

TECHNISCHE UNIVERSITÄT MÜNCHEN

Lehrstuhl E23 für Technische Physik

Walther-Meißner-Institut für Tieftemperaturforschung
der Bayerischen Akademie der Wissenschaften

Magnetoelectric Interactions in Multiferroic Thin Films and Composites

Stephan Geprägs

Vollständiger Abdruck der von der Fakultät für Physik der Technischen
Universität München zur Erlangung des akademischen Grades eines

Doktors der Naturwissenschaften

genehmigten Dissertation.

Vorsitzender: Univ.-Prof. Dr. Harald Friedrich

Prüfer der Dissertation: 1. Univ.-Prof. Dr. Rudolf Gross
2. apl. Prof. Dr. Martin S. Brandt

Die Dissertation wurde am 14.11.2011 bei der Technischen Universität München
eingereicht und durch die Fakultät für Physik am 13.12.2011 angenommen.

Abstract

Multifunctional materials, which unite different functionalities in the same phase, have attracted a lot of attention in recent years due to their rich physics and large variety of potential applications. In particular, the coupling of different functionalities paves the way to novel phenomena as well as enhanced and improved features in future engineered systems. In this field, the interaction of magnetic and dielectric degrees of freedom in magnetoelectric compounds is of particular interest, since they offer the possibility to control the magnetic state via local electric fields, which could be employed in non-volatile, low-power memory devices. This magnetoelectric interaction is expected to be particularly strong in systems which simultaneously exhibit both ferromagnetism and ferroelectricity in the same phase, i.e., in so-called intrinsic magnetoelectric multiferroics. Unfortunately, these materials are scarce in nature. Attractive alternatives are composite material systems, in which ferromagnetic and ferroelectric compounds are artificially assembled. These structures, which are referred to as extrinsic multiferroic composite structures, enable large magnetoelectric effects at room temperature by exploiting the elastic coupling between the two ferroic constituents.

In this thesis, both concepts are quantitatively studied. In the first part, the physical properties of intrinsic multiferroic BiMO_3 ($M = \text{Cr}, \text{Fe}$) thin films are discussed in detail. In particular, for the first time, indications of an enhanced magnetic moment and a strong magnetoelectric coupling at domain walls, separating areas with different electric surface potentials, are found experimentally in BiFeO_3 thin films. In addition, detailed investigations of the multiferroic ground state of BiCrO_3 thin films are carried out, revealing an antiferromagnetic and antiferroelectric ordering below around 145 K. However, no indication for a cross-coupling between these order parameters is observed. Thus, BiCrO_3 should be regarded as an intrinsic multiferroic compound without magnetoelectric interaction.

As discussed in detail in the first part of this thesis, a strong magnetoelectric coupling at room temperature is hardly achievable in intrinsic multiferroic materials, as the origin of the magnetic and dielectric order is largely independent in most intrinsic multiferroics. To improve this situation, the second part of this thesis deals with extrinsic composite structures consisting of ferromagnetic and ferroelectric layers, which are elastically coupled to one another. Two different approaches are considered. First, free standing ferromagnetic/ferroelectric hybrid structures using BaTiO_3 as the ferroelectric layer are examined. In these hybrids, we detect reversible and irreversible changes of the magnetization for different temperatures as well as applied electric fields. Second, ferromagnetic/ferroelectric thin film heterostructures fabricated on adequate substrates are investigated, since, for applications, finite magnetoelectric effects in thin film heterostructures are desirable. Our measurements disclose that magnetoelectric effects are achievable even in extrinsic multiferroic heterostructures exhibiting elastic constraints due to the rigid substrate. This demonstrates that, in principle, strain-mediated extrinsic multiferroic composite structures are ready for application in new designed memory cells combining the best aspects of existing devices.

Kurzfassung

Multifunktionale Materialsysteme, die unterschiedliche Funktionalitäten vereinen, haben in den letzten Jahren großes Interesse erlangt, da sie sowohl für die Grundlagenforschung als auch für potentielle Anwendungen interessant sind. Im Besonderen ermöglicht die Kopplung zwischen verschiedenen Funktionalitäten neue physikalische Phänomene und bietet verbesserte und neuartige Eigenschaften in zukünftigen technischen Systemen. Die Wechselwirkung zwischen magnetischen und dielektrischen Freiheitsgraden in sogenannten magnetoelektrischen Materialien ist hierbei von besonderem Interesse, da sie die Möglichkeit bietet, den magnetischen Zustand über lokale elektrische Felder zu kontrollieren. Dies kann in zukünftigen energiesparenden, nicht flüchtigen Speicherelementen angewendet werden. Die magnetoelektrische Wechselwirkung kann besonders stark in Systemen sein, welche gleichzeitig eine ferromagnetische und ferroelektrische Ordnung besitzen, d.h. in sogenannten intrinsischen, magnetoelektrischen Multiferroika. Bedauerlicherweise sind diese Materialien selten. Eine vielversprechende Alternative stellen Komposite dar, welche ferromagnetische und ferroelektrische Materialien miteinander verbinden. Derartige extrinsische, multiferroische Strukturen nutzen die elastische Kopplung zwischen den ferroischen Komponenten und ermöglichen dadurch große magnetoelektrische Effekte bei Raumtemperatur.

Im Rahmen dieser Dissertation werden sowohl intrinsische als auch extrinsische multiferroische Systeme untersucht. Im ersten Teil der Arbeit werden die physikalischen Eigenschaften von BiMO_3 ($M = \text{Cr}, \text{Fe}$) Dünnschichten im Detail diskutiert. Hierbei konnte zum ersten Mal in BiFeO_3 Dünnschichten Anzeichen eines vergrößerten magnetischen Momentes und einer stärkeren magnetischen Kopplung an ferroelektrischen Domänenwänden nachgewiesen werden, welche Bereiche mit unterschiedlicher, aus der Filmebene heraus zeigender, elektrischer Polarisationskomponente trennen. Zusätzlich wird eine ausführliche Untersuchung des multiferroischen Grundzustandes in BiCrO_3 Dünnschichten durchgeführt. Unsere Experimente zeigen, dass BiCrO_3 für Temperaturen unterhalb von etwa 145 K eine antiferromagnetische und antiferroelektrische geordnete Phase besitzt. Es wurden aber keine Anzeichen einer magnetoelektrischen Kopplung beobachtet. Das bedeutet, dass BiCrO_3 als intrinsisches, multiferroisches Materialsystem ohne magnetoelektrische Kopplung betrachtet werden sollte.

Es hat sich gezeigt, dass eine starke magnetoelektrische Kopplung bei Raumtemperatur in intrinsischen, multiferroischen Materialsystem kaum erreicht werden kann, da in den meisten intrinsischen, multiferroischen Materialien der Ursprung der dielektrischen und magnetischen Ordnung verschieden ist. Große magnetoelektrische Effekte können aber in extrinsischen, verbundartigen Systemen erreicht werden, die aus ferromagnetischen und ferroelektrischen Schichten bestehen. Der zweite Teil dieser Arbeit befasst sich deshalb mit diesen extrinsischen, multiferroischen Strukturen. Hierbei werden zwei verschiedene Ansätze betrachtet. Als erstes werden frei stehende ferromagnetische/ferroelektrische Hybridstrukturen untersucht, wobei BaTiO_3 als ferroelektrisches Substrat verwendet wird. In diesen Hybridstrukturen konnten reversible und irreversible Änderungen der Magnetisierung bei verschiede-

nen Temperaturen und angelegten elektrischen Feldern erreicht werden. Der zweite Ansatz behandelt ferromagnetische und ferroelektrische dünne Schichten, die auf ein geeignetes Substrat aufgebracht werden. Diese Herangehensweise ist besonders für zukünftige Anwendungen von Bedeutung. Unsere Experimente zeigen, dass trotz der starken elastischen Bindung der dünnen Schichten an das verwendete unelastische Substrat magnetoelektrische Effekte nachgewiesen werden können. Dies beweist, dass extrinsische, multiferroische Komposite im Prinzip bereit sind für die Anwendung in zukünftigen Speicherbauelementen, in denen die besten Eigenschaften bestehender Bauteile kombiniert werden.

Contents

1	Introduction	1
2	Experimental techniques	7
2.1	Thin film growth and structural characterization	7
2.1.1	Pulsed laser deposition	8
2.1.2	Reflection high energy electron diffraction	10
2.1.3	X-ray diffraction techniques	12
2.1.4	Transmission electron microscopy	17
2.2	Dielectric characterization techniques	17
2.2.1	Macroscopic dielectric characterization techniques	18
2.2.2	Microscopic dielectric characterization techniques	19
2.3	Magnetic characterization techniques	20
2.3.1	SQUID magnetometry	20
2.3.2	Ferromagnetic resonance	21
2.3.3	Angle-dependent magnetotransport	22
2.3.4	Magnetic force microscopy	23
I	Intrinsic multiferroic materials	25
3	Theory of intrinsic multiferroics	27
3.1	Linear magnetoelectric effect	28
3.2	Symmetry considerations	30
3.3	Multiferroics	33
3.3.1	Lone pair multiferroics	36
3.3.2	Geometric ferroelectrics	36
3.3.3	Electronic ferroelectrics	37
3.3.4	Magnetic ferroelectrics	37
4	The intrinsic multiferroic material system BiMO_3 ($M=\text{Cr, Fe}$)	39
4.1	The lone pair multiferroics BiMO_3 ($M=\text{Cr, Fe}$)	40
4.2	Pulsed laser deposition of BiMO_3 ($M=\text{Cr, Fe}$) thin films	42
4.2.1	Growth conditions	42
4.2.2	Imposed layer-by-layer growth	43
4.3	SrRuO_3 as an electrode material	45
4.3.1	Growth and structural properties of SrRuO_3 thin films	45
4.3.2	Magnetic and transport properties of SrRuO_3 thin films	50
4.4	Physical properties of BiFeO_3 thin films	55
4.4.1	Structural characterization of BiFeO_3 thin films	56
4.4.2	Multiferroic properties of BiFeO_3 thin films	71

4.4.3	Summary: Multiferroic BiFeO ₃ thin films	88
4.5	Physical properties of BiCrO ₃ thin films	90
4.5.1	Structural characterization of BiCrO ₃ thin films	90
4.5.2	Multiferroic properties of BiCrO ₃ thin films	105
4.5.3	Summary: Multiferroic BiCrO ₃ thin films	122
5	Intrinsic multiferroic material systems: Conclusions and Outlook	125
II	Extrinsic multiferroic composite structures	133
6	Magnetoelectric composites	135
6.1	Realizing magnetoelectric coupling in composite structures	135
6.2	Converse magnetoelectric coupling in multiferroic composite structures	139
6.2.1	Thermodynamic model of multiferroic composites	139
6.2.2	Strain-mediated manipulation of the magnetization in multiferroic composite systems	145
6.2.3	Thin film strain tensor	148
6.2.4	Examples of converse magnetoelectric effects in multiferroic composites	152
7	Materials for composite multiferroics	157
7.1	BaTiO ₃ as the ferroelectric material	158
7.2	Crystalline ferromagnetic materials for FM/BaTiO ₃ hybrid structures	169
7.2.1	Magnetite (Fe ₃ O ₄)	169
7.2.2	The ferromagnet Sr ₂ CrReO ₆	179
7.3	Polycrystalline ferromagnetic materials for FM/BaTiO ₃ hybrid systems	188
7.3.1	Ni as ferromagnetic material	188
7.3.2	Fe ₅₀ Co ₅₀ (FeCo) as ferromagnetic material	189
7.4	Summary	190
8	FM/BaTiO₃ multiferroic composite hybrid systems	193
8.1	FM/BaTiO ₃ without ferroelastic domain control	193
8.1.1	Elastic deformation of Sr ₂ CrReO ₆ /BaTiO ₃ hybrid structures	194
8.1.2	Modification of the physical properties of FM/BaTiO ₃ hybrid structures	195
8.2	Ferroelastic domain control in BaTiO ₃ substrates	207
8.3	FM/BaTiO ₃ hybrid structures with ferroelastic domain control	213
8.3.1	Calculation of the BaTiO ₃ strain tensor under electric fields	213
8.3.2	Magnetization changes in FM/BaTiO ₃ hybrid structures as a function of temperature	214
8.4	Electric field control of magnetism in FM/BaTiO ₃ hybrid structures	219
8.4.1	BaTiO ₃ in the tetragonal phase	220
8.4.2	BaTiO ₃ in the orthorhombic phase	241
8.5	Summary	249
9	Thin film heterostructures based on FM/BaTiO₃ multiferroic composites	255
9.1	BaTiO ₃ thin films	256
9.1.1	BaTiO ₃ thin films investigated by molecular dynamics simulations	256
9.1.2	BaTiO ₃ thin films fabricated by pulsed-laser deposition	260

9.2	FM/BaTiO ₃ multiferroic composite heterostructures	270
9.2.1	Modeling of FM/BaTiO ₃ heterostructures	271
9.2.2	Epitaxial 2-2 type Fe ₃ O ₄ /BaTiO ₃ heterostructures	276
9.2.3	Non-epitaxial 2-2 type FeCo/BaTiO ₃ heterostructures	278
9.3	Summary	282
10	Extrinsic multiferroic composite structures: Conclusions and Outlook	285
A	Multiferroic double perovskite Bi₂CrFeO₆ thin films	291
B	Modeling of magnetization hysteresis in ferromagnetic materials	293
	List of publications	297
	Acknowledgements	299
	Bibliography	301

Chapter 1

Introduction

The investigation and engineering of novel multifunctional compounds, which exhibit different functionalities in the same phase, is one of the most fascinating challenges in today's solid-state physics. The use of such compounds bears the promise for an enhanced level of functionality and tailorability while decreasing the cost, size, and power consumption of future engineered systems.

In the field of multifunctional compounds, *multiferroic materials*, which simultaneously possess at least two long-range ordering phenomena in the same phase [1], have attracted widespread interest over the last years. In particular, the coexistence of ferroelectric and ferromagnetic ordering allows to store information in both the ferromagnetic and the ferroelectric phase, enabling novel device concepts [2]. For example, the information can be encoded in the direction of the electric polarization and magnetization, yielding a non-volatile, multi-state memory device [3, 4]. However, these devices may still exhibit the disadvantages of current memories based on ferroelectric and ferromagnetic ordered phases, such as the destructive read process in case of ferroelectric memories [5, 6] and the need of large magnetic fields to write magnetic states [7, 8]. In contrast, an ideal multiferroic memory cell could offer the possibility to electrically write the magnetic state, which then can be read out in a non-destructive manner [9]. Such a multiferroic memory concept combines the high speed of existing electronics with the remanent properties of magnetism and thus joins the best aspects of existing ferroelectric and magnetic data storage memories.

The realization of such devices requires an electrical control of magnetism, i.e., a *magnetoelectric coupling*, which describes the interaction of the magnetic and dielectric degrees of freedom. Magnetoelectric materials are one example of “smart” materials in which the coupling of different functionalities produces new phenomena, which are more than just the sum of the original ones, possessing, e.g., sensing and actuating functions in the same compound [9, 10]. The magnitude of the novel coupling phenomena between dielectric and magnetic properties is bounded by the product of the permittivity and the permeability in case of magnetoelectric materials [11]. Thus, compounds which easily polarize in response of an electric and magnetic field may exhibit large magnetoelectric effects. This requirement is usually fulfilled by multiferroic materials. Note, however, that large permittivity and permeability values are not a prerequisite for a ferroelectric and ferromagnetic behavior, respectively. This means that a finite magnetoelectric coupling is neither always present in multiferroic compounds, nor that only multiferroics can be magnetoelectrics [8]. In case of magnetoelectric multiferroics, the order parameters are coupled and each

can be modified by the respective conjugate field of the other [12] (cf. Fig. 1.1(a)). This paves the way to control the information stored in a memory cell by a local electric field, i.e., by low power consuming electronics [13]. However, it permits a fully electrically controlled, non-volatile memory in which data are written and read by means of electric fields, leading to smaller, more energy-efficient devices [14].

The described concept of a data storage device based on materials exhibiting a finite magnetoelectric interaction is one prominent example of possible applications of multiferroic materials [15–18]. One key requirement for such devices is the presence of a strong magnetoelectric interaction at room temperature. This requirement triggered much activity in searching for new multiferroic materials exhibiting a cross-coupling between the magnetic and dielectric properties. In spite of this tremendous amount of research, there are only a few multiferroic materials known to date, since it was shown that the simultaneous presence of ferromagnetism and ferroelectricity in the same phase tend to be mutually exclusive [19]. Therefore, the definition of multiferroicity is usually extended to include antiferromagnetic and antiferroelectric orderings [8]. We adopt this terminology here and label compounds, which belong to this class of materials, as *intrinsic multiferroics* in the following. However, the origin of the magnetic and dielectric order is largely independent in most intrinsic multiferroics, which results in small magnetoelectric interactions. Therefore, apart from searching for novel intrinsic multiferroic materials, heterogeneous structures consisting of two or more constituent materials have been studied extensively in recent years [20, 21]. In such composite structures, a strong magnetoelectric coupling at room temperature can be achieved via interface-mediated effects even if the constituent materials do not possess a cross-coupling between the magnetic and electric order parameters. This allows to exceed the intrinsic upper bound of single-phase magnetoelectric materials. Since the definition of multiferroics is based on single-phase materials [22], we use the term *extrinsic multiferroics* for composite structures based on ferroelectric and ferromagnetic constituents.

This thesis deals with both intrinsic (Part I) and extrinsic (Part II) multiferroics, such that the two most promising concepts to achieve finite magnetoelectric coupling in multiferroic structures can be compared. In searching for new multiferroic compounds, the first part concentrates on the basic physics of two intrinsic multiferroic materials, providing a better insight on the multiferroic and magnetoelectric behavior. While these studies are part of the field of material science, we investigate the spin-mechanics concept for the realization of large magnetoelectric effects in extrinsic multiferroics in the second part of this thesis.

Intrinsic multiferroics

Since various mechanisms determine the properties of *intrinsic multiferroic materials*, these compounds are usually classified into two main groups, which are denoted as split-order-parameter multiferroics (type-I) or joint-order-parameter multiferroics (type-II) [25]. In the former class, the ferroelectric and magnetic order are independent in origin, leading to weak magnetoelectric effects. In contrast, joint-order-parameter multiferroics exhibit a strong magnetoelectric coupling, as magnetism is

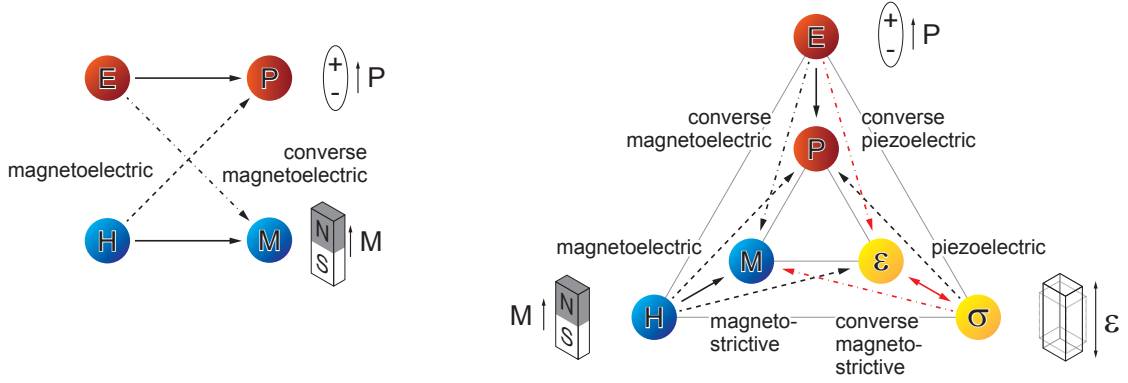


Figure 1.1: Interaction in multiferroics (figure adapted from Refs. [23, 24]). (a) The ferroic order parameters, ferroelectric polarization (\mathbf{P}) and ferromagnetic magnetization (\mathbf{M}), can be controlled by their conjugate electric (\mathbf{E}) and magnetic (\mathbf{H}) fields, respectively. The $\mathbf{P}(\mathbf{E})$ and $\mathbf{M}(\mathbf{H})$ dependence is referred to as the principle effect. Additional interaction channels arise in magnetoelectric multiferroics: cross-coupling allows to modify the order parameters by the respective conjugate field of the other ordering phenomena. These interactions are termed as magnetoelectric (dashed line) and converse magnetoelectric (dash dotted line) coupling. (b) Interaction in multiferroics including ferroelasticity. The strain-mediated manipulation of the magnetization by electric fields (“spin-mechanics” concept) is highlighted by red arrows.

caused by ferroelectricity or vice versa. Thus, in these materials, the emergence of a spontaneous electric (magnetic) polarization is a direct consequence of the magnetic (dielectric) order, which might be exploited in future devices. However, the main drawback of joint-order-parameter multiferroics are the weak values of the spontaneous electric and magnetic polarizations, which are about three orders of magnitudes smaller than in single ferroic materials [26]. Furthermore, so far, the magnetoelectric coupling is restricted to temperatures well below room temperature. Therefore, in terms of application, split-order-parameter multiferroics appear more promising.

In the framework of this thesis, we have focused on two split-order-parameter intrinsic multiferroics. On the one hand, we have studied BiFeO_3 thin films. This compound has recently gained considerable interest, since it is one of the few intrinsic multiferroics, which exhibits a strong ferroelectric and magnetic ordering at room temperature [13]. In particular, BiFeO_3 possesses a large saturation polarization for $T \lesssim 1100$ K [27], which might be exploited to replace existing materials in the field of ferroelectric memory cells [28]. In addition, an antiferromagnetic order superimposed by a cycloidal modulation was found below around 640 K. Apart from the interesting multiferroic behavior of BiFeO_3 , an electric control of the magnetic state was achieved in this compound by changing the direction of the electric polarization [29–31]. The discovery of this effect together with the finding of enhanced magnetism in the pioneering work on BiFeO_3 thin films [32] have triggered renewed interest in BiFeO_3 in recent years [14].

On the other hand, we have studied BiCrO_3 , which is an interesting compound in the perovskite-like family BiMO_3 with $M = \text{Cr}, \text{Mn}, \text{Fe},$ and Co , since it can be

regarded as an ideal model material to elucidate the role of the Bi cation in driving multiferroic phase transitions [33]. In this compound, the transition temperatures are easier to access experimentally than for BiFeO₃. However, little is known about the multiferroic ground state and possible magnetoelectric effects in BiCrO₃ [34–36], because high quality single crystals are not available up to now. This is a direct consequence of the metastable chemical phase of BiCrO₃ [37].

The fabrication as well as the multiferroic properties of BiFeO₃ and BiCrO₃ thin films are discussed in the first part of this thesis, which is organized as follows: After giving a short introduction into the theory of intrinsic multiferroics in Chapter 3, the physical properties of intrinsic multiferroic BiFeO₃ and BiCrO₃ thin films grown using pulsed laser deposition are examined in detail in Chapter 4 using macroscopic and microscopic probe techniques. Since it was shown that the dielectric and magnetic properties of BiFeO₃ depend strongly on extrinsic effects, such as parasitic phases and the used buffer layer [38], we put much effort on the fabrication of highly crystalline BiMO₃ ($M = \text{Cr, Fe}$) thin films on SrRuO₃-buffered SrTiO₃ substrates as well as directly on Nb-doped SrTiO₃ crystals. In these high-quality samples, for the first time, we observed large variations of the magnetic stray field in BiFeO₃ thin films in regions, where the electrostatic potential changes its value. Therefore, our results suggest an enhanced magnetoelectric coupling at ferroelectric domain walls in these thin films. In case of BiCrO₃ thin films, our experiments demonstrate an antiferroelectric and antiferromagnetic ground state without a measurable cross-coupling between these ordered phases. Thus, BiCrO₃ should be considered as intrinsic multiferroic material system possessing an antiferromagnetic and antiferroelectric ordered phase. In spite of the tremendous research activities in the field of intrinsic multiferroics and in particular of BiFeO₃, there are still open questions remaining, which are addressed in Chapter 5.

Extrinsic multiferroics composite structures

The second part of this thesis is devoted to *extrinsic multiferroic composite structures*. These are heterogeneous systems, in which the existing properties are enhanced, or new effects are created by the interaction between the constituents. Within the extrinsic multiferroic composites, a substantial manipulation of the magnetization by electric fields at room temperature is possible using composite structures consisting of ferroelectric and ferromagnetic materials, which are elastically coupled at their interface [20]. In such extrinsic multiferroics, an electric field applied to the ferroelectric layer results in an expansion or contraction of its shape caused by converse piezoelectric effects. Due to the intimate contact of the ferroelectric and ferromagnetic constituents, this distortion is mechanically transferred into the ferromagnetic layer and entails a variation of the magnetization due to converse magnetostriction. In this “spin-mechanics” scheme, the magnetization of the ferromagnetic layer can be manipulated by an electric field applied to the ferroelectric constituent, which results in an indirect strain-mediated magnetoelectric coupling (cf. Fig. 1.1(b)). These strain-mediated, magnetoelectric composite structures can be realized by either magnetic nanoparticles or magnetic pillars em-

bedded in a ferroelectric material, or by horizontal alternating ferroelectric and ferromagnetic layers, which are denoted as 2-2 type composites [21]. In the framework of this thesis, only 2-2-type horizontal structures were investigated by using free standing ferroelectric/ferromagnetic composite *hybrid structures* as well as thin film *heterostructures* consisting of ferromagnetic and ferroelectric layers fabricated on adequate substrates.

The discussion of extrinsic multiferroic composite structures in the second part of this thesis is organized as follows: First, an overview about magnetoelectric composite structures is given in Chapter 6, followed by the discussion of the materials chosen for the ferroelectric and ferromagnetic layers (Chapter 7). While for the ferroelectric layer BaTiO₃ is used through out this thesis, polycrystalline as well as single crystalline thin films consisting of different materials, such as Ni, Fe₅₀Co₅₀, and Fe₃O₄, were employed as the ferromagnetic layers. In addition, the ferromagnetic double perovskite Sr₂CrReO₆ was used, due to its giant magnetostrictive effects caused by an unquenched Re orbital moment. In Chapter 8, the manipulation of the magnetization as a function of temperature and electric field is discussed in free standing ferromagnetic/BaTiO₃ composite hybrid structures. Since the physical properties were found to be strongly dependent on the ferroelastic domain configuration in the BaTiO₃ crystal, a control of ferroelastic domains is mandatory to quantitatively control the magnetization state of the ferromagnetic layer. For the first time, the temperature and electric field dependence of the magnetization in ferromagnetic/BaTiO₃ hybrids were calculated in an ab-initio manner taking advantage of miscut BaTiO₃ substrates. For applications, the realization of magnetoelectric effects in thin film heterostructures consisting of ferromagnetic and ferroelectric layers fabricated on adequate substrates are essential. Thus, in Chapter 9, the fabrication and multiferroic properties of 2-2 type horizontal ferromagnet/BaTiO₃ heterostructures on Nb-doped SrTiO₃ substrates is discussed. In spite of the strong elastic coupling between the BaTiO₃ layer and the rigid SrTiO₃ substrate, a finite magnetoelectric effect in FeCo/BaTiO₃ multiferroic heterostructures was observed around the magnetic coercive field. The second part of this thesis clearly shows that reversible and irreversible manipulations of the magnetization by local electric fields are feasible at room temperature. However, some important issues, which are discussed in Chapter 10, remain to be solved for practical applications.

Chapter 2

Experimental techniques

In this chapter, we present the experimental techniques used in the framework of this thesis. First, the fabrication of polycrystalline and epitaxial thin films as well as the structural characterization of these films employing electron and x-ray diffraction techniques are discussed. Since the aim of this thesis was the investigation of materials and hybrid structures, which simultaneously exhibit a magnetically as well as a ferroelectrically or antiferroelectrically ordered phase, both magnetic and dielectric characterization methods were applied to attest their multiferroic behavior. To this end, the dielectric properties were probed on a macroscopic and microscopic scale. Furthermore, various physical methods were used to reveal the magnetic properties of these thin films. In particular, changes of the magnetic properties as a function of an applied electric field, i.e., converse magnetoelectric effects, were investigated using newly designed sample holders and improved experimental techniques.

2.1 Thin film growth and structural characterization

In the field of solid-state physics, one of the most fascinating challenges is the discovery and application of novel functional materials including artificially designed compounds and heterostructures. This field has been driven largely by the development and understanding of new growth and characterization techniques, which have offered new insight on the physical mechanisms of these compounds. In the course of this thesis, different deposition techniques were applied: electron beam evaporation, sputtering, and pulsed laser deposition (PLD). These techniques have many similarities, but do also differ substantially with respect to the underlying physics [39]. In the case of electron beam evaporation, the material is evaporated in a vacuum chamber by means of an electron beam, and then condenses on a substrate. Electron beam evaporation can therefore be classified as a thermal deposition technique, in which the impinging particles have a kinetic energy of the order of 0.1 eV. This technique was mainly applied to fabricate polycrystalline Ni and Fe₅₀Co₅₀ thin films.¹ In contrast, Au thin films, which were used as electrode materials, were deposited on the respective samples by DC-sputtering using a commercial setup [41]. In this instance, positive ions stemming from an electrical discharge are accelerated onto a solid target material, from which atoms with energies between 10 eV and 100 eV are ejected due to a momentum transfer from the accelerated particle to the atoms of

¹The electron beam evaporation system used during this thesis is described in detail in Ref. [40].

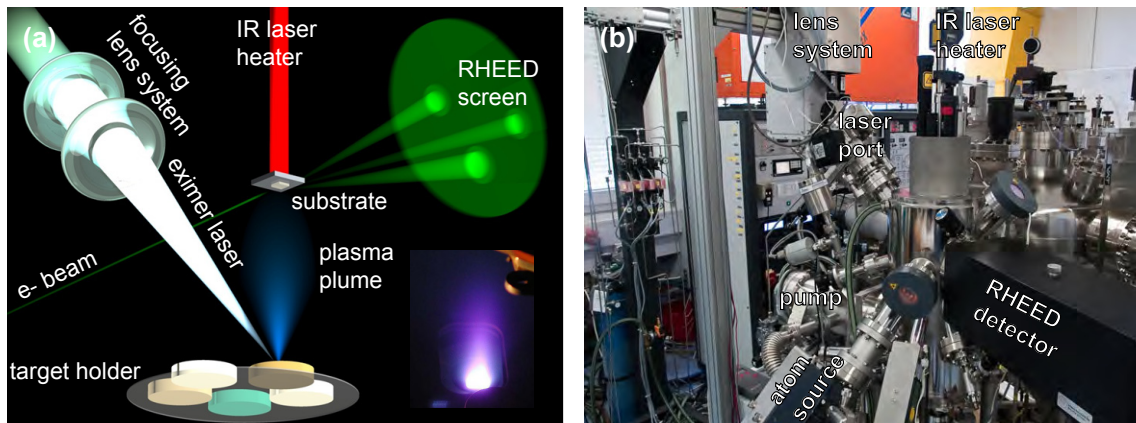


Figure 2.1: (a) Schematic illustration of the pulsed laser deposition (PLD) process (see text for more details). The inset shows an image of a plasma plume (figure adapted from Ref. [46]). (b) The PLD system has been continuously upgraded during the course of this thesis. In particular, a new optical path with a telescope lens system was developed in cooperation with M. Althammer and T. Brenninger. The new system allows to control the laser power density in a well controlled way and extends the range of the laser fluence on the target to $0.5 - 5.5 \text{ J/cm}^2$ (see Ref. [47] for more details). The PLD is part of an ultra-high vacuum cluster system for thin film growth, including a sputter chamber, a metallization chamber based on electron beam evaporation, a surface characterization chamber with a UHV scanning force microscope, and a load-lock chamber.

the target material [42]. However, to fabricate high-quality epitaxial thin films of oxide materials, pulsed laser deposition is one of the best-suited methods [43]. Since all epitaxial thin films discussed in this thesis are fabricated using this technique, the pulsed laser deposition is briefly introduced in the following section.

2.1.1 Pulsed laser deposition

Pulsed laser deposition (PLD) is a powerful method to fabricate epitaxial thin films of complex oxides.² The main advantage of this technique is the versatility, allowing to fabricate different material systems in one and the same setup. Therefore, it is a cost effective method for exploring a wide range of materials. The PLD process can be divided into three parts, which are repeated at each laser pulse: (i) vaporization of the target material, (ii) transport of the vapor plume to the substrate, and (iii) the thin film growth process on the substrate.

The first step of the deposition is the impact of a high energy laser pulse on the surface of a polycrystalline target. In the PLD system used in the present study (cf. Fig. 2.1), the laser pulse is generated by a KrF excimer laser ($\lambda = 248 \text{ nm}$) with a repetition rate between $0.5 - 10 \text{ Hz}$ and focused on the target using an optical system of different lenses, which allows to continuously vary the energy density at the target surface from 0.5 J/cm^2 to 5.5 J/cm^2 . Assuming an energy density of 2 J/cm^2 and a duration of the laser pulse of 20 ns , the power density can be estimated to

²The reader is referred to Refs. [39, 42, 44, 45] for more details on recent advances in pulsed-laser ablation-based techniques.

around 10^8 W/cm², which is more than enough energy to ablate all materials [45]. As schematically shown in Fig. 2.1 (a), the targets are mounted on a target holder, which offers the possibility to select one of five different materials without breaking vacuum. The targets were fabricated by solid-state reactions, as described in Refs. [48–51].³ The absorption of the laser radiation by the surface of the target results in a complex process including evaporation, ablation, excitation, plasma formation and exfoliation of the target material, which is driven by the conversion of the electromagnetic energy of the laser radiation first into electronic excitations, followed by a transformation into thermal, chemical, and even mechanical energy [45]. During this process, a plasma plume is formed, which consists of species with different energies, such as atoms, molecules, electrons, ions, and even clusters of atoms. One of the major disadvantages of the PLD process is the ejection of macroscopic particles commonly labeled as “laser droplets”. These droplets are caused by three phenomena, namely subsurface boiling, recoil ejection, and exfoliation [42]. However, using an appropriate optical system to focus the laser beam on the target, the density of droplets can be minimized (cf. Ref. [52]).

The second step of the thin film growth is the expansion of the nascent erosion plasma towards the substrate. During this process, the plasma adiabatically cools down to temperatures of around 3000 – 5000 K [42]. The angular distribution of the plasma plume can be described by a $\cos^n \theta$ function and consists of two components. The first contribution is mainly caused by thermal energy with $n = 1$ and tends to be non-stoichiometric as in conventional thermal evaporation of complex oxides. However, the main component can be fitted with values of $n = 4 - 14$ [45], which depends strongly on the laser fluence and on the pressure of the ambient atmosphere. This sharp component of the plasma plume is closely stoichiometric and contains particles with kinetic energies up to around 100 eV, depending on the material used. The large kinetic energy of the particles is a key feature of PLD which may give rise to resputtering effects at the substrate. Therefore, the plasma species are often thermalized through multiple collisions using an ambient background atmosphere. Furthermore, in case of oxide materials, O₂ is usually used as background gas to compensate possible oxygen vacancies in the thin film.

The final step of the PLD process is the thin film growth on a substrate, which can be described as a result of a number of microscopic processes, such as adsorption, diffusion and desorption of adatoms [39]. All these processes are strongly dependent on the kinetics of the system, which is determined by the deposition rate, the substrate temperature, the background pressure, etc., resulting in different growth modes. In our PLD system, these parameters can be automatically controlled (cf. Ref. [46] for more details). Since nucleation on the substrate can occur at step edges, defects, etc., a careful pretreatment of the substrate surface is mandatory for the growth of high quality thin films. For example, a TiO₂ termination of (001) oriented SrTiO₃

³In the case of Sr₂CrReO₆ thin films, the target was made in an oxygen-getter-controlled technique to ensure a stoichiometric compound, which was established during this thesis (see the diploma thesis of Oliver Sanganas [49] for more details). Furthermore, non-stoichiometric Bi_{1+x}FeO₃ and Bi_{1+x}CrO₃ targets with $x = 0.05, 0.10, 0.15,$ and 0.20 were used to compensate for the loss of Bi due to its high volatility.

substrate surfaces can be obtained following the procedure developed by Koster and coworkers [53], which was further improved by Ohnishi *et al.*[54]. This uniquely defined substrate surface forms a well defined basis for the thin film growth on SrTiO₃.⁴

In the literature, three major thin film growth modes are distinguished: (1) Volmer-Weber or island growth, (2) Frank-Van der Merwe or layer-by-layer growth, and (3) Stranski-Krastanov growth. In the case of Volmer-Weber growth, clusters nucleate directly on the substrate surface and then grow into three-dimensional islands. This process can be explained by a stronger bonding of the deposited atoms to each other than to the substrate. In contrast, the layer-by-layer growth mode or Frank-Van der Merwe mode describes the deposition of a thin film, where a new monolayer starts to grow only after the previous one is complete, resulting in a two-dimensional growth. In this case, the deposited atoms are more strongly bonded to the substrate than to each other. The intermediate case is called Stranski-Krastanov growth. Here, the growth process starts in a layer-by-layer growth mode, which becomes energetically unstable at a certain film thickness and the growth is continued in a three-dimensional island growth. The different growth modes are usually characterized by the strength of the substrate, film, and vapor interfacial energy using a simple thermodynamic model (see, eg., Ref. [45]). However, since the growth process is by definition a non-equilibrium process [58], it should be described by rate equations accounting for the kinetics and the microscopic pathway. Therefore, the understanding and control of the growth morphologies requires a detailed knowledge of the atomistic processes involved. In particular, atomic diffusion events like terrace, interlayer, exchange and edge diffusion, which are determined by specific activation barriers, are important. However, the calculation of the nucleation and growth of thin films far away from thermodynamic equilibrium is demanding. The reader is referred to Refs. [39, 58, 59] for more details on this issue.

2.1.2 Reflection high energy electron diffraction

The most powerful tool to monitor the growth modes during thin film deposition is reflection high energy electron diffraction (RHEED). Within this technique, an electron beam with energies between 10 – 20 keV and current of around 100 μ A is directed to the sample surface under an incident angle of around 1 – 3°.⁵ Due to the grazing incidence geometry, the penetration depth of the electron beam is less than

⁴A TiO₂ termination of (001) oriented SrTiO₃ substrate surfaces can be obtained by an etching step using NH₄F – HF buffered HF acid followed by an annealing treatment in an oxygen atmosphere at 950 °C for 1 h. For BaTiO₃ substrates, the first step is not appropriate, since it is well known that in ferroelectrics the positive and negative ends of domains etch at a different rate [55, 56]. Therefore, only the annealing step was carried out before the growth process, resulting in a mixture of BaO and TiO₂ at the surface of BaTiO₃ substrates. However, the TiO₂-terminated surface of BaTiO₃ was found to be energetically more favorable than the BaO-terminated one by recent theory calculations, suggesting that the BaTiO₃ surface mostly consists of TiO₂ terminated regions after the annealing process [57].

⁵For more information about the RHEED system used during this thesis, see Refs. [46, 60, 61].

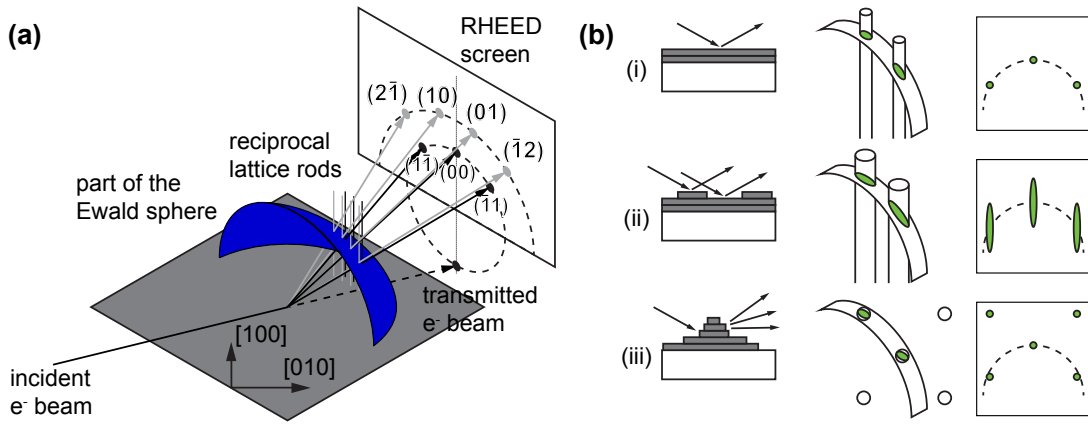


Figure 2.2: (a) Schematic illustration of the reflection high energy electron diffraction (RHEED). The RHEED patterns discussed in the course of this thesis are recorded with the incident electron beam aligned along the $[110]$ direction of the substrate. The Ewald sphere construction is described in the text. For electrons with an energy of 15 keV, the radius of the Ewald sphere is $k_0 \approx 630 \text{ nm}^{-1}$, which is much larger than the dimension of the reciprocal lattice unit. Therefore, in reality, the Ewald sphere is almost a planar cut through the first Brillouin zones of the reciprocal lattice. (b) Expected response of electron diffraction from surfaces exhibiting a different amount of disorder: (i) perfect surface in the case of Frank-Van der Merwe layer-by-layer growth mode, (ii) thin film with weak roughness, and (iii) three dimensional Volmer-Weber growth mode.

a few nm. Therefore, RHEED is strongly surface sensitive and the probed volume can be approximated to be two-dimensional [62]. In this limit, the reciprocal lattice degenerates into a set of one-dimensional parallel, regularly spaced, infinitely thin rods perpendicular to the surface. Considering only elastic scattering, the direction of the constructive interference is given by the crossing points of these rods with the Ewald sphere, which is determined by the incident wave vector $|\mathbf{k}_0| = k_0 = \frac{1}{\hbar}\sqrt{2m_0E}$.⁶ These points lie on concentric circles, which are called Laue circles. The Ewald sphere construction is schematically shown in Fig. 2.2(a).

Accordingly, finite intensities of the scattered electron beam from a perfect thin film surface, which is grown by a layer-by-layer growth mode, can be observed at distinct angles on the RHEED screen and the intensity can be described by a delta distribution (cf. (i) in Fig. 2.2(b)). However, in reality, these spots are broadened due to the limited resolution of the RHEED system and the finite size of the investigated crystal.

In case of a weak surface disorder (cf. (ii) in Fig. 2.2(b)), the reciprocal lattice rods broaden and the intensity is given by a delta distribution superimposed by a diffuse peak caused by the presence of disorder [63]. Therefore, the intensity recorded at a certain angular position on the RHEED screen depends strongly on the surface coverage: A minimum of the intensity occurs at half coverage of the surface layer, while the intensity is maximum, if the two dimensional layer consisting of charge neutral blocks is completely covered. Thus, intensity oscillations are observed in

⁶The relativistic correction is neglected, since it amounts less than 3%.

a true layer-by-layer growth mode. Since in reality substrates are not perfectly flat and exhibit steps and terraces, a two dimensional growth mode can occur, if the atoms adhere at surface steps (step-flow growth). This is normally the case at higher substrate temperatures compared to the deposition parameters for the layer-by-layer growth mode, leading to a higher mobility of the adatoms. In this case, the surface morphology does not change appreciably resulting in a constant intensity evolution of the recorded RHEED reflection as a function of growth time.

In contrast to a two dimensional growth process, the three dimensional Volmer-Weber growth mode results in a large surface roughness. Here, the RHEED pattern is a consequence of electron transmission through three dimensional islands (cf. (iii) in Fig. 2.2(b)). To sum up, Fig. 2.2 reveals that RHEED is a powerful technique to in-situ monitor the growth process of complex oxides. The reader is directed to Refs. [62, 64] for more details on this technique.

2.1.3 X-ray diffraction techniques

Not only information about the morphology of the thin film structure, but also about the structural properties can be derived by the RHEED technique. For example, the relaxation of the epitaxial strain can be monitored during the growth process by measuring the distance of the corresponding diffraction spots [62]. However, since RHEED is a surface sensitive method, the structural information is limited to the first monolayers of the thin film. The most powerful method to get detailed information about the structure of the whole volume of the thin film is x-ray diffraction. In the course of this thesis, x-ray diffraction measurements were carried out using a Bruker D8 Discover four-circle x-ray diffractometer (cf. Fig. 2.3(a)), which is equipped with a Cu tube source, a Göbel mirror to collimate the divergent x-ray beam, a Ge channel-cut monochromator, and a NaI scintillation detector. To be able to apply an electrical voltage as well as to modify the temperature of the sample, a new sample holder was built, which is shown in Fig. 2.3(a). This sample holder enables to perform x-ray diffraction measurements in a temperature range from 150 K to 500 K.⁷ However, as standard x-ray tube sources produce only about 10^7 photons per second (ph/s) and emit them in a divergent and unpolarized manner (cf. Fig. 2.3(d)), synchrotron radiation offers several advantages compared to conventional x-ray tubes: It provides a high incident flux of photons, it is both low-divergence and linearly polarized, and the x-ray energy can be tuned over a large range. To exploit these properties, x-ray diffraction measurements were carried out in cooperation with Dan Mannix (CNRS Grenoble) at the European Synchrotron Radiation Facility (ESRF) beamline BM28 [65] as well as at the Diamond light source (beamline I16) [66]. Both beamlines cover an energy range of the incident photons of around 3 – 15 keV focusing the x-ray diffraction on a sample area of $0.5 \times 0.5 \text{ mm}^2$ and $0.2 \times 0.05 \text{ mm}^2$, respectively. As shown in Figs. 2.3(b) and (c), the BM28 beamline is equipped with a 11-axes and the I16 beamline with a 6-axes kappa diffractometer. However, the emission sources for the high flux synchrotron

⁷The reader is referred to the diploma thesis of Daniel Pantel for more information about the new sample holder [70].

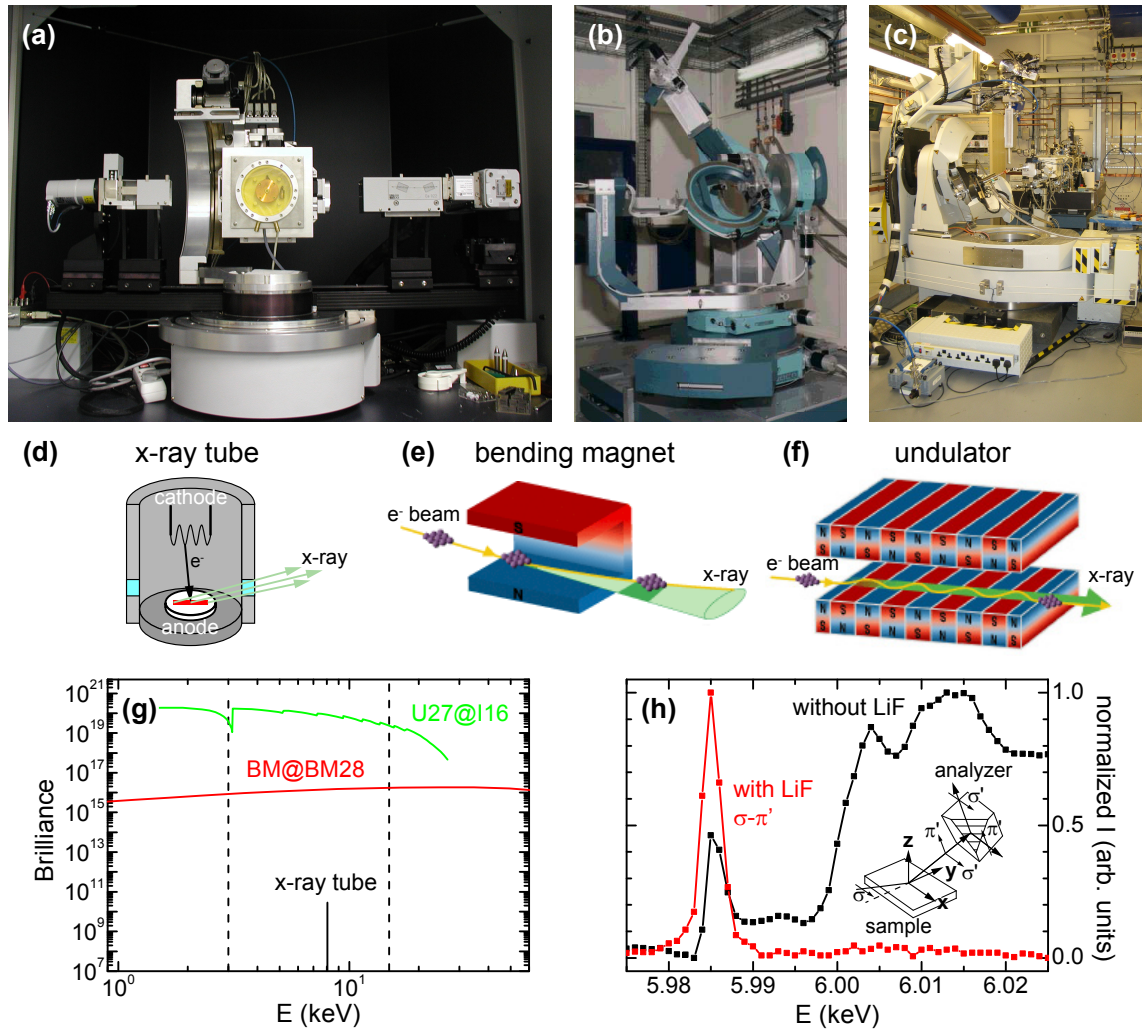


Figure 2.3: X-ray diffraction setups used in the framework of this thesis: (a) Bruker D8 Discover four-circle x-ray diffractometer, (b) Huber 11-axes diffractometer installed at the BM28 beamline at the European Synchrotron Radiation Facility (ESRF) [65], and (c) 6-axes kappa diffractometer located at the I16 beamline at the Diamond light source [66]. A new sample holder was designed for the Bruker D8 Discover diffractometer, which allows to apply an electric field across the investigated sample during the x-ray diffraction measurement and to modify the temperature of the sample within $150 \text{ K} < T < 500 \text{ K}$. The x-ray diffraction setups shown in (a)-(c) use different radiation sources. The Bruker D8 Discover is equipped with a standard Cu-x-ray source (d). The BM28 beamline is located at a bending magnet (BM) (e), while the I16 beamline uses an in-vacuum undulator (U27) (f) as emission source (figures adapted from Refs. [67, 68]). (g) The quality of each radiation source is quantified by its brilliance [69]. Apart from the high brilliance of the x-ray radiation at the BM28 and I16 beamline, a large energy range enclosed by the vertical dashed lines is usable. This enables to investigate weak x-ray diffraction phenomena by tuning the energy of the x-ray beam close to an absorption edge of a thin film element, which results in a resonant enhancement of the intensity. (h) As an example, energy scans close to the Cr K -absorption edge at around 5.985 keV carried out at the pseudo-cubic $(0.75 \ 0.75 \ 0.75)_{\text{PC}}$ reflection of a 46 nm thick BiCrO_3 thin film are shown without (black symbols) and with a LiF analyzer in a σ - π' scattering geometry. While the incident beam is linearly polarized perpendicular to the diffraction plane (σ), the scattered wave has components parallel (π') or perpendicular (σ') to this plane (see inset).

radiation are different at both beamlines. The beamline BM28 at the ESRF is located at a bending magnet (cf. Fig. 2.3(e)), which produces a photon flux of around 10^{10-11} ph/s with a horizontal (H) and vertical (V) divergence of ≈ 1 mrad and ≈ 0.1 mrad, respectively. At the I16 beamline at the Diamond light source, an in-vacuum undulator U27 (cf. Fig. 2.3(f)), which consists of a periodic structure of dipole magnets and results in a significant enhancement of the photon flux to 10^{14} ph/s as well as a reduction of the radiation divergence to ≈ 0.1 mrad (H) and ≈ 0.001 mrad (V), is used. The figure of merit for the comparison between various sources of x-rays is its brilliance. The brilliance, which is measured in units of ph/(s · mm² · mrad² · 0.1% bandwidth), is a quantity related to the intensity (ph/s), the collimation of the beam, the beam size, and the spectral distribution. As evident from Fig. 2.3(g), the I16 beamline has the highest brilliance in the whole used energy range (cf. vertical dashed lines in Fig. 2.3(g)). Furthermore, Fig. 2.3(g) demonstrates the importance of synchrotron radiation, since it exhibits an increase of the brilliance of about 10 orders of magnitudes than those of standard laboratory x-ray tubes. Moreover, a large energy range of x-ray photons can be used. This offers the possibility for the investigation of weak x-ray diffraction phenomena, such as charge and orbital ordering, or magnetic scattering, by tuning the energy of the x-ray beam close to an absorption edge of a thin film element, which results in a resonant enhancement of the intensity. As an example, Fig. 2.3(h) shows the result of an energy scan around the Cr *K*-absorption edge carried out at the pseudo-cubic (0.75 0.75 0.75)_{pc} reflection of a 46 nm thick BiCrO₃ thin film at the I16 beamline. A clear enhancement of the intensity near the *K*-absorption edge at around 5.985 keV is observable.

In principle, diffraction effects occur if electromagnetic radiation with wavelengths comparable to the interatomic distances in crystals impinges on the periodic structure of a crystal and constructive and destructive interference should become observable. In the kinematic theory of elastic scattering the intensity can be expressed as [71]

$$I = \left| \int \rho(\mathbf{r}) \exp(i\mathbf{q}\mathbf{r}) dV \right|^2 \propto |F(\mathbf{q}, \omega) \cdot G(\mathbf{q})|^2, \quad (2.1)$$

where $\rho(\mathbf{r})$ denotes the total electron density at point \mathbf{r} and $\mathbf{q} = \mathbf{k}_f - \mathbf{k}_i$ describes the scattering vector, which is defined by the wave vector difference of the initial \mathbf{k}_i and final \mathbf{k}_f wave vector. Making use of the periodicity of the lattice, the intensity can be rewritten as a function of the structure factor $F(\mathbf{q}, \omega)$ and the lattice factor $G(\mathbf{q})$ with

$$F(\mathbf{q}, \omega) = \sum_j f_j(\mathbf{q}, \omega) \exp(i\mathbf{q} \cdot \mathbf{r}_j), \quad G(\mathbf{q}) = \sum_{m_i} \exp(i\mathbf{q}(m_1\mathbf{a}_1 + m_2\mathbf{a}_2 + m_3\mathbf{a}_3)). \quad (2.2)$$

The structure factor $F(\mathbf{q}, \omega)$ is given by the atomic form factors f_j of the j th atom with position \mathbf{r}_j in the unit cell of the lattice. f_j is a measure of the scattering amplitude of waves by a single atom. In contrast, the lattice factor $G(\mathbf{q})$ only

describes the periodicity of the lattice with $\mathbf{T} = m_1\mathbf{a}_1 + m_2\mathbf{a}_2 + m_3\mathbf{a}_3$. \mathbf{a}_1 , \mathbf{a}_2 , and \mathbf{a}_3 denote the unit vectors. For infinite crystals ($-\infty < m_i < +\infty$), $G(\mathbf{q})$ yields $G_{\text{infinite}}(\mathbf{q}) \propto \sum_{hkl} \delta(\mathbf{q} - \mathbf{G}_{hkl})$, which is an alternative formulation of the Laue equation $\mathbf{q} = \mathbf{G}_{hkl}$ for the Bragg diffraction. In this case, a finite intensity is observed only if the scattering vector \mathbf{q} is equal to a reciprocal lattice vector \mathbf{G}_{hkl} . In reality, this delta-shaped scattering intensity contribution is smeared out mainly owing to the finiteness of the crystal ($0 \leq m_i \leq N - 1$, N denotes the number of the unit cells), which leads to $G_{\text{finite}}(\mathbf{q}) \propto \prod_i [\sin^2(N\mathbf{q} \cdot \mathbf{a}_i/2) / \sin^2(\mathbf{q} \cdot \mathbf{a}_i/2)]$. Thus, in case of scattering by a perfect crystal of finite thickness, intensity oscillation fringes close to the Bragg peaks are observed. From simulations of these fringes, among others, the thickness of the crystal can be obtained. However, $G_{\text{finite}}(\mathbf{q})$ reveals, that a finite intensity is also observed apart from Bragg peaks, which is labeled as diffuse scattering. In general, diffuse scattering arises from imperfection of a perfect infinite crystal. These imperfections can be classified into two groups according to Krivoglaz [72, 73]. While in case of weak defects (point defects and their clusters, small precipitates of another phase in the crystal lattice) the diffracted wave contains coherent and diffuse components, scattering by strong defects (dislocations and their pile-ups) results in a diffuse component only [74]. These imperfections do not only give rise to diffuse scattering, but also affect the Bragg reflection. In the vicinity of a defect, which creates a slight variation of the atomic bond lengths and interplanar spacings d , the crystal lattice is distorted resulting in microstrains causing a broadening of the Bragg reflections [68]. To analyze this effect, the peak broadening caused by the finite size of the crystal as well as by the microstrain have to be separated.

The Williamson-Hall plot is one method to separate size and strain broadening of ($00l$)-reflections ($l = 1 - 4$) in the out-of-plane direction. Assuming that the peak profile has a Gaussian shape, the integral breadth β_{meas} , which is given by the area of the peak divided by its height, is mainly caused by three contributions: $\beta_{\text{meas}}^2 = \beta_{\text{size}}^2 + \beta_{\text{strain}}^2 + \beta_{\text{instr}}^2$, where β_{size} , β_{strain} , and β_{instr} denote the peak broadening by the finite thickness of the thin film, the inhomogeneous strain, and the instrumental resolution of the diffractometer, respectively [75]. Using the Scherrer equation of the form $\beta_{\text{size}} = \frac{K_S}{\langle D \rangle \cos \theta}$, the integral breadth $\beta = \beta_{\text{meas}} - \beta_{\text{instr}}$ yields $\beta^2 = \beta_{\text{size}}^2 + \beta_{\text{strain}}^2 = \left(\frac{K_S \lambda}{\langle D \rangle \cos \theta} \right)^2 + (2K_D \epsilon_{\text{rms}} \tan \theta)^2$, where $\langle D \rangle$, K_S , λ , and θ denote the average crystallite size, the Scherrer constant, the x-ray wavelength, and the diffraction angle, respectively. The root mean square strain $\epsilon_{\text{rms}} = \sqrt{\langle \epsilon^2 \rangle}$ is a function of the normalized variation of the interplanar spacing $\frac{\Delta d}{d}$ as well as a scaling factor K_D , which depends on the nature of the lattice distortions and the underlying model of the microstrain [68]. Using the momentum transfer $q = \frac{4\pi}{\lambda} \sin \theta$, the above equation yields

$$(\Delta K)^2 = \left(\tilde{K}_S \right)^2 + (K_D \epsilon_{\text{rms}} K)^2, \quad (2.3)$$

where $q = 2\pi K$ and $K_S = \tilde{K}_S \langle D \rangle$. Therefore, the Williamson-Hall plot of $(\Delta K)^2$ versus K^2 should give a straight line that allows to determine $K_D \epsilon_{\text{rms}}$ from its slope.

However, Eq. (2.3) is based on the assumption that size broadening does not depend on the length of the scattering vector whereas strain broadening does [68]. Moreover, the Williamson-Hall method was developed for polycrystalline materials rather than for thin films. Therefore, the derived values of the mean micro strain $K_D \epsilon_{\text{rms}}$ using the Williamson-Hall method should be considered as first estimate. Ungár and coworkers modified the classical Williamson-Hall plot by including a dislocation contrast term, which depends on the Miller indices hkl of the reflection, the Burgers vector, the scattering vector, and on elastic constants of the material [76]. In this case, the average microstrain takes a defined meaning and is now among others proportional to the square root of the dislocation density [68].

Apart from imperfection of the crystal, the peak profiles from Bragg reflections are affected by instrumental settings like the emission profile of the x-ray source, the monochromators used, the widths, and other factors. These effects are merged into β_{instr} , which is determined by investigating the peak profile of the Bragg reflections caused by the corresponding substrate. In addition, the x-ray beam might be displaced with respect to the center of the diffractometer. This strongly affects the x-ray diffraction measurements in particular in the context of the precise determination of the lattice parameters. Since the fractional error in the lattice interplanar spacing d , which is a function of the lattice parameter of the crystal, caused by a given error in the diffraction angle θ approaches zero for $\theta \rightarrow 90^\circ$, high order Bragg reflections, which are located close to $2\theta = 180^\circ$, should be used for the calculation of the lattice parameters of the investigated sample. However, in this case the systematic error can not be eliminated entirely, because a reflected beam can not be observed for a diffraction geometry with $2\theta = 180^\circ$. This situation is improved by plotting the measured lattice constants for different order reflections against an analytical function depending on θ . This function should be chosen such that the curve results in a straight line, which may be extrapolated with confidence [77]. In our case, the Nelson-Riley (NR) function [78]

$$\frac{\Delta d}{d} \propto NR = \left(\frac{\cos^2 \theta}{\sin \theta} + \frac{\cos^2 \theta}{\theta} \right) \quad (2.4)$$

is used, which mainly corrects the experimental data in the case of off-centering of the sample and absorption effects. Equation (2.4) reveals, that NR approaches zero for $\theta \rightarrow 90^\circ$. Therefore, the precise lattice parameter can be obtained from the y -axis intercept of the Nelson-Riley plot (d versus NR).⁸

As discussed in the framework of Eqs. (2.1) and (2.2), the scattering intensity is characterized not only by the lattice factor $G(\mathbf{q})$ but also by the structure factor $F(\mathbf{q}, \omega)$. The latter quantity is mainly depending on the atomic form factor f_j , which is in general a complex function:

$$f_j = f_j^{(\text{oa})} + f_j^{(\text{a})}, \quad (2.5)$$

⁸Due to statistical error, the data are scattered around the expected straight line in a Nelson-Riley plot. This additional error can be reduced by applying the Cohen method described in Ref. [77].

where $f_j^{(\text{oa})}$ describes the normal (non-resonant) atomic form factor, which is determined by the Fourier transform of the electron density as well as the orbital and spin magnetization densities of the j th atom.⁹ The complex part of the atomic form factor ($f_j^{(\text{a})} = f_j' + \imath f_j''$) is the resonant scattering factor, which is sensitive to the x-ray photons that are absorbed by the photoelectric effect. If the energy of the incoming photons is close to an electronic resonance, it interacts with the corresponding bound core electrons and is absorbed. Therefore, $f_j^{(\text{a})}$ is strongly frequency dependent and is sensitive to the electronic structure of the scattering atom and its surrounding. This yields valuable information about the spin and orbital moments. In case of magnetic materials, the real part of the scattering amplitude f_j' corresponds to resonant magnetic scattering, while the imaginary part f_j'' gives rise to x-ray magnetic circular dichroism. Furthermore, since the scattering amplitude is highly dependent on the polarization of the incident and scattered wave vector, the contribution due to charge, orbital, or magnetic scattering can be separated. In this sense, a linear basis ($\mathbf{e}_\sigma, \mathbf{e}_\pi$) is a common choice. For more details on x-ray scattering and absorption by magnetic materials, the reader is referred to the book of S. W. Lovesey and S. P. Collins [79]. As an example of resonant x-ray scattering, Fig. 2.3(h) shows the result of resonant x-ray scattering experiments around the Cr K -absorption edge carried out at the beamline I16 at the Diamond light source on a 46 nm thick BiCrO₃ film.¹⁰

2.1.4 Transmission electron microscopy

In the field of thin film deposition, the investigation of the crystalline symmetry and the unit cell structure can be obtained by x-ray diffraction analysis. However, using this technique, the information about the variation of local structures due to defects or fluctuations, which give rise to diffuse scattering, is usually smoothed out. In this case, real-space analysis methods support the structural information obtained by x-ray diffraction techniques. In this sense, transmission electron microscopy (TEM) is a useful method.¹¹ In the framework of this thesis, TEM images of our thin films were recorded by Sven-Martin Hühne (Universität Bonn). The measurements were carried out on a Philips CM300 TEM operating at 300 keV, which is described in detail in Ref. [81].

2.2 Dielectric characterization techniques

As this thesis deals with multiferroic thin films and hybrid structures, the investigation of its magnetic and dielectric properties is mandatory to test their multiferroic behavior. As a first step, the dielectric properties were probed on a macroscopic scale using a commercial tester as well as a LCR meter. Furthermore, piezoelectric

⁹Non-resonant magnetic scattering is much weaker than the usual charge scattering.

¹⁰Resonant x-ray diffraction experiments on BiCrO₃ thin films are under further investigation.

¹¹The reader is referred to a recent review on TEM for more details on this technique [80].

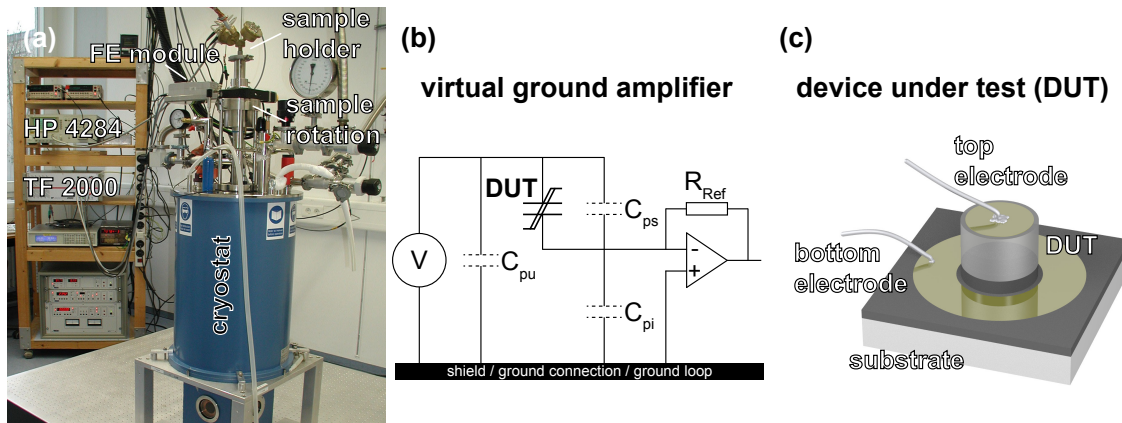


Figure 2.4: (a) Measurement setup used for the investigation of the dielectric behavior of multiferroic as well as single-ferroic ferroelectric compounds. The electronic assembly, which was built-up in the framework of this thesis, consists of a commercial ferroelectric tester (TF Analyzer 2000 HS, aixACCT Systems) as well as an LCR meter (HP 4284A, Hewlett Packard) and a dedicated dip-stick. The TF Analyzer 2000 HS ferroelectric tester consists of a ferroelectric probe head (FE module) connected to the basic unit (TF 2000). The use of a new sample holder, which can be inserted into a magnet cryostat, enables temperature ($2\text{ K} \lesssim T \leq 300\text{ K}$) as well as magnetic field ($|\mu_0 H| = 8\text{ T}$) dependent measurements of the dielectric behavior (see Ref. [84] for more details). (b) The ferroelectric tester uses the virtual ground method, which eliminates parasitic cable capacitances C_{pu} and C_{pi} , to perform dynamic and static $P(E)$ hysteresis measurements [85]. The parasitic stray capacitance C_{ps} is compensated as described in Ref. [86]. Moreover, a dynamic leakage current compensation method is implemented in the measurement software to reduce parasitic effects due to leakage currents [87]. In case of multiferroic or single-ferroic ferroelectric thin films, the device under test (DUT) is patterned into a parallel plate capacitor geometry as schematically shown in (c).

force microscopy was employed to get detailed information on a nanometer length scale.

2.2.1 Macroscopic dielectric characterization techniques

On a macroscopic scale, a commercial ferroelectric tester (TF Analyzer 2000 HS, aixACCT Systems) [82] as well as a LCR meter (HP 4284A, Hewlett Packard) [83] were used as probe equipment to investigate the dielectric properties of our intrinsic multiferroic thin films as well as extrinsic multiferroic composite structures (cf. Fig. 2.4(a)). The TF Analyzer 2000 HS system provides several standard ferroelectric measurement techniques, such as dynamic and static $P(E)$ hysteresis measurements, fatigue, retention and imprint measurements as well as leakage current measurements, which are described in Refs. [70, 82, 85]. The most common ones to characterize ferroelectric or antiferroelectric compounds are dynamic and static $P(E)$ hysteresis measurements, in which the current response to an applied electric excitation signal is recorded. The ferroelectric test module of the TF Analyzer 2000 HS setup (cf. FE module in Fig. 2.4(a)) is based on the virtual ground method displayed in Fig. 2.4(b), which is an improved version of the original Sawyer-

Tower circuit [88] and enables the highest precision for ferroelectric measurements [85]. In particular, parasitic capacitances such as cable capacitance C_{pu} and C_{pi} (cf. Fig. 2.4(b)) are eliminated employing the virtual ground circuit. Furthermore, the parasitic stray capacitance C_{ps} , which is parallel to the device under test (DUT), is compensated within the TF Analyzer 2000 HS as described in Ref. [86].

In case of multiferroic as well as single-ferroic ferroelectric thin films, the respective sample is patterned into the structure shown in Fig. 2.4(c). Since the diameter of the top electrode is $200\ \mu\text{m}$ and since the thin films used in the course of this thesis are thinner than $350\ \text{nm}$, a considerable amount of leakage current, which strongly influences the $P(E)$ hysteresis measurements [89], is unavoidable. This parasitic effect is reduced using the unique dynamic leakage current compensation method (DLCC), which is implemented in the measurement software. The DLCC takes advantage of the different frequency dependencies of the current response caused by dielectric displacement, ferroelectric switching, and leakage currents [87].

In addition to large signal $P(E)$ hysteresis measurements, reversible parts of the ferroelectric polarization switching process can be obtained by small signal capacitance versus voltage $C(V)$ measurements carried out using the LCR meter HP 4284A [90]. Furthermore, relaxation phenomena such as Debye or Maxwell-Wagner relaxation can be investigated by frequency dependent measurements of the real ε_r and imaginary ε_i part of the permittivity [91]. More details on this issue can be found in the diploma thesis of Daniel Pantel [70].

2.2.2 Microscopic dielectric characterization techniques

As the diameter of the top electrodes used for macroscopic $P(E)$ hysteresis measurements are as large as $200\ \mu\text{m}$, the signal recorded during these measurements is based on the current response of more than 750000 ferroelectric domains in case of BiFeO_3 thin films (cf. Fig. 4.17) and therefore an average quantity. To get precise information on the ferroelectric domain structure, piezoelectric force microscopy (PFM) measurements on our samples were performed by Denny Köhler (Technische Universität Dresden).¹² PFM is based on the linear coupling between electrical and mechanical phenomena, i.e., the converse piezoelectric effect. More precisely, a tip is brought into contact with the surface of the sample and the piezoelectric response is detected, while a periodic bias voltage is applied to the tip. Within this technique, information on the polarization direction as well as on the local electromechanical activity can be obtained by analyzing the phase and the amplitude of the tip deflection signal, respectively. Moreover, PFM allows for a simultaneous acquisition of both topographic and piezoelectric responses of the investigated sample surface. Two different setups were used to reveal the piezoelectric response of our samples: a room temperature and low temperature ultra-high vacuum (UHV) system. The former setup provides information on the in-plane as well as out-of-plane domain structure, while the latter is only sensitive to the out-of-plane PFM component due

¹²A summary about the recent progress in applications of piezoresponse force microscopy (PFM) can be found in Ref. [92].

to experimental restrictions. The reader is referred to the PhD thesis of Denny Köhler for a detailed description of the PFM technique and the different PFM setups [93].

2.3 Magnetic characterization techniques

Different techniques were employed to investigate the magnetic properties of multiferroic thin films as well as composite structures consisting of ferromagnetic and ferroelectric layers. In particular, the magnetic response was examined not only as a function of external magnetic fields but also under different electric fields, i.e., detecting converse magnetoelectric effects.

2.3.1 SQUID magnetometry

One of the most sensitive techniques to measure the overall magnetic moment is SQUID magnetometry, since it is based on a superconducting quantum interference device (SQUID) detection system, which allows to precisely convert variations of the magnetic flux into voltage changes. The basic operation mode, which can be divided into three steps, is shown in Fig. 2.5(a). First, the magnetic flux is detected using a pick-up coil in the shape of a second order gradiometer, which suppresses any constant magnetic flux as well as first order gradient magnetic fields. In the second step, the magnetic flux is transferred to a rf SQUID device and converted to a voltage signal. Finally, this signal is amplified by the instrument electronics and the voltage versus sample position curve is fitted using the fit function described in Ref. [95]. From this fitting procedure, the projection of the magnetic moment along the gradiometer axis and thus along the external magnetic field, which is proportional to the amplitude of the SQUID voltage response curve, is obtained. To increase the sensitivity to around 10^{-11} Am², the sample can be periodically moved up and down through the pick-up coil and the SQUID output signal is analyzed using lock-in techniques (RSO mode).

In order to examine magnetoelectric effects, new sample holders were designed in the framework of this thesis, which allow to apply an electric voltage across the investigated sample. Since the pick-up coil is a second order gradiometer, a sample holder will produce no signal as long as it is homogeneously extended over the whole length of the pick-up coil. Therefore, the main challenge for the design of a new SQUID sample holders is to ensure the homogeneity in shape and size, which is fulfilled in our case. The magnetic measurements are by far more affected by the magnetic properties of the substrates used for the thin film deposition than by the sample holder. These contributions are corrected using the magnetic behavior at high magnetic fields, at which the investigated thin film is expected to be magnetically saturated.

Since the SQUID magnetometer yields information about the projection of the magnetic moment on the applied magnetic field, angle-dependent measurements were carried out to reveal the magnetic anisotropy of the sample. To this end,

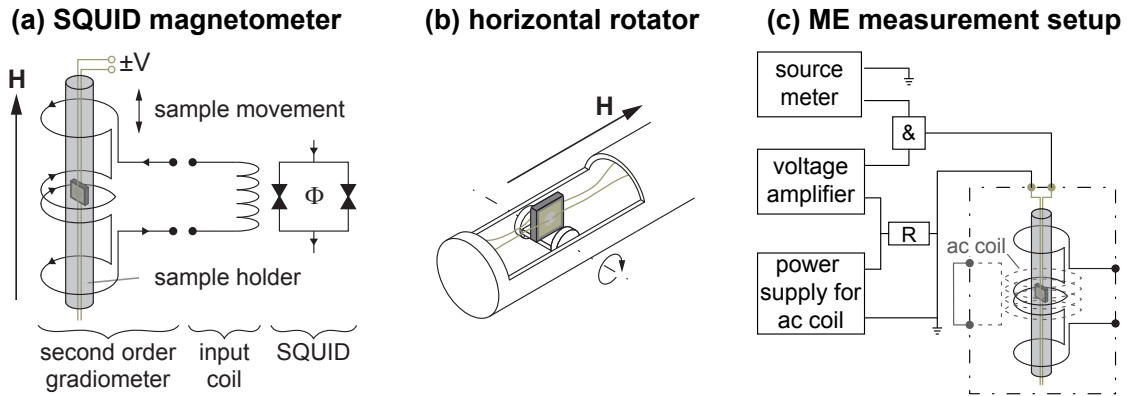


Figure 2.5: (a) Schematic illustration of the SQUID magnetometer MPMS XL-7. The magnetometer is based on a SQUID detection system, which is a highly sensitive flux-to-voltage converter. The MPMS XL-7 system provides a magnetic field of $|\mu_0 H| \leq 7 \text{ T}$ and temperatures in a range of $1.8 \text{ K} \leq T \leq 400 \text{ K}$. In the framework of this thesis, new sample holders were designed, which allow to apply an electric voltage $\pm V$ across the sample. (b) To carry out angle-dependent magnetization measurements as a function of applied magnetic and electric fields at different temperatures, the magnetometer was equipped with a horizontal rotator. Electric contacts were installed to record angle-dependent magnetization measurements as a function of the applied electric field. (Figures (a) and (b) adapted from Ref. [24]) (c) Following Borisov *et al.* [94], the linear converse magnetoelectric effect was measured taking advantage of the ac-option of the MPMS XL-7 SQUID magnetometer. To this end, the ac coil (dashed lines) was short circuited and its power supply was used as an ac current source to apply an ac voltage, which drops across the load resistance R , on the investigated sample. The magnetic response on the voltage was then detected by the ac-option of the magnetometer employing a lock-in-technique. The measurements were performed using an ac frequency in the range of $1 \leq f \leq 10 \text{ Hz}$.

the magnetometer was equipped with a horizontal rotator, which is schematically depicted in Fig. 2.5(b). In this case, the sensitivity is decreased by about one order of magnitude, since the sample is moved through the second order gradiometer in a step mode (dc mode). Again, electric contacts were installed to record angle-dependent magnetization measurements as a function of the applied electric field.

To reveal the linear converse magnetoelectric effect, we followed Borisov *et al.* [94] and took advantage of the ac-option of our SQUID magnetometer (cf. Fig. 2.5(c)). Here, the basic idea is to use the power supply of the ac coil to drive the investigated sample and detect its magnetic response by the SQUID setup employing a lock-in technique. Within this technique, all options of the magnetometer remain available. In particular, the two-point method used for conventional ac measurements, allows to increase the accuracy of the detection, since it nulls all spurious signals (cf. Ref. [95] for more details).

2.3.2 Ferromagnetic resonance

Ferromagnetic resonance (FMR) is a common method to elucidate the magnetic anisotropy of ferromagnets. It is based on the resonant absorption of microwave

radiation in a system of strongly interacting spins. In case of ferromagnets exposed to a static external magnetic field, FMR occurs at a given frequency at which the magnetization precession is resonantly excited. The precession takes place around an effective magnetic field, which comprises the external magnetic field and internal effective fields due to exchange interaction and magnetic anisotropies. Thus, FMR provides substantial information, among others, about the magnetic anisotropy present in the ferromagnet. All FMR data presented in this thesis were obtained by using a commercial Bruker ESP 300 system located at the Walter Schottky Institut, which operates at a constant frequency of 9.3 GHz. The FMR is detected while sweeping the magnitude of the static external magnetic field. At resonance, the first derivative of a resonance line (e.g., a Lorentzian in the simplest case) is observed, since magnetic field modulation and lock-in detection is used. Please refer to the PhD thesis of Andreas Brandlmaier for more details on the theory of ferromagnetic resonance as well as the Bruker ESP 300 system [24].

2.3.3 Angle-dependent magnetotransport

Angle-dependent magnetotransport measurements are another powerful tool to determine the magnetic anisotropy of a ferromagnetic sample, in particular on a local scale. To this end, standard four-point magnetotransport measurements were carried out,¹³ yielding longitudinal ρ_{xx} and transverse ρ_{xy} resistivities, which were measured parallel and perpendicular to the in-plane applied current density $\mathbf{J} = J\mathbf{j}$, respectively.

Following Birss [98] and Limmer *et al.* [99], the relationship between an electric field E_i ($i = 1, 2, 3$) and an applied current density J_j ($j = 1, 2, 3$) in the presence of a magnetic field H_k ($k = 1, 2, 3$) can be, in general, non-linear and is described by¹⁴

$$E_i = \rho_{ij}J_j + R_{ijk}J_jH_k + \dots \quad (2.6)$$

However, if the external magnetic field is high enough to saturate the ferromagnetic sample, Ohm's law $E_i = \rho_{ij}J_j$ becomes valid and the resistivity tensor ρ_{ij} can be expressed as series expansion in powers of the direction cosines m_i of the magnetization $M_i = M_s m_i$, where M_s denotes the saturation magnetization:

$$\rho_{ij} = a_{ij} + a_{kij}m_k + a_{klij}m_k m_l + a_{klmij}m_k m_l m_m + \dots \quad (2.7)$$

a_{ij} , a_{kij} , a_{klij} , and a_{klmij} are galvanomagnetic tensors, which have to comply with the symmetry of the investigated crystal, according to Neumann's principle. In case of isotropic media, such as polycrystalline ferromagnetic thin films, where the magnetization is confined in the film plane, the longitudinal ρ_{xx} and transverse ρ_{xy}

¹³The reader is directed to the diploma theses of Matthias Althammer [96] and Michael Wagner [97] for more details on this technique.

¹⁴Summation over repeated indices is assumed throughout this thesis (Einstein summation convention).

resistivities can be derived by averaging over all possible crystal orientations in space [97, 99]:¹⁵

$$\rho_{xx} = \rho_0 + \rho_1 \cos^2 \Theta, \quad \rho_{xy} = \rho_2 \sin \Theta \cos \Theta, \quad (2.8)$$

where Θ denotes the angle between the current density \mathbf{J} and the magnetization \mathbf{M} . The resistivities ρ_0 , ρ_1 , and ρ_2 are related to the components of the galvanomagnetic tensors a_{ij} , a_{kij} , $a_{kl ij}$, and a_{klmij} for cubic symmetry as follows [99]:

$$\begin{aligned} \rho_0 &= a_{11} + \frac{1}{5} (3a_{1111} + 2a_{1122} + 2a_{2323}), \\ \rho_1 &= \rho_2 = \frac{1}{5} (2a_{1111} - 2a_{1122} + 3a_{2323}). \end{aligned} \quad (2.9)$$

Therefore, Eq. (2.8) depends only on Θ and is in agreement with the classical dependence of the planar Hall effect in isotropic media [100]. Since the magnetization aligns in such a way that the energy density of the system takes its minimum value, the angle Θ can be calculated. Thus, using an appropriate description for the magnetic behavior of the system, the magnetic anisotropy can be derived from Eq. (2.8) by performing angle-dependent magnetotransport measurements, in which the angle of the applied magnetic field is varied with respect to the direction of the current density \mathbf{j} .

2.3.4 Magnetic force microscopy

As discussed above, angle-dependent magnetotransport measurements require a saturated magnetic state, i.e., a single-domain state, to reveal the magnetic anisotropy of the investigated sample. However, since the natural domain structure of the investigated sample recorded at zero external field contains a variety of information concerning the material properties, such as the exchange interaction, magnetic anisotropy, magnetoelastic effects, and even magnetoelectric interactions, the investigation of the domain structure on a microscopic scale is worth to be studied. In this sense, magnetic force microscopy (MFM) is a common tool to image magnetic domains with high spatial resolution. MFM is a special method in the field of non-contact scanning force microscopy. In the dynamic mode, the magnetic tip located at a finite distance above the surface of the sample oscillates with a certain amplitude, exhibiting a phase shift with respect to the driving signal in the presence of a variation of the near-surface magnetic stray field of the investigated sample. The change in the detected frequency of the tip motion is here proportional to the second derivative of the magnetic field in out-of-plane direction. The experimental data discussed in the course of this thesis were measured by Denny Köhler (Technische

¹⁵In the course of this thesis, the conventional notation of the longitudinal ρ_{xx} and transverse ρ_{xy} resistivities is used. In general, ρ_{xx} and ρ_{xy} are defined as $\rho_{xx} = \mathbf{j} \cdot \boldsymbol{\varrho} \cdot \mathbf{j}$ and $\rho_{xy} = \mathbf{t} \cdot \boldsymbol{\varrho} \cdot \mathbf{j}$ with $\boldsymbol{\varrho}$ denoting the resistivity tensor as well as $\mathbf{J} = J\mathbf{j}$ and $\mathbf{t} = \mathbf{n} \times \mathbf{j}$, where \mathbf{n} describes the surface normal.

Universität Dresden) using a commercial low temperature UHV-AFM, which is described in detail in Ref. [93]. In multiferroic materials, which exhibit a magnetic and dielectric order, the tip is not only affected by magnetic but also by electric forces, the contribution due to surface charges has to be subtracted from the measured signal, to reveal the pure magnetic behavior of the sample. This was carried out by simultaneously measuring the surface potential of the sample by Kelvin probe force microscopy (KPFM). The procedure is discussed in detail in Ref. [93].

Intrinsic multiferroic materials

Chapter 3

Theory of intrinsic multiferroics

“Materials should exist, which can be polarized by a magnetic field and magnetized by an electric field.”

Pierre Curie (1894)

Intrinsic multiferroic materials combine two or more of the primary ferroic ordering phenomena in the same phase. Considering time reversal and space inversion symmetries, the primary ferroic properties can be identified as ferromagnetic, ferroelectric, ferroelastic, and ferrotoroidic. While in ferroic materials, the ferroic order parameter changes with its conjugate field, e.g., magnetic (electric) fields change the magnetization (electric polarization) state, in magnetoelectric multiferroics, a magnetic (electric) field can tune the electric polarization (magnetization). This cross-coupling between the magnetic and electric phases is of great interest both for basic physics as well as for technological applications in the field of multifunctional devices, in which the low power and high speed of field-effect electronics are combined with the remanent properties of electric field controlled ferromagnetism.

The magnetoelectric effect was first conjectured by Pierre Curie in 1894 [101]. More than half a century later, Landau and Lifshitz developed symmetry requirements for this new effect [102]. On that basis, Dzyaloshinskii predicted a finite magnetoelectric effect in antiferromagnetic Cr_2O_3 in 1960 [103], which was later on confirmed experimentally by Astrov [104]. However, the maximum value of the linear magnetoelectric coupling in Cr_2O_3 was found to be only 4.13 ps/m. This corresponds to the magnetization obtained after the reversal of only five of every 10^6 spins in the antiferromagnetic lattice [105]. This smallness of the magnetoelectric effect suppressed the research activities in this field for 30 years. Recently, a revival of magnetoelectric effects has occurred, not only due to possible applications for data storage, but also due to developments in the understanding of the microscopic origin [105, 106].

In this chapter, the theory of intrinsic multiferroic materials, which exhibit finite magnetoelectric effects, is introduced in a four dimensional relativistic formulation. On the basis of the covariant formulation of classical electromagnetism, a general four dimensional susceptibility tensor, which covers dielectric, magnetic, and magnetoelectric behavior can be established. Therefore, the dielectric, magnetic, and magnetoelectric effects can be regarded as different manifestations of one general property.

3.1 Linear magnetoelectric effect

The direct (converse) magnetoelectric effect is generally defined as the induced electric polarization (magnetization) of a material in an applied magnetic (electric) field. [102]. Following O'Dell's treatment of the electrodynamics of magnetoelectric media [107], the dielectric, magnetic, and magnetoelectric properties of a medium can be considered as different aspects of one property. In the theory of classical electromagnetism, the three dimensional electric field \mathbf{E} as well as the magnetic field \mathbf{B} are defined in terms of the vector potential \mathbf{A} and the scalar potential ϕ as follows:

$$\mathbf{B} = \nabla \times \mathbf{A} \quad (3.1)$$

$$\mathbf{E} = -\nabla\phi - \frac{\partial \mathbf{A}}{\partial t}. \quad (3.2)$$

While the scalar potential ϕ is implicitly defined by the previous equation, the vector potential \mathbf{A} is only determined up to the gradient of a scalar field. In the covariant formulation of classical electromagnetism, the scalar and the vector potential can be unified by introducing the four-dimensional vector potential $A^\mu = (\phi/c, \mathbf{A})$. On the basis of this vector potential A^μ , a four-dimensional field tensor $F^{\mu\nu}$ ($\mu, \nu = 0, 1, 2, 3$) can be defined as the four-dimensional curl of the vector potential A^μ [107], which yields $F^{\mu\nu} = \partial^\mu A^\nu - \partial^\nu A^\mu$ with $\partial^\mu = (\frac{1}{c}\frac{\partial}{\partial t}, -\nabla)$. By using Eqs. (3.1) and (3.2), the components of the contravariant field tensor $F^{\mu\nu}$ are given by [108]

$$F^{\mu\nu} = \begin{pmatrix} 0 & -1/cE_1 & -1/cE_2 & -1/cE_3 \\ 1/cE_1 & 0 & -B_3 & B_2 \\ 1/cE_2 & B_3 & 0 & -B_1 \\ 1/cE_3 & -B_2 & B_1 & 0 \end{pmatrix}. \quad (3.3)$$

$F^{\mu\nu}$ is antisymmetric ($F^{\mu\nu} = -F^{\nu\mu}$) and therefore possesses six independent components. Since the constitutive relation in vacuum between the electric and magnetic field vectors and the two excitation vectors is given by $D = \varepsilon_0 E$ and $H = \frac{1}{\mu_0} B$, a four-dimensional excitation tensor $G^{\mu\nu}$ can be constructed by $F^{\mu\nu} = \mu_0 c G^{\mu\nu}$, which yields

$$G^{\mu\nu} = \begin{pmatrix} 0 & -D_1 & -D_2 & -D_3 \\ D_1 & 0 & -1/cH_3 & 1/cH_2 \\ D_2 & 1/cH_3 & 0 & -1/cH_1 \\ D_3 & -1/cH_2 & 1/cH_1 & 0 \end{pmatrix}. \quad (3.4)$$

However, the simple relation depicted in the previous equation is only valid in vacuum. In the general case of a magnetic and electric polarizable medium, this equation must be extended to $F^{\mu\nu} = \mu_0 c (G^{\mu\nu} + M^{\mu\nu})$, where $M^{\mu\nu}$ denotes the four-dimensional polarization tensor:

$$M^{\mu\nu} = \begin{pmatrix} 0 & P_1 & P_2 & P_3 \\ -P_1 & 0 & -1/cM_3 & 1/cM_2 \\ -P_2 & 1/cM_3 & 0 & -1/cM_1 \\ -P_3 & -1/cM_2 & 1/cM_1 & 0 \end{pmatrix}. \quad (3.5)$$

Now, assuming a linear response of the magnetic and electric polarizable medium on the applied electromagnetic fields, the polarization tensor $M^{\mu\nu}$ and the field tensor $F^{\mu\nu}$ are connected via a general susceptibility tensor $\xi_{\mu\nu}^{\alpha\beta}$ in the following way

$$\mu_0 c M^{\alpha\beta} = \frac{1}{2} \xi_{\mu\nu}^{\alpha\beta} F^{\mu\nu}. \quad (3.6)$$

The constant $\mu_0 c$ is included in Eq. (3.6) to obtain a dimensionless tensor $\xi_{\mu\nu}^{\alpha\beta}$. As $F^{\mu\nu}$ and $M^{\alpha\beta}$ are antisymmetric tensors (cf. Eq. (3.3) and Eq. (3.5)), $\xi_{\mu\nu}^{\alpha\beta}$ must be antisymmetric in $\mu\nu$ and $\alpha\beta$, which leads to

$$\xi_{\alpha\beta}^{\mu\nu} = -\xi_{\alpha\beta}^{\nu\mu} = \xi_{\beta\alpha}^{\nu\mu} = -\xi_{\beta\alpha}^{\mu\nu}. \quad (3.7)$$

Applying the summation over μ and ν and accounting for the asymmetric behavior of $\xi_{\alpha\beta}^{\mu\nu}$, the electric polarization P_i and the magnetization M_i can be obtained from Eqs. (3.3)-(3.7) ($i, j = 1, 2, 3$):

$$P_i = -\frac{1}{\mu_0 c^2} \chi_{ij}^{(e)} E_j + \frac{1}{\mu_0 c} \chi_{ij}^{(em)} B_j \quad (3.8)$$

$$M_i = +\frac{1}{\mu_0 c} \chi_{ij}^{(me)} E_j + \frac{1}{\mu_0} \chi_{ij}^{(m)} B_j. \quad (3.9)$$

The 3×3 tensors $\chi_{ij}^{(e)}$, $\chi_{ij}^{(m)}$, $\chi_{ij}^{(me)}$, and $\chi_{ij}^{(em)}$ are related to $\xi_{\alpha\beta}^{\mu\nu}$ in the following way:

$$\begin{aligned} \chi_{ij}^{(e)} &= \begin{pmatrix} \xi_{01}^{01} & \xi_{01}^{02} & \xi_{01}^{03} \\ \xi_{01}^{02} & \xi_{01}^{02} & \xi_{01}^{03} \\ \xi_{01}^{03} & \xi_{01}^{03} & \xi_{01}^{03} \\ \xi_{01}^{03} & \xi_{01}^{03} & \xi_{01}^{03} \end{pmatrix}, & \chi_{ij}^{(em)} &= - \begin{pmatrix} \xi_{23}^{01} & \xi_{31}^{01} & \xi_{12}^{01} \\ \xi_{23}^{02} & \xi_{31}^{02} & \xi_{12}^{02} \\ \xi_{23}^{03} & \xi_{31}^{03} & \xi_{12}^{03} \\ \xi_{23}^{03} & \xi_{31}^{03} & \xi_{12}^{03} \end{pmatrix}, \\ \chi_{ij}^{(me)} &= \begin{pmatrix} \xi_{01}^{23} & \xi_{01}^{23} & \xi_{01}^{23} \\ \xi_{01}^{31} & \xi_{01}^{31} & \xi_{01}^{31} \\ \xi_{01}^{31} & \xi_{01}^{31} & \xi_{01}^{31} \\ \xi_{01}^{12} & \xi_{01}^{12} & \xi_{01}^{12} \end{pmatrix}, & \chi_{ij}^{(m)} &= \begin{pmatrix} \xi_{23}^{23} & \xi_{31}^{23} & \xi_{12}^{23} \\ \xi_{23}^{31} & \xi_{31}^{31} & \xi_{12}^{31} \\ \xi_{23}^{31} & \xi_{31}^{31} & \xi_{12}^{31} \\ \xi_{23}^{12} & \xi_{31}^{12} & \xi_{12}^{12} \end{pmatrix}. \end{aligned} \quad (3.10)$$

$\chi_{ij}^{(e)}$ and $\chi_{ij}^{(m)}$ can be identified as the electric and magnetic susceptibility tensors. While $\chi_{ij}^{(e)}$ is identical to the conventional electric susceptibility tensor $\tilde{\chi}_{ij}^{(e)}$ defined by $P_i = \frac{1}{\mu_0 c^2} \tilde{\chi}_{ij}^{(e)} E_j$ except for a change in sign,¹ the magnetic susceptibility tensor $\chi_{ij}^{(m)}$ is clearly different from the conventional one, which is defined as $M_i = \tilde{\chi}_{ij}^{(m)} H_j$ in the linear response theory. However, Equation (3.9) reveals that $\chi_{ij}^{(m)}$ is determined by $M_i = \frac{1}{\mu_0} \chi_{ij}^{(m)} B_j$ in the absence of magnetoelectric effects. O'Dell showed that the new representation will correspond to the conventional one when the medium is only weakly magnetic [107]. In addition to the pure electric and magnetic behavior, a finite electric (magnetic) polarization can be induced by magnetic (electric) fields, if the material under consideration is magnetoelectric. The direct and converse effects are thereby characterized by the susceptibility tensors $\chi_{ij}^{(em)}$ and $\chi_{ij}^{(me)}$, respectively.

¹ $\chi_{ij}^{(e)}$ is measured at constant B_i and differs from that measured at constant H_i in the presence of magnetoelectric effects.

Since Eq. (3.6) is only valid in the limit of the linear response theory, the behavior arising from $\chi_{ij}^{(\text{em})}$ and $\chi_{ij}^{(\text{me})}$ is named linear magnetoelectric effect. As the linear magnetoelectric effect is part of the general susceptibility $\xi_{\alpha\beta}^{\mu\nu}$, $\chi_{ij}^{(\text{em})}$ and $\chi_{ij}^{(\text{me})}$ are treated as dimensionless tensors. However, in literature, considerable confusion exists regarding the unit of the linear magnetoelectric effect (see Ref. [109] and references therein). In the course of this thesis, the induced polarization (magnetization) caused by direct (converse) magnetoelectric effects is normalized by the vacuum impedance $R_0 = \mu_0 c = \sqrt{\frac{\mu_0}{\epsilon_0}} \approx 377 \text{ V/A}$ resulting in a dimensionless quantity. However, since $\chi_{ij}^{(\text{em})}$ is often expressed in units of s/m, $\frac{1}{c}\chi_{ij}^{(\text{em})}$ is used to compare the derived magnetoelectric coupling constants with literature values.

By representing pairs of indices by a single one (01 = 1, 02 = 2, 03 = 3, 23 = 4, 31 = 5, and 12 = 6), the general susceptibility tensor $\xi_{\alpha\beta}^{\mu\nu}$ can be represented as a 6×6 matrix [110]:

$$\xi_{\alpha\beta}^{\mu\nu} = \begin{pmatrix} \chi_{ij}^{(\text{e})} & -\chi_{ij}^{(\text{em})} \\ \chi_{ij}^{(\text{me})} & \chi_{ij}^{(\text{m})} \end{pmatrix}. \quad (3.11)$$

Equation (3.11) reveals that the general susceptibility tensor $\xi_{\mu\nu}^{\alpha\beta}$ covers the dielectric, magnetic and magnetoelectric behavior of the material.

3.2 Symmetry considerations

The antisymmetric behavior in $\mu\nu$ and $\alpha\beta$ of the general susceptibility tensor $\xi_{\alpha\beta}^{\mu\nu}$ was already used for the calculation of the tensor components of the four 3×3 tensors $\chi_{ij}^{(\text{e})}$, $\chi_{ij}^{(\text{m})}$, $\chi_{ij}^{(\text{me})}$, and $\chi_{ij}^{(\text{em})}$ (see Eq. 3.10). However, the intrinsic symmetry of $\xi_{\alpha\beta}^{\mu\nu}$ can be revealed following Ref. [111] to be highly symmetric with respect to an interchange of its upper ($\mu\nu$) and lower ($\alpha\beta$) indices.

By assuming that the elements of the susceptibility tensor $\xi_{\alpha\beta}^{\mu\nu}$ are constant, the total differential of the Gibbs free energy density g can be represented in the following way [110]

$$dg = -\frac{c}{2} F_{\alpha\beta} dM^{\alpha\beta} = -\frac{1}{4\mu_0} F_{\alpha\beta} \xi_{\mu\nu}^{\alpha\beta} dF^{\mu\nu}, \quad (3.12)$$

where $dM^{\alpha\beta}$ was substituted by Eq. (3.6) and $F_{\alpha\beta}$ is defined as $F_{\alpha\beta} = \mathbf{g}_{\alpha\epsilon} \mathbf{g}_{\beta\eta} F^{\epsilon\eta}$. $\mathbf{g}_{\alpha\epsilon} = \mathbf{g}^{\alpha\epsilon}$ denotes the metric tensor, which takes the form

$$\mathbf{g}^{\alpha\epsilon} = \begin{pmatrix} +1 & 0 & 0 & 0 \\ 0 & -1 & 0 & 0 \\ 0 & 0 & -1 & 0 \\ 0 & 0 & 0 & -1 \end{pmatrix}, \quad (3.13)$$

using a Cartesian coordinate system. Since dg is a perfect differential, Eq. (3.12) yields

$$\frac{\partial g}{\partial F^{\mu\nu}} = -\frac{1}{4\mu_0} F_{\alpha\beta} \xi_{\mu\nu}^{\alpha\beta} = -\frac{1}{4\mu_0} \mathfrak{g}_{\alpha\varepsilon} \mathfrak{g}_{\beta\eta} F^{\varepsilon\eta} \xi_{\mu\nu}^{\alpha\beta}. \quad (3.14)$$

Furthermore, as the components of the electromagnetic fields B_i and E_i are treated as independent variables [111], Eq. (3.14) becomes

$$\frac{\partial^2 g}{\partial F^{\mu\nu} \partial F^{\varepsilon\eta}} = -\frac{1}{4\mu_0} \mathfrak{g}_{\alpha\varepsilon} \mathfrak{g}_{\beta\eta} \xi_{\mu\nu}^{\alpha\beta}. \quad (3.15)$$

A similar derivation yields

$$\frac{\partial^2 g}{\partial F^{\varepsilon\eta} \partial F^{\mu\nu}} = -\frac{1}{4\mu_0} \mathfrak{g}_{\alpha\mu} \mathfrak{g}_{\beta\nu} \xi_{\varepsilon\eta}^{\alpha\beta}. \quad (3.16)$$

Using the definition of a perfect differential, Eqs. (3.15) and (3.16) can be equated, which results in

$$\mathfrak{g}_{\alpha\varepsilon} \mathfrak{g}_{\beta\eta} \xi_{\mu\nu}^{\alpha\beta} = \mathfrak{g}_{\alpha\mu} \mathfrak{g}_{\beta\nu} \xi_{\varepsilon\eta}^{\alpha\beta}. \quad (3.17)$$

Employing the properties of the metric tensor $\mathfrak{g}_{\alpha\varepsilon} = \mathfrak{g}_{\varepsilon\alpha}$ in a Cartesian coordinate system, such as $\mathfrak{g}^{\gamma\varepsilon} \mathfrak{g}_{\varepsilon\alpha} = \delta_\alpha^\gamma$ with the four-dimensional Kronecker delta δ_α^γ ($\delta_\alpha^\gamma = 1$ for $\gamma = \alpha$ and $\delta_\alpha^\gamma = 0$ otherwise), Eq. (3.17) can be written as

$$\xi_{\mu\nu}^{\gamma\delta} = \mathfrak{g}^{\gamma\varepsilon} \mathfrak{g}^{\delta\eta} \mathfrak{g}_{\alpha\mu} \mathfrak{g}_{\beta\nu} \xi_{\varepsilon\eta}^{\alpha\beta}. \quad (3.18)$$

By choosing $\gamma = \mu = 0$ and $\delta \neq 0$, $\nu \neq 0$ as well as $\gamma \neq 0$, $\delta \neq 0$, $\mu \neq 0$, and $\nu \neq 0$, Eq. (3.18) reveals that $\xi_{\mu\nu}^{\gamma\delta}$ is symmetric with respect to an interchange of its upper ($\gamma\delta$) and lower ($\mu\nu$) indices. The former represents the situation of the electric susceptibility $\chi_{ij}^{(e)} = \xi_{0j}^{0i}$ (cf. Eq. (3.10)) and leads to the symmetry $\chi_{ij}^{(e)} = \chi_{ji}^{(e)}$:

$$\chi_{ij}^{(e)} = \xi_{0j}^{0i} = \mathfrak{g}^{0\varepsilon} \mathfrak{g}^{i\eta} \mathfrak{g}_{\alpha 0} \mathfrak{g}_{\beta j} \xi_{\varepsilon\eta}^{\alpha\beta} = \xi_{0j}^{0i} = \chi_{ji}^{(e)}. \quad (3.19)$$

The latter typifies the case of the magnetic susceptibility tensor $\chi_{ij}^{(m)}$ and reveals the same symmetry as for the electric susceptibility: $\chi_{ij}^{(m)} = \chi_{ji}^{(m)}$. Therefore, applying the intrinsic symmetry of $\xi_{\alpha\beta}^{\mu\nu}$ to the electric $\chi_{ij}^{(e)}$ and magnetic susceptibility $\chi_{ij}^{(m)}$ tensors, the well known symmetric behavior of these two tensors appears, reducing the independent components to six of either kind [112]. In contrast, Eq. (3.18) reveals that the magnetoelectric tensors $\chi_{ij}^{(me)}$ and $\chi_{ij}^{(em)}$ are not symmetric, but they are the transpose of one another $\chi_{ij}^{(me)} = \chi_{ji}^{(em)}$ (cf. Eq. (3.10)).

Thus, the magnetoelectric susceptibility tensors $\chi_{ij}^{(me)}$ and $\chi_{ij}^{(em)}$ include symmetric α_{ij} and antisymmetric $\alpha_{ij}^{(a)}$ parts:

$$\chi_{ij}^{(me)} = \alpha_{ij} + \alpha_{ij}^{(a)}. \quad (3.20)$$

The nonzero antisymmetric components $\alpha_{ij}^{(a)}$ can be identified with the presence of a toroidal moment \mathbf{T} [1, 113, 114]:

$$\chi_{ij}^{(me)} - \chi_{ji}^{(me)} = \chi_{ij}^{(me)} - \chi_{ij}^{(em)} \propto \varepsilon_{ijk} T_k. \quad (3.21)$$

	\mathbf{E}	\mathbf{P}	\mathbf{B}	\mathbf{M}	$\chi_{ij}^{(\text{me})}$	$\chi_{ij}^{(\text{em})}$	β_{ijk}	γ_{ijk}
\mathcal{P}_s	$-\mathbf{E}$	$-\mathbf{P}$	\mathbf{B}	\mathbf{M}	$-\chi_{ij}^{(\text{me})}$	$-\chi_{ij}^{(\text{em})}$	$-\beta_{ijk}$	γ_{ijk}
\mathcal{P}_t	\mathbf{E}	\mathbf{P}	$-\mathbf{B}$	$-\mathbf{M}$	$-\chi_{ij}^{(\text{me})}$	$-\chi_{ij}^{(\text{em})}$	β_{ijk}	$-\gamma_{ijk}$

Table 3.1: Electric \mathbf{E} and magnetic \mathbf{B} fields, order parameters (\mathbf{P} and \mathbf{M}), and magnetoelectric tensors ($\chi_{ij}^{(\text{me})}$, $\chi_{ij}^{(\text{em})}$, β_{ijk} , and γ_{ijk}) under space \mathcal{P}_s and time \mathcal{P}_t inversion. The table is adapted from Ref. [116].

The toroidal moment arises from at least two non-collinear magnetic moments, or spins in the elementary cell with opposite direction, i.e., magnetic vortices [1, 109, 115].²

Because the magnetoelectric tensors are not symmetric, nine independent components of $\chi_{ij}^{(\text{me})}$ and $\chi_{ij}^{(\text{em})}$ exist. However, the investigated crystal usually exhibits a certain symmetry, which further reduces the number of independent components. More fundamentally, the linear magnetoelectric effect is only observed in crystals, which break time and space symmetry. This is evident by examining the Gibbs free energy density g under space and time inversion. Using Eq. (3.12), g can be written as

$$-g = g_0 + \frac{1}{4\mu_0} F_{\alpha\beta} \xi_{\mu\nu}^{\alpha\beta} F^{\mu\nu}, \quad (3.22)$$

which yields in the linear response theory

$$-g = g_0 - \frac{1}{\mu_0 c^2} \chi_{ij}^{(\text{e})} E_i E_j + \frac{1}{\mu_0} \chi_{ij}^{(\text{m})} B_i B_j + \frac{1}{\mu_0 c} \chi_{ij}^{(\text{me})} B_i E_j + \frac{1}{\mu_0 c} \chi_{ij}^{(\text{em})} E_i B_j. \quad (3.23)$$

The magnetic and electric fields as well as the respective order parameters transform under space and time inversion, which can be described by the parity operators \mathcal{P}_s and \mathcal{P}_t , as shown in Table 3.1. Therefore, since the Gibbs free energy density g has to be invariant upon these transformations, the linear magnetoelectric effects can only be observed in states where both time reversal and space inversion symmetries are broken. This is a fundamental symmetry requirement for the observation of finite linear magnetoelectric effects. As an example, the simultaneous violation of time reversal symmetry and spatial inversion symmetry occurs in magnetically and ferroelectrically ordered systems. Higher order magnetoelectric effects, such as the electrobimagnetic β_{ijk} [117] and the magnetobielectric γ_{ijk} effects [118] are also included in Table 3.1. These effects can even be detected in systems with no magnetic order (β_{ijk}), exhibiting an even transformation under time reversal, or in centrosymmetric magnetic materials prohibiting spontaneous polarization (γ_{ijk}), leading to an even spatial symmetry. More details concerning higher order magnetoelectric coupling can be found in Refs. [119, 120]. Since higher-order effects can play an important role only at relative high fields or if the linear magnetoelectric tensor vanishes $\chi_{ij}^{(\text{me})} = \chi_{ij}^{(\text{em})} = 0$, these effects are neglected in the following.

²The existence of the toroidal moment T_k is still controversially discussed (see Ref. [109]).

The symmetry considerations discussed above do not allow to draw any conclusions about the strength of the magnetoelectric coupling. An upper bound on the magnitude of the linear magnetoelectric effect can be derived from the thermodynamic stability requirement. The free energy density of Eq. (3.23) must have a minimum at $\mathbf{E} = \mathbf{B} = 0$ so that the Hessian matrix has positive eigenvalues [121]. The Hessian matrix H_{ij} of $g(\mathbf{E}, \mathbf{B})$ reads

$$H_{ij} = \frac{2}{\mu_0 c} \begin{pmatrix} \frac{1}{c} \chi_{ij}^{(e)} & \frac{1}{2} \chi_{ij}^{(em)} \\ \frac{1}{2} \chi_{ij}^{(me)} & c \chi_{ij}^{(m)} \end{pmatrix}. \quad (3.24)$$

Equation (3.24) has to be positive definite, which leads to an upper limit of the magnetoelectric effect [115]:

$$\left| \chi_{ij}^{(em)} \right| \lesssim \sqrt{\chi_{ii}^{(e)} \chi_{jj}^{(m)}}. \quad (3.25)$$

A stronger condition can be obtained using second-order thermodynamic perturbation theory [11]:

$$\chi_{ij}^{(em)} < \sqrt{\chi_{ii}^{(e)} \chi_{jj}^{(m)}}, \quad (3.26)$$

where dielectric responses were neglected. Therefore, the linear magnetoelectric coupling is expected to be large in ferroelectric and/or ferromagnetic materials.³ It is worth noting that Eq. (3.26) is not a sufficient condition for the presence of linear magnetoelectric effects. These effects can also be observed in materials with $\chi_{ii}^{(e)} \chi_{jj}^{(m)} \ll 1$, such as antiferromagnets (e.g. Cr_2O_3) or frustrated spin systems. On the other hand, a high geometric mean of the corresponding electric and magnetic susceptibilities does not necessarily imply a large or even any linear magnetoelectric coupling.

3.3 Multiferroics

Equation (3.26) suggests that materials exhibiting simultaneously large electric $\chi_{ii}^{(e)}$ and magnetic $\chi_{jj}^{(m)}$ susceptibilities are good candidates for the appearance of a notable magnetoelectric effect. This requirement is fulfilled in most ferroelectric and ferromagnetic materials. Therefore, the search for compounds, which possess ferroelectric and ferromagnetic ordering in the same phase, is the main challenge in the field of intrinsic magnetoelectric materials. Such systems are called multiferroics:

“Crystals can be defined as multiferroic when two or more of the primary ferroic properties are united in the same phase.”

Hans Schmid

Primary ferroic properties can be defined following the nomenclature of Newnham [122] and Schmid [1, 22]. A ferroic crystal contains two or more possible orientation

³Note that a large $\chi_{ii}^{(e)}$ is not a prerequisite for a material to be ferroelectric (or vice versa), and similarly ferromagnets do not necessarily possess large $\chi_{jj}^{(m)}$.

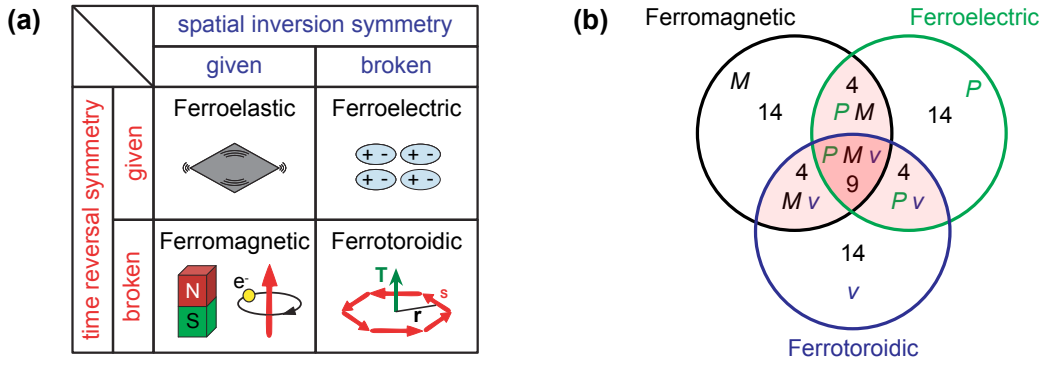


Figure 3.1: (a) Primary ferroic order parameter under space and time inversion according to Refs. [22, 123]. (b) In the absence of ferroelasticity, 31 point groups are possible in each primary ferroic state permitting a spontaneous polarization P_i^s , magnetization M_i^s , and toroidization T_i^s . Among these, 13 groups intersect allowing either a finite spontaneous polarization and magnetization, a finite magnetization and toroidization, or a finite polarization and toroidization in the same phase (light-red area). However, only 9 point groups admit all three kinds of primary ferroics (red area). Note that velocity v can be replaced by linear momentum p or spontaneous toroidization T_i^s with equal transformation properties [22].

states or domains, which can be switched from one state to another under a suitably chosen driving force. On the basis of this definition, four different primary ferroic properties, which are depicted in Fig. 3.1(a), can be identified with respect to space and time inversion. A ferroelastic crystal has two or more orientation states differing in spontaneous strain ϵ_{ij}^s . Using external mechanical stress, reversible switching between these states can be achieved. As evident from Fig. 3.1(a), ferroelasticity is invariant under both time and space inversion. In contrast, the ferroelectric order parameter, i.e., the spontaneous electric polarization P_i^s , changes sign under spatial inversion but remains invariant under time reversal. This results from the finite time independent charge separation created by the spontaneous electric polarization P_i^s . In contrast, ferromagnetism corresponds to a spontaneous magnetization M_i^s , a quantity that changes sign under time reversal but remains invariant under space inversion. As schematically shown in Fig. 3.1(a), we may consider the magnetic moments of atoms in a magnetic material to be the result of electric current loops, which reverse direction when time is reversed. The fourth primary ferroic state, ferrotoroidicity, changes sign under both space or time inversion in accordance with the magnetoelectric effect. The classical example of a toroidal moment is a solenoid that is bent into a torus. In this example, the current induces a circular magnetic field inside the solenoid, giving rise to a toroidal moment perpendicular to the magnetic field [115]. Figure 3.1(a) reveals that ferrotoroidicity does not only give rise to antisymmetric contributions to the magnetoelectric tensor $\chi_{ij}^{(me)}$ (cf. Eq. (3.21)), but seems to be an elementary part of primary ferroics.

In multiferroic materials, two or more of these ferroic properties are unified in the same phase. However, as Fig. 3.1(a) suggests, the occurrence of different ferroic ordering in the same compound requires symmetry constrictions. In the ab-

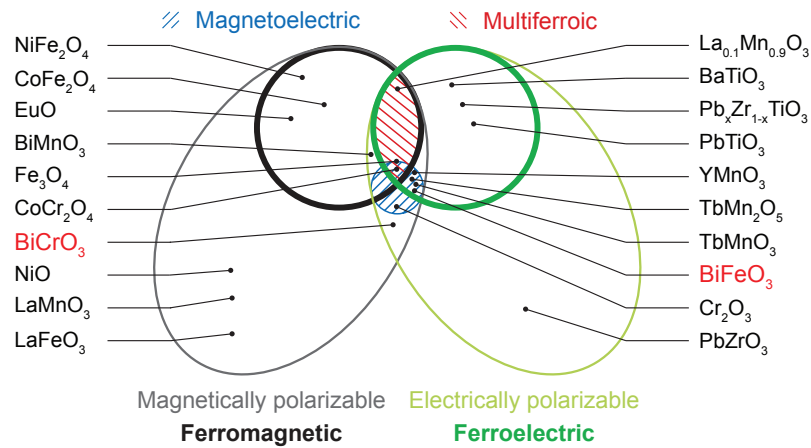


Figure 3.2: Classification of insulating oxides in terms of magnetical and electrical polarizability, after [8, 15]. The compounds BiFeO₃ and BiCrO₃, which are discussed in this part of the thesis, are marked in red.

sence of ferroelasticity, 31 point groups are possible in each primary ferroic state (see Fig. 3.1(b)) permitting a spontaneous polarization P_i^s , magnetization M_i^s , and toroidization T_i^s . Among these 31 point groups, 13 groups intersect allowing simultaneously either a finite spontaneous polarization P_i^s and magnetization M_i^s , a finite magnetization M_i^s and toroidization T_i^s , or a finite polarization P_i^s and toroidization T_i^s in the same phase. However only 9 point groups admit all three kinds of primary ferroics (M_i^s , P_i^s , and T_i^s) [22]. This low number reflects the rareness of multiferroic compounds.

Considering only magnetically and electrically polarizable materials, few compounds in the class of oxide materials are known to be multiferroic (see Fig. 3.2).⁴ Therefore the question arises, why there are so few magnetic ferroelectrics [19]? This can be answered regarding compounds with perovskite structure ABO_3 . In these materials, the transition metal d electrons, which are responsible for conventional magnetism, play an important role, since they reduce the tendency for off-center ferroelectric distortion. In ferroelectric materials (e.g. BaTiO₃) exhibiting no d electrons (d^0), the short range repulsion between adjacent electron clouds, which favors the paraelectric symmetric structure, is small and the bonding, which might stabilize the ferroelectric phase, is large. Therefore, even in the absence of an applied electric field, the stabilizing forces associated with the polarization of the ions when displaced are stronger than the short-range repulsive ion-ion interactions. Needless to note, that ferroelectric materials have to be electric insulators, which is fulfilled with d^0 . However, if there are no d electrons creating localized magnetic moments, no long range ferromagnetic ordering can exist [19]. Therefore, magnetic ferroelectrics seem to be chemically incompatible, since ferroelectricity is favored by d^0 -ness and conventional ferromagnetism requires d electrons. This conclusion is reflected in Fig. 3.2. Consequently, other mechanisms must be considered to create

⁴The dielectric and magnetoelectric behavior of BiMnO₃ is still discussed controversially.

ferromagnetism and ferroelectricity, respectively. However, a considerable number of compounds exhibiting a ferroelectric order are simultaneously magnetically polarizable. These materials are mainly antiferromagnetics/ferroelectrics. To incorporate these materials, the definition of the term multiferroic is commonly extended to include antiferroelectric and antiferromagnetic compounds.

Multiferroic materials can be further classified depending on the microscopic mechanism of ferroelectricity. Ferroelectric order can be caused by hybridization effects, geometric constraints and/or electronic degrees of freedom (spin, charge or orbital) [124]. In this thesis, we follow the classification of multiferroic compounds as introduced by Cheong and Mostovoy [25].

3.3.1 Lone pair multiferroics

Lone pair multiferroics based on the perovskite structure ABO_3 are characterized by A site ions with stereochemically active $6s^2$ lone-pairs ($A = Bi^{3+}, Pb^{2+}$). They cause hybridization between the $6p$ orbitals of the A site ion and the oxygen $2p$ orbitals and drive the off-centering of the B cation towards the neighboring anions resulting in ferroelectricity [125]. Examples of this class of multiferroics are the compounds $BiMO_3$ ($M = Cr, Fe$). However, since the ferroelectricity is caused by the A cations and the transition metal ions occupying the B site are responsible for magnetism, the multiferroic behavior is created by two different cations. Therefore, lone pair multiferroics are classified as split-order-parameter multiferroics. This leads, on the one hand, to strong magnetic and ferroelectric properties resulting in high transition temperatures, but on the other hand to a weak magnetoelectric coupling. However, recently an electric field induced spin flop in $BiFeO_3$ single crystals demonstrates the presence of a finite coupling between the antiferromagnetic and ferroelectric order parameters in $BiFeO_3$ [29]. Up to now, ferroelectrics or multiferroics with structural instabilities, which are mainly forced due to the electronic pairing or hybridization, are discussed. These materials can be classified as “proper” ferroelectrics. In contrast, spontaneous electric polarization of “improper” ferroelectrics appear as “side effect” of an existing ordering or of geometric constraints [25].

3.3.2 Geometric ferroelectrics

One group of improper ferroelectrics are geometric ferroelectrics leading to a multiferroic behavior. In these compounds, the ferroelectric instability has its origin in the topology of the chemical structure, and the ferroelectric distortions are driven by ionic size effects [124]. For example, in hexagonal manganites $RMnO_3$ ($R = Ho - Lu, Y$) a spontaneous electric polarization is induced by a nonlinear coupling to nonpolar lattice distortions, such as a buckling of $R-O$ planes or tilts of oxygen MnO_5 bipyramids [126]. These tilts and rotations of MnO_5 bipyramids lead to ferroelectricity due to the topology of differently charged ions in the distorted lattice. Therefore, the mechanism is driven entirely by electrostatic and size effects, rather than hybridization or significant charge transfer between cations and anions as it is the case in the usual “proper” ferroelectrics. In these geometric ferroelectrics,

the ferroelectricity can coexist with a magnetic order leading to geometric multiferroics. Since ferroelectric and magnetic order parameter are again not directly coupled, this class of materials can again be classified as split-order-parameter multiferroics, similar to lone-pair multiferroics. However, coupling between ferroelectric and antiferromagnetic domain walls was observed in YMnO_3 [127].

3.3.3 Electronic ferroelectrics

Multiferroicity can also be driven by different forms of charge ordering [128]. In this group of multiferroics, LuFe_2O_4 emerges as a prototype. Ferroelectricity is caused by ordering of Fe^{3+} (d^5) and Fe^{2+} (d^6) in an arrangement of polar symmetry in this mixed valence material [129, 130]. Similar to LuFe_2O_4 , recent theoretical and experimental results suggest the presence of charge ordering in Fe_3O_4 below the Verwey transition at around 120 K, but this is still controversially discussed (see Section 7.2.1). However, the finite polarization observed in Fe_3O_4 below 38 K [131] seems to be caused by “shifts” of electronic charges between octahedral Fe sites, leading to a noncentrosymmetric $\text{Fe}^{2+}/\text{Fe}^{3+}$ charge-ordered pattern [132]. Since the ferrimagnetic ordering of Fe_3O_4 already occurs below 840 K, the large difference in the magnetic and electric transition temperature suggests, that the magnetic and electric order parameters are only weakly coupled and Fe_3O_4 can again be classified as split-order-parameter multiferroic. Ferroelectricity induced by charge order constitutes an interesting and unexplored territory in the field of multiferroicity up to now [133].

3.3.4 Magnetic ferroelectrics

Magnetic ferroelectrics are the best candidates to achieve high magnetoelectric coupling, since ferroelectricity is induced by magnetic ordering in these materials. The magnetic ordering breaks inversion symmetry and induces a spontaneous polarization. Therefore, these materials can be classified as joint-order-parameter multiferroics. Within this class, magnetic ferroelectrics can be further divided into two sub-classes depending on whether or not the spin ordering is collinear. For example, $\text{Ca}_3\text{CoMnO}_6$ exhibits a collinear spin structure. In this system with a quasi one dimensional structure, the ions Co^{2+} and Mn^{4+} alternate along the chain with a magnetic up-up-down-down type structure. Since magnetostriction is different for ferro and antiferro bonds, the system distorts, breaking the inversion symmetry. This mechanism leads to unequal bonds. The different charges (Co^{2+} , Mn^{4+}) at the opposite ends of these dimers now induce a finite electric polarization, which was recently observed by Choi and coworkers [134]. Using a magnetic field, the electric polarization can nicely be modified confirming a larger magnetoelectric coupling.

The other sub-class consists of non-collinear magnetic ferroelectrics such as orthorhombic RMnO_3 with $R = (\text{Tb}, \text{Dy})$, MnWO_4 , and CoCr_2O_4 . RMn_2O_5 with $R = (\text{Tb}, \text{Dy}, \text{Y})$ also exhibits a weak non-collinear magnetic order, which is most probably not the origin, but rather the consequence of ferroelectricity [128]. In these compounds, the ferroelectricity is driven mainly by magnetostriction. However, in

non-collinear magnetic ferroelectrics, the magnetic ordering is inhomogeneous, i.e., $\mathbf{M}(\mathbf{r})$ varies over the crystal. This inhomogeneity can be caused due to magnetic frustration [135] leading to a magnetoelectric coupling term g in the Gibbs free energy density of the form [136]:

$$g_{\text{ME}}(\mathbf{r}) \propto \mathbf{P} \cdot \{ \gamma(\nabla\mathbf{M}^2) + \gamma' [\mathbf{M}(\nabla \cdot \mathbf{M}) - (\mathbf{M} \cdot \nabla)\mathbf{M}] + \dots \} . \quad (3.27)$$

Symmetry considerations reveal that Eq. (3.27) is invariant under time and space reversal, since the coupling consists of quadratic terms in \mathbf{M} , is linear in \mathbf{P} , and contains a gradient of \mathbf{M} . Note that the actual form of Eq. (3.27) depends on the symmetry of the lattice. The first term gives a surface contribution only when the free energy is integrated over the spatial coordinates and the polarization \mathbf{P} is assumed to be independent of \mathbf{r} [136]. The second term is called Lifshitz invariant. Since this term is linear in \mathbf{P} , it induces a finite electric polarization even for arbitrarily weak coupling γ' . However, for magnetic states, which have a center of inversion, such as sinusoidal density waves, Eq. (3.27) vanishes. In contrast, the coupling is nonzero for circular cycloidal spiral [135]. In the magnetic ferroelectric TbMnO_3 , giant magnetoelectric and magnetocapacitance effects were observed by Kimura and coworkers, demonstrating the large coupling in these joint-order-parameter multiferroics [26].

The same coupling described by Eq. (3.27) can lead to the converse effect. In compounds such as BiFeO_3 , where the ferroelectric order occurs first breaking the inversion symmetry, the magnetic order parameter can become modulated in space due to the Lifshitz invariant term.

The brief overview of intrinsic multiferroic materials demonstrates that multiferroicity can arise from various mechanisms. However, up to now, no material system has been found, which exhibits a strong coupling between the ferromagnetic and ferroelectric order parameter at room temperature.

Chapter 4

The intrinsic multiferroic material system BiMO_3 ($M=\text{Cr}, \text{Fe}$)

The previous chapter revealed that there are intrinsic multiferroic material systems exhibiting a pronounced magnetoelectric effect. However, this magnetoelectric coupling is restricted to low temperatures ($T \ll 100 \text{ K}$) in almost all of them. One exception is BiFeO_3 . This material system is one of the few known compounds, which possess long range ferroelectric and antiferromagnetic order well above room temperature being a key prerequisite for most applications. Although BiFeO_3 can be classified as split-order parameter multiferroic (cf. Section 3.3), a finite coupling between the antiferromagnetic order parameter and an applied electric field was observed in BiFeO_3 thin films [137] and single crystals [29], which can be exploited to modify the magnetization of an overlying ferromagnet through exchange bias [138]. This might pave the way to electrically writable spintronic devices such as spin valves or magnetic tunnel junctions [15]. Furthermore, the ferroelectric properties alone make BiFeO_3 very attractive in the field of lead-free ferroelectric random access memories [28]. These interesting physical properties have triggered a tremendous flurry of research interest in BiFeO_3 in the past few years (see, e.g., Ref [13]).

In contrast, BiCrO_3 is most likely not a technologically relevant multiferroic material, since the magnetic transition temperature of bulk BiCrO_3 of around 123 K is well below room temperature [139]. However, it is an ideal model material to elucidate the role of the Bi cation in driving structural phase transitions [33].

In this part of the thesis, we discuss the physical behavior of BiMO_3 ($M = \text{Cr}, \text{Fe}$) thin films with a particular focus on their magnetic and dielectric properties. Since these properties are strongly influenced by extrinsic effects such as parasitic phases, a detailed analysis of the crystalline quality of BiFeO_3 thin films grown on either SrRuO_3 -buffered SrTiO_3 as well as on Nb doped SrTiO_3 substrates is performed in the following. Furthermore, new aspects such as the magnetoelectric coupling at domain walls are addressed. In case of BiCrO_3 thin films, the lack of experiments on the physical properties makes a detailed investigation of the crystalline structure at different temperatures as well as of the dielectric and magnetic properties mandatory. In addition, the presence or absence of a finite magnetoelectric coupling in this compound is discussed.

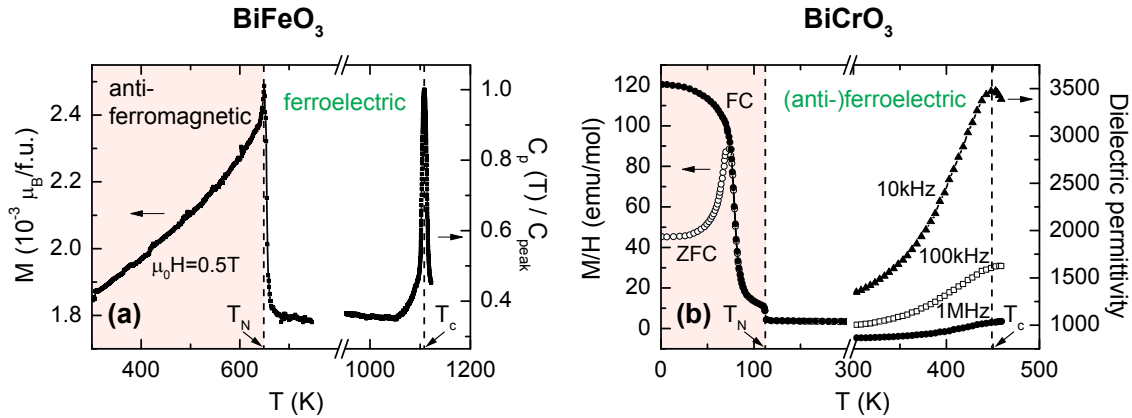


Figure 4.1: (a) Magnetization and normalized specific heat as a function of temperature measured on a BiFeO₃ polycrystalline bulk sample. The antiferromagnetic and ferroelectric transitions at around $T_N \approx 640$ K and $T_c \approx 1100$ K are clearly visible. (b) Magnetic and dielectric permittivity measurements carried out by Niitaka *et al.* [147] on bulk BiCrO₃. Two different transitions are observable at around $T_N \approx 120$ K and $T_c \approx 450$ K, respectively. The temperature region, in which the compounds exhibit a multiferroic behavior, is marked by the red shaded area.

4.1 The lone pair multiferroics BiMO₃ ($M=\text{Cr, Fe}$)

BiFeO₃ was first synthesized in 1957 by Royen and Swars [140]. In spite of numerous studies of mainly polycrystalline samples, the physical properties of BiFeO₃ remained the subject of controversial discussions over many years (see, e.g., Ref. [141] and references therein). The magnetic properties of BiFeO₃ were revealed by Fischer *et al.* [142], who demonstrate that BiFeO₃ possesses a compensated antiferromagnetic G -type structure below the Néel temperature of about $T_N = 670$ K with a cycloidal spin order, which is incommensurate with the lattice [143]. The electric characterization of bulk BiFeO₃ was also demanding, since the polycrystalline BiFeO₃ samples exhibit high leakage currents, which results in a low resistivity. The controversy about whether BiFeO₃ has a ferroelectric or antiferroelectric ground state was finally settled by Teague and coworkers [144]. A ferroelectric hysteresis loop was found in dielectric measurements carried out on BiFeO₃ single crystals, which is in agreement with a rhombohedral polar space group $R3c$ [27, 145]. This ferroelectric/ferroelastic phase was found to be stable up to 1123 K [146].

Figure 4.1(a) shows the temperature dependence of the magnetization measured using a SQUID magnetometer as well as the normalized heat capacity obtained by performing differential scanning calorimetry measurements of a polycrystalline BiFeO₃ sample, which is used as a target material for pulsed laser deposition. The magnetization reveals a paramagnetic-antiferromagnetic transition around $T_N \approx 640$ K. Furthermore, a first order transition at around $T_c \approx 1100$ K is observed in the normalized heat capacity measurements, which can be attributed to the paraelectric-ferroelectric phase transition. Therefore, BiFeO₃ exhibits a multiferroic behavior below 640 K in the sense of the simultaneous presence of ferroelectric and antiferromagnetic long-range order. However, due to the large difference be-

tween T_c and T_N , a weak linear magnetoelectric effect is expected. As discussed in Section 3.3, this is a direct consequence of the split-order-parameter in BiFeO_3 . However, recently, it was shown that the magnetic easy plane could be switched by changing the direction of the electric polarization [29–31], which enables to control the magnetic state by an applied electric field. In BiFeO_3 thin films, the pioneering work of Wang and coworkers has attracted a lot of attention [32], since they reported on the possibility to enhance the magnetic properties in BiFeO_3 thin films due to epitaxial strain. Even though this has not been verified by other groups, the research activities on BiFeO_3 thin films, which led to a better understanding of the physical properties in BiFeO_3 thin films as well as new methods to control the magnetization via electric fields, is still high [14].

Since bulk BiCrO_3 can only be synthesized at high pressure [37], a few reports on BiCrO_3 are available in literature. Sugawara and coworkers observed an antiferromagnetic phase below 123 K accompanied by a weak spontaneous moment due to spin canting [139]. The antiferromagnetic structure of BiCrO_3 was revealed by Belik *et al.* to be G -type [148]. In addition, a spin reorientation between 80 K and 60 K was recently found by Darie and coworkers [36]. In contrast to the magnetic properties of bulk BiCrO_3 , the dielectric behavior remains unclear. Niitaka *et al.* assumed a ferroelectric behavior below a structural phase transition from an orthorhombic $Pnma$ crystal symmetry at temperatures larger than 440 K to a monoclinic $C2$ structure below 420 K [147]. The magnetic properties and the dielectric permittivity measured by Niitaka *et al.* are shown in Fig. 4.1(b). A sudden rise of the magnetic susceptibility is visible at around 115 K. Furthermore, a frequency dependent anomaly of the dielectric permittivity at around 440 K was observed, which was interpreted as a transition from the paraelectric into the ferroelectric state. Therefore, BiCrO_3 seems to be multiferroic below around 115 K. However, up to now, no direct observation of a ferroelectric or antiferroelectric behavior of bulk BiCrO_3 has been reported in the literature, which is a direct consequence of the lack of the availability of high quality BiCrO_3 single crystals. The difficulties in the preparation of bulk BiCrO_3 samples can be avoided by using BiCrO_3 thin films, since the metastable BiCrO_3 phase can be stabilized by epitaxial strain. However, the availability of BiCrO_3 thin films also did not clarify the dielectric ground state of BiCrO_3 . Recently, Murakami and coworkers reported a ferroelectric behavior using piezoelectric force microscopy [149], while Kim *et al.* clearly observed an antiferroelectric double hysteresis using macroscopic contacts [34]. Furthermore, the crystal structure of BiCrO_3 thin films has not been clarified yet. Kim *et al.* and Murakami *et al.* found a triclinic structure of BiCrO_3 thin films [34, 150]. However, recently, David and coworkers detected different areas in the same thin film exhibiting either an orthorhombic or monoclinic symmetry at room temperature from transmission electron diffraction [151]. These results suggest that the intrinsic physical properties of BiCrO_3 thin films are difficult to obtain, which is mainly caused by the strong sensitivity of the dielectric and magnetic behavior on extrinsic effects, such as parasitic phases.

Evidently, high quality thin films are mandatory to reveal the magnetic and dielectric ground state of BiCrO_3 and BiFeO_3 . Therefore, we first discuss the growth process of BiMO_3 ($M = \text{Cr, Fe}$) thin films using pulsed laser deposition.

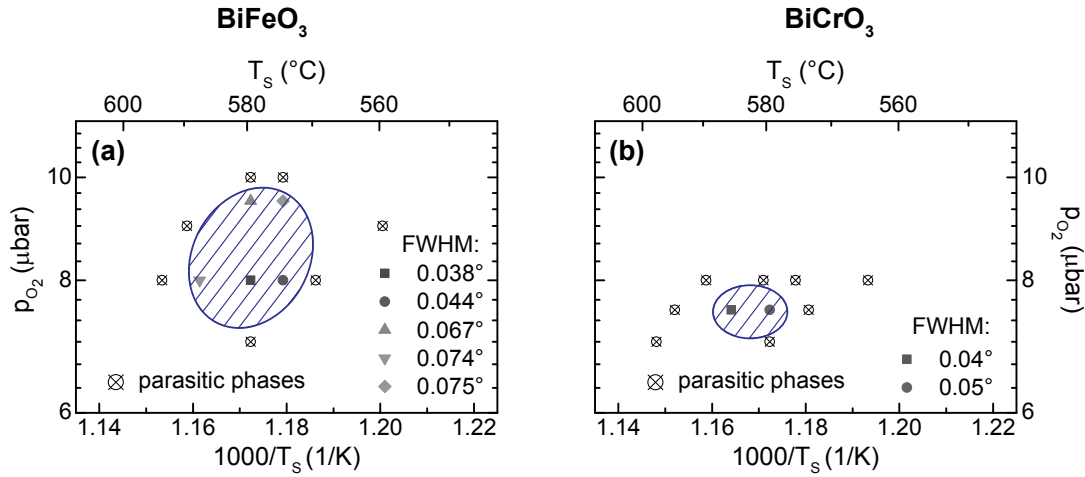


Figure 4.2: Pressure-temperature phase diagram for (a) BiFeO_3 and (b) BiCrO_3 thin films fabricated at different oxygen pressures p_{O_2} and substrate temperatures T_{S} . The blue shaded areas mark the growth window for single phase thin films. In addition, the full width at half maximum (FWHM) of the rocking curves around the pseudo-cubic $(001)_{\text{pc}}$ Bragg reflection is listed, indicating the quality of the single phase thin films.

4.2 Pulsed laser deposition of BiMO_3 ($M=\text{Cr, Fe}$) thin films

In the past years, various groups fabricated BiFeO_3 thin films under quite different growth conditions using different experimental techniques (see, e.g., Refs. [32, 152–156]) and various substrate materials (see, e.g., Refs. [32, 157–159]). In contrast, as mentioned above, only a few studies of BiCrO_3 thin films have been reported so far [34, 150, 151]. To get a better understanding of the physical properties of both material systems, BiMO_3 ($M = \text{Cr, Fe}$) thin films were fabricated using pulsed laser deposition (cf. Section 2.1.1).

4.2.1 Growth conditions

Since parasitic phases have great influence on the physical properties of BiMO_3 ($M = \text{Cr, Fe}$) thin films [38, 160], the proper deposition process of single phase thin films is an important task. In Fig. 4.2, the dependence of the growth conditions such as oxygen pressure p_{O_2} and substrate temperature T_{S} on the quality of BiMO_3 ($M = \text{Cr, Fe}$) thin films is shown. All thin films considered here were deposited on Nb:SrTiO_3 substrates using an energy density of 2 J/cm^2 on the target. Moreover targets with a nominal composition of $\text{Bi}_{1.15}\text{MO}_3$ ($M = \text{Cr, Fe}$) were used to prevent Bi deficiency in these thin films. Figure 4.2(a) reveals that single phase BiFeO_3 thin films were only achieved in a narrow temperature and pressure window. This is in agreement with the data reported by Béa *et al.* [38]. They identify the parasitic phases as $\gamma\text{-Fe}_2\text{O}_3$ and Bi_2O_3 . BiFeO_3 thin films with Bi_2O_3 impurities usually show large leakage currents, while Fe containing parasitic phases affect the magnetic properties. Furthermore, the quality of the single-phase thin

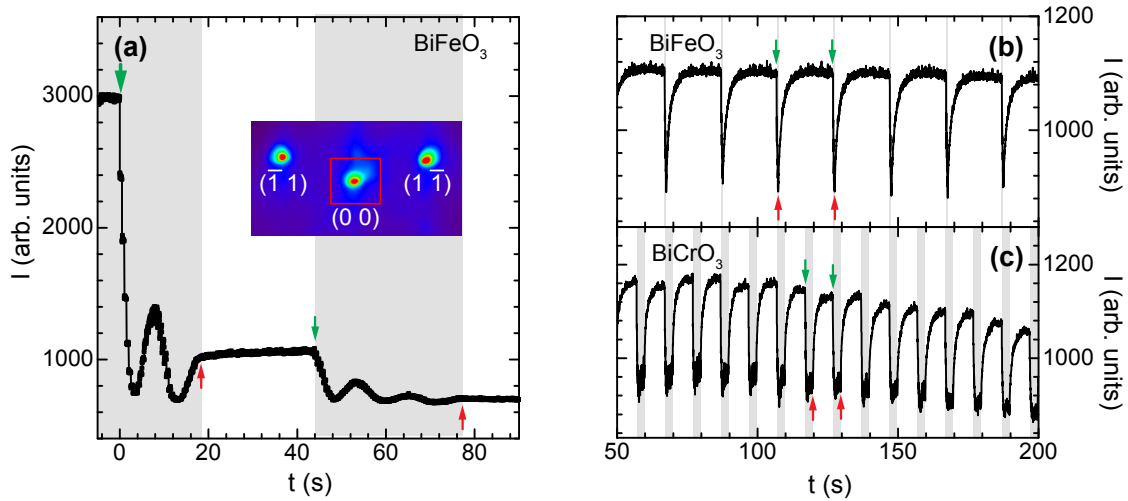


Figure 4.3: Reflection high energy electron diffraction (RHEED) intensity of the (00) reflection monitored during the growth of BiFeO_3 and BiCrO_3 thin films. The intensity was integrated within the area marked by the red rectangle in the RHEED pattern, which is shown in the inset of (a). The start and the end of each deposition sequence (indicated by the gray shaded areas) are marked by green and red arrows, respectively. (a) Growth of BiFeO_3 thin films using a continuous growth mode with a laser repetition rate of 2 Hz. The inset shows the RHEED pattern of the SrTiO_3 before the growth process. (b), (c) Imposed layer-by-layer growth mode of BiFeO_3 and BiCrO_3 thin films.

films is indicated in Fig. 4.2 by listing the full width at half maximum (FWHM) of the rocking curves around the pseudo-cubic $(001)_{\text{pc}}$ Bragg reflection. That is, single phase BiFeO_3 thin films with good crystalline quality were obtained using a substrate temperature of 852 K in pure oxygen atmosphere with a pressure of $8 \mu\text{bar}$. Note that within the deposition window for phase pure BiFeO_3 thin films, it was observed that the Bi/Fe ratio can vary with different oxygen pressures leading to different ferroelectric properties [161, 162].

The parameter window for single phase BiCrO_3 thin films is even more narrow (cf. Fig. 4.2(b)). This reflects the metastable nature of BiCrO_3 , which can be stabilized using epitaxial thin film growth techniques [163, 164]. In particular, a strong dependence on the oxygen pressure is observable. The optimum parameters were found to be $T_{\text{S}} = 858 \text{ K}$ and $p_{\text{O}_2} = 7.5 \mu\text{bar}$. Using SrRuO_3 as bottom electrode, a slightly higher oxygen pressure of $p_{\text{O}_2} = 8 \mu\text{bar}$ was found to be ideal for single phase BiCrO_3 thin films.

4.2.2 Imposed layer-by-layer growth

Defects such as misfit dislocations have an important impact on the properties of ferroelectric thin films [165]. Therefore, it is important to fabricate almost defect-free single crystalline thin films [166]. This requires not only a careful choice of the substrate material to avoid a high density of misfit dislocations due to a large lattice mismatch between the thin film and the substrate, but also appropriate growth parameters to achieve a two dimensional growth mode. Otherwise island boundaries or

even grain boundaries can form during the growth process affecting the ferroelectric properties of the thin film [167]. Furthermore, in order to be able to fabricate superlattices and heterostructures, where a control of the interfaces between the different layers on an atomic level is needed, a two dimensional layer-by-layer growth mode is a prerequisite. In case of BiMO_3 ($M = \text{Cr}, \text{Fe}$) thin films, the achievement of a two dimensional growth mode is a substantial challenge due to the Bi deficiency and the small temperature and pressure window of single phase thin films (cf. Fig. 4.2). Therefore, both the growth parameters and the Bi content in the target should be concurrently optimized.

As discussed in Section 2.1.2, reflection high energy electron diffraction (RHEED) is a powerful tool to investigate in-situ the growth process of BiMO_3 ($M = \text{Cr}, \text{Fe}$) thin films. In Fig. 4.3(a), the intensity evolution of the (00) reflection monitored by RHEED during the deposition of a BiFeO_3 thin film on a SrTiO_3 substrate is shown. The ideal growth conditions as discussed in the previous section as well as a laser repetition rate of $f_L = 2 \text{ Hz}$ were used for the deposition. When starting the deposition, two oscillations emerge ($0 \text{ s} < t < 18 \text{ s}$), which indicates a two dimensional layer-by-layer growth mode. After these oscillations, the deposition was stopped, allowing the surface to relax. During this time the RHEED intensity increases only weakly. Therefore, almost no relaxation of the surface takes place. Continuing the growth process at $t = 44 \text{ s}$, further damped oscillations are observed until the RHEED intensity vanishes nearly completely. Afterwards, the BiFeO_3 thin film starts to grow in a three dimensional growth mode due to the limited mobility of the adatoms at the given pressure and temperature, resulting in BiFeO_3 thin films with a large surface roughness. This situation can be improved by applying the imposed layer-by-layer interval deposition technique [168]. Here, one unit-cell is deposited in a very short time using a high laser repetition rate of at least $f_L = 6 \text{ Hz}$ followed by a break during which the deposited material can rearrange. Within this technique, a two dimensional layer-by-layer growth mode can be imposed, since only small islands are formed during the short deposition intervals due to the high supersaturation typical for pulsed laser deposition. As shown in Fig. 4.3(b) and (c), employing the imposed layer-by-layer interval deposition technique to the growth of BiMO_3 ($M = \text{Cr}, \text{Fe}$), the RHEED intensity stays almost constant during the whole deposition process, resulting in thin films with low surface roughness.¹

Employing the described techniques, a two dimensional growth mode can be achieved, which paves the way to fabricate single-phase thin films with good structural properties as well as heterostructures and superlattices in the future. Another important parameter for the realization of high quality multiferroic thin films is the choice of an adequate bottom electrode. In this sense, SrRuO_3 thin films as well as Nb:SrTiO_3 substrates were used in the course of this thesis.

¹In the case of BiFeO_3 , thin films with low surface roughness of around $0.4 \text{ nm}_{\text{RMS}}$ could also be fabricated using a very slow growth rate employing a laser repetition rate of $f_L = 0.5 \text{ Hz}$ in a continuous deposition mode.

4.3 SrRuO₃ as an electrode material

SrRuO₃ was employed as an electrode material in several oxide-based devices [5, 169, 170] due to its outstanding physical properties such as a highly crystalline growth on SrTiO₃ substrates [171], low resistivity at room temperature [172], good chemical and thermal stability [173, 174], and sharp and clean interfaces in oxide heterostructures [173, 175–177]. Moreover, SrRuO₃ thin films exhibit high work functions up to 5.0 eV [178]. Thus, SrRuO₃ electrodes are suitable for ferroelectric thin film capacitors reducing fatigue, imprint, and leakage currents [179–181].

The compound SrRuO₃ is a well known itinerant ferromagnet with a transition temperature of around 160 K [182, 183] and exhibits an orthorhombic GdFeO₃-type perovskite structure [184] below 600 K [185, 186] with a space group of $Pbnm$, which can be described by a $a^-a^-c^+$ tilted system according to Glazer [187]² and lattice constants of $a = 0.556$ nm, $b = 0.553$ nm, and $c = 0.784$ nm [188]. Moreover, SrRuO₃ has a metal like conductivity due to the strong hybridization of oxygen $2p$ -states with ruthenium d -states, which generates a narrow conduction band [189, 190]. With a conductivity at room temperature of $2.75 \times 10^{-4} \Omega\text{cm}$ and a carrier density of the order of 10^{22}cm^{-3} [191], it can be classified as a bad metal [192].

Since SrRuO₃ is used as an electrode material in the framework of this thesis, a detailed knowledge of the physical properties of our SrRuO₃ thin films is essential. Moreover, SrRuO₃ itself is still an interesting material system, justifying a detailed discussion of the structural, electric, and magnetic behavior of SrRuO₃ thin films in the following.

4.3.1 Growth and structural properties of SrRuO₃ thin films

Epitaxial SrRuO₃ thin films were deposited on TiO₂ terminated, (001)-oriented SrTiO₃ substrates by pulsed laser deposition using an energy density of 2J/cm^2 and a repetition rate of 2 Hz. The deposition was carried out at substrate temperatures of 873 K to 773 K and at a pressure of 0.1 mbar in pure oxygen atmosphere.

As an example of the growth process of SrRuO₃ thin films on SrTiO₃ substrates, Fig. 4.4 shows the evolution of the RHEED intensity of the (00) reflection monitored during the growth of a 29 nm thick SrRuO₃ film. The whole deposition can be separated into three main steps: At the beginning of the growth (cf. (I) in Fig. 4.4) five intensity oscillations are visible indicating a two dimensional layer-by-layer growth mode. Obviously, the oscillation periods are not equal in time. This can be attributed to a termination conversion from TiO₂-terminated SrTiO₃ substrate to a SrO-terminated SrRuO₃ layer [193], which is finished after the growth of one to five monolayers depending on the substrate temperature. Thereafter, the intensity increases slightly (cf. (II) in Fig. 4.4), before the RHEED intensity stays constant until

²The Glazer notation describes a tilted system by rotations of BO_6 octahedra. The notation specifies the magnitude and phase of the octahedral rotations. The letters indicate the magnitude of the rotation about a given axis, e.g., the letters a , b , and c imply unequal tilts about the x , y , and z axes. A superscript is used to mark the phase of the octahedral tilt: + denote the neighboring octahedral tilt in the same direction (in-phase), – implies that neighboring octahedral tilt in the opposite direction (out-of-phase), and 0 signifies no tilt about that axis.

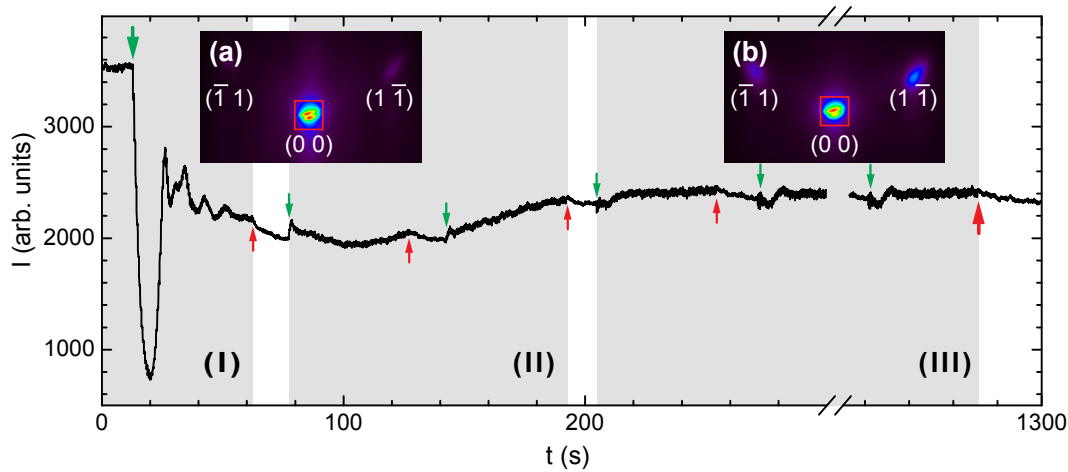


Figure 4.4: RHEED intensity evolution of the (00) reflection (marked by the red rectangle in the insets) monitored during the growth of a 29 nm thick SrRuO₃ film on a (001)-oriented SrTiO₃ substrate. The whole deposition can be separated into three sequences ((I)-(III)). The start and the end of the deposition of each sequence are marked by green and red arrows, respectively. The insets display the RHEED pattern (a) before and (b) after the deposition of a 29 nm thick SrRuO₃ film.

the deposition was stopped (cf. (III) in Fig. 4.4). Thus, the deposition of SrRuO₃ on SrTiO₃ substrates exhibits a transition from a two-dimensional layer-by-layer to a step-flow growth mode after the conversion in termination is complete. This transient behavior can be explained by an enhancement of the surface diffusivity and therefore different mobility of the adatoms deposited [194], as well as strain effects [195].

Since the RHEED technique is strongly surface sensitive (cf. Section 2.1.2), a low surface roughness can be revealed from the two RHEED patterns shown in the insets of Fig. 4.4. The left pattern (Fig. 4.4(a)) displays the diffraction from the TiO₂-terminated SrTiO₃ substrate at the beginning of the growth. This diffraction pattern reveals a splitting of the (00) spot indicating a SrTiO₃ substrate with a certain miscut angle [61]. From the splitting of the diffraction spot a terrace width of around 100 nm can be estimated. Looking closer to Fig. 4.4(b), which shows the diffraction pattern after the growth of 29 nm SrRuO₃, the splitting of the (00) spot is still observable, demonstrating a remaining step-terrace structure after the growth process. This provides evidence that SrRuO₃ thin films can be fabricated with a low surface roughness.

The SrRuO₃ thin films exhibit not only an excellent morphology but also a high crystalline quality. For example, the structural properties of a 22 nm thick SrRuO₃ film deposited on a SrTiO₃ (001) substrate investigated by x-ray diffraction (XRD) are shown in Fig. 4.5. The reciprocal space map and the corresponding q -scans around the SrTiO₃ (002) and SrRuO₃ (220) reflections depicted in the left and upper part of Fig. 4.5(a) reveal a coherent growth of SrRuO₃ on SrTiO₃. This is obvious through the observation of finite thickness fringes, which can be well re-

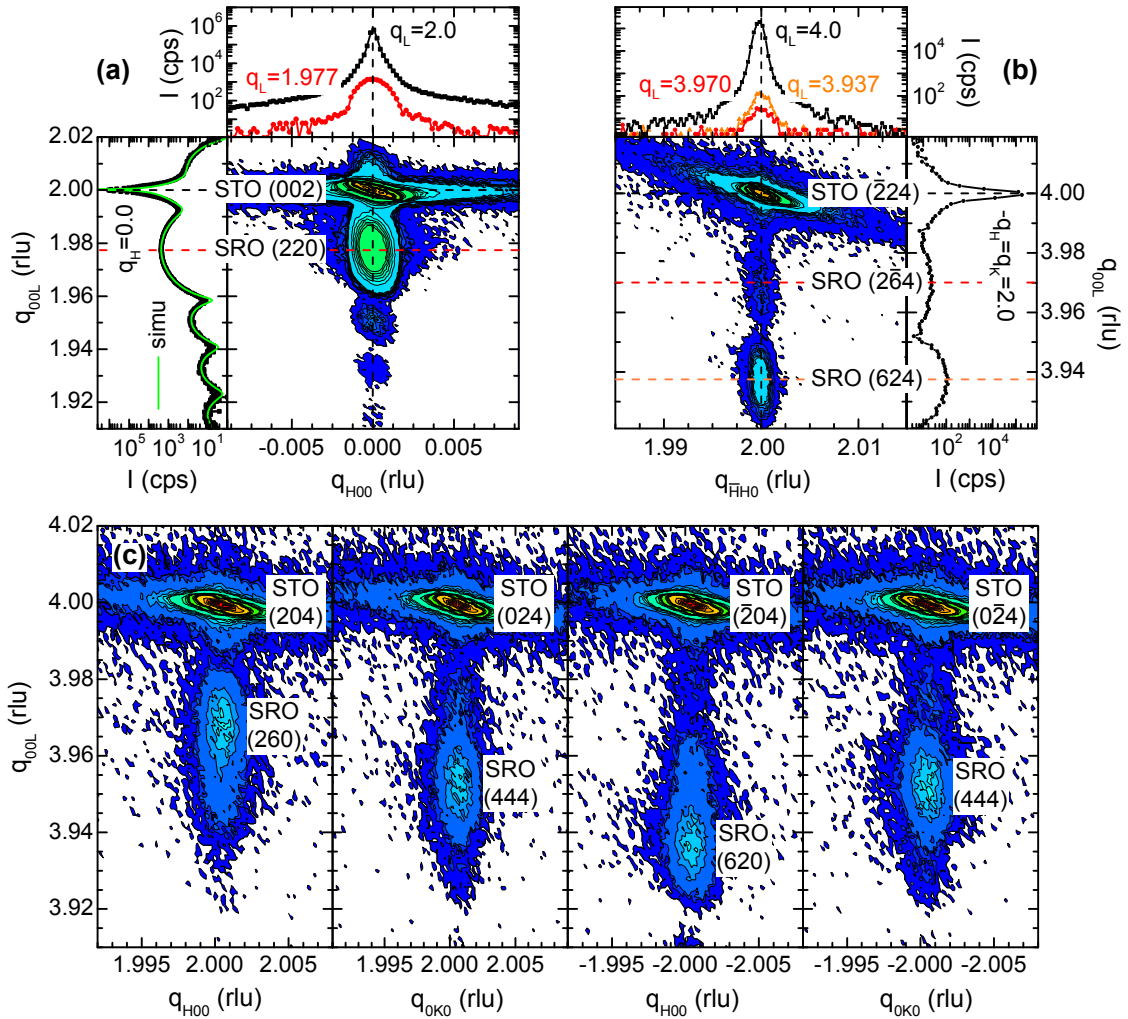


Figure 4.5: Reciprocal space maps and q -scans of a 22 nm thick SrRuO₃ (SRO) film grown on a SrTiO₃ (STO) substrate around (a) SrTiO₃ (002), (b) SrTiO₃ ($\bar{2}24$), and (c) SrTiO₃ (204) carried out under different in-plane orientations of the sample. The finite thickness fringes visible in the q_{00L} -scan around the SrRuO₃ (220) reflection in the left panel of (a) are well reproduced in a simulation using the software LEPTOS (green line).

produced using the software LEPTOS (cf. green line in Fig. 4.5(a)) [196]. The perfect agreement between simulation and experiment proves that there is no inhomogeneous strain relaxation in the out-of-plane direction. Moreover, the overall thickness of 22 nm measured using X-ray reflectometry (not shown here) and the thickness revealed by the simulation are identical. This demonstrates a coherent crystalline growth over the whole thickness of the SrRuO₃ thin film. Furthermore, the SrRuO₃ thin film reveals a low mosaic spread, which can be quantified by the full width at half maximum (FWHM) of the rocking curve around the pseudo-cubic SrRuO₃ (220) Bragg reflection. A value of 0.04° is obtained, demonstrating a good crystalline quality of the SrRuO₃ thin film.

The symmetry of the SrRuO₃ thin films is investigated employing x-ray diffraction

measurements around the SrTiO_3 ($\bar{2}24$) (Fig. 4.5(b)) and SrTiO_3 (204) (Fig. 4.5(c)) reflections under different in-plane orientations of the sample. These measurements suggest an orthorhombic symmetry of the SrRuO_3 thin films. The difference of the q_L -values of the SrRuO_3 (260) and the (620) reflections corresponds to a dissimilarity of the a and b lattice parameters in the orthorhombic symmetry. Furthermore, a finite intensity at the Bragg position of the SrRuO_3 (211) reflection (not shown here) was observed, which is an indication for an orthorhombic symmetry [197]. However, angular resolved magnetoresistance measurements carried out near the Curie temperature of SrRuO_3 suggest a monoclinic symmetry rather than an orthorhombic one.³ This would be in agreement with the results published recently by Ziese *et al.* [198] and theoretical considerations, in which the 90° angle in the out-of-plane direction is altered by epitaxial strain [199]. However, using x-ray diffraction, no indication for a monoclinic symmetry could be found. Thus, the SrRuO_3 thin films will be described in the orthorhombic symmetry in the following.

In principle, if SrRuO_3 is deposited on cubic (001)-oriented SrTiO_3 substrates, three different types of domains can exist. The SrRuO_3 thin film can grow epitaxially with its (001), (110), or ($\bar{1}\bar{1}0$) planes parallel to the SrTiO_3 (001) surface [200]. Therefore, there exist three different domain types (Fig. 4.6) resulting in six domains in total [200]. For multilayers using SrRuO_3 as bottom electrode or buffer layer, it is important to fabricate twin free SrRuO_3 thin films exhibiting a single crystallographic orientation. Otherwise the multidomain state induces crystalline defects like grain boundaries in the thin film deposited on top of the SrRuO_3 layer. Moreover, an existing multidomain state in the SrRuO_3 thin film affects the physical properties of the SrRuO_3 thin film itself [201]. Interestingly, the number of domains formed in SrRuO_3 thin films strongly depends on the surface morphology of the substrate used for the thin film process. While in SrRuO_3 thin films deposited on nominally exact SrTiO_3 (001) substrates with a miscut angle lower than 0.1° , X - and Y -type domains are formed, crystallographically single-domain SrRuO_3 thin films were obtained on SrTiO_3 (001) substrates exhibiting large miscut angles of up to 4° [171, 202]. Z -type domains are not detected in SrRuO_3 thin films grown on SrTiO_3 (001) substrates [200], but all three types of domains coexist in epitaxial SrRuO_3 thin films on LaAlO_3 (001) substrates [203]. Contrary to these accepted observations, recent publications show that a single domain state can also be achieved in fully strained epitaxial SrRuO_3 thin films deposited on nominal exact SrTiO_3 (001) substrates [197, 204]. In the course of this thesis, SrTiO_3 (001) substrates with different miscut angles were used. SrRuO_3 thin films grown on top of SrTiO_3 substrates with miscut angles larger than 0.5° were found to be almost single domain with a ratio of X - and Y -type domains of less than 5%.⁴ Unfortunately, Φ -scans around the SrRuO_3 (221) reflection reveal a broad mosaic in-plane distribution of more than 1° in these thin films. In contrast, the in-plane mosaic spread is reduced to less than 0.2° in SrRuO_3 thin films grown on SrTiO_3 (001) substrates

³See the diploma thesis of Daniel Pantel, for more details on angular resolved magnetoresistance measurements on our SrRuO_3 thin films [70].

⁴Since the miscut angle could only be detected using diffraction techniques such as XRD and RHEED, it exhibits a high degree of uncertainty.

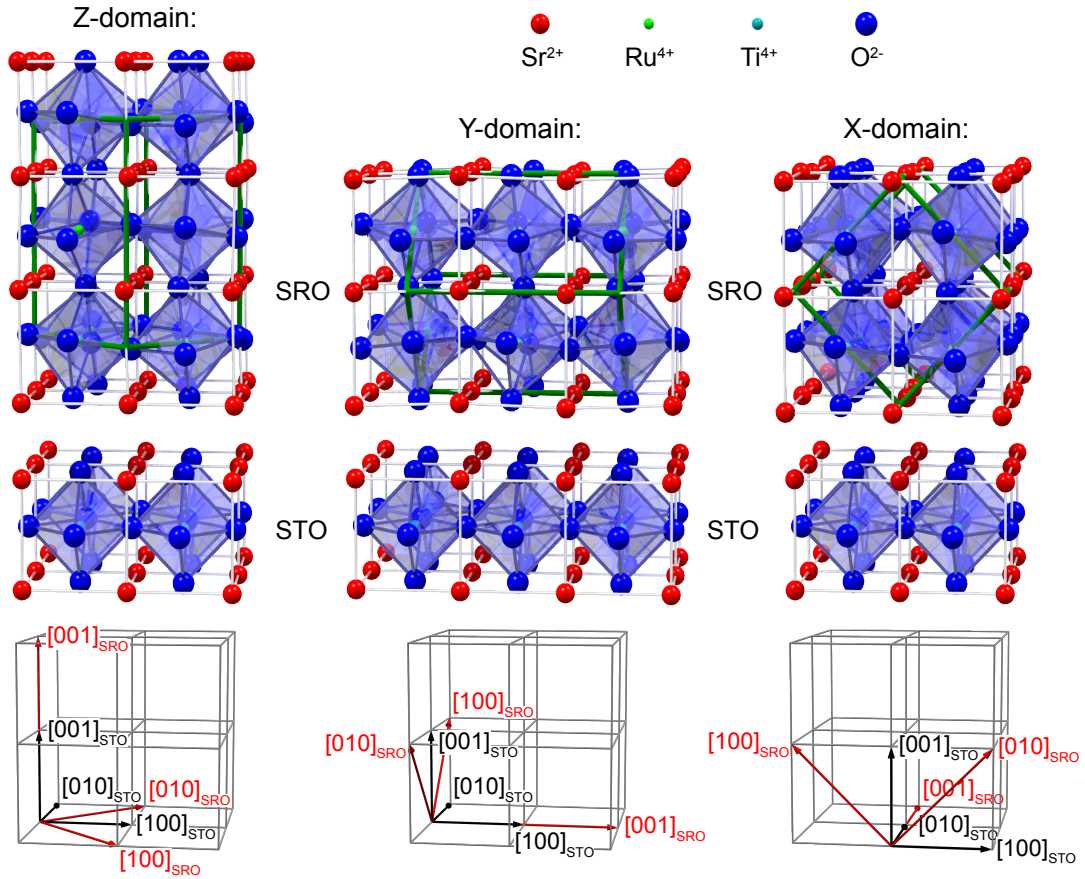


Figure 4.6: Epitaxial relation of orthorhombic SrRuO₃ thin films on (001)-oriented SrTiO₃ substrates. The primitive orthorhombic unit cell is marked by green lines. In general, three different types of domains (Z-, Y-, and X-domain) can be formed simultaneously during the deposition. Each of them can have two different in-plane orientations, resulting in six different domains in total [200]:

$$\begin{aligned}
 \text{Z-domain:} & \text{SrRuO}_3 [100] \parallel \text{SrTiO}_3 [110] \text{ and } \text{SrRuO}_3 [010] \parallel \text{SrTiO}_3 [\bar{1}\bar{1}0] \\
 \text{Z'-domain:} & \text{SrRuO}_3 [100] \parallel \text{SrTiO}_3 [110] \text{ and } \text{SrRuO}_3 [010] \parallel \text{SrTiO}_3 [110] \\
 \text{Y-domain:} & \text{SrRuO}_3 [001] \parallel \text{SrTiO}_3 [100] \text{ and } \text{SrRuO}_3 [\bar{1}\bar{1}0] \parallel \text{SrTiO}_3 [010] \\
 \text{Y'-domain:} & \text{SrRuO}_3 [001] \parallel \text{SrTiO}_3 [100] \text{ and } \text{SrRuO}_3 [\bar{1}\bar{1}0] \parallel \text{SrTiO}_3 [010] \\
 \text{X-domain:} & \text{SrRuO}_3 [001] \parallel \text{SrTiO}_3 [010] \text{ and } \text{SrRuO}_3 [\bar{1}\bar{1}0] \parallel \text{SrTiO}_3 [100] \\
 \text{X'-domain:} & \text{SrRuO}_3 [001] \parallel \text{SrTiO}_3 [010] \text{ and } \text{SrRuO}_3 [110] \parallel \text{SrTiO}_3 [100]
 \end{aligned}$$

The epitaxial relation between the SrRuO₃ (SRO) and the SrTiO₃ (STO) unit cell of each domain type is depicted in the lower part of the figure.

with miscut angles smaller than 0.5°.⁵ This observation is in agreement with Kim *et al.* [205] and might be explained by in-plane strain relaxation processes [205]. Since a perfect crystalline quality, which requires both a low mosaic spread and a crystalline single domain state, is mandatory for a buffer material in epitaxial growth, SrRuO₃ thin films with a finite but low density of secondary domains are used in the following. To determine the density of X- and Y-type domains, reciprocal lattice mappings around SrTiO₃ (204) and SrTiO₃ ($\bar{2}24$) were used. The splitting of

⁵SrTiO₃ (001) substrates exhibiting miscut angles larger than 0.5° were fabricated in-house and do not have a well defined in-plane orientation of the miscut.

the SrRuO₃ (624) and the SrRuO₃ (620) reflections displayed in Figs. 4.5(b) and (c) discloses the existence of 90° rotated double domains. From these measurements, the ratio between the *X*- and *Y*-type domains can be estimated to be around 15% in this sample.

In total, SrRuO₃ thin films with excellent crystalline quality were deposited on SrTiO₃ (001) substrates using pulsed laser deposition. The evolution of the RHEED intensity monitored during the growth process reveals a two-dimensional growth, which results in SrRuO₃ thin films with low surface roughness. Detailed x-ray diffraction measurements disclose a crystalline *X*- and *Y*-type multidomain state with a density of secondary domains of around 15%.

4.3.2 Magnetic and transport properties of SrRuO₃ thin films

As SrRuO₃ thin films are used as bottom electrodes for multilayer systems, which are magnetic and dielectric in one phase, the knowledge of not only the electric but also the magnetic behavior is essential. Therefore, in the following, the magnetic and transport properties of a 22 nm thick SrRuO₃ film are discussed in detail (cf. Fig. 4.7).

Since the x-ray diffraction measurements considered in the previous chapter revealed that our SrRuO₃ thin films are fully strained and exhibit an orthorhombic symmetry, the notation of the crystallographic directions is related to this symmetry in the following. Furthermore, the SrRuO₃ thin films are considered as crystallographic single-domain, exhibiting only orthorhombic *X*-type domains (cf. Fig. 4.6). Note that the crystalline symmetry has great influence on the magnetic and transport properties of SrRuO₃ due to a pronounced spin-orbit coupling [206].

The temperature dependence of the remanent magnetization measured after cooling the sample from 300 K to 5 K in a magnetic field of $\mu_0 H_{FC} = 7$ T reveals a Curie temperature of (139 ± 1) K (cf. Fig. 4.7(a)). This is significantly lower than the Curie temperature $T_C \approx 160$ K of SrRuO₃ single crystals [207]. We attribute this mainly to strain effects in the SrRuO₃ thin film. The compressive strain imposed by the epitaxial growth of SrRuO₃ on SrTiO₃ (001) substrates is likely to affect the distortion of the RuO₆ octahedra [208] leading to a decrease of the transition temperature [209, 210]. The magnetic remanence as a function of temperature measured in the [110] direction follows the scaling law $M = C(T_C - T)^\beta$ around the transition temperature T_C with a critical exponent of $\beta = (0.33 \pm 0.01)$. This value lies in between the theoretical ones for a 3D Heisenberg-type and Ising-type ferromagnet and is in good agreement with $\beta = 0.34$ reported by Kats *et al.* [211]. However, the magnitude of the critical exponent is still discussed controversially in the literature [212–215], indicating a strong dependence of the critical exponent on different domain structure, orientation, and strain effects. The inset of Fig. 4.7(a) shows the magnetic remanence measured along the [110] direction as a function of $T^{\frac{3}{2}}$ in the low temperature limit ($T \lesssim 50$ K). Obviously, the magnetization follows the Bloch's law $M(T) = M(0) - A \cdot T^{\frac{3}{2}}$, which confirms the dominance of spin-wave excitations on the magnetization in this temperature range. However, no further suppression of the magnetization due to Stoner excitations is observable [192]. By comparing the

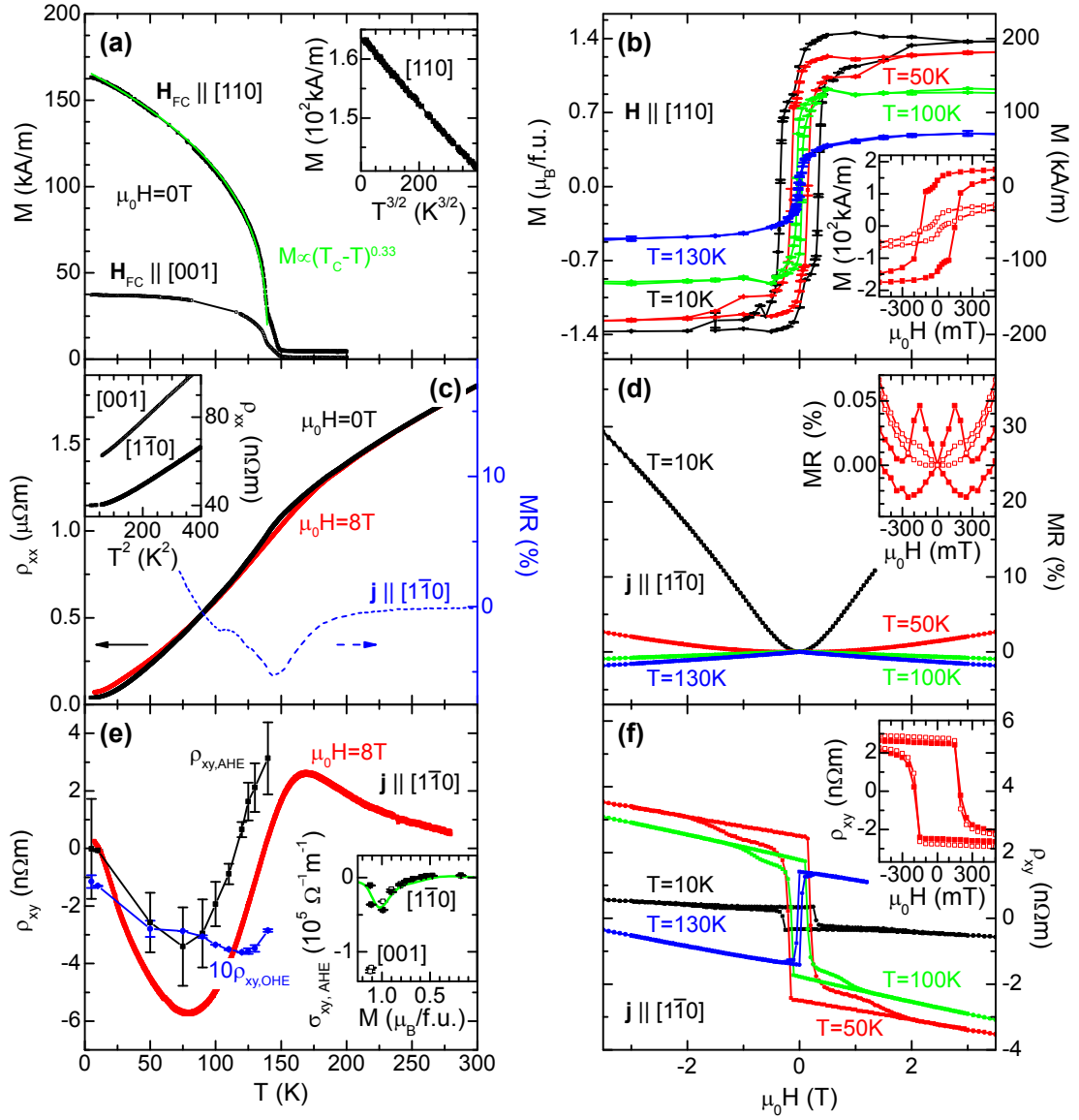


Figure 4.7: Magnetic and electric properties as a function of temperature and magnetic field of a 22 nm thick SrRuO₃ film. (a) Temperature dependence of the magnetic remanence measured along [110] (full symbols) and [001] (open symbols) after field cooled in a magnetic field of $\mu_0 H_{FC} = 7$ T. The magnetic behavior for $\mathbf{H}_{FC} \parallel [110]$ follows the scaling law $M = C(T_C - T)^\beta$ with a critical exponent of $\beta = (0.33 \pm 0.01)$ (green solid line) and can be described within Bloch's law at low temperatures (see inset of (a)). (b) Magnetic hysteresis loops obtained with $\mathbf{H} \parallel [110]$ (full symbols) and $\mathbf{H} \parallel [001]$ (open symbols) at different temperatures reveal a strong magnetic anisotropy in SrRuO₃ (see inset of (b)). The transport properties are displayed in (c)-(f) for different temperatures and external magnetic fields. The current density \mathbf{j} was applied along $[1\bar{1}0]$ (full symbols) and $[001]$ (open symbols). The magnetoresistance is defined as $MR = (\rho_{8T} - \rho_{0T}) / \rho_{8T}$. Our anomalous conductivity $\sigma_{xy,AHE}$ data (symbols) are described by first-principles calculations (green line) adapted from Ref. [206] (inset of (e)). The calculated transverse conductivity $\sigma_{xy,AHE}$ is multiplied by a factor of 2.5 with respect to the calculations in Ref. [206].

projection of the magnetization measured along the [110] and [001] crystallographic orientations, a pronounced magnetic anisotropy in the SrRuO₃ thin film is visible (cf. Fig. 4.7(a)). This is obvious due to the considerable difference in the magnetic remanence for $\mathbf{H}_{\text{FC}} \parallel [110]$ and $\mathbf{H}_{\text{FC}} \parallel [001]$ and suggests an easy axis close to the out of plane [110] direction.

The magnetic field dependence of the magnetization along the [110] direction for different temperatures is depicted in Fig. 4.7(b). The diamagnetic contribution of the SrTiO₃ substrate was determined from the high-field slope ($\mu_0 H \geq \pm 5$ T) of the hysteresis and subtracted from the total magnetic moment (cf. Section 2.3.1). The $M(H)$ loops are rather square-like indicating a magnetic easy axis, which is close to this direction. Furthermore, the saturation magnetization M_s reaches (200 ± 2) kA/m at 10 K, which corresponds to $1.3 \mu_B/\text{f.u.}$. Assuming a valence state of Ru⁴⁺ in a simple ionic picture and a low spin configuration, a maximum moment of $2 \mu_B$ is expected. More sophisticated calculations using density functional theory predict a magnetic moment of $0.98 \mu_B/\text{f.u.}$ for strain free SrRuO₃. By applying a compressive (tensile) stress this value is expected to moderately decrease (increase) by about $0.4 \mu_B/\text{f.u.}$ [199]. However, in the literature saturation magnetizations of $(1.1 - 2.0) \mu_B/\text{f.u.}$ (see, e.g., Refs. [198, 215]) or even higher values [216] are reported. This large variation of saturation magnetization values can be explained by the strong dependence of the magnetic properties of SrRuO₃ thin films on strain effects [208], domain effects [217], and non-stoichiometry [218]. The inset of Fig. 4.7(b) shows two different hysteresis loops measured with $\mathbf{H} \parallel [110]$ (cf. full symbols in Fig. 4.7(b)) and $\mathbf{H} \parallel [001]$ (cf. open symbols in Fig. 4.7(b)) at 50 K. At 130 K no difference of the measurements along the two orientations is observable (not shown here), which indicates an isotropic magnetic behavior close to the Curie temperature. Cooling down to 50 K the magnetic anisotropy becomes dominant. While [110] is close to an easy direction of the magnetization, the in-plane direction [001] is not an energetically favorable one. This prevents the magnetization to saturate along this direction at lower temperatures ($T \leq 130$ K) and at all external magnetic fields ($\mu_0 H \leq 7$ T) available in the magnetometer. Therefore, the method described in Section 2.3.1 to eliminate diamagnetic and paramagnetic parts stemming from the SrTiO₃ substrate and the sample holder is no longer appropriate for measurements along this crystallographic direction. Here, the diamagnetic and paramagnetic contributions measured in the paramagnetic regime at $T = 200$ K were used to detract the measured data neglecting the temperature dependence of these parts.⁶ In principle, magnetic hysteresis loops are sensitive not only to intrinsic properties, but also to impurities, grain boundaries, and defect structures, which largely influence the coercive field $\mu_0 H_c$. On the one hand, the small value of $\mu_0 H_c = (340 \pm 10)$ mT measured at 10 K along the [110] direction, which is in good agreement with previously reported values [198, 215, 216], indicates a low density of pinning centers. On the other hand, some anomalies are visible close to the coercive field of SrRuO₃ (cf. inset of Fig. 4.7(c)), which are also observed by several other groups [215, 217]. These anomalies could be explained by Barkhausen jumps [215] or might be caused by

⁶This method was only applied for temperatures larger than 50 K, since this assumption does no longer hold at low temperatures.

magnetization rotation towards the [110] direction, since it was found that the easy axis and the [110] direction encloses a finite angle, which is strongly temperature dependent [198].

To get further information on the quality of our SrRuO₃ thin films, the temperature and field dependence of the resistivity were investigated (cf. Figs. 4.7(c)-(f)). For this purpose, the SrRuO₃ thin film was patterned into a 375 μm long and 50 μm wide Hall bar and the resistance was recorded in a standard four-point measurement technique. The measurements were carried out with the external magnetic field \mathbf{H} applied along the out of plane [110] direction and with the current density \mathbf{j} flowing along [1 $\bar{1}$ 0] and [001]. The longitudinal resistivity ρ_{xx} as a function of temperature T measured at $\mu_0 H = 0$ T decreases from $\rho_{300\text{K}} = (1.725 \pm 0.001) \mu\Omega\text{m}$ at 300 K to $\rho_{5\text{K}} = (0.062 \pm 0.002) \mu\Omega\text{m}$ at 5 K with a clear discontinuity at the Curie temperature T_C (cf. Fig. 4.7(c)). An important parameter to identify the quality of SrRuO₃ thin films is the residual resistivity ratio defined as $RRR = \rho_{300\text{K}}/\rho_{5\text{K}}$. This value is very sensitive to changes in stoichiometry [219] and any disorder effects [172]. Here, a high RRR value of 27 is obtained, which compares well with the value of 26 found in stoichiometric SrRuO₃ thin films by Siemons *et al.* [219]. For comparison, a value of $RRR = 51$ is reported for high quality single crystals [183] and $RRR = 5 - 7$ for Ru-deficient SrRuO₃ thin films [219]. Note that for the majority of SrRuO₃ thin films in the literature values less than 11 are found (see, e.g., Refs. [172, 198, 208, 212]), demonstrating that our SrRuO₃ thin films are highly stoichiometric and exhibit a low amount of disorder effects. The low temperature behavior of the resistivity measured with $\mathbf{j} \parallel [1\bar{1}0]$ and $\mathbf{j} \parallel [001]$ is depicted in the inset of Fig. 4.7(c). Clearly, no up-turn of the resistivity down to 4 K due to localized carriers is detectable in both measurements, indicating a SrRuO₃ thin film with low density of impurities [192, 220]. Furthermore, the resistivity values for $\mathbf{j} \parallel [001]$ are larger than those for $\mathbf{j} \parallel [1\bar{1}0]$. This can be explained by magnetic domain wall scattering, since the domain walls are preferential orientated along the [1 $\bar{1}$ 0] direction [221, 222]. In addition to the resistivity measured at $\mu_0 H = 0$ mT, the temperature dependence resistivity obtained with an applied magnetic field of $\mu_0 H = 8$ T is displayed in Fig. 4.7(c). Obviously, the discontinuity at the Curie temperature T_C is suppressed. Therefore, the negative magnetoresistance $MR = \frac{\rho_{8\text{T}} - \rho_{0\text{T}}}{\rho_{8\text{T}}}$ near the Curie temperature T_C (cf. dashed line in Fig. 4.7(c)) can be qualitatively understood as being related to spin dependent scattering and the suppression of spin fluctuations [223]. Below $T < 60$ K, the MR becomes positive, which we attribute to mean free path shortening due to the Lorentz force and is more pronounced in samples with low residual resistivities. However, the positive MR calculated using a mean free path of 45 nm and a Larmor radius of 900 nm reveal a MR value of $MR \approx 0.0025$ [224]. This value is obviously too small to explain the experimental data. The discrepancy could be resolved by taking into account more than one type of carriers and band structure effects [224]. The magnetic field dependence of the magnetoresistance for different temperatures is shown in Fig. 4.7(d). In agreement with Fig. 4.7(c), the change in sign of the MR takes place between 100 K and 50 K. Furthermore, the pronounced positive MR at 10 K does not show a H^2 dependence expected for a MR caused by Lorentz forces. This further proves that the positive MR is dominated

by band structure effects. The anisotropic behavior of the MR effect is also visible in the inset of Fig. 4.7(c). Here, the magnetoresistance measured with $\mathbf{j} \parallel [001]$ (open symbols) and $\mathbf{j} \parallel [1\bar{1}0]$ (full symbols) at $T = 50$ K is displayed. The difference of both curves can be explained in terms of magnetic anisotropy [198] as well as a preferential orientation of the magnetic domain walls in SrRuO_3 [221, 222].

In addition to the above described physical properties, the extraordinary Hall effect in SrRuO_3 exhibiting a non-monotonic temperature dependence makes SrRuO_3 very interesting in the condensed-matter community. The transverse resistivity ρ_{xy} of SrRuO_3 measured at $\mu_0 H = 8$ T with $\mathbf{j} \parallel [1\bar{1}0]$ is displayed in Fig. 4.7(e) as a function of temperature. A finite value of ρ_{xy} can be observed even above the Curie temperature, exhibiting a Curie-Weiss like behavior. This indicates the existence of localized magnetic moments in the paramagnetic phase [225, 226]. Below the Curie temperature, the resistivity has a non-monotonic temperature dependence, including a change of sign. This unusual behavior is also visible in the magnetic field dependence of the transverse resistivity depicted in Fig. 4.7(f). Note that the shoulder in the resistivity for magnetic fields larger than the coercive field is also present in the hysteresis loops displayed in Fig. 4.7(b) and can therefore be attributed to rotation of the magnetization away from the easy axis. In the ferromagnetic phase the transverse resistivity ρ_{xy} can be separated into the ordinary Hall resistivity $\rho_{xy,\text{OHE}}$ and the anomalous $\rho_{xy,\text{AHE}}$ one. This separation is crucial in SrRuO_3 due to the difficulty to fully saturate the magnetization. Employing two different methods to distinguish between the ordinary and the anomalous part may yields different results [227]. One promising technique to separate both components was reported by Kats *et al.* [228], utilizing the different angle dependence of the anomalous and ordinary resistivity at low magnetic fields. However, in this thesis the common method of extrapolating the high field dependence of the transverse resistivity $\rho_{xy,\text{AHE}}$ to $\mu_0 H = 0$ T was used to determine $\rho_{xy,\text{OHE}}$ and $\rho_{xy,\text{AHE}}$ (cf. Fig. 4.7(f)).⁷⁸ The ordinary Hall resistivity $\rho_{xy,\text{OHE}}$ is negative in the whole temperature range, which indicates electron-like charge carriers. A carrier density n of the order of 10^{22} cm^{-3} , which was calculated using a one-band relationship and corresponds to about 1 electron/f.u., was reported by some authors (see, e.g., Refs. [224, 230]). This is misleading, since SrRuO_3 is an intrinsically multi-band material and thus electrons and holes contribute to the transport properties [189]. Thus an estimation of the carrier density derived from the ordinary Hall effect will not be given here. In contrast to $\rho_{xy,\text{OHE}}$, the anomalous resistivity $\rho_{xy,\text{AHE}}$ is strongly temperature dependent and exhibits a sign change below 120 K. This can be understood considering band structure effects. As the anomalous conductivity $\sigma_{xy,\text{AHE}}$ was found to be roughly independent of the longitudinal conductivity σ_{xx} for $j \parallel [1\bar{1}0]$ below 90 K,⁹ the transport properties are dominated by intrinsic contributions and can be theoretically calculated [206, 231]. In the inset of Fig. 4.7(f), $\sigma_{xy,\text{AHE}}$ derived by the group of Tokura using

⁷The reader is referred to the diploma thesis of Matthias Althammer [96] and Wolfgang Kaiser [229] for more details on this issue.

⁸The described uncertainty is expressed in the error bars of $\rho_{xy,\text{OHE}}$ and $\rho_{xy,\text{AHE}}$.

⁹The longitudinal and the transverse conductivity are given by $\sigma_{xx} = \frac{1}{\rho_{xx}}$ and $\sigma_{xy} = \frac{\rho_{xy}}{\rho_{xx}^2}$, respectively.

first-principles calculations on the basis of an orthorhombic symmetry [206] along with the experimental results of our SrRuO₃ thin film are plotted as a function of the magnetization. The anomalous conductivity $\sigma_{xy,\text{AHE}}$ measured with the current aligned along the $[1\bar{1}0]$ direction (full squares) matches fairly well the theoretical calculation (solid line).¹⁰ In contrast, the anomalous conductivity $\sigma_{xy,\text{AHE}}$ obtained with $\mathbf{j} \parallel [001]$ exhibits a totally different dependence. Therefore, while the anomalous Hall effect measured with $\mathbf{j} \parallel [1\bar{1}0]$ is of intrinsic origin and is highly dependent on band structure effects, extrinsic scattering effects dominates the transport behavior with $\mathbf{j} \parallel [001]$. Approaching the Curie temperature, $\sigma_{xy,\text{AHE}}$ is no longer independent of σ_{xx} for $\mathbf{j} \parallel [1\bar{1}0]$ and $\mathbf{j} \parallel [001]$. Thus, the intrinsic-dominated picture described by Fang *et al.* [206] is likely to be incomplete near T_C [228] and additional contributions to the anomalous conductivity should be taken into account.

In summary, state of the art SrRuO₃ thin films were fabricated exhibiting excellent magnetic and electric properties. In particular, a high residual resistivity ratio was detected, which demonstrates SrRuO₃ thin films with the correct stoichiometric composition and a low density of defects. Furthermore, the anomalous conductivity measured with $\mathbf{j} \parallel [1\bar{1}0]$ can be well described by theoretical calculations based on first-principles methods. This confirms that the electronic transport is of intrinsic origin in our SrRuO₃ thin films.

4.4 Physical properties of BiFeO₃ thin films

As revealed in the previous section, SrRuO₃ thin films are applicable as bottom electrode in multiferroic thin film heterostructures. Therefore, BiFeO₃ thin films were fabricated on Nb:SrTiO₃ as well as on SrRuO₃-buffered SrTiO₃ substrates. However, apart from the choice of the bottom electrode, the physical properties of BiFeO₃ thin films are directly linked to the growth conditions. A non-stoichiometric Bi/Fe ratio and the presence of oxygen vacancies or parasitic phases have significant influence on the structural, magnetic, and dielectric behavior. Therefore, an important part of this thesis was devoted to achieve high quality BiFeO₃ thin films (cf. Section 4.2). In this section, the physical properties of these thin films are investigated in detail. First, the structural characterization with respect to crystal symmetry and strain relaxation mechanisms is discussed, and second, the multiferroic behavior of BiFeO₃ thin films on Nb:SrTiO₃ substrates is examined. Since Wang and coworkers reported a large enhancement of the magnetization from $M < 10$ kA/m to 150 kA/m ($\approx 1 \mu_B/\text{f.u.}$) due to epitaxial strain in their pioneering work on BiFeO₃ thin films [32], we restricted our research on BiFeO₃ to strained thin films with thicknesses lower than 120 nm.

¹⁰The calculated transverse conductivity $\sigma_{xy,\text{AHE}}$ is multiplied by a factor of 2.5 with respect to the published calculations [206]. Therefore, the calculated conductivity is smaller compared to the experiment (cf. Ref. [228]).

4.4.1 Structural characterization of BiFeO₃ thin films

The crystal structure of bulk BiFeO₃ has been widely studied over the last 30 years [145]. However, until recently, no conclusive data on the evolution of the crystal structure in the vicinity of the ferroelectric Curie temperature T_c and above was available. In 2009, Arnold and coworkers performed high-temperature neutron diffraction experiments revealing a GdFeO₃-type $Pbnm$ (Glazer notation: $a^-a^-c^+$) orthorhombic symmetry in the temperature range of $T_c < T < T_c + 95$ K [232]. The crystal structure of this high temperature phase is displayed in Fig. 4.8(a) based on a pseudo-cubic lattice. Therefore, above the Curie temperature, BiFeO₃ behaves like other perovskite orthoferrites, where the long-range order vanishes. Below T_c , the BiFeO₃ crystal exhibits a non-centrosymmetric rhombohedral $R3c$ symmetry [145] with lattice parameters of $a_{R3c} = 0.56343$ nm and $\alpha_{R3c} = 59.35^\circ$ (cf. Fig. 4.8(b)) [141]. Neutron diffraction experiments suggest a phase coexistence of the orthorhombic high temperature and the rhombohedral low temperature phase around T_c [232]. This is consistent with the first-order nature of the transition and should also be visible in specific-heat measurements. However, this could not be confirmed in our experiments on polycrystalline BiFeO₃ samples, where no anomalies around 1000 K could be found (cf. Fig. 4.2(a)).

In the low temperature phase, not only an antiphase rotation of the oxygen octahedra with an angle of $11^\circ - 14^\circ$ [141, 145] along the pseudo-cubic $\langle 111 \rangle_{pc}$ directions exists (Glazer notation: $a^-a^-a^-$) but also a strong distortion of the FeO₆ octahedra. This is caused by the Bi lone pair and results in an off-centering of the Fe ion by 0.0134 nm [141], which yields a finite electric polarization. The distortion can be classified by the Goldschmidt tolerance factor t with $t = 0.89$ [13] using the ionic radii published by Shannon [233] with Bi³⁺ in eightfold coordination (the value for 12-fold coordination is not reported). This value deviates largely from the ideal tolerance factor of $t = 1$ for the cubic perovskite structure $Pm\bar{3}m$ (Glazer notation: $a^0a^0a^0$). Therefore, the oxygen octahedra have to buckle in order to fit into a cell that is too small leading to an Fe-O-Fe angle of about 154° [141].

We now turn to BiFeO₃ thin films. Since the thin film fabrication process takes place at temperatures below 873 K, the rhombohedral symmetry is the base for BiFeO₃ thin films and no crystalline phase transitions are expected on cooling from the growth temperature to room temperature.

In recent years, the structural properties of BiFeO₃ thin films have been extensively studied. Tetragonal [234], rhombohedral [235], monoclinic [236], and triclinic [237] symmetries were reported as a function of the thin film thickness [238–240], substrate material [241, 242], and substrate orientation [243, 244]. This suggests that the epitaxial strain arising from the difference in the lattice parameters of the thin film and the substrate strongly affects the crystal structure, which should have significant influence on the physical properties of ferroelectric thin films [245]. This might be exploited to engineer the physical properties of BiFeO₃ thin films through strain. As an example, recently, different groups have tried to stabilize a tetragonal symmetry through epitaxial strain [246, 247], which, in principle, should lead to a giant axial ratio enhancing the ferroelectric polarization [248, 249]. However, it was

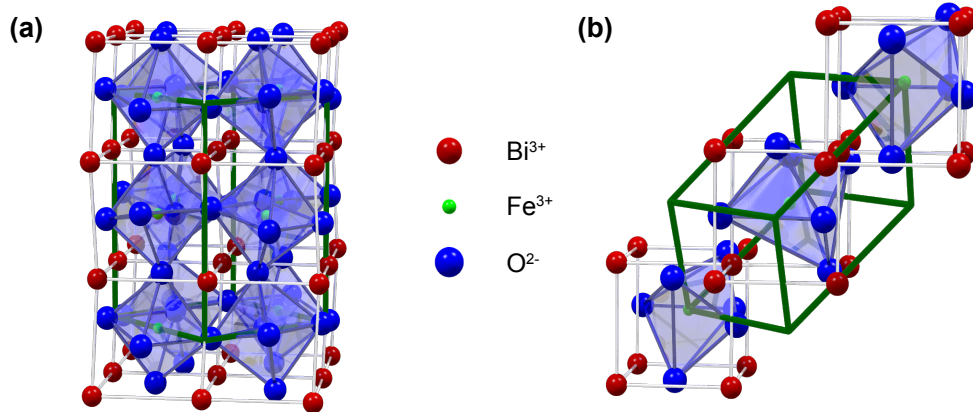


Figure 4.8: (a) High-temperature $Pbnm$ and (b) low-temperature $R3c$ crystal structure of BiFeO₃ single crystals sketched in a pseudo-cubic reference setting. The primitive cell of each phase is marked in green. The structural parameters were taken from Refs. [232] and [141], respectively.

found, that neither the ferroelectric nor the magnetic properties vary significantly with strain at room temperature [160, 246, 250]. One exception seems to be the strain dependence of the Curie temperature T_c , which was recently observed by Infante and coworkers in BiFeO₃ thin films [242]. This is surprising, since ferroelectric materials are normally very sensitive to strain effects [251]. However, extrinsic effects such as imperfections of the crystal lattice or a multiphase state strongly affect the physical properties and should be taken into account when describing ferroelectric thin films under epitaxial strain [165, 252–254]. As an example, recently, large electric field-induced strains were reported in BiFeO₃ thin films, which exhibit regions with tetragonal- and rhombohedral-like symmetries, i.e., a crystalline multiphase state [255]. In these thin films, a reversible electric-field-induced strain of more than 5% was found due to moving the boundaries between tetragonal- and rhombohedral-like phases.

In this thesis, we focus on BiFeO₃ thin films deposited directly on Nb:SrTiO₃ (001)-oriented substrates as well as on SrRuO₃-buffered SrTiO₃ (001) crystals. The rhombohedral structure of bulk BiFeO₃ can be described in a pseudo-cubic lattice with lattice parameter $a_{pc} = 0.396$ nm [243]. Using this value and a lattice parameter of 0.3905 nm for SrTiO₃ [256], the lattice mismatch between BiFeO₃ and SrTiO₃ can be estimated to -1.4% . From the theoretical point of view, employing density functional calculations, thin films grown on cubic substrates under compressive epitaxial strain should be monoclinic with either Cm or Cc symmetry [247, 249]. The two space groups differ by the absence (Cm) and presence (Cc) of oxygen octahedral rotations along the out-of-plane direction leading either to a $a^+a^+c^0$ or $a^-a^-c^-$ tilted system [257]. The $a^-a^-c^-$ system is similar to the rhombohedral $a^-a^-a^-$ one, justifying the notation “ R -phase” for BiFeO₃ thin films exhibiting a Cc symmetry [241, 249]. Using the standard setting, the unit-cell axes of the Cc

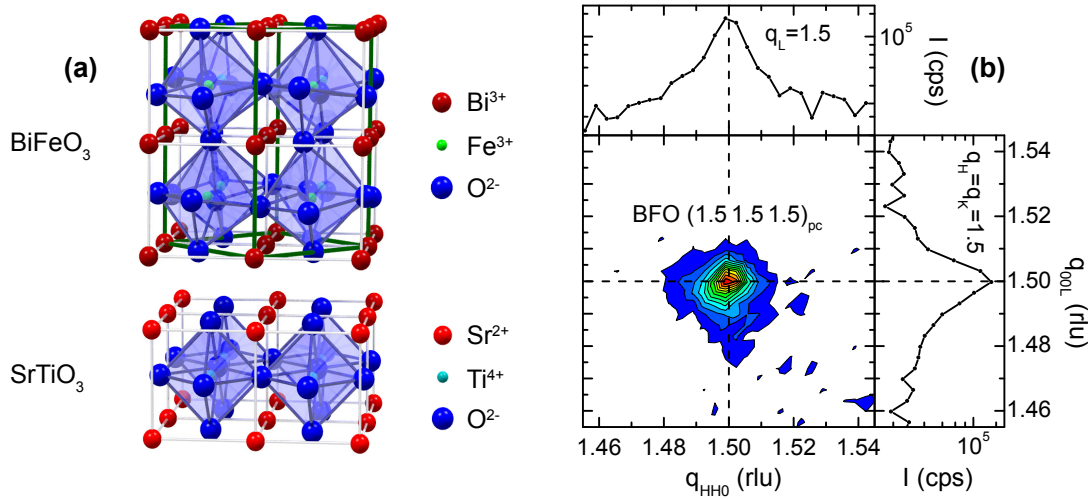


Figure 4.9: (a) Schematic illustration of the growth of BiFeO₃ (BFO) thin films with Cc symmetry (R -phase) on SrTiO₃ (001)-oriented substrates. The unit cell of the Cc symmetry in a pseudo-cubic reference setting ($I1a1$ space group) is marked in green. (b) Reciprocal space map around the BiFeO₃ (1.5 1.5 1.5)_{pc} reflection using synchrotron x-ray diffraction. The reciprocal lattice units (rlu) are related to the pseudo-cubic BiFeO₃ lattice. The measurement was performed on a 23 nm thick BiFeO₃ film deposited on a SrRuO₃-buffered SrTiO₃ substrate at the XMaS beamline BM28 located at the European Synchrotron Radiation Facility (ESRF).

space group, (\mathbf{a}_{Cc} , \mathbf{b}_{Cc} , \mathbf{c}_{Cc}) are related to the pseudo cubic axes (\mathbf{a}_{pc} , \mathbf{b}_{pc} , \mathbf{c}_{pc}) as $\mathbf{a}_{Cc} = \mathbf{a}_{pc} + \mathbf{b}_{pc} + 2\mathbf{c}_{pc}$, $\mathbf{b}_{Cc} = -\mathbf{a}_{pc} + \mathbf{b}_{pc}$, and $\mathbf{c}_{Cc} = -\mathbf{a}_{pc} - \mathbf{b}_{pc}$. With a new choice of axes, the space group Cc can equivalently be transformed into a $I1a1$ space group, resulting in a simpler correlation with the pseudo-cubic cell: $\mathbf{a}_{Cc} = \mathbf{a}_{pc} + \mathbf{b}_{pc}$, $\mathbf{b}_{Cc} = -\mathbf{a}_{pc} + \mathbf{b}_{pc}$, and $\mathbf{c}_{Cc} = 2\mathbf{c}_{pc}$ [258]. This basis is used to describe the Cc space group in the following (cf. Fig. 4.9(a)). Within this setting, the unit cell is built up by two Cm -type subcells stacked along the out-of-plane direction exhibiting an anti-phase tilt of the neighboring FeO₆ octahedra. This antiferrodistortive arrangement of the oxygen octahedral tilt will cause superlattice reflections represented by all-odd or two-odd type indices with respect to the pseudo-cubic cell [258], which can be observed using x-ray diffraction. Figure 4.9(b) shows the results of x-ray diffraction measurements on a 23 nm thick BiFeO₃ film deposited on a SrRuO₃-buffered SrTiO₃ substrate using synchrotron radiation. The measurements were carried out at the XMaS beamline BM28 located at the European Synchrotron Radiation Facility (ESRF) (cf. Section 2.1.3). Clearly, a finite intensity is visible around the (1.5 1.5 1.5)_{pc} reflection, which is indexed with respect to the pseudo-cubic lattice of BiFeO₃. This reflection is absent in the rhombohedral $R3c$ space group [259], confirming a monoclinic Cc symmetry of BiFeO₃ thin films fabricated on SrRuO₃-buffered SrTiO₃ substrates. Therefore, the rotation of the oxygen octahedra is not fully clamped by the substrate even in BiFeO₃ thin films with thicknesses as low as 23 nm. However, at larger epitaxial strain, the rotation of the oxygen octahedra can be destroyed. For example, the superstructure peak was observed for BiFeO₃ thin films grown on SrTiO₃ substrates (lattice mismatch: -1.4%), but not detectable for

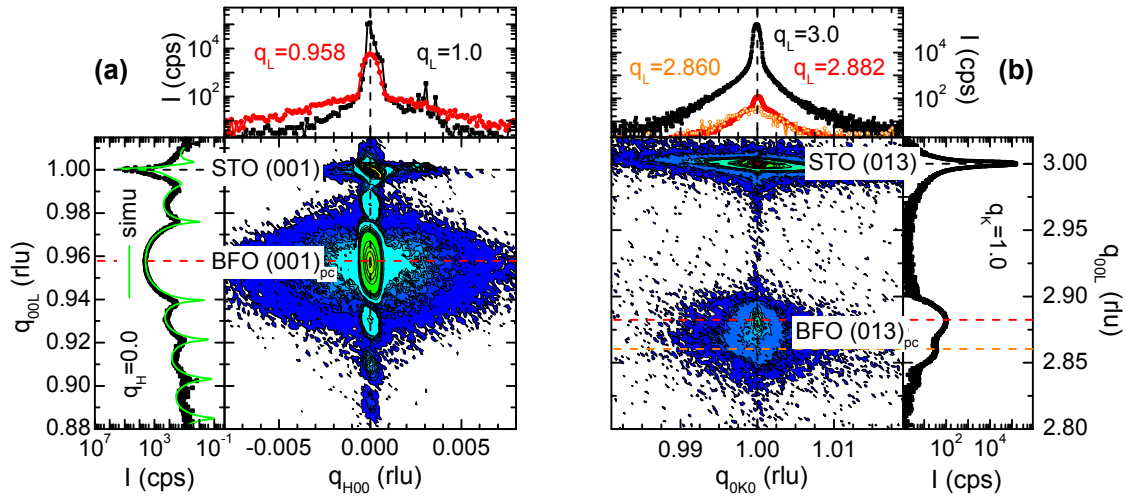


Figure 4.10: Reciprocal space maps and q -scans around (a) SrTiO₃(001) and (b) SrTiO₃(013) of a 22 nm thick BiFeO₃ film grown on a Nb:SrTiO₃ substrate. The finite thickness fringes are simulated using the software LEPTOS (green line in the left panel of (a)).

BiFeO₃ thin films on LaAlO₃ (lattice mismatch: -4.8%) [247]. Thus, depending on the lattice mismatch either Cm or Cc are favored in BiFeO₃ thin films. Since in this thesis we restrict our discussion to BiFeO₃ thin films grown on (001)-oriented SrTiO₃ substrates, the BiFeO₃ thin films will be indexed with respect to the $I1a1$ space group utilizing the Cc symmetry.

BiFeO₃ thin films on Nb:SrTiO₃ substrates

As Nb-doped SrTiO₃ substrates satisfy the requirements for an electrode material in dielectric measurements [260, 261], BiFeO₃ thin films are deposited directly on (001)-oriented Nb:SrTiO₃ substrates. As an example, Fig. 4.10 shows the structural properties obtained by x-ray diffraction measurements carried out at room temperature on a 22 nm thick BiFeO₃ film. The reciprocal space map as well as the q_{00L} -scan around SrTiO₃(001) depicted in the left panel of Fig. 4.10(a) reveal finite thickness fringes attesting a high crystalline quality. The simulation of these fringes using the software LEPTOS [196] fits nicely to the experimental data (cf. green solid line in Fig. 4.10(a)). The coherent thickness of 22 nm arising from the simulation coincides well with the thickness revealed using x-ray reflectometry measurements (not shown here), indicating a coherent growth of the BiFeO₃ thin film over the whole thickness. Furthermore, the simulation, which assumes a homogeneous spacing of the crystallographic planes parallel to the surface, proves that strain gradients along the out of plane direction can be neglected. The mosaicity in the out of plane direction disclosed by the full width at half maximum (FWHM) of 0.038° of the rocking curve around the pseudo-cubic BiFeO₃(001)_{pc} reflection is very low in terms of oxide materials grown by pulsed laser deposition [262]. This low mosaicity is also visible in the transverse q_{H00} -scan at $q_L = 0.958$ rlu shown in the upper panel of Fig. 4.10(a). Moreover, no tilt of the scattering planes in the out of plane direction is detectable,

which indicates that the [001] direction of the BiFeO_3 thin film is fixed to the out of plane direction of the substrate. However, Fig. 4.10(a) reveals that the q_{H00} -scan consists of two components: a sharp one occurring at the specular condition as well as diffuse scattering, which results in a broad distribution. The former component arises from long-range order and the latter one from short-scale disorder, which might be caused by weak defects (point defects and their clusters) as well as by strong defects (dislocations and their pile-ups) [74].

Since BiFeO_3 thin films on SrTiO_3 (001) exhibit a monoclinic symmetry, different crystalline domains are unavoidable. These domains can be investigated using x-ray diffraction (XRD) measurements around asymmetric reflections. As an example, the result of XRD measurements around the SrTiO_3 (013) reflection are shown in Fig. 4.10(b). The splitting of the pseudo-cubic BiFeO_3 (013)_{pc} reflection, which is even more pronounced in the q_{00L} -scan at $q_{\text{K}} = 1.0$ (cf. right panel of Fig. 4.10(b)), reveals different monoclinic domains present in the BiFeO_3 thin film. This suggests that the critical thickness for pseudomorphic growth of BiFeO_3 on SrTiO_3 (001) is slightly lower than 22 nm, which is in agreement with the experimental results previously reported by Daumont *et al.* [240] as well as by Chu and coworkers [262]. In contrast, other groups found critical thicknesses even up to 90 nm [160, 238, 239, 263, 264]. This confirms that the determination of the symmetry and the strain state of BiFeO_3 thin films is demanding. From XRD measurements around SrTiO_3 (001), SrTiO_3 (013), and SrTiO_3 (113) (not shown here), the BiFeO_3 lattice constants can be derived in a Cc symmetry: $a = (0.553 \pm 0.002)$ nm, $b = (0.551 \pm 0.002)$ nm, $c = (0.8154 \pm 0.0004)$ nm, and $\beta = (90.6 \pm 0.1)^\circ$. Since the reflections caused by the different monoclinic domains are not well separated from each other, a precise determination of the lattice constants is difficult, resulting in large uncertainties. Using these lattice parameters, the in-plane and out-of-plane strain state can be calculated to -1.43% and 2.8% , respectively. Therefore, BiFeO_3 thin films with a thickness of 22 nm are nearly fully strained and exhibit a large out of plane elongation, which results in a Poisson ratio of about $\nu = 0.49$. This ratio is unusual, since a typical value for oxide thin films is around $\nu = 0.25$ [235], and might be explained by an anisotropic elastic behavior [265]. Using the lattice constants of BiFeO_3 thin films published by other groups [236, 238, 240, 243, 244], Poisson ratios in the range of 0.45 to 0.50 can be calculated, which confirms our results. Smaller values of $\nu < 0.45$, which are reported by Refs. [246, 263], might be attributed to non-stoichiometric effects. You and coworkers recently found a decrease of the out-of-plane lattice parameter when decreasing the Bi/Fe ratio in BiFeO_3 thin films [266]. Since only a small variation of the in-plane lattice parameter due to substrate clamping effects are expected, the decrease of the Bi/Fe ratio will change the Poisson ratio to lower values by simply decreasing the volume of the unit cell. This suggests that BiFeO_3 thin films with Poisson ratios between 0.45 and 0.50 exhibit the correct stoichiometric Bi/Fe ratio.

With the knowledge of the Poisson ratio the critical thickness of BiFeO_3 thin films can be estimated. Two different models are commonly used to calculate the critical thickness of epitaxial thin films, which describes the onset of strain relaxation by misfit dislocations at the growth temperature [267]. Employing the Matthews-

Blakeslee criteria [268] with a Poisson ratio of $\nu = 0.49$, the critical thickness for the formation of misfit dislocations can be calculated to be 4 nm [269], which is by far too low to describe the experimentally derived value.¹¹ The People-Bean model, which is applicable to thin film systems with moderate misfit strain, could be more appropriate in ferroelectric thin films [269]. This model assumes that dislocations have to nucleate, which leads to a simple energy balance of the strain energy versus the energy cost of dislocation nucleation. Within this model a critical thickness of 24 nm was calculated, which is in good agreement with experiment even without considering kinetic contributions [267, 272]. Therefore, a measured Poisson ratio of about $\nu = 0.49$ not only suggests that we have BiFeO₃ thin films with the correct stoichiometric composition but also naturally explains the experimentally obtained value of the critical thickness in the limit of the phenomenological People-Bean model.

As discussed in the context of Fig. 4.10, the relaxation of the misfit strain in BiFeO₃ thin films takes place by forming different domains. In principle, growing materials with monoclinic symmetry on cubic substrates not only leads to elastic strains caused by the lattice mismatch, but also to finite shear strains in the thin films. The former can be diminished by the formation of misfit dislocations and the latter can be reduced by the formation of structural domains with an alternating sign of shear strain [273]. Since we only consider BiFeO₃ thin films with moderate compressive strain, the thin films are similar to the rhombohedral parent phase (*R*-phase) and exhibit four monoclinic domains. Following the notation of Streiffer and coworkers [274], the four distinct ferroelastic variants (r_i with $i = 1 - 4$) can be described as shown in Fig. 4.11(a). Each domain exhibits two possible ferroelectric polarizations ($\pm \mathbf{P}_i$ with $i = 1 - 4$), which are assumed to be oriented along the body diagonal of the distorted pseudo-cubic unit cell (cf. Fig. 4.11(a)). In order to determine the domain structure of BiFeO₃ thin films, q_{00L} -scans around the asymmetric SrTiO₃ (103) and SrTiO₃ (113) reflections with different in-plane orientations of the sample were carried out (Fig. 4.11(b) and (c)). While two of the four domains are distinguishable in the q_{00L} -scans around SrTiO₃ (103) (cf. Fig. 4.11(b)), XRD measurements around the asymmetric SrTiO₃ (113) reflection allows to separate three of the four variants (see Ref. [240] for more details). Figures 4.11(b) and (c) reveal peak splittings of both types of pseudo-cubic BiFeO₃ reflections for each in-plane orientation, which proves the presence of all four domains even for a BiFeO₃ thin film with a thickness as low as 22 nm [275]. This is in agreement with several reports on BiFeO₃ thin films deposited on SrRuO₃-buffered SrTiO₃ substrates [155, 240, 276]. Here, no preferential formation of the four ferroelastic domains was reported for BiFeO₃ thin films with thicknesses lower than 87 nm [240].¹²

The presence of different monoclinic domains, which are accompanied by domain walls imposing edge dislocations in BiFeO₃ thin films [274, 277], certainly influences

¹¹Here, a strain value of 1.34% at the growth temperature of 853 K was used [256, 270]. Although, the reported values for the coefficient of the thermal expansion differ significantly [270, 271], they alone cannot explain the low critical thickness.

¹²The preferential formation of monoclinic domains is discussed in the context of SrRuO₃-buffered SrTiO₃ substrates at the end of this section.

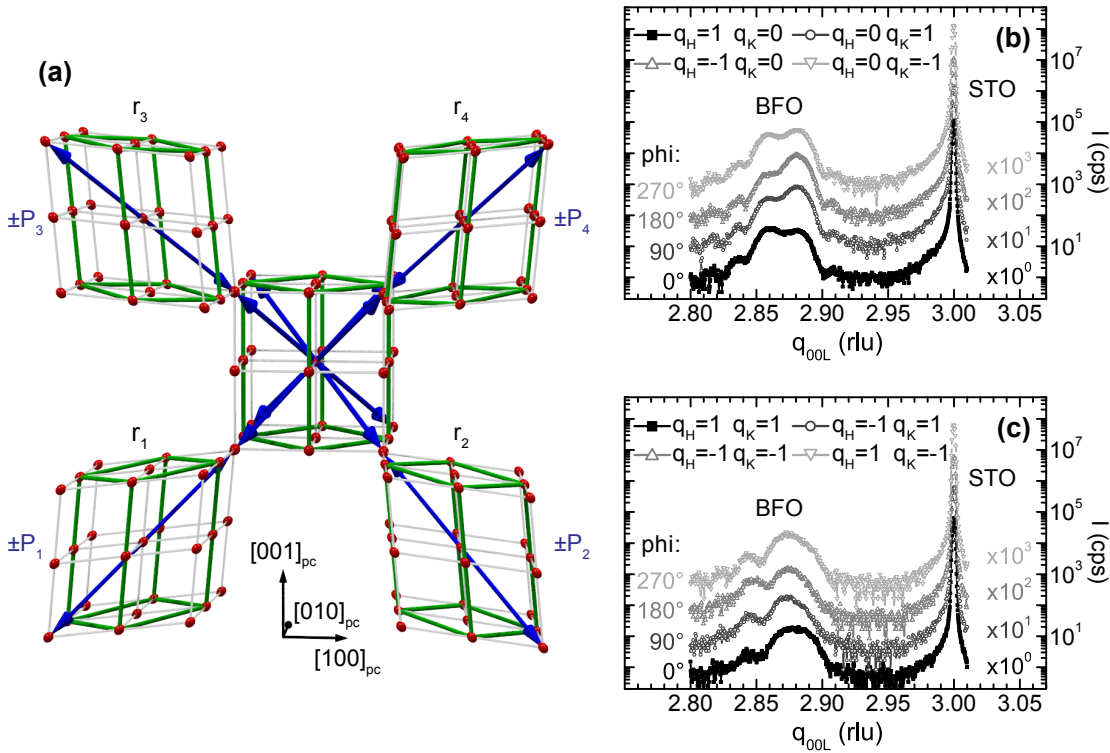


Figure 4.11: (a) Schematic illustration of the four ferroelastic domains in the *R*-phase of BiFeO₃. The monoclinic unit cells are represented by green lines. To enhance the visibility, the unit-cells are greatly simplified and only the Bi ions are shown (red dots). The polarization (blue arrows) is assumed to be oriented along the body diagonal of the pseudo-cubic unit cell. To determine the domain structure of BiFeO₃ thin films, q_{00L} -scans around the asymmetric (b) SrTiO₃ (103) and (c) SrTiO₃ (113) reflections were performed with different in-plane orientations of the sample, i.e., different ϕ angles. The intensity of each scan is scaled by the given factor.

the physical properties of these thin films. In particular, a high leakage current caused by conducting domain walls [278] together with a low remanent polarization [276] are expected in dielectric measurements. On the other hand, novel functionalities such as a strong magnetoelectric coupling were observed at the domain walls in BiFeO₃ [137, 278].

With increasing thickness of BiFeO₃ thin films, relaxation of the misfit strain occurs mainly by the formation of dislocations [279], which can be investigated by diffraction techniques (cf. Section 2.1.3). In Fig. 4.12(a), q_{00L} -scans along ($q_H = 0.0$) and just beside ($q_H = 0.025$) the crystal truncation rod around the symmetric pseudo-cubic BiFeO₃ (001)_{pc} reflection carried out on BiFeO₃ thin films with thicknesses ranging from 22 nm to 88 nm, which are fabricated in a continuous growth mode using a slow growth rate (cf. Section 4.2), are shown. The intensity of the former type of q_{00L} -scans is a superposition of the intensity caused by coherent and diffuse scattering, while diffuse scattering mainly contributes to the intensity in the q_{00L} -scans at $q_H = 0.025$. At a thickness of 22 nm, the maximum of the Bragg reflection of BiFeO₃ (001)_{pc} and the maximum of the diffuse scattering coincide, confirm-

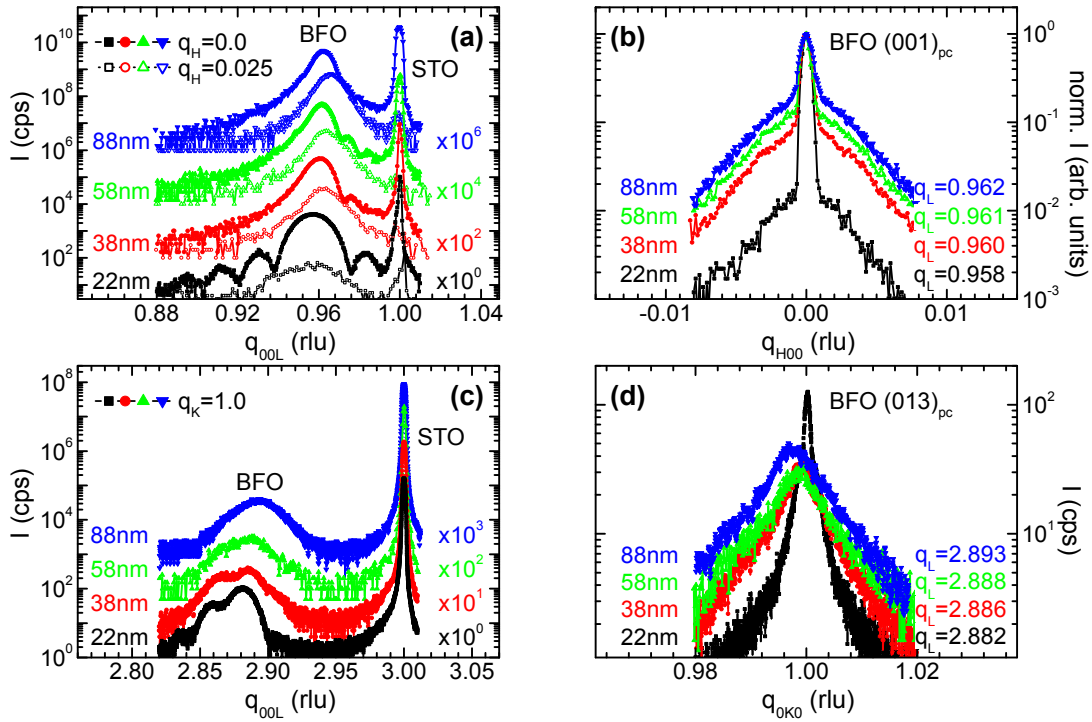


Figure 4.12: X-ray diffraction measurements on BiFeO₃ thin films with different thicknesses deposited on Nb:SrTiO₃ (001) substrates: (a) q_{00L} -scans and (b) transverse q_{H00} -scans around the pseudo-cubic BiFeO₃ (001)_{pc} reflections as well as (c) q_{00L} -scans and (d) transverse q_{0K0} -scans around BiFeO₃ (013)_{pc}. The intensity of the q_{00L} -scans in (a) and (c) are multiplied by the given factors. To reveal the influence of dislocations on the diffraction profile, q_{00L} -scans along ($q_H = 0.0$, full symbols) and just beside ($q_H = 0.025$, open symbols) the crystal truncation rod are displayed in (a).

ing a low density of dislocations [280]. Increasing the film thickness, the maximum of the diffuse scattering shifts to higher q_L -values than the specular reflection, which implies a lower, partially relaxed, out-of-plane lattice constant. Furthermore, the intensity of the diffuse part increases from 22 nm to 88 nm indicating an increase of the dislocation density in these thin films. This is also observable in the transverse q_{H00} -scans around the pseudo-cubic BiFeO₃ (001)_{pc} reflection (Fig. 4.12(b)). These scans disclose two components. Whereas the long range mosaicity revealed by the full width at half maximum (FWHM) of the sharp component around the specular reflection slightly increases with increasing film thickness (FWHM of rocking curves around BiFeO₃ (002) ranges from 0.04° to 0.06°), the intensity of the broad component caused by diffuse scattering strongly raises between $d = 22$ nm and $d = 38$ nm. Thus, in this thickness range, the misfit strain seems to relax by the formation of misfit dislocations. Interestingly, the intensity of the broad component is only slightly enhanced by further increasing the film thickness.

As revealed by the q_{00L} -scans, in the intermediate thickness range ($22 \text{ nm} < d < 88 \text{ nm}$), an asymmetric shape of the BiFeO₃ (001)_{pc} Bragg reflections together with asymmetric finite thickness fringes are observed, indicating inhomogeneities within the crystalline lattice (cf. Fig. 4.12(a)). Since for symmetric Bragg reflections only

the lattice parameter perpendicular to the surface is accessible, solely the effect of the inhomogeneities along the surface normal is visible. The reason for these inhomogeneities can be strain gradients as well as changes of the chemical composition. The former will arise due to strain relaxation and the latter from variations of the Bi/Fe ratio as a function of film thickness, which can be attributed to the high volatility of Bi at the growth temperature. Assuming a stoichiometric thin film, the relaxation of misfit strain causes a shift of the specular reflection along the relaxation line, which connects the Bragg position of a completely relaxed and fully strained thin film in the reciprocal space. In contrast, in thin films with a constant strain state exhibiting a gradient in the chemical composition, a broadening and shift along lines that connect the reciprocal lattice points of the substrate and the thin film are observed. By performing x-ray diffraction measurements around asymmetric reflections of BiFeO_3 thin films with different thickness, the effects stemming from strain relaxation and non-stoichiometry can be separated. Figures 4.12(c) and (d) depict q_{00L} - as well as q_{0K0} -scans around the asymmetric BiFeO_3 $(013)_{\text{pc}}$ reflection. Again the q_{00L} -scans reveal several monoclinic domains. Concentrating on the monoclinic domains with the highest intensity, the transverse q_{0K0} -scans shown in Fig. 4.12(d) disclose a relaxation of the in-plane lattice constants of thin films with thicknesses larger than $d = 22$ nm. The relaxation process can be visualized in a q_L - q_K -diagram using the q_L and q_K positions of the maximum intensity of BiFeO_3 $(013)_{\text{pc}}$ reflections. In addition, the relaxation line was calculated employing the Poisson ratio of 0.49 (cf. dashed line in Fig. 4.13(a)). As evident from Fig. 4.13(a), the experimentally derived data (cf. full symbols in Fig. 4.13(a)) follows the relaxation line, but they are shifted by $\Delta q_L = 0.005$ compared to the theoretical line. This can be explained by a reasonable systematic error mainly caused by a displacement of both the sample and the x-ray beam with respect to the center of the diffractometer. This error can be reduced by taking into account BiFeO_3 $(00l)_{\text{pc}}$ reflections up to the fourth order ($l = 4$) and utilizing the Nelson-Riley method (cf. Section 2.1.3). This results in positions of the BiFeO_3 $(013)_{\text{pc}}$ reflections as shown by the open symbols in Fig. 4.13(a), which follow nicely the theoretical relaxation line. Therefore, the variation of the Bragg reflections visible in Fig. 4.12 can be attributed to strain relaxation rather than changes of the Bi/Fe ratio, which further proves the correct stoichiometry in our BiFeO_3 thin films.

The relaxation of the in-plane lattice spacing along the pseudo cubic $[010]_{\text{pc}}$ direction, which corresponds to the monoclinic $[110]_{\text{m}}$ direction of the BiFeO_3 lattice in the Cc symmetry (cf. Fig. 4.9(a)), is in agreement with x-ray diffraction measurements published by Chu and coworkers [262]. However, other groups reported a nearly independent behavior of the lattice constants along $[110]_{\text{m}}$ and $[001]_{\text{m}}$ below a thickness of 100 nm using SrRuO_3 as buffer layer [240, 263]. As discussed in the context of Fig. 4.12(b), the relaxation of nearly pseudomorphic to partially relaxed BiFeO_3 thin films increases the density of dislocations. To investigate this in more detail, the integrated intensities caused by coherent and diffuse scattering was derived by extracting the intensity evolution of transverse $q_{\text{H}00}$ -scans in the range of $0.94 < q_L < 0.985$ around the symmetric BiFeO_3 $(001)_{\text{pc}}$ reflection. For this purpose, reciprocal space maps were recorded using BiFeO_3 thin films with different

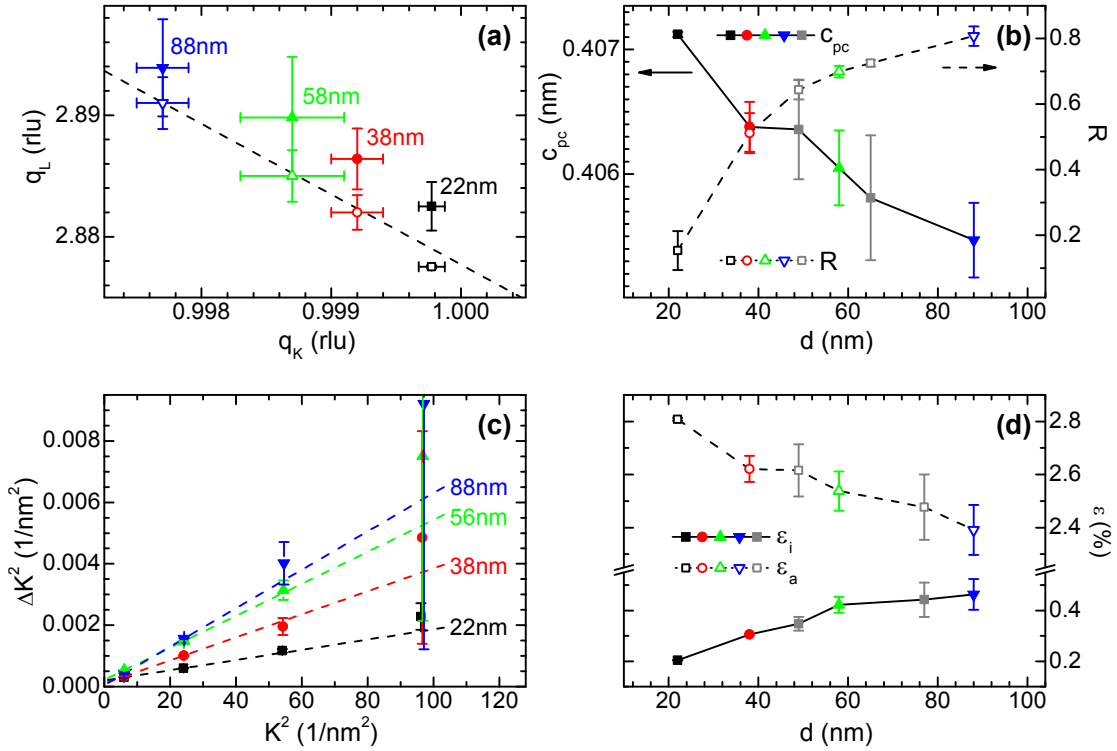


Figure 4.13: (a) The q_L - q_K -diagram of BiFeO₃ thin films grown on Nb:SrTiO₃ substrates with different thicknesses illustrates the strain relaxation process. The q_L and q_K positions of the BiFeO₃ (013)_{pc} reflections are marked by full symbols. The systematic error in the out-of-plane direction can be reduced by taking into account BiFeO₃ (00 l)_{pc} reflections up to the fourth order ($l = 4$) and utilizing the Nelson-Riley method (open symbols). The relaxation line calculated using a Poisson ratio of 0.49 is marked by the dashed line. (b) Pseudo-cubic out-of-plane lattice constant c_{pc} (full symbols), which is determined using the Nelson-Riley method (cf. Section 2.1.3), and the normalized integrated intensity caused by diffuse scattering $R = I_{diffuse}/I_{total}$ (open symbols) as a function of the film thickness d . $I_{diffuse}$ denotes the integrated intensity caused by diffuse scattering and $I_{total} = I_{coherent} + I_{diffuse}$ the total integrated intensity. Both values were obtained by extracting the intensity evolution of transverse q_{H00} -scans in the range of $0.94 < q_L < 0.985$ around the symmetric BiFeO₃ (001)_{pc} reflection. (c) Conventional Williamson-Hall plot as discussed in Section 2.1.3. The microstrain of the BiFeO₃ thin films ϵ_i can be determined from the slope of the linear dependence between the change of the momentum transfer $\Delta K = \frac{\Delta Q}{2\pi}$ and $K = \frac{Q}{2\pi}$. For this purpose the pseudo-cubic BiFeO₃ (00 l)_{pc} reflections with $l = 1 - 3$ are used (dashed lines). (d) The microstrain ϵ_i and the average out-of-plane strain ϵ_a , which is derived using the pseudo-cubic out-of-plane lattice constant c_{pc} , reveal an inverse behavior as a function of the film thickness d . The gray symbols mark the BiFeO₃ samples, which are fabricated using the imposed layer-by-layer technique described in Section 4.2.

thicknesses (not shown here). In Fig. 4.13(b), the normalized integrated intensity caused by diffuse scattering $R = I_{diffuse}/I_{total}$ with $I_{total} = I_{coherent} + I_{diffuse}$ as well as the pseudo cubic out-of-plane lattice constant c_{pc} are plotted as a function of the BiFeO₃ film thickness. Furthermore, data, which were derived from BiFeO₃ thin films fabricated using the imposed layer-by-layer technique are also included in the

figure (gray symbols). As evident from Fig. 4.13(b), these data fit nicely into the thickness behavior of BiFeO₃ thin films fabricated in a continuous growth mode with a slow growth rate. Therefore, it seems that there is no significant difference in the structural properties for both fabrication techniques. Figure 4.13(b) further reveals that the pseudo cubic lattice constant c_{pc} and the normalized integrated intensity caused by diffuse scattering R are correlated. While c_{pc} decreases with increasing film thickness, the R value increases continuously. This suggests that the relaxation of the pseudomorphic growth creates defects in BiFeO₃ thin films, which increases the diffuse scattering.

It is generally implied that this strain relaxation takes place at or near the interface between thin film and substrate [165]. Thus, the strain field associated by misfit dislocations should be localized at the interface and apart from the first monolayers the strain state across the thin film should be homogeneous and only dependent on the total thickness. In contrast, the asymmetric peak shape along the out-of-plane direction visible in the q_{00L} -scan around the BiFeO₃ (001)_{pc} reflection of thin films with thicknesses in the range of $22 \text{ nm} < d < 88 \text{ nm}$ suggests a strain gradient over the whole thickness of the thin film. Therefore, the strain should be described not only depending on the total thickness d , but also as a function of the distance z to the film-substrate interface $\epsilon(z, d)$ [75]. One thus expects that the strain relaxation $\Delta\epsilon(z, d)/\Delta z$ should be proportional to the strain itself, which yields an exponential behavior

$$\epsilon(z, d) = \epsilon_0 \exp\left(-\frac{z}{\delta}\right),$$

where ϵ_0 is the strain at the film-substrate interface at $z = 0$ and δ is a characteristic decay length of the strain [281].¹³ Both parameters can be derived by estimating the local mean strain ϵ_i of the thin film using a Williamson-Hall-type approach (cf. Section 2.1.3) [75], which is one method to separate size and strain broadening of x-ray diffraction peak profiles [283]. The conventional Williamson-Hall relation predicts a linear dependence of the change of the momentum transfer $\Delta K = \frac{\Delta Q}{2\pi}$ and $K = \frac{Q}{2\pi}$. However, in case of our BiFeO₃ thin films using the pseudo-cubic (00 l)_{pc} reflections with $l = 1 - 4$, Fig. 4.13(c) reveals that the data corresponding to the fourth order of diffraction significantly deviate from the linear behavior, which might be attributed to larger uncertainties in determining the instrumental resolution, since peak broadening caused by the diffractometer itself becomes significant at higher diffraction order. Furthermore, the intensity of the pseudo-cubic BiFeO₃ (004)_{pc} reflection is weak, resulting in a large error in measuring the integral breadth β_{meas} of this reflection (cf. Section 2.1.3). However, using the BiFeO₃ (00 l)_{pc} reflections with $l = 1 - 3$, the mean microstrain $\epsilon_i = K_{\text{D}}\epsilon_{\text{rms}}$, where ϵ_{rms} denotes the local root mean square strain and K_{D} depends on the nature of the lattice distortion as well as the underlying model of the microstrain [68], can be derived as a function of the film thickness (cf. Fig. 4.13(d)). By comparing ϵ_i and the average out-of-plane strain ϵ_a , which is obtained from the pseudo-cubic lattice constant c_{pc} shown in

¹³If the strain gradient is only caused by dislocations, a more precise calculation of the vertical profile can be found in Ref. [282].

Fig. 4.13(b), an inverse behavior is revealed. With increasing thickness of the BiFeO₃ thin film, the relaxation reduces the average out-of-plane strain ϵ_a and increases the internal strain ϵ_i mainly due to the formation of dislocations. Now, following Catalan and coworkers [75], the strain profile can be determined by calculating the parameters ϵ_0 and δ . For this purpose, the scaling factor K_D is set to unity and asymmetric effects are neglected, so that $\epsilon_i = \epsilon_{\text{rms}} = \sqrt{\langle \epsilon^2 \rangle} = \bar{\epsilon}^2 - \bar{\epsilon}_a^2 = \epsilon^2 - \epsilon_a^2$. Using the average out-of-plane strain ϵ_a depicted in the inset of Fig. 4.10(c) and the derived internal strains ϵ_i , ϵ_0 and δ are determined to $\epsilon_0 = (0.036 \pm 0.002)$ and $\delta(d) = (15.4 \pm 1.7) \text{ nm} + (0.71 \pm 0.03) \cdot d$, respectively. However, both values are larger than expected. This could be an indication for a significant density of imperfections such as point defects, impurities, and/or threading dislocations at the interface between thin film and substrate. On the other hand, quantitative values may vary depending on the approach used (cf. Ref. [284]). In particular, peak profile fitting including finite thickness fringes would be more appropriate for thin films with low thickness [285]. However, Catalan and coworkers found similar results using either a detailed peak profile fit or employing the Williamson-Hall method [75].

In summary, BiFeO₃ thin films with high crystalline quality were deposited on (001)-oriented Nb doped SrTiO₃ substrates. Using advanced diffraction techniques, the stoichiometry of our thin films could be demonstrated. A detailed analysis of the structural properties revealed a critical thickness of pseudomorphic growth of less than 22 nm. BiFeO₃ thin films with larger thicknesses start to release the misfit strain by formation of dislocations, which enhances the diffuse part of the diffraction intensity. Furthermore, an asymmetric shape of the diffraction profile was detected. This indicates that a strain gradient along the out-of-plane direction is present in these thin films. This was analyzed in more detail using the Williamson-Hall method. Strain gradients certainly have strong influence on the physical properties of ferroelectric thin films [75, 165, 252, 254, 286]. Therefore, reducing the internal strain gradient is essential for ferroelectric thin films with high dielectric quality. As discussed in Section 4.3, BiFeO₃ thin films fabricated on SrRuO₃-buffered SrTiO₃ substrates might exhibit less internal microstrain than BiFeO₃ thin films on Nb:SrTiO₃.

BiFeO₃ thin films on SrRuO₃-buffered SrTiO₃ substrates

Using SrRuO₃ as buffer layer for the growth of BiFeO₃ thin films seems to be promising, since SrRuO₃ is widely used not only as bottom electrode but also as buffer material providing clean and nearly defect free surfaces (cf. Section 4.3). BiFeO₃ thin films were grown on SrRuO₃-buffered SrTiO₃ substrates using the same deposition parameters as described in Chapter 4.2.1, which were found to be optimal for the growth of BiFeO₃ thin films on Nb:SrTiO₃ substrates. In order to compare the structural properties of BiFeO₃ thin films fabricated on Nb:SrTiO₃ and on SrRuO₃-buffered SrTiO₃ substrates, the same analysis as discussed above for BiFeO₃ thin films grown on Nb:SrTiO₃ is carried out in the following.

Figure 4.14 shows the structural properties of BiFeO₃ thin films grown on SrRuO₃-buffered SrTiO₃ (001) substrates with different thicknesses. In analogy to Fig. 4.13, the experimental data depicted in Fig. 4.14 are mainly based on BiFeO₃ thin films

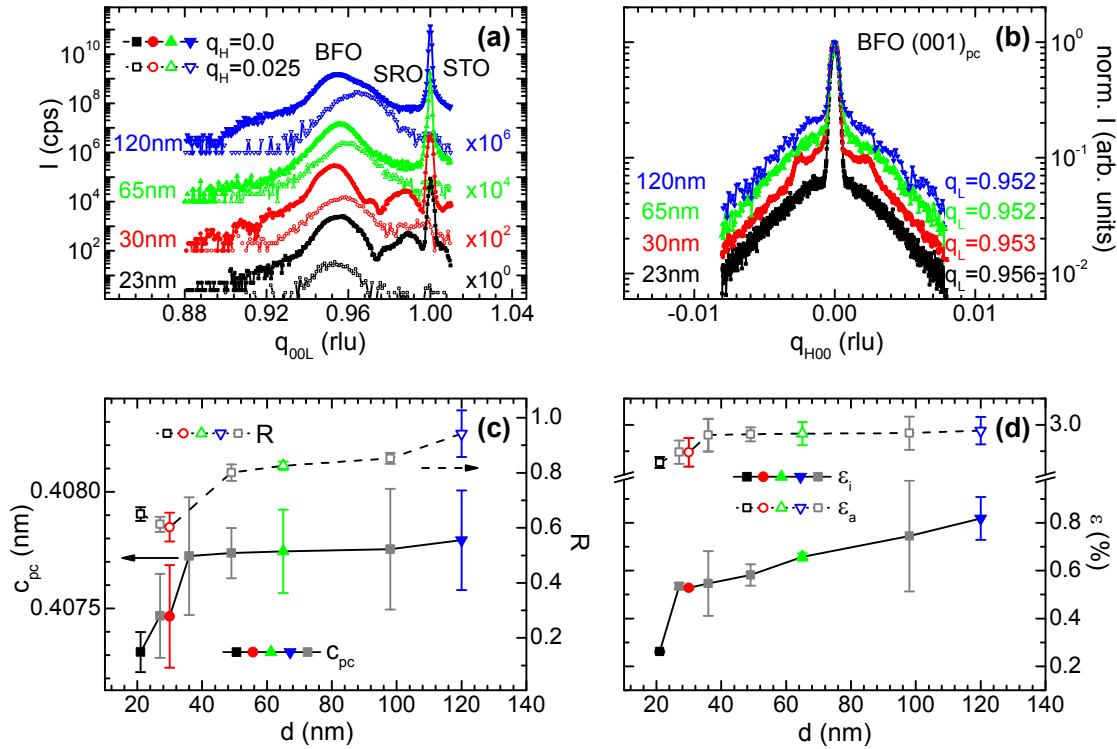


Figure 4.14: X-ray diffraction measurements on BiFeO_3 thin films with different thickness grown on SrRuO_3 -buffered SrTiO_3 (001)-oriented substrates with different thicknesses: (a) q_{00L} -scans and (b) transverse q -scans around the BiFeO_3 (001)_{pc} reflection, (c) out-of-plane pseudo-cubic lattice constant c_{pc} and normalized integrated intensity caused by diffused scattering R as a function of BiFeO_3 film thickness d , (d) out-of-plane strain ϵ_a and internal strain ϵ_i as a function of d . The gray symbols label the data derived from BiFeO_3 samples, which were fabricated using the imposed layer-by-layer technique (cf. Section 4.2).

fabricated using a continuous growth mode with a slow repetition rate of the laser of 0.5 Hz, while the structural results from BiFeO_3 thin films grown by the imposed layer-by-layer technique are depicted by gray symbols (cf. Figs. 4.14(c) and (d)).

X-ray diffraction measurements on BiFeO_3 thin films grown on SrRuO_3 -buffered SrTiO_3 reveal a similar crystalline quality as BiFeO_3 thin films deposited on Nb doped SrTiO_3 substrates (cf. Figs. 4.12(a), (b) and Figs. 4.14(a), (b)). The FWHM of rocking curves around the pseudo-cubic BiFeO_3 (001)_{pc} reflection ranges from 0.040° to 0.046° , which proves that BiFeO_3 thin films have low mosaic spread up to a thickness of 120 nm. However, q_{00L} -scans measured along ($q_H = 0.0$) and close ($q_H = 0.0025$) to the coherent crystal truncation rod depicted in Fig. 4.14(a) disclose an increasing intensity due to diffuse scattering with increasing thickness d of the BiFeO_3 thin film. The diffuse scattering even contributes to the q_{00L} -scan at $q_H = 0.0$ resulting in a double peak around the BiFeO_3 (001)_{pc} reflection (cf. full blue symbols in Fig. 4.14(a)). Note that the shoulder observed at around $q_L = 0.91$ rlu can be attributed to finite thickness fringes caused by the 10 nm thick SrRuO_3 buffer layer. The increase of the intensity due to diffuse scattering is also visible in the

transverse q_{H00} -scans around the BiFeO₃ (001)_{pc} reflection displayed in Fig. 4.14(b). Similar to the growth of BiFeO₃ thin films on Nb:SrTiO₃ substrates, the overall intensity of these scans can be explained by a superposition of scattering on long range mosaicity as well as intensity caused by diffuse scattering. Interestingly, the sample with a thickness of 30 nm reveals satellite peaks at around $q_H = \pm 0.0025$, which might be explained by an ordered network of misfit dislocations [280]. In general, a detailed analysis of the x-ray diffraction results in terms of strain relaxation and diffuse scattering reveals a different behavior of BiFeO₃ thin films fabricated on SrRuO₃-buffered SrTiO₃ substrates as compared to BiFeO₃ thin films deposited on Nb:SrTiO₃ crystals. First, the pseudo-cubic out-of-plane lattice constant c_{pc} , which was derived using the Nelson-Riley method, discloses a slight increase with increasing film thickness up to 38 nm. This is in agreement with the reported values in Refs. [244, 276], but in contrast to Ref. [240]. Assuming stoichiometric thin films with no defects, the out-of-plane lattice constant should always decrease or at most stay constant, since BiFeO₃ thin films fabricated on SrRuO₃-buffered SrTiO₃ are under tensile out-of-plane strain. Therefore, the increase in the lattice along the out-of-plane direction could be an indication for extrinsic effects, such as non-stoichiometry like oxygen vacancies or variations of the Bi/Fe ratio. Moreover, the structural properties of BiFeO₃ thin films are also strongly affected by the quality of the SrTiO₃ substrate and the SrRuO₃ buffer layer [276, 287]. On the other hand, recent theoretical calculations reveal an unusual dependence of the lattice volume on the lattice strain in the limit of moderate compressive in-plane strain of 0% to -2% [249]. However, to conclusively explain the elastic behavior of our BiFeO₃ thin films with thicknesses lower than 38 nm, further measurements are needed. As obvious from Fig. 4.14(c), BiFeO₃ thin films with thicknesses larger than 38 nm exhibit an almost constant out-of-plane lattice parameter, which is in agreement with other publications [240, 263]. This suggests that the strain relaxation takes place in the film plane for $38 \text{ nm} < d < 120 \text{ nm}$ [240]. Similar to the evolution of the out-of-plane lattice constant c_{pc} , the integrated intensity ratio caused by diffuse scattering R strongly increases between $d = 30 \text{ nm}$ and 49 nm , indicating a significant growth of the defect density. At larger thickness, R stays almost constant resembling the evolution of the out-of-plane lattice parameter. Almost the same behavior is observed for the microstrain ϵ_i , which is determined by the Williamson-Hall method (cf. Fig. 4.13(c)), and the average out-of-plane strain ϵ_a . This is in contrast to the behavior found in BiFeO₃ thin films fabricated on Nb:SrTiO₃ substrates. Therefore, the relaxation of the misfit strain seems to be different in BiFeO₃ thin films deposited on SrRuO₃-buffered SrTiO₃ substrates than on Nb:SrTiO₃ crystals, which would be worth to be studied in the future using synchrotron radiation. By comparing the absolute values of the intensity ratio R as well as the microstrain ϵ_i of BiFeO₃ thin films grown on SrRuO₃-buffered SrTiO₃ substrates with values derived for BiFeO₃ thin films fabricated directly on Nb:SrTiO₃ crystals, a larger intensity due to diffuse scattering as well as an enhanced microstrain is obtained in BiFeO₃ thin films on SrRuO₃-buffered SrTiO₃ substrates. Since the SrRuO₃ buffer layer shows finite thickness fringes above $q_L > 0.91 \text{ rlu}$, it will certainly influence the intensity ratio R . But reciprocal space maps around the SrRuO₃ (220) reflection reveal only a very low

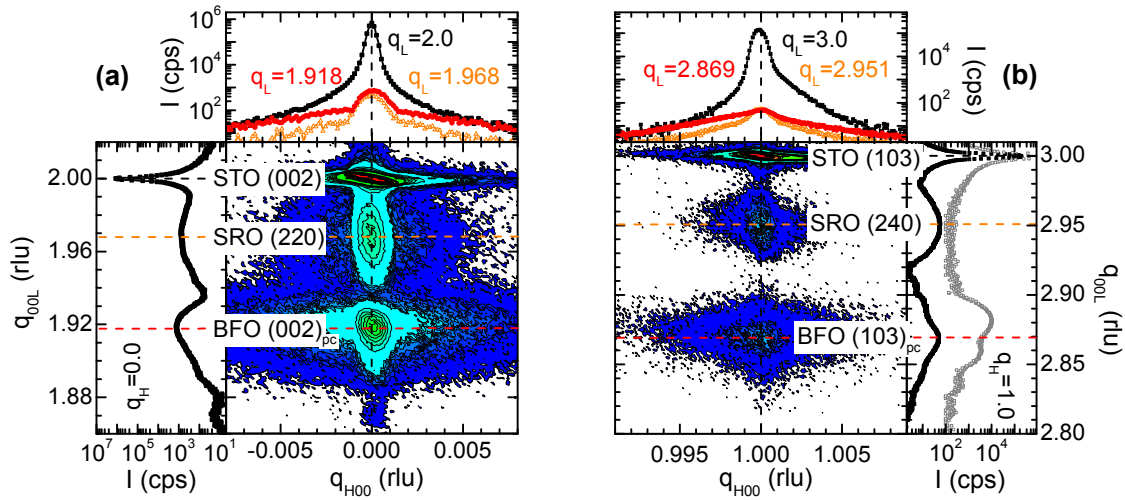


Figure 4.15: Reciprocal space maps around (a) SrTiO₃ (002) and (b) SrTiO₃ (103) of a 22 nm thick BiFeO₃ film grown on a SrRuO₃-buffered SrTiO₃ (001) substrate exhibiting a miscut angle of about 1°. For comparison, the q_{00L} -scan carried out on a 22 nm thick BiFeO₃ film directly grown on a Nb:SrTiO₃ substrate with low miscut angle ($< 0.1^\circ$) is shown in the right panel of (b) (gray open symbols).

intensity due to diffuse scattering. Therefore, the SrRuO₃ buffer layer alone cannot explain the surprising high R and ϵ_i values.¹⁴ These values could be decreased by reducing the number of monoclinic domains. As depicted in Fig. 4.11(a), different monoclinic domains reduce the shear strain in BiFeO₃ thin films fabricated on SrTiO₃ (001)-oriented substrates. In analogy to SrRuO₃ (cf. Section 4.3), a preferential formation of monoclinic domains can be achieved by using miscut substrates, making it possible to engineer the domain state in BiFeO₃ thin films [276].

Figure 4.15 shows the structural properties of a 23 nm thick BiFeO₃ film fabricated on a SrRuO₃(22 nm)-buffered SrTiO₃ substrate exhibiting a miscut angle of about 1°. The reciprocal space map around the SrTiO₃ (002) reflection reveals a tilt of the out-of-plane [001]_{pc} direction of the BiFeO₃ thin film with respect to the [001] direction of the substrate and the [110] direction of the SrRuO₃ buffer layer. This behavior is also observable in the transverse q_{H00} -scan around the BiFeO₃ (002)_{pc} reflection at $q_L = 1.918$ rlu shown in the upper panel of Fig. 4.15(a). While the broad component is symmetric with respect to $q_H = 0$ rlu, the sharp component is shifted to higher q_H values. The difference of the intensity due to Bragg reflection and diffuse scattering is also visible in the reciprocal space map. The maximum intensity of the diffuse scattering is not located around the BiFeO₃ (002) Bragg reflection, but shifted to higher q_L -values. This indicates that the position of the Bragg peak is not affected by dislocations, which are therefore separated from one another by more than the lattice spacing [280]. The tilt of the scattering planes with respect to the SrTiO₃ substrate can be determined to $(0.06 \pm 0.01)^\circ$. The number of monoclinic

¹⁴ q_{00L} -scans depicted in Fig. 4.14(a) reveal a significant peak broadening due to the increase of diffuse scattering for thicknesses larger than 90 nm, which is taken into account in larger uncertainties in ϵ_i .

domains can be investigated by performing x-ray diffraction measurements around SrTiO₃(103) (cf. Fig. 4.11(b)). Figure 4.15(b) reveals no splitting of the pseudocubic BiFeO₃(103)_{pc} reflection. The small humps visible around $q_L = 2.90$ rlu in the q_{00L} -scan depicted in the right panel of Fig. 4.15(b) can be attributed to finite thickness fringes. The q_{00L} -scan carried out on a 22 nm thick BiFeO₃ film grown on a Nb:SrTiO₃ substrate with low miscut angle is shown for comparison (cf. open gray symbols in Fig. 4.11(b)). Since only two of the four monoclinic domains are distinguishable in the reciprocal space around SrTiO₃(103), the single reflection observed in Fig. 4.15(b) suggests the existence of only two monoclinic domain-types in this sample. However, the preferential formation of certain monoclinic domains should also decrease the number of twin-domain boundaries, which reduces the intensity due to diffuse scattering. In fact, the intensity ratio of the diffuse scattering R is reduced to 0.35 compared to 0.65 for BiFeO₃ thin films grown on SrRuO₃-buffered SrTiO₃ substrates exhibiting low miscut angles. Therefore, the use of highly miscut SrTiO₃ substrates allows us to engineer the domain configuration in BiFeO₃ thin films, which certainly has great influence on the physical properties of these thin films. Recently, Baek and coworkers fabricated even monodomain BiFeO₃(001)-oriented samples [288].

To conclude, BiFeO₃ thin films with excellent crystalline quality in terms of mosaic spread were fabricated on SrRuO₃-buffered SrTiO₃ substrates. However, no reduction of the microstrain as well as the intensity contribution due to diffuse scattering were found in these thin films compared to BiFeO₃ thin films deposited directly on Nb:SrTiO₃ crystals. This suggests that BiFeO₃ thin films on SrRuO₃-buffered SrTiO₃ substrates exhibit a considerable amount of crystalline defects, such as dislocations. The intensity of the diffuse scattering could be significantly reduced by decreasing the number of monoclinic domains in BiFeO₃ thin films using a SrTiO₃ substrate with a miscut angle of 1°. It was found that the four possible structural domains are reduced to two, resulting in an intensity ratio of the diffuse scattering, which is comparable to BiFeO₃ thin films deposited on Nb:SrTiO₃.

4.4.2 Multiferroic properties of BiFeO₃ thin films

The multiferroic properties, which are by far the most interesting aspects with regard to BiFeO₃, are discussed in the following. Since the structural properties of BiFeO₃ thin films reveal no significant improvement by using SrRuO₃ buffer layers, we focus only on thin films fabricated directly on Nb:SrTiO₃ substrates.

Dielectric properties of BiFeO₃ thin films

The dielectric properties and in particular the ferroelectric domain configuration of a 38 nm thick BiFeO₃ film grown on a Nb:SrTiO₃ substrate are discussed in the following. Since we focus on BiFeO₃ thin films with thicknesses lower than 120 nm in this thesis, measurements of the ferroelectric properties of these thin films using a standard ferroelectric tester with macroscopic contacts (cf. Section 2.2.1) have not been successful due to high leakage currents present in these samples. Therefore,

the ferroelectric properties of BiFeO_3 thin films were investigated by piezoelectric force microscopy (PFM) (cf. Section 2.2.2). These measurements were carried out by Denny Köhler (Institute of Applied Photophysics, Technische Universität Dresden).¹⁵

The ferroelectric state in BiFeO_3 is realized by a large displacement of Bi relative to the FeO_6 octahedron, which is driven by the active lone pair of the $6s$ Bi^{3+} ion [125]. This leads to a distortion along the $\langle 111 \rangle_{\text{pc}}$ direction of the orthorhombic pseudo-cubic cell upon crossing the phase transition from the paraelectric to the ferroelectric state (cf. Section 4.4.1). As a consequence, four different ferroelastic domains can form (cf. Fig. 4.11(a)). Each of them exhibits two polarization directions resulting in eight possible polarization variants $\pm \mathbf{P}_i$ ($i = 1 - 4$) with the polarization vectors aligned along the four pseudo-cubic diagonals $\langle 111 \rangle_{\text{pc}}$. The domain walls separating the different domain states are characterized by the rotational angle needed to match the spontaneous polarization on both sides of the wall. Each of the eight polarization vectors can therefore be separated by either 71° , 109° , or 180° domain walls in BiFeO_3 [274, 278]. These domains can be investigated using piezoelectric force microscopy (PFM).

The results of piezoelectric force microscopy (PFM) measurements sensitive to the out-of-plane and in-plane component performed at ambient conditions on an as-grown 38 nm thick BiFeO_3 film fabricated on a Nb:SrTiO_3 substrate are shown in Fig. 4.16. In addition, the topography of the BiFeO_3 thin film measured simultaneously with the PFM signal is depicted in Fig. 4.16(a) and (d), respectively. The measurements were carried out using an ac modulation with an amplitude between 0.5 V and 1.0 V as well as a frequency of 24 kHz.

As obvious from Fig. 4.16(a), this particular BiFeO_3 sample was grown in an island growth mode, resulting in a large root mean square (rms) roughness of more than 10 nm. Furthermore, no drift effects are detectable, which is proven by an excellent reproducibility of the topography recorded simultaneously during the out-of-plane and in-plane PFM measurements (cf. Fig. 4.16(a) and (d)). This enables us to compare both measurements and derive the ferroelectric domain configuration of this thin film area. We start with the out-of-plane PFM measurements. The amplitude and the phase, which respectively are sensitive to the local piezoelectric coefficient and the polarization direction, of the out-of-plane PFM measurements reveal different results (cf. Fig. 4.16(b) and (c)). While the PFM phase shows a homogeneous contrast, finite structures observed in the PFM amplitude suggest the presence of different domains. This can be explained by taking into account a crosstalk between one of the in-plane components of the PFM signal and the out-of-plane PFM signal [93]. On the other hand, the finite in-plane component visible in the out-of-plane contrast could also be an indication for polarization vectors deviating from the pseudo-cubic $\langle 111 \rangle_{\text{pc}}$ directions, which would confirm recent theoretical predictions [240, 247, 249]. However, the PFM phase measured along the out-of-plane direction suggests a constant out-of-plane component of the ferroelectric polarization, which can be attributed to the existence of a self-poling effect as a consequence of the

¹⁵More details on the PFM technique as well as on the results of our BiFeO_3 samples can be found in the PhD thesis of Denny Köhler [93].

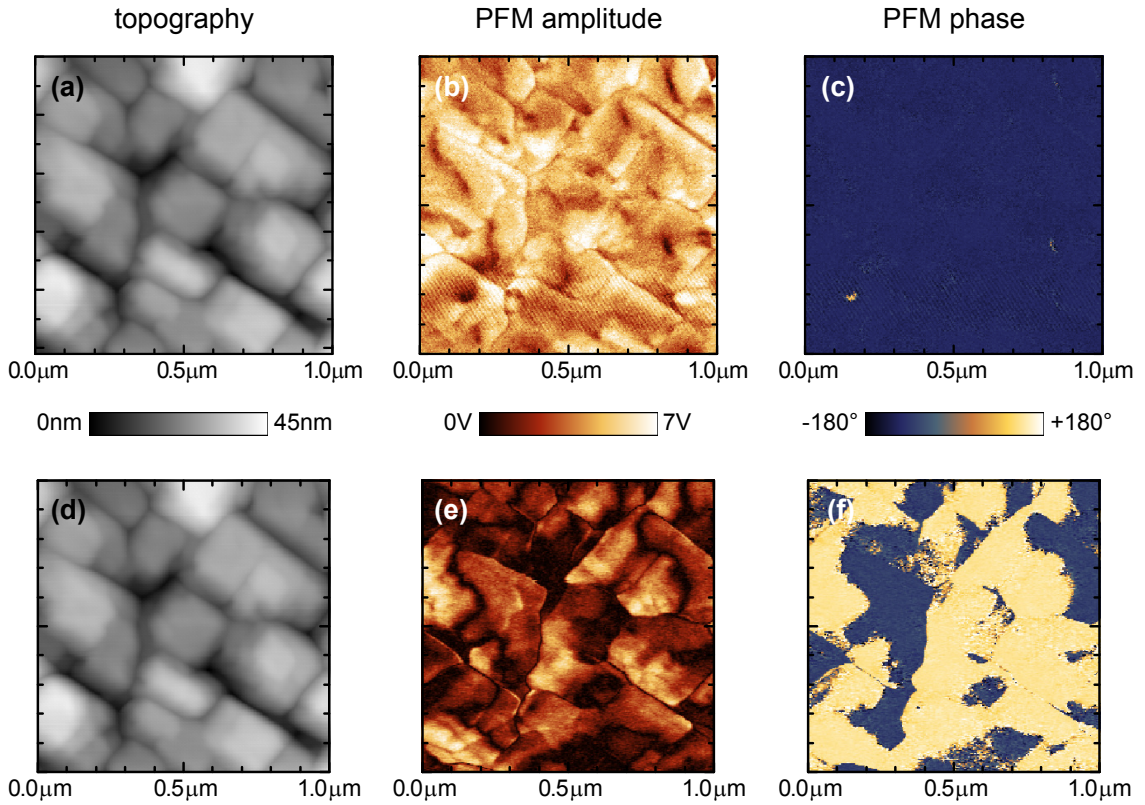


Figure 4.16: Piezoelectric force microscopy (PFM) measurements performed at ambient conditions on a 38 nm thick BiFeO₃ film grown on Nb doped SrTiO₃: out-of-plane PFM (b) amplitude and (c) phase signal as well as in-plane PFM (e) amplitude and (f) phase signal. The topography, which is recorded simultaneously during measuring the out-of-plane PFM and in-plane PFM signal, is shown in (a) and (d), respectively.

conducting Nb:SrTiO₃ substrate [275, 289, 290], as well as to epitaxial strain effects [240]. Therefore, the number of possible polarization variants is reduced to four ($+\mathbf{P}_i$ with $i = 1 - 4$). This is in agreement with BiFeO₃ thin films grown on SrRuO₃-buffered substrates exhibiting moderate thicknesses of $d \lesssim 130$ nm [240, 262, 291]. The in-plane PFM measurements reveal a finite contrast in the amplitude and phase images (cf. Fig. 4.16(e) and (f)). To investigate the domain configuration in more detail, the PFM amplitude A_{PFM} and the PFM phase signal Φ_{PFM} was converted into $X_{\text{PFM}} = A_{\text{PFM}} \cdot \cos(\Phi_{\text{PFM}} + \alpha_{\text{PFM}})$ and $Y_{\text{PFM}} = A_{\text{PFM}} \cdot \sin(\Phi_{\text{PFM}} + \alpha_{\text{PFM}})$ [93], where the phase factor α_{PFM} can be chosen such that $Y_{\text{PFM}} \approx 0$. Due to this transformation X_{PFM} shows the whole information about the domain configuration, whereas Y_{PFM} contains only noise.

In Fig. 4.17(a) and (b), the X_{PFM} signals derived from the out-of-plane and in-plane measurements depicted in Fig. 4.16 are shown. Since the out-of-plane X_{PFM} signal might be caused by artifacts, only the X_{PFM} signal stemming from the in-plane measurements are discussed in the following. In principle, in ferroelectric materials exhibiting a rhombohedral symmetry with polarization vectors $\pm\mathbf{P}_i$ ($i = 1 - 4$) aligned along the pseudo-cubic $\langle 111 \rangle_{\text{pc}}$ directions, the in-plane PFM images taken

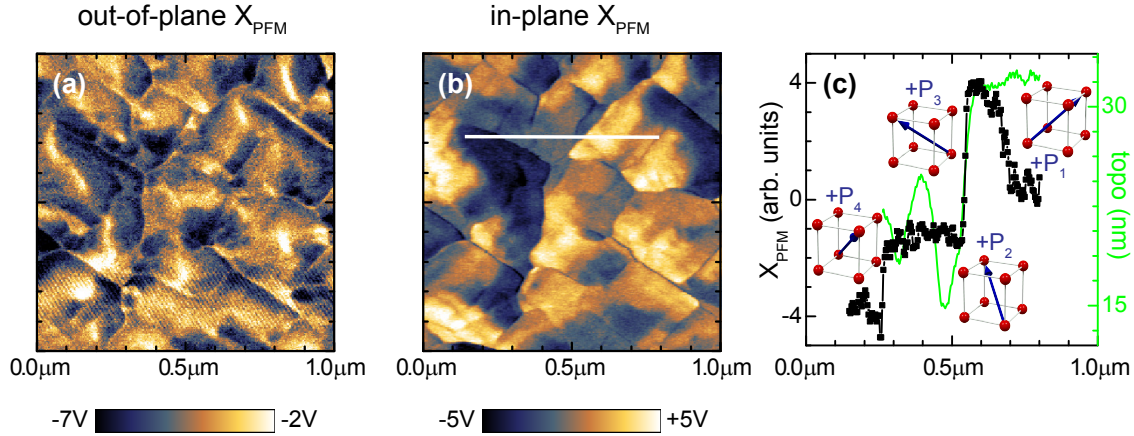


Figure 4.17: The PFM amplitude A_{PFM} and the PFM phase Φ_{PFM} were converted into $X_{\text{PFM}} = A_{\text{PFM}} \cdot \cos(\Phi_{\text{PFM}} + \alpha_{\text{PFM}})$ and $Y_{\text{PFM}} = A_{\text{PFM}} \cdot \sin(\Phi_{\text{PFM}} + \alpha_{\text{PFM}})$. The phase factor α_{PFM} can be chosen such that $Y_{\text{PFM}} \approx 0$ [93]. Therefore, the out-of-plane (a) and in-plane (b) X_{PFM} -signal holds the whole ferroelectric domain information. (c) X_{PFM} -signal and the topography along the white line marked in (b). The polarization direction $+\mathbf{P}_i$ ($i = 1 - 4$) is schematically shown in each region.

with the cantilever pointing along $\langle 100 \rangle_{\text{pc}}$ reveal two different contrast levels, since in this case only two of the four domains can be distinguished. However, three different tones are expected for measurements with the cantilever's long axis aligned along $\langle 110 \rangle_{\text{pc}}$, as domains exhibiting in-plane components of the polarization vector parallel to $\langle 110 \rangle_{\text{pc}}$ do not produce any torque required for a finite contrast in in-plane PFM measurements [289, 292]. Assuming that the islands visible in the topography images are aligned along the pseudo-cubic axes of BiFeO_3 [293], Figs. 4.16(a) and (d) reveal a misalignment of the cantilever's long axis of 35° with respect to the $[010]_{\text{pc}}$ direction. Therefore, all four polarization vectors $+\mathbf{P}_i$ with $i = 1 - 4$ should be visible and four contrast levels are expected. Indeed, Fig. 4.17(b) reveals four contrast levels, which can be used to determine the polarization direction. As an example, the evolution of the polarization along the white line marked in Fig. 4.17(b) was analyzed (cf. Fig. 4.17(c)). The X_{PFM} signal reveals four domains, each of them separated by 71° domain walls. The existence of mainly 71° domain walls in as-grown BiFeO_3 thin films is in agreement with previous reports [240, 289, 290]. These domain walls cause a twinning of the monoclinic unit cell and reduce the in-plane strain state of BiFeO_3 thin films on $\text{SrTiO}_3(001)$ substrates [240, 290]. Furthermore, it was shown that the out-of-plane polarization switching in BiFeO_3 thin films is strongly affected by these domain walls [290]. We note, however, that 71° domain walls are non-conducting and are therefore not responsible for the high leakage current in these thin films [278].

In addition to the X_{PFM} signal, the topography along the white line is also shown in Fig. 4.17(c). A clear correlation between the in-plane PFM signal and the topography is visible around $0.55 \mu\text{m}$. Therefore, as expected, BiFeO_3 thin films with a high surface roughness strongly affect the ferroelectric properties. Therefore, to improve the ferroelectric properties of BiFeO_3 thin films, a two-dimensional growth

process is mandatory (cf. Section 4.2.2).

In total, the dielectric properties of a 38 nm thick BiFeO₃ film fabricated on a Nb:SrTiO₃ substrate were investigated using piezoelectric force microscopy. These measurements reveal a ferroelectric state of the BiFeO₃ thin film at room temperature. Moreover, a constant out-of-plane component of the polarization was detected. In contrast, in-plane measurements reveal a ferroelectric domain structure with mainly 71°-type domain walls. On the one hand, it was reported that these domain walls strongly affect the polarization reversal in BiFeO₃ thin films [290]. On the other hand, polarization switching by either 71° or 109° changes the orientation of the easy magnetization plane [137]. Furthermore, magnetoelectric coupling in BiFeO₃ thin films is suggested to be enhanced at ferroelectric domain walls [294]. Therefore, while the ferroelectric properties can be enhanced by using single-domain BiFeO₃ thin films, it seems that finite magnetoelectric coupling requires 71° and 109° domain walls.

Magnetic properties of BiFeO₃ thin films

On a local level, bulk BiFeO₃ exhibits an antiferromagnetic arrangement of antiparallel aligned Fe magnetic moments of nearest neighbors in all three Cartesian directions due to superexchange interaction. This results in a *G*-type antiferromagnetic order, where the magnetic moments are coupled ferromagnetically within the pseudo-cubic {111}_{pc} planes perpendicular to the polarization direction and antiferromagnetically between these planes [295, 296]. In this order, the Fe³⁺ cations are surrounded by six nearest Fe³⁺ neighbors, with opposite spin directions. In reality, the spins are not perfectly antiparallely aligned, resulting in a weak moment induced by a Dzyaloshinskii-Moriya interaction [297, 298]. This interaction, which arises from the interplay between superexchange and spin-orbit coupling [298], can be expressed as $E_{ij}^{\text{DM}} = D_{ij} \cdot (\mathbf{S}_i \times \mathbf{S}_j)$, where D_{ij} is the Dzyaloshinskii-Moriya vector and \mathbf{S}_i and \mathbf{S}_j are two localized magnetic moments. E_{ij}^{DM} is minimized if the two magnetic moments form an angle of 90°. However, since the much stronger Heisenberg-type interaction $E_{ij}^{\text{H}} = J_{ij} \cdot (\mathbf{S}_i \cdot \mathbf{S}_j)$ favors either 0° or 180° angles, the Dzyaloshinskii-Moriya interaction leads only to a small canting between the interacting moments. As D_{ij} is zero in materials, which exhibit an inversion symmetry, the ferroelectric distortion in ferroelectric antiferromagnets may trigger a Dzyaloshinskii-Moriya interaction, leading to canting of the antiferromagnetic sublattice magnetizations, which results in a net magnetic moment [299]. In such materials, which exhibit an antiferromagnetic order with an antiferromagnetic vector \mathbf{L} ¹⁶ and a finite ferroelectric polarization \mathbf{P} , where the polarization \mathbf{P} and the Dzyaloshinskii-Moriya vector D_{ij} are based on the same structural distortion, the system can lower its energy by $E^{\text{PLM}} \sim \mathbf{P} \cdot (\mathbf{L} \times \mathbf{M})$ [299]. A reversal of the polarization \mathbf{P} without changing the orientation of \mathbf{L} then leads to a sign change in the net magnetization \mathbf{M} , and thus a magnetoelectric coupling, where the magnetization can be reversed by an electric field, is achieved. However, symmetry analysis and first principles calculations revealed that this seems

¹⁶Recent calculations revealed that the lowest energy is provided when the antiferromagnetic vector \mathbf{L} lies along the pseudo-cubic $[\bar{1}10]$ direction [300].

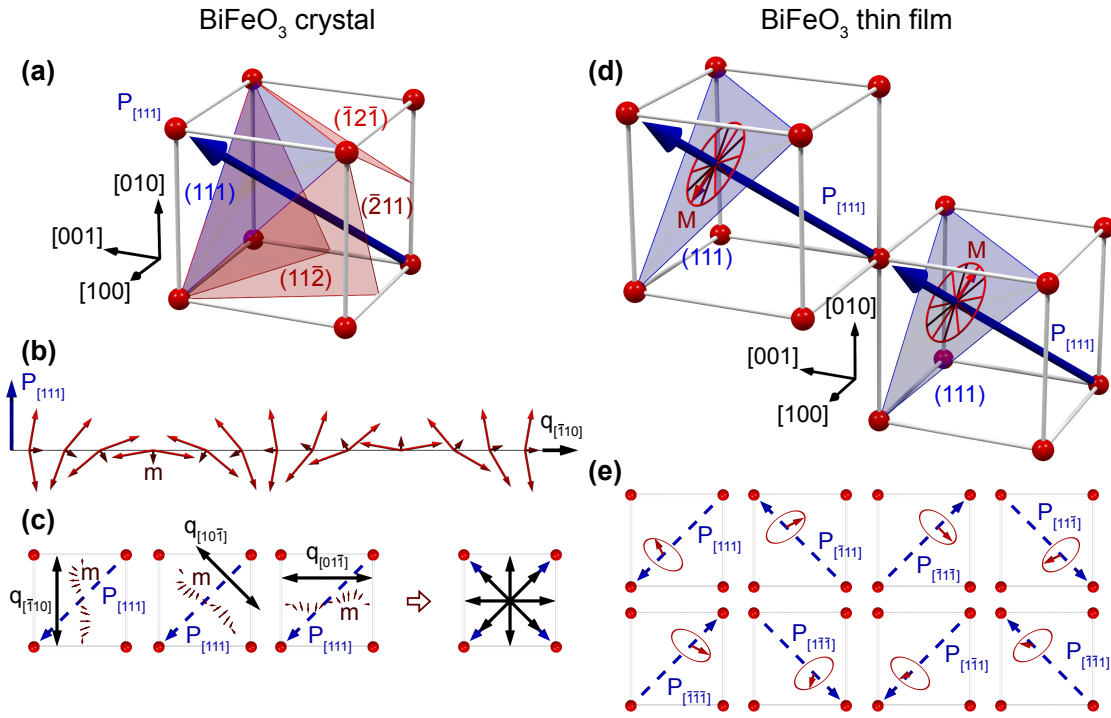


Figure 4.18: Schematic representation of the magnetic structure of BiFeO_3 single crystals and BiFeO_3 thin films. The figure is adapted from Ref. [305]. (a), (b) In case of BiFeO_3 single crystals, the canted magnetic moments are arranged in a cycloidal ordering: nearest Fe^{3+} magnetic moments are arranged in a 62 – 64 nm long cycloid in one of the $\{121\}_{\text{pc}}$ planes (cf. red shaded areas in (a)) for $\mathbf{P} \parallel \langle 111 \rangle_{\text{pc}}$. (c) The projection of the canted magnetic moments \mathbf{m} on the $(010)_{\text{pc}}$ plane is modulated along $[100]_{\text{pc}}$, $[101]_{\text{pc}}$, and $[001]_{\text{pc}}$ for the cycloid propagation vector \mathbf{q} parallel to $[\bar{1}10]_{\text{pc}}$, $[10\bar{1}]_{\text{pc}}$, and $[01\bar{1}]_{\text{pc}}$, respectively. Taking into account all possible orientations of the polarization, the weak canted moment is modulated along the $\langle 110 \rangle_{\text{pc}}$ or $\langle 100 \rangle_{\text{pc}}$ directions. (d), (e) In BiFeO_3 thin films, the spin cycloid is believed to be destroyed by epitaxial strain, leading to a collinear antiferromagnetic arrangement. In this case, the magnetization of the magnetic sublattices \mathbf{M} are located in the magnetic easy plane perpendicular to the polarization $\mathbf{P} \parallel \langle 111 \rangle_{\text{pc}}$. The epitaxial strain further lifts the degeneracy within the $\{111\}$ planes (cf. blue shaded area in (d)). According to Ref. [306], BiFeO_3 thin films under either compressive or tensile strain exhibit preferred magnetic axes along $\langle 112 \rangle$ (cf. light red lines in (d)) or $\langle 1\bar{1}0 \rangle$ (cf. dark red lines in (d)), depending on the polarization direction. (e) Projection of the magnetic easy axes $\langle 112 \rangle$ on the (010) plane for different directions of the electric polarization. The BiFeO_3 unit cells are greatly simplified by showing only the Bi ions (red dots).

not to be the case in BiFeO_3 [296, 299, 301, 302]. In this material system, the weak ferromagnetism of around $0.1 \mu_{\text{B}}/\text{f.u.}$, which corresponds to a 1° canting from the collinear direction, might be induced by octahedral rotations rather than polar distortions [296]. However, the lack of the coupling between D_{ij} and \mathbf{P} in BiFeO_3 is still discussed controversially [13, 303, 304].

In addition to the spin canting of the magnetic moments, BiFeO_3 crystals exhibit a long-range spiral spin structure in which the antiferromagnetic axis rotates through the crystal with an incommensurate long-wavelength period of about 62 – 64 nm [29, 143, 307, 308]. The propagation vector of this spin cycloid was found to be

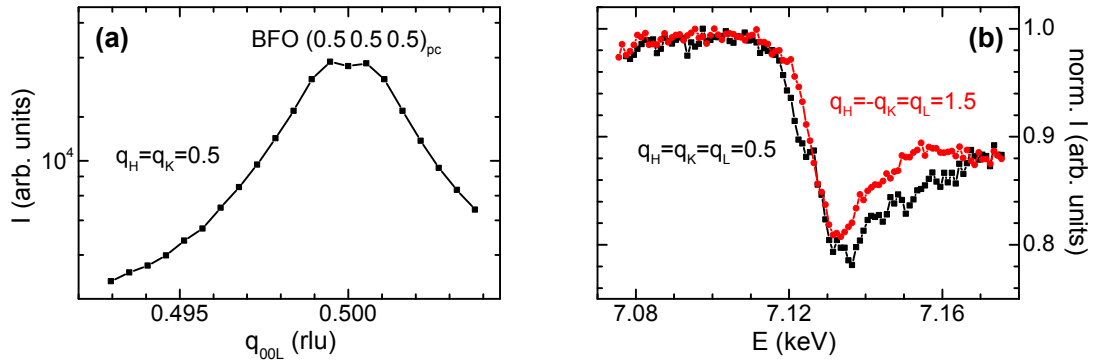


Figure 4.19: (a) Non-resonant x-ray scattering around BiFeO₃ (0.5 0.5 0.5)_{pc} and (b) energy scans around the Fe *K*-edge at BiFeO₃ (0.5 0.5 0.5)_{pc} and (1.5 – 1.5 1.5)_{pc} reflections measured on a BiFeO₃ (30 nm) thin film grown on a SrRuO₃-buffered SrTiO₃ substrate. The energy profiles were performed under constant scattering vector \mathbf{q} and were not corrected for absorption. The experiments were carried out at the BM28 beamline at the ESRF (Grenoble).

along one of the three equivalent pseudo-cubic $\langle 110 \rangle_{pc}$ directions, which is schematically shown in Figs. 4.18(a)-(c). This spin cycloid averages out the macroscopic canting moment resulting in a vanishing macroscopic magnetization in bulk single crystals [162] and can be destroyed with high magnetic fields, recovering the canted magnetic state and its associated remanent magnetization [309]. Furthermore, the volume averaged magnetoelectric effect vanishes in the presence of a spin cycloid. Therefore, the destruction of the spin cycloidal structure is essential for a finite linear magnetoelectric coupling in BiFeO₃. However, in the presence of the spin cycloid structure, the magnetic easy plane defined by the propagation vector \mathbf{q} and the direction of the ferroelectric polarization can be modified by either 71° or 109° switching of the polarization [29–31]. Therefore, the magnetic easy plane, within which the spins rotate, can be switched only if the polarization changes direction, but not if it merely changes polarity [13].

In BiFeO₃ thin films, the spin cycloid is believed to be destroyed by epitaxial strain [310]. Therefore, the antiferromagnetic structure was reported to be collinear *G*-type [311]. This directly results in a net magnetization, since the canted magnetic moment is not averaged out. Therefore, a weak magnetic moment is expected in BiFeO₃ thin films. Furthermore, in collinear *G*-type antiferromagnets, the {111} planes can be considered as effective easy planes of the magnetization [305]. However, it was recently found that the degeneracy between all directions within the {111} planes is lifted in BiFeO₃ thin films due to epitaxial strain [306]. For BiFeO₃ thin films under either compressive or tensile strain, the antiferromagnetic direction lies along the $\langle 112 \rangle$ or $\langle 1\bar{1}0 \rangle$ axes (cf. Figs. 4.18(d), (e)). Therefore, Fig. 4.18 reveals that the magnetic properties of BiFeO₃ thin films should be quite different compared to the magnetic behavior of BiFeO₃ single crystals, which is mainly caused by epitaxial strain.

In general, strain can strongly affect the magnetic properties in epitaxial thin films, changing not only the magnetic transition temperature [312] but also the

magnetic anisotropy [313] as well as the saturation magnetization [208]. To investigate the strain dependence of the magnetic properties of BiFeO₃ thin films, we first discuss the kind of antiferromagnetic order. The magnetic *G*-type structure in bulk BiFeO₃ results in a doubling of the magnetic unit cell so that magnetic reflections are expected to appear at $(hkl) = (vvv)_{\text{pc}}$ with $v = 0.5 \cdot n$ and $n \in \mathbb{Z}$ in a pseudo-cubic notation (cf. Fig. 4.18(d)). Since these reflections are not only of magnetic origin but contain also structural information in BiFeO₃ thin films (cf. Fig. 4.9(b)), the *G*-type magnetic order gives rise to superstructure peaks at the same positions to those associated with the tilt of the oxygen octahedra. Therefore, due to the high magnetic transition temperature in BiFeO₃, it is difficult to separate magnetic and structural information, in particular when using neutron diffraction experiments. Therefore, we used resonant x-ray magnetic scattering (RXMS) to evaluate the magnetic structure of BiFeO₃ thin films (cf. Section 2.1.3). The x-ray diffraction experiment were performed at the BM28 beamline at the ESRF. A vertical scattering geometry was used, so that the incident photons were σ -polarized. However, no polarization analyzer was installed in this case, thus the intensity shown in Fig. 4.19 is the total scattering intensity. A 30 nm thick BiFeO₃ film grown on a SrRuO₃-buffered SrTiO₃ substrate was used for the experiment. The *q*-scan along the pseudo-cubic $[111]_{\text{pc}}$ direction with $q_{\text{H}} = q_{\text{K}} = q_{\text{L}}$ using an energy near the Fe *K*-edge reveals a finite intensity at $(0.5\ 0.5\ 0.5)_{\text{pc}}$ (Fig. 4.19(a)). This again confirms a monoclinic *Cc* symmetry for BiFeO₃ thin films in the limit of moderate epitaxial strain (cf. 4.4.1). To reveal the magnetic structure, energy scans around the Fe *K*-edge were performed at BiFeO₃ $(0.5\ 0.5\ 0.5)_{\text{pc}}$ and $(1.5\ \bar{1}.5\ 1.5)_{\text{pc}}$ reflections. The results are shown in Fig. 4.19(b). Tuning the energy of the incoming beam to the *K*-edge of Fe, a significant reduction of the scattering intensity is observable, but no resonant behavior is visible. The absence of any resonant x-ray magnetic scattering suggests that $(0.5\ 0.5\ 0.5)_{\text{pc}}$ and $(1.5\ \bar{1}.5\ 1.5)_{\text{pc}}$ are no magnetic reflections. This is surprising, since several groups found a *G*-type antiferromagnetic order also in thin films [239, 242, 246, 311] by investigating the $(0.5\ 0.5\ 0.5)_{\text{pc}}$ reflection using neutron diffraction experiments. However, as stated above, this reflection could also be of nuclear origin only. Therefore, the conclusion of a *G*-type magnetic order solely from using neutron diffraction techniques should be considered with care even in case of temperature dependent measurements [242]. In contrast, either *A*-type or *C*-type antiferromagnetism in BiFeO₃ thin films, which would result in magnetic $(0\ 0\ 0.5)_{\text{pc}}$ or $(0.5\ 0.5\ 0)_{\text{pc}}$ reflections, appear unlikely, since theoretical calculations predicted a change of the bulk *G*-type magnetic ordering not until the epitaxial strain exceeds -4.5% [249]. Taking together, the absence of any resonance behavior in our measurements remains unsolved and RXMS measurements should be repeated in more detail in the near future using BiFeO₃ thin films with different thicknesses, i.e., different strain states.

While the antiferromagnetic ordering could not be resolved, a magnetic hysteresis exhibiting a small saturation magnetization of around 2.3 kA/m, which corresponds to $0.04\ \mu_{\text{B}}/\text{f.u.}$, is detectable from SQUID magnetometry measurements at $T = 25\ \text{K}$ on BiFeO₃ thin films deposited on Nb:SrTiO₃ crystals (cf. Fig. 4.20(a)). Thus, our BiFeO₃ thin films exhibit a weak ferromagnetic phase, which can be

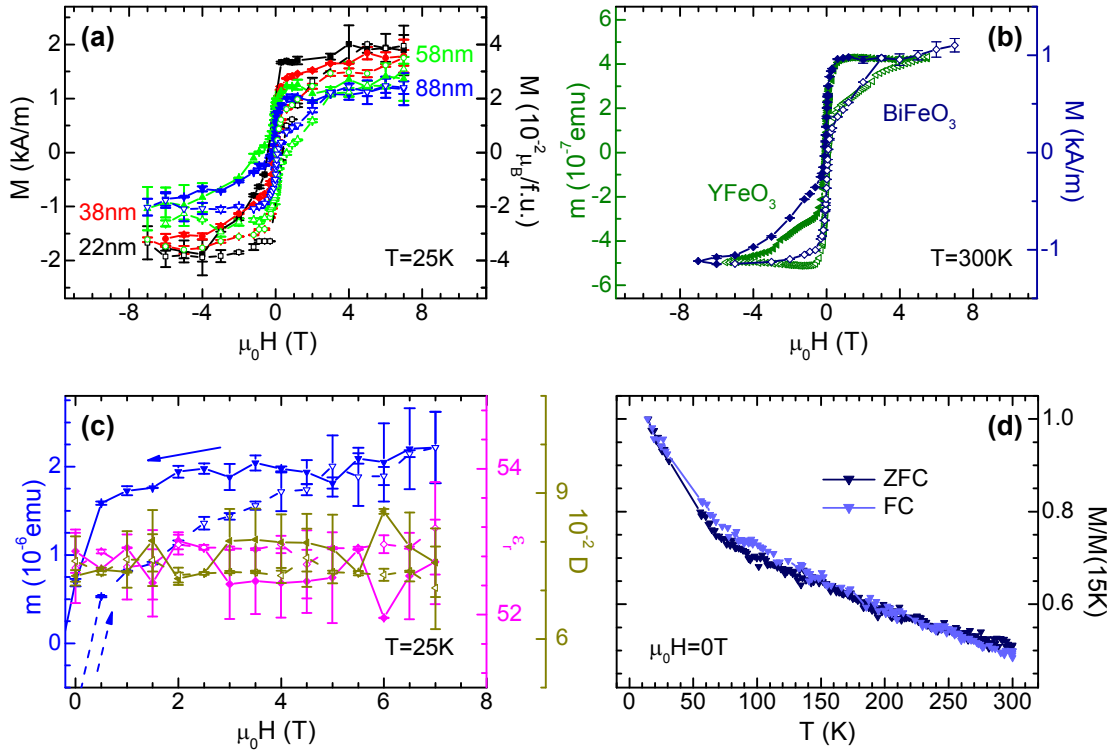


Figure 4.20: Macroscopic magnetic behavior of BiFeO₃ thin films deposited on Nb:SrTiO₃ substrates with the magnetic field applied along the pseudo-cubic BiFeO₃ [100]_{pc} direction. (a) The magnetic field dependence of the magnetization at 25 K reveals only a small enhancement of the weak magnetic moment with decreasing the thin film thickness, i.e., increasing the strain state of the BiFeO₃ thin films. (b) Comparison between the M - H -loop of a 120 nm thick BiFeO₃ thin film measured at 300 K (full symbols) with the magnetic field dependence of YFeO₃ (open symbols) indicating a spin reorientation process in both kinds of material systems. The data for YFeO₃ are taken from Ref. [314]. (c) To detect a possible destruction of the spin cycloid structure in a 88 nm thick BiFeO₃ film at high magnetic fields, the magnetic moment, the real part of the dielectric constant, and the dielectric loss were measured simultaneously at 25 K. No indication of a phase transition from a cycloidal to a homogeneous antiferromagnetic spin order is visible. The down sweep (+7 T \rightarrow -7 T) is marked by full symbols, while the open symbols denote the up sweep (-7 T \rightarrow +7 T). (d) Remanent magnetization as a function of temperature measured after cooling the sample from 390 K to 5 K in either zero magnetic field (ZFC) or $\mu_0 H = 7$ T (FC).

attributed to spin canting of the antiferromagnetic sublattices. However, in the pioneering experimental work by Wang *et al.* on BiFeO₃ thin films, a tremendous enhancement of the saturation magnetization of around $1 \mu_B/\text{f.u.}$ under compressive strain was found [32]. This is not confirmed in our measurements. Figure 4.20(a) reveals that the saturation magnetization decreases from (1.8 ± 0.4) kA/m ($(0.032 \pm 0.007) \mu_B/\text{f.u.}$) to (1.1 ± 0.2) kA/m ($(0.019 \pm 0.003) \mu_B/\text{f.u.}$) with increasing the thin film thickness from 22 to 88 nm, which is equivalent to a decrease of the out-of-plane strain by 0.4% (cf. Fig. 4.13(d)). This is in agreement with recent publications [38, 160, 239, 250, 315] and indicates the absence of magnetic parasitic phases containing iron, since these phases will strongly increase the satu-

ration magnetization [38, 149, 160]. Therefore, the strong ferromagnetism found in strained BiFeO₃ samples by Wang and coworkers [32] probably is of extrinsic origin. Our measurements suggest that there is a finite strain dependence of the saturation magnetization, increasing its value by a factor of 1.6 in agreement with other measurements [250, 315]. Note that strain relaxation can also lead to multiphase formation. Such BiFeO₃ thin films exhibit a much faster reduction of the saturation magnetization with increasing thickness of BiFeO₃ thin films [315]. Therefore, the thickness dependence of the saturation magnetization displayed in Fig. 4.20(a) further proves the absence of magnetic parasitic phases in our BiFeO₃ thin films.

A closer look on the magnetic hysteresis loops displayed in Figs. 4.20(a) and (b) reveal a S-shaped component exhibiting a high magnetic saturation field. This magnetic field dependence of the magnetization might be explained by either a destruction of the spin cycloid structure by high magnetic fields or a spin reorientation process. The former was experimentally observed in bulk BiFeO₃ samples at a magnetic field strength of 20 T [316] and the latter is common in orthoferrites [317]. For comparison, the M - H -loop caused by spin reorientation in YFeO₃ is displayed in Fig. 4.20(b).¹⁷ However, both effects should be reversible with respect to decreasing or increasing the magnetic field strength. Thus, the irreversibility of the M - H -loops could be an indication of interdomain coupling [314].

The destruction of the spin cycloid structure should not only enhance the magnetization but also affect the electric polarization as well as the dielectric constant [316, 318, 319]. Therefore, the magnetic field dependence of the magnetic moment, the dielectric constant, and the dielectric loss are measured simultaneously sweeping the magnetic field strength from +7 T to -7 T (cf. full symbols in Fig. 4.20(c)) and vice versa (cf. open symbols in Fig. 4.20(c)). The measurement was carried out on a 88 nm thick BiFeO₃ film grown on Nb:SrTiO₃. Figure 4.20(c) discloses that no changes of the dielectric properties were observed within the experimental error at the magnetic field of $\mu_0 H_{\text{critical}} = 5$ T. Furthermore, no other magnetocapacitance effects were detected in our BiFeO₃ thin films [320]. Therefore, no experimental evidence of a magnetic field induced phase transition from a spin cycloidal order to a homogeneous spin structure was found. This phase transition occurs, when the Gibbs free energy density of the cycloidal state g_{cycloid} is equal to that of a homogeneous antiferromagnetic spin structure $g_{\text{homogeneous}}$ and can be induced not only by high magnetic fields but also by epitaxial strain. An estimation of the critical strain can be made following Refs. [310, 318, 321]. Within a phenomenological theory, the Gibbs free energy density of the cycloidal state g_{cycloid} can be expressed as

¹⁷The experimental data are taken from Ref. [314].

$$\begin{aligned}
- g_{\text{cycloid}} - g_0 &= g_{\text{LI}} + g_{\text{exch}} + g_{\text{an}} + g_{\text{ME}} + g_{\text{pert}} \\
&= +\gamma' P_z \left(l_x \frac{\partial}{\partial x} l_z + l_y \frac{\partial}{\partial y} l_z \right) \\
&\quad - A \left[\left(\frac{\partial}{\partial x} \mathbf{l} \right)^2 + \left(\frac{\partial}{\partial y} \mathbf{l} \right)^2 + \left(\frac{\partial}{\partial z} \mathbf{l} \right)^2 \right] \\
&\quad + K_u l_z^2 \\
&\quad + \mu_0 c^2 \frac{\chi}{\alpha_{33}^2} (P_z^2 (l_x^2 + l_y^2) + (dY\varepsilon)^2) + \dots, \tag{4.1}
\end{aligned}$$

where \mathbf{l} denotes the antiferromagnetic unit vector $\mathbf{l} = \mathbf{L}/(2M_0)$ with M_0 as the magnetization of the magnetic sublattice. \mathbf{l} can be written in terms of the polar Θ and azimuthal Φ angles: $\mathbf{l} = (l_x, l_y, l_z) = (\sin \Theta \cos \Phi, \sin \Theta \sin \Phi, \cos \Theta)$. Moreover, P_z is the z -component of the polarization in a hexagonal setting with $[001]_{\text{hex}} \parallel [111]_{R3\bar{c}}$. The first term $g_{\text{LI}} = \gamma' P_z \left(l_x \frac{\partial}{\partial x} l_z + l_y \frac{\partial}{\partial y} l_z \right) = -\gamma' P_z \sin^2 \Theta \left(\cos \Phi \frac{\partial \Theta}{\partial x} + \sin \Phi \frac{\partial \Theta}{\partial x} \right)$ represents an inhomogeneous magnetoelectric interaction with coupling constant γ' . This effect is odd with respect to electric field \mathbf{E} and does not change sign with the reversal of \mathbf{l} . g_{LI} causes a spin cycloidal structure in BiFeO₃. The next term of Eq. (4.1) is the exchange energy, which is given as $g_{\text{exch}} = -A \sum_i (\nabla l_i)^2 = -A ((\nabla \Theta)^2 + \sin^2 \Theta (\nabla \Phi)^2)$, where A denotes the stiffness exchange constant [322]. Furthermore, $g_{\text{an}} = K_u l_z^2 = K_u \cos^2 \Theta$ accounts for the magnetic anisotropy, where K_u is the uniaxial magnetic anisotropy constant. Here, higher order effects are neglected. The last term in Eq. (4.1) represents a Dzyaloshinskii-Moriya like coupling as well as the linear magnetoelectric effect. Both interactions can be written in terms of an effective Zeeman energy $g_{\text{ME}} = \mu_0 c^2 \frac{\chi}{\alpha_{33}^2} P_z^2 (l_x^2 + l_y^2)$ with the magnetic susceptibility $\chi_{ij}^{(\text{m})} = \chi$ and the linear magnetoelectric coupling $\chi_{ij}^{(\text{em})} = \alpha_{33}$ (cf. Chapter 3). In case of the linear magnetoelectric effect $g_{\text{pert}} = \mu_0 c^2 \frac{\chi}{\alpha_{33}^2} (d \cdot Y \cdot \epsilon_{33})^2$, the polarization P_z is substituted by $d \cdot Y \cdot \epsilon_{33}$, where d , Y , and ϵ_{33} denote the piezoelectric moduli, Young's modulus, and the epitaxial strain. Neglecting the last three terms (g_{an} , g_{ME} , and g_{pert}) in Eq. (4.1), which can be treated as perturbations, the minimization of $g_{\text{LI}} + g_{\text{exch}}$ yields $\Phi_0 = \text{const} = \arctan(q_y/q_x)$ and $\Theta_0 = q_x x + q_y y$, where $\mathbf{q} = (q_x, q_y, q_z)$ denotes the spiral wave vector. This perturbation ansatz is valid as long as the anisotropy constant is much smaller than the exchange energy, which is fulfilled for BiFeO₃ [323], otherwise anharmonic effects should be taken into account. Φ_0 and Θ_0 require that the spins lie in the plane of the wave vector, which is in agreement with a cycloidal spin structure. Using these values, the minimization of the volume-averaged Gibbs free energy g_{cycloid} occurs for $q = \frac{\gamma' P_z}{4A}$ and $\Phi = \frac{\pi}{2}$. Therefore, the free energy for a harmonic spin cycloid can be written as

$$- g_{\text{cycloid}} - g_0 = \frac{1}{4A} (\gamma' \cdot P_z)^2 + \frac{\mu_0 c^2}{4} \frac{\chi}{\alpha_{33}^2} (P_z^2 + d^2 Y^2 \epsilon_{33}^2) - \frac{1}{2} K_u. \tag{4.2}$$

For strains larger than a critical strain ϵ_{33}^c , a phase transition from the cycloidal to the homogeneous antiferromagnetic spin state, which can be described by $(\Theta = \Phi = \frac{\pi}{2})$

$$-g_{\text{homogeneous}} - g_0 = \frac{\mu_0 c^2}{2} \frac{\chi}{\alpha_{33}^2} (P_z^2 - d^2 Y^2 \epsilon_{33}^2) - K_u, \quad (4.3)$$

occurs. Therefore, the critical strain value ϵ_{33}^c can be derived using the condition $g_{\text{cycloid}} = g_{\text{homogeneous}}$:

$$\epsilon_{33}^c = \frac{1}{d \cdot Y} \sqrt{\frac{4}{\mu_0} \frac{\alpha_{33}^2 c^2}{\chi} \left(\frac{(\gamma' \cdot P_z)^2}{4A} + \frac{K_u}{2} \right) - P_z^2}. \quad (4.4)$$

The product $\gamma' \cdot P_z$ and the exchange constant A can be estimated to be $6 \times 10^{-4} \text{ J/m}^2$ and $3 \times 10^{-12} \text{ J/m}$, respectively [318]. With the reported value for the perpendicular susceptibility of $\chi = 5 \times 10^{-5}$ [324], the uniaxial anisotropy constant K_u can be approximated from ESR data to be $K_u = 7 \times 10^4 \text{ J/m}^3$ [321]. Using a magnetoelectric coupling of $\frac{1}{c} \alpha_{33} = 4 \times 10^{-9} \text{ s/m}$ [32], a spontaneous polarization of $P_z = 6 \times 10^{-2} \text{ As/m}^2$ [318], and an elastic value of $d \cdot Y = 10 \text{ As/m}^2$ [310], the critical strain ϵ_{33}^c can be estimated to be 0.8%. However, since Eq. (4.4) reveals the strain component ϵ_{33}^c along the hexagonal $[001]_{hex}$ direction, which is equivalent to the rhombohedral $[111]_{R3\bar{c}}$ direction, the strain tensor ϵ_{ij}^c has to be transformed with respect to the SrTiO_3 (001) coordinate system. This can be done by employing the transformation law of a second-rank tensor $\epsilon_{ij} = a_{ik} a_{jl} \epsilon_{kl}$, where a_{ik} denotes the cosine of the angle between the rhombohedral x_i and cubic x_k axes [112]. The absolute value of the critical in-plane strain for the growth of BiFeO_3 on (001)-oriented SrTiO_3 substrates can then be estimated to $|\epsilon_{ip}^c| = 0.6\%$. Therefore, in all investigated BiFeO_3 thin films the cycloidal spin order should be destroyed, since x-ray diffraction measurements reveal an in-plane strain of these thin films, which is larger than $|\epsilon_{ip}^c|$ (cf. Sec 4.4.1). Thus, the weak magnetic moment observed in BiFeO_3 thin films can be attributed to canting of the Fe spins in the absence of a cycloidal spin structure (cf. Fig. 4.20). This is also observed experimentally. Béa and coworkers found no evidence for the presence of a spin cycloid order performing neutron diffraction of a 240 nm thick BiFeO_3 thin film grown on a SrRuO_3 -buffered SrTiO_3 (001) substrate [239]. In addition, an enhanced polarization and a release of latent magnetization was observed in $(111)_{pc}$ -oriented BiFeO_3 thin films, which was explained by the destruction of the modulated spin structure due to epitaxial strain [310]. Furthermore, recently, much attention has been focused on domain walls in multiferroic materials, which can be ferromagnetic in principle [325]. Such domain wall effects might be small in bulk, but can increase the magnetic moment in thin films due to the high volume density of these walls. However, since the cycloidal spin structure is expected to be destroyed by epitaxial strain, the reason for the S-shaped magnetic hysteresis loops visible in Figs. 4.20(a) and (b) might be attributed to spin reorientations of the antiferromagnetic sublattice (cf. Fig. 4.20(b)). Whether the finite magnetic moment and the S-shaped magnetic field dependence of the magnetization in BiFeO_3 thin films are caused by a marginal concentration of ferromagnetic clusters or are of intrinsic origin cannot be completely answered at present.

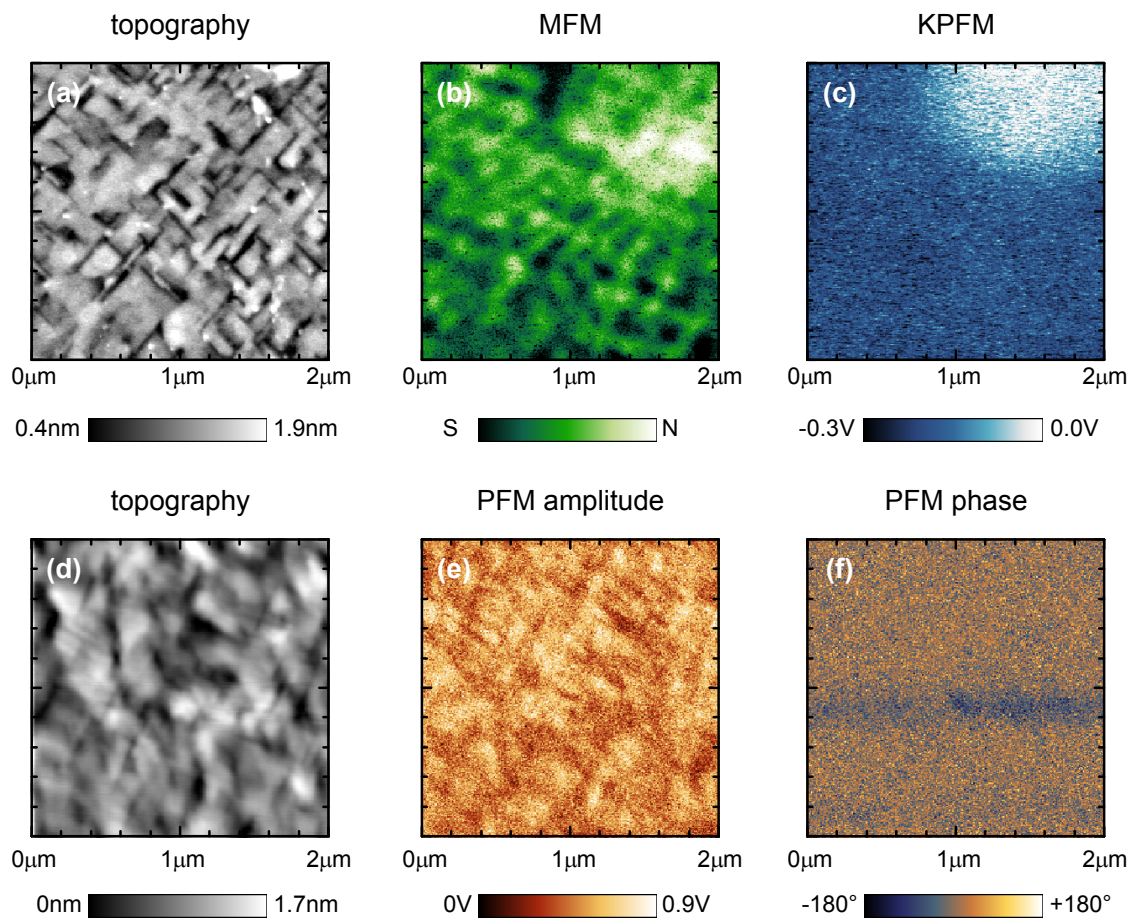


Figure 4.21: (b) Magnetic force microscopy (MFM), (c) Kelvin probe force microscopy (KPFM) and (e), (f) piezoelectric force microscopy (PFM) carried out on a 22 nm thick BiFeO₃ film grown on a Nb:SrTiO₃ substrate. The MFM measurements were performed at 80 K in an ultra-high vacuum chamber. The topography of each measurement area is shown in (a) and (d), respectively.

To further investigate the quality of our BiFeO₃ thin films, field cooled (FC) and zero-field cooled (ZFC) magnetization measurements were performed. No magnetic anomalies or even phase transitions are visible (cf. Fig. 4.20(d)). Since the reported phase or glass transitions for temperatures larger than 50 K [326, 327] most likely indicate impurity phases in samples of limited quality [162], the almost perfect agreement of FC and ZFC data further confirms a high purity of our BiFeO₃ thin films.

In Fig. 4.20, the macroscopic magnetic behavior of BiFeO₃ thin films obtained using SQUID magnetometry is displayed. To investigate the microscopic magnetic structure, magnetic force microscopy (MFM) measurements (cf. Section 2.3.4) were carried out on a 22 nm thick BiFeO₃ film grown on a Nb:SrTiO₃ substrate. These measurements were performed by Denny Köhler (Technische Universität Dresden). The topography of this sample reveals a very small rms surface roughness of only 0.3 nm (cf. Fig. 4.21(a)). Comparing the topography of the present BiFeO₃ thin film with that shown in Fig. 4.16(a), a tremendous reduction of the surface roughness

is visible. This is mainly due to the growth optimization processes discussed in Section 4.2.2. For MFM measurements, a low surface roughness is mandatory to avoid topographic artifacts. Furthermore, in thin films with excellent morphology, the tip-sample distance can be reduced, which improves the MFM signal. The MFM images were taken at 80 K in an ultra-high vacuum chamber using a constant average height of the cantilever of 20 nm with respect to the sample surface in a dynamic non-contact mode. Since the force on the cantilever is around 10^{-12} N, which is one or two orders of magnitude larger than the thermal noise [93], the reduction of the temperature, the pressure, as well as the distance between the thin film surface and the cantilever is essential for the detection of a magnetic signal in BiFeO₃ thin films using the MFM technique. However, due to the multiferroic nature of BiFeO₃, the cantilever is not only attracted by magnetic stray fields but also by electrostatic forces. Therefore, a correction of the MFM signal is mandatory to obtain the pure magnetic contrast of the BiFeO₃ sample. The compensation of the MFM signal is carried out by simultaneously performing MFM and Kelvin probe force microscopy (KPFM) measurements, which is sensitive to the surface potential only.¹⁸ In Figs. 4.21(b) and (c), the MFM and KPFM images are displayed. The MFM image reveals structures ranging in size from 50 nm to 100 nm. The finite MFM contrast is caused mainly by a finite magnetization component pointing out-of-plane and/or by magnetic domain walls. As discussed in the context of Fig. 4.18, the six-fold magnetic easy axes are reduced to one in the absence of a spin spiral structure due to epitaxial strain in BiFeO₃ thin films. These magnetic easy axes are aligned along the pseudo-cubic $\langle 112 \rangle_{pc}$ directions. Thus, the weak ferromagnetic moment caused by spin-canting is located perpendicular to these axes, exhibiting an out-of-plane component, which can be detected using MFM. Therefore, the finite contrast visible in Fig. 4.21(b) can be related to magnetic domains of the BiFeO₃ phase rather than to extrinsic effects such as ferromagnetic parasitic phases. This finite surface magnetic moment is a key requirement for the realization of electrically controllable exchange bias in ferromagnetic/BiFeO₃ composites [305, 311, 328]. Recently, a robust electric control of the exchange bias in composites based on the magnetoelectric antiferromagnet Cr₂O₃ was demonstrated [329]. In this system, a surface magnetization with magnetoelectrically controllable domains was detected [330]. Such a magnetoelectric coupling was also found in BiFeO₃ thin films [137]. Since as-grown BiFeO₃ thin films exhibit a ferroelectric multidomain state with mainly 71° domain walls (cf. Fig. 4.16 and Fig. 4.17), an antiferromagnetic multidomain state is generated due to the coupling between the ferroelectric and antiferroelectric order parameters [29, 137]. This coupling results in pinning of antiferromagnetic domain walls on the ferroelectric ones, which was revealed by theoretical calculations based on the Gibbs free energy density presented in Eq. (4.1) [331, 332]. To compare the size and the structure of the magnetic and ferroelectric domains and domain walls in our BiFeO₃ thin films, PFM measurements were performed on the same sample but not on the same area. The findings are shown in Figs. 4.21(d), (e), and (f). Due to experimental constraints, only out-of-plane PFM measurements are viable

¹⁸See Ref. [93] for more details on the KPFM technique.

under ultra-high vacuum conditions at 80 K. Therefore, the PFM amplitude and phase signal shown in Figs. 4.21(e) and (f) should be sensitive to the out-of-plane component of the polarization. However, in analogy to Fig. 4.16(b) and (c), a finite contrast is visible in the PFM amplitude image, which can again be attributed to a crosstalk between the in-plane and the out-of-plane PFM component. Thus, the in-plane ferroelectric domain structure can be revealed in the amplitude signal of out-of-plane PFM measurements (cf. Fig. 4.16(b) and Fig. 4.21(e)). Figure 4.21(e) suggests that the ferroelectric in-plane domains have a similar size as the magnetic structure visible in Fig. 4.21(b). Therefore, the ferroelectric and antiferromagnetic order parameters seem to be coupled. However, to correlate the magnetic and ferroelectric properties in detail, in-plane and out-of-plane PFM measurements as well as MFM scans have to be carried out on the same area in future experiments.

Contrary to the homogeneous contrast in the phase images obtained by out-of-plane PFM measurements (cf. Fig. 4.21(f) and Fig. 4.16(c)),¹⁹ which implies a constant z -component of the polarization, i.e., a constant surface potential, the results of the KPFM measurement reveal a change of the potential in the upper right corner of the scanned area (cf. Fig. 4.21(c)). This higher electrostatic potential is very likely caused by a reversal of the out-of-plane component of the ferroelectric polarization, since the topography reveals no artifacts or adsorbates in this area of the BiFeO₃ thin film (cf. Fig. 4.21(a)). Interestingly, at the border of this region, an accumulation of white and black magnetic contrast is visible in the MFM image (cf. Fig. 4.21(b)). This is shown in more detail in Fig. 4.22, scanning a larger area. The scan window used for the MFM measurement of Fig. 4.21(b) is marked by the blue rectangle.

Interestingly, the magnetic contrast at regions, where the surface potential changes, is substantially enhanced as compared to areas with constant electrostatic potential (cf. Fig. 4.21 and Fig. 4.22). Assuming that the changes of the electrostatic potential are caused by a reversal of the out-of-plane component of the electric polarization, the MFM measurements suggest an enhancement of the local magnetic moment located at ferroelectric domain walls where the out-of-plane component changes its sign. Therefore, a reorientation of the antiferromagnetic domains by switching the ferroelectric polarization by either 71° or 109°, which was uncovered by Zhao and coworkers [137], might not only explain the experimental results, since these domains are also present within regions of constant electrostatic potential, i.e., constant out-of-plane component of the polarization (cf. Fig. 4.16 and Fig. 4.17). Therefore, additional mechanisms have to be considered. For example, first-principles studies of ferroelectric domain walls suggest an increase of the local canting by 33% due to changes of Fe-O-Fe bonds, which can enhance the local moment at the domain walls [333]. Furthermore, magnetoelectric pinning is observed in multiferroic material systems [127]. In this case, antiferromagnetic domain walls can be stabilized by ferroelectric domains or grain boundaries. However, one has to keep in mind that KPFM is only sensitive to a difference in the electrostatic potential but insensitive to polarization directions. Therefore, to confirm the experimental findings in our

¹⁹The finite contrast in Fig. 4.21(f) is likely an artifact of the measurement.

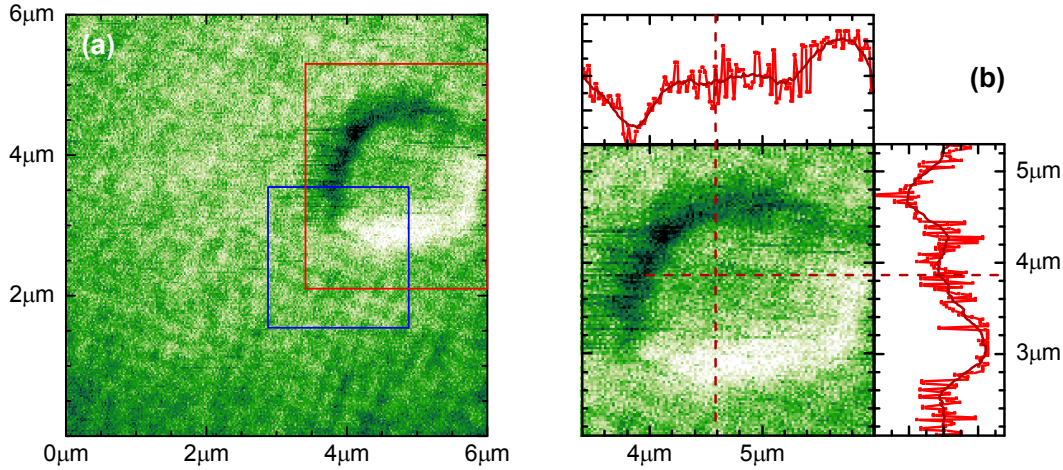


Figure 4.22: (a) Magnetic force microscopy (MFM) carried out on the same sample as in Fig. 4.21(b), scanning a larger area. The scan window used for the MFM measurement in Fig. 4.21(b) is marked by a blue rectangle. (b) Enlarged view of the part of the MFM image where an increase of the electrostatic surface potential is suggested (cf. red rectangle in (a)). The line scan depicted in the upper and right panels in (b) reveal an increase and decrease of the magnetic contrast in regions where the surface potential changes.

BiFeO₃ thin films, detailed PFM and MFM measurements are mandatory.

From a theoretical point of view, the enhancement of the local moment at ferroelectric domain walls in a magnetoelectric multiferroic without spin cycloid structure can be explained on the basis of a Landau-Ginzburg potential. Following Darakchiev and coworkers [325], the Gibbs potential of such a system can be written as

$$G_{\text{ME}} = G_0 + \frac{\kappa}{2} (\nabla P)^2 + \frac{\lambda}{2} (\nabla M)^2 + G_{\text{MP}}(P, M) \quad (4.5)$$

with $G_{\text{MP}}(P, M)$ defined as

$$G_{\text{MP}}(P, M) = \frac{\alpha}{2} P^2 + \frac{a}{2} M^2 + \frac{\beta}{4} P^4 + \frac{b}{4} M^4 + \frac{\eta}{6} P^6 + \frac{n}{6} M^6 + \frac{\gamma}{2} P^2 M^2 + \dots \quad (4.6)$$

The gradient terms $(\nabla P)^2$ and $(\nabla M)^2$ arise from an increase of the free energy when P or M slowly vary in space and are the remaining part of Eq. (3.27) in systems, which do not exhibit an spin spiral order ($\gamma' = 0$). In the center of a domain, i.e., far away from any domain walls, these terms are negligible and the system is mainly described by the potential $G_{\text{MP}}(P, M)$. This potential, which is based on an expansion of the order parameters P and M up to the sixth order, contains a biquadratic coupling term $\frac{\gamma}{2} P^2 M^2$ allowed by every symmetry. This term describes the coupling between P and M . The expansion coefficients are chosen such that the potential G_{MP} is positive definite at high values of P and M [325].

In this formalism, BiFeO₃ is treated as a material, which is both ferroelectric and (weakly) ferromagnetic leading to negative first order coefficients of the polarization

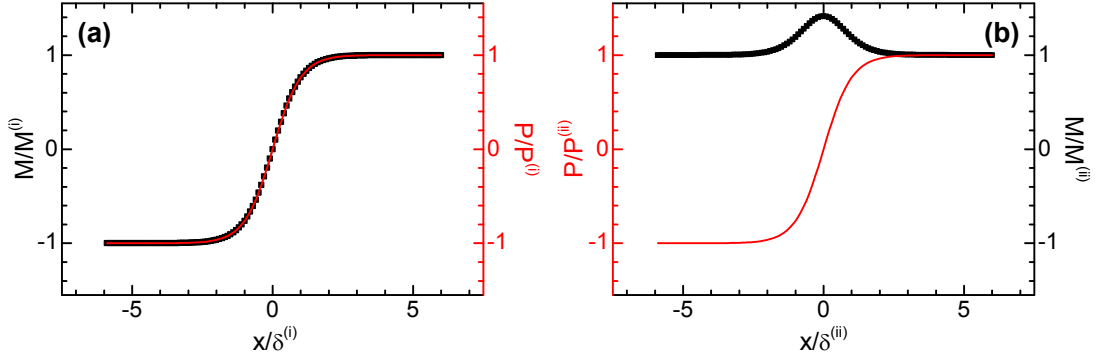


Figure 4.23: Calculations of the polarization and magnetization profiles across a domain wall in multiferroics according to Ref. [325]. Polarization $P(x)$ and magnetization $M(x)$ profile in case of (a) domain walls that invert P and M simultaneously and (b) walls that invert P but not M . Both profiles are plotted for positive $P^{(i)}$, $P^{(ii)}$, $M^{(i)}$, and $M^{(ii)}$ values (cf. Eq. (4.7)).

and magnetization (α and a). The domain wall is introduced in the \mathbf{z} - \mathbf{y} plane. Therefore, $P(x)$ as well as $M(x)$ are one-dimensional functions of x . In this case, the potential G_{MP} exhibits four minima, with each of them defining positive and negative directions of P and M , respectively. Therefore, two different situations can be considered: (i) domain walls that invert P and M simultaneously as well as (ii) walls that invert P but not M [325]:²⁰

$$\begin{aligned}
 (i) \quad P(x) &= \pm P^{(i)} \tanh\left(\frac{x}{\delta^{(i)}}\right) & M(x) &= \pm M^{(i)} \tanh\left(\frac{x}{\delta^{(i)}}\right), \\
 (ii) \quad P(x) &= \pm P^{(ii)} \tanh\left(\frac{x}{\delta^{(ii)}}\right) & M(x) &= \pm M^{(ii)} \sqrt{2 - \tanh^2\left(\frac{x}{\delta^{(ii)}}\right)}. \quad (4.7)
 \end{aligned}$$

The polarization $P(x)$ as well as the magnetization $M(x)$ domain wall profiles are plotted in Fig. 4.23 for both cases. For simplicity the coherence lengths $\delta^{(i)} = \sqrt{-2\frac{\kappa}{\alpha}}$ and $\delta^{(ii)} = 2\sqrt{\frac{\kappa b}{a\gamma - \alpha\beta}}$ are assumed to be equal for both order parameters. While in (i) the magnetization follows the polarization (cf. Fig. 4.23(a)), an increase of the magnetization is visible in the center of the domain wall in case (ii) (cf. Fig. 4.23(b)). The maximum enhancement can be estimated with $M = \sqrt{2}M_{\text{domain}}$ [325]. Our measurements reveal a similar magnetization profile as calculated for case (ii) (cf. Fig. 4.23(b) and Fig. 4.22(b)). However, the region in which the local magnetization varies was found to be around 500 nm, which is too large in terms of domain walls in magneto-electric multiferroic compounds. In such systems, the thickness of the domain walls is affected by the finite coupling of the ferroelectric polarization and the magnetization. This should result in thicker ferroelectric domain walls, being intermediate between the thickness of a purely ferroelectric wall and that of a purely magnetic one [325]. The correlation of the magnetic contrast and the electrostatic surface

²⁰ $P^{(i)}$, $P^{(ii)}$, $M^{(i)}$, and $M^{(ii)}$ are functions of the expansion coefficients [325].

potential could be an indication for an enhanced magnetoelectric coupling at the ferroelectric domain walls. Furthermore, our measurements suggest an increase of the local magnetic moment at regions where the out-of-plane component of the polarization changes its polarity. However, whether the enhancement of the magnetic moment arises from intrinsic coupling effects at ferroelectric domain walls or is caused by extrinsic defects, such as oxygen vacancies [334], which might be stabilized at domain walls, could not be resolved completely and further MFM measurements are mandatory.

4.4.3 Summary: Multiferroic BiFeO₃ thin films

In summary, high quality BiFeO₃ thin films exhibiting excellent structural and multiferroic properties were fabricated. Neither an indication of parasitic phases nor any evidence for non-stoichiometric effects were found. X-ray diffraction measurements on these thin films using synchrotron light revealed a monoclinic structure with a Cc symmetry. This confirms recent calculations [249] and demonstrates that a finite rotation of the oxygen octahedra along the out-of-plane direction is present in BiFeO₃ thin films with a thickness as low as 23 nm. To investigate the multiferroic properties, BiFeO₃ thin films were grown directly on Nb:SrTiO₃ as well as on SrRuO₃-buffered SrTiO₃ substrates. In both cases, BiFeO₃ thin films with low mosaic spread up to a thickness of 120 nm were achieved, demonstrating a high crystalline quality of all investigated BiFeO₃ thin films. However, in the past, some ambiguous reports on the magnetic properties of strained BiFeO₃ thin films were published in literature. Therefore, BiFeO₃ thin films with different thicknesses were fabricated and studied in detail by x-ray diffraction. Our results revealed a critical thickness of pseudomorphic growth of around 22 nm, which is in agreement with the calculated one using the People-Bean model. Moreover, since BiFeO₃ thin films with moderate epitaxial strain exhibit a monoclinic symmetry, which is similar to the parent rhombohedral bulk symmetry, different structural domains were found. By increasing the thickness of BiFeO₃ thin films, relaxation of the misfit strain mainly by dislocation formation was detected. In particular, an inverse behavior of the out-of-plane strain and the averaged microstrain as a function of the thickness was found in BiFeO₃ thin films grown on Nb:SrTiO₃ employing the Williamson-Hall method. This is in contrast to BiFeO₃ thin films fabricated on SrRuO₃-buffered SrTiO₃ substrates. In these thin films, a different relaxation behavior of the misfit strain together with a larger amount of diffuse scattering, which suggests a higher density of dislocations compared to BiFeO₃ thin films on Nb:SrTiO₃, was observed. A decrease of the diffuse scattering by reducing the number of monoclinic domains could be achieved in BiFeO₃ thin films fabricated on SrRuO₃-buffered SrTiO₃ substrates exhibiting a miscut angle of around 1°.

Overall, the dislocation density in all investigated BiFeO₃ thin films is not exceeding the low density limit of dislocations. In this limit, the Bragg peak is not affected by dislocations, which are separated from one another by more than the lattice spacing. Furthermore, the structural properties of BiFeO₃ thin films grown on SrRuO₃-buffered SrTiO₃ substrates were not found to be enhanced compared to

BiFeO₃ thin films directly grown on Nb:SrTiO₃. Therefore, only the multiferroic properties of BiFeO₃ thin films grown on Nb:SrTiO₃ substrates were discussed.

The ferroelectric state was analyzed by means of piezoelectric force microscopy measurements, which were carried out by Denny Köhler (Technische Universität Dresden). These measurements revealed that as grown BiFeO₃ thin films exhibit a constant out-of-plane component of the polarization due to self-poling effects of the conducting substrate. Furthermore, mainly 71° domain walls were detected, which is in agreement with literature reports [240]. The magnetic properties of these thin films were investigated in more detail using x-ray magnetic scattering, SQUID magnetometry as well as magnetic force microscopy. An antiferromagnetic *G*-type ordering in BiFeO₃ thin films, which was predicted by theory [249] and detected using neutron diffraction [239, 311], could not be confirmed in our samples using x-ray resonant techniques. Therefore, the detailed antiferromagnetic structure remains unsolved and future experiments should be carried out on this issue. The macroscopic magnetic behavior of BiFeO₃ thin films grown on Nb:SrTiO₃ substrates examined using SQUID magnetometry reveals a magnetic hysteresis with a small saturation magnetization in all investigated BiFeO₃ thin films. In particular, only a small increase of the saturation magnetization up to 1.8 kA/m, which corresponds to 0.03 μ_B /f.u., was found by decreasing the thin film thickness, i.e., increasing the epitaxial strain. The moderate enhancement of the saturation magnetization by a factor of 1.6 while increasing the film thickness from 22 nm to 88 nm is in contrast to the pioneering work on BiFeO₃ thin films [32] but in agreement with several recent publications (see, e.g., Ref. [250]) and confirms the absence of magnetic parasitic phases in our BiFeO₃ thin films. The finite macroscopic magnetic moment suggests the destruction of the spin cycloid structure caused by epitaxial strain in BiFeO₃ thin films. Indeed, the critical strain, at which the spin cycloid structure is destroyed, could be estimated to 0.8% by comparing the Gibbs free energy density of BiFeO₃ in a spin cycloid state with that of BiFeO₃ exhibiting a collinear antiferromagnetic order. Moreover, a S-shaped component was detected in the magnetic hysteresis, which might be attributed to spin reorientation processes, which is common in orthoferrites.

In recent years, large magnetoelectric effects via exchange bias were found in ferromagnet/BiFeO₃ composites structures. These effects are mainly based on uncompensated spins, leading to a finite surface magnetic moment [311]. We addressed the surface magnetic moment by employing magnetic force microscopy. To obtain a magnetic contrast, which is not affected by topography features, a reduction of the rms surface roughness to 0.3 nm by applying the growth optimization processes discussed in Section 4.2 was mandatory. The magnetic contrast could be related to magnetic domains of the BiFeO₃ phase rather than to extrinsic effects such as ferromagnetic parasitic phases. Moreover, the dark and bright contrast have similar lateral dimensions compared to ferroelectric domains, which were observed using piezoelectric force microscopy. In addition, an increase and decrease of the magnetic contrast was detected at regions where the electrostatic surface potential changes its value, which was interpreted as ferroelectric domain walls at which the out-of-plane component of the polarization changes polarity. These results suggest a

finite magnetoelectric coupling and an enhanced magnetic moment at ferroelectric domain walls separating regions with opposite sign of the out-of-plane component of the ferroelectric component. The latter could be theoretically explained using a Landau-Ginzburg based Gibbs free energy. However, since the ferroelectric domain distribution was not recorded on the same area as the magnetic force microscopy measurements, the interpretation of the local surface magnetic moment is only preliminary. To correlate the magnetic and ferroelectric results in detail, in-plane and out-of-plane piezoelectric force microscopy as well as magnetic force microscopy measurements have to be carried out on the same area in future experiments. Nevertheless, our findings would confirm recent suggestions on an enhanced magnetic moment at ferroelectric domain walls [335].

4.5 Physical properties of BiCrO₃ thin films

In contrast to BiFeO₃, BiCrO₃ is hardly a technologically relevant multiferroic material as evident from the bulk behavior depicted in Fig. 4.1(b). However, to elucidate the role of the Bi cation in driving structural phase transitions in the BiMO₃ perovskite-like family with $M = \text{Cr, Mn, Fe, Co}$, the physical properties of BiCrO₃ thin films are investigated in detail in the following. In this context, the structural behavior as a function of temperature is discussed first, followed by the analysis of the multiferroic properties of these thin films. Furthermore, the possibility of a magnetoelectric coupling in BiCrO₃ is examined by investigating the electric field control of exchange bias effects in ferromagnet/BiCrO₃ composite heterostructures.

4.5.1 Structural characterization of BiCrO₃ thin films

The structural properties of BiCrO₃ have hardly been investigated up to now, since bulk BiCrO₃ can only be synthesized at high pressure [37, 139, 336]. Bulk BiCrO₃ exhibits a phase transition at around $T_{\text{phase, bulk}} \approx 410 \text{ K} - 440 \text{ K}$ (cf. Fig. 4.1(b)) accompanied by a change of the structural symmetry [36, 147]. Recently, the crystalline structure of the high-temperature ($T > T_{\text{phase, bulk}}$) and the low temperature ($T < T_{\text{phase, bulk}}$) phase was investigated by diffraction techniques using neutrons [36, 148] and synchrotron light [147]. Consistently, it was found that bulk BiCrO₃ exhibits an orthorhombic $Pbnm$ symmetry with an orthoferrite GdFeO₃ structure for $T > T_{\text{phase, bulk}}$ (similar to the crystal structure of SrRuO₃ depicted in Fig. 4.6). The lattice parameters were found to be $a = 0.5543 \text{ nm}$, $b = 0.5426 \text{ nm}$, and $c = 0.7752 \text{ nm}$ at $T = 470 \text{ K}$ [36]. An orthorhombic $Pbnm$ symmetry was also identified in the paraelectric phase of BiFeO₃ (cf. Section 4.4.1) and BiMnO₃ [337]. Therefore, the perovskite-like family BiMO₃ with ($M = \text{Cr, Mn, Fe}$) exhibits the same crystalline symmetry above the temperature, at which the long-range order vanishes. Below the phase transition, a monoclinic symmetry of either $C2$ or $C2/c$ kind was found in bulk BiCrO₃ [36, 147, 148]. The identification of the correct symmetry is important, since the former is non-centrosymmetric allowing for ferroelectricity and the latter prohibits a long-range ferroelectric order, as it is cen-

trosymmetric.²¹ Recently, neutron diffraction experiments revealed no evidence for a $C2$ space group [36, 148]. Therefore, $C2/c$ seems to be the correct symmetry of the low temperature phase of bulk BiCrO₃.

In BiCrO₃ thin films, the crystal structure has not yet been finally clarified. Two groups found a triclinic structure at room temperature [34, 150]. However, David and coworkers recently reported on three structural variants in a BiCrO₃ thin film at room temperature using transmission electron diffraction [151]. Two of them can be related to either the bulk high temperature orthorhombic structure or the low-temperature monoclinic structure, respectively. In addition, they observed extra diffraction spots along the [101] direction, which could be caused by a modulated structure related to the bulk monoclinic phase.

However, up to now, no data are available on the structural properties of BiCrO₃ thin films as a function of temperatures, e.g. above and below the phase transition. Therefore, in the following, the crystal structure of our BiCrO₃ thin films is investigated and discussed in detail using x-ray diffraction.

Structural properties of BiCrO₃ thin films at temperatures above the phase transition

Since BiCrO₃ thin films are fabricated at a substrate temperature of 858 K (cf. Section 4.2), the orthorhombic $Pbnm$ symmetry is the parent phase. As discussed in the context of SrRuO₃ thin films (cf. Section 4.3), in this symmetry, X -, Y -, and Z -type domains can be formed. Depending on the domain type, a lattice mismatch ranging between 0.85% and 0.90% of BiCrO₃ thin films on SrTiO₃ can be estimated.²² Since these values are very similar, all three domain types are expected to be present in BiCrO₃ thin films grown on (001)-oriented SrTiO₃ substrates. By performing x-ray diffraction measurements at 500 K, i.e., well above $T_{\text{phase, bulk}}$, the crystalline symmetry as well as the domain state can be revealed.

As an example, Fig. 4.24 shows the results of x-ray diffraction measurements carried out on a 177 nm thick BiCrO₃ film grown on a SrRuO₃-buffered SrTiO₃ (001) substrate. The reciprocal space map around SrTiO₃ (001) as well as the q_{H00} - and q_{00L} -scans depicted in the left and upper panel of Fig. 4.24(a) reveal a BiCrO₃ thin film with high crystalline quality. This is not only proved by the finite thickness fringes indicating a coherent growth even at a thickness of 177 nm, but also by the low mosaic spread revealed by the narrow BiCrO₃ (001)_{pc} reflection along the [100] direction. The crystalline quality can be quantified by the full width at half maximum of the rocking curve around this reflection of 0.04°, which is an excellent value in terms of BiCrO₃ thin films of thicknesses as large as 177 nm. At this thickness, strain relaxation certainly takes place by forming dislocations and different crystallographic domains. The splitting of the pseudo-cubic BiCrO₃ (113)_{pc} reflection observable in the reciprocal space map around SrTiO₃ (113) depicted

²¹In analogy to BiCrO₃, the identification of the crystal symmetry ($C2$ or $C2/c$) of BiMnO₃ has been controversially discussed over the last years (cf. Ref. [338]).

²²The lattice mismatch was calculated at 470 K using the structural parameters obtained by neutron diffraction [36], since no data are available on the thermal expansion of BiCrO₃.

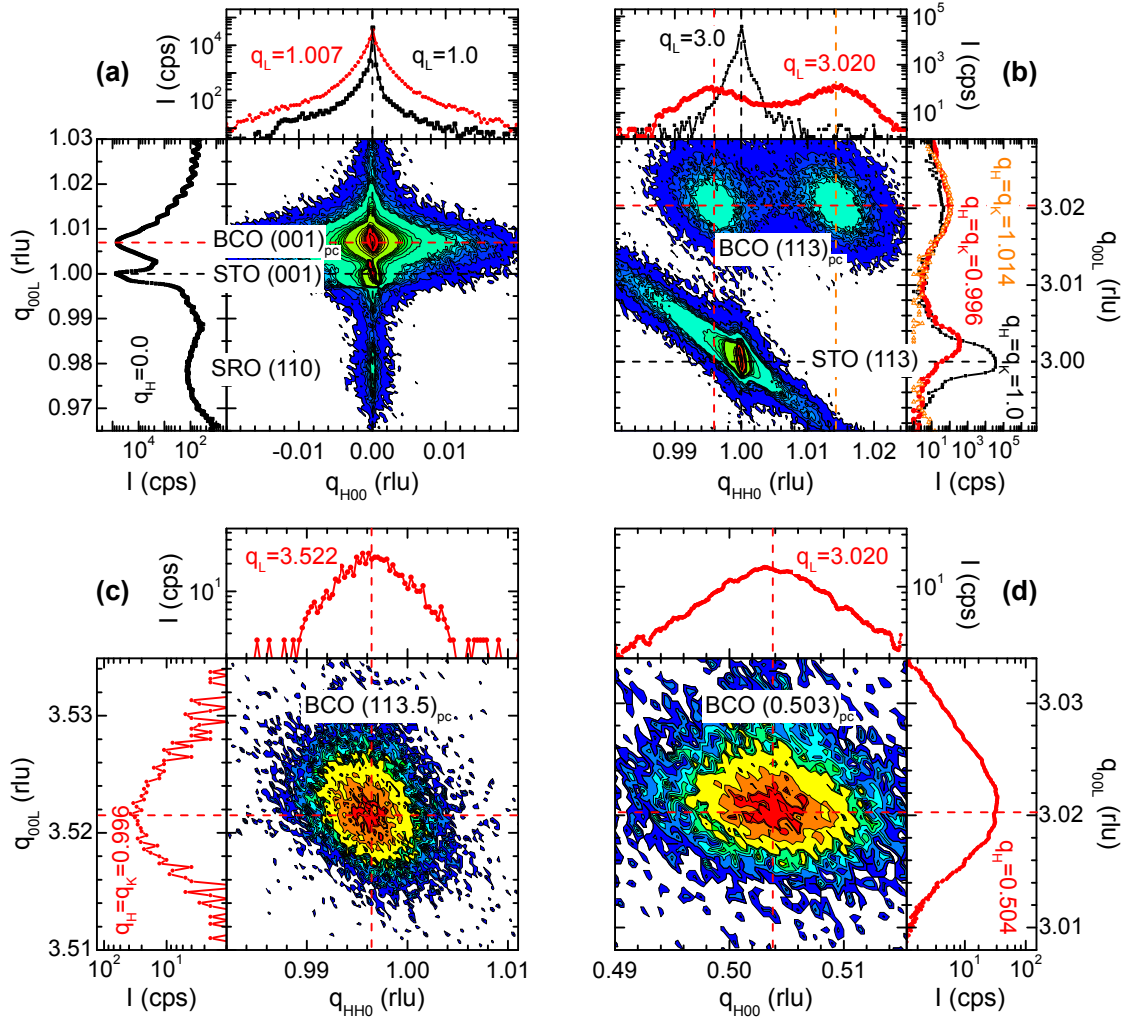


Figure 4.24: X-ray diffraction measurements carried out on a 177 nm thick BiCrO_3 film grown on a SrRuO_3 -buffered SrTiO_3 (001) substrate at 500 K. Reciprocal space maps and q -scans around (a) SrTiO_3 (001) and (b) SrTiO_3 (113). The splitting of the pseudo cubic BiCrO_3 (113)_{pc} reflection reveals a difference of the a and b lattice parameters in the orthorhombic symmetry. Superstructure reflections of orthorhombic Z - as well as Y -type domains (cf. Fig.4.6) are depicted in (c) and (d), respectively.

in Fig. 4.24(b) indicates a difference of the a and b lattice parameters at a constant c value. Therefore, Fig. 4.24(b) reveals the presence of orthorhombic Z - and Z' -domains (cf. Fig. 4.6). These domains exhibit a doubling of the unit cell in the out-of-plane direction, causing a superstructure peak around the pseudo-cubic (113.5)_{pc} reflection. Since this reflection is allowed in the orthorhombic symmetry, but forbidden in the monoclinic $C2/c$ and rhombohedral $R3c$ space group, the finite intensity visible in Fig. 4.24(c) proves that the crystal symmetry of the high temperature phase of BiCrO_3 thin films is orthorhombic and equal to the parent bulk phase. In analogy to orthorhombic Z -type domains, X - and Y -type domains cause superstructure reflections along the pseudo-cubic $[100]_{\text{pc}}$ and $[010]_{\text{pc}}$ directions with $q_{00L} \geq 1 \text{ rlu}$, respectively (cf. Fig. 4.6). Indeed, these superstructure

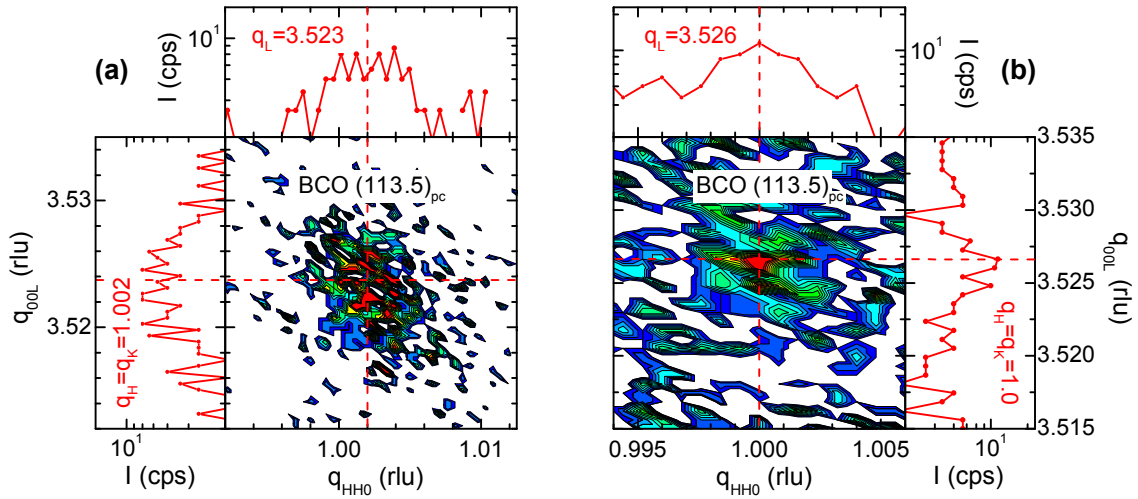


Figure 4.25: X-ray diffraction measurements carried out (a) on a 28 nm thick BiCrO₃ film grown on a SrRuO₃-buffered SrTiO₃ substrate as well as (b) on a BiCrO₃ (43 nm) thin film deposited directly on Nb:SrTiO₃. Both measurements were performed at 500 K around the superstructure reflection BiCrO₃ (1 1 3.5)_{pc}.

peaks are clearly resolved at $q_{00L} = 3$ rlu (cf. Fig. 4.24(d)).²³ Therefore, at the deposition temperature, all three orthorhombic domain types are formed in BiCrO₃ thin films on SrRuO₃-buffered SrTiO₃ (001) substrates leading to a crystalline multidomain state. The orthorhombic lattice parameters of the 177 nm thick BiCrO₃ film were calculated to $a_{500K} = (0.552 \pm 0.001)$ nm, $b_{500K} = (0.543 \pm 0.002)$ nm, and $c_{500K} = (0.7759 \pm 0.0004)$ nm. Therefore, this BiCrO₃ thin film is almost fully relaxed, exhibiting an in-plane strain of $\varepsilon_{xx} = -0.4\%$ and $\varepsilon_{yy} = +0.1\%$ as well as an out-of-plane strain of $\varepsilon_{zz} = +0.2\%$. These values yield a Poisson ratio of $\nu = (0.40 \pm 0.05)$, which is nearly as high as for BiFeO₃ thin films (cf. Section 4.4.1). The in-plane lattice parameters a_{500K} and b_{500K} reveal that the strain relaxation is not symmetric around the SrTiO₃ in-plane lattice constant $\sqrt{2}a_{\text{STO}} = 0.5535$ nm as it could be expected for thin films exhibiting an orthorhombic symmetry (cf. Ref. [339]).

The superstructure reflections caused by X -, Y -, and Z -type domains were also observed in BiCrO₃ thin films with thicknesses down to 28 nm (cf. Fig. 4.25(a)), indicating the presence of an orthorhombic symmetry for thicknesses as low as 28 nm. Furthermore, almost no difference was detected for BiCrO₃ thin films fabricated on SrRuO₃-buffered SrTiO₃ substrates compared to BiCrO₃ thin films on Nb:SrTiO₃. Figure 4.25(b) reveals that an orthorhombic symmetry was also found in BiCrO₃ thin films with a thickness of 43 nm grown on Nb:SrTiO₃ at $T = 500$ K.

In summary, detailed x-ray diffraction measurements carried out at $T = 500$ K shown in Fig. 4.24 disclose an orthorhombic symmetry of the high temperature phase of our BiCrO₃ thin films. Moreover, all different types of orthorhombic domains were detected, which proves a crystalline multidomain state of BiCrO₃ thin films grown on (001)-oriented SrTiO₃ substrates.

²³A finite intensity was also detected in the q_{0K0} - q_{00L} plane (not shown).

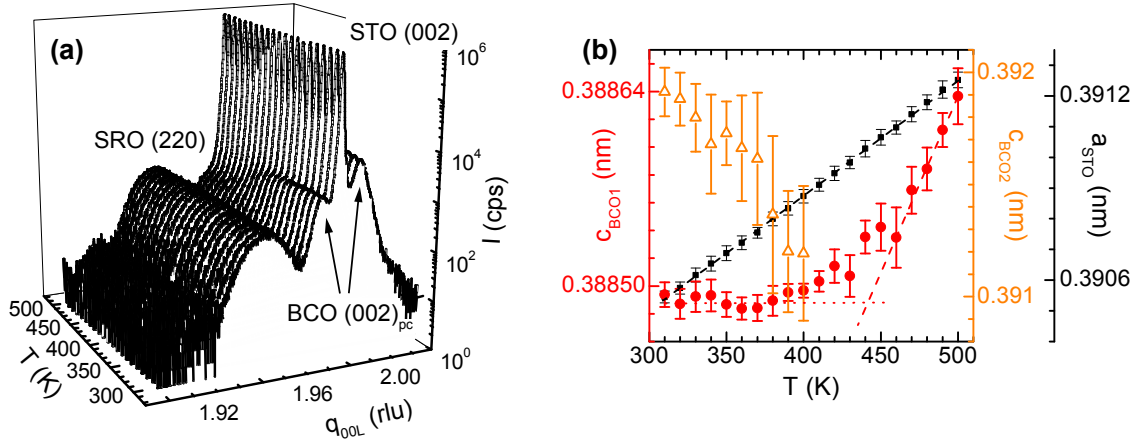


Figure 4.26: Structural phase transition in BiCrO_3 thin films: (a) q_{00L} -scans measured at $q_H = 0$ rlu for different temperatures revealing the presence of two distinct BiCrO_3 peaks below around 410 K. (b) Pseudo-cubic out-of-plane lattice constants for BiCrO_3 (c_{BCO1} , c_{BCO2}) and SrTiO_3 (a_{STO}) calculated by using the Nelson-Riley method described in Section 2.1.3. The red dashed and dotted lines are guides to the eye.

Structural phase transition in BiCrO_3 thin films

As stated above, upon lowering the temperature from 500 K to room temperature, a structural phase transition occurs at around 410 K – 440 K in bulk BiCrO_3 . To investigate this transition in our BiCrO_3 thin films, x-ray diffraction measurements were carried out at different temperatures.

Figure 4.26(a) shows the result of q_{00L} -scans performed on a 220 nm thick BiCrO_3 film grown on a SrRuO_3 -buffered SrTiO_3 substrate as a function of temperature. An automatic alignment procedure was employed to correct for the thermal expansion of the sample and sample holder. Upon lowering the temperature from 500 K to 300 K, the single pseudo-cubic BiCrO_3 (002)_{pc} reflection splits into two distinct BiCrO_3 peaks. This suggests that crystalline domains exist below $T \approx 410$ K, which exhibit different out-of-plane pseudo-cubic lattice constants. These lattice constants were extracted from the q_{00L} -scans using the Nelson-Riley method described in Section 2.1.3. In Fig. 4.26(b), both pseudo-cubic lattice constants (c_{BCO1} , c_{BCO2}) of a 177 nm thick BiCrO_3 film as a function of temperature are shown. In addition, the cubic unit cell parameter a_{STO} of the SrTiO_3 substrate is included in the figure for comparison. While the lattice constant of SrTiO_3 decreases linearly with decreasing the temperature from 500 K to 300 K with a thermal expansion coefficient of about $\alpha_{\text{STO}} = 9.8 \cdot 10^{-6} \text{ 1/K}$, which is close to the literature value of $\alpha_{\text{STO}} = 9.6 \cdot 10^{-6} \text{ 1/K}$ [256], the temperature behavior of the BiCrO_3 lattice strongly changes at around 430 K. Above 450 K, the pseudo-cubic lattice constant c_{BCO1} of BiCrO_3 exhibits an about linear dependence on temperature. In this region, the thermal expansion coefficient $\alpha_{\text{BCO,HT}}$ can be estimated to $\alpha_{\text{BCO,HT}} \simeq 6.5 \cdot 10^{-6} \text{ 1/K}$. Reaching the temperature range $400 \text{ K} \leq T \leq 450 \text{ K}$, c_{BCO1} deviates significantly from the linear temperature dependence and crosses over in an almost temperature independent lat-

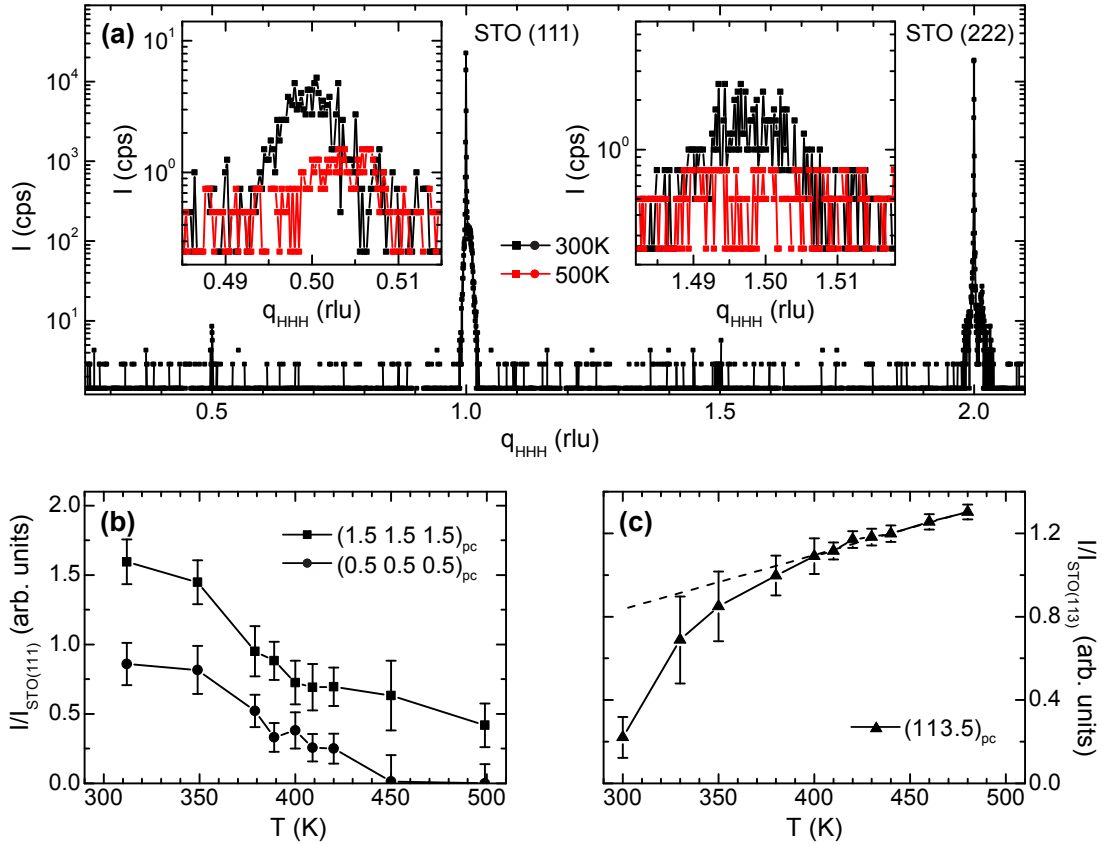


Figure 4.27: (a) X-ray diffraction measurements along q_{HKL} with $q_{\text{H}} = q_{\text{K}} = q_{\text{L}}$ carried out at 300 K (black symbols) and 500 K (red symbols) on a (177 nm) BiCrO₃ thin film grown on a SrRuO₃-buffered SrTiO₃ substrate. The insets show the monoclinic superstructure reflections $(0.5\ 0.5\ 0.5)_{\text{pc}}$ and $(1.5\ 1.5\ 1.5)_{\text{pc}}$ in more detail. (b), (c) A finite normalized intensity $I/I_{\text{SrTiO}_3(111)}$ and $I/I_{\text{SrTiO}_3(113)}$ of the monoclinic and orthorhombic $((1\ 1\ 3.5)_{\text{pc}})$ superstructure reflections was detected in the whole temperature range $300\text{ K} \leq T \leq 500\text{ K}$, proving a coexistence of both phases.

tice constant upon further cooling the sample. Furthermore, a second peak emerges at around 410 K. The corresponding pseudo-cubic lattice constant $c_{\text{BCO}2}$ is larger than $c_{\text{BCO}1}$ and increases its value with decreasing temperature. Figure 4.26 reveals significant changes of the BiCrO₃ lattice at around $T_{\text{phase}} = 410\text{ K} - 440\text{ K}$, which can be attributed to a bulk-like structural phase transition, since T_{phase} is similar to $T_{\text{phase, bulk}}$.

In analogy to bulk BiCrO₃, which exhibits a change in symmetry from orthorhombic to monoclinic at the phase transition, a monoclinic symmetry is assumed for $T \leq 410\text{ K}$. The monoclinic symmetry can be revealed by investigating the pseudo-cubic superstructure reflections $(0.5\ 0.5\ 0.5)_{\text{pc}}$ and $(1.5\ 1.5\ 1.5)_{\text{pc}}$, as they correspond to the $(002)_{\text{m}}$ and $(004)_{\text{m}}$ reflections in the monoclinic $C2/c$ symmetry. These reflections can be observed by performing x-ray diffraction measurements along the pseudo-cubic $[111]_{\text{pc}}$ direction, i.e., q -scans with $q_{\text{H}} = q_{\text{K}} = q_{\text{L}}$. As an example, the q_{HHL} -scan depicted in Fig. 4.27(a), which was measured on a 177 nm thick

BiCrO₃ film at 300 K, reveals a finite intensity at $q_H = q_K = q_L = 0.5$ as well as at $q_H = q_K = q_L = 1.5$. The observation of only one kind of superstructure reflections is certainly not sufficient to unambiguously determine the symmetry of epitaxial thin films. But as we expect a bulk like behavior in this BiCrO₃ thin film, the detection of the $(0.5\ 0.5\ 0.5)_{\text{pc}}$ and $(1.5\ 1.5\ 1.5)_{\text{pc}}$ reflections strongly suggests a monoclinic symmetry at 300 K. Therefore, the BiCrO₃ thin film undergoes a structural phase transition at T_{phase} , where the orthorhombic symmetry is lowered to a monoclinic one.

For temperatures larger than T_{phase} , the intensity of the pseudo-cubic $(0.5\ 0.5\ 0.5)_{\text{pc}}$ and $(1.5\ 1.5\ 1.5)_{\text{pc}}$ reflections should vanish, since these reflections are forbidden in the orthorhombic phase. Nevertheless, the insets of Fig. 4.27(a) reveal still a finite intensity around the $(0.5\ 0.5\ 0.5)_{\text{pc}}$ reflection at 500 K. This surprising result indicates a coexistence of both phases in a large temperature interval. Indeed, detailed x-ray diffraction measurements carried out at different temperatures between 500 K and 300 K around the monoclinic $(0.5\ 0.5\ 0.5)_{\text{pc}}$, $(1.5\ 1.5\ 1.5)_{\text{pc}}$ as well as the orthorhombic $(1\ 1\ 3.5)_{\text{pc}}$ superstructure reflections disclose a finite intensity at both types of reflections in the whole temperature range (cf. Figs. 4.27(b) and (c)). Note that the normalized intensity $I/I_{\text{SrTiO}_3(113)}$ of the $(1\ 1\ 3.5)_{\text{pc}}$ reflection depicted in Fig. 4.27(c) is derived from two dimensional reciprocal space maps, while the normalized intensity of the monoclinic superstructure $I/I_{\text{SrTiO}_3(111)}$ is obtained from one dimensional q_{HHH} -scans. Thus, the temperature evolution of the intensity shown in Fig. 4.27(c) is more accurate than the temperature dependence of the monoclinic superstructure displayed in Fig. 4.27(b). However, in both measurements, a change of the temperature dependence of the intensity ratio is visible for $T \leq 410$ K, which further corroborates a structural phase transition around $T_{\text{phase}} \approx 410$ K.

The coexistence of the high-temperature and low-temperature phase around T_{phase} was also observed in BiMnO₃ [337] and BiCr_{0.5}Mn_{0.5}O₃ [340] and could be caused by several reasons. First, the structural transition could be extended over a large temperature range. In this case, the coexistence of both phases is caused by the first order nature of the structural transition. For example, in BiCr_{0.5}Mn_{0.5}O₃, the temperature range for the coexistence of the high-temperature and low-temperature phase was recently found to be larger than 100 K around the phase transition [340]. To investigate this possibility, x-ray diffraction measurements were carried out at $T = 300$ K and $T = 60$ K on a 46 nm thick BiCrO₃ sample fabricated on a SrRuO₃-buffered SrTiO₃ substrate using grazing incidence diffraction (GID). The GID measurements were performed at the BM28 beamline at the ESRF (cf. Section 2.1.3). As shown in Fig. 4.28(a), the q_{HK0} -scans with $q_H = q_K$ recorded at $T = 300$ K and $T = 60$ K reveal no qualitative difference. This suggests that no additional crystalline phase transition takes place between $T = 300$ K and $T = 60$ K. Furthermore, a splitting of the pseudo-cubic BiCrO₃ $(220)_{\text{pc}}$ reflection into three peaks is observable. To understand this, x-ray diffraction measurements around the pseudo-cubic BiCrO₃ $(113)_{\text{pc}}$ reflection were carried out around the phase transition using a standard Cu x-ray source. As obvious from Fig. 4.28(b), in the orthorhombic high temperature phase at 500 K, the BiCrO₃ $(113)_{\text{pc}}$ reflection is split into two peaks (cf. Fig. 4.24(b)). Upon lowering the temperature to 420 K, a third reflection

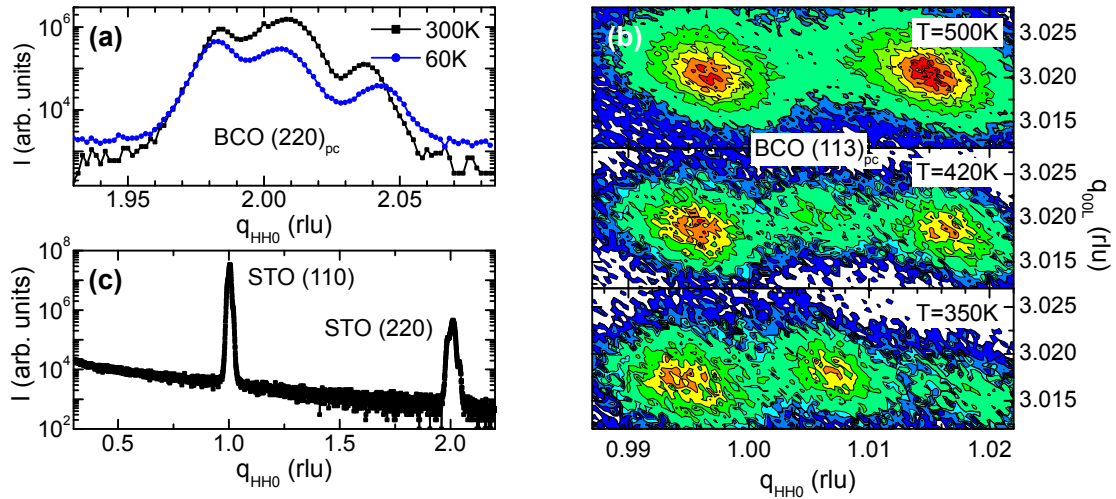


Figure 4.28: (a) Grazing incidence x-ray diffraction along $q_{\text{HK}0}$ with $q_{\text{H}} = q_{\text{K}}$ carried out at 300 K and 60 K on a 46 nm thick BiCrO₃ film. Both measurements were performed at the BM28 beamline at ESRF. The pseudo-cubic BiCrO₃ (220)_{pc} reflection is split into three peaks. (b) These peaks corresponds to the high temperature orthorhombic and low temperature monoclinic phases as revealed by x-ray diffraction measurements at different temperatures around the pseudo-cubic BiCrO₃ (113)_{pc} reflection using a standard Cu x-ray tube. (c) No superstructure was observed along the pseudo-cubic $\langle 110 \rangle$ direction. Therefore, no indication for the existence of a monoclinic $P2_1/c$ symmetry was found in our samples.

emerges, which is caused by the monoclinic symmetry. This reflection becomes more intense by further cooling down the sample. Therefore, from Fig. 4.28(b), the finite intensity detected at around $q_{\text{H}} = q_{\text{K}} = 1.015$ rlu, can be attributed to the high temperature orthorhombic phase. In analogy to x-ray diffraction measurements on the pseudo-cubic BiCrO₃ (113)_{pc} reflection, the splitting of the BiCrO₃ (220)_{pc} reflection along the $[110]_{\text{pc}}$ direction reflects the coexistence of the monoclinic and orthorhombic phases. Thus, from Figs. 4.28(a) and (b), we draw the conclusion that the orthorhombic phase is still present down to a temperature of 60 K, which is more than 350 K lower than the phase transition temperature. Therefore, the coexistence of both phases can not only be explained by an extended phase transition.

Recently, David and coworkers suggested another explanation for the coexistence of different phases in BiCrO₃ thin films [151]. Since epitaxial strain relaxation can cause inhomogeneous strain distributions, BiCrO₃ can be locally exposed to different internal pressures, altering the structural properties. In the material system BiMnO₃, high pressure synchrotron studies reveal different structural symmetries depending on the applied pressure [341]. Three different crystalline structures were detected. In the low pressure regime, BiMnO₃ remains monoclinic. Increasing the pressure to above 1.5 GPa, BiMnO₃ changes its monoclinic symmetry to $P2_1/c$. Finally, at high pressures ($p \gtrsim 6$ GPa), the orthorhombic high temperature symmetry becomes stable. As the structural properties of BiMnO₃ are closely related to BiCrO₃, a similar dependence is expected in BiCrO₃. In this regard, in BiCrO₃ thin films, which exhibit a strain distribution from a fully strained state at the

interface between the BiCrO₃ and SrRuO₃ layer to a fully relaxed state at the surface of the BiCrO₃ thin film, all three crystalline phases are expected. Therefore, in particular the monoclinic $P2_1/c$ symmetry, which causes superstructure reflections along the pseudo-cubic $\langle 110 \rangle_{\text{pc}}$ directions [151], should exist in our BiCrO₃ thin films. However, no indication of any superstructure reflections along this crystallographic direction were found in our measurements using synchrotron radiation (cf. Fig. 4.28(c)). This confirms that the monoclinic $C2/c$ symmetry is the dominant phase below the phase transition and inhomogeneous strain distributions might not be the main reason for the existence of different crystallographic phases. Note that a strain relaxation mechanism, which takes place over the whole film thickness, would affect the peak profile in x-ray diffraction measurements (cf. Section 4.4.1), which was not observed in our measurements. However, recent density functional calculations performed for epitaxial BiCrO₃ films with lattice constants determined by the SrTiO₃ substrate reveal an orthorhombic high temperature phase, which was found to be stable down to 10 K [342]. This result confirms the strong sensitivity of the crystalline structure on the epitaxial strain proposed by David *et al.* [151].

The additional monoclinic $P2_1/c$ symmetry found by David and coworkers might be attributed to oxygen non-stoichiometric effects. Again, utilizing the structural similarity of BiMnO₃ and BiCrO₃, different phases exhibiting monoclinic and orthorhombic symmetries were found in oxygen deficient BiMnO₃ samples [343]. Therefore, oxygen non-stoichiometric effects might be another reason for the existence of different phases in BiCrO₃ thin films. However, this possibility can not be ruled out, since the precise determination of the oxygen content in thin films is virtually impossible.

In summary, temperature dependent x-ray diffraction measurements reveal a structural phase transition from the high-temperature orthorhombic phase to a monoclinic structure at around $T_{\text{phase}} = T_{\text{phase, bulk}} = 410 \text{ K} - 440 \text{ K}$. However, a coexistence of both structures was found in the whole investigated temperature range of $60 \text{ K} \leq T \leq 500 \text{ K}$. The exact mechanism responsible for this structural behavior remains unresolved and might be attributed to a combination of strain effects, oxygen non-stoichiometry, and a large temperature range at which the structural phase transition takes place. Therefore, the transition at 410 K – 440 K should be regarded as a change in volume fraction of different BiCrO₃ regions exhibiting an orthorhombic and monoclinic symmetry.

Structural properties of BiCrO₃ thin films at low temperature

As discussed in the previous section, the BiCrO₃ thin films exhibit a crystalline multiphase state in the temperature range $60 \text{ K} \leq T \leq 500 \text{ K}$. Since x-ray diffraction revealed that the reflections of the low temperature monoclinic phase are by far more intense than the corresponding orthorhombic ones as well as no indication of further structural phase transitions was found down to 60 K (cf. Figs. 4.27 and 4.28), the monoclinic structure is the dominant phase for $T < T_{\text{phase}}$. To investigate this structure in more detail, x-ray diffraction measurements were carried out at room temperature using a standard Cu x-ray source or synchrotron radiation at the I16

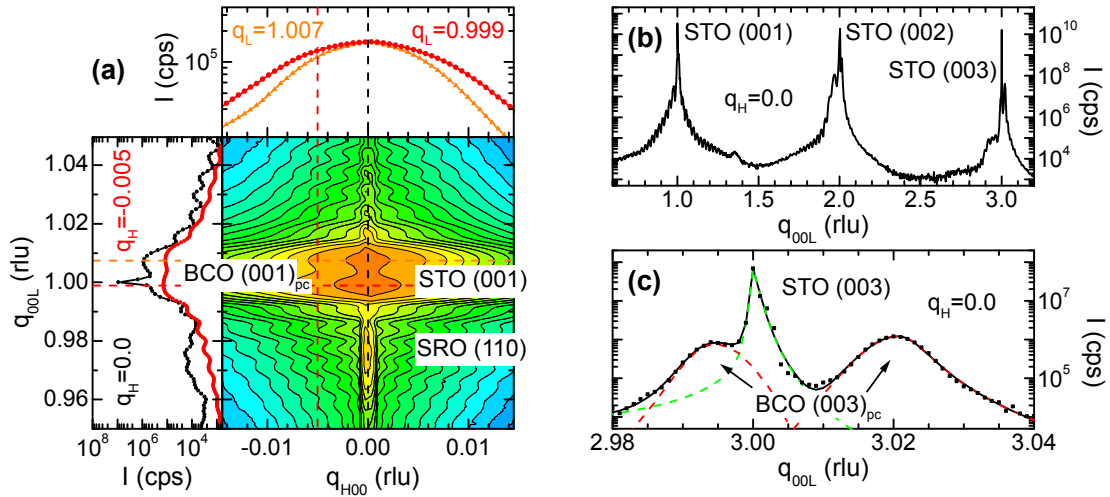


Figure 4.29: X-ray diffraction measurements on a 65 nm thick BiCrO₃ film grown on a SrRuO₃-buffered SrTiO₃ (001) substrate, carried out at room temperature at the I16 beamline located at the Diamond light source. (a) The finite thickness fringes around the pseudo-cubic BiCrO₃ (001)_{pc} reflections disclose an excellent coherent growth. A splitting of this reflection into two peaks is visible in the q_{00L} -scans with $q_H = 0$ rlu and $q_H = -0.005$ rlu. (b) An additional reflection with low intensity at around $q_H = 1.35$ rlu, which might be caused by a small impurity phase, was detected in the q_{00L} -scan. This impurity phase could not be resolved when using a standard laboratory diffractometer with a Cu x-ray source. (c) To estimate the volume ratio of the monoclinic domain types exhibiting a different out-of-plane lattice constant, the profile of the SrTiO₃ (003) reflection (green dashed line) as well as the BiCrO₃ peaks (red dashed lines) were fitted. The derived intensity evolution of the q_{00L} -scan is marked by the black solid line.

beamline at the Diamond light source as well as the BM28 beamline at the ESRF.

In BiCrO₃ thin films grown on SrRuO₃-buffered SrTiO₃ (001) substrates, BiCrO₃ reflections with two different out-of-plane constants were detected at room temperature. As an example, Fig. 4.29(a) shows x-ray diffraction measurements around SrTiO₃ (001) measured on a 65 nm thick BiCrO₃ film using synchrotron radiation. Obviously, this thin film exhibits a high crystalline quality, since finite thickness fringes are visible over the whole investigated reciprocal space demonstrating an excellent coherent growth. Furthermore, the q_{00L} -scans at $q_H = 0$ rlu and more pronounced at $q_H = -0.005$ rlu reveal a splitting of the pseudo-cubic BiCrO₃ (001)_{pc} reflection into two peaks (cf. left panel of Fig. 4.29(a)). This confirms the result of x-ray diffraction measurements on a 177 nm thick BiCrO₃ film shown in Fig. 4.26 and suggests that monoclinic domains with different out-of-plane lattice parameters are present in BiCrO₃ thin films at room temperature. To estimate the volume ratio of both type of domains distinguishable in the out-of-plane direction, the Scherrer formula [68] was employed using the full width at half maximum derived by fitting the q_{00L} -scan around the SrTiO₃ (003) reflection (cf. Figs. 4.29(b) and (c)). Within this simple model, a ratio of 60 : 40 was derived, suggesting a slight preferential formation of the domain type exhibiting a smaller out-of-plane lattice constant. The two different monoclinic domains can be identified by (111)- and ($\bar{1}01$)-type domains

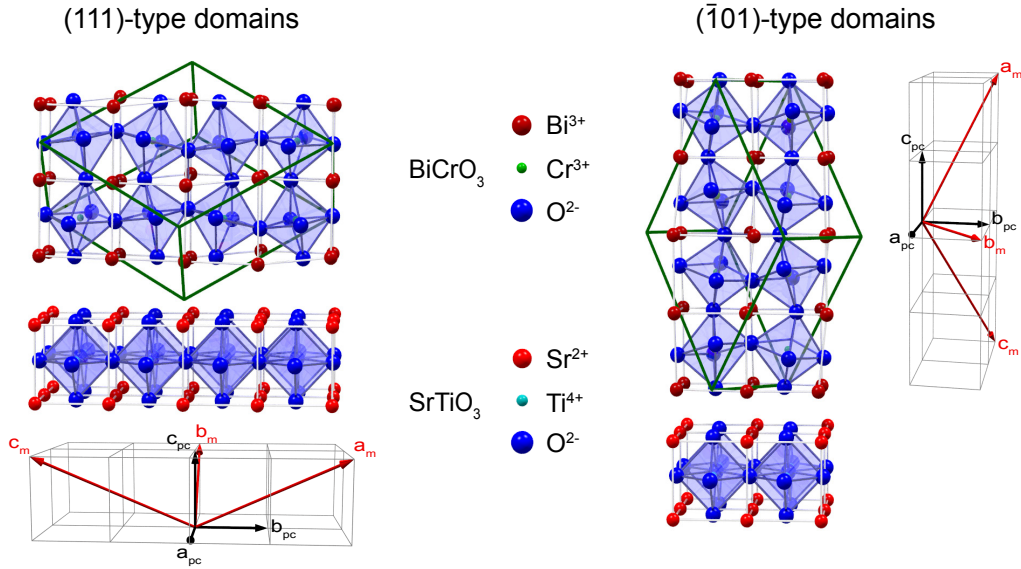


Figure 4.30: Schematic illustration of (111)- and $(\bar{1}01)$ -type monoclinic domains. The epitaxial relations between BiCrO_3 and the SrTiO_3 (001) substrate can be described as:

(111)-type domains: BiCrO_3 (111) \parallel SrTiO_3 (001) and BiCrO_3 $[\bar{1}01]$ \parallel SrTiO_3 [010]

$(\bar{1}01)$ -type domains: BiCrO_3 $(10\bar{1})$ \parallel SrTiO_3 (001) and BiCrO_3 [121] \parallel SrTiO_3 [010].

Within this setting, the monoclinic unit cell is related to the perovskite cubic axes by the matrices:

$$\begin{aligned} \text{(111)-type domains:} \quad & \begin{pmatrix} \mathbf{a}_m \\ \mathbf{b}_m \\ \mathbf{c}_m \end{pmatrix} = \begin{pmatrix} 1 & 2 & 1 \\ \bar{1} & 0 & 1 \\ 1 & \bar{2} & 1 \end{pmatrix} \begin{pmatrix} \mathbf{a}_{pc} \\ \mathbf{b}_{pc} \\ \mathbf{c}_{pc} \end{pmatrix} \\ \text{(\bar{1}01)-type domains:} \quad & \begin{pmatrix} \mathbf{a}_m \\ \mathbf{b}_m \\ \mathbf{c}_m \end{pmatrix} = \begin{pmatrix} \bar{1} & 1 & 2 \\ 1 & 1 & 0 \\ \bar{1} & 1 & \bar{2} \end{pmatrix} \begin{pmatrix} \mathbf{a}_{pc} \\ \mathbf{b}_{pc} \\ \mathbf{c}_{pc} \end{pmatrix}. \end{aligned}$$

(cf. Fig. 4.30). Using the lattice constants of bulk BiCrO_3 , which were recently published by Darie *et al.* [36], a misfit strain between BiCrO_3 and SrTiO_3 of -0.2% and -0.6% for (111)- and $(\bar{1}01)$ -type domains can be derived. Since the difference in strain of both values is small, the BiCrO_3 thin films can have (111)- and $(\bar{1}01)$ -oriented regions. Furthermore, the preferential formation of (111)-type domains, which is revealed by the volume ratio 60 : 40 derived from Fig. 4.29(c) and found in all investigated BiCrO_3 thin films independent of thickness and presence or absence of SrRuO_3 buffer layers, can be explained by the lower misfit strain.

In Fig. 4.30, only one variant of each domain-type with a fixed in-plane relation is shown for simplicity. Allowing different in-plane orientations, the BiCrO_3 thin film will form further structural domains, which can be distinguished by x-ray diffraction measurements performed around asymmetric reflections. As an example, the result of such measurements around SrTiO_3 (103) is shown in Fig. 4.31(a). In principle, Fig. 4.31(a) should disclose six different BiCrO_3 variants, but they are barely distinguishable using a standard Cu x-ray source. However, two domain types with different out-of-plane lattice constants, which can be indexed within the monoclinic symmetry by $(424)_m$ and $(51\bar{7})_m$, are marked by white dashed lines. The in-plane

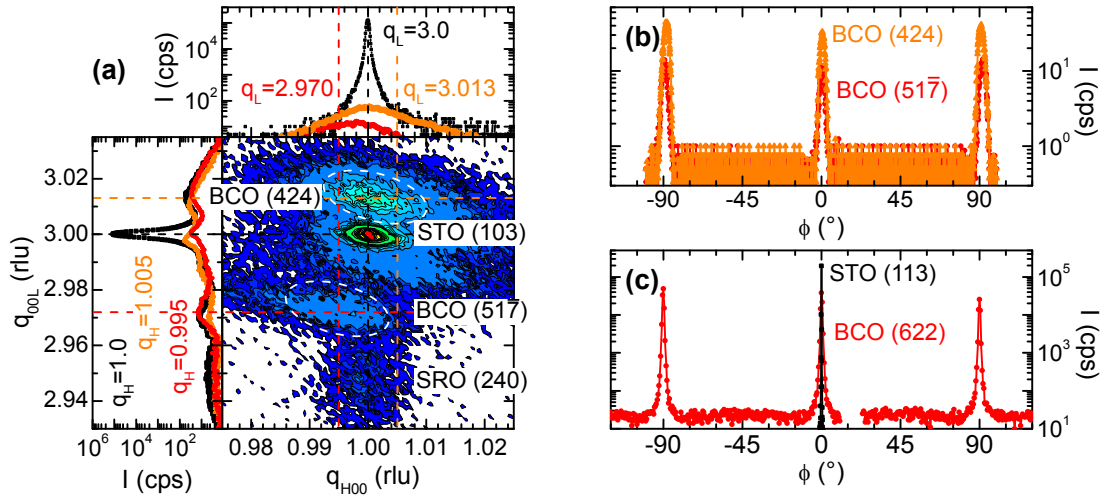


Figure 4.31: (a), (b) X-ray diffraction measurements on a 177 nm thick BiCrO₃ film grown on a SrRuO₃-buffered SrTiO₃ substrate carried out around the asymmetric SrTiO₃ (103) reflection using a standard Cu x-ray source. (a) Two of six possible in-plane domains of BiCrO₃, which are marked by white dashed lines, are resolved and indexed with respect to the monoclinic symmetry. (b) ϕ -scans reveal a four-fold symmetry of both domains. This indicates a cube-on-cube growth of the pseudo-cubic BiCrO₃ unit cells on the SrRuO₃-buffered SrTiO₃ substrate. (c) Using ϕ -scans carried out on the six-circle diffractometer of the BM28 beamline at the ESRF, the quality of the in-plane orientation can be derived from the full width at half maximum (FWHM) around the BiCrO₃ (622) reflection yielding 0.95°.

orientation of these two domain-types exhibits a fourfold symmetry revealed by azimuthal ϕ -scans (cf. Fig. 4.31(b)). This demonstrates a cube-on-cube growth of the pseudo-cubic BiCrO₃ unit cells on SrTiO₃ (001) substrates, as it is depicted in Fig. 4.30. Using ϕ -scans measured along the monoclinic BiCrO₃ (622)_m reflection carried out on the six-circle diffractometer of the BM28 beamline at ESRF (cf. Fig. 4.31(c)), the quality of the in-plane orientation can be derived from the full width at half maximum (FWHM). A FWHM of 0.95° was found for BiCrO₃, which is one order of magnitude larger compared to the SrTiO₃ substrate, but more than two times smaller than reported for BiMnO₃ thin films [164]. This demonstrates a good in-plane orientation of the crystalline domains in BiCrO₃ with the SrRuO₃-buffered SrTiO₃ substrate.

To get a deeper understanding of the in-plane structure, measurements using grazing incidence diffraction (GID) were performed at the BM28 beamline at the ESRF on a 65 nm thick BiCrO₃ thin film grown on a SrRuO₃-buffered SrTiO₃ substrate. The result of the GID measurements around the SrTiO₃ (030), SrTiO₃ (300), and SrTiO₃ (330) reflections are depicted in Fig. 4.32. All three measurements reveal the presence of several in-plane domains. Due to the low incidence angles used in the GID measurements, which results in a low penetration depth of the x-ray radiation, the contributions caused by the 20 nm thick SrRuO₃ buffer layer as well as the SrTiO₃ substrate can be neglected. This assumption is also justified by the large

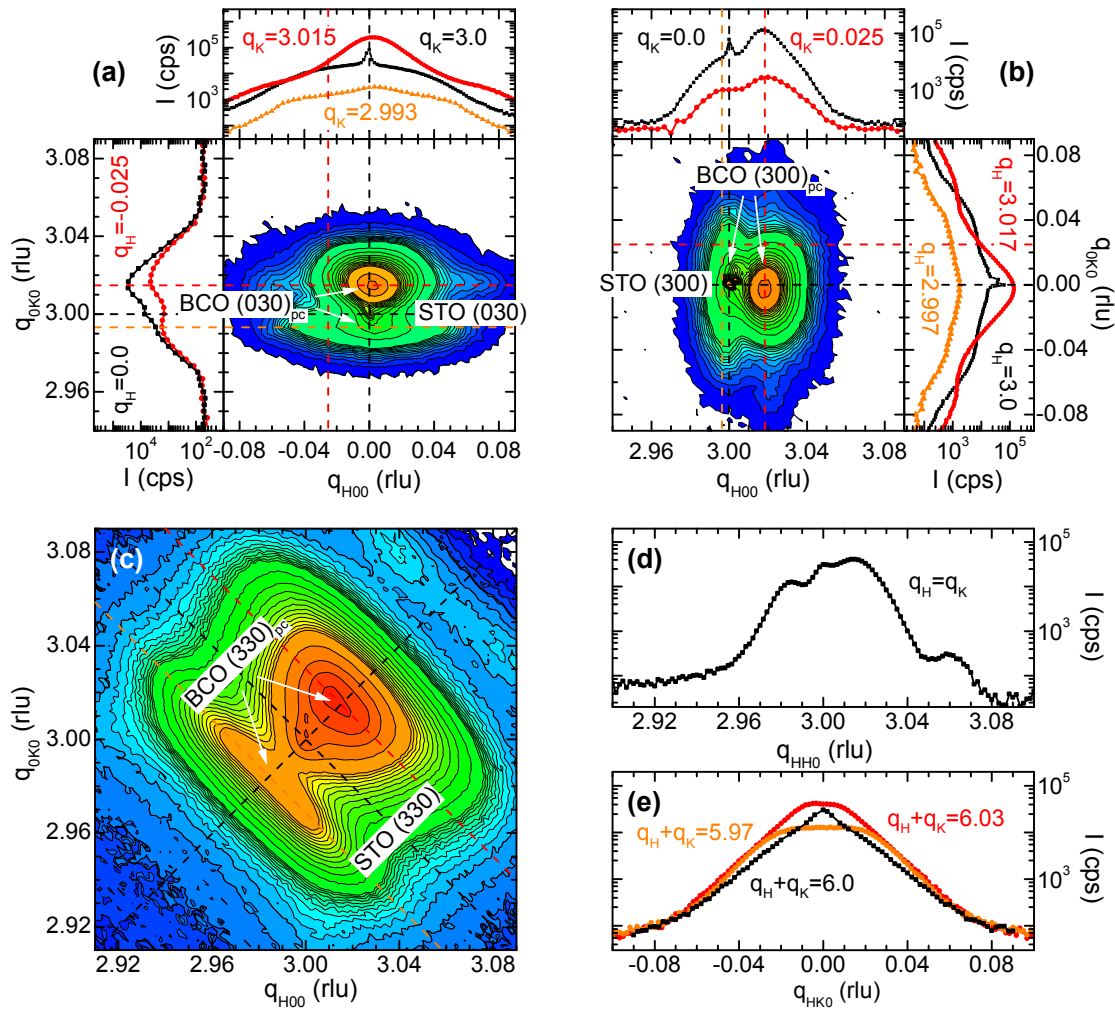


Figure 4.32: Grazing incidence diffraction around the (a) SrTiO₃ (030), (b) SrTiO₃ (300), and (c), (d), (e) SrTiO₃ (330) reflections carried out at the BM28 beam-line at the ESRF on a 65 nm thick BiCrO₃ film grown on a SrRuO₃-buffered SrTiO₃ substrate.

scattering power of bismuth atoms.²⁴

X-ray diffraction performed around the SrTiO₃ (030) reflection reveals clearly two main peaks attributed to the scattering from the BiCrO₃ layer, which are better resolved in the q_{0K0} -scan recorded at $q_H = -0.025$ rlu (cf. left panel of Fig. 4.32(a)). The peaks correspond to the monoclinic $(\bar{3}\bar{3}\bar{3})_m$ and $(\bar{6}06)_m$ reflections at higher and lower q_{0K0} -values with respect to the SrTiO₃ substrate. The q_{H00} -scans and the corresponding reciprocal space map reveal a slight shift of the maximum intensity of both peaks to positive q_{H00} -values (cf. upper panel of Fig. 4.32(a)). This suggests that the coherency of the BiCrO₃ thin film with the SrTiO₃ substrate is lifted and the relaxation of the misfit strain has started. A similar behavior was detected by

²⁴However, a finite intensity caused by scattering from the SrTiO₃ substrate is still visible in Fig. 4.32.

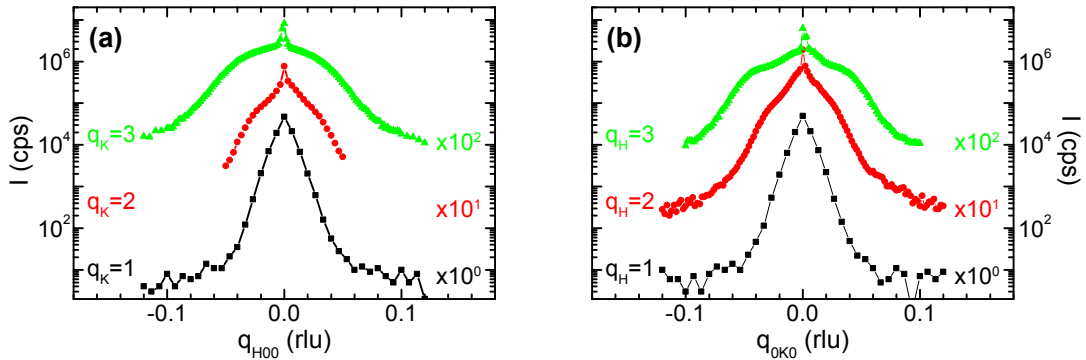


Figure 4.33: (a), (b) Grazing incidence diffraction ($q_L = 0$ rlu) carried out along the pseudo-cubic $[100]_{pc}$ ($[010]_{pc}$) direction for different q_K -values (q_H -values) around SrTiO₃ (100), SrTiO₃ (200), and SrTiO₃ (300).

GID around the SrTiO₃ (300) reflection depicted in Fig. 4.32(b). Again, two crystalline domains are observed (cf. upper panel of Fig. 4.32(b)), and both are shifted to negative q_{0K0} -values (cf. right panel of Fig. 4.32(b)). However, a detailed analysis of the peak positions of the pseudo-cubic BiCrO₃ (300)_{pc} and BiCrO₃ (030)_{pc} reflections, which are both split into two peaks, reveal a shift of the BiCrO₃ (300)_{pc} peaks to higher q_H -values compared to the BiCrO₃ (030)_{pc} peaks, which are located at lower q_K -values (cf. Figs. 4.32(a) and (b)). This might be an indication for a triclinic symmetry of the BiCrO₃ thin film, in agreement with the structural properties of BiCrO₃ thin films reported by Murakami *et al.* [150].

The low symmetry of the BiCrO₃ thin films also results in a splitting of the pseudo-cubic BiCrO₃ (330)_{pc} reflection shown in Fig. 4.32(c). The q_{HK0} -scan with $q_H = q_K$ along the $[110]_{pc}$ direction reveals four reflections (cf. Fig. 4.32(d)). One of them is caused by the SrTiO₃ substrate ($q_H = q_K = 3.0$ rlu). As discussed in the context of Fig. 4.28, the reflection located at $q_H = q_K = 3.06$ rlu can be attributed to the (060)_o and (600)_o reflections of the orthorhombic high temperature phase. The remaining two peaks are additionally split along the $[1\bar{1}0]_{pc}$ direction, since q -scans along this direction with either $q_H + q_K = 5.97$ rlu or $q_H + q_K = 6.03$ rlu reveal a broadening of these reflections (cf. Fig. 4.32(e)). In principle, the pseudo-cubic BiCrO₃ (330)_{pc} reflection splits into four different domains taking into account all possible in-plane orientations of (111)- and ($\bar{1}01$)-type domains. However, these domains are only barely resolvable (cf. Fig. 4.32(e)). Therefore, no final conclusion can be drawn on the detailed in-plane domain configuration from the GID measurements depicted in Fig. 4.32.

However, the transverse q_{H00} - as well as q_{0K0} -scans shown in Fig. 4.32(a) reveal broad shoulders at around $|q_{H00}| \simeq 0.05$ rlu and $|q_{0K0}| \simeq 0.05$ rlu, respectively. This is shown in more detail in Fig. 4.33. The additional component can be attributed to small twin domains exhibiting a low degree of ordering [259]. This is in agreement with the observation of an anisotropic peak broadening associated with diffuse scattering in polycrystalline BiCrO₃ samples revealed by neutron diffraction [36, 37]. These effects were attributed to the existence of twin domains with sizes of the order of 10 nm. However, no modulated domain structure was found, since the position of

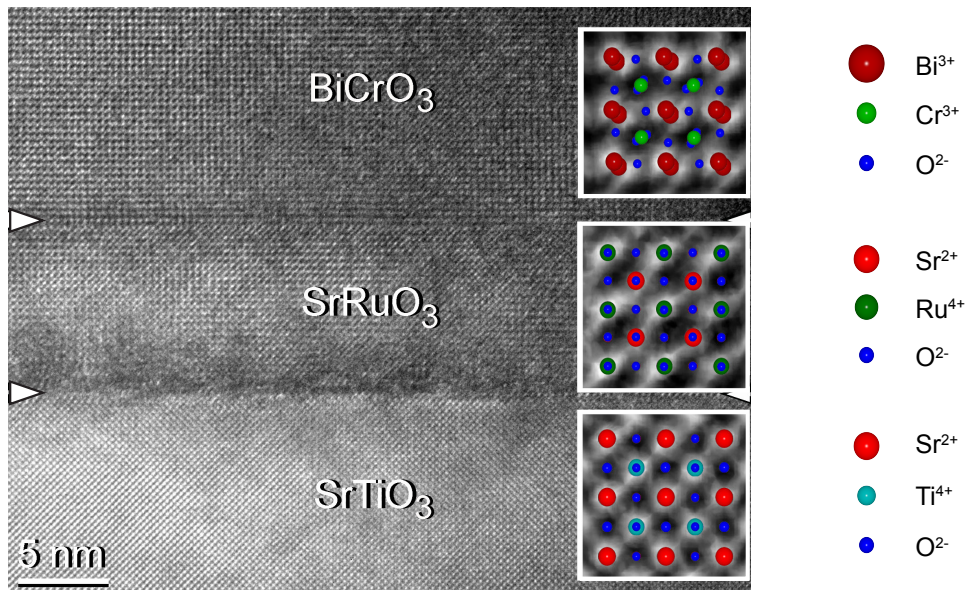


Figure 4.34: High resolution transmission electron microscopy image of a 28 nm thick BiCrO_3 film grown on a SrRuO_3 ($d = 10$ nm)-buffered SrTiO_3 substrate, measured by Sven-Martin Hühne (Universität Bonn). To illustrate the contrast in each perovskite layer, high magnification images are depicted in the insets. On the right, the scattering power of the different ions are illustrated by different diameters of the spheres.

the side peaks observed in $q_{\text{H}00}$ -scans ($q_{0\text{K}0}$ -scans) performed at different q_{K} -values (q_{H} -values) depend on the scattering vector $|\mathbf{q}|$.²⁵

The existence of twin domains as well as of (111)- and $(\bar{1}01)$ -type domains should be visible using transmission electron microscopy [37, 151, 345, 346]. Figure 4.34 shows a high resolution transmission electron microscopy image of a 28 nm thick BiCrO_3 film grown on a SrRuO_3 ($d = 10$ nm)-buffered SrTiO_3 substrate. The measurements were performed by Sven-Martin Hühne (Universität Bonn). The low magnification transmission electron microscopy image (not shown here) reveals a thickness of 28 nm (10 nm) of the BiCrO_3 (SrRuO_3) layer. These values correspond well with the thicknesses disclosed by x-ray reflectivity measurements, which were found to be 28.5 nm and 10 nm, respectively. This demonstrates an uncertainty of less than 1 nm in determining the thin film thickness using x-ray diffraction. Furthermore, Fig. 4.34 reveals a difference in the image contrast caused by the different scattering power of the present ions, since the scattering potential scales with the atomic number Z (cf. right side of Fig. 4.34). To illustrate the contrast in each perovskite layer, high magnification images are depicted in the insets of Fig. 4.34. These images reveal that in case of the BiCrO_3 layer, the contrast is mainly caused by the Bi atoms, while for SrTiO_3 and SrRuO_3 , the Sr^{2+} , Ti^{4+} and Ru^{4+} ions contribute. In addition, Fig. 4.34 proves a continuation of the oxygen sublattices of the three perovskite layers across the interfaces. The rotations of the oxygen octahedra, which are present in the SrRuO_3 and BiCrO_3 layers (cf. Fig. 4.30 and Fig. 4.6), are

²⁵An in-plane modulation of twin domains would lead to satellite peaks located at a distance $\pm|\mathbf{q}|$ from the center, independent of the momentum transfer [344].

not resolved due to the low scattering power of the oxygen columns. Furthermore, neither crystallographic (111)-type and ($\bar{1}01$)-type domains nor twin domains have been observed so far. Therefore, in the framework of this thesis, no direct evidence of the presence of twin domains in BiCrO₃ thin films was found.

However, the high crystalline quality is demonstrated by the high resolution transmission electron microscopy image shown in Fig. 4.34. Furthermore, an atomically flat interface between SrRuO₃ and BiCrO₃ was found, which confirms the excellent growth behavior of BiCrO₃ on SrRuO₃-buffered SrTiO₃ substrates.

In summary, the dominant crystalline structure of BiCrO₃ thin films for $T < T_{\text{phase}}$ was found to be monoclinic. In agreement with the temperature dependent x-ray diffraction measurements shown in Fig. 4.26, monoclinic domains with different pseudo-cubic out-of-plane lattice constants were detected. These domains can be identified to be either monoclinic (111)- or ($\bar{1}01$)-type domains. In analogy to BiMnO₃ thin films [164], the determination of the in-plane domain structure is a difficult task, since the low symmetry of the BiCrO₃ thin film results in a significant number of reflections, which furthermore overlap one another. As no indication of a preferred in-plane domain configuration was found, it is assumed that all possible monoclinic in-plane domains are present in the BiCrO₃ with equal probability.

4.5.2 Multiferroic properties of BiCrO₃ thin films

The multiferroic properties of BiCrO₃ thin films are discussed in the following section. Since there are conflicting reports on the dielectric ground state of BiCrO₃ thin films, we investigated the macroscopic and microscopic dielectric behavior of our BiCrO₃ thin films in detail, using both a commercial ferroelectric tester as well as piezoelectric force microscopy measurements. In addition, the macroscopic and microscopic magnetic properties above and below the magnetic transition temperature of the BiCrO₃ thin films were examined by means of SQUID magnetometry and magnetic force microscopy. Furthermore, exchange bias effects were observed in ferromagnet/BiCrO₃ composite heterostructures.

Dielectric behavior of BiCrO₃ thin films

The dielectric properties of bulk BiCrO₃ have not been conclusively resolved up to now. Niitaka and coworkers stated that bulk BiCrO₃ exhibits ferroelectricity below 420 K without giving any proof [147]. The ferroelectric behavior would be in agreement with the observation of a ferroelectric hysteresis in $(1-x)$ [LaCrO₃] x [BiCrO₃] bulk samples [270]. Both experimental findings are in contrast to first principles density functional calculations [33]. These calculations reveal an antiferroelectric behavior of BiCrO₃, similar to PbZrO₃.

For BiCrO₃ thin films, only two reports on the dielectric properties have been published so far. While microscopic measurements using piezoelectric force microscopy revealed a ferroelectric-like behavior [150], antiferroelectricity was observed in macroscopic measurements using a ferroelectric tester [34]. To resolve this controversy, we investigated the dielectric properties of our BiCrO₃ both on macroscopic

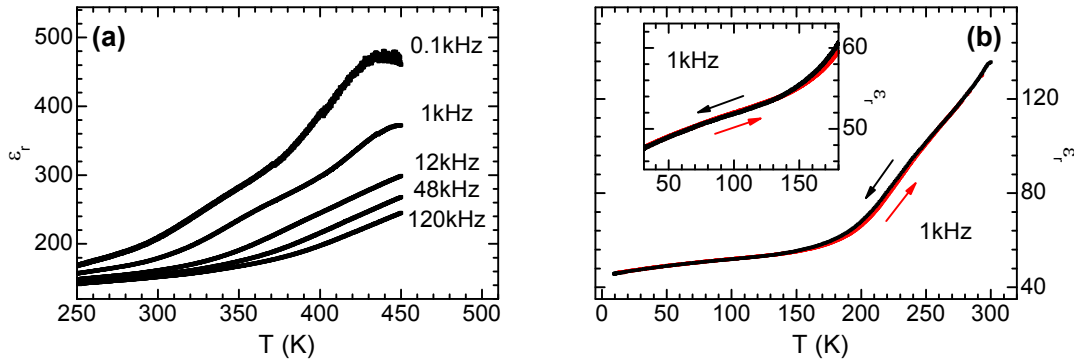


Figure 4.35: Temperature dependence of the real part of the dielectric permittivity ϵ_r (a) as a function of the measurement frequency as well as (b) depending on heating or cooling the sample. The measurements were carried out on a 220 nm thick BiCrO₃ film grown on a SrRuO₃-buffered SrTiO₃ substrate.

and microscopic scales using a commercial ferroelectric tester as well as piezoelectric force microscopy (cf. Section 2.2).

As pointed out in the previous section, BiCrO₃ exhibits a phase transition at around 410 K – 440 K. Since this phase transition is expected to be not only structural, but also between a paraelectric and a ferroelectric or antiferroelectric phase, the real part of the dielectric permittivity ϵ_r should change at the phase transition. Figure 4.35(a) shows the temperature dependence of ϵ_r measured on a 220 nm thick BiCrO₃ film grown on a SrRuO₃-buffered SrTiO₃ substrate.²⁶ For a measurement frequency of 0.1 kHz, an anomaly is visible at the phase transition temperature of about 430 K. This anomaly shifts to higher temperatures with increasing measurement frequency. A similar behavior is also observed in bulk BiCrO₃ (cf. Fig. 4.1(b)) [147] and, e.g., in the material system YCrO₃ [347]. The dependence of the transition temperature on the measurement frequency can be understood in terms of defects leading to a relaxor like behavior [348]. Such a phase transition usually leads to a thermal hysteresis in the dielectric permittivity depending on whether the measurement is carried out during cooling or heating. However, no hysteresis in the temperature range between 300 K and 5 K was observed in our samples (cf. Fig. 4.35(b)). Furthermore, the inset of Fig. 4.35(b) reveals no further anomalies around the expected magnetic transition temperature at around 120 K. This suggests that no strong magnetoelectric or magnetocapacitance effects are present in BiCrO₃ [337]. This is in contrast to the results published by Kim *et al.* [34], who found anomalies at 140 K as well as at 107 K and attributed them to a finite magnetoelectric coupling and structural transition, respectively.

To reveal the intrinsic dielectric properties in Bi containing multiferroics, a detailed analysis of the dielectric properties is essential [162]. Therefore, the temperature and frequency dependence of the real part of the dielectric permittivity ϵ_r as well as the dielectric loss D are discussed in detail in the following. In Fig. 4.36(a), ϵ_r and D are shown as a function of temperature. The measurements were carried out

²⁶See Section 2.2 for more details on dielectric permittivity measurements.

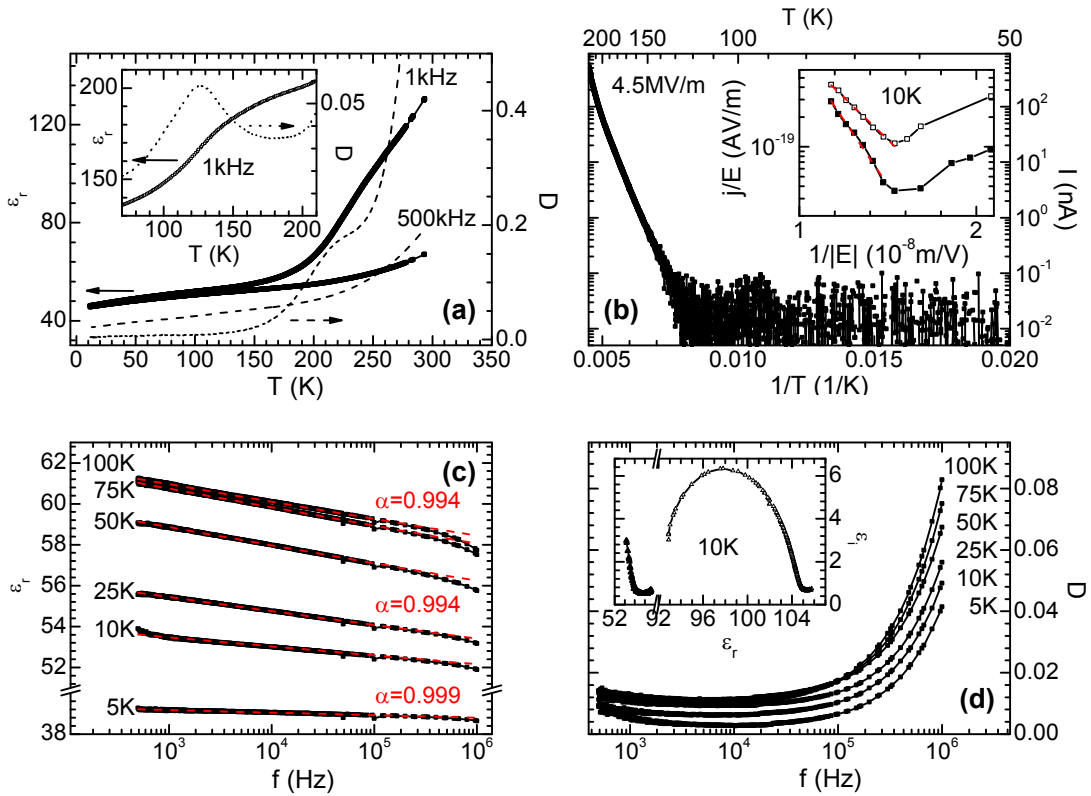


Figure 4.36: (a) The real part of the dielectric permittivity ϵ_r (full symbols) and the dielectric loss D (dashed lines) as a function of temperature measured at 1 kHz and 500 kHz. The measurements were carried out on a 177 nm thick BiCrO₃ film fabricated on a SrRuO₃-buffered SrTiO₃ substrate. For comparison, the temperature dependence of ϵ_r and D measured on a 220 nm thick BiCrO₃ film fabricated using a lower oxygen pressure compared to the ideal deposition parameters described in Section 4.2 is shown in the inset. (b) Leakage current measurements performed at an electric field of 4.5 MV/m applied across the 177 nm thick BiCrO₃ film. The inset reveals a Fowler-Nordheim tunnel process at $T = 10$ K in the limit of high electric fields following Eq. (4.9) (red dashed lines). (c), (d) Frequency dependence of the dielectric permittivity ϵ_r and dielectric loss D for different temperatures. (c) ϵ_r follows a Curie-von Schweidler law for $f \leq 10^5$ Hz (red dashed lines). The dielectric behavior of the nominally stoichiometric 177 nm thick BiCrO₃ film (full symbols) as well as the oxygen deficient 220 nm thick one (open symbols) is plotted in a Cole-Cole diagram in the inset of (d).

on a 177 nm thick BiCrO₃ film fabricated on a SrRuO₃-buffered SrTiO₃ substrate. No frequency dependence of the dielectric permittivity and the dielectric losses was observed below 150 K. Increasing the temperature, not only an increase of ϵ_r , but also a strong frequency dependence was found accompanied by an increase of the dielectric loss. Furthermore, a peak in D is observable at a measurement frequency of 1 kHz. This can be attributed to dielectric relaxation [70], which can be caused, in principle, by space charge polarization, Maxwell-Wagner polarization, domain-wall motion, long-range structural disorder, and defects in the BiCrO₃ thin film at low frequencies ($f < 1$ MHz) [349]. In analogy to BiFeO₃, we attribute the behavior vis-

ible in Fig. 4.36(a) to a Maxwell-Wagner type relaxation caused by a space charge polarization located at the film-electrode interface [162, 350, 351]. Therefore, this relaxation should strongly depend on extrinsic effects like the Schottky barrier heights defined by the electrode materials [352] and the type of contacts [162]. Moreover, the oxygen partial pressure during the growth process and therefore the amount of oxygen vacancies in BiCrO_3 thin films is crucial in terms of reducing the leakage current and destroying relaxation processes. As an example, the inset of Fig. 4.36(a) shows the results of dielectric measurements on a 220 nm thick BiCrO_3 film fabricated using a lower oxygen pressure compared to the ideal deposition condition described in Section 4.2. In spite of the similar thickness, frequency dependent anomalies are observed even below 100 K leading to an enhanced dielectric permittivity as well as an increase of the dielectric loss. This furthermore reveals the high sensitivity of the physical properties on the growth parameters in Bi containing perovskite-like material systems. In SrTiO_3 thin films as well as in Bi doped SrTiO_3 , similar modes were observed and attributed to impurities and local disorder [353, 354].²⁷

One of the main drawbacks of Bi containing multiferroics is the high leakage current found in these material systems [355]. Figure 4.36(b) shows the result of dc current measurements with a constant electric field of 4.5 MV/m applied across the BiCrO_3 thin film. The leakage current rapidly increases above $T = 130$ K, which can be mainly attributed to a thermally activated electric conductivity caused by Bi and/or oxygen vacancies. In general, the major leakage mechanisms in insulating thin films are commonly classified in four basic conduction processes: Schottky emission, space charge limited bulk conduction, Poole-Frenkel emission, and Fowler-Nordheim tunneling [356]. For a given insulator, each process may dominate in a certain temperature range. The Schottky emission process arises from thermionic emission across the metal-insulator interface. When a metal is attached to an insulating material, a potential barrier is formed, if the metal work function ϕ_m is greater than the electron affinity χ of the insulating material. Using SrRuO_3 and Au as electrode materials with a work function ϕ_m of either 5.2 eV [357] or 5.3 eV [358], respectively, as well as an electron affinity of $\chi = 3.3$ eV, which was estimated for BiFeO_3 [352], a barrier height ϕ_b of the metal- BiCrO_3 device can be estimated to $\phi_b = \phi_m - \chi \approx 1.9$ eV. However, in reality, dopants or surface states lead to band bending effects at the interface of the electrode and the thin film forming a Schottky barrier. BiCrO_3 thin films are likely oxygen deficient and are presumed to be slightly nonstoichiometric due to the high volatility of Bi. While Bi deficiencies create an acceptor level above the valence band, oxygen vacancies are donor type defects. Since typically the regions of the capacitor near the interface are more oxygen deficient than the bulk, a transition from n -type behavior at the interface to p -type behavior in the center of the BiCrO_3 film might occur [5]. Following Cowley and Sze [359], the barrier height can be calculated using the expression

$$\phi_b = S(\phi_m - \chi) + (1 - S)(E_g - \phi_0), \quad (4.8)$$

where E_g is the band gap of BiCrO_3 and ϕ_0 is defined as the energy below which the

²⁷The reader is referred to the diploma thesis of Daniel Pantel for more details on this issue [70].

surface states must be filled for charge neutrality at the surface. S is the Schottky barrier pinning factor ranging from 0 to 1 [5]. Using an energy band gap of 2.5 eV for BiCrO₃ [360] and a pinning factor of 0.23, which was calculated for BiFeO₃ [352], the barrier height can be estimated to 0.80 eV (0.82 eV) in case of SrRuO₃ (Au) as electrode material. However, Equation (4.8) is only valid in the limit of low density of defect concentrations ($n_D \lesssim 10^{16} \text{ cm}^{-3}$). In case of a higher density of defects, such as oxygen vacancies, the barrier height is expected to be further reduced. For example, a maximum reduction of about 0.3 eV was found in Pt-SrTiO₃ junctions [5]. Nevertheless, at low temperatures the energy barrier is still sizable making emission of electrons from the electrode into the ferroelectric unlikely.

In analogy to BiFeO₃ [355, 356, 361], the current response observed in BiCrO₃ for temperatures larger than 120 K is more probably caused by bulk-limited Poole-Frenkel emission, which is due to field-enhanced thermal excitation of trapped electrons. In this case, the barrier height is given by the trap potential well and a linear dependence of $\ln(j/E^2)$ as a function of $(1/T)$ is expected [362], which is fulfilled in the temperature range $120 \text{ K} < T < 200 \text{ K}$ (cf. Fig. 4.36(b)). Oxygen vacancies can be identified as the cause of Poole-Frenkel emission, since these defects induce trap centers in Bi containing perovskite-like thin films [361, 363].

At low temperature ($T \leq 10 \text{ K}$), the conduction process can be attributed to an interface-limited Fowler-Nordheim tunneling. Since the thickness of the BiCrO₃ thin film is 177 nm, the tunneling does not take place across the whole thin film, but instead through a potential barrier formed at the thin film/electrode interface. In case of Fowler-Nordheim tunneling, a linear relation between $\ln(j/E^2)$ and $(1/E)$ can be observed in the limit of high electric fields (cf. inset of Fig. 4.36(b)) as the leakage current j is described by

$$j = BE^2 \exp\left(-\frac{C\phi_b^{3/2}}{E}\right), \quad (4.9)$$

where B and C are constants and ϕ_b denotes the height of the potential barrier [362]. The inset of Fig. 4.36(b) reveals different slopes measured for negative (open symbols) and positive bias (full symbols), which indicates a different amount of oxygen vacancies at the bottom and top of the BiCrO₃ [5].

Since the leakage current detected for temperatures larger than 130 K certainly influences the dielectric measurements, the dielectric behavior for temperatures lower than 100 K is discussed in the following. At these temperatures, an intrinsic behavior of the BiCrO₃ thin film is expected. In Fig. 4.36(c) and (d), the real part of the relative permittivity ϵ_r as well as the loss tangent D are plotted as a function of the measurement frequency f recorded for different temperatures T . While a very weak frequency dispersion of the dielectric constant is visible, the loss tangent varies considerably with frequency. At low frequency, the slight increase of the loss tangent can be attributed to the presence of a finite dc leakage current, whereas the decrease of ϵ_r and the increase of D for frequencies larger than 10^5 Hz indicate a relaxation process which might take place above 10^6 Hz .²⁸ To illustrate the dielectric behavior

²⁸Due to experimental restrictions, the maximum frequency is limited to 10^6 Hz .

measured at 10 K in more detail, the imaginary part ε_i is plotted versus the real part ε_r of the dielectric function (Cole-Cole diagram) [91, 364]. For comparison, the real ε_r and imaginary ε_i part of the dielectric function derived from the 220 nm thick oxygen deficient BiCrO_3 film discussed in the inset of Fig. 4.36(a) is also included in the Cole-Cole diagram (cf. open symbols in the inset of Fig. 4.36(d)). Clearly, a semi-circle is observable in this sample, indicating a Debye-like relaxation at low temperatures. This relaxation seems to be shifted to higher frequencies in BiCrO_3 thin films grown under nominally optimal conditions. However, in the observed frequency range, the BiCrO_3 thin films fabricated under these conditions exhibit only a small dependence of the dielectric permittivity ε_r on the frequency f (cf. Fig. 4.36(c)). This behavior can be explained within a Curie-von Schweidler law, which is also called the “universal dynamic current response” [365]:

$$j_R(t) = \beta \cdot t^{-\alpha}, \quad (4.10)$$

where j_R denotes the polarization charging current of the dielectric material and α as well as β are constants. Following Waser *et al.* [91], the frequency dependence of the electric susceptibility χ_e can be obtained by the Fourier transform of the relaxation current response to a step function of the electric field $E(t) = E_0$ for $0 \leq t \leq \infty$:

$$\chi_e = \chi'_e(\omega) + i\chi''_e(\omega) = \frac{1}{\varepsilon_0 E_0} \left(\int j_R(t) \cdot \exp(i\omega t) dt \right). \quad (4.11)$$

From Eq. (4.11), the real part of the relative permittivity as well as the loss factor can be calculated to

$$\begin{aligned} \varepsilon_r(\omega) &\approx \chi'_e(\omega) = k_0 \cdot \omega^{\alpha-1} + \chi_\infty \\ D &= \left| \frac{\varepsilon_i(\omega)}{\varepsilon_r(\omega)} \right| \approx \left| \frac{\chi''_e(\omega)}{\chi'_e(\omega)} \right| = \cot\left(\frac{\alpha\pi}{2}\right) = \text{const}, \end{aligned} \quad (4.12)$$

where χ_∞ is the electric susceptibility in the limit of high frequency and k_0 is a constant, which depends on, among others, E_0 as well as on α . Therefore, $\varepsilon_r(\omega)$ should be a function of $\omega^{\alpha-1}$ in the regime of the Curie-von Schweidler law. Using Eq. (4.12), the dispersion of the BiCrO_3 thin film can be obtained for different temperatures. As shown in Fig. 4.36(c), the Curie-von Schweidler law is in good agreement with the experimental data for frequencies lower than 10^5 Hz. This law is reported for a wide range of materials [366, 367] including ferroelectrics such as BiFeO_3 [154] and the dielectric compound SrTiO_3 [368]. To explain this behavior, different models were proposed in the literature, such as a distribution of relaxation times, of hopping probabilities, or space charge trapping [365, 367, 369–371]. However, the origin of the power law dependence of the dielectric permittivity is poorly understood, especially in highly-crystalline thin films. Since Jonscher pointed out that this behavior is invariably occurring in disordered systems [370], the crystalline polydomain state present in BiCrO_3 thin films on $\text{SrTiO}_3(001)$ substrates might be the main reason for the observed dielectric behavior. However, to increase the

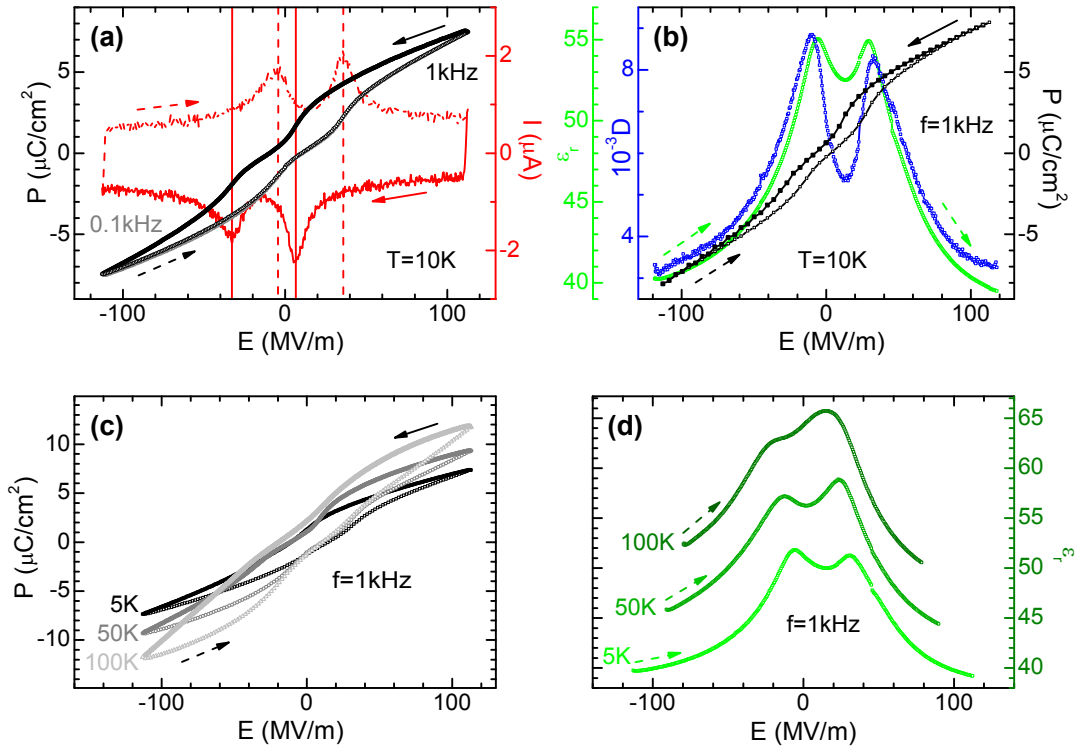


Figure 4.37: (a) Electric polarization P as a function of the applied electric field E measured at 10 K on a 177 nm thick BiCrO₃ film grown on a SrRuO₃-buffered SrTiO₃ substrate by employing the dynamic hysteresis mode with 0.1 kHz (grey symbols) and 1 kHz (black symbols). The current response recorded during the $P(E)$ measurement is plotted as red lines. Two distinct current peaks are visible in each sweep direction, which are marked by vertical lines. (b) To eliminate any frequency dependence of the electric polarization, $P(E)$ loops were also measured using the quasi-static hysteresis mode of the commercial ferroelectric tester (black symbols). The electric field dependence of the real part of the dielectric permittivity ϵ_r (green line) as well as the dielectric loss D (blue line) are also included into the figure. For better visibility, only the up sweep (-119 MV/m \rightarrow $+119$ MV/m) is shown for ϵ_r and D . (c), (d) The dynamic $P(E)$ and $\epsilon_r(E)$ loops at higher temperatures are strongly affected by the increase of the leakage current in the BiCrO₃ sample.

understanding on this issue, dielectric measurements on high quality mono-domain BiCrO₃ thin films are mandatory.

To reveal the existence of a long range order of electric dipoles, the electric polarization P as a function of the applied electric field E was investigated at different temperatures as well as different measurement frequencies using a commercial ferroelectric tester. Figure 4.37(a) discloses a double hysteresis $P(E)$ loop with four distinct current peaks at $T = 10$ K, which are located at the step sections of the polarization curve (cf. vertical dashed lines in Fig. 4.37(a)). This is a clear sign of an antiferroelectric behavior, with an electric field-forced transition into a ferroelectric state above $E \approx 40$ MV/m, which is possible due to a small difference in free energy between the ferroelectric and antiferroelectric state. The finite remanent polarization at $E = 0$ is caused by leakage currents present in the BiCrO₃ thin film. Such

leakage currents can also contribute to the measured surface charges, which falsifies the electric polarization response of the sample. Using different measurement frequencies to obtain the $P(E)$ hysteresis, the contribution caused by finite leakage currents can be identified, since the ferroelectric displacement is almost frequency independent in the used frequency range ($f < 1$ kHz), while the leakage charge is proportional to the integration time [89]. As an example, Fig. 4.37(a) shows two $P(E)$ loops measured using a frequency of 0.1 kHz and 1 kHz. Almost no difference is observable. The slight increase of the polarization value at $E = \pm 100$ MV/m and 0.1 kHz can be attributed to a small amount of a dc leakage current. However, the shape of the $P(E)$ loops remains similar revealing an antiferroelectric behavior independent of the frequency. Furthermore, the frequency dependent change of the area enclosed by the $P(E)$ loop is marginal, indicating saturated $P(E)$ loops [372]. Therefore, extrinsic effects causing the observed polarization response as a function of the electric field can be excluded and Fig. 4.37(a) reveals an antiferroelectric ground state of BiCrO₃ thin films, which is in agreement with theoretical calculations [33] and experimental results published by Kim and coworkers [34]. A possible frequency dependence of the polarization can be excluded by recording quasi static $P(E)$ hysteresis loops (cf. Section 2.2.1). This method allows the electric polarization to relax for several seconds at each data point. The $P(E)$ loop measured with the static hysteresis procedure using a relaxation time of 2 s is displayed in Fig. 4.37(b), again revealing a double hysteresis in agreement with the $P(E)$ loop obtained using the dynamic measurement mode (cf. Fig. 4.37(a)). However, by comparing both measurement techniques, a reduction of the area enclosed by the $P(E)$ loop is observable, which can be mainly attributed to the absence of any dielectric relaxation in quasi-static $P(E)$ loops. Moreover, the quasi-static polarization versus electric field loop is horizontally shifted by 1 MV/m with respect to $E = 0$ MV/m, indicating a small but finite imprint effect. Various efforts were made to understand the origin of the imprint in dielectric materials in the past. Two main reasons are considered to be responsible for the occurrence of imprint effects: defect dipoles related to oxygen vacancies [373] as well as the existence of a non switching layer (“dead layer”) between the ferroelectric layer and the bottom electrode, which is possibly formed by the relaxation of lattice misfit strain in the heteroepitaxial ferroelectric thin film [374]. To get further insight into this issue, the electric field dependence of the real part of the dielectric permittivity $\varepsilon_r(E)$ as well as the dielectric loss $D(E)$ measured at 1 kHz, which reveal additional information about reversible and irreversible domain wall and pinning effects, were recorded. For clarity, only the up sweep (-119 MV/m \rightarrow $+119$ MV/m) is shown in Fig. 4.37(b) revealing two maxima of each curve. However, the position of the maxima of the simultaneously measured $\varepsilon_r(E)$ and $D(E)$ curves do not match, which is an indication for pinning centers, since pinned domain walls contribute to the dielectric permittivity losslessly [368]. Therefore, a finite amount of pinning centers most likely is responsible for the finite imprint effect detectable in the quasi-static $P(E)$ double hysteresis [375].

The temperature evolution of the $P(E)$ and $\varepsilon_r(E)$ loops is displayed in Figs. 4.37(c) and (d). Clearly, an increase of the saturation polarization and the remanent polarization as well as the dielectric permittivity is visible, which is caused by an increase

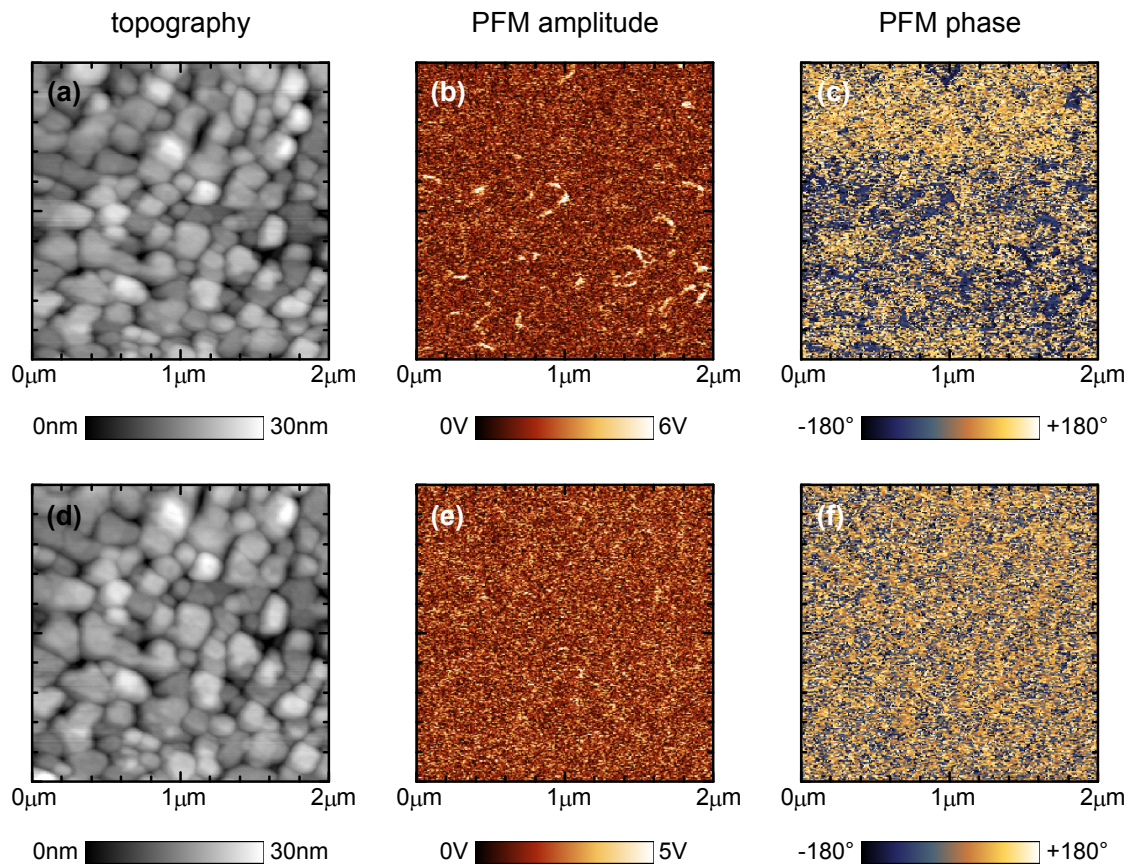


Figure 4.38: (b), (c) Out-of-plane and (e), (f) in-plane piezoelectric force microscopy (PFM) measurements carried out at ambient conditions on a 68 nm thick BiCrO₃ film deposited directly on a Nb:SrTiO₃ substrate. The corresponding topography, which is recorded simultaneously, is displayed in (a) and (d), respectively.

of the leakage current. At 100 K, the antiferroelectric nature of the BiCrO₃ thin films is hardly resolved. Therefore, high quality thin films with a low amount of leakage currents are mandatory to exclude extrinsic artefacts and to reveal the ground state of multiferroic materials [89]. The reader is referred to the diploma thesis of Daniel Pantel for more details on the dielectric properties of BiCrO₃ thin films [70].

Figure 4.37 unambiguously reveals an antiferroelectric behavior in BiCrO₃ thin films observed from dielectric measurements using macroscopic contacts.²⁹ However, Murakami and coworkers reported the presence of ferroelectricity in BiCrO₃ thin films employing piezoelectric force microscopy (PFM) measurements [150]. To investigate this discrepancy, PFM experiments were performed on our BiCrO₃ thin films by Denny Köhler (Technische Universität Dresden). Figure 4.38 shows out-of-plane ((b), (c)) and in-plane ((e), (f)) PFM images as well as the corresponding topography measurements ((a), (d)) recorded at room temperature on a 68 nm thick BiCrO₃ film deposited directly on a Nb:SrTiO₃ substrate. The topography images

²⁹The diameter of the electric contacts used for the dielectric measurements of BiCrO₃ thin films was 200 μm (cf. Section 2.2).

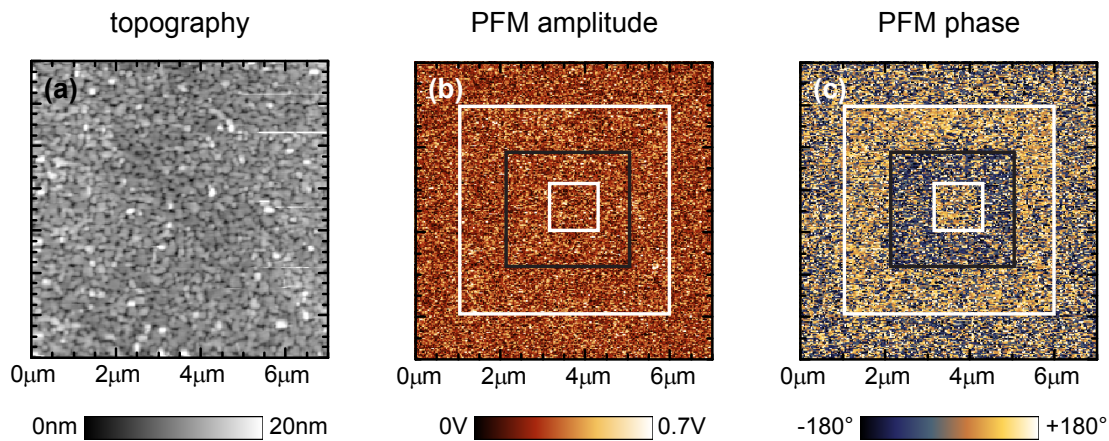


Figure 4.39: (b), (c) Out-of-plane piezoelectric force microscopy (PFM) measurements carried out at 80 K under ultra-high vacuum conditions after poling the area marked by the white and black rectangles using a voltage of ± 10 V. First, the area enclosed by the large white rectangle was poled using $+10$ V, then -10 V was used for the region marked by the black square, and finally the area of the inner white rectangle was poled using a positive voltage again. The topography of the whole scan area is depicted in (a).

(cf. Figs. 4.38(a) and (d)) reveal that this particular sample is grown in an island growth mode resulting in a high rms surface roughness of 4.8 nm. However, the amplitude and phase signal of in-plane as well as out-of-plane PFM measurements exhibit almost a constant signal over the whole scanned area. The finite contrast visible in the out-of-plane measurements is caused by topography artefacts. Two different conclusions can be drawn from the observed constant signals: (i) either the BiCrO_3 thin film exhibits a ferroelectric single domain state with no domain structure, or (ii) the BiCrO_3 thin film has an antiferroelectric ground state, suggested by the macroscopic measurements discussed above. The first explanation is very unlikely, since the crystallographic polydomain state in BiCrO_3 thin films at least leads to an in-plane ferroelectric domain structure similar to BiFeO_3 thin films (cf. Fig. 4.16). Assuming an antiferroelectric ground state of BiCrO_3 thin films, an increase of noise is expected in the PFM signal [93]. This is visible by comparing the phase signal of the out-of-plane PFM measurement of BiCrO_3 (cf. Fig. 4.38(c)) with the respective out-of-plane measurement of BiFeO_3 (cf. Fig. 4.16(c)). Therefore, Fig. 4.38(c) confirms the dielectric macroscopic measurements.

In addition, Murakami *et al.* found a reversible switching of ferroelectric domains in BiCrO_3 thin films using PFM after poling different areas of the BiCrO_3 thin film [150]. To understand these findings, we repeated the same experiment on a 38 nm thick BiCrO_3 film deposited directly on a Nb:SrTiO_3 substrate. The PFM measurement was carried out at 80 K under ultra-high vacuum conditions. Three different areas were poled applying ± 10 V to the conducting tip. First, the area enclosed by the outer white rectangle depicted in Figs. 4.39(b) and (c) was poled by applying $+10$ V to a conducting tip while scanning this area in contact mode. Afterwards, a negative voltage of -10 V was used to scan the region marked by the black

square, and finally another poling procedure was performed with a positive voltage of +10 V while scanning the inner area (cf. small white rectangle in Figs. 4.39(b) and (c)). After the poling procedure, the out-of-plane PFM amplitude and phase signal was recorded. As obvious from Figs. 4.39(b) and (c), a homogeneous signal was observed in the out-of-plane PFM amplitude, while a finite contrast is visible in the PFM phase image. This contrast can not be attributed to different ferroelectric domains, since the difference in the PFM phase signal between the poled areas was found to be only 56° [93]. Furthermore, the contrast is not stable in time and vanishes after three more scans of the same area. Therefore, this relaxor-type behavior is most likely caused by extrinsic effects [93]. One explanation could be the presence of charged oxygen vacancies and short range polar regions, which cause a relaxor like behavior in normal ferroelectrics [347, 376]. Therefore, the microscopic measurements depicted in Figs. 4.38 and 4.39 confirm the antiferroelectric ground state of BiCrO₃ thin films revealed by dielectric measurements using macroscopic contacts.

In total, the dielectric properties of BiCrO₃ thin films reveal a relaxor-like phase transition at around 430 K, which might be attributed to defects. Since electric polarization measurements carried out at 10 K reveal an antiferroelectric behavior of these thin films, this phase transition can be attributed to a transition from the paraelectric phase above 430 K to an antiferroelectric one below this temperature. The antiferroelectric ground state was further confirmed by piezoelectric measurements (PFM). The finite contrast visible in PFM phase images recorded after poling different areas of the BiCrO₃ thin films with ±10 V can be mainly attributed to extrinsic effects, such as oxygen vacancies and short range polar regions, rather than switching of ferroelectric domains as reported by Murakami *et al.* [150]. Furthermore, the frequency dependence of the real part of the dielectric permittivity reveals a Curie-von Schweidler behavior for temperatures lower than 100 K, which might be explained by the crystalline polydomain state of the BiCrO₃ thin films. At higher temperatures, the dielectric properties are strongly affected by an increase of the leakage currents in the sample. However, no anomalies were found around the expected magnetic transition temperature of BiCrO₃ at around 120 K, which suggests no strong magnetocapacitance or magnetoelectric effects in BiCrO₃.

Magnetic properties of BiCrO₃ thin films

The magnetic properties of bulk BiCrO₃ were first investigated by Sugawara and Iida [139]. They found a transition temperature of $T_N = 123$ K, which was interpreted as the Néel temperature of BiCrO₃. Furthermore, a parasitic ferromagnetic moment was detected below T_N . Recently, the antiferromagnetic structure was identified using neutron diffraction to be *G*-type [36, 148], which is in agreement with theoretical calculations [33, 342, 360, 377]. Within this magnetic structure, the magnetic moments were found to be aligned along the monoclinic *b* axis (cf. Fig. 4.30) [148]. However, detailed neutron diffraction measurements revealed a reorientation of the magnetic moments for $T \leq 80$ K [36]. In addition, several anomalies of magnetic origin were found in bulk BiCrO₃ at temperatures lower than T_N , which were attributed

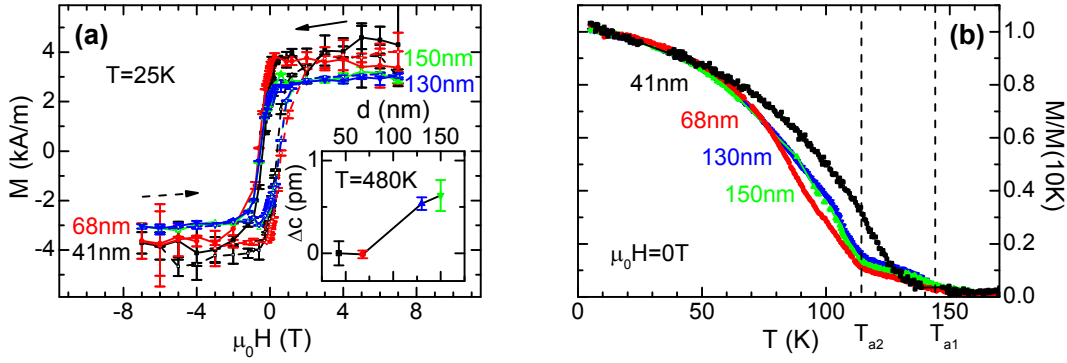


Figure 4.40: Magnetization as a function of (a) the applied magnetic field at $T = 25$ K as well as (b) temperature for $\mu_0 H = 0$ T after field cooling in a magnetic field of $\mu_0 H = 7$ T. The measurements were carried out on BiCrO_3 thin films with different thicknesses grown on Nb:SrTiO_3 substrates using SQUID magnetometry. The inset of (a) displays the difference of the pseudo-cubic out-of-plane lattice constant $\Delta c = c - c(41 \text{ nm})$ as a function of the thin film thickness. Two anomalies at temperatures T_{a1} and T_{a2} , which are marked by vertical dashed lines, are visible in the temperature dependence of the remanent magnetization depicted in (b).

to a change of the magnetic easy axis, the presence of an orthorhombic modification of the low-temperature monoclinic structure, and inhomogeneities [147, 378, 379]. In BiCrO_3 thin films a small saturation magnetic moment of $0.05 \mu_B/\text{f.u.}$ was found, which is consistent with canting of Cr^{3+} spins [150]. Furthermore, magnetization versus temperature scans reveal a magnetic transition temperature ranging from 120 K to 140 K and magnetic anomalies at 50 K [150] as well as 105 K [34]. However, no further details about the magnetic properties of BiCrO_3 thin films have been published to date.

Since SrRuO_3 is ferromagnetic below $T \lesssim 150$ K (cf. Section 4.3), the magnetic investigation shown in Fig. 4.40 were performed on BiCrO_3 thin films with different thicknesses grown on Nb:SrTiO_3 substrates. The magnetic field dependence of the magnetization measured at $T = 25$ K reveals a ferromagnetic behavior of all investigated BiCrO_3 thin films with a weak saturation magnetization smaller than $M_S < 4$ kA/m, which corresponds to $M_S \lesssim 0.03 \mu_B/\text{f.u.}$ (cf. Fig. 4.40(a)). This finite ferromagnetic moment can be attributed to a spin canting along the b axis, which is allowed in the monoclinic $C2/c$ symmetry [378] as well as in the orthorhombic high temperature phase [342]. Furthermore, similar to the discussion of the magnetic properties of BiFeO_3 thin films (cf. Section 4.4.2), the weak magnetic moments observed in BiCrO_3 thin films suggest the absence of magnetic parasitic phases in these samples. However, Fig. 4.40(a) reveals a small increase of the saturation magnetization for BiCrO_3 thin films with thicknesses lower than 100 nm. This can be explained by a finite strain dependence of the saturation magnetization. In the inset of Fig. 4.40(a), the difference of the pseudo-cubic out-of-plane lattice parameter $\Delta c = c - c(41 \text{ nm})$ with respect to the 41 nm thick BiCrO_3 thin film measured in the orthorhombic phase at 480 K is shown as a function of the film thickness. Clearly, an increase of the lattice constant is visible for BiCrO_3 thin films with thicknesses

larger than 100 nm, which can be attributed to a change of the epitaxial strain. Therefore, Fig. 4.40(a) indicates a small strain dependence of the saturation magnetization. The different strain state of the investigated BiCrO₃ thin films might also affect the magnetic transition temperature. For example, Kim and coworkers found an enhancement of the transition temperature and related this to epitaxial strain [34]. However, as shown in Fig. 4.40(b), the temperature dependence of the normalized magnetic remanence is quite different for BiCrO₃ thin films with a thickness of 41 nm and 68 nm, although the equal pseudo-cubic out-of-plane constants depicted in the inset of Fig. 4.40(a) suggest a similar epitaxial strain state in both thin films. Therefore, different strain effects might not be the main origin for the different magnetization behavior in the vicinity of the transition temperature. While the 41 nm thick BiCrO₃ film reveals an onset of the ferromagnetic moment due to spin-canting at $T_C \approx 130$ K, anomalies around $T_{a1} = 145$ K and $T_{a2} = 115$ K were detected in BiCrO₃ thin films with larger thicknesses. This two step transition was also observed by Kim *et al.* on a 1400 nm thick BiCrO₃ film grown on a SrRuO₃-buffered SrTiO₃ substrate [34]. Furthermore, several anomalies in the temperature dependence of the magnetic susceptibility were found in bulk BiCrO₃ samples [378]. Two of them were observed at 165 K and 109 K, respectively. Belik and coworkers attributed the first one to the transition temperature of BiCrO₃ regions exhibiting an orthorhombic symmetry and the second one was explained by the long-range *G*-type antiferromagnetic order of the monoclinic *C2/c* phase [379]. Within the orthorhombic domains the Cr and O bond angles are closer to 180°, increasing the magnetic transition temperature as compared to the highly distorted monoclinic symmetry. This explanation might also be applicable to our samples. As discussed in Section 4.5.1, a finite volume fraction with an orthorhombic symmetry was observed in the whole investigated temperature range ($60 \text{ K} \leq T \leq 500 \text{ K}$). Therefore, in analogy to bulk BiCrO₃, T_{a1} and T_{a2} might be attributed to the transition temperatures of the orthorhombic and monoclinic phases in BiCrO₃. The BiCrO₃ thin film with a thickness of 41 nm seems to be exceptional. In this particular BiCrO₃ thin film, no indication for an orthorhombic phase was found at room temperature. However, the intensity of a standard x-ray tube used for diffraction measurements on BiCrO₃ thin films with thicknesses as low as 41 nm might not be sufficient (cf. Fig. 4.25(b)) and the use of synchrotron radiation is mandatory to draw a definite conclusion on this issue (cf. Section 2.1.3). In summary, Fig. 4.40 suggests that the magnetic behavior of BiCrO₃ thin films on Nb:SrTiO₃ (001) substrates stems from a complex interplay between the strain state of the BiCrO₃ thin films and the effects caused by different crystalline phases.

The magnetic behavior was further investigated on the microscale by means of magnetic force microscopy (MFM) carried out on a 38 nm thick BiCrO₃ film on a Nb:SrTiO₃ substrate by Denny Köhler (Technische Universität Dresden) [93]. The MFM images were taken at constant temperature below (Fig. 4.41(a) and (c)) and above (Fig. 4.41(b)) the magnetic transition temperature on the same thin film area (cf. Fig. 4.40(b)). The images represent the remanent magnetic behavior, since no magnetic field was applied, neither during the temperature cycles nor while taking the MFM images. The MFM measurements depicted in Fig. 4.41 were performed

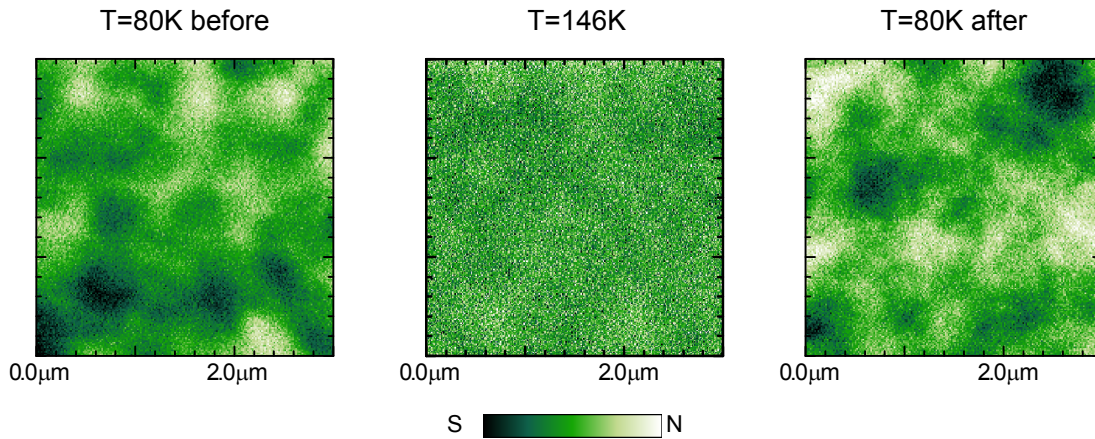


Figure 4.41: Magnetic force microscopy (MFM) measurements performed by Denny Köhler (Technische Universität Dresden) on a 38 nm thick BiCrO_3 film grown on a Nb:SrTiO_3 substrate. The MFM measurements were carried out in an ultrahigh vacuum chamber at 80 K and 146 K on the same thin film area. Since this BiCrO_3 thin film exhibits a higher surface roughness of $2.7 \text{ nm}_{\text{RMS}}$ compared to the BiFeO_3 thin film used in Fig. 4.21, the tip-sample distance was increased to 60 nm to avoid topographical artefacts.

as follows. First, the BiCrO_3 thin film was cooled down to 80 K, well below the magnetic transition temperature. At this temperature, MFM measurements reveal a magnetic contrast with magnetic domains exhibiting a lateral size of the order of 400 nm (cf. Fig. 4.41(a)). These domains are therefore almost twice as large as in case of BiFeO_3 thin films (cf. Fig. 4.21(b)). To ensure that the finite contrast visible in Fig. 4.41(a) is of magnetic origin, the sample was heated to 146 K, i.e., above the magnetic transition temperature (cf. Fig. 4.40(b)). MFM measurements carried out at this temperature disclose no magnetic contrast (cf. Fig. 4.41(b)).³⁰ However, the contrast emerges again upon cooling down the sample to 80 K (cf. Fig. 4.41(c)) and thus can be attributed to be of magnetic origin caused by uncompensated spins of the antiferromagnetic ground state, which form a surface magnetization [311]. By comparing both measurements carried out at 80 K, which are depicted in Figs. 4.41(a) and (c), a different magnetic domain distribution is visible. This indicates that there is no coupling of the magnetic structure neither on the topography nor on the ordered network of electric dipoles, since this arrangement should remain unchanged during the temperature cycle 80 K \rightarrow 146 K \rightarrow 80 K as the transition temperature of the antiferroelectric ordering is around 410 K (cf. Fig. 4.35(a)). Therefore, the magnetic and electronic structure are unpinned and no magnetoelectric coupling is expected in BiCrO_3 thin films. However, the uncompensated spins, which are mainly responsible for this finite surface magnetism observed by MFM measurements, should create exchange bias effects in ferromagnet/ BiCrO_3 composite heterostructures in the same way as in case of BiFeO_3 thin films [305, 311].³¹

³⁰The finite contrast visible in Fig. 4.41(b) can be attributed to thermal noise and topographic artefacts [93].

³¹More details on composite heterostructures can be found in Part II of this thesis.

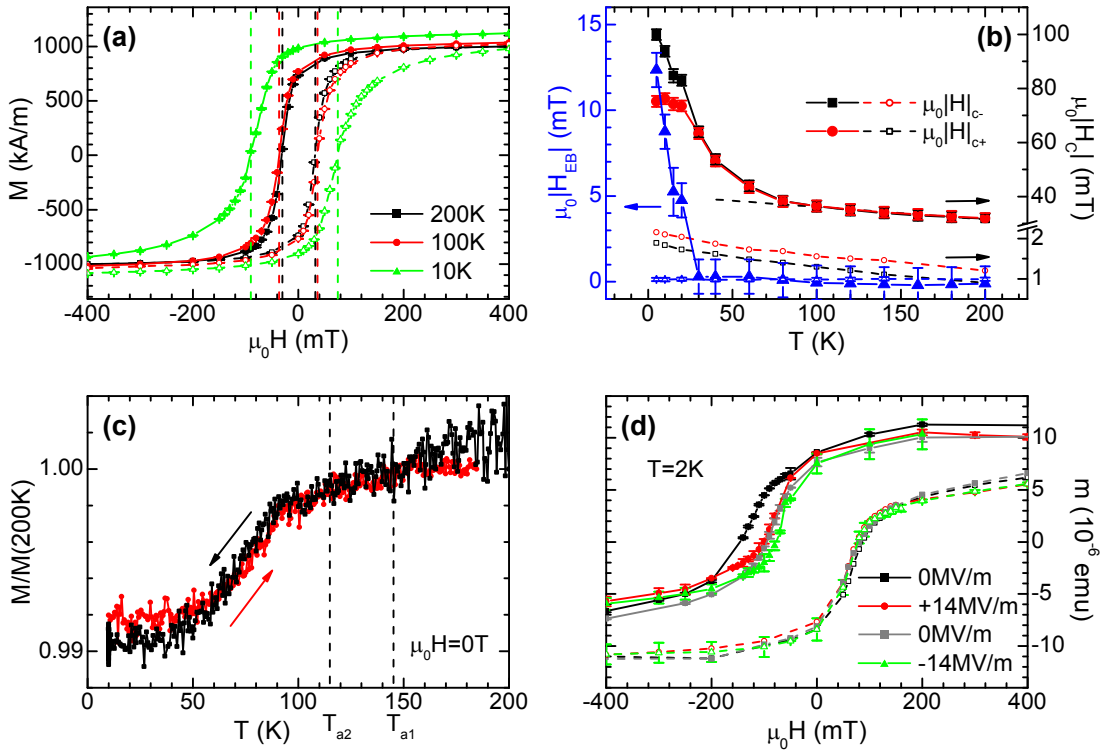


Figure 4.42: Magnetic properties of a Fe₁₀Co₉₀(10 nm)/BiCrO₃(350 nm) composite structure grown on a SrRuO₃(25 nm)-buffered SrTiO₃ substrate. (a) The magnetic hysteresis loops measured at different temperatures reveal a finite exchange bias at 10 K. The positive ($\mu_0 H_{C+}$) and negative ($\mu_0 H_{C-}$) coercive fields are marked by vertical dashed lines. (b) Temperature evolution of the coercive fields as well as the exchange bias field $\mu_0 H_{BC}$ (full symbols), which is calculated from $\mu_0 H_{C+}$ and $\mu_0 H_{C-}$. A change of the temperature dependence of these fields is visible below 90 K (cf. black dashed line). The coercive fields and the derived exchange bias field of a 10 nm thick Fe₁₀Co₉₀ film deposited on a SrTiO₃ substrate is added for comparison (open symbols). (c) The temperature dependent remanent magnetization of the Fe₁₀Co₉₀/BiCrO₃ composite heterostructure changes in the temperature range $40 \text{ K} \lesssim T \lesssim 90 \text{ K}$, i.e., well below the transition temperatures of the monoclinic T_{a2} and orthorhombic T_{a1} phases, which are indicated by vertical dashed lines. This can be attributed to spin reorientation in the BiCrO₃ layer. (d) Magnetic hysteresis loops measured at $T = 2 \text{ K}$ while biasing the BiCrO₃ layer with $E = \pm 14 \text{ MV/m}$. In order to apply an electric field across the Fe₁₀Co₉₀/BiCrO₃ composite, the heterostructure was patterned into a similar structure as shown in Fig. 2.4(c) with a diameter of the top contact of 0.5 mm.

To investigate this effect, a $t_{\text{FM}} = 10 \text{ nm}$ thick ferromagnetic Fe₁₀Co₉₀ film was deposited on top of a BiCrO₃ ($t_{\text{AF}} = 350 \text{ nm}$) thin film, which was grown on a SrRuO₃ (25 nm)-buffered SrTiO₃ substrate. To prevent oxidation of the Fe₁₀Co₉₀ thin film, the layer was capped in-situ with a 5 nm thin layer of gold. The alloy Fe₁₀Co₉₀ combines a large saturation magnetization of around $M_{\text{FM}} \approx 1750 \text{ kA/m}$ with a negligible magnetoelastic coupling [380]. Therefore, magnetoelastic effects can be neglected in the following experiments. Since the Fe₁₀Co₉₀ layer exhibits a large magnetic moment which dominates the magnetic measurements, the magnetic

contribution of the SrRuO₃ buffer layer can be ignored. Neutron diffraction experiments carried out on bulk BiCrO₃ revealed that the spins are aligned along the crystallographic *b* axis [148]. Therefore, a finite exchange bias between the BiCrO₃ layer or more precisely the BiCrO₃ ($\bar{1}01$)-type domains and the Fe₁₀Co₉₀ layer is expected below the blocking temperature T_B , which is usually close to the antiferromagnetic transition temperature of the monoclinic phase $T_B \approx T_N \approx T_{a2} = 115$ K (cf. Fig. 4.30). The exchange bias arises from the exchange coupling J_{EB} at the Fe₁₀Co₉₀/BiCrO₃ interface, which transfers an unidirectional anisotropy from the antiferromagnet (BiCrO₃) into the ferromagnetic (Fe₁₀Co₉₀) layer, and manifests itself by a shift of the magnetic hysteresis of the Fe₁₀Co₉₀ layer with respect to $\mu_0 H = 0$ mT.³² From a theoretical point of view, the magnitude of the exchange bias field $\mu_0 H_{EB}$ can be estimated by [381]

$$\mu_0 H_{EB} = \frac{1}{2} \cdot \mu_0 (H_{C+} + H_{C-}) = \mu_0 H_{EB}^{\infty} \sqrt{1 - \frac{1}{4R^2}}, \quad (4.13)$$

where $\mu_0 H_{EB}^{\infty} = -J_{EB} / (M_{FM} \cdot t_{FM})$ is the value of the exchange bias field when the anisotropy of the antiferromagnetic layer K_u is infinitely large, and $R = K_u \cdot t_{AF} / J_{EB}$ is the ratio between the antiferromagnetic anisotropy and the interface exchange energy per unit area J_{EB} , which can be calculated by $J_{EB} = \zeta \cdot \sqrt{A \cdot K_u}$ [384]. ζ is found to be close to unity in BiFeO₃ [311] and $A \cdot K_u$ denotes the product of the exchange stiffness A as well as the magnetic anisotropy of the antiferromagnetic layer K_u . The calculation of J_{EB} accounts for a finite interface roughness, which results in domain-like regions in the antiferromagnet [384]. Using the values found for bulk BiFeO₃ (cf. Section 4.4.2), the exchange energy J_{EB} can be estimated to be $J_{EB} \approx 0.4$ mJ/m². Therefore, in BiCrO₃ thin films with thicknesses as large as $t_{AF} = 350$ nm, the antiferromagnetic anisotropy term $K_u \cdot t_{AF}$ dominates, which results in $R \gg 1$. Thus Eq. (4.13) reduces to $\mu_0 H_{EB} \approx \mu_0 H_{EB}^{\infty}$. This equation is similar to the original phenomenological model proposed by Meiklejohn and Bean [385, 386]. In this limit, the magnitude of the exchange bias field is expected to be around $\mu_0 H_{EB} \approx -23$ mT. The negative sign indicates a shift of the hysteresis loops in the $-\mathbf{H}$ direction.

However, as shown in Fig. 4.42(a), magnetic hysteresis loops measured at 200 K and 100 K reveal no significant difference. This is surprising, since the antiferromagnetic transition temperature of the monoclinic phase, which was identified by $T_{a2} = 115$ K (cf. Fig. 4.20(b)), is larger than 100 K and a finite exchange bias is expected. However, the situation changes upon further cooling down the composite heterostructure. At 10 K, a large enhancement of the coercive field together with a finite shift of the $M(H)$ loop with respect to $\mu_0 H = 0$ mT is observable. Both effects are caused by a finite exchange bias effect [381]. The experimentally derived exchange bias field $\mu_0 H_{EB}$ is strongly temperature dependent and by a factor of two smaller than expected from theory, which can be attributed to the unknown interface exchange energy per unit area J_{EB} of BiCrO₃ thin films. However, in contrast

³²Recent reviews on exchange bias effect of ferro-/antiferromagnetic heterostructures can be found in Refs. [381–383].

to the expectation of exchange biased magnetic hysteresis loops for $T < T_{a2}$, an enhancement of the coercive field as well as a finite exchange bias were observed not until $T < 100$ K and $T < 30$ K, respectively. Therefore, the blocking temperature T_B , at which the exchange bias field approaches zero, is significantly lower than the antiferromagnetic transition temperature, $T_B < T_{a2} \approx 115$ K, in BiCrO₃ thin films. In general, T_B is strongly dependent on the thickness of the ferromagnetic [387] and the antiferromagnetic layer [388] as well as on the quality of the antiferromagnetic thin film [389]. However, Fig. 4.42(b) reveals that the coercive field is first enhanced in the temperature range $30 \text{ K} < T < 100 \text{ K}$ and then a finite exchange bias was detected below this temperature range. Interestingly, in bulk BiCrO₃, a spin reorientation was recently found by neutron diffraction between 60 K and 80 K, i.e., in between this temperature range [36]. The rotation of the spins takes place in the plane determined by the b and c lattice parameters and forms a 50° angle with the b axis direction. A similar behavior is expected in BiCrO₃ thin films. Since the alignment of the ferromagnetic spins in Fe₁₀Co₉₀ is determined by the spin direction in the underlying antiferromagnetic layer [390],³³ the magnetic moments rotate away from the magnetic field direction in this temperature range, resulting in a reduction of the detected magnetization projection. Therefore, the overlying ferromagnetic layer in ferromagnetic/antiferromagnetic composite structures can be used as a tracer of possible spin reorientation processes of the basic antiferromagnetic thin film. As revealed by Fig. 4.42(c), a reduction of the remanent magnetization is detected in the temperature range $40 \text{ K} \lesssim T \lesssim 90 \text{ K}$ upon cooling the sample from 200 K to 5 K in zero external magnetic field. Above and below this temperature range, the remanent magnetization was found to be nearly constant. Therefore, Fig. 4.42(c) suggests that, in analogy to bulk BiCrO₃, a gradual reorientation of the antiferromagnetic spins takes place in the BiCrO₃ thin film as well. Thus, the temperature dependence of the coercive field as well as the appearance of a finite exchange bias field at temperatures below 30 K can be interpreted as follows. The temperature range $40 \text{ K} \lesssim T \lesssim 90 \text{ K}$, at which the coercive field strongly increases, corresponds to the temperature range, where a reorientation of the spins in the antiferromagnetic BiCrO₃ layer is suggested. Below this temperature range, this spin reorientation process is complete and a finite exchange bias effect is observed. Therefore, the results shown in Figs. 4.42(a)-(c) suggest that a finite exchange bias is only present after the spin reorientation is completed in the BiCrO₃ thin film.

As mentioned in Section 4.4.2, in antiferromagnetic materials exhibiting a finite magnetoelectric effect, the magnetization of a ferromagnetic thin film, which is closely attached to the antiferromagnetic layer, can be indirectly modified by an electric field applied to the antiferromagnetic layer. This mechanism was first demonstrated by Borisov and coworkers using the archetypical magnetoelectric Cr₂O₃ [138, 392]. Afterwards, other magnetoelectric materials, such as BiFeO₃ [311] or YMnO₃ [393], were used. In composite heterostructures based on BiFeO₃, robust and reversible changes of the magnetization by an electric field were demonstrated even at room temperature [394]. Very recently, a magnetization reversal by decou-

³³The reorientation of the antiferromagnetic spins, which takes place by depositing a ferromagnetic thin film on an antiferromagnetic layer [391], is neglected.

pling of magnetic and ferroelectric domain walls was found in multiferroic LuMnO₃ based heterostructures [395]. However, since the mechanism behind the described effects is based on the electric field control of the antiferromagnetic state, changes of the exchange bias field $\mu_0 H_{EB}$ as a function of the applied electric field E in the Fe₁₀Co₉₀/BiCrO₃ heterostructure indirectly prove a possible magnetoelectric behavior in the BiCrO₃ compound. To this end, magnetic hysteresis loops were measured using SQUID magnetometry, while biasing the BiCrO₃ thin film with different electric fields. The measurements were performed at 2 K after cooling the sample from room temperature in an external magnetic field of $\mu_0 H = 1$ T. As shown in Fig. 4.42(d), no clear change of the exchange bias field related to the applied electric field is visible. The large change of the negative coercive field in case of $E = 0$ MV/m can be attributed to training effects, which is common in exchange bias systems [381]. These effects are caused by irreversible changes of the antiferromagnetic domain structures as well as of the interface magnetization [381]. Therefore, the data displayed in Fig. 4.42(d) suggests that neither a suppression nor an enhancement of the exchange bias field can be achieved in ferromagnetic/BiCrO₃ composite heterostructures by an applied electric field. Thus, no clear evidence for a magnetoelectric coupling in BiCrO₃ was found. This result confirms the MFM measurement depicted in Fig. 4.41, where no pinning of the magnetic domains on the electric ones was detected, but is in contrast to recent ab initio calculation of the magnetoelectric response of Bi containing multiferroic materials [35].

4.5.3 Summary: Multiferroic BiCrO₃ thin films

In summary, for the first time, a detailed analysis of the physical properties of BiCrO₃ thin films was carried out. At first, the crystalline properties of high quality BiCrO₃ thin films were investigated in the temperature range $60 \text{ K} \leq T \leq 500 \text{ K}$. A structural transition from an orthorhombic to a monoclinic symmetry was found at $T_{\text{phase}} = 410 \text{ K} - 440 \text{ K}$. However, a coexistence of both phases was observed in the whole investigated temperature range, which might be caused by a combination of epitaxial strain effects, oxygen non-stoichiometry, and a temperature-extended structural phase transition. Therefore, the transition should be regarded as a change in volume fraction of regions in the BiCrO₃ thin film exhibiting an orthorhombic and monoclinic symmetry. Above T_{phase} , BiCrO₃ thin films mainly consist of regions with orthorhombic symmetry forming three different domain types, while at $T < T_{\text{phase}}$ the monoclinic phase dominates. In this phase, various crystallographic domains were found to be present. These domains can be classified into (111)- and ($\bar{1}01$)-type domains depending on whether the BiCrO₃ (111) or the BiCrO₃ ($\bar{1}01$) plane is parallel to SrTiO₃ (001). In addition, both domain types exhibit different in-plane orientations forming a multitude of domains. In spite of performing grazing incidence diffraction using synchrotron radiation, the determination of the in-plane domain structure of our BiCrO₃ thin films failed, since the different reflections are poorly separated from one another. Therefore, no preferred in-plane orientation of the domains was inferred.

As the dielectric behavior of BiCrO₃ in bulk and thin film form was discussed

controversially in the past, substantial efforts were undertaken to reveal the dielectric ground state of BiCrO₃ thin films. An antiferroelectric behavior was found in measurements, which were carried out using macroscopic contacts. This is further confirmed by piezoelectric microscopy. However, on the microscale a ferroelectric-like characteristic was observed, which is not stable in time and was attributed to charged defects. In addition, no indication for a finite magnetocapacitance effect was found in the vicinity of the expected magnetic transition temperature. Therefore, magnetoelectric effects might be small or not present in the BiCrO₃ compound.

To reveal the magnetic properties of BiCrO₃ thin films, SQUID magnetometry as well as magnetic force microscopy measurements were performed on BiCrO₃ thin films with different thicknesses. A small but finite ferromagnetic moment was found below around 145 K, which can be attributed to canting of the spins in the antiferromagnetic structure. Epitaxial strain considerations disclosed an increase of the saturation magnetization by a factor of 1.3 upon decreasing the thin film thickness from 150 nm to 41 nm. However, the temperature dependence of the magnetization revealed a two step magnetic transition in almost all BiCrO₃ thin films with anomalies at 145 K and 115 K. This behavior can be explained by the crystalline multi-phase state of the BiCrO₃ thin films. Since the bond angle between Cr and O is closer to 180° in the orthorhombic symmetry than in the monoclinic one, the magnetic transition temperature of parts of the BiCrO₃ thin film exhibiting an orthorhombic phase is higher as compared to BiCrO₃ regions with monoclinic symmetry. Therefore, the onset of the magnetic moment at 145 K was interpreted as magnetic transition temperature of the orthorhombic phase of BiCrO₃, while 115 K was identified with the transition temperature of the monoclinic structure. The magnetic properties of BiCrO₃ thin films in the vicinity of the magnetic transition temperature was further examined by magnetic force microscopy. These measurements disclose a finite magnetic contrast, which might be attributed to uncompensated spins of the antiferromagnetic structure, leading to a finite surface magnetization. This offers the possibility to observe exchange bias effects in ferromagnet/BiCrO₃ composite heterostructures. Indeed, exchange biased magnetic hysteresis loops were detected by SQUID magnetometry at temperatures lower than 30 K in Fe₁₀Co₉₀/BiCrO₃, which indirectly proves that BiCrO₃ has an antiferromagnetic ground state. Interestingly, a finite exchange bias was detected only when a spin reorientation process, which is suggested by temperature dependent measurements of the remanent magnetization, was finished. Therefore, the low blocking temperature might be attributed to modifications of the spin structure of the antiferromagnetic BiCrO₃ layer rather than the quality of the antiferromagnetic BiCrO₃ thin film. However, in recent years, the composite heterostructures based on magnetoelectric antiferromagnets have been employed to achieve large and robust changes of the magnetization in the ferromagnet as a function of the electric field, which is applied across the antiferromagnetic layer. A similar experiment was carried out using a Fe₁₀Co₉₀/BiCrO₃ composite structure. Unfortunately, no electric field dependence of the exchange bias was found, which suggests that BiCrO₃ does not exhibit a magnetoelectric coupling. Therefore, the compound BiCrO₃ should be regarded as an antiferroelectric/antiferromagnetic material without a cross-coupling between both phases.

Chapter 5

Intrinsic multiferroic material systems: Conclusions and Outlook

A material, which unites different ferroic properties in the same phase, is termed as intrinsic multiferroic. The primary forms of ferroic order are ferromagnetism, ferroelectricity, ferroelasticity, and ferrotoroidicity in case of time reversal and space inversion symmetries (cf. Chapter 3). However, since intrinsic multiferroic materials are rare, the definition of multiferroicity is usually extended to include antiferromagnetic and antiferroelectric phases. In these material systems, the order parameter of the ferroic phase is typically modified by its conjugate field, e.g., magnetic (electric) fields change the magnetization (electric polarization) state. In magnetoelectric multiferroics, an additional coupling between these order parameters exists, which enables to control the electric polarization by external magnetic fields and the magnetization by electric fields.

In this class of materials, presently BiFeO_3 is the most popular one, since it exhibits both a ferroelectric and an antiferromagnetic transition well above room temperature (cf. Section 4.1). In the course of this thesis, a detailed study of the physical properties of BiFeO_3 thin films on SrRuO_3 -buffered as well as on Nb:SrTiO_3 substrates was carried out (cf. Sections 4.4.1 and 4.4.2). Apart from the examination of the structural and dielectric properties, the main focus was set on the magnetic behavior of these thin films. In particular, for the first time, a clear indication for an enhanced magnetic moment was found in regions, where the electrostatic potential changes its value. These regions were interpreted as ferroelectric domain walls, separating areas with opposite sign of the out-of-plane component of the ferroelectric polarization. However, in studying the basic physics of this compound, the high antiferromagnetic ($T_N \approx 670$ K) and ferroelectric ($T_c \approx 1100$ K) transition temperatures are a main drawback, since the paraelectric and paramagnetic phases are hardly reachable experimentally. Therefore, we also studied BiCrO_3 thin films. BiCrO_3 exhibits transition temperatures of the electric and magnetic phases at around 410 K and 120 K, respectively. Thus, it is ideal for basic studies, as it can be regarded as model system for Bi containing perovskite-like compounds [125]. Since little is known so far about this compound, a detailed study of its crystalline, magnetic, and electric properties was carried out (cf. Sections 4.5.1 and 4.5.2). For the first time, the crystalline characteristic of BiCrO_3 thin films was investigated in a large temperature range of $60 \text{ K} < T < 500 \text{ K}$. Moreover, an antiferroelectric ground state was revealed in macroscopic as well as microscopic measurements and

an antiferromagnetic behavior was confirmed by observing an exchange bias effect in ferromagnet/BiCrO₃ composite heterostructures. However, no indication for a magnetoelectric coupling was found in our thin films.

Before drawing conclusions and presenting further possibilities for the realization of room temperature intrinsic multiferroic compounds, the results of the first part of this thesis will be summarized first.

Summary

Several literature reports of Bi containing perovskite thin films suggest that the physical properties of these thin films are strongly affected by extrinsic effects, which are directly linked to the growth conditions (see, e.g., Ref. [38]). Therefore, much efforts were devoted to fabricate BiMO₃ ($M = \text{Cr, Fe}$) thin films with excellent crystalline and physical properties (cf. Section 4.2).

To disclose the multiferroic behavior of these BiMO₃ ($M = \text{Cr, Fe}$) thin films, a detailed investigation of their physical properties have to be carried out as a function of external magnetic and electric fields. To this end, SrRuO₃ thin films as well as Nb-doped SrTiO₃ substrates were used as bottom electrode materials. Since, in particular, the SrRuO₃ layer may contribute to the experimental results obtained in BiMO₃ ($M = \text{Cr, Fe}$) thin films grown on SrRuO₃-buffered SrTiO₃ substrates, a detailed knowledge of the structural, magnetic, and electrical behavior of SrRuO₃ thin films is essential for the interpretation of these results. Thus, the properties of SrRuO₃ thin films are discussed in detail in Section 4.3. The structural characterization of these thin films revealed an orthorhombic symmetry with the presence of *X*- and *Y*-domains as well as a high crystalline quality. The excellent electric behavior was demonstrated by the high residual resistivity ratio detected in our SrRuO₃ thin films. This provides clear evidence for thin films, which exhibit the correct stoichiometric composition and a low density of structural defects. Furthermore, the electric transport was found to be of intrinsic origin, since the anomalous conductivity could be well described by theory calculations based on first-principles methods. Therefore, our SrRuO₃ thin films satisfy the conditions of an electrode material in BiMO₃ ($M = \text{Cr, Fe}$)/SrRuO₃ heterostructures with excellent structural and physical properties.

In case of BiFeO₃ thin films (cf. Section 4.4), synchrotron x-ray diffraction measurements revealed a monoclinic *Cc* symmetry at room temperature. This monoclinic space group is similar to the bulk rhombohedral *R3c* symmetry and leads to the formation of four different ferroelastic domains, which were detected by piezoelectric force microscopy. In contrast to the common notion, no improvement of the crystalline quality of BiFeO₃ thin films grown on SrRuO₃-buffered SrTiO₃ substrates compared to BiFeO₃ thin films directly fabricated on SrTiO₃ crystals was found by detailed x-ray diffraction measurements. However, the possibility of reducing the number of ferroelastic domains was demonstrated in BiFeO₃ thin films fabricated on SrRuO₃-buffered SrTiO₃ substrates with a miscut angle of around 1°. The multiferroic properties of BiFeO₃ thin films were examined by BiFeO₃ thin films fabricated on Nb:SrTiO₃ substrates (cf. Section 4.4.2). To this end, piezoelectric

force microscopy¹ was employed to disclose a ferroelectric ground state of as-grown BiFeO₃ thin films. In these measurements, a constant out-of-plane component was detected, while ferroelectric in-plane domains were found to be separated by mainly 71° domain walls. These domain walls certainly affect the ferroelectric properties. On the other hand, an electric field control of the magnetic phase by a ferroelectric multidomain state was reported in literature [137]. In the course of this thesis, indication of an enhanced magnetic moment located in the center of a ferroelectric domain wall separating regions with opposite sign of the out-of-plane component of the ferroelectric polarization was found. This is in agreement with calculations using a phenomenological Landau-Ginzburg model. However, magnetic force microscopy images revealed that this net magnetic moment is averaged out over the ferroelectric multidomain state and therefore, it is not the reason for the observed finite ferromagnetic moment. Since an in-plane epitaxial strain of $|\epsilon_{ip}| = 0.6\%$ is enough to destroy the spin cycloidal state, which was observed in bulk BiFeO₃ [29], the net magnetization of $M \approx 2 \text{ kA/m}$ could rather be attributed to canting of the Fe³⁺ spins in the antiferromagnetic ground state of BiFeO₃.

In addition, the physical properties of BiCrO₃ thin films were investigated (cf. Sections 4.5). The structural properties of these thin films revealed a phase transition at $T_{\text{phase}} = 410 \text{ K} - 440 \text{ K}$, where a change of the volume fraction of BiCrO₃ thin film regions exhibiting an orthorhombic and monoclinic symmetry was found. Therefore, no abrupt structural phase transition occurs in these thin films and two different crystalline phases coexist in the whole investigated temperature range. Furthermore, a multidomain state was detected in both phases. This multiphase and multidomain state certainly affects the physical properties of BiCrO₃ thin films. Nevertheless, a clear antiferroelectric behavior was observed in measurements using macroscopic contacts (cf. Sections 4.5.2). On the one hand, piezoelectric force microscopy measurements confirmed these findings, while on the other hand a relaxor-like behavior was detected, which might be attributed to charged defects present in the thin films. As BiCrO₃ is expected to be multiferroic (in the extended definition of multiferroicity), the magnetic properties of BiCrO₃ thin films were also examined. A magnetic two-step transition with anomalies at 145 K and 115 K was found in almost all BiCrO₃ thin films. These anomalies were attributed to the magnetic transition temperature of BiCrO₃ regions exhibiting an orthorhombic and monoclinic symmetry, respectively. Furthermore, a small ferromagnetic moment was revealed by SQUID magnetometry measurements, which was explained by the canting of the Cr³⁺ spins in an antiferromagnetic ground state. Using a ferromagnetic Fe₁₀Co₉₀ layer of 10 nm thickness, which was deposited on top of a 350 nm thick BiCrO₃ film, the antiferromagnetic state was confirmed by detecting a finite exchange bias field at low temperatures in the magnetic field dependence of the magnetization stemming from the Fe₁₀Co₉₀ layer. However, detailed investigations of the magnetic properties of this Fe₁₀Co₉₀/BiCrO₃ composite heterostructure indicated the presence of a spin reorientation process in the BiCrO₃ thin film between 40 K and 90 K. Furthermore, a finite exchange bias field could only be detected for temperatures

¹The piezoelectric force microscopy as well as the magnetic force microscopy measurements were carried out by Denny Köhler (Technische Universität Dresden).

lower than 30 K. Therefore, these results suggest that an exchange bias field can be observed only when the spin reorientation process is completed. As discussed in the literature, the exchange bias field can be controlled by an electric field, if the antiferromagnetic layer exhibits a finite magnetoelectric coupling [138]. Therefore, magnetic hysteresis loops were recorded under different electric fields applied to the BiCrO₃ thin film. Unfortunately, no electric field dependence of the exchange bias field was observed. Thus, the compound BiCrO₃ seems not to be a magnetoelectric multiferroic. This negative result was also confirmed by magnetic force microscopy measurements carried out above and below the magnetic transition temperature. In these measurements, no pinning of the magnetic structure on the dielectric one was examined. These measurements demonstrate that BiCrO₃ should be regarded as a material system exhibiting an antiferromagnetic and antiferroelectric behavior below 115 K without cross-coupling between both phases.

Conclusions and Outlook

In the field of multiferroics, new developments are occurring at a rapid pace.² In particular, the multiferroic perovskite BiFeO₃ has generated much interest, due to the interesting physics and the potential applications. However, as discussed in this part of the thesis, some physical aspects of BiFeO₃ thin films still remain unclear. While there exists a full theoretical and experimental understanding of the ferroelectric behavior, which originates from the lone-pair active Bi cation, the modification of the magnetic state in BiFeO₃ thin films compared to the magnetic bulk properties are still under investigation.

The magnetic order is mainly caused by the oxygen-mediated superexchange interaction between the Fe cations, resulting in a *G*-type antiferromagnetic ordering. This antiferromagnetic structure was predicted by theory, but not well confirmed by experiments. In previous diffraction experiments using neutrons, the *G*-type structure was confirmed by the observation of the pseudo-cubic BiFeO₃ (0.5 0.5 0.5)_{pc} reflection (eg. Ref. [311]). However, since this reflection is not only of magnetic but also of structural origin, the obtained results should be considered with care. Recently, temperature dependent neutron diffraction measurements of BiFeO₃ thin films indicate a *G*-type antiferromagnetic ordering [242], but resonant magnetic x-ray studies might be the better choice to unambiguously determine the magnetic structure in future (cf. Section 4.4.2).

In addition to the antiferromagnetic spin ordering, a cycloidal-type spatial spin modulation occurs in bulk BiFeO₃ below the Néel temperature. As discussed above, this cycloidal spin structure is believed to be destroyed in BiFeO₃ thin films due to an epitaxial strain of around $|\epsilon_{ip}| = 0.6\%$. This implies that the spin modulation should be observable in fully relaxed BiFeO₃ thin films. However, this is not confirmed experimentally up to now. Neutron diffraction measurements carried out on 240 nm thick BiFeO₃ films, which should exhibit an epitaxial strain of less than 0.6%, reveal no indication of a spin cycloidal structure [239]. The presence or absence of this structure is of particular interest, since a finite magnetic moment due

²Recent reviews on intrinsic multiferroics can be found in Refs. [13, 14, 396]

to spin canting of the antiferromagnetic sublattices as well as a linear magnetoelectric coupling is only possible, if the cycloidal spin structure is destroyed. Therefore, future experiments on BiFeO₃ thin films exhibiting different epitaxial strains are mandatory to reveal the detailed magnetic structure. Furthermore, since the cycloidal spin structure does not only depend on the strain state of BiFeO₃ but also on magnetic fields, an external control parameter exists to switch on and off the linear magnetoelectric coupling in BiFeO₃ [309].

This magnetoelectric interaction, i.e., the coupling between the magnetic and ferroelectric properties of BiFeO₃, seems to be caused by the structural distortion associated with the ferroelectric polarization rather than the polarization itself [14, 299]. Therefore, ferroelastic switching events, i.e., changing the ferroelectric polarization orientation by 71° and 109° (cf. Section 4.4.1), were found to reorient the magnetization plane in BiFeO₃ [29, 137]. This result and recent Raman measurements [397] suggest that the magnetoelectric coupling might be mediated by magnetostriction and piezoelectric effects, which is further confirmed by recent neutron diffraction measurements of Bi_{1-x}Nd_xFeO₃ crystals exposed to small uniaxial pressures [398]. However, as discussed in Section 4.4.2, the lack of the coupling between the electric polarization and the magnetic properties of BiFeO₃ is still discussed controversially and further experiments are essential to clearly reveal the nature of the magnetoelectric coupling on a microscopic level in BiFeO₃.

Up to now, the change of the magnetic easy direction within one ferroelastic domain compared to the neighboring one was discussed in the literature. But what happens at the border of these domains, i.e., at ferroelectric domain walls? Regarding only the ferroelectric properties, it was found that 109° and 180° domain walls in BiFeO₃ are electrically conducting, which paves the way for new applications [14, 16]. One of the main result of this thesis is the detection of an enhanced magnetic contrast at regions, where the electrostatic potential changes. This was interpreted as ferroelectric domain wall, in which the out-of-plane component of the ferroelectric polarization changes its sign. Therefore, an enhanced magnetic moment could be created and controlled by the ferroelectric domain structure in BiFeO₃, which could be employed as electrically controlled memory bit. However, a full understanding of this behavior is still lacking and further measurements of the local magnetic moment together with the ferroelectric domain structure are necessary. For example, recently, a magnetization reversal by decoupling of magnetic and ferroelectric domain walls forced by an applied electric field was discovered in ferroelectric/antiferroelectric composite heterostructures based on LuMnO₃, which is an antiferromagnetic multiferroic compound [395]. This demonstrates the importance of the understanding of the behavior of ferroelectric and/or magnetic domain walls in multiferroic compounds. As the internal structure of domain boundaries, interfaces, twin walls, etc. can have significant effects on the macroscopic behavior and, in specific cases, can even outperform these properties, one would like to optimize the interfacial properties rather than the domain structure itself, which leads to the field of “domain boundary engineering” [399].

Therefore, the most promising field for future discoveries regarding multiferroics might be interfacial phenomena [14, 400]. In addition to spontaneously formed

domain walls, interfaces can be artificially engineered in heterostructure devices. One example is the fabrication of exchange coupled ferromagnet/BiFeO₃ composite heterostructures. In such devices, the exchange field can be modified by an external electric field, resulting in a robust control of the magnetization at room temperature [401]. However, the mechanism leading to interfacial coupling is far from being well understood [14]. A detailed discussion of engineering larger magnetoelectric coupling using interfacial effects between ferromagnetic and ferroelectric constituents of composite structures is addressed in the second part of this thesis.

To conclude, BiFeO₃ has been a focal point of research in recent years, since it is a material for various potential applications. In particular, employing the multiferroic behavior of BiFeO₃, memory cells could be written electrically and read magnetically, which has advantages in terms of the non-volatility of the stored information, power consumption and scalability [13]. The first condition can be realized due to the electrically switchable easy plane of the antiferromagnetic phase [137], which might be read out by exchange bias effects [311]. A second potential use of BiFeO₃ thin films in the field of spintronic applications could be magnetic tunnel junctions using BiFeO₃ as tunnel barrier [3], where the ferroelectric state of the BiFeO₃ barrier controls the magnetic state of the ferromagnetic electrode. Both concepts show, in principle, the possibility to develop a magnetoelectric random access memory (MeRAM) [9]. In addition, Bea and coworkers proposed different potential applications based on conducting domain walls in BiFeO₃ thin films [16]. Apart from the multiferroic behavior, the outstanding ferroelectric properties alone make BiFeO₃ a possible candidate in next generation ferroelectric memory devices [28], since BiFeO₃ thin films exhibit a large remanent polarization of around 100 $\mu\text{C}/\text{cm}^2$ [27] as well as lead-free constituents, which is important in terms of health and safety compared to the most widely used ferroelectric material: $\text{Pb}_{1-x}\text{Zr}_x\text{TiO}_3$. Furthermore, it was found that BiFeO₃ thin films emit THz radiation, when hit with a femtosecond laser pulse [402]. Since the radiation is correlated to the poling state of the BiFeO₃ thin film, this is a non-destructive method to read out the information stored in a ferroelectric memory cell, resulting in a prototype for optically accessible BiFeO₃ memory [403]. Recently, a second line of work on BiFeO₃ has emerged, driven by the search for new materials in the field of renewable energy production. In this regard, BiFeO₃ has attracted attention, since photoconductivity as well as a photovoltaic effect was found in this material [404–406]. This further demonstrates that BiFeO₃ is an attractive and intriguing compound. However, in spite of the tremendous research efforts in this area, many questions remain, which were highlighted above. These topics are worth to be investigated in future experiments.

The second multiferroic compound investigated during the course of this thesis is hardly relevant for future applications. As summarized above, crystalline, dielectric, and magnetic properties of BiCrO₃ thin films were investigated in detail for the first time. However, the multiphase and multidomain state hamper the correct determination of the in-plane domain structure as well as strongly influence the dielectric and magnetic properties. In particular, the magnetoelectric coupling of BiCrO₃ might be averaged out due to its multidomain state [35]. Therefore, the

fabrication of single-phase and single-domain BiCrO_3 thin films is mandatory to get a deeper insight of the physical properties of this compound. This could be realized by using (111)-oriented SrTiO_3 substrates, since then the monoclinic (111) domain type is preferred compared to the $(\bar{1}01)$ one. Furthermore, as demonstrated in case of BiFeO_3 (cf. Section 4.4.1), the use of miscut substrates can further reduce the number of in-plane monoclinic domains.

As became clear in this part of the thesis, BiCrO_3 resembles more the multiferroic BiMnO_3 compound than BiFeO_3 . However, since BiMnO_3 seems to be ferroelectric and ferromagnetic,³ the question arises, why Bi containing perovskite-like multiferroics behave so differently? Theory calculations and experimental results suggest that in BiMO_3 with $M = \text{Cr, Mn, Fe, Co}$ the stereochemical activity of the Bi lone pair induces local electric moments, which allow ferroelectricity only if the symmetry of the compound does not have a center of inversion. In case of an inversion symmetry, the net polarization turns to zero [408]. Therefore, the crystal structure mainly determines the dielectric ground state in these systems. However, BiMnO_3 seems to be exceptional. In this compound, the emergence of an electric moment might be connected with inversion symmetry breaking by the noncollinear antiferromagnetic order [338].

Since the magnetic transition temperature of BiMnO_3 is as low as that of BiCrO_3 , there are two possible candidates for a room temperature multiferroic behavior in the sense of combining ferroelectric and antiferromagnetic phases: BiFeO_3 and BiCoO_3 . BiCoO_3 has a giant tetragonal lattice distortion of $c/a = 1.27$ and is therefore expected to exhibit a large spontaneous polarization of up to $179 \mu\text{C}/\text{cm}^2$ [409], but a ferroelectric hysteresis loop has not yet been observed. Therefore, it was proposed that BiCoO_3 is a pyroelectric material rather than a ferroelectric one [410]. However, this compound is of particular interest, since a giant magnetoelectric coupling was predicted by density functional calculations [411]. These calculations reveal a pressure- or electric field-induced metamagnetic transition, where Co^{3+} transforms from the high-spin state to a nonmagnetic low-spin state accompanied by an insulator-metal transition.

The main disadvantage of BiCoO_3 and all other perovskite-like BiMO_3 ($M = \text{Cr, Mn, Fe}$) compounds is their low magnetic moment (cf. Sections 4.4.2 and 4.5.2). In order to give rise to an intrinsic ferromagnetic behavior, compounds exhibiting a ferroelectric and ferromagnetic ordering are synthesized by combining two materials of the BiMO_3 ($M = \text{Cr, Mn, Fe}$) family, forming a double-perovskite structure. Among others, the compound $\text{Bi}_2\text{CrFeO}_6$ has attracted a lot of attention, since an enhanced magnetism [412] and even a multiferroic behavior at room temperature in epitaxially patterned $\text{Bi}_2\text{CrFeO}_6$ thin films [413] as well as a photovoltaic effect [414] were observed. However, our measurements on $\text{Bi}_2\text{CrFeO}_6$ thin films (see Appendix A), which are in agreement with Refs. [415, 416], do not confirm these results. Theory calculations reveal a magnetic transition temperature around 130 K [417]. Therefore, the magnetic transition temperature of $\text{Bi}_2\text{CrFeO}_6$ and thus the multiferroic behavior is unlikely to be above room temperature [418]. In this sense, the

³The magnetic and dielectric ground state is still discussed controversially in the literature [407].

compound $\text{Bi}_2\text{FeCoO}_6$ seems to be more promising in terms of room temperature multiferroic behavior, since the magnetic as well as ferroelectric transition temperature of both constituents (BiFeO_3 and BiCoO_3) are well above room temperature and an increase in magnetization was recently observed at 300 K in Co-substituted BiFeO_3 samples [419, 420]. However, in the double perovskite $\text{Bi}_2\text{BB}'\text{O}_6$, an ordering of the B and B' cations are difficult to achieve, as their ionic charges and ionic radii are very similar.

As discussed in Chapter 3, the perovskite-like BiMO_3 ($M = \text{Cr}, \text{Mn}, \text{Fe}, \text{Co}$) compounds are classified as split-order-parameter multiferroics. Thus, their expected magnetoelectric coupling may be small. In contrast, in joint-order-parameter multiferroics, in which the magnetic order induces the ferroelectric one, any reversal of the spontaneous polarization is directly coupled to changes in the magnetic order and thus a large magnetoelectric coupling is likely. However, the quest for compounds exhibiting a magnetoelectric coupling at room temperature is still far from being solved, since the strong magnetoelectric coupling is mainly based on competing interactions, which are destroyed by thermal energy at room temperature. Therefore, these materials are fascinating compounds in the field of basic research rather than for practical applications.

To overcome the limitations of the low transition temperatures as well as the weak ferromagnetic and ferroelectric polarizations, new mechanisms for a strong coupling between magnetic and ferroelectric ordering were recently proposed. As an example, it was found that magnetically ordered insulators that are neither ferroelectric nor ferromagnetic are transformed into ferroelectric ferromagnets using a single control parameter: strain [421, 422]. These results demonstrate that strain controls multiple order parameters, which can lead to enhanced magnetoelectric effects. This will be employed in detail in the second part of this thesis.

Extrinsic multiferroic composite structures

Chapter 6

Magnetoelectric composites

“A new class of physical properties of composite materials is that of “product properties” in which the phases or submaterials of the composite are selected in such a way that an effect in one of the phases of submaterials leads to a second effect in the other phase.”

J. van Suchtelen (1972) [423]

The small linear magnetoelectric response of intrinsic magnetoelectric materials known to date hampers the development of next-generation electronic devices in this field. Up to now, no single phase multiferroic material, which combines large, robust, electric and magnetic polarizations at room temperature, has been reported [21]. An alternative way to achieve enhanced magnetoelectric coupling is the use of heterogeneous hybrid structures, where proximity and interface-mediated effects are exploited to realize a finite coupling between the magnetic and dielectric degrees of freedom of the constituents [424]. In these hybrids, a converse pseudo-magnetoelectric coupling can be realized although no magnetoelectric effect exists in the constituent phases [423].¹ This allows to overcome the intrinsic upper limit of the linear magnetoelectric coupling characteristic of intrinsic magnetoelectric multiferroics (cf. Eq. (3.26)). In particular, magnetoelectric coupling coefficients larger than $\sqrt{\chi_{ii}^{(e)} \cdot \chi_{jj}^{(m)}}$ are possible in hybrid structures. In recent years, these composites therefore have drawn significant interest, also regarding the viable technological applications [21, 105, 425].

6.1 Realizing magnetoelectric coupling in composite structures

On a microscopic scale, composites are built up of two or more constituent materials that are in intimate contact. The interaction between the constituents can lead to an enhancement of existing properties (sum and scaling properties), or to

¹The magnetoelectric effect in composites is extrinsic. However, the term pseudo-magnetoelectric and magnetoelectric coupling is used synonymously in this part of the thesis.

new effects (product properties), which are absent in the single-phase submaterials [105, 423]. In the former case, for example, the magnitude of the magnetoelectric coupling can be increased by exchange bias effects coupling the antiferromagnetic order of multiferroics or magnetoelectrics to a ferromagnetic layer [392]. This mechanism was exploited in Part I of this thesis to demonstrate a possible magnetoelectric coupling in the multiferroic compound BiCrO_3 using a $\text{FeCo}/\text{BiCrO}_3$ composite system (cf. Section 4.5.2).

To achieve a finite magnetoelectric coupling in case of “product properties”, different mechanisms have been developed, relying on (i) the ferroelectric field effect, which controls the spin state by charge modulation [426–429], or (ii) the elastic coupling at the interface.²

The charge-mediated magnetoelectric coupling at the interface of multiferroic hybrid structures have been extensively investigated theoretically in recent years. For example, first principles calculations predict a large surface magnetoelectric coupling in Fe/BaTiO_3 (001) [57, 431] and $\text{Fe}_3\text{O}_4/\text{BaTiO}_3$ (001) [432] systems, originating from chemical bonding at the interface. Furthermore, a sizable magnetoelectric coupling is predicted to arise from spin-dependent screening of the ferroelectric polarization. In this case, a change of the magnetization is caused by the accumulation of spin-polarized electrons or holes at the interface due to an applied electric field [433]. Other charge-mediated magnetoelectric coupling mechanisms are predicted for ferromagnetic layers near the boundary between the ferromagnetic and paramagnetic state [434], as well as the ferromagnetic and antiferromagnetic ground state [435]. However, in the field of charge-induced magnetoelectric effects, only the magnetoelectric coupling using ferroelectric field effects has been experimentally verified up to now [427, 436–441], exploiting the charge sensitivity of the magnetic state in complex oxides [437]. Recently, a large magnetoelectric response of about $\Delta M/\Delta E \approx 6 \times 10^{-4} \text{ A/V}$ has been reported in $\text{Pb}(\text{Zr}_{0.2}\text{Ti}_{0.8})\text{O}_3/\text{La}_{0.8}\text{Sr}_{0.2}\text{MnO}_3$, i.e., in ferroelectric/ferromagnetic hybrid structures [427]. Using x-ray absorption near edge spectroscopy, it was shown that this magnetoelectric coupling is purely electronic in origin [428]. However, since the ferroelectric layer ($\text{Pb}(\text{Zr}_{0.2}\text{Ti}_{0.8})\text{O}_3$ in this case) is also piezoelectric, a superposition of charge and strain-mediated magnetoelectric coupling is, in principle, expected [438].

The strain-mediated coupling has been exploited early on to realize large magnetoelectric effects in composite material systems [424]. In this case, the electric and magnetic degrees of freedom are elastically coupled at the interface between the piezomagnetic (or magnetostrictive) and piezoelectric constituents. The strain-mediated magnetoelectric (ME) effect is therefore a product tensor property and can be described phenomenologically by [442]

$$\text{Direct ME effect} = \frac{\text{Magnetic}}{\text{Mechanical}} \times \frac{\text{Mechanical}}{\text{Electric}}$$

²Note that a compositional ordering that breaks inversion symmetry, such as three different materials (A , B , and C) in an A - B - C - A - B - C -... arrangement, is not sufficient to produce a significant switchable polarization and therefore seems not to be an alternative route to composite multiferroics [430].

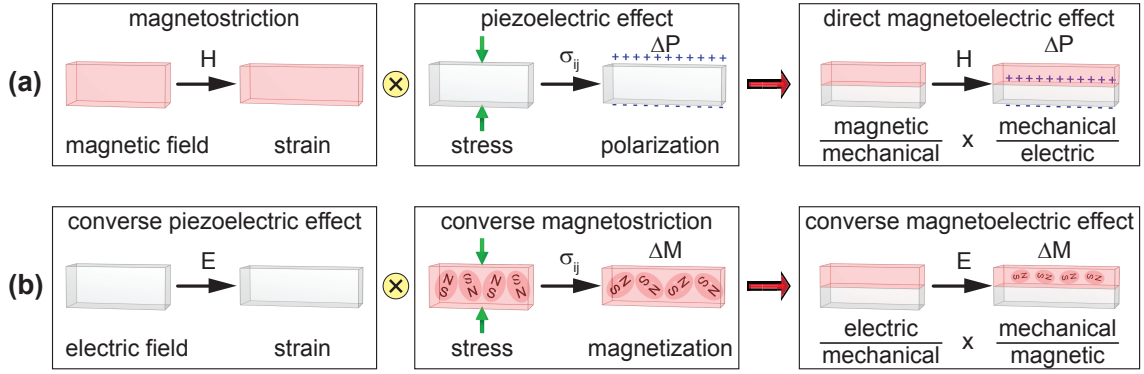


Figure 6.1: Schematic illustration of the product property of strain-mediated magnetoelectric composite systems consisting of 2-2-type horizontal magnetostrictive/piezoelectric hybrid structures [443]. The magnetostrictive layer is marked in red and the piezoelectric layer in gray. (a) Direct magnetoelectric effect: an in-plane magnetic field \mathbf{H} induces strain in the magnetostrictive layer due to the magnetostrictive effect. Since the piezoelectric layer is bonded on the magnetostrictive layer, the resulting stress σ_{ij} in the piezoelectric layer induces a finite polarization $\Delta\mathbf{P}$ through the piezoelectric effect. Thus in the composite, an in-plane magnetic field \mathbf{H} leads to a finite electric polarization $\Delta\mathbf{P}$. (b) Converse magnetoelectric effect: An electric field \mathbf{E} applied out of plane to the sample causes a finite strain in the piezoelectric layer due to the converse piezoelectric effect, which is mechanically transferred to the magnetostrictive layer, inducing a change of the magnetization $\Delta\mathbf{M}$ due to the inverse effect of magnetostriction. Therefore, the converse magnetoelectric effect is double indirect, causing a change of the magnetization $\Delta\mathbf{M}$ due to an electric field \mathbf{E} in the composite.

$$\text{Converse ME effect} = \frac{\text{Electric}}{\text{Mechanical}} \times \frac{\text{Mechanical}}{\text{Magnetic}}, \quad (6.1)$$

as is schematically shown in Fig. 6.1. In the corresponding composites, the magnetoelectric coupling relies on strain to induce crystal deformations on either the magnetic phase through the converse piezoelectric effect, or in the piezoelectric phase through magnetostriction. The effect is doubly indirect, since a first conversion occurs in translating the applied field to strain, and a second in converting stress to a polarization, i.e., the coupling is the product of two distinct interactions [424].

The direct and converse magnetoelectric effect has been realized in the form of particulate composites [444], laminated composites [445], nanostructured composites [446], and epitaxial multilayers [447]. Since the interface mediates the elastic coupling, it is common to classify the different forms of strain-mediated magnetoelectric composites using the notation 0-3, 1-3, 2-2, etc., where the numbers denote the connectivity of each phase [122]. The connectivity is defined as the number of dimensions through which the material is continuous. While 0-3 and 1-3 composites are based on either magnetic nanoparticles (0 D) or magnetic pillars (1 D) embedded in ferroelectric materials (3 D) [446, 448], alternating piezoelectric and magnetostrictive layers in horizontal structures are denoted as 2-2 type composites (see Fig. 6.1) [449].

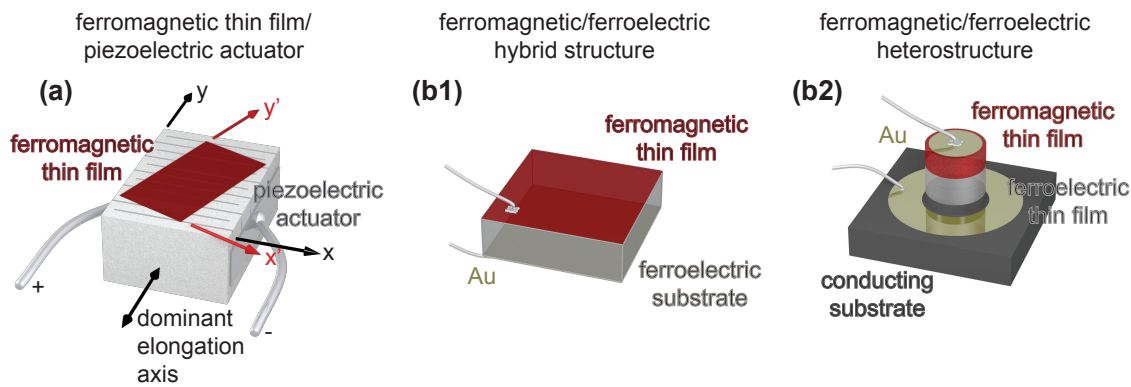


Figure 6.2: Variable schemes for the realization of 2-2-type horizontal strain-mediated structures investigated during this thesis: (a) A ferromagnetic thin film/piezoelectric actuator hybrid is realized by either depositing or cementing of ferromagnetic thin films onto piezoelectric $\text{Pb}(\text{Zr}_x\text{Ti}_{1-x})\text{O}_3$ -based actuators. (b) Ferromagnetic/ferroelectric structures fabricated by depositing ferromagnetic thin films onto ferroelectric layers. The ferroelectric layer can be a ferroelectric substrate, which results in free-standing ferromagnetic/ferroelectric hybrid structure (b1), or a ferroelectric thin film, which is grown on a suitable substrate first (b2). To apply an electric field across the ferromagnetic/ferroelectric structure, a metallic (Au) bottom electrode is deposited on the backside of the hybrid structure (b1), or the ferromagnetic/ferroelectric heterostructure is patterned into the mesa geometry shown in (b2).

In the scope of this thesis, only 2-2-type horizontal structures were investigated.³ Two different schemes were used for the realization of such 2-2-type horizontal structures. One approach is to fabricate ferromagnetic thin film/piezoelectric actuator structures by either depositing or cementing ferromagnetic thin films onto piezoelectric $\text{Pb}(\text{Zr}_x\text{Ti}_{1-x})\text{O}_3$ -based actuators (Fig. 6.2(a)). This technique allows to fabricate model systems for strain-mediated magnetization control using a large variety of ferromagnetic materials. Furthermore, the effect of strain on the magnetic properties can be tuned by simply changing the direction of the dominant elongation axis of the piezoelectric actuator with respect to the ferromagnetic thin film. This is addressed in Fig. 6.2(a) by two different coordinate systems. The reader is referred to Refs. [451–454] and the doctoral thesis of Andreas Brandlmaier [24] for more details on this approach. Obviously, the transfer of the concept shown in Fig. 6.2(a) to thin film heterostructures is desirable. As a first step, this can be realized by growing ferromagnetic thin films directly onto ferroelectric substrates (Fig. 6.2 (b1)) to create a free-standing ferromagnet/ferroelectric bilayer. However, for applications based on magnetoelectric composites, thin film heterostructures consisting of ferromagnetic and ferroelectric layers fabricated on adequate substrates are essential (Fig. 6.2 (b2)). The two main advantages of the approaches shown in Fig. 6.2(b) are a better control over the crystal structure and an almost perfect mechanical coupling between the magnetostrictive and the ferroelectric layer [424].

The expected magnetoelectric effects of free-standing ferromagnetic/ferroelectric

³More details on the different forms of strain-mediated magnetoelectric composites can be found in recent review articles [105, 425, 443, 450] and references therein.

hybrid structures (cf. Fig. 6.2(b1)) as well as horizontal ferromagnetic/ferroelectric heterostructures (cf. Fig. 6.2(b2)) are discussed in the following. Since the control of the magnetization by a local electric field is a major challenge in today's magnetic memory cells as described in the introduction (see Chapter 1), we will restrict our consideration to the discussion of the converse magnetoelectric effect (see Fig. 6.1(b)). Furthermore, as the converse magnetoelectric effect $\chi_{ij}^{(me)}$ in composites arises from the coupling of magnetostrictive and piezoelectric materials, $\chi_{ij}^{(me)}$ is highly frequency dependent [450]. Within this thesis, we focus on magnetoelectric effects at low-frequencies, i.e., in the DC limit, where no resonance phenomena (e.g. electromechanical or magnetoacoustic resonances) are expected. A quantitative understanding of DC coupling effects are a mandatory requirement for future studies of high-frequency magnetoelectric coupling.

6.2 Converse magnetoelectric coupling in multiferroic composite structures

Modeling of magnetoelectric effects in composite material systems has been extensively investigated since 1991 by Harshe as well as Bichurin and coworkers ([455] and references therein). Their calculations are based on solving combined elastostatic, electrostatic and magnetostatic equations to obtain an effective magnetoelectric coupling constant [456]. Within this theoretical model, the boundary conditions between the constituents of the composite seems to be crucial [457]. However, since these calculations yield magnetoelectric constants, which are proportional to the piezomagnetic coefficient, this is not applicable in our 2-2 type horizontal structures consisting of ferromagnetic materials as magnetostrictive layer. In magnetostrictive ferromagnetic materials exhibiting a homogeneous magnetization throughout the sample, a piezomagnetic effect is not expected. Therefore, we follow a different approach and examine the control of the magnetization \mathbf{M} as a function of the applied electric field \mathbf{E} on the basis of a phenomenological thermodynamic model.

6.2.1 Thermodynamic model of multiferroic composites

Since multiferroic composite structures consist of magnetostrictive and ferroelectric layers, the Gibbs free energy densities \tilde{g} of both constituents have to be considered. The total Gibbs free energy density $\tilde{g}^{(c)}$ of 2-2-type horizontal composites can then be found by adding the correctly weighted energy densities of the magnetostrictive $\tilde{g}^{(m)}$ and piezoelectric $\tilde{g}^{(e)}$ layer:

$$\tilde{g}^{(c)} = \frac{1}{v^{(m)} + v^{(e)}} (v^{(m)}\tilde{g}^{(m)} + v^{(e)}\tilde{g}^{(e)}) = \frac{1}{d^{(m)} + d^{(e)}} (d^{(m)}\tilde{g}^{(m)} + d^{(e)}\tilde{g}^{(e)}) , \quad (6.2)$$

where $v^{(m)}$ ($d^{(m)}$) and $v^{(e)}$ ($d^{(e)}$) denote the volume (thickness) of the magnetostrictive and piezoelectric layer. Here, we have assumed that the areas of both layers are identical.

Magnetostrictive layer

Assuming that the magnetostrictive layer is a ferromagnetic thin film, the magnetic response of the ferromagnetic material on external magnetic fields H_i and mechanical stresses $\sigma_{ij}^{(m)}$ can be calculated phenomenologically using the Gibbs free energy density $g^{(m)}(p, H_i, \sigma_{ij}^{(m)}; T) = u^{(m)}(M_i, \epsilon_{ij}^{(m)}) - Ts + p - \sigma_{ij}^{(m)} \epsilon_{ij}^{(m)} - \mu_0 M_i H_i$, where s (u) denotes the entropy (internal energy) per unit volume, T the temperature, p the pressure and $\epsilon_{ij}^{(m)}$ the elastic strain tensor.

For strain-mediated composites with no external stresses σ_{ij} applied to the composite, the Gibbs free energy density $g^{(m)}$ does not describe the equilibrium thermodynamic state, because of the rigid interaction of the magnetostrictive thin film with the piezoelectric constituent (cf. Figs. 6.2 (b1) and (b2)) [458]. Assuming a perfect clamping of both layers and a single-crystalline single-domain magnetostrictive thin film, the homogeneous in-plane strains of the magnetostrictive thin film $\epsilon_{11}^{(m)}$, $\epsilon_{22}^{(m)}$, and $\epsilon_{12}^{(m)}$ are fixed due to the rigid mechanical coupling of both layers, inducing homogeneous stresses $(\sigma_{11}^{(m)}, \sigma_{22}^{(m)}, \sigma_{12}^{(m)})$ in the magnetostrictive thin film [459]. In contrast, the stress components $\sigma_{33}^{(m)}$, $\sigma_{23}^{(m)}$, and $\sigma_{31}^{(m)}$ must be zero, because there are no mechanical forces acting on the free surface of the magnetostrictive layer. Since the Gibbs free energy density is only defined for fixed external stresses $\sigma_{ij}^{(m)}$ as independent variables, $g^{(m)}$ has to be modified by the Legendre transformation $\tilde{g}^{(m)}(p, H_i, \epsilon_{ij}^{(m)}; T) = g^{(m)}(p, H_i, \sigma_{ij}^{(m)}; T) + \sigma_{ij}^{(m)} \epsilon_{ij}^{(m)}$ [458]. $\tilde{g}^{(m)}$ is therefore a function of the natural variables T , p , H_i , and $\epsilon_{ij}^{(m)}$ and reaches a minimum in the equilibrium thermodynamic state of the system at constant temperature T , pressure p and magnetic field H_i as well as constant strain $\epsilon_{ij}^{(m)}$.

To determine $\tilde{g}^{(m)}$, first the magnetic energy density $u^{(m)}(M_i, \epsilon_{ij}^{(m)})$ of a ferromagnetic thin film is calculated [380]. We restrict ourselves to situations where the magnetization $\mathbf{M} = M_s \cdot \mathbf{m}$ is well defined and the unit vector \mathbf{m} of the magnetization direction is uniform throughout the sample. This is fulfilled for temperatures well below the Curie temperature in the absence of any magnetic domains. The direction of the magnetization \mathbf{M} can then be expressed by the components of the unit vector \mathbf{m} , i.e., by the direction cosines m_i ($i = 1, 2, 3$) of the Cartesian axes⁴ as well as the saturation magnetization M_s . Since the converse magnetoelectric interaction is based on the coupling of \mathbf{M} and the strain tensor ϵ_{ij} in ferromagnetic/piezoelectric composites, the magnetic energy density $u^{(m)}$ must contain magnetoelastic terms. To take into account the magnetoelastic coupling, the magnetic energy density $u^{(m)}(m_i, \epsilon_{ij}^{(m)})$ can be expanded in powers of m_i and $\epsilon_{ij}^{(m)}$ for small and homogeneous deformations [98, 460].⁵

⁴The direction cosines fulfill the normalization $m_1^2 + m_2^2 + m_3^2 = 1$.

⁵The exchange interaction is isotropic and is included in $u_0^{(m)}$.

$$\begin{aligned}
u^{(m)}(m_i, \epsilon_{ij}^{(m)}) - u_0^{(m)} &= k_{ij}m_i m_j + k_{ijkl}m_i m_j m_k m_l + k_{ijklmn}m_i m_j m_k m_l m_m m_n + \dots \\
&+ c_{ijkl}^{(m)}\epsilon_{ij}^{(m)}\epsilon_{kl}^{(m)} + \dots \\
&+ B_{ijkl}\epsilon_{ij}^{(m)}m_k m_l + \dots
\end{aligned} \tag{6.3}$$

Equation (6.3) contains the lowest-order terms of three contributions. The first line describes the magnetic anisotropy depending only on the direction of the magnetization m_i : $u_{\text{ani}}^{(m)} = k_{ij}m_i m_j + k_{ijkl}m_i m_j m_k m_l + k_{ijklmn}m_i m_j m_k m_l m_m m_n + \dots$, where the expansion tensors are denoted as k_{ij} , k_{ijkl} , k_{ijklmn} . Since ferromagnetic crystals are not symmetrical with respect to time-inversion, all terms of odd rank in m_i are zero [98]. The pure elastic energy $u_{\text{el}}^{(m)} = c_{ijkl}^{(m)}\epsilon_{ij}^{(m)}\epsilon_{kl}^{(m)} + \dots$ depicted in the second line is only a function of the strain tensor $\epsilon_{ij}^{(m)}$. The dependence of the elastic tensor $c_{ijkl}^{(m)}$ on the magnetization direction m_i known as the morphic effect [461], which is of the order of 1% in Ni [462], is neglected in the following. Therefore, the components of the stiffness tensors $c_{ijkl}^{(m)}$ are regarded as material constants. Assuming an undeformed state with $\epsilon_{ij}^{(m)} = 0$, the internal stresses are zero also, i.e., $\sigma_{ij} = \frac{\partial u_{\text{el}}^{(m)}}{\partial \epsilon_{ij}^{(m)}} = 0$.

Therefore, there is no linear term in the expansion of $u_{\text{el}}^{(m)}(\epsilon_{ij}^{(m)})$ [463]. The third contribution of the expansion depends on the strain components $\epsilon_{ij}^{(m)}$ and the direction of the magnetization m_i and therefore represents the interaction between the elastic and magnetic anisotropy energies. This term can be identified by the first-order magnetoelastic energy density $u_{\text{magnet}}^{(m)} = B_{ijkl}\epsilon_{ij}^{(m)}m_k m_l + \dots$ with the magnetoelastic coupling tensor B_{ijkl} . The magnetoelastic energy density can significantly alter the magnetization direction and is therefore often regarded as another form of magnetic anisotropy. Note that the linear coupling between the magnetization and the mechanical strain in the magnetoelastic energy $u_{\text{magnet}}^{(m)}$ is missing. This term describes piezomagnetic effects, which are not expected in ferromagnetic materials exhibiting a homogeneous magnetization. However, a ‘‘pseudo’’ piezomagnetic effect may be observed in ferromagnetic materials in a narrow external magnetic field range below the saturation field (see Section 9.2.1) [464].

Since the internal energy density $u^{(m)}(m_i, \epsilon_{ij}^{(m)})$ is a scalar and therefore independent of the choice of axes, each term has to satisfy the requirements of the crystal symmetry [465]. All ferromagnetic thin films discussed in this part of the thesis exhibit a pseudo-cubic crystal structure, so that it is convenient to transform Eq. (6.3) into [322, 380, 466]⁶

⁶The addition theorem $m_1^4 + m_2^4 + m_3^4 = 1 - 2(m_1^2 m_2^2 + m_2^2 m_3^2 + m_3^2 m_1^2)$ was used to further simplify the magnetic anisotropy contribution.

$$\begin{aligned}
u^{(\text{m.cubic})}(m_i, \eta_i^{(\text{m})}) - u_0 &= -\frac{1}{2}K_c (m_1^4 + m_2^4 + m_3^4) + \dots \\
&+ \frac{1}{2}c_{11}^{(\text{m})} \left[\left(\eta_1^{(\text{m})} \right)^2 + \left(\eta_2^{(\text{m})} \right)^2 + \left(\eta_3^{(\text{m})} \right)^2 \right] \\
&+ c_{12}^{(\text{m})} \left(\eta_1^{(\text{m})} \eta_2^{(\text{m})} + \eta_2^{(\text{m})} \eta_3^{(\text{m})} + \eta_1^{(\text{m})} \eta_3^{(\text{m})} \right) \\
&+ \frac{1}{2}c_{44}^{(\text{m})} \left[\left(\eta_4^{(\text{m})} \right)^2 + \left(\eta_5^{(\text{m})} \right)^2 + \left(\eta_6^{(\text{m})} \right)^2 \right] + \dots \\
&+ B_1 \left[\eta_1^{(\text{m})} \left(m_1^2 - \frac{1}{3} \right) + \eta_2^{(\text{m})} \left(m_2^2 - \frac{1}{3} \right) + \eta_3^{(\text{m})} \left(m_3^2 - \frac{1}{3} \right) \right] \\
&+ B_2 \left(\eta_4^{(\text{m})} m_2 m_3 + \eta_5^{(\text{m})} m_1 m_3 + \eta_6^{(\text{m})} m_1 m_2 \right) + \dots, \quad (6.4)
\end{aligned}$$

neglecting higher order terms.⁷ The *matrix* or *Voigt notation* [112] is exploited in Eq. (6.4) to reduce the number of independent components in $\epsilon_{ij}^{(\text{m})}$ and $c_{ijkl}^{(\text{m})}$. For more clarity, a new symbol for the strain components η_k with $k = 1, \dots, 6$ is used throughout this thesis while applying the matrix notation ($\eta_1 = \epsilon_{11}$, $\eta_2 = \epsilon_{22}$, $\eta_3 = \epsilon_{33}$, $\frac{1}{2}\eta_4 = \epsilon_{23}$, $\frac{1}{2}\eta_5 = \epsilon_{13}$, $\frac{1}{2}\eta_6 = \epsilon_{12}$).⁸

As in the cubic symmetry, the three axes are indistinguishable [98], the first term in $u_{\text{ani}}^{(\text{m})}(m_i)$ results in $k_{ij}m_i m_j = k_{11}(m_1^2 + m_2^2 + m_3^2) = k_{11}$. Therefore, the first non-zero term, which is a function of m_i is of fourth order, with the first order cubic anisotropy constant $K_c = 6k_{1122}$. However, the lowest order of the magnetoelastic contribution $u_{\text{magel}}^{(\text{m})}$ obviously contains terms quadratic in m_i . Since the symmetry is in general lowered under strain, $u_{\text{magel}}^{(\text{m})}$ may contain anisotropy terms that are forbidden in the unstrained state. In $u_{\text{magel}}^{(\text{m})}$, the magnetoelastic coupling constants B_i are linear combinations of B_{ijkl} tensor components ($B_0 = \frac{2}{3}B_{1122} - \frac{1}{3}B_{1111}$, $B_1 = B_{1111} - B_{1122}$ and $B_2 = 2B_{2323}$) [98]. For bulk magnetostrictive samples, B_i can be expressed as a function of the magnetostriction constants λ_{100} and λ_{111} by minimizing the sum of the magnetoelastic and elastic energies [459]:

$$\lambda_{100}^{\text{bulk}} = -\frac{2}{3} \frac{B_1}{(c_{11}^{\text{m}} - c_{12}^{\text{m}})}, \quad \lambda_{111}^{\text{bulk}} = -\frac{1}{3} \frac{B_2}{c_{44}^{\text{m}}}, \quad (6.5)$$

with the three independent components of the stiffness matrix $c_{ij}^{(\text{m})}$. For a sample magnetized in the [100] ([111]) direction, the strain due to magnetoelastic effects is defined as $\lambda_{100}^{\text{bulk}}$ ($\lambda_{111}^{\text{bulk}}$), starting from an ideal demagnetized state. The ideal demagnetized state can be defined as [466]

$$\lambda_0 = -3 \frac{B_0}{\left(c_{11}^{(\text{m})} - c_{12}^{(\text{m})} \right)}. \quad (6.6)$$

⁷The term $B_0 \left(\eta_1^{(\text{m})} + \eta_2^{(\text{m})} + \eta_3^{(\text{m})} \right) = B_0 \partial V / V$, which describes volume magnetoelastic effects, is neglected, since it is only significant near the Curie temperature of the ferromagnetic material [466].

⁸The standard notation is used for the stress and strain tensor components [112]. Furthermore, the calculation is based on a standard Cartesian coordinate system.

For polycrystalline ferromagnetic bulk materials, the magnetostrictive strain is isotropic ($\lambda_{100}^{\text{bulk}} = \lambda_{111}^{\text{bulk}} = \bar{\lambda}^{\text{bulk}}$) and can be expressed as [467]

$$\bar{\lambda}^{\text{bulk}} = a\lambda_{100}^{\text{bulk}} + (1 - a)\lambda_{111}^{\text{bulk}}, \quad (6.7)$$

with the Akulov relation $a = 2/5$ [468]. Furthermore, the c_{44} component of the stiffness matrix c_{ij} of isotropic materials is given by $\frac{1}{2}(c_{11} - c_{12})$ [112]. Thus, as expected, the magnetoelastic coupling constants are equal ($B_1 = B_2$). However, this is only justified for untextured polycrystals and for amorphous alloys [380].

In bulk samples, the quantities B_i and λ_{ij} are often used synonymously. In case of ferromagnetic thin films, the equivalence between B_i and λ_{ij} is not given due to the elastic constraints caused by the rigid substrate. Therefore, the concept of magnetostriction should be avoided. Instead, the magnetoelastic coupling B_i should be used [459]. In general, B_i^{film} deviates from the bulk value B_i^{bulk} in ferromagnetic thin films due to surface effects and the influence of strain on the magnetoelastic coupling coefficients [459]. In the past, the difference between B_i^{film} and B_i^{bulk} was discussed in view of surface effects and thickness dependent magnetoelastic coupling coefficients B_i^{film} were proposed [469]. Within this theory B_i^{film} reaches the bulk value with increasing film thickness. However, measurements on ferromagnetic thin films with the same thickness but exposed to different stress states reveal different magnetoelastic coupling coefficients [470]. Therefore, the deviation of B_i^{film} from the respective bulk value might be due to strain dependence of B_i rather than surface effects [471]. The strain dependence of B_i can be phenomenologically described by $B_i^{\text{eff}}(\epsilon_{\parallel}^{\text{m}}) = B_{0,i} + D_i\epsilon_{\parallel}^{\text{(m)}}$ with the average in-plane strain $\epsilon_{\parallel}^{\text{(m)}}$ [471]. B_i^{eff} is therefore a combination of first and second order magnetoelastic coupling coefficients [471, 472]. Since the values for $B_{0,i}$ and D_i have been determined only for a few ferromagnetic materials, bulk B_i^{bulk} values were used throughout this thesis. To account for the difference in B_i^{film} and B_i^{bulk} , a correction factor k^λ was included in the following calculations.

Since Eq. (6.4) is only valid for an infinitely extended sheet with \mathbf{M} aligned in the plane [380], an additional term must be added to the magnetic internal energy density $u^{\text{(m)}}(m_i, \epsilon_{ij}^{\text{(m)}}$) accounting for the shape anisotropy in ferromagnetic thin films with finite dimensions. Since $\nabla \cdot \mathbf{B} = 0$ requires $\nabla \cdot \mathbf{H} = -\nabla \cdot \mathbf{M}$, the magnetic field diverges at the surface of a ferromagnetic material and produces demagnetization fields originating from magnetic dipolar interactions [473]. The energy associated with the demagnetization field can be expressed as $u_{\text{demag}}^{\text{(m)}} = \frac{1}{2}\mu_0 M_s^2 m_i N_{ij} m_j$, where N_{ij} denotes the demagnetization tensor. For ferromagnetic thin films extended parallel to the (001) plane, for example, only $N_{33} = 1$ is different from zero and the demagnetization energy $u_{\text{demag}}^{\text{(m)}}$ in the limit of thin films with thickness of around 100 nm results in [474]

$$u_{\text{demag}}^{\text{(m)}}(m_3) = \frac{1}{2}\mu_0 M_s^2 m_3^2 \quad (6.8)$$

Neglecting any other energy contributions, $u_{\text{demag}}^{\text{(m)}}$ forces the magnetization into the film plane.

Using Eqs. (6.4) and (6.8), the modified Gibbs free energy density of the magnetic layer $\tilde{g}^{(m)}(p, H_i, \epsilon_{ij}^{(m)}; T)$ can be calculated on the basis of the internal energy density $u^{(m)}(m_i, \epsilon_{ij}^{(m)})$. At constant temperature T and pressure p , as well as elastic strain $\epsilon_{ij}^{(m)}$, the magnetization $M_i^{(m)}$ of the ferromagnetic layer can then be derived from

$$M_i^{(m)} = -\frac{1}{\mu_0} \left. \frac{\partial \tilde{g}^{(m)}}{\partial H_i} \right|_{T, p, \epsilon_{ij}^{(m)}}. \quad (6.9)$$

Piezoelectric layer

As discussed in Fig. 6.2, ferroelectric materials, which are piezoelectric by nature, are used for the piezoelectric layer in multiferroic composite structures. Therefore, in analogy to Eq. (6.3), the modified Gibbs free energy density of the ferroelectric layer $\tilde{g}^{(e)}$ can be described by $\tilde{g}^{(e)}(p, E_i, \epsilon_{ij}^{(e)}; T) = u^{(e)}(P_i, \epsilon_{ij}^{(e)}) - Ts + p - E_i^{(e)} D_i^{(e)}$. The internal energy density $u^{(e)}(P_i, \epsilon_{ij}^{(e)})$ is thereby a function of the polarization P_i and the elastic strain $\epsilon_{ij}^{(e)}$ and can be expanded into powers of P_i and $\epsilon_{ij}^{(e)}$ near the ferroelectric phase transition [475]:

$$\begin{aligned} u^{(e)}(P_i, \epsilon_{ij}^{(e)}) - u_0^{(e)} &= a_{ij} P_i P_j + a_{ijkl} P_i P_j P_k P_l + a_{ijklmn} P_i P_j P_k P_l P_m P_n + \dots \\ &+ c_{ijkl}^{(e)} \epsilon_{ij}^{(e)} \epsilon_{kl}^{(e)} + \dots \\ &+ d_{ijk} \epsilon_{ij}^{(e)} P_k + Q_{ijkl} \epsilon_{ij}^{(e)} P_k P_l + \dots \end{aligned} \quad (6.10)$$

Surface and depolarization energy contributions are neglected, since the piezoelectric layer is considered under closed circuit conditions. The first term in Eq. (6.10) can be identified by a Landau-Ginzburg-Devonshire type expansion with coefficients a_{ij} , a_{ijkl} , and a_{ijklmn} . Since most ferroelectric materials undergo a first-order transition, the expansion in powers of the electric polarization P_i must have terms at least up to the sixth order of P_i [260]. The phenomenological Landau-Ginzburg-Devonshire models are widely used to study ferroelectric phase transitions and domain pattern formation. In addition to the expansion in powers of P_i , gradient terms, which account for inhomogeneous structures such as domains or interfaces, are normally added to $u^{(e)}(P_i, \epsilon_{ij}^{(e)})$. However, this is not considered here. The elastic energy of the piezoelectric layer can be expressed as $u_{el}^{(e)} = c_{ijkl}^{(e)} \epsilon_{ij}^{(e)} \epsilon_{kl}^{(e)} + d_{ijk} \epsilon_{ij}^{(e)} P_k + Q_{ijkl} \epsilon_{ij}^{(e)} P_k P_l + \dots$, where $c_{ijkl}^{(e)}$, d_{ijk} , and Q_{ijkl} represent the elastic stiffness tensor of the ferroelectric layer, the piezoelectric tensor, and the electrostrictive tensor. The presence of symmetry in the crystal reduces the number of independent components in these tensors. The internal energy density $u^{(e)}(P_i, \epsilon_{ij}^{(e)})$ for a specific symmetry of the ferroelectric layer can be derived by using the correct form of the Landau-Ginzburg-Devonshire type model [476] as well as the $c_{ij}^{(e)}$, d_{ij} , Q_{ijk} matrices [112].

With the Gibbs free energy densities of the magnetostrictive thin film $\tilde{g}^{(m)}$ and the ferroelectric layer $\tilde{g}^{(e)}$, the composite system is well described. This is the starting point to calculate converse magnetoelectric effects in strain-mediated multiferroic composites.

6.2.2 Strain-mediated manipulation of the magnetization in multiferroic composite systems

Considering the multiferroic composite as a homogeneous system, the linear magnetoelectric susceptibilities $\chi_{ij}^{(\text{me})}$ and $\chi_{ij}^{(\text{em})}$ (cf. Section 3.1) can be treated as symmetric tensors $\chi_{ij}^{(\text{me})} = \chi_{ji}^{(\text{me})} = \chi_{ji}^{(\text{em})} = \alpha_{ij}^{(\text{c})}$, since no antisymmetric contribution $\alpha_{ij}^{(\text{a})}$, which is related to the presence of a toroidal moment \mathbf{T} , is expected. Therefore, the converse linear magnetoelectric coupling $\alpha_{ij}^{(\text{c})}$ can be expressed as (cf. Eq. (3.9))

$$\alpha_{ij}^{(\text{c})} = \mu_0 c \frac{\partial M_i^{(\text{c})}}{\partial E_j^{(\text{c})}} = \mu_0 c \frac{\Delta M_i^{(\text{c})}}{\Delta E_j^{(\text{c})}}, \quad (6.11)$$

where all physical quantities are related to the composite structure. Because the multiferroic composite consists of a ferromagnetic thin film on top of a ferroelectric layer (cf. Fig. 6.2), the magnetization of the composite $M_i^{(\text{c})} = v^{(\text{m})}/(v^{(\text{e})} + v^{(\text{m})})M_i^{(\text{m})}$ is identical to the magnetization of the ferromagnetic layer $M_i^{(\text{m})}$, which can be derived by using Eq. (6.9), scaled by the volume fraction $v^{(\text{m})}/(v^{(\text{e})} + v^{(\text{m})})$. $v^{(\text{m})}$ and $v^{(\text{e})}$ denote the volume of the ferromagnetic thin film and the ferroelectric layer, respectively. Since we further presume that the ferromagnetic thin film is a conductor and therefore acts as a top electrode, the electric field of the composite structure $E_j^{(\text{c})}$ is the same as the electric field across the ferroelectric layer $E_j^{(\text{e})}$. Following the arguments above, the converse linear magnetoelectric effect $\alpha_{ij}^{(\text{c})}$ in strain-mediated composite hybrids scales with the volume fraction of the magnetic and ferroelectric constituents $v^{(\text{m})}/(v^{(\text{e})} + v^{(\text{m})})$, which is equal to the thickness ratio $d^{(\text{m})}/(d^{(\text{e})} + d^{(\text{m})})$ in 2-2-type horizontal composites:

$$\alpha_{ij}^{(\text{c})} = \frac{d^{(\text{m})}}{d^{(\text{e})} + d^{(\text{m})}} \tilde{\alpha}_{ij}^{(\text{c})} = \frac{d^{(\text{m})}}{d^{(\text{e})} + d^{(\text{m})}} \mu_0 c \frac{\Delta M_i^{(\text{m})}}{\Delta E_j^{(\text{e})}} = \frac{d^{(\text{m})}}{d^{(\text{e})} + d^{(\text{m})}} \mu_0 c \frac{\Delta M_i^{(\text{m})}}{\Delta \epsilon_{mn}^{(\text{c})}} \frac{\Delta \epsilon_{mn}^{(\text{c})}}{\Delta E_j^{(\text{e})}}. \quad (6.12)$$

In numerous publications, giant sharp and persistent converse magnetoelectric effects were reported, neglecting the thickness of the ferroelectric substrate ($d^{(\text{e})} \rightarrow 0$) (eg. [20, 477, 478]). This is obviously incorrect, since the definition of the linear magnetoelectric tensor $\alpha_{ij}^{(\text{c})}$ is only valid in homogeneous systems. For $d^{(\text{m})}/d^{(\text{e})} = 10^{-3}$, the reported pseudo magnetoelectric effect $\tilde{\alpha}_{ij}^{(\text{c})}$ is around three orders of magnitudes larger than in reality. For example, a giant pseudo-converse magnetoelectric effect of up to $\frac{1}{c} \tilde{\alpha}_{13}^{(\text{c})} \approx 2.3 \times 10^{-7}$ s/m was observed in $\text{La}_{0.67}\text{Sr}_{0.33}\text{MnO}_3/\text{BaTiO}_3$ hybrid structures [20]. Taking into account the scaling factor $d^{(\text{m})}/(d^{(\text{e})} + d^{(\text{m})})$, this giant pseudo-converse magnetoelectric effect transforms into a large converse magnetoelectric effect of around $\frac{1}{c} \alpha_{13}^{(\text{c})} \approx 10^{-10}$ s/m, which is comparable to magnetoelectric effects at low temperatures of intrinsic magnetoelectric materials such as TbMn_2O_5 [479], TbMnO_3 [26], and $\text{Ni}_3\text{B}_7\text{O}_{13}\text{I}_3$ [480].

In Eq. (6.12), the strain tensor of the composite $\epsilon_{mn}^{(\text{c})}$ reflects the origin of the converse magnetoelectric effect in strain-mediated composite materials. If the ferromagnetic thin film is perfectly clamped to the ferroelectric layer, the in-plane strain

of the ferromagnetic thin film and the ferroelectric layer are equal. Since the physical properties of the ferromagnetic and ferroelectric layer are defined within the crystal axes of each system, the in-plane strain components of the ferromagnetic thin film $\epsilon_{mn}^{(m)}$ ($mn = 11, 22, 12$) are derived from the transformation of the ferroelectric strain tensor $\epsilon_{op}^{(e)}$ into the crystal axes of the ferromagnetic system: $\epsilon_{mn}^{(m)} = a_{mo}a_{np}\epsilon_{op}^{(e)}$ for $mn = 11, 22, 12$, where a_{mo} are the cosine of the angle between the crystal axes of the ferromagnetic and the ferroelectric system [112]. We assume, without loss of generality, that the coordinate system of the composite is the same as for the ferromagnetic thin film. Furthermore, neglecting any variations of the magnetization with respect to the out-of-plane components of $\epsilon_{mn}^{(c)}$ ($mn = 33, 13, 23$), the in-plane components of $\epsilon_{mn}^{(c)}$ are equal to $\epsilon_{mn}^{(m)} = a_{mo}a_{np}\epsilon_{op}^{(e)}$ ($mn = 11, 22, 12$). Using the matrix notation, this yields $\eta_k^{(c)} = \eta_k^{(m)} = T_{kk'}\eta_{k'}^{(e)}$ for $k = 1, 2, 6$ with the transformation matrix $T_{kk'}$. Since only the in-plane components of $\eta_k^{(c)}$ are relevant for the calculation, a new strain matrix η is defined as $\eta_{1,2,3} = \eta_{1,2,6}^{(c)}$. In this sense, the converse linear magnetoelectric effect can be expressed as

$$\alpha_{ij}^{(c)} = \mu_0 c \frac{d^{(m)}}{d^{(e)} + d^{(m)}} \frac{\Delta M_i^{(m)}}{\Delta \eta_{\tilde{k}}} T_{\tilde{k}k'} \frac{\Delta \eta_{k'}^{(e)}}{\Delta E_j^{(e)}}, \quad (6.13)$$

where \tilde{k} runs from 1 to 3 and $T_{\tilde{k}k'}$ is a 3×6 transformation matrix accounting for the difference in the coordinate systems of the magnetic thin film and the ferroelectric layer.

Equation (6.13) reveals that the converse magnetoelectric effect in multiferroic hybrid structures is based on the strain coupling between the magnetostrictive and the piezoelectric constituents, which leads to a finite manipulation of the magnetization $M_i^{(m)} = M_i$ by an electric field $E_j^{(e)} = E_j$. To calculate the converse linear magnetoelectric effect in composites, the change of the magnetization ΔM_i caused by a variation of the strain state $\Delta \eta_{\tilde{k}}$ is evaluated first. $\Delta M_i / \Delta \eta_{\tilde{k}}$ can be expressed in the low frequency limit as the difference of the final $m_i^{(f)}$ and initial $m_i^{(i)}$ magnetization direction calculated at constant in-plane strains $\eta_{\tilde{k}}^{(f)}$ and $\eta_{\tilde{k}}^{(i)}$ of the ferromagnetic layer using the modified Gibbs free energy density $\tilde{g}^{(m)}$ (cf. Section 6.2.1):

$$\frac{\Delta M_i}{\Delta \eta_{\tilde{k}}} = M_s \frac{m_i^{(f)} \Big|_{\eta_{\tilde{k}}^{(f)} = \text{const}} - m_i^{(i)} \Big|_{\eta_{\tilde{k}}^{(i)} = \text{const}}}{\eta_{\tilde{k}}^{(f)} - \eta_{\tilde{k}}^{(i)}}. \quad (6.14)$$

Up to now, the saturation magnetization M_s was assumed to be independent of $\eta_{\tilde{k}}$. However, M_s can vary, for example, as a consequence of the strain-dependent magnetic Curie temperature [481], which is a result of the high sensitivity of the transfer integral t on external pressure of double-exchange ferromagnets [312, 482]. This results in large changes of the magnetization as a function of the applied electric field in ferromagnetic/piezoelectric hybrid structures at temperatures near the magnetic transition temperature [20, 481]. Furthermore, an enhancement of the crystal field splitting by external stress can induce a spin-state transition from a magnetic intermediate-spin to a nonmagnetic low-spin state in (La, Sr)CoO₃ [483].

Both examples reveal that not only magnetic anisotropy effects can lead to a finite converse magnetoelectric effect due to the change of the orientation of the magnetization (see Eq. (6.14)), but also modification of the exchange interaction caused by strain effects can alter the magnetization. Therefore, \mathbf{M} must be expressed as $\mathbf{M}(M_s, \mathbf{m}) = M_s(\eta_{\bar{k}}) \cdot \mathbf{m}(\eta_{\bar{k}})$ and Eq. (6.14) should be extended to

$$\frac{\Delta M_i}{\Delta \eta_{\bar{k}}} = M_s \frac{m_i^{(f)} \Big|_{\eta_{\bar{k}}^{(f)} = \text{const}} - m_i^{(i)} \Big|_{\eta_{\bar{k}}^{(i)} = \text{const}}}{\eta_{\bar{k}}^{(f)} - \eta_{\bar{k}}^{(i)}} + m_i \cdot \frac{\Delta M_s}{\Delta \eta_{\bar{k}}}. \quad (6.15)$$

The driving force of the manipulation of the magnetization by an electric field in composite hybrid structures is the electric field dependence of the strains $\eta_{\bar{k}}$ (cf. Eq. (6.13)). As discussed above, $\eta_{\bar{k}}$ consists of the in-plane strain components of the ferromagnetic thin film $\eta_k^{(m)}$ ($k = 1, 2, 6$), which are a function of the strain matrix of the ferroelectric layer $\eta_{k'}^{(e)}$. The electric field dependence of $\eta_{k'}^{(e)}$ is known as the converse piezoelectric effect, which can be divided into two parts. One part arises from switching or movement of ferroelastic domains in a multi-domain state as well as from polarization reorientation and the other from the linear dependence of the strain tensor on the electric field [484]. The latter leads to converse linear piezoelectric effects expressed as⁹

$$\eta_{k'}^{(e)}(E) = d_{jk'} E_j \quad \text{with } k' = 1 - 6, j = 1 - 3, \quad (6.16)$$

where $d_{jk'}$ is the piezoelectric moduli of the ferroelectric layer [112]. Therefore, piezoelectric or ferroelectric materials with large piezoelectric responses are preferable for the fabrication of composite structures. A second method to impose large strains into the ferromagnetic material arises from ferroelastic domain switching in multi-domain states of the ferroelectric material. As an example, BaTiO₃ displays large piezoelectric strains of around 1% at room temperature, due to the coupled ferroelectric and ferroelastic phases [260]. To account for both piezoelectric effects, the electric field dependence of the strain state of the ferroelectric substrate $\epsilon_{mn}^{(e, \text{domain})}$ can be expressed as

$$\frac{\Delta \eta_{k'}^{(e)}(E)}{\Delta E_j} = d_{jk'} + \frac{\Delta \eta_{k'}^{(e, \text{domain})}}{\Delta E_j}. \quad (6.17)$$

In total, the converse linear magnetoelectric effect $\alpha_{ij}^{(c)}$ in composite structures can be described as $\alpha_{ij}^{(c)} = \frac{d^{(m)}}{d^{(e)} + d^{(m)}} \tilde{\alpha}_{ij}^{(c)}$, with

$$\tilde{\alpha}_{ij}^{(c)} = \mu_0 c \left[M_s \frac{m_i^{(f)} \Big|_{\eta_{\bar{k}}^{(f)} = \text{const}} - m_i^{(i)} \Big|_{\eta_{\bar{k}}^{(i)} = \text{const}}}{\eta_{\bar{k}}^{(f)} - \eta_{\bar{k}}^{(i)}} + m_i \cdot \frac{\Delta M_s}{\Delta \eta_{\bar{k}}} \right] T_{\bar{k}k'} \left[d_{jk'} + \frac{\Delta \eta_{k'}^{(e, \text{domain})}}{\Delta E_j} \right]. \quad (6.18)$$

⁹Higher order effects, such as electrostriction, which results from a quadratic dependence of ϵ_{ij} on E_i , are neglected.

Eq. (6.18) emphasizes the doubly indirect effect in which a first conversion occurs in translating the applied electric field to strain $\Delta E_j \rightarrow \Delta \eta_{\bar{k}}$, and a second in converting strain in a manipulation of the magnetization $\Delta \eta_{\bar{k}} \rightarrow \Delta M_i$.

With the knowledge of the converse piezoelectric effect of the ferroelectric layer $\eta_{k'}^p(E)$ and neglecting the dependence of the saturation magnetization on the in-plane strain components $\Delta M_s / \Delta \eta_{\bar{k}}$, the main challenge in the calculation of $\alpha_{ij}^{(c)}$ is therefore to compute the magnetization direction m_i at constant strain state $\eta_{\bar{k}}$. This can be done by exploiting the inverse magnetoelastic effect described in Eq. (6.3), since \mathbf{M} aligns in such a way, that $\tilde{g}^{(m)}$ takes its minimum value. However, $\tilde{g}^{(m)}$ is a function of the strain tensor $\eta_k^{(m)}$ of the ferromagnetic layer. Therefore, the calculation of $\eta_k^{(m)}$ as a function of $\eta_{k'}^{(e)}$ is the remaining step.

6.2.3 Thin film strain tensor

In 2-2-type horizontal hybrid structures exhibiting a strain-mediated magnetoelectric effect, two or more submaterials are coupled to each other. Assuming a perfect elastic coupling without defects, this clamping produces a well-defined strain in the plane of each submaterial. For the approaches sketched in Fig. 6.2, the in-plane components $\eta_1^{(m)}$, $\eta_2^{(m)}$, and $\eta_6^{(m)}$ of the strain tensor of the overlying thin film are fixed by the thick substrate or by the piezoelectric actuator, respectively. To determine the whole strain matrix $\eta_k^{(m)}$ of the thin film, the knowledge of the remaining components $\eta_3^{(m)}$, $\eta_4^{(m)}$, and $\eta_5^{(m)}$ is essential. This situation is the general case of pseudomorphic or coherent growth of epitaxial thin films (f) on crystalline substrates (s). Following Marcus and Jona [485, 486], the strain matrix of the thin film η_k^f can be calculated using elastic theory.

Pseudomorphic growth

Assuming a vector in two dimensions with components (x_1, x_2) , which is stretched to have components $(x_1 + u_1, x_2 + u_2)$, the deformation can be described by a linear transformation $U_{ij}x_j = x_i + u_i$, with $(i, j = 1, 2)$. By using the definition of the strain tensor $\epsilon_{ij} = \frac{1}{2} \left(\frac{\partial u_i}{\partial x_j} + \frac{\partial u_j}{\partial x_i} \right)$ [112], the strain components ϵ_{ij} can be expressed as a function of the transformation matrix U_{ij} by $\epsilon_{ij} = \frac{1}{2} (U_{ij} + U_{ji}) - \delta_{ij}$ in the limit of the linear transformation (δ_{ij} denotes the Kronecker symbol). In the general case of pseudomorphic growth of a thin film described in the coordinate system $(\mathbf{x}_1^f, \mathbf{x}_2^f)$ with the surface vectors $(\mathbf{a}_1^f, \mathbf{a}_2^f)$ in the equilibrium state on a substrate defined by $(\mathbf{x}_1^s, \mathbf{x}_2^s)$ and $(\mathbf{a}_1^s, \mathbf{a}_2^s)$ (see Fig. 6.3(a)), the linear transformation can be written as

$$\begin{pmatrix} U_{11} & U_{12} \\ U_{21} & U_{22} \end{pmatrix} \begin{pmatrix} a_1^f & a_2^f \cos \theta^f \\ 0 & a_2^f \sin \theta^f \end{pmatrix} = \begin{pmatrix} a_1^s & a_2^s \cos \theta^s \\ 0 & a_2^s \sin \theta^s \end{pmatrix}. \quad (6.19)$$

Therefore, the in-plane strain tensor coefficients are simply determined by the mismatch between film and substrate at the growth temperature:

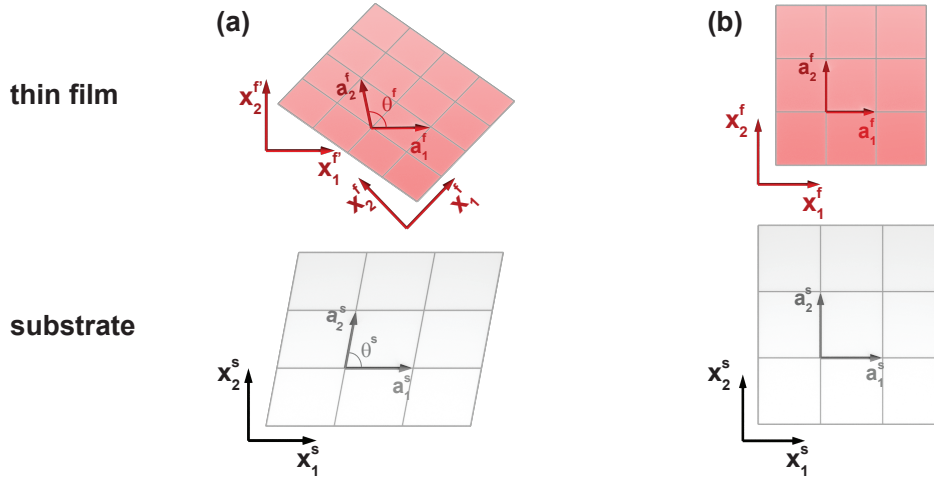


Figure 6.3: (a) General case of the growth of a material with low symmetry on a substrate. The surfaces of both materials are characterized by the surface vectors $(\mathbf{a}_1^f, \mathbf{a}_2^f)$, which are described in the surface coordinate system $(\mathbf{x}_1^f, \mathbf{x}_2^f)$, and $(\mathbf{a}_1^s, \mathbf{a}_2^s)$ as well as the angles θ^f and θ^s in the equilibrium state. The pseudomorphic growth of the thin film on the substrate requires a rotation of the coordinate system of the thin film $(\mathbf{x}_1^f, \mathbf{x}_2^f)$ with respect to the coordinate system of the substrate $(\mathbf{x}_1^s, \mathbf{x}_2^s)$ and a deformation of the unit mesh of the films equilibrium phase into the unit mesh of the substrate, which certainly imposes in-plane strain in the thin film. (b) Deposition of a cubic material with lattice constant a_0^f on a substrate exhibiting in-plane cubic symmetry with lattice constant a_0^s .

$$\begin{aligned}
 \epsilon_{11}^{f'} &= \eta_1^{f'} = \frac{a_1^p}{a_1^m} - 1, \\
 \epsilon_{12}^{f'} &= \frac{1}{2}\eta_6^{f'} = \frac{1}{2} \left(\frac{a_2^p \cos \theta^p}{a_2^m \sin \theta^m} - \frac{a_1^p \cos \theta^m}{a_1^m \sin \theta^m} \right), \\
 \epsilon_{22}^{f'} &= \eta_2^{f'} = \frac{a_2^p \sin \theta^p}{a_2^m \sin \theta^m} - 1.
 \end{aligned} \tag{6.20}$$

Due to different thermal expansion coefficients between the thin film and the substrate, additional strains might be created in the thin film during cooling down from the deposition temperature to room temperature, which are neglected for simplicity. The strain components in Eq. (6.20) are calculated with respect to the surface coordinate system defined by $(\mathbf{x}_1^f, \mathbf{x}_2^f)$, which is, in general, not equal to the crystal coordinate system $(\mathbf{x}_1^f, \mathbf{x}_2^f)$. The transformation of the strain components $\epsilon_{mn}^{f'}$ into the crystal coordinate system can be carried out utilizing the transformation law of the components of a second-rank tensor [112]:

$$\tilde{\epsilon}_{ij}^f = s_{im}s_{jn}\epsilon_{mn}^{f'}, \tag{6.21}$$

where s_{im} are the direction cosines between x_i^f and $x_m^{f'}$.

To calculate the total strain tensor ϵ_{ij}^f ($i, j = 1, 2, 3$), which contains the in-plane strain components given by Eq. (6.21) and satisfies the vanishing stress condition

$0 = c_{ijkl}^f \epsilon_{kl}^f$ for $ij = 13, 23, 33$, three in-plane unit stresses ($h = 1 : \sigma_{11}^{f'} = 1$, $h = 2 : \sigma_{22}^{f'} = 1$, and $h = 3 : \sigma_{12}^{f'} = 1$) are considered first. In each case all other components of the stress tensor are taken to vanish. To compute the elastic response on the unit stresses, the three unit stress tensors have to be transformed into the crystal coordinate system of the thin film, since the elastic constants c_{ijkl}^f are referred to these axes. In analogy to Eq. (6.21), the stress tensor in the thin film coordinate system ($\mathbf{x}_1^f, \mathbf{x}_2^f$) can be derived by $\sigma_{ij}^f = s_{ik}s_{jl}\sigma_{kl}^{f'}$. Using the unit stresses defined above, the strains ϵ_{ij}^f can be calculated to

$$\begin{aligned}\sigma_{ij,h}^f &= s_{hi}s_{hj} = c_{ijkl}^f \epsilon_{kl,h}^f \quad \text{for } h = 1, 2 \\ \sigma_{ij,3}^f &= s_{1i}s_{2j} + s_{1j}s_{2i} = c_{ijkl}^f \epsilon_{kl,3}^f.\end{aligned}\quad (6.22)$$

To get the total strain tensor, the three strain tensors $\epsilon_{ij,h}^f$ are superimposed with three different weight factors f_h , which are determined by putting the weighted sum of the values ϵ_{11}^f , ϵ_{22}^f , and ϵ_{12}^f equal to the values obtained in Eq. (6.21):

$$\epsilon_{ij}^f = \sum_{h=1}^3 f_h \epsilon_{ij,h}^f \quad \text{with} \quad \epsilon_{ij}^f = \tilde{\epsilon}_{ij}^f \quad \text{for } ij = 13, 23, 33. \quad (6.23)$$

The total strain tensor of the thin film ϵ_{ij}^f in Eq. (6.23), which was calculated with respect to the thin film crystal coordinate system ($\mathbf{x}_1^f, \mathbf{x}_2^f$), contains the correct in-plane strain components and the desired out-of-plane strains.

Ferromagnetic thin film with cubic symmetry

The simplest example of the method described above is the growth of a thin film with cubic symmetry and lattice constant a_0^f on a substrate exhibiting an in-plane cubic symmetry with lattice constant a_0^s (see Fig. 6.3(b)). In this case the surface coordinate system ($\mathbf{x}_1^{f'}, \mathbf{x}_2^{f'}$) and the crystal coordinate system ($\mathbf{x}_1^f, \mathbf{x}_2^f$) of the thin film as well as the coordinate system of the substrate ($\mathbf{x}_1^s, \mathbf{x}_2^s$) are identical (see Fig. 6.3(b)). This situation yields

$$\epsilon_{ij}^{f,\text{cubic}} = \begin{pmatrix} \epsilon_{\text{ip}}^f & 0 & 0 \\ 0 & \epsilon_{\text{ip}}^f & 0 \\ 0 & 0 & -2 \frac{c_{12}^f}{c_{11}^f} \epsilon_{\text{ip}}^f \end{pmatrix}, \quad (6.24)$$

with $\epsilon_{\text{ip}}^f = \epsilon_{11}^f = \epsilon_{22}^f = \frac{a_0^s}{a_0^f} - 1$.

Up to now, only the elastic properties of the overlying thin films have been considered. However, in ferromagnetic thin films, magnetoelastic effects lead to additional contributions to the strain components. To account for magnetoelastic effects in the calculation of the strain tensor ϵ_{ij}^f , the stress in Eq. (6.22) should be extended to $\sigma_{ij,h}^f = c_{ijkl}^f \epsilon_{kl,h}^f + B_{ijkl} m_k m_l$, which yields

$$\epsilon_{ij}^{\text{f,cubic,ME}} = \begin{pmatrix} \epsilon_{\text{ip}}^{\text{f}} & 0 & -\frac{B_2}{c_{44}^{\text{f}}} m_1 m_3 \\ 0 & \epsilon_{\text{ip}}^{\text{f}} & -\frac{B_2}{c_{44}^{\text{f}}} m_2 m_3 \\ -\frac{B_2}{c_{44}^{\text{f}}} m_1 m_3 & -\frac{B_2}{c_{44}^{\text{f}}} m_2 m_3 & -2\frac{c_{12}^{\text{f}}}{c_{11}^{\text{f}}} \epsilon_{\text{ip}} - \frac{B_1}{c_{11}^{\text{f}}} \left(m_3^2 - \frac{1}{3}\right) \end{pmatrix}, \quad (6.25)$$

in the cubic symmetry. Equation (6.25) is in agreement with the equilibrium deformation of the thin film calculated by minimizing the sum of the magnetic and elastic energies with respect to the strain components ϵ_{ij}^{f} ($ij = 13, 23, 33$) using Eq. (6.4).

To minimize the computational cost, the magnetoelastic effects are neglected in the determination of the thin film strain tensor ϵ_{ij}^{f} in the following. By comparing Eq. (6.24) and Eq. (6.25) this is only valid for $\epsilon_{\text{ip}}^{\text{f}} \gg B_1/c_{12}^{\text{f}}$ and $B_2/c_{44}^{\text{f}} \ll 1$, which results in $\epsilon_{\text{ip}}^{\text{f}} \gg \lambda_{100}$ and $\lambda_{111} \ll 1$ in the bulk limit. In general, λ_{100} and λ_{111} range from $\pm 10^{-7}$ up to $\pm 10^{-3}$ in some $4f$ metals [380]. However, in this thesis, ferromagnetic $3d$ metals such as Ni and FeCo as well as spinel-type ferrites (Fe_3O_4) and ferromagnetic double perovskite ($\text{Sr}_2\text{CrReO}_6$) are used as ferromagnetic materials. For all of these materials, the method described above is valid for in-plane strains larger than $\epsilon_{\text{ip}}^{\text{f}} > 10^{-3}$. Therefore, the calculation of the total strain tensor employing the general method of pseudomorphic epitaxial growth neglecting magnetoelastic effects is only applicable for systems with moderate and large strains, where pure elastic effects overbalance possible magnetoelastic contributions.

Multiferroic composite structures

In case of multiferroic composite structures, a ferromagnetic thin film is deposited onto a ferroelectric layer (cf. Fig. 6.2). To account for the converse piezoelectric effect in the above described method, the lattice parameter of the substrate are a function of the applied electric field. However, since the converse piezoelectric effect $\epsilon_{op}^{(e)}(E)$ is derived with respect to the coordinate system of the substrate ($\mathbf{x}_1^s, \mathbf{x}_2^s$), the resulting strain is treated as an additional contribution to the misfit strain derived in Eq. (6.21). Furthermore, the calculation of the misfit strain ϵ_{mn}^{f} is carried out at the growth temperature using constant substrate lattice parameters. Therefore, the in-plane strain components of the ferromagnetic thin film in composite hybrid structures read

$$\epsilon_{mn}^{(m)} = \epsilon_{mn}^{\text{f}} + a_{mo} a_{np} \epsilon_{op}^{(e)}(E), \quad (6.26)$$

with $mn = 11, 22, 12$. As mentioned in the previous section, a_{mo} are the direction cosines of x_m^{f} with respect to x_o^s . Note that, again, any additional strain resulting from different thermal expansion coefficients of the substrate and the thin film is neglected. Using the in-plane strain components $\epsilon_{mn}^{(m)}$, which are denoted as $\eta_{\tilde{k}}$ ($\tilde{k} = 1, 2, 3$) (cf. Eq. (6.13)) in the previous section, the total strain tensor of the ferromagnetic thin film can be calculated using the method described above. The resulting components of the strain tensor are now a function of the applied electric field due to the converse piezoelectric effect $\epsilon_{op}^{(e)}(E)$.

So far, the elastic coupling between the ferromagnetic thin film and the ferroelectric layer is assumed to be ideal. However, in case of imperfect clamping, the in-plane components of the strain tensors $\epsilon_{ij}^{(m)}$ and $\epsilon_{ij}^{(e)}$ are not identical. This can be described by a coupling parameter k^c , with $k^c = 1$ for ideal elastic coupling between both constituents and $k^c = 0$ in the case of vanishing coupling. Therefore, the strain components $\eta_{\bar{k}}$ are attenuated to $k^c \eta_{\bar{k}}$ and Eq. (6.13) transforms into

$$\alpha_{ij}^{(c)} = \mu_0 c \frac{d^{(m)}}{d^{(e)} + d^{(m)}} \frac{\Delta M_i}{\Delta (k^c \eta_{\bar{k}})} T_{kk'} \frac{\Delta \eta_{k'}^{(e)}}{\Delta E_j^{(e)}}. \quad (6.27)$$

Additionally, k^c must also be taken into account in the calculation of the magnetization changes ΔM_i . By neglecting the strain dependence of the saturation magnetization $\frac{\Delta M_s}{\Delta \eta_{\bar{k}}} = 0$, the change of the magnetization of the ferromagnetic thin film ΔM_i is calculated on the basis of the Gibbs free energy density $\tilde{g}^{(m)}$ (cf. Section 6.2.1). To reduce the number of unknown parameters, the correction factor k^λ , which accounts for the difference of magnetostrictive stress in thin films B_i^{film} and bulk B_i^{bulk} (cf. Section 6.2.1), and the coupling parameter k^c are merged together to one factor k , which is determined experimentally. Therefore, k is included in the calculation modifying the first-order magnetoelastic term $u_{\text{magel,thin film}}^{(m)} = k \cdot u_{\text{magel}}^{(m)}$.

6.2.4 Examples of converse magnetoelectric effects in multiferroic composites

With the knowledge of the strain response of the piezoelectric layer on applied electric fields $\epsilon_{ij}^{(e)}(E)$, the strain tensor of the overlying thin film $\epsilon_{ij}^{(m)}$ can be calculated using the method described in the previous section. As an example, a polycrystalline ferromagnetic thin film with a magnetostriction constant of $\bar{\lambda} = -30 \times 10^{-6}$ fabricated on top of a tetragonal piezoelectric layer without any misfit strain ($\epsilon_{mn}^f = 0$) exhibits the following in-plane strain (cf. Eq. (6.26)): $\epsilon_{mn}^{(m)} = \epsilon_{mn}^{(e)}(E)$ with $mn = 11, 22, 12$. Neglecting magnetoelastic effects in the calculation of the out-of-plane components of the thin film strain tensor, $\epsilon_{ij}^{(m)}$ can be expressed in the form of Eq. (6.24). However, assuming a tetragonal symmetry with space group $4mm$ of the piezoelectric layer (such as BaTiO₃ at room temperature), the converse linear piezoelectric effect yields $\epsilon_{mn}^{(e)}(E) = \eta_k^{(e)} = d_{31} E_3$ with $mn = 11, 22$; $k = 1, 2$ and $\epsilon_{12}^{(e)}(E) = \frac{1}{2} \eta_6^{(e)} = 0$. These strain components are displayed in Fig. 6.4(a) for $d_{31} = -1 \text{ nm/V}$ in the electric field range $E > 200 \text{ kV/m}$. In this electric field range, the strain tensor of the ferromagnetic thin film $\epsilon_{ij}^{(m)}$ can be expressed as

$$\epsilon_{ij}^{(m)} = \begin{pmatrix} d_{31} E_3 & 0 & 0 \\ 0 & d_{31} E_3 & 0 \\ 0 & 0 & -2 \frac{c_{12}^f}{c_{11}^f} d_{31} E_3 \end{pmatrix}, \quad (6.28)$$

assuming a perfect elastic coupling between the ferromagnetic thin film and the piezoelectric layer ($k^c = 0$). $\epsilon_{ij}^{(m)}$ is therefore a linear function of the applied electric field and the magnetization direction m_i can now be computed by minimizing the

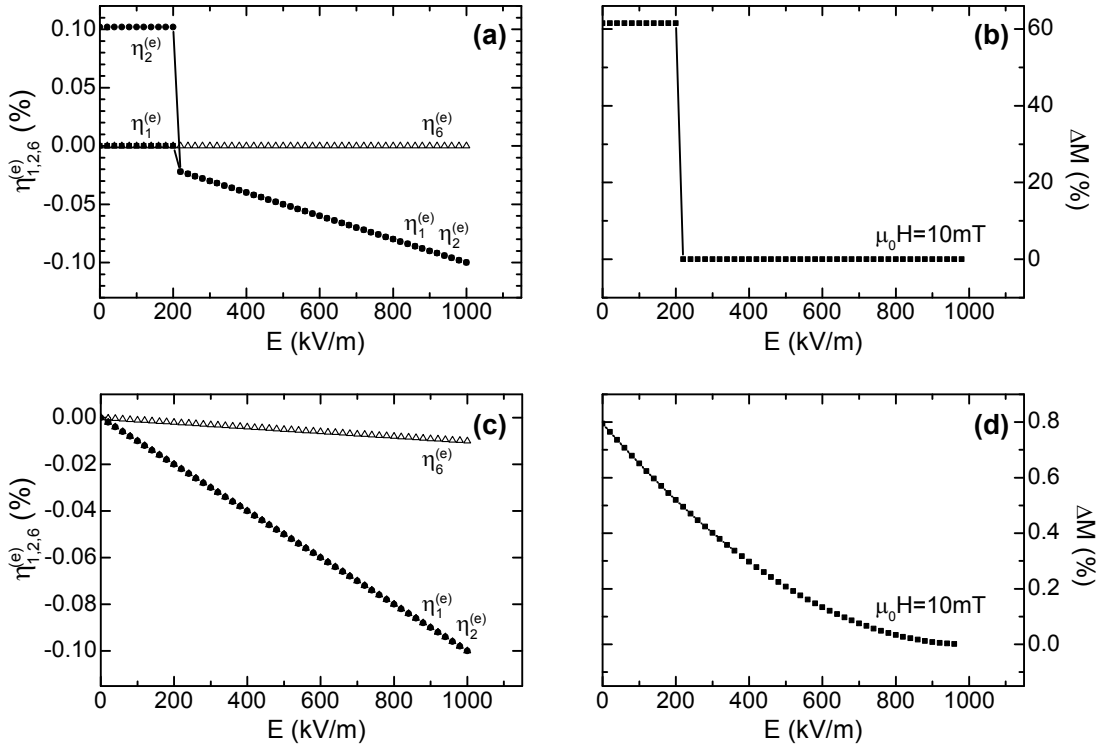


Figure 6.4: Evolution of in-plane strain components $\eta_k^{(e)}$ ($k = 1, 2, 6$) of a virtual substrate exhibiting a (a) tetragonal and (c) trigonal symmetry. (a) In addition to the converse linear piezoelectric effect for electric fields larger than 200 kV/m, the substrate considered in (a) is ferroelastic and domain switching occurs at a critical field of 200 kV/m. For the calculation of the converse linear effects the following values of the piezoelectric moduli were used: $d_{31} = -1$ nm/V and $d_{36} = -0.1$ nm/V. (b), (d) Assuming a perfect clamping ($k^c = 1$) of a polycrystalline ferromagnetic material with a magnetostriction constant of $\bar{\lambda} = -30 \times 10^{-6}$ deposited on top of the considered layer as well as $k^\lambda = 1$, the variation of the magnetization projection along the external magnetic field ΔM is calculated by minimizing the modified Gibbs free energy density \tilde{g}^m using an external magnetic field of $\mu_0 H = 10$ mT.

modified Gibbs free energy $\tilde{g}^{(m)}$. As evident from Fig. 6.4(b), no variation of the magnetization ΔM can be observed for electric fields larger than 200 kV/m. Thus, for isotropic in-plane strains ($\eta_1^{(e)} = \eta_2^{(e)} = \eta_1^{(e)} = \eta_2^{(e)}$) and vanishing shear strains ($\eta_6^{(e)} = \eta_6^{(m)} = 0$), the magnetization direction is not affected by the strain state and the magnetization remains constant. However, the isotropic in-plane strain behavior can be broken up by using a ferroelastic/ferroelectric layer. In such kind of materials, the coupled ferroelectric and ferroelastic domains can be reoriented by external electric fields. For example, assuming a tetragonal ferroelectric substrate with the longer polar axis oriented in-plane, this axis will align parallel to the external field, which is applied along the out-of-plane direction, at a critical electric field strength. Since in most ferroelectrics, the ferroelectric and ferroelastic properties are coupled, the reorientation of the polar axis is accompanied by changes of the strain state. This is exemplary shown in Fig. 6.4(a). At low electric fields ($E < 200$ kV/m), where the

polar axis is aligned in-plane, no strain response of the ferroelastic substrate as a function of the external electric field is expected in the tetragonal $4mm$ symmetry. By increasing the external electric field, the electric polarization switches at a critical field strength (e.g. 200 kV/m) into the out-of-plane direction parallel to the external electric field. At this critical field, a jump of the in-plane strain components $\eta_1^{(e)}$ and $\eta_2^{(e)}$ occurs. Figures 6.4(a) and (b) reveal, that this discontinuity results in a large change of the magnetization (ΔM) of the composite structure. Increasing the electric field strength further ($E > 200$ kV/m), the strain response of the single ferroelastic domain is caused by the converse linear piezoelectric effect as described above.

As shown in Figs. 6.4(a) and (b), a finite variation of the projection of the magnetization along the external magnetic field is only observable for $\eta_1^{(m)} \neq \eta_2^{(m)}$ in case of tetragonal ferroelectric materials. However, for piezoelectric materials with lower symmetry, magnetization changes can be obtained even for $\eta_1^{(m)} = \eta_2^{(m)}$. As an example, for a piezoelectric substrate exhibiting a trigonal symmetry, an evolution of the in-plane strains as shown in Fig. 6.4(c) is expected. While the in-plane strains $\eta_1^{(e)}$ and $\eta_2^{(e)}$ are equal, the in-plane shear component $\eta_6^{(e)}$ is finite. Using magnetoelastic theory, the variation of the magnetization can again be calculated. As shown in Fig. 6.4(d), the finite variation of $\eta_6^{(m)} = \eta_6^{(e)}$ as a function of the electric field enables a manipulation of the magnetization in hybrid composite materials. However, by comparing Figs. 6.4(b) and (d), a much larger converse magnetoelectric effect is expected by domain switching in ferroelastic substrate. Although Fig. 6.4 reveals that the variation of the magnetization projection ΔM is not linear as a function of the applied electric field E , an average converse linear magnetoelectric constant $\alpha_{13}^{(c)}$ can be estimated on the basis of Eq. (6.18). In the case of polycrystalline ferromagnetic thin films deposited on top of a piezoelectric/ferroelectric layer, the physical properties of both materials are referred to the same coordinate system. Therefore, the transformation matrix $T_{kk'}$ yields

$$T_{kk'} = \begin{pmatrix} 1 & 0 & 0 & 0 & 0 & 0 \\ 0 & 1 & 0 & 0 & 0 & 0 \\ 0 & 0 & 0 & 0 & 0 & 1 \end{pmatrix}. \quad (6.29)$$

Using this tensor, the average converse linear magnetoelectric constant α_{13} in the case of ferroelastic domain switching displayed in Figs. 6.4(a) and (b) can be calculated to

$$\frac{1}{c}\alpha_{13}^{(c)} \approx \frac{d^{(m)}}{d^{(e)} + d^{(m)}} \cdot 3 \times 10^{-7} \text{ s/m}, \quad (6.30)$$

while the smaller variation of the magnetization caused by the converse linear piezoelectric effect shown in Fig. 6.4 (d) yields

$$\frac{1}{c}\alpha_{13}^{(c)} \approx \frac{d^{(m)}}{d^{(e)} + d^{(m)}} \cdot 4 \times 10^{-9} \text{ s/m}. \quad (6.31)$$

The latter converse linear magnetoelectric constant is, of course, a strong function of the piezoelectric moduli. However, for the calculation shown in Fig. 6.4, piezo-

electric constants, which are around one order of magnitude larger than for typical ferroelastic materials (e.g. BaTiO₃), were used.

Thus, not only piezoelectric materials exhibiting large values of the piezoelectric moduli d_{ij} are interesting for the realization of multiferroic composites, but also ferroelectrics, where abrupt strain changes $\Delta\eta_k^{(e,\text{domain})}$ are expected due to ferroelastic domain reorientations.

Chapter 7

Materials for composite multiferroics

In composite multiferroics, each constituent can be independently selected and optimized to tailor the desired coupling [8]. In the case of strain-mediated magneto-electric effects, the piezoelectric layer should feature an efficient transformation of the applied electric field to elastic strain, while ferromagnetic materials exhibiting large magnetoelastic coupling should be selected for the magnetostrictive constituent (cf. Equation (6.18)).

In recent years, relaxor based ferroelectric materials have become increasingly popular as a substrate material for epitaxially grown thin films (cf. Refs. [477, 478, 481]), since they provide electrically tunable in-plane strains of up to 0.5 % [487]. However, these substrates have several drawbacks, such as the need of high electric field to achieve this strain level [481]. Furthermore, the commonly used materials are based on Pb-containing compounds (e.g. $(1 - x)[\text{Pb}(\text{Mg}_{1/3}\text{Nb}_{2/3})\text{O}_3]x[\text{PbTiO}_3]$ (PMN-Pt)), which is problematic due to the possible Pb loss at high temperatures during the epitaxial growth of the overlying magnetostrictive constituent. Alternatively, in spite of the small converse linear piezoelectric effect, BaTiO_3 is still widely used as the ferroelectric material in composite hybrids (cf. Refs. [20, 424, 447]). Although, the strain achieved by the converse linear piezoelectric effect in BaTiO_3 is around two orders of magnitude smaller than for PMN-Pt [488], BaTiO_3 can provide large strains up to 1% due to ferroelastic domain switching.

In case of the magnetostrictive layer, different ferromagnetic material systems, which offer a large variety of magnetostriction constants, were used in this thesis for multiferroic hybrid structures. On the one hand, crystalline hybrid structures were fabricated using the well known ferrimagnet Fe_3O_4 [380] as well as the double perovskite ferromagnet $\text{Sr}_2\text{CrReO}_6$. The latter exhibits a high Curie temperature well above room temperature [489], strong magnetoelastic effects [490], and is expected to have a high spin polarization at the Fermi level [491]. On the other hand, polycrystalline Ni and $\text{Fe}_{50}\text{Co}_{50}$ thin films were implemented in composite hybrid structures.

In the following, the physical properties of these materials are discussed in the context of strain-mediated multiferroic hybrid systems.

7.1 BaTiO₃ as the ferroelectric material

BaTiO₃ is one of the most widely studied ferroelectric material and was long regarded as prototypic displacive ferroelectric perovskite.¹ Below the Curie temperature T_c of 393 K [493], BaTiO₃ undergoes successive transitions to three different ferroelectric phases as the temperature is lowered [494–496]. Each transition is accompanied by a change of the crystallographic symmetry and the dielectric properties (Fig. 7.1) [497].

In the paraelectric state above 393 K, BaTiO₃ crystallizes in the ideal centrosymmetric cubic perovskite structure with $Pm\bar{3}m$ symmetry. As the temperature is lowered, BaTiO₃ becomes ferroelectric and a finite spontaneous polarization P_s , which is depicted in Fig. 7.1, emerges at 393 K. In this first ferroelectric phase, BaTiO₃ has a tetragonal (T) structure ($P4mm$ symmetry) with polar axes along the original cubic $\langle 100 \rangle_{pc}$ directions. Since there are six equivalent $\langle 100 \rangle_{pc}$ axes, the polar axis can be parallel to any of these axes, which results in ferroelastic and ferroelectric domain structures. The three ferroelastic domains sketched in Fig. 7.1(c) can be denoted as: c -domains with the spontaneous electric polarization $\pm \mathbf{P}_s$ aligned along $[001]$, a_1 -domains with $\pm \mathbf{P}_s \parallel [100]$, and a_2 -domains with $\pm \mathbf{P}_s \parallel [010]$. Within the ferroelectric state, the lattice symmetry is further reduced to orthorhombic (O) with crystal symmetry $Amm2$ (below 278 K). It is convenient to treat the orthorhombic unit cell described by the lattice constants a , b , and c in a pseudo-cubic notation, i.e., as a distortion of the parent cubic cell stable above 393 K. This distortion consists in an elongation of one of the face diagonals of the original cube. Therefore the polar axes are $\langle 110 \rangle_{pc}$, which corresponds to the c -directions in the orthorhombic notation. As a result the unit cells shown in Fig. 7.1 are monoclinic with lattice parameters a_m , c_m , and α_m . The relation between the primitive orthorhombic unit cell (a , b , c) and the pseudo-monoclinic unit cell (a_m , c_m , α_m) is given by $a = a_m$, $b = 2c_m \sin(\alpha_m/2)$, and $c = 2c_m \cos(\alpha_m/2)$. The monoclinic angle of $\alpha_m = 90.14^\circ - 90.15^\circ$ changes only slightly in the temperature range between 174.5 K and 281.2 K [496]. Since twelve equivalent $\langle 110 \rangle_c$ directions are present in the orthorhombic phase, six ferroelastic domains can be distinguished (see Fig. 7.1(c)). A third phase transition occurs at around 183 K accompanied by a symmetry change of BaTiO₃ to rhombohedral (R) (with crystal symmetry $R3c$). Within this third ferroelectric phase the polar axes are $\langle 111 \rangle_{pc}$ with respect to the pseudo-cubic notation leading to a stretch of the original cubic cell along one of the body diagonals, which results in an almost temperature independent rhombohedral angle of $\alpha_r = 89.80^\circ - 89.83^\circ$ [496]. As there are eight equivalent $\langle 111 \rangle_{pc}$ axes, four ferroelastic domains exist (see Fig. 4.11 for comparison).

All three phase transitions are of first order causing an abrupt change of the dielectric constants, ferroelectric polarization, and the lattice constants accompanied by a thermal hysteresis (see Fig. 7.1). By employing the Keve-Abrahams notation, the sequence of the BaTiO₃ phase changes can be summarized as follows [260]: $PPP(m3m) \rightarrow F_cF_cP(4mm) \rightarrow F_cF_cP(mm2) \rightarrow F_cF_cP(3m)$. The first symbol refers to the dielectric state, the second to the elastic state, and the third to the magnetic

¹A detailed description of BaTiO₃ can be found in Refs. [492] and [260].

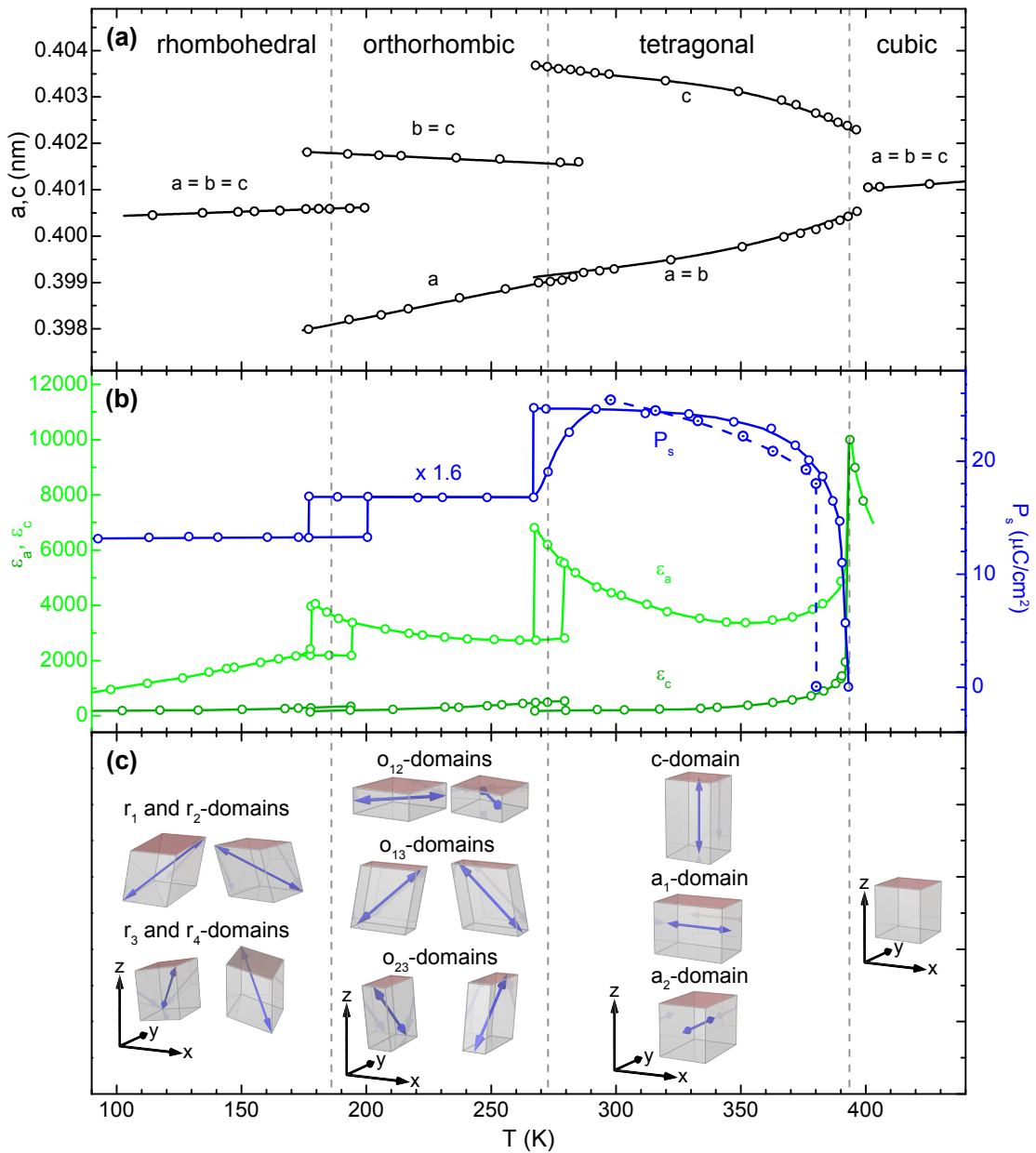


Figure 7.1: Phase diagram of BaTiO₃: (a) lattice constants a , b , and c , (b) dielectric constants ϵ_a and ϵ_c as well as spontaneous polarization P_s , and (c) possible ferroelastic domains of BaTiO₃ as a function of temperature [496, 497]. The phase transition temperatures are indicated schematically by gray dashed lines. The orthorhombic phase (a_o , b_o , and c_o) is displayed in a pseudo-monoclinic setting (a , b , and $\alpha_m = 90.14^\circ - 90.15^\circ$) (see (a)). The two different branches of the dielectric constant observed in the rhombohedral phase can be attributed to domain clamping [492] (see (b)). The measurement of the spontaneous polarization P_s was carried out along the pseudo-cubic [100] direction [497]. To account for the different direction of P_s , the experimental results were multiplied by $\sqrt{2}$ and $\sqrt{3}$ in the orthorhombic and rhombohedral phase, respectively. Newer measurements (blue dashed line) on BaTiO₃ single crystals with better qualities reveal a first order transition at the Curie temperature T_c (see (b)). The different Curie temperatures can be attributed to different Ti concentration in BaTiO₃ [493]. (c) The notation of the possible ferroelastic domains are according to Ref. [274, 498, 499].

state of the crystal. BaTiO_3 is therefore, paraelectric, paraelastic, and paramagnetic in the high temperature cubic PPP-phase with a point group of $(m3m)$. However, the nonmagnetic, ferroelectric, and ferroelastic low temperature phases of BaTiO_3 can be denoted by F_cF_cP . The subscript c describes the coupling of the ferroelectric and ferroelastic order parameter.

Early theories suggested that the phase transitions are classical examples of displacive soft mode type transitions [500]. More recent experiments have reopened the question of the origin of ferroelectricity in BaTiO_3 [501]. While neutron scattering [502] studies confirm the displacive model, x-ray absorption fine structure experiments (XAFS) [503] and the observation of diffuse x-ray scattering [504] seem to contradict this theory and point to an order-disorder type 8-site model [505]. In contrast, nuclear magnetic resonance (NMR) studies observed a coexistence of both displacive and order-disorder components [506]. The displacive model is based on the assumption that the soft mode becomes unstable on cooling through T_c as its frequency goes to zero. As a consequence, the lattice stabilizes with an off-centered Ti atom. On the other hand, an order-disorder transition is characterized by local atomic configurations which do not necessarily share the symmetry elements of the macroscopic crystal. In BaTiO_3 , a local rhombohedral distortion with eight equivalent $\langle 111 \rangle$ displacements (8-site model) was found in all BaTiO_3 phases. In the rhombohedral phase only one of the eight $\langle 111 \rangle$ displacements is occupied. As the temperature increases, hopping processes average out one of the cubic components leading to a $[110]$ orthorhombic average periodic structure. In the same way, additional hopping barriers are overcome at the orthorhombic to tetragonal transition producing a $[100]$ tetragonal structure. At the Curie temperature all sites were occupied and the local displacements average to zero. The difficulties to reveal the nature of the phase transition of BaTiO_3 might also arise from the different time scales of different experimental methods such as NMR and XAFS [506]. Theoretical calculations based on “ab initio” effective Hamiltonian numerical simulations suggest that the long standing problem of the displacive versus the order-disorder character might only be a measurement problem and the instantaneous mechanism of the phase transition in BaTiO_3 corresponds to a mechanism very similar to the 8-site model [507, 508]. However earlier calculations found the transitions to be intermediate between order-disorder and displacive character [509, 510]. Both calculations are based on an effective Hamiltonian developed by Zhong, Vanderbilt, Rabe and Waghmare [509–512].

In this part of the thesis, the ferroelectric as well as ferroelastic properties of BaTiO_3 were calculated using molecular dynamics simulations based on this Hamiltonian [513]. The basic idea of this Hamiltonian is to decrease the number of degrees of freedom from a 15-dimensional atomic displacement vector to a three dimensional amplitude vector representing collective motions of the atoms in each unit cell [514]. A reasonable approximation for the study of phase transitions is to consider (i) local modes $\mathbf{u} = \mathbf{u}(\mathbf{R})$ that roughly represents the polar displacements of the atoms, and (ii) homogeneous η_H and inhomogeneous η_I strains, where the inhomogeneous strain can be expressed as a function of the local acoustic displacement vector $\mathbf{w} = \mathbf{w}(\mathbf{R})$. This corresponds to the assumption that only the lower part of the phonon spec-

trum is relevant for the phase transition. Since BaTiO₃ exhibits 5 atoms in the primitive unit cell, 3 acoustic and 12 optical normal mode coordinates should be considered. But at low energy, only the lowest optical modes (soft modes) and long-wavelength acoustic phonons significantly contribute to the phonon density of states [260]. Following Zhong et al. [510] and Takeshi et al. [514], the effective Hamiltonian can be written as a function of \mathbf{u} and the inhomogeneous and homogeneous strain $\eta = \eta_H + \eta_I$:

$$\begin{aligned} \mathcal{H}^{\text{eff}}(\{\mathbf{u}\}, \eta) = & V^{\text{self}}(\{\mathbf{u}\}) + V^{\text{dpl}}(\{\mathbf{u}\}) + V^{\text{short}}(\{\mathbf{u}\}) + V^{\text{elastic}}(\eta_H, \eta_I) \\ & + V^{\text{coup}}(\{\mathbf{u}\}, \eta) - Z^* \sum_{\mathbf{R}} \mathbf{E} \cdot \mathbf{u}(\mathbf{R}) . \end{aligned} \quad (7.1)$$

$\mathcal{H}^{\text{eff}}(\{\mathbf{u}\}, \eta)$ consists of a self energy $V^{\text{self}}(\{\mathbf{u}\})$, a long range dipole-dipole interaction $V^{\text{dpl}}(\{\mathbf{u}\})$, a short range interaction between soft modes $V^{\text{short}}(\{\mathbf{u}\})$, an elastic energy $V^{\text{elastic}}(\eta_H, \eta_I)$, an interaction between the local modes and the local strains $V^{\text{coup}}(\{\mathbf{u}\}, \eta)$, and finally an electric field \mathbf{E} is taken into account through its vector product with each dipole moment $V^{\text{E}}(\mathbf{u}) = Z^* \sum_{\mathbf{R}} \mathbf{E} \cdot \mathbf{u}(\mathbf{R})$ with the Born effective charge Z^* associated with the soft mode. Z^* can be obtained as $Z^* = \xi_{\text{Ba}} Z_{\text{Ba}}^* + \xi_{\text{Ti}} Z_{\text{Ti}}^* + \xi_{\text{O1}} Z_{\text{O}}^* + \xi_{\text{O2}} Z_{\text{O}}^* + \xi_{\text{O3}} Z_{\text{O}}^*$ from the eigenvector of the soft mode, once the Born effective charges for the ions are known [509]. Note that the braces $\{\}$ denote a set of \mathbf{u} in a simulation supercell. Furthermore the homogeneous strain components $\eta_{H,I}$ are expressed in matrix notation (e.g. $\eta_{H,1} = \epsilon_{11}$, $\eta_{H,4} = 2\epsilon_{23}$).

The local mode self energy $V^{\text{self}}(\{\mathbf{u}\})$ is the summation of the energy of an isolated local mode $E(\mathbf{u}_i)$ at the position \mathbf{R}_i :

$$V^{\text{self}}(\{\mathbf{u}\}) = \sum_i E(\mathbf{u}_i) = \sum_i (\kappa_2 u_i^2 + \alpha u_i^4 + \gamma (u_{ix}^2 u_{iy}^2 + u_{iy}^2 u_{iz}^2 + u_{iz}^2 u_{ix}^2)) , \quad (7.2)$$

where u_i is the absolute value of $|\mathbf{u}_i|$: $u_i = |\mathbf{u}_i|$ and κ_2 , α , and γ are expansion coefficients. $V^{\text{self}}(\{\mathbf{u}\})$ contains anharmonic as well as harmonic contributions. Since the reference structure is cubic, only even-order terms can contribute [510]. Higher-order terms in $V^{\text{self}}(\{\mathbf{u}\})$ do not significantly improve the description of the double-well potentials associated with the ferroelectric instabilities and are therefore neglected [515].

In the long range interaction between local modes $V^{\text{dpl}}(\{\mathbf{u}\})$, only dipole-dipole interactions are considered, since higher order terms tend to be of short range, which is included in the short range contribution $V^{\text{short}}(\{\mathbf{u}\})$. $V^{\text{dpl}}(\{\mathbf{u}\})$ can be expressed as

$$V^{\text{dpl}}(\{\mathbf{u}\}) = \frac{Z^{*2}}{\epsilon_{\infty}} \sum_{i < j} \frac{\mathbf{u}_i \cdot \mathbf{u}_j - 3 (\hat{\mathbf{R}}_{ij} \cdot \mathbf{u}_i) (\hat{\mathbf{R}}_{ij} \cdot \mathbf{u}_j)}{|\mathbf{R}_{ij}|^3} . \quad (7.3)$$

Here, ϵ_{∞} denotes the optical dielectric constant of the material, $\mathbf{R}_{ij} = \mathbf{R}_i - \mathbf{R}_j$, and $\hat{\mathbf{R}}_{ij} = \mathbf{R}_{ij}/|\mathbf{R}_{ij}|$. $|\mathbf{R}_{ij}|$, which appears in Eq. (7.3) in the denominator, should

be strain dependent. Since strain induced dipole-dipole interactions are of higher order, this effect can be neglected [510].

The next term in the potential energy represents the short range interaction $V^{\text{short}}(\{\mathbf{u}\})$. This contribution is caused by short range repulsion and electronic hybridization between two adjacent local modes and two isolated local modes. Up to the third nearest neighbor, $V^{\text{short}}(\{\mathbf{u}\})$ can be written as

$$V^{\text{short}}(\{\mathbf{u}\}) = \frac{1}{2} \sum_{i \neq j} \sum_{\alpha\beta} J_{ij,\alpha\beta} u_{i\alpha} u_{j\beta}, \quad (7.4)$$

where $J_{ij,\alpha\beta}$ is the short range interaction matrix, which depends on \mathbf{R}_{ij} and should decay rapidly with increasing $|\mathbf{R}_{ij}|$. $J_{ij,\alpha\beta}$ can be classified into seven independent interaction parameters, which were calculated in Ref. [510] for a cubic lattice. α and β denote the Cartesian directions $\alpha, \beta = (x, y, z)$. Higher-order terms in $V^{\text{short}}(\{\mathbf{u}\})$ represent anharmonic couplings between neighboring local modes and provide a correction to the local-anharmonicity approximations in $V^{\text{self}}(\{\mathbf{u}\})$. However, Tinte *et al.* found that these terms are small and can thus be neglected [515].

The elastic energy $V^{\text{elastic}}(\eta_{\text{H}}, \eta_{\text{I}})$ is further divided into homogeneous $V^{\text{elastic,homo}}(\eta_{\text{H}})$ and inhomogeneous $V^{\text{elastic,inho}}(\eta_{\text{I}})$ parts. $V^{\text{elastic,homo}}(\eta_{\text{H}})$ is simply given by the elastic energy calculated for cubic symmetry:

$$\begin{aligned} V^{\text{elastic,homo}}(\eta_{\text{H}}) &= \frac{1}{2} N \cdot a_0^3 \cdot c_{ij} \eta_{\text{H},i} \eta_{\text{H},j} \\ &= \frac{1}{2} N \cdot a_0^3 \cdot c_{11} (\eta_{\text{H},1}^2 + \eta_{\text{H},2}^2 + \eta_{\text{H},3}^2) \\ &\quad + N \cdot a_0^3 \cdot c_{12} (\eta_{\text{H},2} \eta_{\text{H},3} + \eta_{\text{H},3} \eta_{\text{H},1} + \eta_{\text{H},1} \eta_{\text{H},2}) \\ &\quad + \frac{1}{2} N \cdot a_0^3 \cdot c_{44} (\eta_{\text{H},4}^2 + \eta_{\text{H},5}^2 + \eta_{\text{H},6}^2), \end{aligned} \quad (7.5)$$

where c_{11} , c_{12} , and c_{44} are components of the elastic stiffness matrix c_{ij} and N is the number of primitive unit cells in the super-cell used for the calculation. The inhomogeneous elastic energy $V^{\text{elastic,inho}}$, which corresponds to bond stretching, bond correlation, and bond bending [510], can be expressed as a function of the local acoustic displacement vector $\mathbf{w}(\mathbf{R}_i)$ of the unit cell at the position \mathbf{R} . Two different invariants have to be fulfilled by the elastic strain energies. First, $V^{\text{elastic,inho}}$ must be invariant under an arbitrary displacement of the lattice as a whole. This ensures that $V^{\text{elastic,inho}}$ can depend only on the differences between nuclear positions. Furthermore, $V^{\text{elastic,inho}}$ must also be invariant under a rigid rotation [516]. Hence, $V^{\text{elastic,inho}}$ can be expressed as an expansion in scalar products of differences between $\mathbf{w}(\mathbf{R}_i)$:

$$\begin{aligned}
V^{\text{elastic, inho}}(\{\mathbf{w}\}) = & \sum_i \left\{ \gamma_{11} [w_x(\mathbf{R}_i) - w_x(\mathbf{R}_i \pm \mathbf{x})]^2 \right. \\
& + \gamma_{12} [w_x(\mathbf{R}_i) - w_x(\mathbf{R}_i \pm \mathbf{x})] [w_y(\mathbf{R}_i) - w_y(\mathbf{R}_i \pm \mathbf{y})] \\
& + \gamma_{44} [w_x(\mathbf{R}_i) - w_x(\mathbf{R}_i \pm \mathbf{y}) + w_y(\mathbf{R}_i) - w_y(\mathbf{R}_i \pm \mathbf{x})]^2 \\
& \left. + \text{cyclic permutations} \right\}, \tag{7.6}
\end{aligned}$$

where $\mathbf{x} = a\hat{\mathbf{x}}$, $\mathbf{y} = a\hat{\mathbf{y}}$, and $\mathbf{z} = a\hat{\mathbf{z}}$. Furthermore \pm indicates that multiple terms have to be summed. The coefficients γ are related to the elastic constants by $\gamma_{11} = a_0^3 \cdot c_{11}/4$, $\gamma_{12} = a_0^3 \cdot c_{12}/8$, and $\gamma_{44} = a_0^3 \cdot c_{44}/8$. The average differential displacements can be expressed as a function of inhomogeneous strain η_{I} : $\eta_{\text{I},1}(\mathbf{R}_i) = \Delta w_{xx}/4$, $\eta_{\text{I},2}(\mathbf{R}_i) = \Delta w_{yy}/4$, $\eta_{\text{I},3}(\mathbf{R}_i) = \Delta w_{zz}/4$, $\eta_{\text{I},4}(\mathbf{R}_i) = (\Delta w_{yz} + \Delta w_{zy})/4$, $\eta_{\text{I},5}(\mathbf{R}_i) = (\Delta w_{xz} + \Delta w_{zx})/4$, and $\eta_{\text{I},6}(\mathbf{R}_i) = (\Delta w_{xy} + \Delta w_{yx})/4$ [510]. Therefore, the elastic energy $V^{\text{elastic}}(\eta_{\text{H}}, \eta_{\text{I}})$ is a function of homogeneous η_{H} and inhomogeneous η_{I} strains.

The coupling between the elastic deformations and the local modes is described in the limit of lowest order by an electrostrictive term [260]

$$V^{\text{coup}}(\{\mathbf{u}\}, \eta) = \frac{1}{2} \sum_i \sum_{\alpha\beta} B_{\alpha\beta} \eta_{\text{I}}(\mathbf{R}_i) u_{\alpha}(\mathbf{R}_i) u_{\beta}(\mathbf{R}_i) \tag{7.7}$$

with the coupling coefficients $B_{\alpha\beta}$. Using a cubic symmetry, there are only three independent coupling constants (B_{1xx} , B_{1yy} , and B_{4yz}) defined in Ref. [510]. Equation (7.7) contains both homogeneous η_{H} and inhomogeneous η_{I} strains and can therefore be separated in a homogeneous $V^{\text{coup, homo}}(\{\mathbf{u}\}, \eta_{\text{H},i})$ and inhomogeneous $V^{\text{coup, inh}}(\{\mathbf{u}\}, \eta_{\text{I},i})$ coupling.

With Eqs. (7.2)-(7.7) the effective Hamiltonian is defined. On the basis of this effective Hamiltonian the physical properties of BaTiO₃ can be simulated by computing the ground-state of the system using density functional theory (DFT) and performing ab initio molecular dynamics (MD) simulations exploiting the results of the DFT calculations, i.e., combining MD and DFT [517]. Using DFT within the local density approximation (LDA) the parameters specifying the effective Hamiltonian were determined by Zhong and coworkers [509, 510]. These parameters can be employed to perform MD calculations. Within MD calculations the validity of classical mechanics to describe ionic motion is assumed. Therefore the time evolution of the displacements \mathbf{u} and \mathbf{w} can be calculated by solving the classical equation of motion:

$$\begin{aligned}
M_{\text{dipole}}^* \frac{d^2 \mathbf{u}_i}{dt^2} &= - \frac{\partial \mathcal{H}^{\text{eff}}(\{\mathbf{u}\}, \eta)}{\partial \mathbf{u}_i} = \mathbf{f}_{\text{dipole},i} \\
M_{\text{acoustic}}^* \frac{d^2 \mathbf{w}_i}{dt^2} &= - \frac{\partial \mathcal{H}^{\text{eff}}(\{\mathbf{u}\}, \eta)}{\partial \mathbf{w}_i} = \mathbf{f}_{\text{acoustic},i}, \tag{7.8}
\end{aligned}$$

where M_{dipole}^* and M_{acoustic}^* are the effective masses for the local soft modes and acoustic modes [514]. The calculation of the forces is done in reciprocal space using

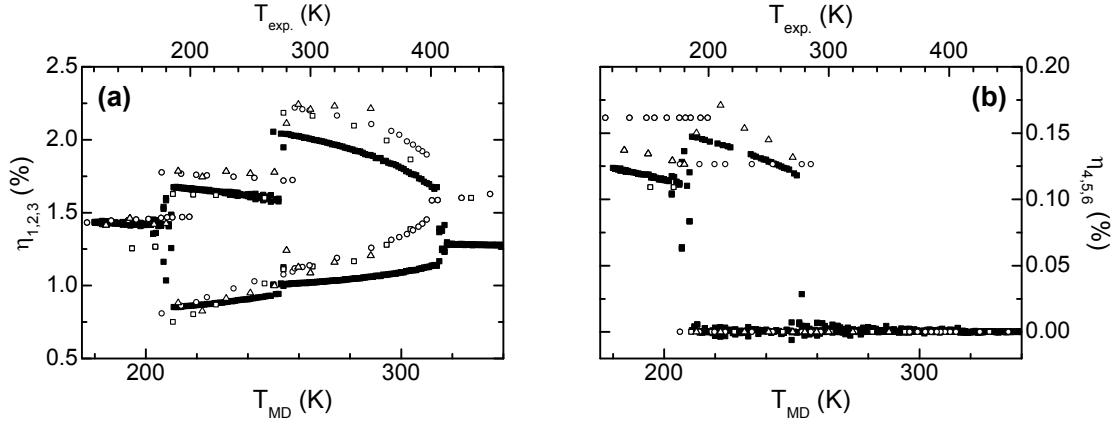


Figure 7.2: (a), (b) Average homogeneous strains $\eta_{H,i} = \eta_i$ with $i = 1, \dots, 6$ as a function of temperature T_{MD} simulated during cooling down using a $16 \times 16 \times 16$ supercell. A pressure of -5 GPa was applied to overcome the underestimation of the phase transition temperatures. For comparison, open symbols represent experimental data from Ref. [495] (open squares), Ref. [496] (open circles), and Ref. [519] (open triangles). Since the temperatures of the experiment and the simulation slightly varies, the experimental data are plotted versus $T_{exp.}$. The strains were calculated relative to the lattice constant of 0.3948 nm, which is derived from local-density approximation simulations.

fast Fourier transformation [512, 514], since the effective Hamiltonian (Eq. (7.1)) and in particular the long range dipole-dipole interaction $V^{dpl}(\{\mathbf{u}\})$ is computationally demanding. The forces in real space are then obtained by the inverse fast Fourier transformation. The MD calculations are performed by using the open source code FERAM developed by Takeshi Nishimatsu [513]. During the calculation the temperature is kept constant within each temperature step in the canonical ensemble using the Nosé-Poincaré thermostat [518]. The homogeneous strain components $\eta_{H,i}$ with $i = 1, \dots, 6$ are derived by solving

$$\frac{\partial}{\partial \eta_{H,i}} [V^{\text{elastic,homo}}(\eta_{H,i}) + V^{\text{coup,homo}}(\{\mathbf{u}\}, \eta_{H,i})] = 0 \quad (7.9)$$

at each time step according to $\{\mathbf{u}\}$ [514]. Furthermore, the local acoustic displacement $\mathbf{w}(\mathbf{R})$ is not treated as described in Eq. (7.8). $\mathbf{w}(\mathbf{R})$ is instead determined by minimizing $V^{\text{elastic,inh}}(\eta_{l,i}) + V^{\text{coup,inh}}(\{\mathbf{u}\}, \eta_{l,i})$. Note that $\eta_{l,i}$ is a function of $\mathbf{w}(\mathbf{R})$. It is worth noting that MD calculations combined with DFT allow to compute the dynamics of polarization as well as structural properties, but not the electronic states [5].

The physical properties of BaTiO_3 were calculated using a $16 \times 16 \times 16$ supercell. Furthermore, the system was thermalized within 60000 time steps, and the properties were averaged over 60000 calculations. Since the LDA calculated lattice constants are typically 1% too small, which leads to large errors in the zero-pressure transition temperatures, a negative pressure of -5 GPa was exerted to overcome this underestimation of phase transition temperatures [510]. Figures 7.2(a) and (b) show the average homogeneous strains $\eta_{H,i} = \eta_i$ with $i = 1, \dots, 6$ of BaTiO_3 as a function of temperature T_{MD} simulated during cooling from 420 K. The strains are calculated

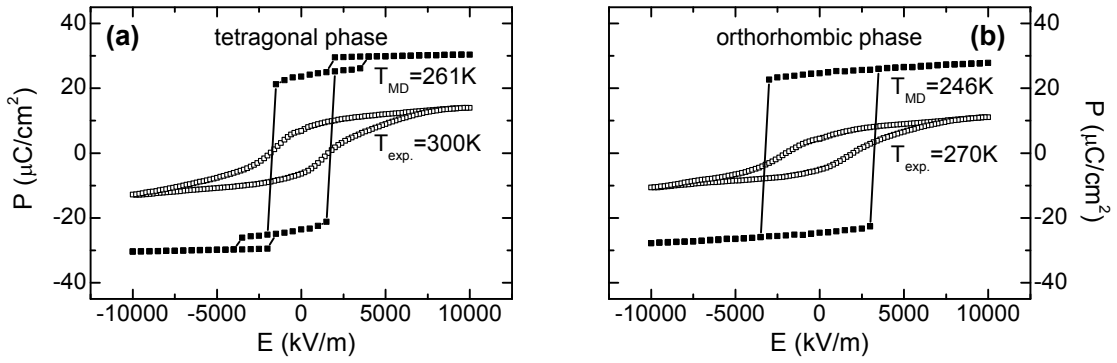


Figure 7.3: Simulations (full symbols) and experimental results (open symbols) of BaTiO₃ $P(E)$ -loops in the (a) tetragonal and (b) orthorhombic phase with the electric field aligned along the out-of-plane direction. The simulations were performed at temperatures of $T_{\text{MD}} = 261$ K and $T_{\text{MD}} = 246$ K using the same parameters as for the simulation in Fig. 7.2. In particular, electrode effects were neglected. These quasi-static $P(E)$ -loops are compared with hysteresis loops measured at $T_{\text{exp.}} = 300$ K and $T_{\text{exp.}} = 270$ K using the static hysteresis mode on an unpoled BaTiO₃ single crystal with 1 mm thickness.

relative to the equilibrium cubic lattice structure derived using LDA simulations ($a = 0.3948$ nm). Thus the obtained strains are non-zero throughout the temperature range. To compare the theoretical results with experimental data, literature values published by different groups are included in Figs. 7.2(a) and (b) [495, 496, 519]. Obviously, the MD calculations reveal the correct sequence of phase transitions. Moreover the difference between theoretical calculated homogeneous strains and the experimental data is acceptable up to a temperature of $T_{\text{exp.}} = 300$ K. However, in spite of the negative pressure applied to the calculations the transition temperatures are still underestimated. Therefore, the temperature scales of the MD calculation T_{MD} and the experiment $T_{\text{exp.}}$ do not coincide (see Fig. 7.2). The underestimation of the phase transition as well as the increased discrepancies for $T_{\text{exp.}} > 300$ K can mainly be attributed to the poor description of thermal expansion effects in the effective Hamiltonian (Eq. (7.1)) and to the errors in first-principles calculations using LDA [515]. The former can be partially corrected using a T -dependent pressure (e.g. $p = -0.005$ GPa/K $\cdot T$ [520]), while the latter can be improved by employing a more accurate generalized-gradient approximation for solids developed by Wu and Cohen [521]. Recently, Nishimatsu and coworkers showed that a clear advancement of the cubic to tetragonal transition temperature in BaTiO₃ can be obtained by utilizing both methods [520]. However, the other ferroelectric transition temperatures are marginally improved. Therefore, further corrections in the description of the effective Hamiltonian as well as on the parameter set derived by DFT will have to be made in the future. In particular, lattice anharmonicity and phonon-strain coupling, which is essential for describing thermal expansion, have to be taken into account more precisely. In the course of this thesis, we will employ the results obtained by MD simulation described above using the parameter set derived by Zhong *et al.* using LDA calculations [509, 510] and using a constant pressure of -5 GPa.

By utilizing the described effective Hamiltonian and the molecular dynamics simulation method, not only the strain state of BaTiO₃ single crystals and thin films can be calculated, but also the electric field dependence of the polarization $P(E)$. Figure 7.3 shows the results of molecular dynamics simulations carried out at $T_{\text{MD}} = 261$ K and $T_{\text{MD}} = 246$ K, i.e., in the tetragonal and orthorhombic phases of BaTiO₃, using the same parameters as for the simulation in Fig. 7.2. Therefore, the $P(E)$ -loops are simulated in a quasi-static method. While these $P(E)$ -loops have almost ideal saturation polarizations (see Fig. 7.1), steps and plateaus are observable in case of $T_{\text{MD}} = 261$ K. This might be attributed to neglected electrodes, which leads to large depolarization fields [514].² However, in $P(E)$ -loops measured at $T_{\text{exp.}} = 300$ K and $T_{\text{exp.}} = 270$ K using the static hysteresis mode (cf. Section 2.2.1) on an unpoled BaTiO₃ single crystal with 1 mm thickness, much lower saturation polarization values were obtained. Since a large saturation polarization value is a hallmark for the quality of BaTiO₃ single crystals [498] (cf. Fig. 7.1(b)), the BaTiO₃ single crystals used in this thesis are not of high quality. However, the simulated and measured coercive fields are almost identical in the tetragonal phase, while a deviation of nearly a factor of two is observed in the orthorhombic phase. The overestimation of the coercive electric fields is well known for theoretical simulations based on effective Hamiltonians [522, 523] and can mainly be attributed to defect-mediated nucleation of domains mainly at ferroelectric interfaces, which is not taken into account in the theoretical simulations [514]. From the theoretical point of view, figure 7.3 reveals that an electric field of around $E = 4$ MV/m is needed to reach the saturation state in both phases.

Figure 7.2 discloses large changes of the strain components η_i with $i = 1, \dots, 6$ at the phase transitions. Therefore, using BaTiO₃ as a ferroelectric material in ferromagnetic/ferroelectric heterostructures different strain states can be achieved by simply varying the temperature. Moreover, BaTiO₃ displays large piezoelectric strains of around 1% associated with ferroelastic domain switching in the tetragonal and orthorhombic phases. Therefore, the magnetic properties of ferromagnetic thin films grown on top of BaTiO₃ can also be altered by employing the converse piezoelectric effect at constant temperature. As discussed in Sec. 6.2.2, the converse piezoelectric effect consists of two parts in ferroelastic materials. One part arises from the multi-domain state of BaTiO₃ and the other from the converse linear piezoelectric effect (see Eq. (6.16)). Assuming an electric field along the pseudo-cubic [001]_{pc}-direction ($E_3 \neq 0$ and $E_{1,2} = 0$), the strain components can be calculated in the tetragonal phase with symmetry $4mm$: $\eta_{1,2} = d_{31}E_3$, $\eta_3 = d_{33}E_3$, and $\eta_i = 0$ for $i = 4, 5, 6$. The maximum in-plane strains $\eta_{1,2}$ generated by the linear piezoelectric effect can be estimated using the highest reported value for $d_{31} = -103.3$ pm/V [488] in the literature³ and an experimental reasonable electric field of 500 kV/m. Thus, the converse linear piezoelectric effect induces an in-plane strain of about $\eta_{1,2} = -0.005\%$. This value can be increased by polarization rotation, i.e., measur-

²A detailed discussion on the simulation of ferroelectric properties with and without electrodes can be found in Section 9.1.1.

³The reported piezoelectric coefficient d_{31} values range from -33.4 pm/V [524] to -103.3 pm/V [488]. This large discrepancy can be mainly attributed to imperfect poling [525].

ing the piezoelectric response along a direction different from the polar axis [484]. Within this method, it is possible to enhance the linear piezoelectric coefficient by around 60% close to the [111] direction at room temperature in the $4mm$ symmetry [526]. Taking the orthorhombic and rhombohedral phases into account, the maximum in-plane strain due to the converse linear piezoelectric effect is estimated to be smaller than $\eta_{1,2} < -2 \times 10^{-4}$ for an electric field of 500 kV/m applied along the $[001]_{pc}$ -direction [527]. This value is about two orders of magnitudes smaller than strains arising from ferroelastic domain switching. Thus, manipulations of the magnetization induced by electric fields via magnetoelastic effects in FM/BaTiO₃ hybrid structures is mainly caused by ferroelastic domain effects rather than the converse linear piezoelectric effect in the temperature range from 396 K to 183 K, i.e., in the tetragonal and orthorhombic phases of BaTiO₃. Therefore, to achieve large magnetoelastic effects in FM/BaTiO₃ hybrid structures a ferroelastic multi-domain state is essential.

In general, in the absence of external electric fields, a ferroelectric material minimizes its free energy by forming different domains [260]. Assuming a single ferroelectric domain, a finite spontaneous polarization creates surface charges, which produce an electric field E_d oriented oppositely to the spontaneous polarization. The electrostatic energy associated with this depolarizing field E_d may be minimized by forming different domains with oppositely oriented polarization. Additionally, the surface charges can be compensated by electric conduction through the crystal or by charges from the surrounding material such as electrodes connected to an electric circuit. Furthermore, the splitting of a ferroelectric crystal into a multi-domain state also occurs due to the reduction of the mechanical stress fields and therefore the elastic energy [528]. Since the domain walls themselves carry energy, the resulting domain configuration will be such that the sum of the domain wall energy, crystal surface energy, and elastic and electric fields energy is minimal [260].⁴

The type of domain walls depends also on the symmetry of the crystal [531].⁵ For example, cooling down a BaTiO₃ crystal from the paraelectric cubic phase to the tetragonal phase at room temperature, the emerging c , a_1 , and a_2 domains are separated by 180° or by 90° domain walls. As can be seen in Fig. 7.4(a), 180° domain walls reduce the effects of the depolarizing electric field, but the formation of these domains do not alter the elastic energy. Therefore, 180° domain walls are pure ferroelectric walls, separating antiparallel polarizations. In contrast, 90° domain walls, which separate regions exhibiting polarizations aligned perpendicular to each other, also minimize the elastic energy. Thus, 90° domain walls are both ferroelectric and ferroelastic walls. Since domain walls can only exist if the two domains meet without infinite stresses or cracks in the bulk of an infinite crystal, the spontaneous strain of neighboring domains must be equal in the plane of the domain wall. This is called mechanical compatibility [260]. Due to the difference in a and c lattice constants in the tetragonal phase of BaTiO₃ (see Fig. 7.1), the

⁴A detailed calculation of the ferroelectric domain walls in BaTiO₃ based on the phenomenological Landau-Ginzburg-Devonshire theory can be found in Refs. [529, 530].

⁵The domain structure also depends on extrinsic effects such as defects or the history of the crystal preparation.

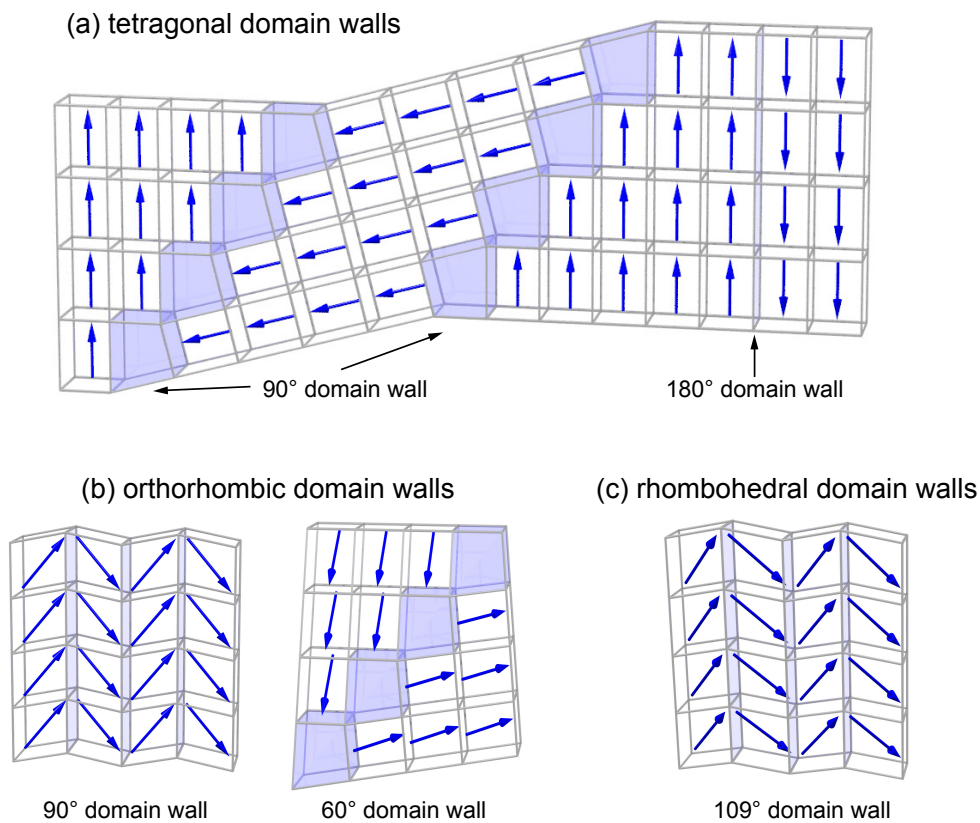


Figure 7.4: Domain walls in the (a) tetragonal, (b) orthorhombic, and (c) rhombohedral phases of BaTiO_3 . For simplicity, not all possible types of domain walls are shown in each phase. The blue arrows depict the polarization vector \mathbf{P} .

mechanical compatibility leads to wedge-shaped 90° domain walls (see Fig. 7.4(a)) [532]. Across a 90° domain wall, the angle of the polarization of adjacent domains differs from 90° by $2 \cdot \arctan \frac{c}{a} \approx 0.57^\circ$. This difference leads to an increase of the depolarization energy, since $\nabla \cdot \mathbf{P}$ is finite at the domain boundary, which acts as the source for a depolarization field [260]. As the wedge shaped angle is small, the increase of the depolarization energy can be neglected compared to the reduction of the elastic energy due to wedge shaped domain boundaries. The second condition for the stability of a 90° domain wall is that no charge is accumulated on the wall, since this would lead to $\nabla \cdot \mathbf{P} \neq 0$. This requires a “head-to-tail” arrangement of the polarizations of the adjacent domains in ideal non-conducting ferroelectrics. The thickness of wedge-shaped 90° domain walls is more than one magnitude larger than for 180° domain walls.⁶ While 180° domain boundaries are very thin ($0.5 - 2 \text{ nm}$), the energy of the domain wall (10 mJ/m^2) is more than twice as large as the energy of 90° domain walls [260], indicating a higher mobility of 90° domain walls. By repeating the domain sequence displayed in Fig. 7.4(a), different domain patterns can be formed, such as laminar and square-net structures [534].

⁶Large discrepancies exist in the literature for theoretically and experimentally determined BaTiO_3 90° domain wall widths (see Ref. [533] and references therein).

Below the second and third phase transitions, BaTiO₃ crystals become highly twinned [534, 535]. In the orthorhombic phase, in principle, three different mechanically compatible domain walls exist: 60°, 90°, and 180° walls [492]. In Fig. 7.4(b) only the 60° and 90° domain walls are shown for simplicity. 90° domain walls are parallel to pseudo-cubic {001}_{pc} planes, which is equivalent to the orthorhombic {110}_o planes, resulting in a twin structure with an angle of $2\alpha_m - 180^\circ \approx 0.3^\circ$. As can be seen in Fig. 7.4(b), no surface distortion is found at orthorhombic 90° domain walls. In contrast, 60° domain walls alter the pseudocubic (001) surface, forming 60° wedges. These domain walls are parallel to pseudo-cubic {011}_{pc} planes ({111}_o planes), resulting in twinning on {011}_{pc} planes. The angle between the planes across the domain boundary is $90^\circ - 2 \arctan(c_m/a_m) \approx 0.4^\circ$. Furthermore, 180° walls separate domains with antiparallel electric polarizations similar to the tetragonal phase. While the width of 90° and 180° domain walls is around 0.7 nm, which is similar to 180° domain boundaries in the tetragonal phase, 60° walls exhibit a higher thickness of around 3 nm. In the rhombohedral phase, 71°, 109°, and 180° domain walls exist (cf. Section 4.4.1). As an example, Fig. 7.4(c) shows the twin structure due to 109° walls. In this phase the domain walls are pseudocubic {100}_{pc} planes [492].

Figures 7.4 and 7.1(c) schematically show that the three ferroelectric phases of BaTiO₃, which can be simply addressed by varying the temperature, exhibit different ferroelastic domains. All these electrically addressable ferroelastic domains impose different strain states in the overlying ferromagnetic thin film, which can alter the magnetization due to magnetoelastic effects. Therefore, using BaTiO₃ as ferroelectric layer in multiferroic composite structures, large converse magnetoelectric effects are expected due to ferroelastic domain switching.

7.2 Crystalline ferromagnetic materials for FM/BaTiO₃ hybrid structures

Various ferromagnetic materials (FM) exhibiting different magnetostriction constants were used for FM/BaTiO₃ hybrid structures in this thesis. In particular, crystalline ferromagnetic materials fabricated using pulsed laser deposition and polycrystalline ferromagnets deposited by electron beam evaporation on BaTiO₃ substrates are utilized for magnetoelectric composite systems (cf. 2.1).

7.2.1 Magnetite (Fe₃O₄)

Magnetite, Fe₃O₄, is known since ancient times. It was discovered 2500 years ago, but it still attracts significant attention due to its interesting magnetic and electronic properties [131]. Fe₃O₄ has a ferrimagnetic ordering with a transition temperature of 850 K [380], which is caused by the interaction of Fe³⁺ and Fe²⁺ occupying different sites in the Fe₃O₄ inverse spinel lattice AB₂O₄ [536, 537]. While A denotes the tetrahedral sites occupied by only one oxidation state (Fe³⁺), a mixed oxidation

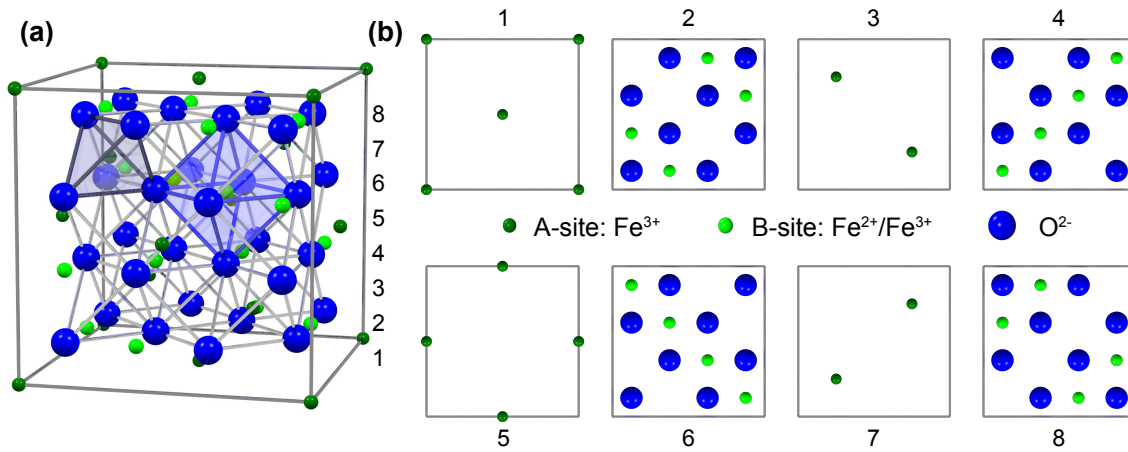


Figure 7.5: (a) Inverse spinel lattice AB_2O_4 of Fe_3O_4 in the cubic $Fd\bar{3}m$ symmetry: The tetrahedrally coordinated A sites and octahedrally coordinated B sites are depicted as dark green and light green spheres, respectively. The A sites are occupied by Fe^{3+} , while Fe^{2+} and Fe^{3+} are present on the B sites. One tetrahedron and one octahedron are exemplary highlighted. (b) Layer-by-layer structure and A - and B -site termination of Fe_3O_4 . The crystal structure of Fe_3O_4 is built up by four stoichiometric sub-units (1 and 2, 3 and 4, 5 and 6, 7 and 8). Fe_3O_4 thin films can have two differently terminated surfaces. While $Fe(A)$ -terminated surfaces (1, 3, 5, and 7) contain Fe cations on tetrahedron A -sites, $FeO_2(B)$ -terminated surfaces (2, 4, 6, and 8) have Fe cations on octahedron B sites

state (Fe^{3+} and Fe^{2+}) is present at the octahedrally coordinated B sites. Both sites are schematically shown in Fig. 7.5(a).

The oxygen mediated exchange interaction between the iron $3d$ cations leads to moments on the A -site (Fe^{3+}), which are parallel to each other and antiparallel to all moments on the B -site (Fe^{3+} and Fe^{2+}). Thus, the trivalent moments compensate each other out and the saturation magnetization is given by the divalent Fe^{2+} resulting in $4 \mu_B/f.u.$. The saturation magnetization of $4 \mu_B/f.u.$ derived within this simple ionic picture is confirmed by recent experiments using spin-dependent Compton scattering [538]. Not only the strong magnetic behavior well above room temperature, but also a high negative spin polarization up to 80%,⁷ which was confirmed by theoretical calculations [541, 542] and different experiments [543, 544], makes Fe_3O_4 a promising candidate for applications in the field of spintronics [545, 546].

Moreover, a pronounced magnetostriction can be observed in Fe_3O_4 . In Fig. 7.6(a) the magnetostriction constants measured by Arai and coworkers along the [100] and [111] direction are shown as a function of temperature [547]. The temperature dependence can be fitted in the temperature range of 170 K to 300 K using first-order polynomials.⁸ Therefore, the described physical properties as well as the good epitaxial growth of Fe_3O_4 thin films on perovskite substrates [548] makes Fe_3O_4 a suitable compound for crystalline FM/ $BaTiO_3$ hybrid structures. To calculate the magnetoelastic response in $Fe_3O_4/BaTiO_3$ hybrids, the knowledge of the magnetoe-

⁷The measured spin polarization of Fe_3O_4 depends strongly on the surface orientation and surface states ([539, 540] and references therein).

⁸ $\lambda_{100}(T) = -8.92 \times 10^{-7} - 4.5 \times 10^{-8} \cdot T$; $\lambda_{111}(T) = 25.93 \times 10^{-6} + 1.8 \times 10^{-7} \cdot T$

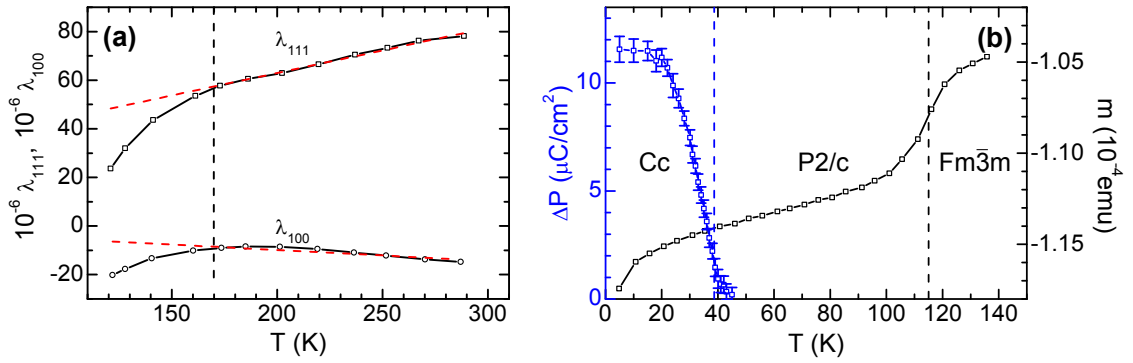


Figure 7.6: (a) Temperature dependence of the magnetostriction constants λ_{100} and λ_{111} for bulk Fe_3O_4 after Arai *et al.* [547]. Both constants are fitted using first-order polynomials (red dashed lines). The fits are valid for temperatures above 170 K (black dashed line). (b) Magnetic moment m and the switchable polarization P reveal a multiferroic state of Fe_3O_4 below 38 K. The magnetic moment was measured in a magnetic field of 0.01 T after zero field cooling and the PUND (positive-up-negative-down) method [153] was employed to measure the switching polarization $\Delta P = 2P_r$. The Verwey transition at around 115 K and the onset of the switchable polarization are marked by vertical dashed lines. Furthermore, the assumed evolution of the crystal symmetry ($Fd\bar{3}m$ - $P2/c$ - Cc) is shown. The data were taken from Alexe *et al.* [131].

lastic coupling B_i is essential (see Eq. (6.4)). In the bulk limit, the magnetoelastic stresses B_i can be calculated using Eq. (6.5). For this purpose, the elastic behavior described by Schwenk *et al.* for temperatures larger than 150 K is used in the following [549].⁹

However, in spite of the extensive research, there are still conflicting reports concerning the behavior of Fe_3O_4 at low temperatures [550, 551]. Fe_3O_4 undergoes a first order phase transition (Verwey transition) at $T_V \approx 120$ K [552] accompanied by a structural transition from a face centered cubic structure $Fd\bar{3}m$ with lattice constant $a = 0.83941$ nm [553, 554] (see Fig. 7.5(a)) to a monoclinic structure.¹⁰ The change of the physical properties below T_V , such as electrical conductivity [559], magnetism [560], thermal expansion [561] and specific heat [562, 563], might be caused by a charge ordering of the Fe^{2+} and Fe^{3+} ions, which was first proposed by Verwey [564]. The presence [550, 565–569] or absence [551, 570–572] of charge ordering in Fe_3O_4 as well as the detailed charge ordering pattern are a matter of intense theoretical and experimental research in recent years [132, 573]. As pointed out in Section 3.1, charge ordering can induce ferroelectricity by a noncentrosymmetric $\text{Fe}^{2+}/\text{Fe}^{3+}$ ordered pattern and can therefore lead to multiferroicity in Fe_3O_4 . Indeed, ferroelectric switching was observed in Fe_3O_4 below around 38 K (see Fig. 7.6(b)) [131]. The difference between the onset of switching polarization and the Verwey temperature was explained by a change of the $P2/c$ monoclinic symmetry,

⁹ $c_{11} - c_{12} = 9.8 \times 10^{10} \text{ N/m}^2 - 1.2 \times 10^7 \text{ 1/K} \cdot T$; $c_{44} = 6.4 \times 10^{10} \text{ N/m}^2 \cdot (T - 66 \text{ K}) / (T - 56 \text{ K})$

¹⁰Up to now, the crystal structure at $T < T_V$ is still not completely understood. Newer measurements suggest a triclinic [555] or monoclinic structure with either $P2/c$ [556] or Cc [557] symmetry, which is also found to be the ground state from theoretical calculations [558].

which prohibits ferroelectricity, to a Cc monoclinic symmetry allowing spontaneous polarization at 38 K. This transition might be accompanied by a transfer from a full charge order pattern to a mixed-charge order state [131, 132]. Furthermore, a local magnetoelectric effect was recently detected in Fe_3O_4 using nonreciprocal x-ray scattering [574] as well as a magnetically addressable polarization [575]. Therefore, Fe_3O_4 seems to be not only the oldest magnetic material but also the first magnetoelectric multiferroic compound known to mankind. Until today, in our Fe_3O_4 thin films fabricated on MgO substrates, we could not clearly detect charge ordering using resonant x-ray diffraction techniques confirming the results found by the group of J. Garcia [551] and the recent critical statements by S.D. Matteo *et al.* [576, 577]. Furthermore, no clear indication of ferroelectricity in Fe_3O_4 thin films grown on TiN buffered MgO substrates was found. Here, one crucial parameter seems to be the choice of the bottom and top electrode material [131, 578]. However, resonant x-ray diffraction experiments as well as dielectric measurements will be continued in the near future.

In the scope of this thesis, Fe_3O_4 is only regarded as a “single-ferroic” ferromagnetic material in FM/ BaTiO_3 hybrids exhibiting a pronounced magnetoelastic effect. $\text{Fe}_3\text{O}_4/\text{BaTiO}_3$ hybrids were recently investigated by different groups, mainly by exploiting the phase transitions of BaTiO_3 [579–582]. In these studies, large discontinuities of the magnetic behavior were observed at the temperatures corresponding to the phase transition of BaTiO_3 . However, Vaz and coworkers suggest that the quantitative explanation of this behavior is more complex than a simple elastic coupling via epitaxy [424]. Therefore, additional contributions than the pure elastic approach discussed in Section 6.2.2 might be taken into account to describe the behavior of FM/ BaTiO_3 hybrids.

The applied strain also alters the electronic structure in Fe_3O_4 . Theoretical calculations reveal that strain reduces the calculated band gap of the majority spin band and destroys the half-metallic state at high in-plane strains of -1.3% and 2.1% [542]. The loss of the half metallic behavior can be related to charge imbalance effects at the interface of Fe_3O_4 and BaTiO_3 [583]. By incorporating oxygen vacancies into the structure, the half-metallic ground state is recovered [432, 583]. Therefore, oxygen vacancies are one of the candidates among the native defects for restoring the halfmetallicity near the interface of $\text{Fe}_3\text{O}_4/\text{BaTiO}_3$ hybrid systems. Moreover, an enhancement of the magnetoelectric coupling was found at the interface for oxygen deficient $\text{Fe}_3\text{O}_4/\text{BaTiO}_3$ hybrids [432].

The $\text{Fe}_3\text{O}_4/\text{BaTiO}_3$ hybrid structures investigated in this thesis were fabricated using pulsed laser deposition monitored by an in-situ high pressure RHEED system (cf. Section 2.1.2). In contrast to Fe_3O_4 thin films grown on lattice matched MgO (001) substrates with a lattice mismatch of -0.3% , slightly different growth parameters of Fe_3O_4 thin films fabricated on BaTiO_3 (001) were found to be ideal. While a substrate temperature of 593 K was used for the growth of Fe_3O_4 thin films on MgO substrates, the optimum substrate temperature was found to be 733 K for the deposition of Fe_3O_4 on BaTiO_3 , i.e., in the cubic phase of BaTiO_3 . The increase of the substrate temperature maintains a flat surface of the BaTiO_3 substrate, and Fe_3O_4 thin films with acceptable crystalline quality as well as good physical prop-

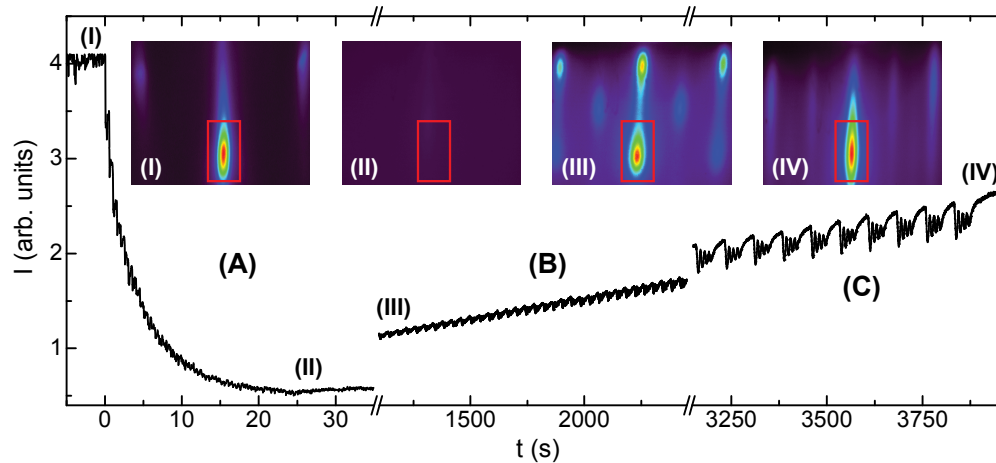


Figure 7.7: Intensity evolution of the RHEED (00) spot monitored during the fabrication of a 64 nm thick Fe₃O₄ thin film on a BaTiO₃ substrate. The intensity was integrated within the red rectangle around the (00) spot marked in the RHEED patterns, which are shown in the upper part of the figure. The growth process can be divided into three main steps: highly disordered growth (A) - three dimensional growth mode (B) - layer-by-layer growth mode (C). The time at which the RHEED patterns shown in the inset are recorded is marked by (I)-(IV).

erties, such as high saturation magnetizations and pronounced Verwey transitions, are obtained. The remaining growth parameters are identical to the well established growth of Fe₃O₄ on MgO [584]. The thin films were deposited in an atmosphere of pure argon with a pressure of 1.6×10^{-3} mbar, a laser fluence at the target of 3.1 J/cm^2 and a repetition rate of 2 Hz.

The growth process is illustrated in Fig. 7.7 on the basis of the intensity evolution of the RHEED (00) spot, which was recorded during the growth of a 64 nm thick Fe₃O₄ thin film on BaTiO₃. The RHEED pattern of the BaTiO₃ substrate (I) shown in the upper part of Fig. 7.7 reveals three spots, which belong to the first Laue circle and can be indexed with $(\bar{1}1)$, (00), and $(1\bar{1})$ (cf. Fig. 4.3). At the beginning of the deposition, the high intensity of the (00) spot drastically decreases. At around 25 s (II), the deposition was stopped. The almost vanished intensity of the RHEED reflections indicates a highly disordered and nearly amorphous growth mode. This behavior is mainly caused by the high lattice mismatch of Fe₃O₄ and BaTiO₃ of 4.7% at the growth temperature.¹¹ Due to this large compressive strain, the critical thickness of pseudomorphic growth is small and hence the Fe₃O₄ thin film relaxes by creating a high density of dislocations in the early stage of the growth. Further deposition leads to a three dimensional crystalline growth indicated by a checkerboard RHEED pattern (cf. RHEED patten (III) in Fig. 7.7). This three dimensional growth mode fades into a two dimensional growth mode with increasing intensity and RHEED oscillations emerge. In the last stage of the growth process ($t > 3000$ s), a real two dimensional layer-by-layer growth mode can be

¹¹The thermal expansion coefficient $\alpha_{\text{Fe}_3\text{O}_4} = 15.26 \times 10^{-6} \text{ 1/K}$ of Fe₃O₄ [585] and the unit cell parameters published by Shebanov [496] were used for the calculation of the lattice mismatch.

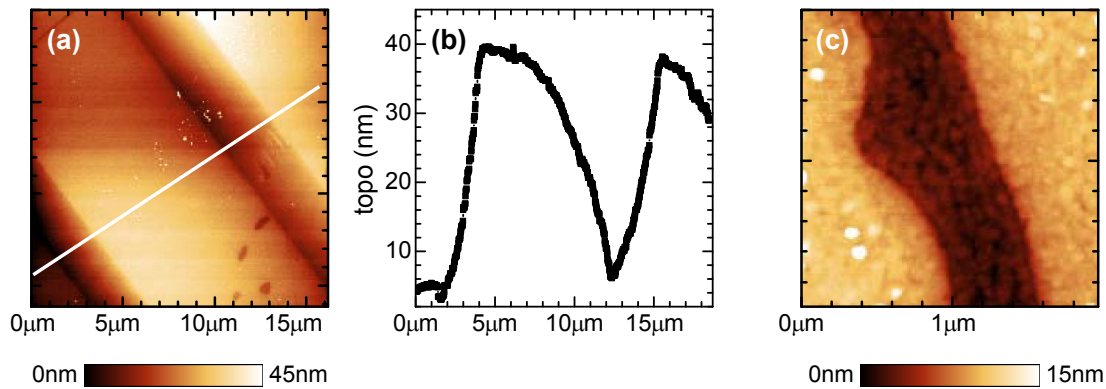


Figure 7.8: Atomic force microscopy images of a 64 nm thick Fe_3O_4 thin film deposited on a BaTiO_3 substrate. The experiments were carried out at room temperature by Denny Köhler, Technische Universität Dresden. The large area displayed in (a) and the line scan shown in (b) reveal a step-like terrace structure, which is caused by a ferroelastic a - c domain structure in the BaTiO_3 substrate. (c) The scan of a smaller area reveals small droplets on the surface of Fe_3O_4 .

obtained. In this stage, one unit cell of Fe_3O_4 indicated by four RHEED oscillations (cf. RHEED pattern (IV) in Fig. 7.5) was deposited followed by a growth interruption of 30 s allowing the film surface to relax. At the end of the growth (cf. (IV) of Fig. 7.7 (IV)), the RHEED pattern is streaky but shows no indication of transmission spots indicating a smooth surface in contrast to the RHEED pattern recorded at (III). As the lattice constant of Fe_3O_4 is about twice as large as the lattice constant of BaTiO_3 at 733 K, the RHEED pattern reveals stripes at positions half the spacing of the diffraction spots for BaTiO_3 . In total, the growth of Fe_3O_4 on BaTiO_3 can be divided into three main steps. First an almost amorphous growth was observed at the beginning of the deposition (A). Then a three dimensional growth mode was detected (B), which evolves into a two dimensional one and finally, a true layer-by-layer growth mode was achieved (C).

This layer-by-layer growth mode should result in a low surface roughness. Atomic force microscopy (AFM) measurements by Denny Köhler, Technische Universität Dresden, shown in Fig. 7.8 reveal a step-like terrace structure, which can be attributed to a ferroelastic a - c domain structure in the BaTiO_3 substrate (Fig. 7.4(a)), since the AFM measurements were carried out at room temperature in the tetragonal phase of BaTiO_3 . However, within one terrace, a surface roughness between $2.5 \text{ nm}_{\text{RMS}}$ and $0.8 \text{ nm}_{\text{RMS}}$ depending on the scanned area were observed. The larger surface roughness is caused by small droplets visible in Fig. 7.8(c). However, the AFM measurements indicate that $\text{Fe}_3\text{O}_4/\text{BaTiO}_3$ hybrids can be fabricated exhibiting a low surface roughness.

However, the highly disordered growth at the beginning of the deposition, which is mainly caused by the high lattice mismatch, certainly influences the structural properties of Fe_3O_4 thin films on BaTiO_3 substrates. In Fig. 7.9(a), x-ray diffraction measurements around the Fe_3O_4 (004) reflection of a Fe_3O_4 thin film grown on a BaTiO_3 substrate are shown. The reciprocal space map and the q -scans depicted in

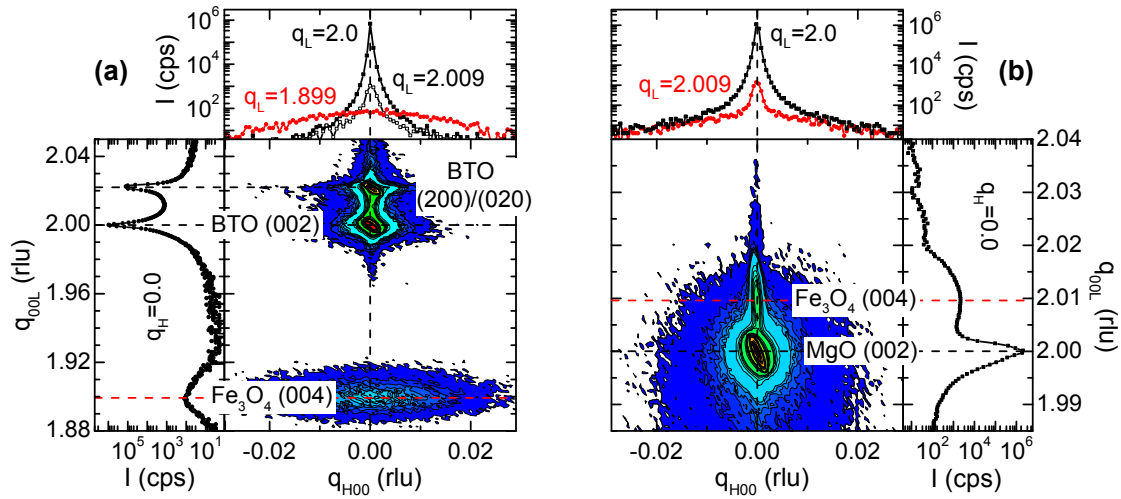


Figure 7.9: X-ray diffraction measurements on Fe₃O₄ thin films grown on (a) BaTiO₃ (BTO) and (b) MgO substrates. The splitting of the BaTiO₃ substrate reflection into BaTiO₃ (002) and BaTiO₃ (200)/BaTiO₃ (200) indicate the presence of a ferroelastic multi-domain state (*c*- and *a*-domains) in the BaTiO₃ substrate. The reciprocal lattice units (rlu) are calculated with respect to BaTiO₃ (001), i.e., the *c*-domains of BaTiO₃. This definition of the reciprocal lattice units will be used in reciprocal space maps of FM/BaTiO₃ hybrid structures throughout this thesis.

the upper and left part of the figure reveal a crystalline growth of the Fe₃O₄ thin film. However, the q_{H00} -scan along the [100] direction at $q_L = 1.899$ rlu discloses a large mosaicity in the out-of-plane direction. This is confirmed by the full width at half maximum (FWHM) of around 0.65° of the rocking curve of the Fe₃O₄ (004) reflection. This high mosaic spread can be mainly attributed to two effects: the large lattice mismatch of Fe₃O₄ thin films grown on BaTiO₃ substrates and the ferroelastic multi-domain nature of BaTiO₃. The effect of the former is illustrated by comparing the structural data of a Fe₃O₄ thin film grown on a BaTiO₃ substrate (see Fig. 7.9(a)) with results of x-ray diffraction measurements around the Fe₃O₄ (004) reflection of a Fe₃O₄ thin film grown on a lattice matched MgO substrate displayed in Fig. 7.9(b). The mesh scan and the q_{H00} -scan along the [100] direction at $q_L = 2.009$ rlu reveal a much smaller mosaic spread compared to Fe₃O₄ thin films grown on BaTiO₃ substrates. This result can be explained by the generation of a high density of dislocations during the process of strain relaxation. The second reason for the low crystalline quality can be found in the ferroelectric nature of the BaTiO₃ substrate. Crossing the ferroelectric transition temperature of around 393 K while cooling the sample from the growth temperature to room temperature, the large strain of more than 1% between *c*- and *a*-domains in the tetragonal phase of BaTiO₃ causes crystalline defects, which increase the measured mosaicity. Furthermore the measurements in Fig. 7.9 are performed without an electric field applied to the BaTiO₃ substrate. Figure 7.9(a) reveals a splitting of the BaTiO₃ (002) reflection into two distinct spots at around $q_L = 2.0$ rlu and $q_L \approx 2.02$ rlu, which correspond to *c*- and *a*-domains, respectively. These domains impose different strains into the Fe₃O₄ thin film leading to a widening of the rocking curve. However, by applying

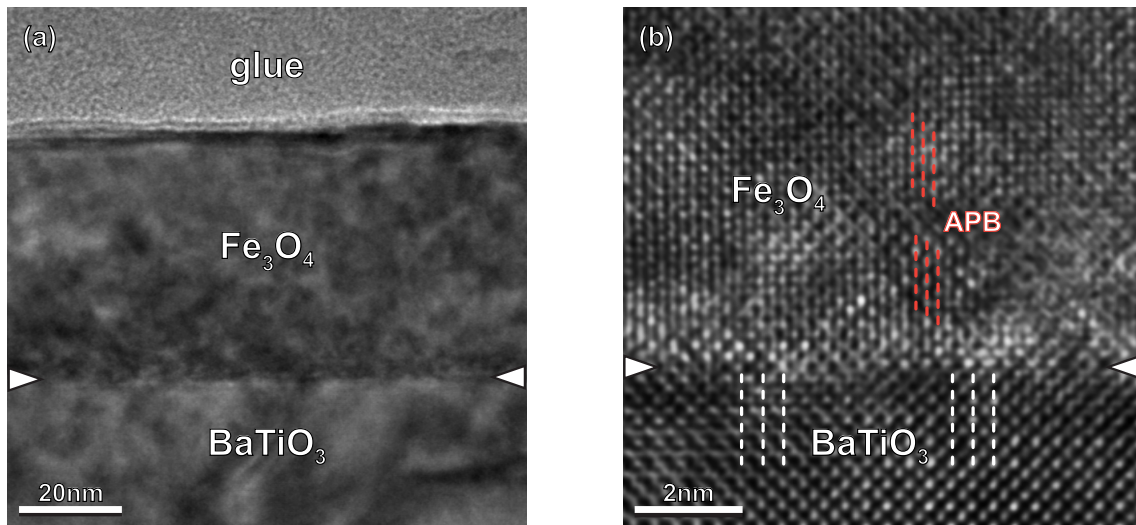


Figure 7.10: (a) Low-magnification and (b) high resolution transmission electron microscopy TEM images of a 50 nm thick Fe_3O_4 thin film grown on a BaTiO_3 substrate. The interface is marked by white triangles. An anti-phase boundary (APB) is located between the red dashed lines. Furthermore, discontinuities at the interface is indicated by white dashed lines. The measurements were performed by Sven-Martin Hühne, Universität Bonn.

an electric field of 400 kV/m along the out-of-plane direction, a ferroelastic single domain state consisting of nearly 100% c -domains can be achieved. X-ray diffraction experiments under this condition reveal a reduction of the FWHM of the rocking curve around the Fe_3O_4 (004) reflection by around 0.05° , which is strongly dependent on the ferroelastic domain configuration of the sample. Furthermore, the room temperature in-plane and out-of-plane lattice constants of (0.8296 ± 0.0008) nm and (0.8492 ± 0.0005) nm indicate a strained Fe_3O_4 thin film exhibiting a compressive in-plane strain of -1.2% and a tensile out-of-plane strain of $+1.2\%$ with respect to the bulk values. This is in contrast to x-ray diffraction measurements published recently [580, 582]. However, the measurements presented in Refs. [580, 582] were performed without any electric field applied to the sample, i.e., in a ferroelastic multi-domain state. The in-plane and out-of-plane strain yields a Poisson ratio of 0.33, which is in agreement with Ref. [549]. Assuming Fe_3O_4 thin films, which are fully clamped to the BaTiO_3 substrate, a remaining in-plane strain of -0.8% at the growth temperature can be calculated by employing the thermal expansion of Fe_3O_4 [585] and the phase diagram of BaTiO_3 [496]. This implies, that Fe_3O_4 thin films relax only partially during the deposition.

This relaxation should result in the formation of dislocations and so-called anti-phase boundaries (APB). APB are a disruption of cation chains in a continuous oxygen lattice, resulting from two symmetry breakings. First, the lattice constant of BaTiO_3 at the growth temperature ($a_{\text{BaTiO}_3} = 0.4031$ nm) is nearly half that of Fe_3O_4 ($a_{\text{Fe}_3\text{O}_4} = 0.8445$ nm) leading to a disruption of the translation symmetry and second, the symmetry of BaTiO_3 in the cubic phase ($Pm3m$) is higher than the symmetry of Fe_3O_4 ($Fd3m$) [586]. As a result, BaTiO_3 unit cells rotated by 90° around an axis

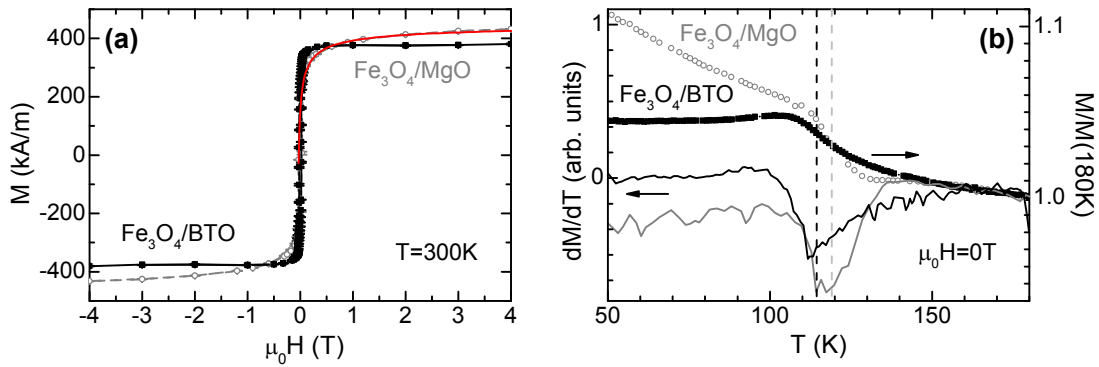


Figure 7.11: Magnetic properties of Fe₃O₄ thin films fabricated on a BaTiO₃ (001) (BTO) (black full symbols) and a MgO (001) (gray open symbols) substrate. (a) Magnetization as a function of the applied magnetic field measured at 300 K reveal a high density of anti-phase boundaries in case of Fe₃O₄/MgO thin films. The magnetic saturation process of the antiferromagnetically coupled anti-phase boundaries (APB) is fitted by using the function $(1 - b/H^{0.5})$ (red line) with $b = 423 \sqrt{\text{A/m}}$. (b) Normalized remanent magnetization (symbols) as well as the derivative of the magnetization (lines) as a function of temperature are shown around the Verwey transition. The transition temperatures of both thin films are indicated by dashed lines. The data were taken in zero applied field with increasing temperature after field cooling in 7 T.

perpendicular to the interface fall onto themselves, but Fe₃O₄ does not (see Fig. 7.5 and Fig. 7.1). Furthermore, recently, it was shown that in systems exhibiting large lattice mismatch, partial dislocations can form APB [587]. Therefore, APB can not only be considered as natural growth defects but also as an additional strain-relaxation mechanism, which can be observed by transmission electron microscopy (TEM) (cf. Section 2.1.4). In Figs. 7.10(a) and (b), cross-sectional low-magnification and high resolution TEM images recorded by Sven-Martin Hühne, Universität Bonn, of a 50 nm thick Fe₃O₄ thin film grown on a BaTiO₃ substrate are shown. The low-magnification TEM image reveals a continuous and homogeneous Fe₃O₄ thin film with no grain boundaries. However, using higher magnification, different defects are visible in the Fe₃O₄ thin film (see Fig. 7.10(b)). First, the interface of BaTiO₃ and Fe₃O₄ is not continuous confirming the partial release of the compressive strain at the interface. Furthermore, APBs are observed within the Fe₃O₄ thin film. These APBs strongly influence not only the structural properties, but also the electronic and magnetic behavior of Fe₃O₄ thin films [588–590].¹²

The magnetic behavior of Fe₃O₄ thin films grown on a lattice matched MgO as well as on a BaTiO₃ substrate is shown in Fig. 7.11. The magnetic field dependent magnetization $M(H)$ hysteresis loops (see Fig. 7.11(a)) measured at 300 K reveal a high saturation magnetizations up to $M_s = 438 \text{ kA/m}$, which corresponds to $3.5 \mu_B/\text{f.u.}$. A slightly lower M_s of $3.1 \mu_B/\text{f.u.}$ is observed for Fe₃O₄ thin films fabricated on BaTiO₃ substrates. The difference between these values and the bulk value of $4.1 \mu_B/\text{f.u.}$ is generally explained due to the presence of APBs [588]. APBs

¹²More details on the characterization of anti-phase boundaries in epitaxial magnetite films can be found in Ref. [591].

exhibit a strong antiferromagnetic coupling, which leads to high saturation fields up to 30 T [592]. Furthermore, the magnetization is found to follow the function $(1 - b/H^n)$, where b is a parameter depending on the density of APBs and n is equal to 0.5 [590]. Using this function, the magnetic behavior of Fe_3O_4 thin films grown on MgO can be nicely fitted (red line in Fig. 7.11(a)), corroborating the presence of APBs in this thin film. In contrast, the magnetic behavior of Fe_3O_4 thin films grown on BaTiO_3 reveals a square shaped hysteresis with a much lower saturation field (see Fig. 7.11(a)). This surprising result might be explained by the disordered growth in the first stage of the fabrication process leading to a disconnection of the Fe_3O_4 thin film with the surface structure of the BaTiO_3 substrate, which results in a lower amount of APBs. If the defects (dislocations), which are created in the first monolayer, are not mobile at room temperature, they cannot reduce the strain in the Fe_3O_4 thin film created by the ferroelectric BaTiO_3 substrate. Therefore, the disconnection of the Fe_3O_4 thin film and the BaTiO_3 surface does not decouple the ferromagnetic layer and the ferroelectric substrate in case of elastic strain.

The stoichiometry of Fe_3O_4 thin films is another important issue, since oxygen non-stoichiometry strongly influences the electric and magnetic properties [550, 564]. The degree of non-stoichiometry can be investigated by measuring the Verwey transition T_V , since this transition is a hallmark of the quality of Fe_3O_4 thin films. It was shown that T_V in $\text{Fe}_{3(1-\delta)}\text{O}_4$ diminishes with increasing δ [564, 593].¹³ Moreover, beyond a critical value of $\delta_c = 0.0039$ a change from a first-order to a second-order phase transition takes place. For $\delta < \delta_c$, T_V decreases linearly with increasing δ from 121 K to about 108 K. At δ_c , a discontinuous drop of roughly 8 K can be observed. Further increase of the non-stoichiometry δ again leads to a linear dependence of T_V with δ . Finally, the transition is lost at $\delta = 3\delta_c$. Beyond this point, Fe_3O_4 is unstable and one enters the Fe_2O_3 region [594]. In Fig. 7.11(b), the normalized remanent magnetization as well as the derivative of the magnetization of Fe_3O_4 thin films fabricated on BaTiO_3 and on MgO substrates as a function of temperature measured after field cooled in an external magnetic field of $\mu_0 H = 7$ T are shown. Verwey transitions are observed in both thin films. This indicates that Fe_3O_4 thin films grown on MgO as well as on BaTiO_3 substrates have the correct phase and other iron oxides such as maghemite, which has the same crystallographic structure as magnetite, can be excluded. However, while the Verwey transition of Fe_3O_4 thin films fabricated on MgO takes place at (118 ± 1) K, which is close to the ideal value of 121 K, Fe_3O_4 thin films grown on BaTiO_3 exhibit a lower transition temperature of (114 ± 2) K. Furthermore, the transition is much broader than the transition observed in Fe_3O_4 thin films fabricated on MgO. Assuming only non-stoichiometric effects, both transition temperatures can be translated in $\delta_{\text{MgO}} = 0.0009$ in case of the $\text{Fe}_3\text{O}_4/\text{MgO}$ thin film and $\delta_{\text{BTO}} = 0.0021$ for the $\text{Fe}_3\text{O}_4/\text{BaTiO}_3$ sample, respectively. Both values are lower than the critical thickness δ_c . This indicates that the broadening of the transition in $\text{Fe}_3\text{O}_4/\text{BaTiO}_3$ thin films does not primarily originate from non-stoichiometric effects, but might be due to inhomogeneous

¹³Each oxide compound is named by the stoichiometric formula (e.g. Fe_3O_4 , BiFeO_3 , ...) throughout this thesis. Since in oxide materials, oxygen defects are always present, these formulas inherently contain non-stoichiometric effects (e.g. $\text{Fe}_{3(1-\delta)}\text{O}_4$, $\text{BiFeO}_{3\pm\delta}$, ...).

stress fields in the Fe₃O₄ layer, caused by rhombohedral ferroelastic domains in BaTiO₃ present in this temperature range [595]. It is well known that hydrostatic pressure also decreases the Verwey transition [596] and falls off rapidly above a pressure of 8 GPa [595, 597]. At this value a quantum critical behavior was suggested. Recently, a novel pressure-induced magnetic transition was additionally observed between 10 GPa and 12 GPa [598], but this is still controversially discussed [599]. Taking into account stress effects due to epitaxial strain, the calculated degrees of non-stoichiometry δ_{MgO} and δ_{BTO} can be regarded as upper bound.

To summarize, Fe₃O₄/BaTiO₃ hybrid structures can be fabricated in a layer-by-layer growth mode at the last stage of the growth process, which results in a low surface roughness. These hybrids exhibit acceptable crystalline quality and satisfying magnetic properties with low oxygen non-stoichiometry.

7.2.2 The ferromagnet Sr₂CrReO₆

The search for new ferromagnetic materials exhibiting a high spin polarization together with a high Curie temperature well above room temperature represents an important challenge in the field of spin electronics [546]. Such materials are highly desirable for utilization as electrodes for spin valves, magnetic tunnel junctions and logic devices. In this class of materials, ferromagnetic double perovskites $A_2BB'O_6$ (with A an alkaline earth element, B a magnetic transition metal ion, and B' a non-magnetic ion) are suitable candidates [600, 601]. Moreover, in combination with BaTiO₃ as a perovskite ferroelectric material, ferromagnetic double perovskites are ideal candidates for epitaxial FM/BaTiO₃ hybrid structures with good crystalline and interfacial qualities.¹⁴

The crystalline structure of double perovskites $A_2BB'O_6$ exhibiting the cubic $Fm\bar{3}m$ symmetry is depicted in Fig. 7.12(a). The structure reveals a large distance between the magnetic B ions, which at first glance makes high magnetic transition temperatures T_C up to 725 K surprising [603]. However, to explain the high T_C values, Sarma and coworkers proposed a generalized double exchange or kinetic energy driven model, which was extended to other materials by Kanamori and Terakura [604–606]. In this model, the hybridization of the $B'-d-t_{2g}$ and $B-d-t_{2g}$ states plays the key role in stabilizing ferromagnetism at high temperatures. The mechanism is sketched in Fig. 7.12(b) for the case of Sr₂CrReO₆. In this compound, the exchange splitting $J_{\text{H,Cr}}$ of the Cr³⁺-3d-levels in spin-up and spin-down states is much larger than the crystal field splitting Δ_{Cr} into e_g and t_{2g} states. Furthermore, all three t_{2g} orbitals are fully occupied in the ionic picture. In contrast, at the Re⁵⁺ site, the crystal field splitting Δ_{Re} is large, whereas the exchange splitting $J_{\text{H,Re}}$ is vanishingly small. This situation is displayed by solid curves in Fig. 7.12(b) in the absence of hopping interactions. Note that, strictly speaking, the Re 5d-O 2p hybridized states should be considered instead of the Re⁵⁺ 5d states only. Now permitting a finite coupling between Cr and Re, hybridization takes place between states with the same symmetry and spin (denoted by dashed arrows in Fig. 7.12(b)). As the majority

¹⁴For more details on ferromagnetic double perovskites see Ref. [490].

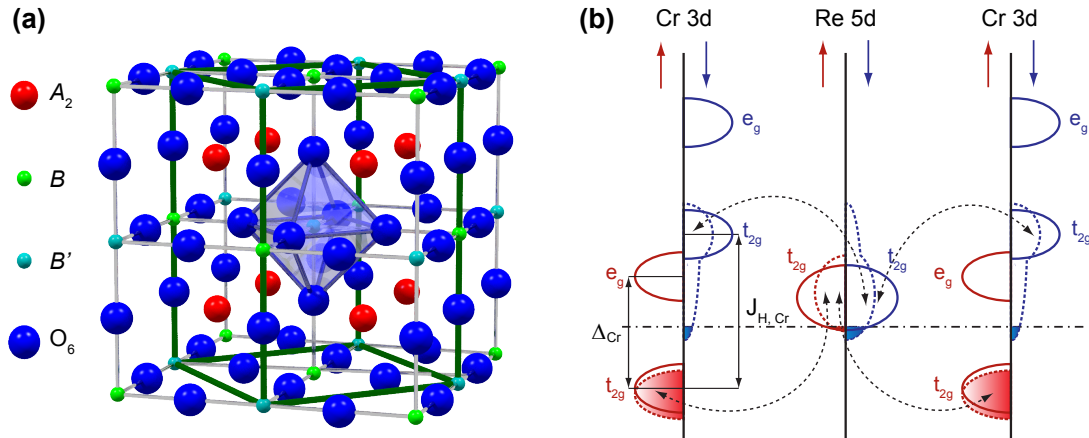


Figure 7.12: (a) Crystal structure of a double perovskite $A_2BB'O_6$ exhibiting the cubic $Fm\bar{3}m$ symmetry (Glazer notation: $a^0a^0a^0$). One oxygen octahedron is highlighted. The dimensions of a tetragonal unit cell with $I4/m$ symmetry is marked in green. (b) Schematic illustration of the Sarma-Fang-Kanamori-Terakura model for Sr_2CrReO_6 . Owing to the large crystal-field splitting of Re ($2-3$ eV [602]), only the Re $5d-t_{2g}$ bands are shown.

spin bands at the magnetic site are occupied ($Cr t_{2g,\uparrow}$), kinetic energy gain can only be obtained by hopping of the minority spin electrons from the nonmagnetic site ($Re t_{2g,\downarrow}$) into the empty minority spin bands of the magnetic ion ($Cr t_{2g,\downarrow}$). This hopping interaction not only leads to an admixture of the states and therefore results in a band broadening, but also to a shift of the energy levels. In particular, the $Re t_{2g,\uparrow}$ spin-up states are pushed up, whereas the $Re t_{2g,\downarrow}$ states are lowered in energy, leading to an induced magnetic moment and a finite spin polarization (up to 100%) at the Fermi level. The kinetic energy driven mechanism results in an anti-ferromagnetic coupling between the delocalized Re $5d$ and localized Cr $3d$ electrons. This model works only if the bandwidth is smaller than the exchange splitting Δ and if the Fermi energy lies in the t_{2g} band of the non-magnetic ion B' .

The above described model can be experimentally verified by investigating the induced magnetic moment at the original non-magnetic B' site. For this purpose, we performed x-ray magnetic circular dichroism (XMCD) measurements at the European Synchrotron Radiation Facility (ESRF) at beam line ID12 on different ferromagnetic double perovskites (A_2CrWO_6 with $A = Ca, Sr$ and Sr_2CrReO_6). Using this technique, the measurement of spin m_s and orbital m_l magnetic moments is possible exploiting magneto-optical sum rules. Furthermore, since XMCD is an element selective technique, the moments on the B' site can be obtained. The measurements were carried out on polycrystalline samples fabricated using an oxygen-getter-controlled technique to ensure stoichiometric compounds [607], which was established during this PhD thesis. More details on the XMCD technique and on the sample preparation can be found in the PhD thesis of Petra Majewski [608] and the diploma thesis of Oliver Sanganas [49].

The XMCD measurements indeed reveal a negative effective spin moment $-m_s$

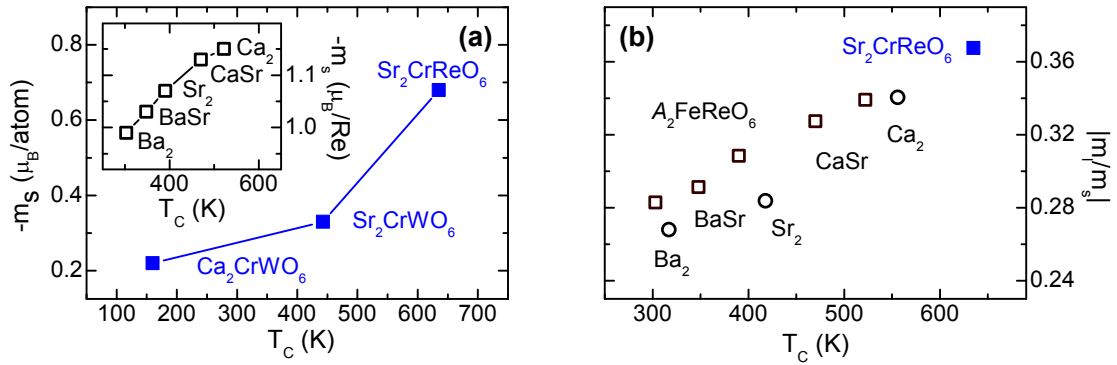


Figure 7.13: (a) Negative effective spin moment $-m_s$ and (b) ratio between orbital and spin contribution $|m_l/m_s|$ as a function of the Curie temperature T_C for different ferromagnetic double perovskites [609, 610]. Data measured on the double perovskite $AA'\text{FeReO}_6$ by other groups are also included in figures (a) and (b): open square symbols $AA'\text{FeReO}_6$ with $AA' = \text{Ba}_2, \text{BaSr}, \text{Sr}_2, \text{SrCa}, \text{Ca}_2$ [611], open circle symbols $A_2\text{FeReO}_6$ with $A = \text{Ba}, \text{Sr}, \text{Ca}$ [612].

on the W site in $A_2\text{CrWO}_6$ ($A = \text{Ca}, \text{Sr}$) as well as on the Re site in the ferromagnetic double-perovskite $\text{Sr}_2\text{CrReO}_6$ confirming the model suggested by Sarma and Fang [609, 610]. Recently, Vaitheeswaran *et al.* argued that this Re moment is induced and not intrinsic. However, a small but finite intrinsic spin moment at the Re^{5+} of $m_s = 0.013 \mu_B/\text{f.u.}$ was observed performing XMCD measurements using the double perovskite $\text{Sr}_2\text{ScReO}_6$ with $B = \text{Sc}$ being non-magnetic [612]. Since this intrinsic moment is negligibly small in comparison with the induced moment, the B' ion can still be denoted as non-magnetic. In Fig. 7.13(a), the effective spin moment $-m_s$ is plotted versus the Curie temperature T_C of each compound. From this figure, a dependence of the macroscopic magnetic transition temperature T_C and the local magnetic moment $-m_s$ can be suggested. A large effective spin moment $-m_s$ at the original non-magnetic site should lead to a strengthening of the magnetic interaction. This dependence was also observed in the double perovskite system $AA'\text{FeReO}_6$ with $AA' = \text{Ba}_2, \text{BaSr}, \text{Sr}_2, \text{SrCa}, \text{Ca}_2$ by Sikora and coworkers [611] (see inset of Fig. 7.13(a)). However, since the absolute values of m_s and m_l depend strongly on the number of $5d$ holes as well as on the white line intensity [608, 611], different experimental data derived by different groups on different compounds can hardly be compared. In contrast, the ratio between orbital and spin contribution $|m_l/m_s|$ is an independent quantity. Focusing on ferromagnetic double perovskite compounds containing Re, which are the most promising in terms of high T_C , Fig. 7.13(b) reveals a linear dependence of $|m_l/m_s|$ on T_C . Surprisingly, the compound $\text{Ca}_2\text{FeReO}_6$ fits nicely into this scaling law. Among the ferromagnetic double perovskites, $\text{Ca}_2\text{FeReO}_6$ which exhibits a highly monoclinically distorted crystal structure [613], is regarded as exceptional compound [612], since it does not confirm the accepted rule that a high Curie temperature is associated with an ideal cubic double perovskites structure [614]. Therefore, in spite of the strong influence of hybridization and site occupation on the T_C [615], these findings qualitatively support the model of ferromagnetism mediated by itinerant minority spin carriers.

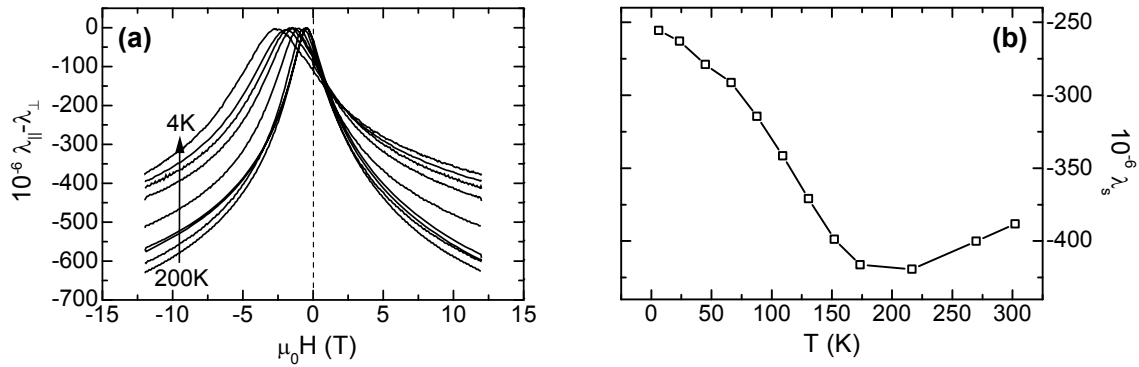


Figure 7.14: (a) Magnetostriction $\lambda_{||} - \lambda_{\perp}$ as a function of the applied magnetic field of $\text{Sr}_2\text{CrReO}_6$. The data were recorded with decreasing the magnetic field strength from +12 T to -12 T. (b) Saturation magnetostriction $\lambda_s = 2/3 \cdot (\lambda_{||} - \lambda_{\perp})$ as a function of temperature. Data were taken from Serrate *et al.* [490, 616].

Figure 7.13(b) reveals that the orbital moment m_l of Re is not quenched due to the crystal field. Therefore, a significant spin-orbit coupling of about 0.3 eV exists in the $\text{Sr}_2\text{CrReO}_6$ double perovskite leading to a splitting of the t_{2g} energy levels [491]. As a consequence, a new ground state occurs with a finite orbital moment [602]. The finite spin-orbit coupling leads to a break-down of the half-metallic behavior in $\text{Sr}_2\text{CrReO}_6$. However, the spin polarization was calculated to be 86% using density functional calculations including spin-orbit coupling, which is still considerably high [491].

As a consequence of the unquenched Re orbital moment, giant magnetostriction effects were observed in polycrystalline $\text{Sr}_2\text{Fe}_{1-x}\text{Cr}_x\text{ReO}_6$ samples [616]. The magnetostriction constant of $\text{Sr}_2\text{CrReO}_6$ as a function of the magnetic field strength ($\lambda_{||} - \lambda_{\perp}$) is shown in Fig. 7.14(a). The data were taken from Serrate and coworkers [616]. Clearly, a high magnetostriction is visible, reflecting nicely the large orbital moment in the Re atom in $\text{Sr}_2\text{CrReO}_6$. Furthermore, Fig. 7.14(a) reveals that the magnetostriction does not saturate even at high magnetic fields of 12 T. Therefore, the saturation magnetostriction λ_s calculated at 12 T (see Fig. 7.14(b)) should be considered as approximation. However, λ_s is three times larger than the value measured for polycrystalline CoFe_2O_4 but is less than half of $\text{Sr}_2\text{FeReO}_6$.¹⁵

On the theoretical side, recently, the first order magnetoelastic coupling coefficients B_i were calculated ab initio within the framework of the density-functional theory for $\text{Sr}_2\text{CrReO}_6$ by M. Komelj [617]. The calculations reveal that the magnetoelastic behavior of $\text{Sr}_2\text{CrReO}_6$ is almost cubic-like, although the double-perovskite $\text{Sr}_2\text{CrReO}_6$ exhibits a tetragonal $I4/m$ symmetry. Therefore, calculations of the magnetoelastic effects of $\text{Sr}_2\text{CrReO}_6$ on the basis of Eq. (6.4) with $B_1 = 70 \text{ MJ/m}^3$ are justified. Since it was found that the magnetoelastic response is dominant along the direction of the external magnetic field [617], no other components of the magnetoelastic coupling tensor B_{ijkl} are considered in the following calculations of mag-

¹⁵The up turn of the magnetostriction below 150 K can be attributed to an enhancement of the magnetocrystalline anisotropy at low temperatures [616].

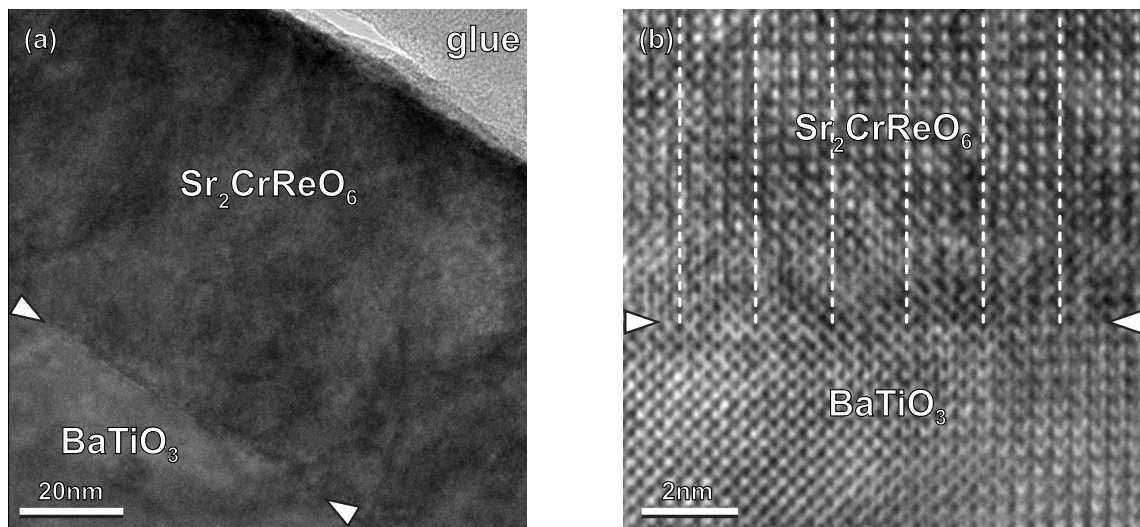


Figure 7.15: Cross-sectional (a) low-magnification and (b) high resolution transmission electron microscopy TEM images of a 76 nm thick Sr₂CrReO₆ thin film fabricated on a BaTiO₃ substrate. The interface is marked by the white triangles. Furthermore, the Re-Cr columns are indicated by white dashed lines. The measurements were performed by Sven-Martin Hühne, Universität Bonn.

netoelastic effects.

In total, Sr₂CrReO₆ is a suitable compound for the realization of extrinsic multiferroic hybrid structures exhibiting a giant magnetostrictive behavior as well as a high Curie temperature of 635 K [489], well above room temperature. Moreover, from the viewpoint of applications in the field of spintronics a high spin polarization is desirable, which is fulfilled by Sr₂CrReO₆.

To realize Sr₂CrReO₆/BaTiO₃ hybrid structures, the growth process for Sr₂CrReO₆ thin films had to be optimized. First, the deposition on non-ferroelectric substrates of SrTiO₃ was established to obtain reference samples. Only few reports are available in the literature for the growth of Sr₂CrReO₆ thin films on SrTiO₃ substrates [618–620] demonstrating the complicated growth process of high quality Sr₂CrReO₆ thin films. Since the magnetic properties of ferromagnetic double perovskites are strongly influenced by antisite defects [621], i.e., the occupation of *B* (*B'*) sites with *B'* (*B*) ions, not only a low mosaicity of Sr₂CrReO₆ thin films but also a high degree of sublattice order is essential. A substrate temperature of $T_S = 973$ K and an oxygen pressure of 6.6×10^{-4} mbar as well as a laser fluence on the target of 2.0 J/cm^2 and a repetition rate of 2 Hz during the laser ablation were found to be optimal.¹⁶ A detailed study on the growth process of Sr₂CrReO₆ as well as the physical properties of Sr₂CrReO₆ thin films can be found in the diploma thesis of Franz Czeschka [623]. The same parameters were used for the growth of Sr₂CrReO₆/BaTiO₃ hybrid structures.

Sr₂CrReO₆ thin films grow on BaTiO₃ substrates in a homogeneous way with no indications of columnar or textured structures, as evident from the cross-sectional low-magnification transmission electron microscopy (TEM) image shown in

¹⁶Oxygen seems to be essential to achieve a low density of antisite defects [622].

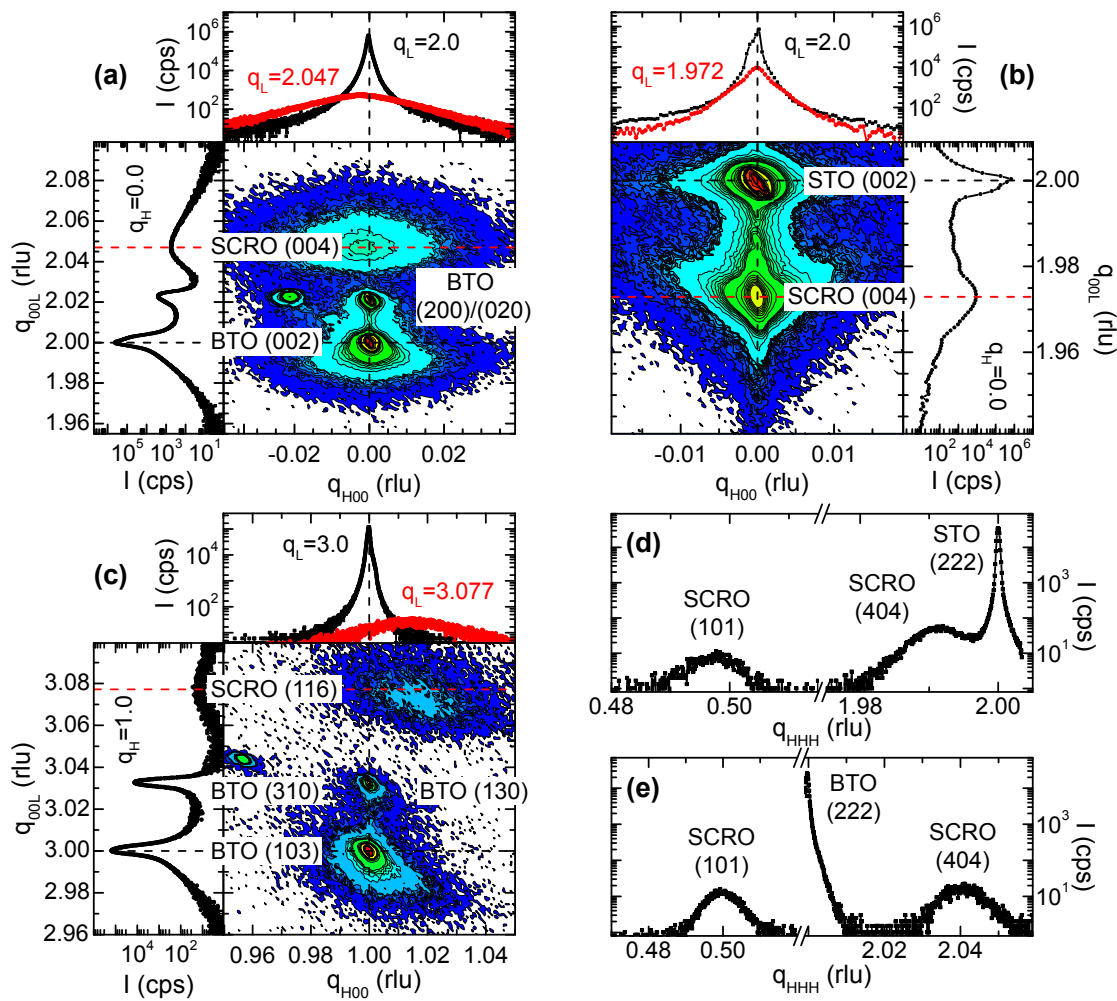


Figure 7.16: High resolution x-ray diffraction of a 31 nm thick Sr₂CrReO₆ (SCRO) thin film grown on a BaTiO₃ (001) (BTO) substrate ((a), (c), (e)) as well as a 76 nm thick Sr₂CrReO₆ thin film deposited on SrTiO₃ (001) (STO) ((b), (d)). In (a), (b), and (c), reciprocal space maps around Sr₂CrReO₆ (004) and Sr₂CrReO₆ (116) are shown, respectively. The Cr/Re sublattice order of Sr₂CrReO₆/SrTiO₃ (d) and Sr₂CrReO₆/BaTiO₃ (e) can be inferred from the intensity ratio $I_{(101)}/I_{(404)}$ of the Sr₂CrReO₆ (101) and Sr₂CrReO₆ (404) reflections.

Fig. 7.15(a) recorded on a 76 nm thick Sr₂CrReO₆ thin film. Furthermore the high resolution TEM image reveal a well-defined interface between Sr₂CrReO₆ and BaTiO₃ and a well ordered growth of Sr₂CrReO₆ (see Fig. 7.15(b)). The lattice image contrast in the Sr₂CrReO₆ thin films is clearly dominated by the Re-Cr columns, i.e., the *B* and *B'* atoms in the double perovskite $A_2BB'O_6$ structure, leading to an arrangement marked by white dashed lines in Fig. 7.15(b). On the contrary, the image contrast in the BaTiO₃ substrate is predominantly caused by the Ba atoms (*A* atoms in the perovskite ABO_3 lattice). Therefore, a gradual shift of the dots by half of the lattice parameter is observed at the interface proving the continuity of the *A* and *B/B'* site positions. Hence, Sr₂CrReO₆ grows on BaTiO₃ with an undisturbed transition of the oxygen sublattices.

The structural properties of Sr₂CrReO₆ thin films fabricated on BaTiO₃ (001) and SrTiO₃ (001) substrates are summarized in Fig. 7.16. A tetragonal $I4/m$ symmetry is observed for both types of substrates from in-plane ϕ -scans, which are not shown here [623]. The reciprocal space maps around Sr₂CrReO₆ (004) reveal a crystalline growth of Sr₂CrReO₆ for both substrates (see Figs. 7.16(a) and (b)). However, a large difference of the crystalline quality can be observed by recording q_{H00} -scans, which are depicted in the upper panel of Figs. 7.16(a) and (b). In case of Sr₂CrReO₆ grown on SrTiO₃ substrates, the small full width at half maximum (FWHM) of 0.05° of the rocking curve of the Sr₂CrReO₆ (004) reflections indicate a good epitaxial growth of Sr₂CrReO₆. In contrast, Sr₂CrReO₆ thin films fabricated on BaTiO₃ substrates exhibit a considerable mosaic spread expressed by a large FWHM of 0.6°. Similar to Fe₃O₄/BaTiO₃ hybrid structures, this high mosaic spread can be mainly attributed to a considerable lattice mismatch of Sr₂CrReO₆ thin films on BaTiO₃ substrates and the multi-domain state of the BaTiO₃ substrate during the measurement. The lattice mismatch of Sr₂CrReO₆ thin films grown on SrTiO₃ substrates is only 0.6% at 973 K, while it is -2.6% for thin films grown on BaTiO₃ [489].¹⁷ Therefore, the lattice mismatch is lower than for Fe₃O₄/BaTiO₃ hybrid structures, but still high enough to cause a high density of dislocations and a low critical thickness for pseudomorphic growth. Indeed, the critical thickness of Sr₂CrReO₆ thin films on BaTiO₃ substrates is much lower than 76 nm [623]. The reciprocal space map around the asymmetric (103) BaTiO₃ reflection shown in Fig. 7.16(c) reveals a distinct shift of the Sr₂CrReO₆ (116) film peak with respect to the corresponding BaTiO₃ substrate reflections. Therefore the 76 nm thick Sr₂CrReO₆ thin film is partially relaxed with lattice parameters of $a = 0.561$ nm and $c = 0.788$ nm. Another reason for the high mosaic spread can be found in the multi-domain state of the BaTiO₃ substrate. The reciprocal space map around the Sr₂CrReO₆ (004) reflection reveals a splitting of the BaTiO₃ (002) peak into three reflections, which unambiguously disclose the presence of c - and a -domains in the BaTiO₃ substrate. Therefore, a ferroelastic multi-domain state is present in the sample, which broadens the FWHM (cf. Section 7.2.1).

However, Sr₂CrReO₆ thin films grown on SrTiO₃ as well as on BaTiO₃ substrates exhibit an ordered network of Cr and Re ions along the pseudo-cubic $[111]_{pc}$ direction. The Cr/Re sublattice order can be inferred from the intensity ratio of $I_{(101)}/I_{(404)}$ (see Figs. 7.16(c) and (d)), since the superstructure (101) reflection has only a finite intensity in the presence of a finite amount of ordering. Using the software PowderCell, the concentration of the antisite defects, i.e., the imperfection created by interchanging Cr and Re ionic positions, as a function of the intensity ratio $I_{(101)}/I_{(404)}$ can be simulated [608]. Depending on the sample a sublattice order of 20% to 30% was observed in Sr₂CrReO₆ independent of the substrate used. Therefore, the BaTiO₃ substrate has only minor influence on the antisite defects. Here, 50% antisite disorder characterizes a fully disordered “double perovskite” ABO_3 - $AB'O_3$ alloy. Recently, Chakraverty *et al.* reported a new way to control the B -site ordering in Sr₂CrReO₆ thin films using the pulsed laser interval

¹⁷A thermal expansion of 2×10^{-5} 1/K [624] for Sr₂CrReO₆ was used to calculate the lattice constant at the growth temperature.

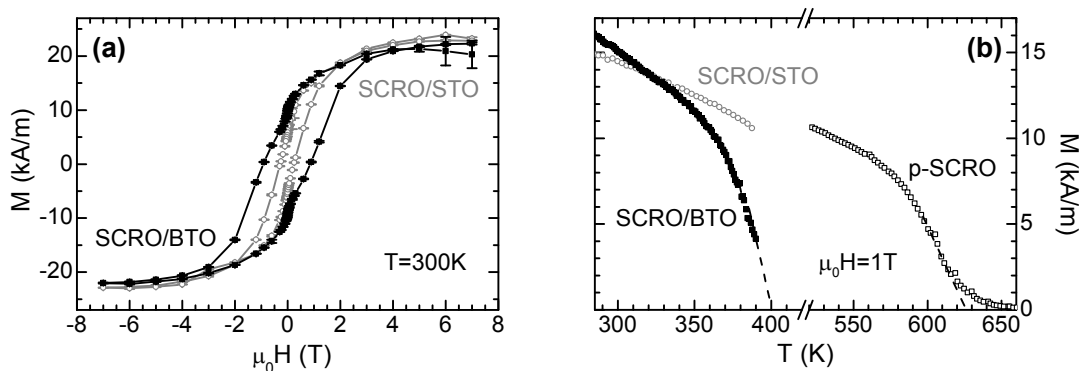


Figure 7.17: Magnetic behavior of $\text{Sr}_2\text{CrReO}_6$ thin films fabricated on BaTiO_3 (001) (BTO) (black full symbols) with a thickness of 70 nm and on SrTiO_3 (001) (STO) (31 nm) (gray open symbols) substrates. (a) Magnetization versus magnetic field measured at 300 K reveal similar magnetization values at 7 T but quite different coercive fields of both thin films. (b) The temperature dependence of the magnetization discloses a low Curie temperature in case of the $\text{Sr}_2\text{CrReO}_6/\text{BaTiO}_3$ hybrid structure. The transition is marked by dashed lines. For comparison, the $M(T)$ curve of the polycrystalline target material (p-SCRO) is also depicted in Fig. (b) (black open symbols). The available maximum temperature for magnetic measurements of thin films is limited to 390 K due to experimental restrictions.

technique (cf. Section 4.2.2) [620]. However, they reached a sublattice ordering of not less than 20% in good agreement with our samples, which were fabricated with the standard continuous growth mode.

Antisite defects drastically influence various physical properties of ferromagnetic double perovskites, e.g. changing the band structure [625] and affecting the electronic, magnetic, and spin transport properties [626]. In particular, the magnetic properties are highly dependent on the number of antisite defects. For instance, the saturation magnetization is reduced in the presence of antisite defects. This experimentally observed reduction mainly arises from an antiferromagnetic coupling of B - O - B bonds in ferromagnetic double perovskites $A_2BB'O_6$ [627]. Figure 7.17(a) shows the magnetic hysteresis at 300 K for $\text{Sr}_2\text{CrReO}_6$ thin films grown on either SrTiO_3 or BaTiO_3 substrates. The S-shaped $M(H)$ hysteresis curves reveal that the saturation field $\mu_0 H_{\text{sat}}$ is not reached at 7 T. This is in accordance with high-field magnetization measurements, where a saturation field of around 20 T is observed [628].¹⁸ The magnetic hardness accompanied by a strong magnetic anisotropy is thought to be caused by the strong spin-orbit coupling of Re ions in Re-based double perovskites [490]. However, the difference in coercive fields of around 0.64 mT of $\text{Sr}_2\text{CrReO}_6$ thin films fabricated on BaTiO_3 and SrTiO_3 substrates reveal the sensitivity of the magnetic anisotropy of $\text{Sr}_2\text{CrReO}_6$ to additional contributions such as magnetoelasticity.

Figure 7.17(a) discloses saturation magnetization values of around $M_s \approx 22$ kA/m, which corresponds to $0.6 \mu_B/\text{f.u.}$, of $\text{Sr}_2\text{CrReO}_6$ thin films deposited on BaTiO_3 as

¹⁸The term “saturation magnetization”, as used herein, denotes the magnetization at a magnetic field of 7 T. The difference between M_{sat} and $M(7\text{ T})$ is of the order of $0.1 \mu_B/\text{f.u.}$ [628].

well as on SrTiO₃ substrates. This confirms the results from the x-ray diffraction measurements, which reveal a similar number of antisite defects in both cases. Theoretical calculations including spin-orbit coupling predicted $M_s = 1.28 \mu_B/\text{f.u.}$ for a perfect sublattice order [491]. Assuming that M_s decreases about linearly with increasing antisite disorder [621], the measured saturation magnetization M_s translates into an amount of antisite defects of less than 26%. This is in good agreement with the measured value, since the calculation is valid only for 0 K. However, this simple model implies a vanishing magnetization for fully disordered double perovskites, but this is not observed experimentally (e.g. Ref. [608]). Recent x-ray diffraction as well as x-ray absorption fine structure experiments on the ferromagnetic double perovskite Sr₂FeMoO₆ reveal the presence of a high degree of local order even in samples with an absence of any long range sublattice order [629]. These findings may indicate that the antisite defects are not randomly distributed over the whole sample, but segregated locally forming anti-phase boundaries [630]. Anti-phase boundaries are located in between two ordered double perovskite domains and are therefore driven by an imperfection of the sublattice ordering. However, in double perovskite thin films fabricated on perovskite substrates such as SrTiO₃ and BaTiO₃, anti-phase boundaries can also be regarded as natural growth defects similar to Fe₃O₄ thin films on BaTiO₃ substrates (cf. Section 7.2.1). In our Sr₂CrReO₆ thin films on BaTiO₃ substrates, the high resolution TEM image shown in Fig. 7.15(b) reveals that the square dot array does not change crossing the interface between Sr₂CrReO₆ and BaTiO₃. This suggests that close to the interface the image contrast is not dominated by the heavy Re atoms. Therefore, a high density of antisite defects might be located at the thin film/substrate interface. The above mentioned anti-phase boundaries are expected to affect the coercive field, since it was shown recently that magnetic domain walls are mostly pinned to anti-phase boundaries in ferromagnetic double perovskites [631]. However, the large increase of the coercive field of Sr₂CrReO₆ thin films grown on BaTiO₃ substrates ($\mu_0 H_c^{\text{BTO}} = (0.90 \pm 0.03) \text{ T}$) compared to Sr₂CrReO₆ thin films fabricated on SrTiO₃ substrates ($\mu_0 H_c^{\text{STO}} = (0.26 \pm 0.02) \text{ T}$) visible in Fig. 7.17(a), might not be explained by anti-phase boundaries, because of the similar amount of antisite defects. Since the measurements are carried out at 300 K, i.e., in the tetragonal phase of BaTiO₃, the difference in the coercive field rather reflects a change of the magnetic anisotropy of the Sr₂CrReO₆ thin film as a function of the BaTiO₃ strain state. Furthermore, the lower crystalline quality leads to pinning effects of magnetic domains, which enhance the coercive field.

In contrast to the minor differences in the saturation magnetizations, the Curie temperature T_C clearly deviates in the two samples. The magnetization as a function of temperature is shown in Fig. 7.17(b). While Sr₂CrReO₆ thin films grown on SrTiO₃ have transition temperatures well above 390 K, the Curie temperature of Sr₂CrReO₆ thin films fabricated on BaTiO₃ substrates is expected to be around 400 K. Unfortunately, the available maximum temperature for magnetic measurements of thin films is limited to 390 K due to experimental restrictions. The $M(T)$ curve of the polycrystalline target material is also depicted in Fig. 7.17(b) for comparison, revealing a Curie temperature of 625 K. Since both Sr₂CrReO₆ thin films were fabricated under nominally identical conditions, the observed low Curie tem-

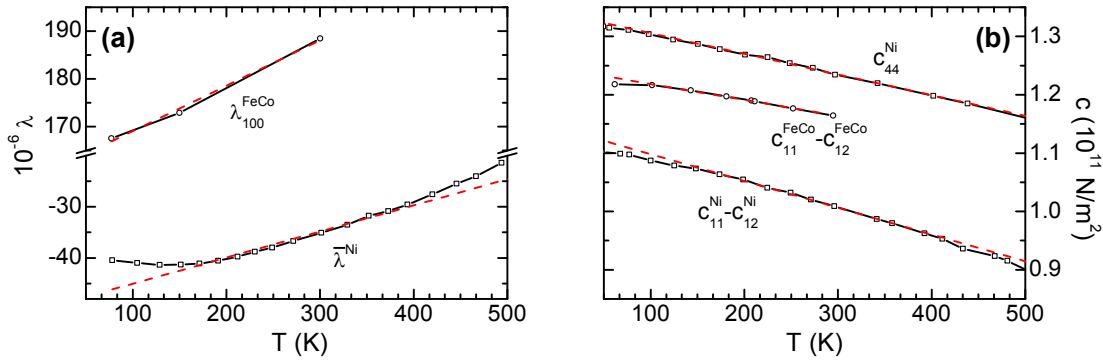


Figure 7.18: (a) Magnetostriction constants and (b) elastic stiffness constants for Ni and Fe₅₀Co₅₀ (FeCo) alloy as a function of temperature. $\bar{\lambda}$ denotes the isotropic polycrystalline magnetostrictive strain. The data were taken from Ref. [635–637]. In the temperature range of interest ($150 \text{ K} < T < 400 \text{ K}$), the magnetostrictive behavior and the elastic constants can be fitted by straight lines (red dashed lines).

perature can mainly be attributed to the different strain state in the Sr₂CrReO₆ thin film fabricated on BaTiO₃ substrate [312].

In summary, Sr₂CrReO₆/BaTiO₃ hybrids were successfully fabricated with high structural and physical qualities. The difference in the magnetic properties compared to Sr₂CrReO₆/SrTiO₃ thin films suggests that the magnetization of Sr₂CrReO₆ is indeed highly sensitive to strain-related effects.

7.3 Polycrystalline ferromagnetic materials for FM/BaTiO₃ hybrid systems

For the realization of FM/BaTiO₃ hybrid structures, not only epitaxial systems, but also polycrystalline ferromagnetic thin films were used. These thin films with a thickness ranging from 50 nm to 100 nm are deposited on BaTiO₃ substrates using electron beam evaporation described in Section 2.1. To prevent oxidation of these ferromagnetic thin films, a 5 nm Au layer was deposited in-situ on top. Two different ferromagnetic materials exhibiting different magnetostrictive behavior were studied for FM/BaTiO₃ hybrid structures.

7.3.1 Ni as ferromagnetic material

Along with iron and cobalt, nickel is one of the three elemental metals that are ferromagnetic at room temperature. The 3*d*-transition itinerant ferromagnet exhibits a Curie temperature of $T_C = 627 \text{ K}$ [632] and a saturation magnetization of $M_s = 493 \text{ kA/m}$ [633]. Ni crystallizes in the face centered cubic (fcc) structure with a lattice constant of $a_{\text{Ni}} = 0.3524 \text{ nm}$ [634].

The temperature dependence of the magnetostriction constant $\bar{\lambda}^{\text{Ni}}$ as well as the elastic stiffness constants ($c_{11}^{\text{Ni}} - c_{12}^{\text{Ni}}$) and c_{44}^{Ni} of polycrystalline Ni are displayed in

Fig. 7.18. The magnetostriction constant of Ni is negative throughout the temperature range and the absolute value is comparable to Fe₃O₄. Due to the negative magnetostriction constant of Ni, a compressive strain will result in a reduction of the magnetic energy in the direction of the strain. In the temperature range of interest ($150 \text{ K} < T < 400 \text{ K}$), the magnetostrictive behavior $\bar{\lambda}^{\text{Ni}}(T)$ as well as the elastic constants $(c_{11}^{\text{Ni}} - c_{12}^{\text{Ni}})(T)$ and $c_{44}^{\text{Ni}}(T)$ can be fitted by straight lines.¹⁹ These functions are used to calculate the magnetoelastic stress components B_1^{Ni} and B_2^{Ni} using Eq. (6.5). For the case of isotropic magnetostriction, B_1^{Ni} and B_2^{Ni} results in $B_1^{\text{Ni}} = 5 \text{ MJ/m}^3$ and $B_2^{\text{Ni}} = 13 \text{ MJ/m}^3$ at room temperature. As discussed in Sec. 6.2.1, these values deviate in thin films due to possible strain dependence of B_i^{film} . Tian and coworkers derived the following strain relation of B_i^{eff} for Ni thin films [471]:

$$\begin{aligned} B_1^{\text{eff}} &= (1.3 \pm 1.0) \text{ MJ/m}^3 + (273 \pm 197) \text{ MJ/m}^3 \times \epsilon_{\parallel} \\ B_2^{\text{eff}} &= (6.6 \pm 1.0) \text{ MJ/m}^3 - (408 \pm 107) \text{ MJ/m}^3 \times \epsilon_{\parallel}. \end{aligned} \quad (7.10)$$

Using Eq. (7.10), the effective B_i^{eff} values can be calculated to $B_1^{\text{eff}} = (4 \pm 3) \text{ MJ/m}^3$ and $B_2^{\text{eff}} = (2.5 \pm 2) \text{ MJ/m}^3$ by assuming an average in-plane strain of $\epsilon_{\parallel} = 0.01$. By comparing the effective B_i^{eff} values with the non-isotropic bulk magnetoelastic stress components, a deviation in B_2^{bulk} is observed, while for B_1^{bulk} no conclusion can be drawn due to the large experimental uncertainty. Thus, by calculating the magnetoelastic stress components B_1^{bulk} and B_2^{bulk} using Eq. (6.5), a difference mainly in B_2^{bulk} is expected due to the neglected strain dependence of B_i . As mentioned in Section 6.2.1, a correction factor k is incorporated in Eq. (6.4) to account for the deviation of B_i^{film} and B_i^{bulk} as well as possible non-ideal elastic coupling effects between thin film and substrate.

7.3.2 Fe₅₀Co₅₀ (FeCo) as ferromagnetic material

Iron-cobalt compounds (Fe_{1-x}Co_x) exhibit the highest saturation magnetization of all known magnetic alloys [638]. Although the maximum saturation magnetization is obtained for $x = 0.35$, the highest magnetostriction constant along the [100] direction is achieved for $x \approx 0.5$ ($\lambda_{100}^{\text{FeCo}} \approx 150 \times 10^{-6}$) [639]. Therefore, the alloy Fe₅₀Co₅₀ (FeCo) is another candidate as ferromagnetic constituent in FM/BaTiO₃ hybrid structures. FeCo has a high Curie temperature of $T_C \approx 1200 \text{ K}$ [640] as well as a large saturation magnetization of $M_s = 1950 \text{ kA/m}$ [380]. At room temperature, it crystallizes in the body centered cubic (bcc) structure [641] with a lattice constant of $a_{\text{FeCo}} = 0.2849 \text{ nm}$ [640].

The temperature dependence of the magnetostriction constant of single crystalline FeCo measured along the cubic [100] direction is shown in Fig. 7.18(a) [637]. In contrast to Ni, the magnetostriction constant of FeCo is positive. Therefore, a tensile strain reduces the magnetic energy in the direction of strain. Due

¹⁹ $\bar{\lambda}^{\text{Ni}}(T) = -50.1 \times 10^{-6} + 0.05 \times 10^{-6} \text{ 1/K} \cdot T$
 $(c_{11}^{\text{Ni}} - c_{12}^{\text{Ni}})(T) = 1.14 \times 10^{11} \text{ N/m}^2 - 4.59 \times 10^7 \text{ N/(m}^2\text{K)} \cdot T$
 $c_{44}^{\text{Ni}}(T) = 1.34 \times 10^{11} \text{ N/m}^2 - 3.54 \times 10^7 \text{ N/(m}^2\text{K)} \cdot T$

to the lack of experimental data, the same temperature dependence of $\lambda_{100}^{\text{FeCo}}$ and $\lambda_{111}^{\text{FeCo}}$ was assumed to calculate the isotropic magnetostriction constant $\bar{\lambda}^{\text{FeCo}}(T) = \alpha(T - 300 \text{ K}) + \frac{2}{5}\lambda_{100}^{\text{FeCo}}(300 \text{ K}) + \frac{3}{5}\lambda_{111}^{\text{FeCo}}(300 \text{ K})$, using the magnetostriction strains $\lambda_{100}^{\text{FeCo}}(300 \text{ K})$ and $\lambda_{111}^{\text{FeCo}}(300 \text{ K})$ measured by Hall et al. [639]. α is derived from the linear regression in Fig. 7.18(a).²⁰ Furthermore, the difference of the elastic stiffness constants c_{11}^{FeCo} and c_{12}^{FeCo} as a function of temperature is displayed in Fig. 7.18(b) [637].²¹ To our knowledge, no experimental data for c_{44}^{FeCo} is reported in the literature. For our purpose, the calculated value $c_{44}^{\text{FeCo}} = 158 \times 10^{11} \text{ N/m}^2$ [642] and the same temperature dependence of $c_{11}^{\text{FeCo}} - c_{12}^{\text{FeCo}}$ were used to derive $c_{44}^{\text{FeCo}}(T)$. With the knowledge of these values, the magnetoelastic coupling constants B_i^{FeCo} can be obtained in the bulk limit.

7.4 Summary

In the case of multiferroic composite structures with strain-mediated coupling, large magnetoelectric effects are expected when combining piezoelectric materials with strong piezoelectric responses with magnetostrictive compounds exhibiting large magnetoelastic effects. These requirements are normally fulfilled by ferroelastic and ferromagnetic materials, respectively.

In this thesis, BaTiO₃ was chosen as the piezoelectric material, as it provides large strain effects due to electrically addressable ferroelastic domain switching. Moreover, BaTiO₃ crystals exhibit different ferroelastic phases, which allows to investigate the physical properties of the overlying magnetostrictive thin film under different strain states by simply varying the temperature. To describe these effects in a quantitative way, the strain state of BaTiO₃ as a function of temperature and/or electric field was calculated on the basis of an effective Hamiltonian (cf. Eq. (7.1)). The method described in this chapter enables an ab initio like calculation of the strain tensor of BaTiO₃ even at finite temperatures, since it combines density functional theory and molecular dynamics simulations. The BaTiO₃ strain tensor thus obtained is the starting point for the simulation of magnetization changes in the overlying ferromagnetic thin film (cf. Section 6.2).

Various ferromagnetic material systems offering different magnetoelastic behavior were applied for the strain-mediated composite structures. In particular, Fe₃O₄ and Sr₂CrReO₆ thin films were used for epitaxial composite structures and polycrystalline Ni as well as Fe₅₀Co₅₀ thin films for non-epitaxial ones. Fe₃O₄ is known since ancient times. However, up to now, the low temperature behavior is still discussed controversially. Since an electrically controllable finite polarization was observed below around 40 K, Fe₃O₄ seems to be not only the oldest magnetic material but also the first magnetoelectric material known to mankind. In this part of the thesis, Fe₃O₄ is treated as “single-ferroic” ferromagnetic material. To realize multiferroic composite hybrid structures, Fe₃O₄ thin films were deposited onto

²⁰In total, $\bar{\lambda}(T)$ can be expressed as $\bar{\lambda}^{\text{FeCo}}(T) = 78 \times 10^{-6} + 0.095 \times 10^{-6} (T - 300 \text{ K})$ for polycrystalline FeCo.

²¹The linear fit in Fig. 7.18(b) yields $c_{11}^{\text{FeCo}} - c_{12}^{\text{FeCo}} = 1.25 \times 10^{11} \text{ N/m}^2 - 2.73 \times 10^7 \text{ N}/(\text{m}^2\text{K}) \cdot T$.

BaTiO₃ substrates. As evident from the time evolution of the intensity recorded at the (00) RHEED reflection, the growth of Fe₃O₄ can be divided into an almost amorphous growth at the beginning, which evolves into a three-dimensional crystalline deposition. At the end, a two-dimensional layer-by-layer growth mode is achieved. This growth behavior is mainly caused by the high lattice mismatch of Fe₃O₄ and BaTiO₃ of 4.7% and certainly influences the physical properties of these thin films. While a low surface roughness of around 0.8 nm_{RMS} was detected, a much larger mosaic spread was observed in Fe₃O₄/BaTiO₃ structures compared to Fe₃O₄ thin films deposited on lattice matched MgO substrates. However, the magnetic properties revealed a distinct Verwey transition, which is a hallmark for the correct iron-oxygen phase, as well as a high saturation magnetization close to the theoretical value. Therefore, we achieved to fabricate Fe₃O₄/BaTiO₃ hybrid structures with acceptable crystalline quality and satisfying physical properties.

In addition to Fe₃O₄, the ferromagnetic double perovskite Sr₂CrReO₆ was used as a material system for epitaxial composite structures based on BaTiO₃. As Sr₂CrReO₆ combines a high Curie temperature of around 635 K, which is caused by a generalized double exchange model, and a predicted large spin polarization at the Fermi level, this compound is an ideal candidate for new materials in the field of spin-electronic devices. In the course of this thesis, Sr₂CrReO₆ thin films were fabricated on SrTiO₃ substrates as well as for the first time on BaTiO₃. Since the physical properties of Sr₂CrReO₆ are strongly dependent on anti-site defects, i.e., the imperfection created by interchanging Cr and Re in the Sr₂CrReO₆ lattice, much efforts were devoted to realize Sr₂CrReO₆ thin films exhibiting a highly ordered network of Cr and Re ions accompanied with excellent magnetic properties. However, in analogy to Fe₃O₄/BaTiO₃ hybrids, the crystalline quality of Sr₂CrReO₆ thin films on BaTiO₃ is much lower than for Sr₂CrReO₆ thin films deposited on lattice matched SrTiO₃ substrates due to the high lattice mismatch of -2.6% .

Besides crystalline multiferroic composite structures, non-epitaxial hybrids were fabricated using polycrystalline Ni and Fe₅₀Co₅₀ thin films.

In the following, these material systems are investigated with respect to strain-mediated magnetoelectric effects.

Chapter 8

FM/BaTiO₃ multiferroic composite hybrid systems

Strain-mediated multiferroic composite hybrid structures based on BaTiO₃ as a ferroelastic substrate material offer a wide range of opportunities to tune the magnetic properties of a ferromagnetic (FM) thin film layer. A free-standing FM/BaTiO₃ bilayer should allow for large magnetoelectric effects, since, in principle, the strain imposed by the BaTiO₃ substrate is transferred to the ferromagnetic layer without constraints (cf. Fig. 6.2). Moreover, by employing the different ferroelastic phases of BaTiO₃, the physical properties of one and the same ferromagnetic layer under different strain conditions can be studied by simply varying the temperature. However, as the following chapter will demonstrate, the physical properties of ferromagnetic thin films in FM/BaTiO₃ are highly dependent on the ferroelastic domain configuration of BaTiO₃. Therefore, the control of ferroelastic domains in BaTiO₃ is a prerequisite for a quantitative discussion of such strain-mediated multiferroic composite systems. For instance, biasing electric fields can be used to alter and control the coupled ferroelectric/ferroelastic domain pattern in BaTiO₃. Furthermore, the number of ferroelastic domain variants can be reduced by applying electric fields along a nonpolar axis. By using miscut BaTiO₃ substrates, the formation of specific domains is preferred in each ferroelectric/ferroelastic phase of BaTiO₃. As it was demonstrated in the previous chapter, the strain tensor of BaTiO₃ can be well calculated for temperatures lower than $T_{\text{exp.}} = 300$ K by using molecular dynamic simulations. This allows to simulate the temperature dependence and electric field dependence of the magnetic behavior of FM/BaTiO₃ hybrid structures in an ab initio manner.

In this chapter, we present a detailed investigation on the temperature and electric field dependence of the magnetization of FM/BaTiO₃ hybrid structures.

8.1 FM/BaTiO₃ without ferroelastic domain control

As discussed in Section 7.1, BaTiO₃ exhibits different ferroelectric/ferroelastic phases, which allow to study the physical properties of a thin film clamped on BaTiO₃ substrates under different strain states [447]. In particular, the phase transitions between different ferroelectric phases in BaTiO₃ impose large strain changes into the overlying ferromagnetic thin film. In other words, elastic deformations of the lattice

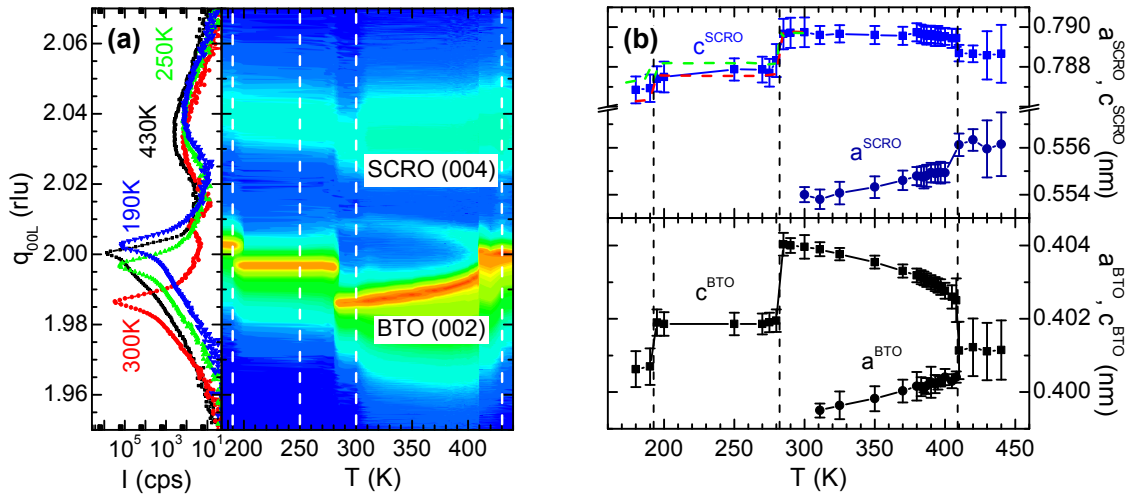


Figure 8.1: X-ray diffraction measurements as a function of temperature of a 76 nm thick $\text{Sr}_2\text{CrReO}_6$ film deposited on a (001) oriented BaTiO_3 substrate. (a) q_{00L} line scans around the $\text{Sr}_2\text{CrReO}_6$ (004) reflection are shown. The reciprocal lattice units (rlu) are calculated with respect to the BaTiO_3 (002) reflection at 440 K. The slight reduction of the intensity below 300 K is caused by the use of the low temperature sample stage described in Section 2.1.3. (b) Lattice constants a (full circles) and c (full squares) of $\text{Sr}_2\text{CrReO}_6$ (blue) and BaTiO_3 (black) as a function of temperature reveal distinct changes at the phase transitions. The evolution of the out-of-plane $\text{Sr}_2\text{CrReO}_6$ lattice constant c^{SCRO} was calculated for $T \leq 300$ K, by using the average Poisson ratio $\nu^{\text{SCRO}} = 0.22$ and (i) the measured out-of-plane constant c^{BTO} of the BaTiO_3 substrate (red dashed line) as well as (ii) the calculated strain tensor of BaTiO_3 from molecular dynamics simulations (green dashed line). Both agree well with the experimental data. For the molecular dynamics simulation, the temperature axis was shifted to coincide with the experimental data.

of epitaxially grown thin films are expected as a function of temperature, which should alter their physical properties.

8.1.1 Elastic deformation of $\text{Sr}_2\text{CrReO}_6/\text{BaTiO}_3$ hybrid structures

The elastic deformation of epitaxial FM/ BaTiO_3 hybrids was investigated as a function of temperature by x-ray diffraction measurements (XRD) using the home-made temperature stage described in Section 2.1.3.

Figure 8.1 shows XRD measurements of a $\text{Sr}_2\text{CrReO}_6/\text{BaTiO}_3$ hybrid structure at different temperatures between 180 K and 440 K. The q_{00L} line scans around the $\text{Sr}_2\text{CrReO}_6$ (004) reflection reveal distinct changes of the $\text{Sr}_2\text{CrReO}_6$ (004) peak positions when crossing the phase transitions of BaTiO_3 (see Fig. 8.1(a)). From the q_{00L} values of both the BaTiO_3 substrate reflection as well as the $\text{Sr}_2\text{CrReO}_6$ (004) peak position, the out-of-plane lattice constant c^{SCRO} can be calculated assuming a tetragonal symmetry of $\text{Sr}_2\text{CrReO}_6$ in the whole temperature range. The in-plane lattice constant of $\text{Sr}_2\text{CrReO}_6$ was derived by measuring the $\text{Sr}_2\text{CrReO}_6$ (116) reflection. The lattice parameters of the BaTiO_3 substrate a^{BTO} and c^{BTO} nicely follow

the bulk behavior shown in Fig. 7.1(a). From the change of the in-plane constants a^{BTO} and a^{SCRO} crossing the cubic-tetragonal phase transition, a nearly ideal elastic coupling between the BaTiO₃ substrate and the Sr₂CrReO₆ thin film can be observed, since both lattice parameters change by about -0.2% . Therefore, in spite of the partial relaxation of the Sr₂CrReO₆ thin film during deposition, the change in the lattice parameter of the ferroelectric substrate is almost perfectly transferred into the overlying Sr₂CrReO₆ thin film. Furthermore, considering the change of the in-plane a^{SCRO} (a^{BTO}) and out-of-plane c^{SCRO} (c^{BTO}) lattice constants of Sr₂CrReO₆ (BaTiO₃) in the cubic and tetragonal phase of BaTiO₃, an average Poisson ratio of $\nu^{\text{SCRO}} = 0.22$ and $\nu^{\text{BTO}} = 0.30$ can be calculated. The value for BaTiO₃ is close to $\nu = 0.29$ reported by Don Berlincourt and coworkers [643]. Neglecting a temperature dependence of the Poisson ratio and shear strains in the orthorhombic and rhombohedral phase, the relative change of the out-of-plane lattice constant c^{SCRO} of Sr₂CrReO₆ for temperatures lower than 300 K can be calculated employing the out-of-plane constant c^{BTO} of the BaTiO₃ substrate as well as the average Poisson ratios ν^{SCRO} and ν^{BTO} (see red dashed line in Fig. 8.1(b)). In spite of the above assumptions and neglecting ferroelectric domains, the temperature behavior of the Sr₂CrReO₆ lattice can be well simulated, which further proves a good elastic coupling of the ferroelectric BaTiO₃ substrate and the Sr₂CrReO₆ thin film. Furthermore, by using ab initio calculations on the basis of molecular dynamics simulations of the strain tensor of BaTiO₃ (see Fig. 7.2), the temperature evolution of the out-of-plane lattice constant c^{SCRO} can be calculated (green dashed line in Fig. 8.1(b)).¹ Clearly the elastic deformation of ferromagnetic thin films in FM/BaTiO₃ hybrids can be derived within ab initio calculations. This confirms that the low temperature evolution of the elastic deformation can be well described by the molecular dynamics simulation presented in Section 7.1.

8.1.2 Modification of the physical properties of FM/BaTiO₃ hybrid structures

Figure 8.1 reveals abrupt changes of the lattice constants of Sr₂CrReO₆ at the phase transitions of BaTiO₃. Therefore, whenever the BaTiO₃ substrate undergoes a structural phase transition, the associated change of the lattice parameters should have a substantial effect on the electronic and magnetic properties of a ferromagnetic thin film clamped to its surface.

Modification of the physical properties of Sr₂CrReO₆/BaTiO₃ hybrids

Fig. 8.2(a) shows the temperature dependence of the longitudinal resistance $R(T)$ of a 70 nm thick Sr₂CrReO₆ thin film grown on BaTiO₃ measured at zero external magnetic field $\mu_0 H = 0$ T. The Sr₂CrReO₆ thin film was patterned into a 375 μm long and 50 μm wide Hall bar and the resistance was recorded in a standard four-point measurement. Upon cooling the Sr₂CrReO₆/BaTiO₃ hybrid structure

¹For the molecular dynamics simulation, the temperature axis was shifted to coincide with the experimental data.

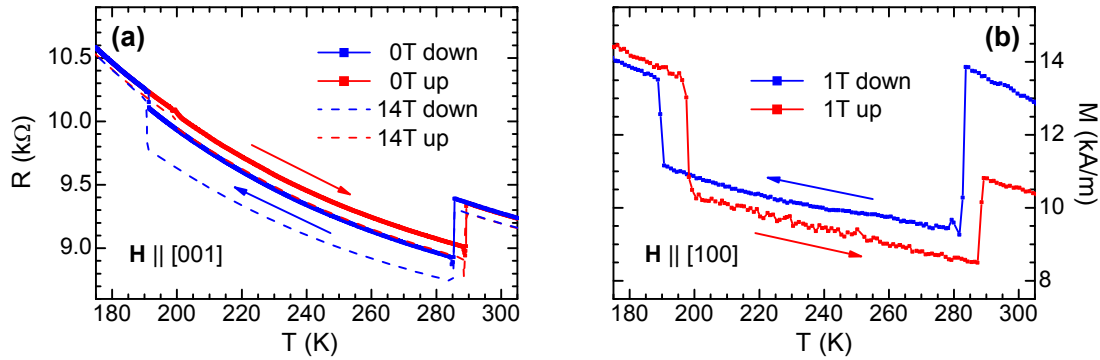


Figure 8.2: (a) Temperature dependence of the longitudinal resistance $R(T)$ of a 70 nm thick $\text{Sr}_2\text{CrReO}_6$ film grown on BaTiO_3 measured at an external magnetic field of $\mu_0 H = 0$ T (full symbols) and $\mu_0 H = 14$ T applied out of the film plane (dashed lines) while cooling (blue curve) and heating (red curve) of the $\text{Sr}_2\text{CrReO}_6/\text{BaTiO}_3$ hybrid structure. (b) Temperature evolution of the magnetization projection M along an external magnetic field $\mu_0 H = 1$ T. The magnetic field was applied in the $\text{Sr}_2\text{CrReO}_6$ film plane. Due to the first order nature of the structural transitions of the BaTiO_3 substrate, thermal hysteresis are observed in the temperature dependence of the resistance and the magnetization.

from 320 K (blue curve), the resistance increases slightly until it suddenly drops at the tetragonal-orthorhombic phase transition of BaTiO_3 at around 285 K. Between 285 K and 191 K the resistance again increases continuously until it jumps to higher values at 191 K, i.e., at the temperature at which the BaTiO_3 substrate becomes rhombohedral. Below 191 K, the resistance increases continuously again. The temperature dependent resistance measured during heating of the sample (red curve) almost reproduces the described behavior. In particular, the difference in the resistance for heating and cooling is negligibly small in the temperature range of the tetragonal and rhombohedral phase of the BaTiO_3 substrate. This proves that cracking of the BaTiO_3 substrate and thus of the $\text{Sr}_2\text{CrReO}_6$ thin film due to the large changes in strain does not explain the abrupt jumps observed in the resistance. The same measurement was also carried out at $\mu_0 H = 14$ T orthogonal to the film plane (cf. dashed lines in Fig. 8.2(a)). Interestingly, only the resistance values in the orthorhombic phase depend strongly on the magnetic field as well as on heating or cooling of the sample. This can be attributed to different ratios of ferroelastic o_{12} , o_{23} , and o_{13} orthorhombic domains in the BaTiO_3 substrate depending on whether the previous phase was rhombohedral or tetragonal (see Fig. 7.1) [644]. The resistance jumps evident in Fig. 8.2(a) are as large as 5.0% at the rhombohedral-orthorhombic phase transition and 4.2% at the orthorhombic-tetragonal phase transition of the BaTiO_3 substrate.

The change of electrical resistance as a function of the applied stress or transferred strain in FM/ BaTiO_3 hybrids is commonly known as piezoresistance effect [645, 646]. Following Parker *et al.* [647], the electric resistance R is given by $R = \rho \cdot l/A$, where ρ denotes the resistivity of $\text{Sr}_2\text{CrReO}_6$, l the length of the Hall bar, and A the cross-sectional area. If the BaTiO_3 substrate undergoes a structural phase transition, the

change in resistance $\Delta R/R$ of the Hall bar in the elastic limit is

$$\frac{\Delta R}{R} = \frac{\Delta \rho}{\rho} - \frac{\Delta A}{A} + \frac{\Delta l}{l} = (1 + 2\nu) \frac{\Delta l}{l} + \frac{\Delta \rho}{\rho}, \quad (8.1)$$

where ν denotes the Poisson ratio of an isotropic material. By using the strain component along the direction of the Hall bar ϵ_{xx} , Eq. (8.1) can be expressed as

$$\gamma = \frac{1}{R} \frac{\Delta R}{\epsilon_{xx}} = (1 + 2\nu) + \frac{1}{\rho} \frac{\Delta \rho}{\epsilon_{xx}} = (1 + 2\nu) + \epsilon_{\rho}. \quad (8.2)$$

γ is commonly termed as gauge factor and ϵ_{ρ} as the strain coefficient of resistivity. Equations (8.2) and (8.1) indicate that the change in resistance is due to two different effects. The term $(1 + 2\nu)$ represents a purely geometrical effect, which corresponds to an increase (decrease) in length, and a decrease (increase) in the cross-sectional area for $\epsilon_{xx} > 0$ ($\epsilon_{xx} < 0$). The second term ϵ_{ρ} is caused by physical effects, since it describes changes in the resistivity of the material as a function of strain. Using the average Poisson ratio $\nu^{\text{SCRO}} = 0.22$ of Sr₂CrReO₆, the geometrical term $(1 + 2\nu)$ yields 1.44. Since the maximum negative strain can be estimated to be $\epsilon_{xx} = -0.011$ due to $a_1 \rightarrow o_{23}$ ferroelastic domain transitions of BaTiO₃ at the orthorhombic-tetragonal phase transition (see Fig. 7.2 and Fig. 7.1), pure geometric effects, which are smaller than $\frac{\Delta R}{R} = 1.6\%$, cannot explain the large resistance jumps shown in Fig. 8.2(a) [447]. Therefore, ϵ_{ρ} plays an important role in Sr₂CrReO₆. Some possible mechanisms for the piezoresistivity term are discussed in Refs. [646–649], such as the alteration in the electron-scattering probability and the modification of the electronic structure. Furthermore, in thin films with thickness smaller than the mean free path of the electrons, the gauge factor increases sharply and is strongly affected by the surface morphology [650]. While for non-magnetic metals the strain-resistance curve is linear and mainly dominated by geometric effects, the zero-field strain-resistance curve for magnetic materials is highly non-linear due to domain-rotation and the anisotropic magnetoresistance effects [647, 651, 652]. For ferromagnetic materials with positive magnetostriction, such as Sr₂CrReO₆, an applied tensile strain causes magnetic domain reorientation such that the direction of the magnetization is parallel to the strain direction and a change in R is observed. However, since Fig. 8.2(a) reveals that the largest variation of the resistivity is observed at an external magnetic field of $\mu_0 H = 14$ T, where the magnetization is nearly saturated [628], these effects are not the main reason for the resistivity variation at the phase transitions. On the other hand, similar to the class of manganites [653], ferromagnetic double perovskites are highly sensitive to distortions of the crystal and thus to changes in the orbital overlap [614]. Therefore, the strength of the magnetic and electronic interaction in Sr₂CrReO₆ is expected to be dependent on the length and angle of the Cr-O-Re bonds. We therefore mainly attribute the observed changes in the temperature dependent resistance to strain induced modifications of the orbital overlap in Sr₂CrReO₆.

Since the ferromagnetic interaction in Sr₂CrReO₆ is mediated by minority spin electrons (see Sec. 7.2.2), the strain induced changes of the orbital overlap should also affect the hopping integral and thus the magnetic properties. Fig. 8.2(b) displays

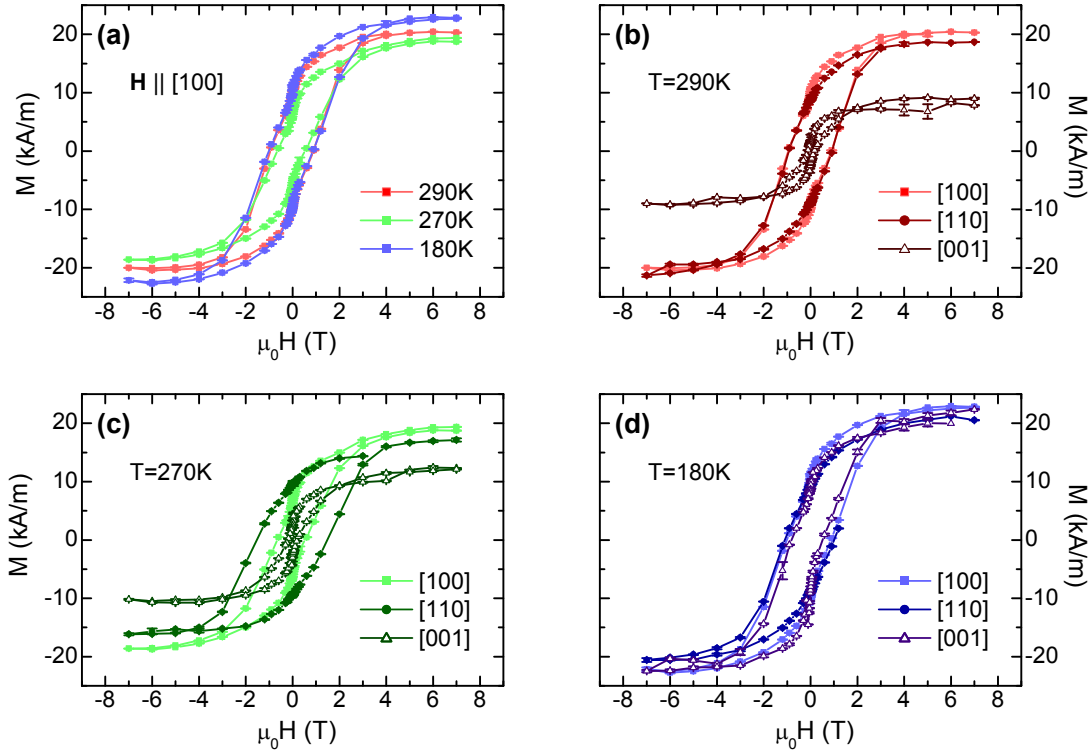


Figure 8.3: (a)-(d) Magnetic hysteresis $M(H)$ measured at different temperatures (290 K, 270 K, and 180 K) and orientations of the external magnetic field. The magnetic field was aligned along the pseudo-cubic $[100]_{\text{pc}}$, $[110]_{\text{pc}}$, and $[001]_{\text{pc}}$ directions of $\text{Sr}_2\text{CrReO}_6$. (a) shows $M(H)$ loops at different temperatures with the external field applied along the pseudo-cubic $\text{Sr}_2\text{CrReO}_6$ $[100]_{\text{pc}}$ direction and (b)-(d) the projection of the magnetization M along the external magnetic field H measured under different orientations of $\mu_0 H$.

the evolution of the magnetization M as a function of temperature T during cooling (blue curve) and heating (red curve) in an external magnetic field of $\mu_0 H = 1$ T applied along the pseudo-cubic $[100]_{\text{pc}}$ in-plane direction of $\text{Sr}_2\text{CrReO}_6$. Just as $\rho_{xx}(T)$, the projection M of the magnetization along the external magnetic field $\mu_0 H$ abruptly changes its magnitude at the phase transitions of BaTiO_3 . These modifications can be caused by strain induced changes of the magnetic interaction as well as variations of the magnetic anisotropy. The former alters the saturation magnetization M_s , while the latter mainly changes the shape of magnetic hysteresis loops $M(H)$. Since the $\text{Sr}_2\text{CrReO}_6$ thin film is not magnetically saturated at an external field of $\mu_0 H = 1$ T, the difference of the initial and final magnetization values at 310 K can be attributed to changes of the magnetic domain structure due to magnetoelastic effects [654].

To distinguish between the variation of the magnetic anisotropy and the magnetic interaction caused by imposed strain effects, the magnetic field dependence of the magnetization $M(H)$ was measured at different temperatures, i.e., in the three different ferroelastic phases of the BaTiO_3 substrate. The evolution of the magnetization projection M along the pseudo-cubic $[100]_{\text{pc}}$ direction of the $\text{Sr}_2\text{CrReO}_6$ thin

films recorded in the tetragonal ($T = 290$ K), orthorhombic ($T = 270$ K), and rhombohedral phase ($T = 180$ K) of BaTiO₃ are shown in Fig. 8.3(a). The $M(H)$ loops look very similar except for the absolute value of the magnetization at a magnetic field of $\mu_0 H = 7$ T, which is denoted in the following as saturation magnetization (see footnote on page 186). The saturation magnetization reaches its maximum at $T = 180$ K, while a lower saturation magnetization is observed at $T = 290$ K and at $T = 270$ K. This further suggests a weakening of the magnetic interaction due to imposed strain effects mainly in the temperature range of the orthorhombic phase of BaTiO₃. However, the shape of the magnetic hysteresis loops indicate no significant changes of the magnetic anisotropy along this direction. To investigate the magnetic anisotropy in more detail, the projections of the magnetization along three different orientations were measured. Figures 8.3(b)-(d) display $M(H)$ loops for the external magnetic field applied along the pseudo-cubic $[100]_{\text{pc}}$, $[110]_{\text{pc}}$, and $[001]_{\text{pc}}$ directions of the Sr₂CrReO₆ thin film recorded in three different ferroelastic phases of BaTiO₃. Clearly, large differences in the shape of the $M(H)$ loops are visible. In particular, at $T = 270$ K, a huge difference in the coercive fields of around 0.9 T can be observed for external magnetic fields applied in-plane. In contrast, in the tetragonal phase of BaTiO₃ at 290 K (see Fig. 8.3(b)), the measurements along $[100]_{\text{pc}}$ and $[110]_{\text{pc}}$ reveal a negligible in-plane anisotropy of the Sr₂CrReO₆ thin film. A similar dependence is visible in the rhombohedral phase measured at $T = 180$ K (see Fig. 8.3(d)). Since the possible four ferroelastic BaTiO₃-domains in the rhombohedral phase (see Fig. 7.1) are present with equal probability without any external field applied, the strain imposed into the Sr₂CrReO₆ thin film is isotropic in the plane. Therefore, Sr₂CrReO₆ thin films fabricated on BaTiO₃ seem to have no in-plane crystalline anisotropy. This is in contrast to Sr₂CrReO₆ thin films deposited on SrTiO₃ substrates, where a complicated magnetic anisotropy was found (see the diploma thesis of Franz Czeschka [623] for more details). Furthermore, in the rhombohedral phase of the BaTiO₃ substrate, the out-of-plane hysteresis loop ($\mathbf{H} \parallel [001]_{\text{pc}}$) agrees well with the in-plane measurements. This suggests that the magnetic behavior of the Sr₂CrReO₆ is isotropic, with no evidence of shape anisotropy. Thus, the magnetoelastic energy contribution balances out the anisotropy caused by demagnetization fields. However, since the saturation magnetization of Sr₂CrReO₆ ($M_s \approx 22$ kA/m) is low compared to normal magnetic materials like Fe₃O₄ or Ni and on the other hand the magnetoelastic coupling is strong, a small isotropic strain of less than $\epsilon_{11} = \epsilon_{22} = 0.0022\%$ is enough to overcome the demagnetization energy. Using the vanishing magnetic anisotropy of Sr₂CrReO₆ in the rhombohedral phase of BaTiO₃ as a new starting point, the tremendous in-plane anisotropy measured at $T = 270$ K in the orthorhombic phase of BaTiO₃, which becomes apparent by large difference in the coercive fields of the in-plane $M(H)$ loops (cf. Fig. 8.3(c)), can be explained by the presence of different ferroelastic domains in the BaTiO₃ substrate.

Figure 8.4 shows the results of $M(H)$ -simulations along $[100]_{\text{pc}}$, $[110]_{\text{pc}}$, and $[001]_{\text{pc}}$ of Sr₂CrReO₆ thin films on top of different ferroelastic BaTiO₃-domains by minimizing the modified thermodynamic potential $\tilde{g}^{(m)}$ (cf. Section 6.2.1) with respect to the direction of the magnetization assuming a magnetic single domain state in a Stoner-Wohlfarth type of approach. The strain tensors of the ferromagnetic thin film $\epsilon_{ij}^{\text{SCRO}}$

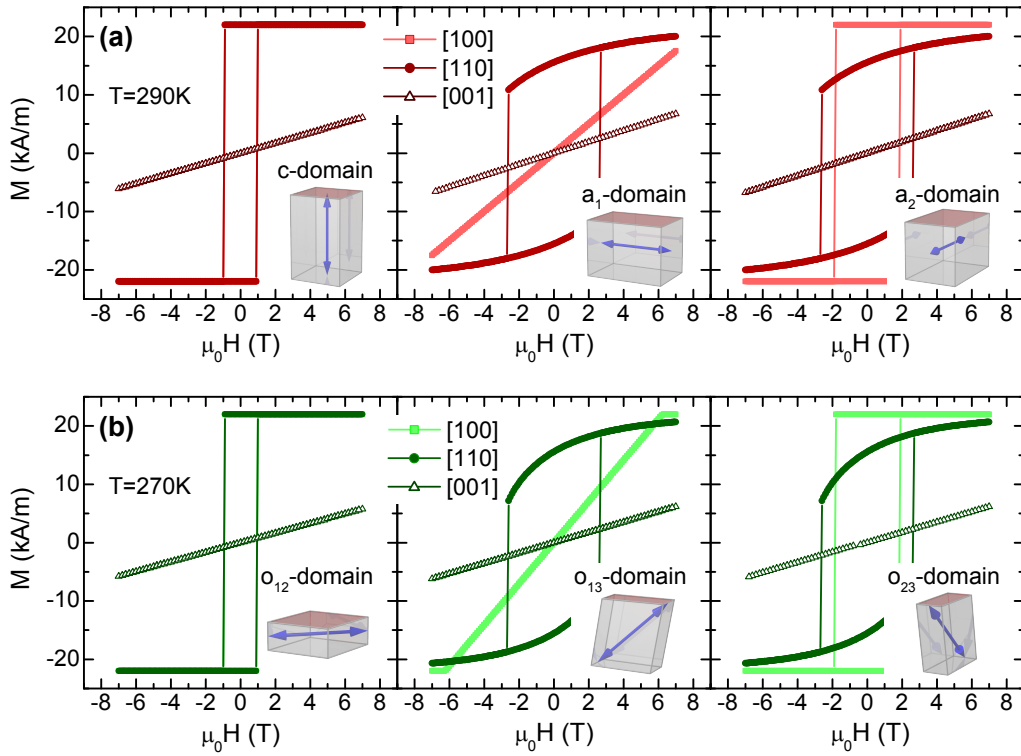


Figure 8.4: $M(H)$ -simulations along $[100]_{pc}$, $[110]_{pc}$, and $[001]_{pc}$ of $\text{Sr}_2\text{CrReO}_6$ thin films on top of different ferroelastic BaTiO_3 -domains in the (a) tetragonal and (b) orthorhombic phase by minimizing the modified thermodynamic potential $\tilde{g}^{(m)}$ with respect to the direction of the magnetization m_i assuming a magnetic single domain state in a Stoner-Wohlfarth type of approach. The $M(H)$ loops along $[100]_{pc}$ and $[110]_{pc}$ are indistinguishable in case of c - as well as o_{12} -domains. To account for the finite coercive field for the simulation of c - as well as o_{12} -domains, an energy barrier of $\Delta E/M_s = 900 \text{ mT}$ was used to describe pinning and domain wall formation energies (see Appendix B).

were calculated using the results of molecular dynamics simulations (cf. Fig. 7.2) as well as the average Poisson ratio of 0.22 (cf. Fig. 8.1). The calculations yield the following strain tensors in the orthorhombic phase for different ferroelastic domains

$$\epsilon_{r \rightarrow o_{12}}^{\text{SCRO}} = \begin{pmatrix} -0.019 & 0 & 0 \\ 0 & -0.019 & 0 \\ 0 & 0 & +0.011 \end{pmatrix}; \epsilon_{r \rightarrow o_{13}}^{\text{SCRO}} = \begin{pmatrix} -0.012 & 0 & 0 \\ 0 & -0.019 & 0 \\ 0 & 0 & +0.009 \end{pmatrix}. \quad (8.3)$$

The components of the strain tensors are calculated with respect to the rhombohedral phase and shear strains were neglected ($\epsilon_{12} = \epsilon_{13} = \epsilon_{23} = 0$). Furthermore, the strain tensor $\epsilon_{r \rightarrow o_{23}}^{\text{SCRO}}$ for the ferroelastic domain transition $r \rightarrow o_{23}$ can be obtained by interchanging the strain components $\epsilon_{11}^{\text{SCRO}}$ and $\epsilon_{22}^{\text{SCRO}}$ in $\epsilon_{r \rightarrow o_{13}}^{\text{SCRO}}$. In the same way, the strain tensors for different ferroelastic domains in the tetragonal symmetry are derived as follows:

$$\epsilon_{r \rightarrow c}^{\text{SCRO}} = \begin{pmatrix} -0.018 & 0 & 0 \\ 0 & -0.018 & 0 \\ 0 & 0 & +0.010 \end{pmatrix}; \epsilon_{r \rightarrow a_1}^{\text{SCRO}} = \begin{pmatrix} -0.008 & 0 & 0 \\ 0 & -0.018 & 0 \\ 0 & 0 & +0.010 \end{pmatrix}. \quad (8.4)$$

Again, for $\epsilon_{r \rightarrow a_2}^{\text{SCRO}}$, the strain components $\epsilon_{11}^{\text{SCRO}}$ and $\epsilon_{22}^{\text{SCRO}}$ in $\epsilon_{r \rightarrow a_1}^{\text{SCRO}}$ were interchanged. For the magnetoelastic calculation, the magnetoelastic coupling strength was weakened by a factor of $k = 0.1$ (cf. Section 6.2.3), which describes an incomplete elastic strain coupling of the Sr₂CrReO₆ thin film on the BaTiO₃ substrate. Moreover, the process of the magnetization reversal was simulated by assuming a pinning and domain wall formation energy of $\Delta E/M_s = 900 \text{ mT}$.² Since the $M(H)$ simulations depicted in Fig. 8.4 are based on numerous assumptions, the $M(H)$ loops should be considered as predictions of the magnetic properties of Sr₂CrReO₆ thin films under different strain states imposed by the BaTiO₃ substrate.

Figure 8.4 reveals that the isotropic in-plane anisotropy measured in the tetragonal phase at $T = 290 \text{ K}$ suggests a minor concentration of BaTiO₃ a -domains in this BaTiO₃ substrate. Since a_1 (a_2)-domains force the Sr₂CrReO₆ thin film to elongate along the $[100]_{\text{pc}}$ ($[010]_{\text{pc}}$) direction, the magnetic energy increases in the $[100]_{\text{pc}}$ ($[010]_{\text{pc}}$) direction and decreases along the $[010]_{\text{pc}}$ ($[100]_{\text{pc}}$) direction due to the positive value of B_i (cf. Section 7.2.2). a_1 (a_2)-domains would therefore induce an easy direction of the magnetization along $[010]_{\text{pc}}$ ($[100]_{\text{pc}}$). In contrast, the magnetic behavior of Sr₂CrReO₆ thin film on top of c -domains is isotropic. Thus, Figure 8.3(b) and Fig. 8.4(a) suggest that the BaTiO₃ substrate is dominated by ferroelastic c -domains in the tetragonal phase. The finite coercive field measured in the tetragonal phase is evidence of pinning effects (see Appendix B). In the $[001]_{\text{pc}}$ direction, no magnetic saturation is observed. Therefore, removing the diamagnetic contribution by subtracting a straight line (cf. Section 2.3.1) does not seem to be the correct way, since the magnetic response of the Sr₂CrReO₆ thin film is also affected. This might explain the low saturation magnetization visible in Figure 8.3(b) along $[001]_{\text{pc}}$. In the orthorhombic phase, the difference of the coercive fields measured along $[100]_{\text{pc}}$ and $[110]_{\text{pc}}$ at $T = 270 \text{ K}$ might be explained by Sr₂CrReO₆ thin film areas, which are clamped to BaTiO₃ o_{23} -domains (cf. Fig. 8.3(c) and Fig. 8.4(b)). However, since no electric field nor any elastic stress was applied on the Sr₂CrReO₆/BaTiO₃ hybrid during the measurement, a ferroelastic multi-domain state is expected in each phase of the BaTiO₃ substrate. Therefore, the measured overall magnetization is the summation of the volume normalized magnetic moments stemming from Sr₂CrReO₆ thin film regions on top of different ferroelastic domains, i.e., the weighted sum over the $M(H)$ hysteresis loops displayed in Fig. 8.4. Thus, even if we assume a magnetic single domain state in each region, different ferroelastic domains present in the BaTiO₃ substrate produce a magnetically heterogeneous state in the overlying ferromagnetic thin film due to magnetoelastic effects. To explain the magnetic field dependence of the magnetization shown in Fig. 8.3 in a quantitative manner, the knowledge of the ferroelastic domain pattern is essential.

²For more details on the simulation of magnetic hysteresis loops, see Appendix B.

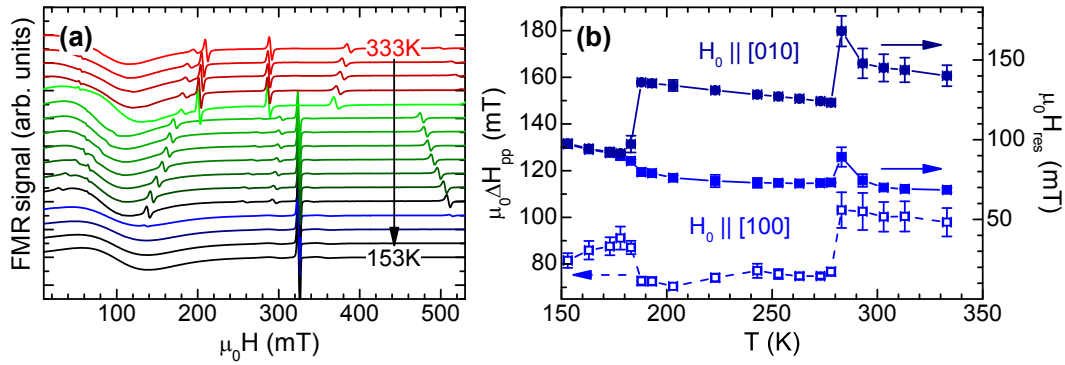


Figure 8.5: Ferromagnetic resonance (FMR) measurements on a $\text{Fe}_3\text{O}_4/\text{BaTiO}_3$ hybrid: (a) X-band FMR spectra as a function of temperature with the external static magnetic field H_0 applied along the pseudo-cubic $[100]_{\text{pc}}$ direction of Fe_3O_4 , (b) temperature dependence of ferromagnetic resonance fields $\mu_0 H_{\text{res}}$ derived from FMR measurements with $H_0 \parallel [100]_{\text{pc}}$ and $H_0 \parallel [010]_{\text{pc}}$ as well as the FMR line width $\mu_0 \Delta H_{\text{pp}}(T)$ for $H_0 \parallel [100]_{\text{pc}}$.

Magnetoelastic effects in $\text{Fe}_3\text{O}_4/\text{BaTiO}_3$ hybrid structures

Not only in $\text{Sr}_2\text{CrReO}_6$ thin films deposited on BaTiO_3 but also in $\text{Fe}_3\text{O}_4/\text{BaTiO}_3$ hybrids, a change of the magnetic anisotropy is observable. In Fig. 8.5, temperature dependent ferromagnetic resonance (FMR) measurements with the external static magnetic field applied along the pseudo-cubic $[100]_{\text{pc}}$ and $[010]_{\text{pc}}$ in-plane directions of Fe_3O_4 are shown. The FMR measurements were carried out at a microwave frequency of 9.3 GHz using a Bruker ESP 300 spin resonance spectrometer described in Section 2.3.2. Furthermore, a nitrogen cryostat was used to vary the temperature of the $\text{Fe}_3\text{O}_4/\text{BaTiO}_3$ hybrid. The measurement series displayed in Fig. 8.5 was performed while decreasing the temperature from 333 K to 153 K. This temperature interval encloses all three ferroelastic BaTiO_3 phases. Each single spectrum shows one broad line around 100 mT, which can be identified as a ferromagnetic resonance of Fe_3O_4 . Several electron paramagnetic spin resonance (EPR) lines caused by mainly Mn, Fe, and Co impurities in the BaTiO_3 substrate are further observed [655]. To investigate the change of the magnetic in-plane anisotropy of the Fe_3O_4 thin film with respect to the different ferroelastic phases of BaTiO_3 , the FMR resonance fields $\mu_0 H_{\text{res}}$ are extracted by fitting the spectra with the first derivative of a Lorentzian line. The FMR resonance fields $\mu_0 H_{\text{res}}$ are shown in Fig. 8.5(b) as a function of temperature for two different orientations of the external static magnetic field. Discontinuous shifts of $\mu_0 H_{\text{res}}$ at the phase transitions of BaTiO_3 can be clearly observed. By comparing the resonance fields of both orientations, large changes of the in-plane magnetic anisotropy in $\text{Fe}_3\text{O}_4/\text{BaTiO}_3$ hybrids become evident. While the FMR resonance fields obtained by aligning the external magnetic field along $[100]_{\text{pc}}$ and $[010]_{\text{pc}}$ coincide below 185 K, i.e., in the rhombohedral phase of BaTiO_3 , a clear difference is observed in the orthorhombic and tetragonal phase. This indicates the presence of an additional uniaxial magnetic anisotropy due to magnetoelastic effects caused by orthorhombic o_{13} - and o_{23} -domains as well as tetragonal

a_1 - and a_2 -domains. By analyzing the line width of the ferromagnetic resonance $\mu_0\Delta H_{pp}$, a distinct temperature dependence is observed (see Fig. 8.5(b)). The line width is considerably reduced in the orthorhombic phase of the BaTiO₃ substrate. However, the absolute value of $\mu_0\Delta H_{pp}$ is around three times larger than for Fe₃O₄ thin films grown on lattice matched MgO substrates [656]. This can be explained by expressing the line width as a sum over the intrinsic damping of the magnetization (homogeneous contribution) and extrinsic effects caused by inhomogeneities of the sample. The inhomogeneous contributions arise from sample imperfections, such as mosaic structures and defects. Since the mosaic spread is much higher in Fe₃O₄ thin films grown on BaTiO₃ substrates than on lattice matched MgO substrates, the enhancement of the line width can be mainly attributed to crystalline defects. Furthermore, the line width is also highly sensitive to internal stresses [657, 658]. In the orthorhombic phase, the BaTiO₃ substrate is expected to be highly twinned [535]. Surprisingly, the line width is smaller in the orthorhombic phase compared to the rhombohedral and tetragonal phases. However, no detailed conclusion can be drawn on this matter without the detailed knowledge of the domain configuration in the BaTiO₃ substrate. Different ferroelastic domains present in the BaTiO₃ substrate at a given temperature induce different amounts of strain into the Fe₃O₄ thin film, which leads to different FMR lines overlapping each other. However, the large line width of the ferromagnetic resonance in Fe₃O₄/BaTiO₃ hybrid samples prevents a separation of these individual FMR lines. Therefore, the ferromagnetic resonance fields μ_0H_{res} displayed in Fig. 8.5(b) can be interpreted as indicator for an averaged magnetic anisotropy in the Fe₃O₄ thin film. To resolve this issue, a full control of the ferroelastic domain configuration is mandatory.

BaTiO₃ based hybrid structure using polycrystalline ferromagnetic thin films

In FM/BaTiO₃ hybrids using polycrystalline ferromagnetic thin films, the situation is even more complicated. In these samples, the ferromagnetic thin film was deposited at room temperature on the BaTiO₃ substrate. At this temperature, the BaTiO₃ substrates exhibit a certain ferroelastic domain structure on which the ferromagnetic thin film is deposited in an unstrained state. The detailed domain structure of the BaTiO₃ substrate during the fabrication process is unknown, since no external fields can be applied during the deposition. Therefore, the starting point for the description of strain-mediated changes of the magnetization in FM/BaTiO₃ hybrids is also unknown. However, changes of the magnetic anisotropy can be observed in polycrystalline ferromagnetic thin films deposited on BaTiO₃ substrates. As an example, Figure 8.6 shows the result of angle-dependent magnetoresistance (ADMR) measurements carried out in Ni/BaTiO₃ hybrids at 300 K (see Figs. 8.6(a) and (b)), i.e., in the tetragonal phase of BaTiO₃, and in the orthorhombic phase at 270 K (see Figs. 8.6(c) and (d)). For these measurements, a 50 nm thick Ni thin film was patterned into Hall bars with the current direction j along the pseudo-cubic $[010]_{pc}$ direction of the BaTiO₃ substrate. The resistivities along the direction of the current density ρ_{xx} as well as perpendicular to the current density ρ_{xy} were recorded

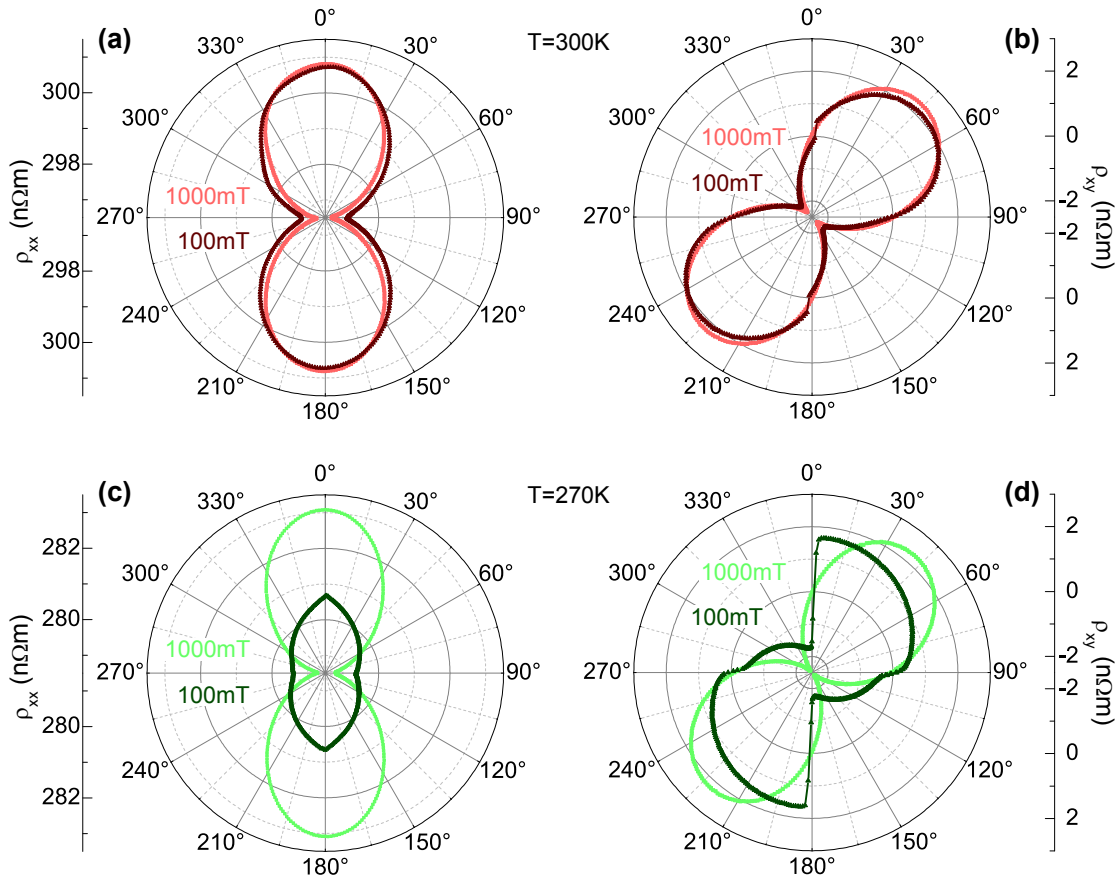


Figure 8.6: Longitudinal resistivity ρ_{xx} and transverse resistivity ρ_{xy} of a 50 nm thick Ni thin film on a BaTiO₃ substrate measured at (a), (b) 300 K and (c), (d) 270 K for external magnetic field strengths of 1000 mT and 100 mT. The external magnetic field was rotated within the film plane, i.e., in the pseudo-cubic (001)_{pc} plane of the BaTiO₃ substrate. 0° is equal to the pseudo-cubic [010]_{pc}-direction of the BaTiO₃ substrate.

at a fixed external magnetic field strength via angle-dependent magnetoresistance measurements, where the magnetic field is rotated in the (001)_{pc} plane of the BaTiO₃ substrate. At sufficiently high magnetic field strength of $\mu_0 H = 1000$ mT, the magnetization follows the magnetic field and the resistivity tensor depends only on the crystal symmetry of the ferromagnetic material. In case of a polycrystalline ferromagnetic materials, the resistivity does not depend on the direction of the current density \mathbf{j} relative to the crystal axis (cf. Section 2.3.3). By lowering the magnetic field strength, the magnetic anisotropy becomes significant. For small magnetic fields, the magnetization tends to remain oriented close to a magnetic easy axis. ρ_{xx} and ρ_{xy} therefore are constant over a broad range of external magnetic field orientations nearby a magnetic easy axis. The difference in shape of the angle-dependent resistivity ρ_{xx} and ρ_{xy} recorded at 300 K and 270 K with an external magnetic field of $\mu_0 H = 100$ mT clearly confirms changes of the magnetic anisotropy by crossing the phase transition of the BaTiO₃ substrate from the tetragonal to the orthorhombic symmetry. These changes are mainly explained by different ferroelastic domains present in the BaTiO₃ substrate.

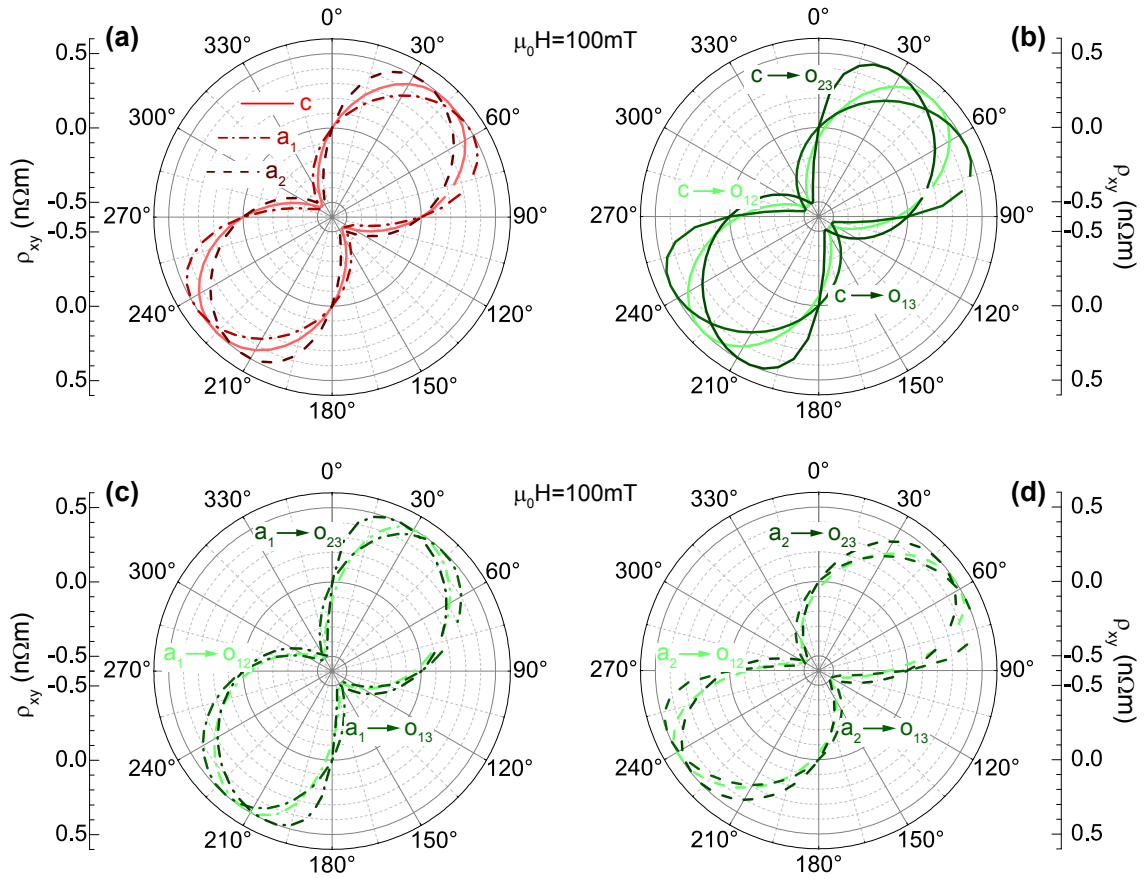


Figure 8.7: Schematic illustration of angle-dependent transverse magnetoresistance ρ_{xy} for polycrystalline Ni simulated for an external magnetic field of $\mu_0 H = 100$ mT and a resistivity parameter ρ_2 of 1 n Ω . The magnetoelastic coupling is attenuated by a factor of $k = 0.1$. (a) ρ_{xy} at 300 K calculated for tetragonal c -, a_1 -, and a_2 -domains of the BaTiO₃ substrate. The BaTiO₃ substrate was assumed to consist of only c -domains during the deposition of the Ni thin film. (b)-(d) ρ_{xy} simulated for different ferroelastic domain transformations while crossing the phase transition from the tetragonal phase to the orthorhombic phase. The calculation was carried out for $T = 270$ K. 0° is equal to the pseudo-cubic $[010]_{pc}$ -direction of the BaTiO₃ substrate.

To illustrate the effect of different ferroelastic domains in the BaTiO₃ substrate on ADMR measurements, Figure 8.7 shows simulations of the angle-dependent transverse magnetoresistance ρ_{xy} for a polycrystalline Ni thin film. The simulation was carried out according to the method described in Section 2.3.3 using an external magnetic field of $\mu_0 H = 100$ mT as well as a resistivity parameter ρ_2 of 1 n Ω . Without any external fields applied, the BaTiO₃ substrate exhibits a ferroelastic multi-domain state. In particular at 300 K, the BaTiO₃ substrate can consist of ferroelastic c -, a_1 -, and a_2 -domains (see Fig. 7.1). Assuming that the Ni thin film is deposited on top of c -domains, the following strain tensors of the Ni thin film can be calculated for different ferroelastic domains present in the tetragonal symmetry of the BaTiO₃ substrate (cf. Section 7.1):

$$\epsilon_c^{\text{Ni}} = \begin{pmatrix} 0 & 0 & 0 \\ 0 & 0 & 0 \\ 0 & 0 & 0 \end{pmatrix}; \epsilon_{a_1}^{\text{Ni}} = \begin{pmatrix} 0.010 & 0 & 0 \\ 0 & 0 & 0 \\ 0 & 0 & -0.006 \end{pmatrix}; \epsilon_{a_2}^{\text{Ni}} = \begin{pmatrix} 0 & 0 & 0 \\ 0 & 0.010 & 0 \\ 0 & 0 & -0.006 \end{pmatrix}.$$

The in-plane strain components are derived from molecular dynamics simulations (cf. Fig. 7.2). Using these strain tensors, the orientation of the magnetization can be calculated using the magnetoelastic energy density u_{magel} (cf. Eq. (6.4)). A reduction of the magnetoelastic coupling by $k = 0.1$ with respect to a ideal clamping of the Ni thin film on the BaTiO₃ was used. The results of the ADMR simulations assuming c -, a_1 -, and a_2 -domains in the BaTiO₃ substrate are depicted in Fig. 8.7(a). A distinct difference in ρ_{xy} is observable for all three ferroelastic domains. Upon crossing the phase transition from tetragonal to orthorhombic, each of the tetragonal domains can transform into different orthorhombic ones. Figures 8.7(b)-(d) display the transverse magnetoresistance ρ_{xy} simulated for all possible transformations on the basis of the strain tensors³

$$\epsilon_{c \rightarrow o_{12}}^{\text{Ni}} = \begin{pmatrix} 0.006 & 0.001 & 0 \\ 0.001 & 0.006 & 0 \\ 0 & 0 & -0.007 \end{pmatrix}; \epsilon_{c \rightarrow o_{13}}^{\text{Ni}} = \begin{pmatrix} 0.006 & 0 & 0 \\ 0 & -0.009 & 0 \\ 0 & 0 & -0.003 \end{pmatrix}.$$

The strain tensor $\epsilon_{c \rightarrow o_{23}}^{\text{Ni}}$ can be derived by interchanging the ϵ_{11} and ϵ_{22} components of $\epsilon_{c \rightarrow o_{13}}^{\text{Ni}}$. Furthermore, $\epsilon_{a_1 \rightarrow o_{12}}^{\text{Ni}}$, $\epsilon_{a_1 \rightarrow o_{13}}^{\text{Ni}}$, and $\epsilon_{a_1 \rightarrow o_{23}}^{\text{Ni}}$ as well as $\epsilon_{a_2 \rightarrow o_{12}}^{\text{Ni}}$, $\epsilon_{a_2 \rightarrow o_{13}}^{\text{Ni}}$, and $\epsilon_{a_2 \rightarrow o_{23}}^{\text{Ni}}$ can be obtained in an analogous manner. Depending on the domain types present in the BaTiO₃ substrate at 300 K (tetragonal phase) and at 270 K (orthorhombic phase), different shapes of the transverse magnetoresistance ρ_{xy} are visible as a function of the in-plane angle. However, the measured transverse resistivity is a parallel or series connection of these different transverse magnetoresistance traces, which makes a quantitative simulation of the experimental results virtually impossible. Again, to obtain results, which can be directly compared to theory, a control of the ferroelastic domain configuration of the BaTiO₃ substrate is essential.

In summary, by employing different techniques, it was shown that physical properties such as lattice constants, resistance and magnetization of ferromagnetic thin films fabricated on top of ferroelastic BaTiO₃ substrate can clearly be modified by simply varying the temperature. In particular, the out of plane lattice constant of Sr₂CrReO₆ nicely follows the lattice constant of the BaTiO₃ substrate proving a nearly perfect elastic coupling between the Sr₂CrReO₆ thin film and the BaTiO₃ substrate in this sample. This is further demonstrated by distinct steps in the temperature dependence of the magnetization and the resistance. A finite strain-mediated coupling between the magnetization and the ferroelastic BaTiO₃ substrate is not limited to Sr₂CrReO₆/BaTiO₃ hybrid structures, but could also be observed

³The probability of the transformation of tetragonal c -domains into orthorhombic o_{12} -domains is small, since the ferroelectric polarization has to switch by 90° during the $c \rightarrow o_{12}$ -domain transition.

in ferromagnetic resonance measurements carried out on epitaxial Fe₃O₄ thin films as well as in angle-dependent magnetotransport measurements in polycrystalline Ni thin films deposited on BaTiO₃ substrates

8.2 Ferroelastic domain control in BaTiO₃ substrates

As has become clear in the previous section, the physical properties of ferromagnetic thin films in FM/BaTiO₃ hybrid structures are highly dependent on the ferroelastic domain configuration present in the BaTiO₃ substrates. Therefore, a ferroelastic domain control in each phase of the BaTiO₃ is essential for a quantitative analysis of the experimental results. Ferroelastic domain control leads to a well-defined strain state in the BaTiO₃ substrate. Changes of this strain state cause modifications of the magnetic anisotropy in the clamped ferromagnetic thin film, which can be described by magnetoelastic theory. Different methods can be used to realize domain engineering in ferroelectric and ferroelastic materials, e.g. by applying electric and elastic fields, inserting charged point defects or structural defects, or creating disorder in an ordered system using physical means other than chemical doping [659–662]. One of the simplest ways to obtain ferroelastic crystals with preferred domain configuration is to pole the crystal in an electric field applied along a specific direction. The poling procedure applied here consists of heating the sample to 450 K (well above the ferroelectric Curie temperature T_c of BaTiO₃) and cooling it back to room temperature using a cooling rate of 2 K/min in an electric field of 400 kV/m applied along the out-of-plane direction. To be able to apply an electric field of sufficient magnitude across the hybrid structure, the BaTiO₃ substrate was polished down to a thickness of 500 μm from the back followed by the deposition of a Au electrode on the backside of the substrate. Both steps were carried out after the fabrication of the overlying ferromagnetic thin film.

When the BaTiO₃ substrate crosses the phase transition from the non-polar paraelectric to the polar ferroelectric phase without any external field applied, the reduction of the symmetry leads to the formation of three different ferroelastic variants (see Fig. 7.1), so that the energy density is minimized. The resulting domain configuration can be investigated by using x-ray diffraction (Fig. 8.8(a)). The reciprocal space map around the BaTiO₃ (002) reflection of a Fe₃O₄/BaTiO₃ hybrid structure recorded at 300 K after the deposition of Fe₃O₄ reveals several *a*- and *c*-domains, which are tilted in different directions. In contrast, cooling down the sample in an electric field, a subset of ferroelastic variants will be selected which are energetically favored by the applied electric field. In Fig. 8.8(b) the same reciprocal mesh scan recorded after poling the BaTiO₃ substrate is displayed. A change of the preferred ferroelastic domain type can be observed. While the BaTiO₃ substrate used in this thesis mainly consist of *a*-domains after the deposition, (cf. Fig. 8.8(a)), during the poling procedure, *c*-domains are primarily formed, such that a BaTiO₃ single crystal with preferred *c*-domains can be obtained. Therefore, poling should evoke a ferroelastic single domain state along the poling direction [85]. Furthermore, the

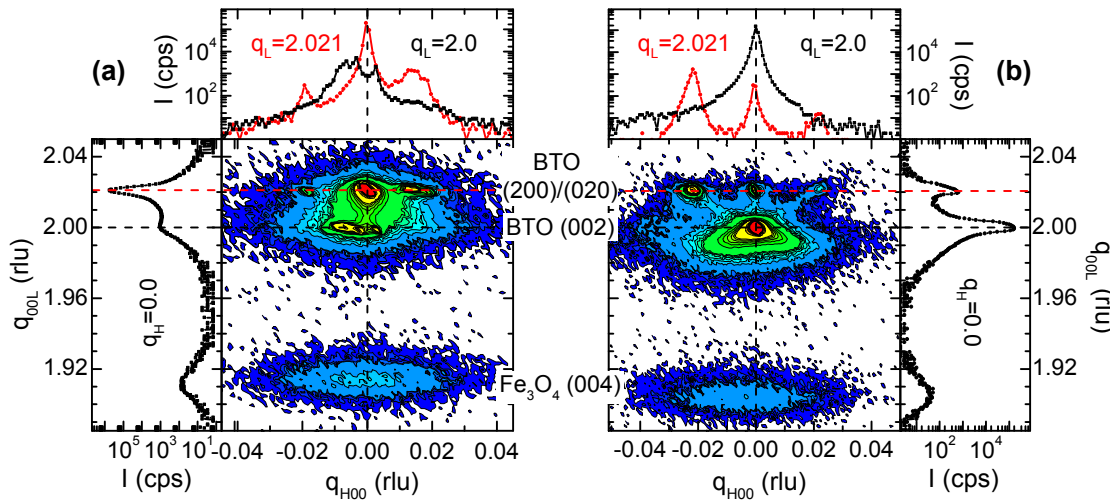


Figure 8.8: Room temperature x-ray diffraction diagrams of a $\text{Fe}_3\text{O}_4/\text{BaTiO}_3$ hybrid structure recorded (a) before and (b) after the poling procedure described in the text. a -domains are denoted by $\text{BaTiO}_3(200)/(020)$ and c -domains by $\text{BaTiO}_3(002)$, respectively.

magnetolectric response was enhanced by carrying out electric field poling procedures in laminate magnetolectric composites [663]. The change of the preferred ferroelastic domain configuration in the BaTiO_3 substrate also influences the structural properties of the overlying ferromagnetic thin film due to elastic coupling. By comparing Figs. 8.8(a) and (b), an increase of the out-of-plane lattice constant of Fe_3O_4 of about 0.003 nm after applying the poling procedure is observed.

However, poling does not completely suppress a_1 -/ a_2 -domains. Rather, a ferroelastic multi-domain state with tilted a_1 -/ a_2 -domains and c -domains can still be detected in poled BaTiO_3 crystals. To further simplify the domain structure, BaTiO_3 substrates exhibiting a certain miscut are used in the following. To investigate the surface of these crystals with respect to the crystalline orientation of the c -domains, the specular reflection was measured by performing rocking curves at a low detector angle of $2\theta = 0.4^\circ$ (below the critical angle for total reflection) under different in-plane orientations of the BaTiO_3 substrate. A finite deviation $\Delta\omega$ between the measured angle ω_{\max} , where the rocking curve shows maximum intensity, from the ideal angle 0.2° proves a certain miscut angle of the BaTiO_3 substrate (see Fig. 8.9(a)). To extract ω_{\max} , each rocking curve was fitted with a Gaussian line. Figure 8.9(b) reveals that $\Delta\omega_{\max} = \omega_{\max} - 0.2^\circ$ follows a sine curve, from which a miscut angle of 0.9° as well as an in-plane misalignment of 7° with respect to the ferroelastic c -domains is derived. Other BaTiO_3 substrates used in this work exhibit a miscut angle between 0.8° and 1.0° .

The finite miscut has tremendous influence on the ferroelastic domain structure of BaTiO_3 . First, x-ray diffraction measurements recorded on these substrates after performing the poling procedure described above reveal a -domains, which are tilted in one particular direction. In Figs. 8.10(a) and (b) reciprocal space maps around the $\text{BaTiO}_3(002)$ reflection measured for two different in-plane orientations of the sam-

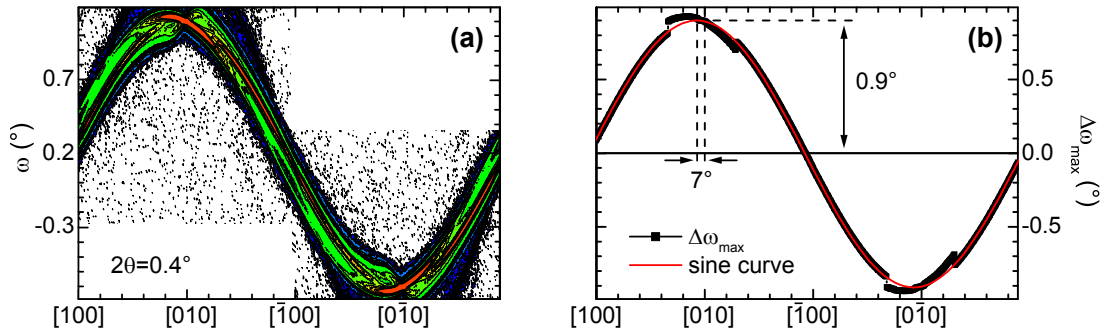


Figure 8.9: (a) Investigation of the surface of BaTiO₃ substrates exhibiting a certain miscut angle. (a) Color-coded rocking curves (vertical axis) carried out at a low detector angle of $2\theta = 0.4^\circ$ for different in-plane orientations (horizontal axis). Before the measurement series, the in-plane orientation of the sample was aligned along the $[100]_{pc}$ direction of the BaTiO₃ c -domains. To extract the angle of the maximum intensity ω_{\max} , each rocking curve is fitted by a Gaussian line. (b) $\Delta\omega_{\max} = \omega_{\max} - 0.2^\circ$ follows a sine curve (red line) from which an in-plane misalignment of 7° and a miscut angle of 0.9° with respect to the ferroelastic c -domains can be derived.

ple are shown. While x-ray diffraction measurements in the q_{H00} - q_{00L} -plane suggest parallel scattering planes for both c - and a -domains, tilting of a -domains is clearly detectable in the q_{0K0} - q_{00L} -plane (cf. Fig. 8.10(b)). A careful analysis yields a tilt angle of $(0.58 \pm 0.01)^\circ$, which is in good agreement with the angle across 90° -domain walls displayed in Fig. 7.4(a). To get detailed information about the tilt direction, q_{H00} -line scans were performed at $q_{00L} = 2$ rlu and $q_{00L} = 2.021$ rlu under different in-plane orientations of the BaTiO₃ substrate, i.e., different Φ -angles. The resulting q_{H00} - q_{0K0} planes are displayed in Figs. 8.10(c) and (d). These measurements prove that a -domains are mainly tilted in the $[0\bar{1}0]$ direction with respect to c -domains in these miscut BaTiO₃ substrates.

The second consequence of miscut BaTiO₃ crystals is the existence of only one type of a -domains. Figure 8.11 shows x-ray diffraction measurements along the asymmetric BaTiO₃ (204) reflection carried out under different in-plane orientations of the BaTiO₃ substrate. The reciprocal space maps reveal two reflections (cf. Figs. 8.11(a) and (b)). One is caused by c -domains at $q_{00L} = 4.0$ rlu and the other by a_2 -type domains. The second type of a -domains could not be detected, neither in the q_{H00} - q_{00L} -plane, nor in the q_{0K0} - q_{00L} -plane. Therefore, only one type of a -domains are present in miscut BaTiO₃ substrates. Since reciprocal space maps are normally recorded at fixed in-plane orientation of the sample, the in-plane angle of the sample with the maximum intensity of both reflections should be chosen. To identify this orientation, reciprocal space maps with different Φ -angles around BaTiO₃ (204) and BaTiO₃ (024) were recorded and the intensity of each mesh scan was integrated for $q_{00L} \leq 4.2$ rlu and for $q_{00L} > 4.2$ rlu, respectively (Figs. 8.11(c) and (d)). The former is an indication for c -domains and the latter for a -domains. Figures 8.11(c) and (d) reveal a coincidence of the maximum integrated intensity of both domain types only around BaTiO₃ (024), i.e., in the q_{00L} - q_{0K0} plane. Therefore, an estimation of

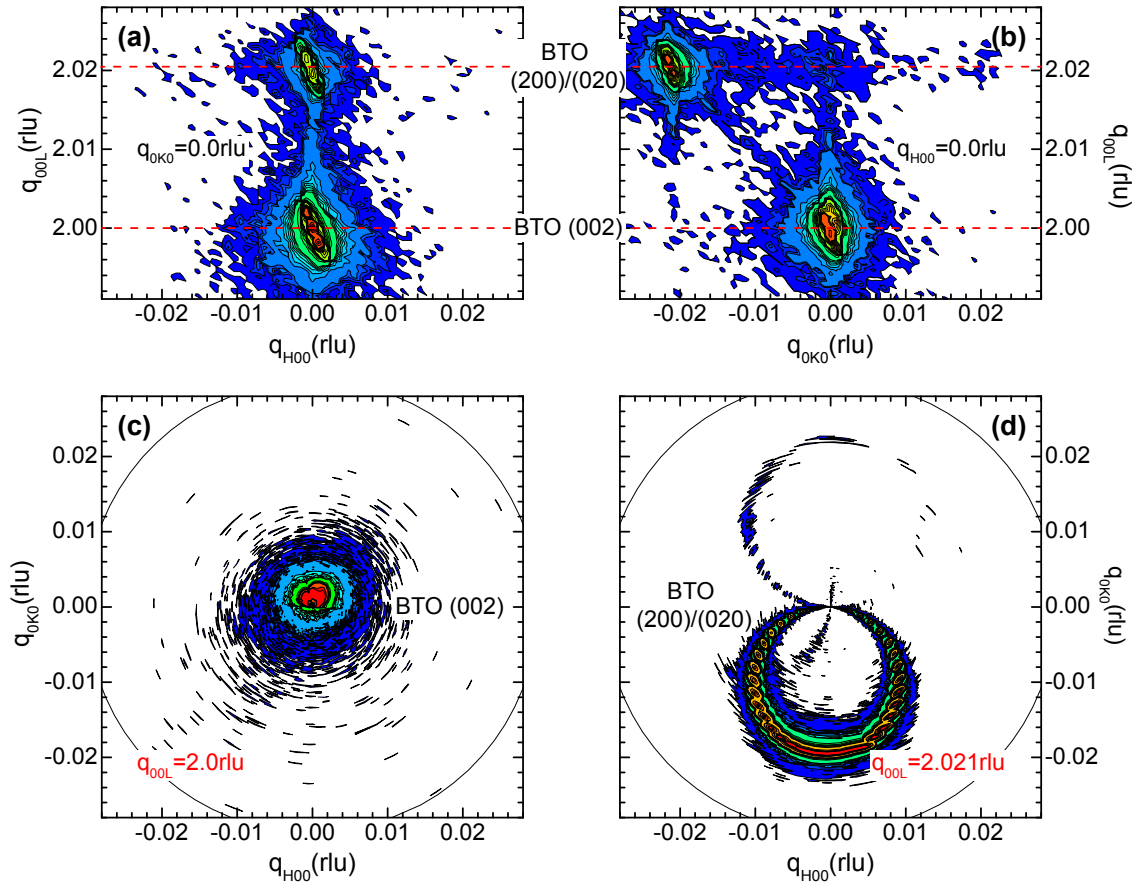


Figure 8.10: X-ray diffraction measurements around the BaTiO_3 (002) reflection measured for two different in-plane orientations: (a) q_{H00} - q_{00L} -plane and (b) q_{0K0} - q_{00L} -plane. To get three dimensional information about the tilted a -domains, q_{H00} -line scans were performed at (c) $q_{00L} = 2$ rlu and (d) $q_{00L} = 2.021$ rlu under different in-plane angles. The color-coded intensities are depicted in q_{H00} - q_{0K0} planes for both q_{00L} values. The measurement ranges are marked by black circles.

the volume fraction of c - and a -domains by using x-ray diffraction should always be done by mapping the q_{00L} - q_{0K0} plane.

The absence of a_1 -domains in miscut BaTiO_3 substrates used for FM/ BaTiO_3 hybrid structures obviously changes the in-plane periodicity of the magnetic properties. Since only a_2 -domains are present in the BaTiO_3 substrates, only one preferred direction of the magnetization is induced in a ferromagnetic thin film deposited on top of c -domains due to the transformation of c -domains into a -domains in the underlying BaTiO_3 substrate. This preferred direction can be investigated, for example, by using ferromagnetic resonance (FMR) spectroscopy (Fig. 8.12(a)). The corresponding measurements were carried out in the tetragonal phase of the BaTiO_3 substrate at room temperature on a Ni/ BaTiO_3 hybrid structure. Two different ferromagnetic resonances are observed in all spectra confirming two ferromagnetic regions with different magnetic anisotropies. One ferromagnetic resonance line can be attributed to those parts of the Ni thin film on top of c -domains and the other

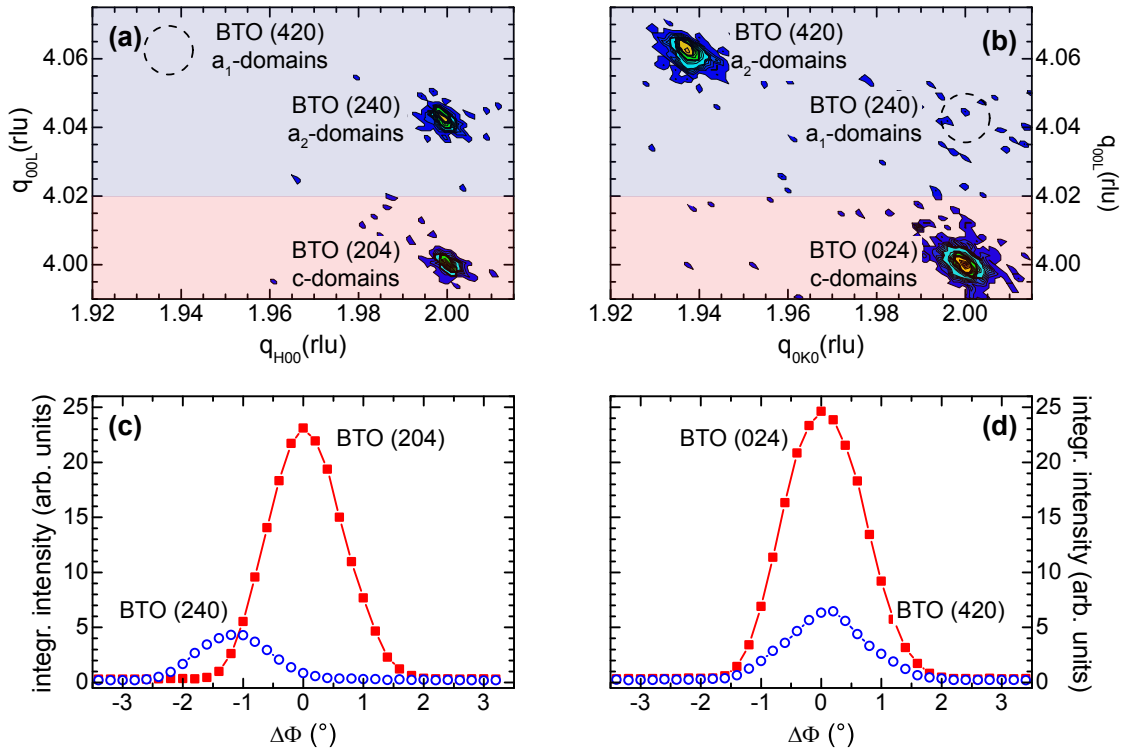


Figure 8.11: X-ray diffraction measurements around the asymmetric (a) BaTiO₃ (204) and (b) BaTiO₃ (024) reflections. Only reflections caused by *c*- and tilted *a*₂-domains are visible. The expected positions of x-ray diffraction on tilted *a*₂-domains are marked by dashed circles. To get three dimensional information about the tilted *a*₂-domains, reciprocal space maps with different Φ -angles around BaTiO₃ (204) and BaTiO₃ (024) were recorded. The intensity of each mesh scan is integrated for $q_{00L} \leq 4.2$ rlu (red shaded area) and $q_{00L} > 4.2$ rlu (blue shaded area) and plotted as a function of the in-plane orientation around (c) BaTiO₃ (204) and (d) BaTiO₃ (024).

to regions on *a*-domains. The ferromagnetic resonance fields are labeled with H_{res}^c and H_{res}^a in Fig. 8.12(b), respectively. The FMR spectra can be simulated by first derivatives of Lorentzian lines (cf. black dashed lines in Fig. 8.12(b)) using ferromagnetic resonance fields calculated from magnetoelastic theory. In this numerical calculation, the magnetoelastic coupling had to be attenuated by $k = (0.23 \pm 0.02)$ to fit the experimental data. Furthermore, a small uniaxial anisotropy with an anisotropy field of $K_{\text{uniax}}/M_s = 2$ mT, probably induced during the deposition of Ni, is included into the simulation. The experimental results can only be described by the assumption of one type of *a*-domains present in the BaTiO₃ substrate. The pronounced second ferromagnetic resonance for $\mathbf{H}_0 \parallel [010]$ at $\mu_0 H_{\text{res}} = 197$ mT is caused by the transformation of *c*-domains into *a*₂-domains. The tetragonal unit cells of *a*₂-domains are oriented with their longer *c*-axis parallel to the BaTiO₃ surface along the pseudo-cubic $[010]_{\text{pc}}$ direction, which is close to the *y*-direction of the BaTiO₃ crystal. Therefore, tensile strain is induced in the Ni thin film, which causes a large uniaxial magnetic anisotropy due to converse magnetostriction shifting the ferromagnetic resonance to higher magnetic fields compared to the $[100]_{\text{pc}}$ direction.

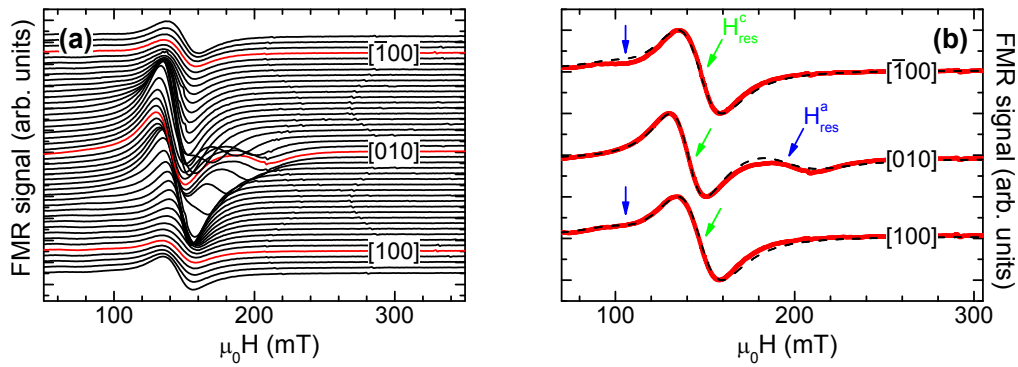


Figure 8.12: (a) Ferromagnetic resonance (FMR) spectra for different in-plane orientations of a Ni/BaTiO₃ hybrid structure measured in the tetragonal phase of BaTiO₃ at room temperature. (b) The FMR spectra can be simulated by first derivatives of Lorentzian lines (black dashed lines). The two ferromagnetic resonance fields are labeled with H_{res}^c and H_{res}^a . The magnetoelastic coupling must be attenuated by $k = (0.23 \pm 0.02)$ to obtain a good fit to the experimental data. Furthermore, a uniaxial anisotropy ($K_{\text{uniax}}/M_s = 2 \text{ mT}$) is included in the simulation.

This preferred y -direction observable in the FMR spectra confirms the results from x -ray diffraction measurements displayed in Fig. 8.11.

In total, a reduction of the number of ferroelastic domain types were achieved by using BaTiO₃ substrates exhibiting a certain miscut angle. Figure 8.13 schematically shows a BaTiO₃ substrate with a possible ferroelastic domain configuration. Note that x -ray diffraction measurements reveal that the crystalline orientation of the ferroelastic domains does not coincide with the BaTiO₃ substrate edges. Therefore, the sample edges of BaTiO₃ substrates are denoted as $(\mathbf{x}, \mathbf{y}, \mathbf{z})$ and the crystallographic axes of the ferroelastic domains as $\langle 100 \rangle_{\text{pc}}$ in the pseudo-cubic notation. However, these BaTiO₃ substrates, which are used in the following for FM/BaTiO₃ hybrid structures, pave the way to study the manipulation of the magnetization in FM/BaTiO₃ systems in a more quantitative manner.

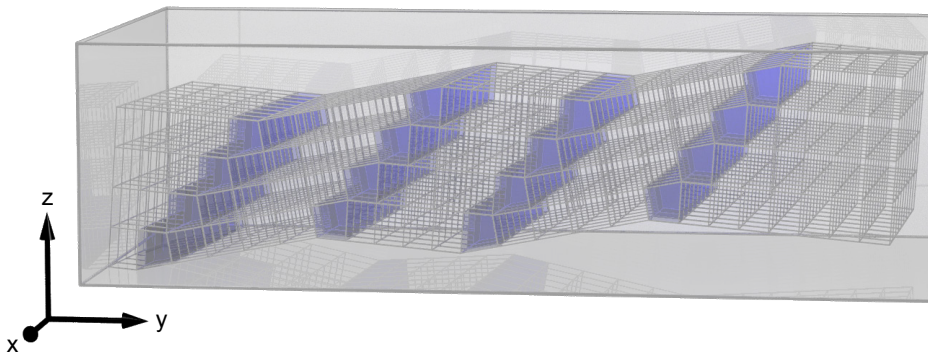


Figure 8.13: Schematic representation of the BaTiO₃ substrate used for FM/BaTiO₃ hybrid structures. The 90° domain walls are marked in blue.

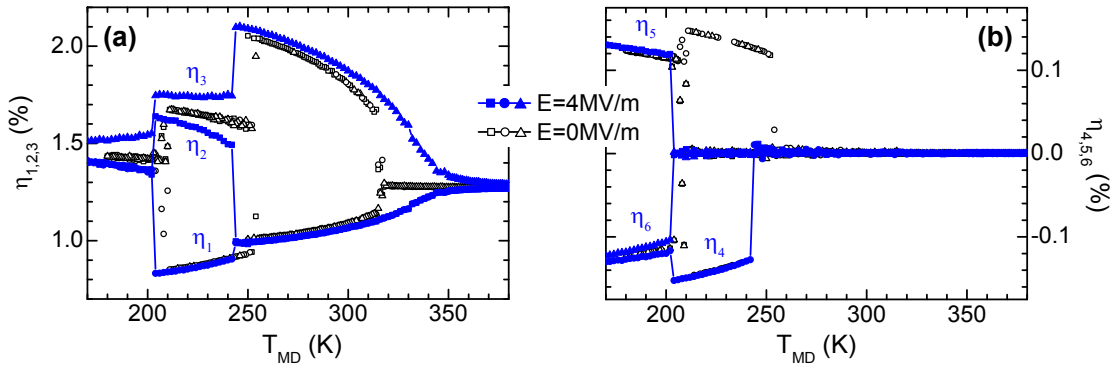


Figure 8.14: Molecular dynamics simulations based on the effective Hamiltonian described in Section 7.1 as a function of temperature T_{MD} and electric field E . The strain components η_i with $i = 1\dots 6$ are calculated with respect to the lattice constant of 0.3948 nm. The BaTiO₃ phase diagram was simulated using a $16 \times 16 \times 16$ supercell and each temperature was thermalized within 60000 steps and averaged over 60000 calculations. Moreover, the electric field was applied along the \mathbf{z} -direction of the BaTiO₃ crystal.

8.3 FM/BaTiO₃ hybrid structures with ferroelastic domain control

As discussed above, crossing the ferroelastic phase transitions of BaTiO₃ has substantial effects on the magnetic and electronic properties of the overlying ferromagnetic thin film. However, each BaTiO₃ phase exhibits a certain number of different ferroelastic domains, imposing different strain states in the ferromagnetic thin film. Furthermore, the transition between the different domains is only partly deterministic and reproducible at each phase transition. For the measurements discussed in the following, an electric field is therefore applied across the miscut BaTiO₃ substrate along the \mathbf{z} -direction to control the ferroelastic domain transformation at each phase transition in the spirit of Section 8.2.

8.3.1 Calculation of the BaTiO₃ strain tensor under electric fields

When an electric field is applied to a ferroelectric material the shape of the crystal changes due to the converse piezoelectric effect. The change in shape of miscut BaTiO₃ substrates can be calculated using the method described in Section 7.1. In this spirit, we performed molecular dynamics simulations for an electric field of 4 MV/m applied along the \mathbf{z} -direction of the BaTiO₃ substrate (cf. Fig. 8.13) and for different temperatures. 4 MV/m is theoretically needed to ensure a single ferroelastic state in each phase of BaTiO₃ (cf. Fig. 7.3).

The resulting BaTiO₃ phase diagram is shown in Fig. 8.14. For comparison, the calculation for $E = 0\text{MV/m}$ is also included in the figure (cf. Fig. 7.2). The strain components η_i were calculated by using the same parameters as described in Sec-

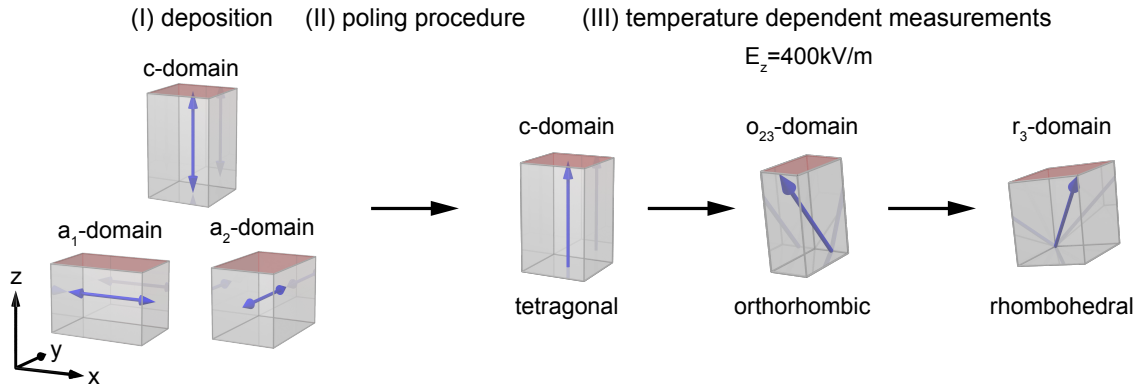


Figure 8.15: Schematic illustration of the time evolution of the fabrication and temperature dependent measurements of FM/BaTiO₃ hybrid structures using polycrystalline FeCo and Ni thin films deposited at room temperature in the tetragonal phase of BaTiO₃ (I). The applied electric field of 400 kV/m along the z -direction and the use of miscut BaTiO₃ substrates does not only create (II) a nearly single domain state at room temperature in the tetragonal phase (c -domains), but also select (III) particular domains in the orthorhombic (o_{23} -domains) and rhombohedral (r_3 -domains) phase of BaTiO₃.

tion 7.1. Figure 8.14(a) reveals that the temperature range of the tetragonal phase expands upon applying a finite electric field. Furthermore, the cubic to tetragonal phase transition becomes diffuse and the transition temperature increases by about 40 K. At first glance, the influence of the applied electric field on the strain components of the orthorhombic and rhombohedral phase is minor. A slight change of the transition temperatures can again be observed. However, a finite electric field reduces the symmetry of the orthorhombic and rhombohedral phases. The new symmetry can be identified to be monoclinic with \mathbf{P} aligned along $[0uv]$ where $u \neq v$ (M_C phase) or along $[uvw]$ with $u < v$ (M_A phase), respectively [664, 665]. In spite of these symmetry changes, both phases are consistently labeled by the parent orthorhombic and rhombohedral phase throughout this thesis. Using the strain components displayed in Fig. 8.14, the change of the magnetization as a function of temperature in FM/BaTiO₃ hybrid structures can be calculated employing magnetoelastic theory as described in Section 6.2.

8.3.2 Magnetization changes in FM/BaTiO₃ hybrid structures as a function of temperature

The temperature dependence of the magnetization in FM/BaTiO₃ hybrid structures was investigated experimentally, for an applied electric field of 400 kV/m. For FM/BaTiO₃ hybrid structures using polycrystalline FeCo and Ni as ferromagnetic materials, the time evolution of the fabrication and temperature dependent measurements can be described as follows (see Fig. 8.15). First, FeCo and Ni are deposited on BaTiO₃ at room temperature, i.e., in the tetragonal phase (cf. (I) in Fig. 8.15). During the deposition, the BaTiO₃ substrate exhibits an unknown multi-domain configuration with a certain concentration of c -domains (x_c^{dep}), a_1 -domains ($x_{a_1}^{\text{dep}}$),

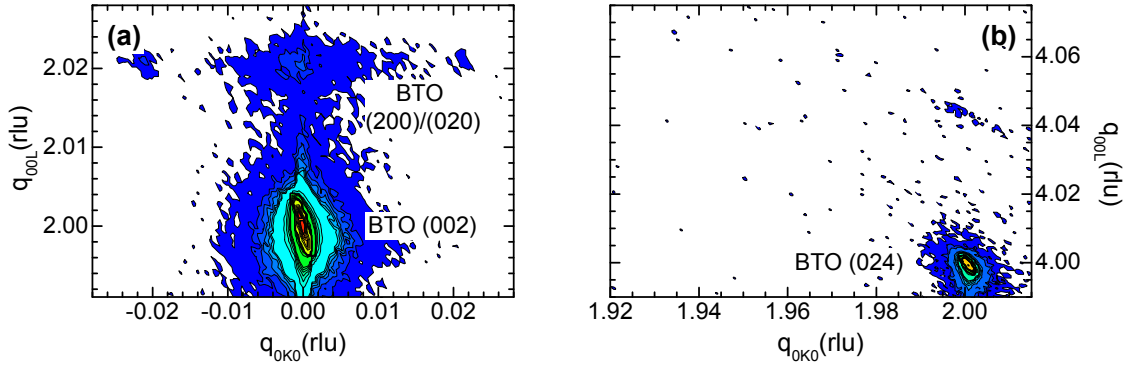


Figure 8.16: X-ray diffraction measurements around (a) BaTiO₃(002) and (b) BaTiO₃(024) carried out at 300 K with an electric field of 400 kV/m applied along the z -direction.

and a_2 -domains ($x_{a_2}^{\text{dep}}$). After the deposition, the poling procedure described in Section 8.2 was carried out on the FM/BaTiO₃ hybrids creating the particular domain configuration sketched in Fig. 8.13. Afterwards the magnetization of FeCo/BaTiO₃ and Ni/BaTiO₃ was measured as a function of temperature in an electric field of 400 kV/m applied along the z -direction (cf. (III) in Fig. 8.15). At this electric field, poled FM/BaTiO₃ hybrid structures exhibit a single domain state at room temperature.

Figure 8.16 shows x-ray diffraction measurements around the BaTiO₃(002) and BaTiO₃(024) reflections recorded at 300 K with an electric field of 400 kV/m applied along the z -direction. In contrast to Figs. 8.10(b) and 8.11(b), almost no intensity is observable at the Bragg positions of a -domains. This indicates that the BaTiO₃ substrate transforms into an almost single ferroelastic domain state at an electric field of 400 kV/m. By integrating the intensity above and below $q_{00L} = 2.01$ r.l.u., the remaining concentration of a -domains can be estimated to be less than 1%. The critical electric field of 400 kV/m is one order of magnitude smaller than the value needed to ensure a single domain state from theoretical simulations and experiments carried out in an unpoled BaTiO₃ crystal with a thickness of 1 mm (see Fig. 7.3). Therefore, the use of poled miscut BaTiO₃ substrates significantly reduces the electric field strength needed to achieve a ferroelastic single domain state at room temperature.

However, the applied electric field and the use of miscut BaTiO₃ substrates does not only create a single domain state at room temperature, but also selects particular domains in the orthorhombic and rhombohedral phases of BaTiO₃, which are energetically favored (cf. Fig. 8.15). Therefore, a controlled strain state can be imposed in the ferromagnetic thin film at each ferroelastic phase of the BaTiO₃ substrate.

In order to simulate the magnetic response of the ferromagnetic thin film clamped to the BaTiO₃ substrate on the basis of the calculated BaTiO₃ strain components (cf. Fig. 8.14) by utilizing magnetoelastic theory, the only unknown parameters are the volume fraction of the a -domains during deposition ($x_{a_1}^{\text{dep}}$ and $x_{a_2}^{\text{dep}}$) and the

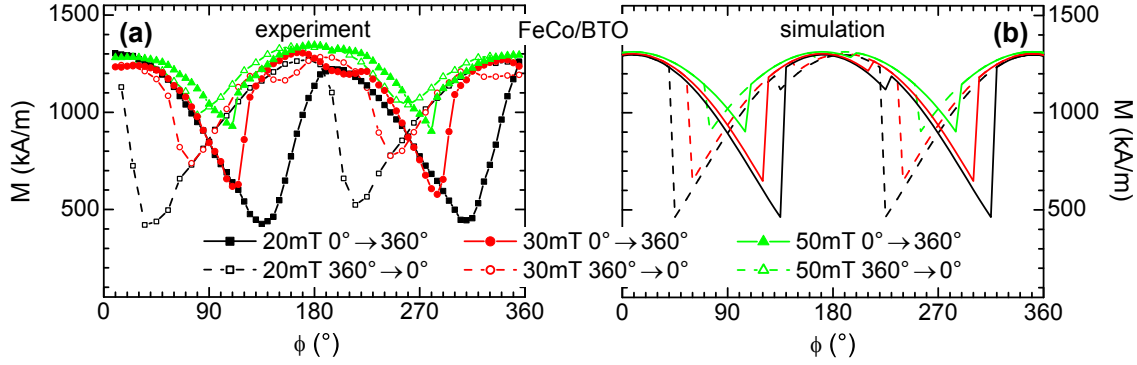


Figure 8.17: (a) Magnetometry measurements of a 50 nm thick FeCo thin film deposited on a BaTiO₃ substrate, performed under different in-plane orientations ϕ of the external magnetic field. The measurements were carried out for different magnetic field strength at 300 K with an electric field of 400 kV/m applied along the \mathbf{z} -direction. After magnetizing the FeCo/BaTiO₃ structure along the \mathbf{x} -direction ($\phi = 0^\circ$) with $\mu_0 H = 1$ T, the angular sweeps were recorded three times in both positive and negative direction of rotation in different magnetic fields. (b) Simulation of the angular dependence of the magnetization by means of magnetoelastic theory. The best fit between experiment and simulation was found for assuming a concentration of a -domains during the deposition of $x_{a_1}^{\text{dep}} = 18\%$ and $x_{a_2}^{\text{dep}} = 40\%$ as well as a reduction of the magnetoelastic coupling strength of $k = (0.42 \pm 0.05)$ from an ideal elastic coupling between thin film and substrate. An energy barrier of $\Delta E/M_s = 7.5$ mT is used to account for the difference in the up (full symbols/solid lines) and down sweep (open symbols/dashed lines), which can be attributed to pinning effects (see Appendix B).

factor k describing the strength of the magnetoelastic coupling. These parameters can be indirectly determined by measuring the magnetization of the FM/BaTiO₃ hybrid structure under different in-plane orientations ϕ of the external magnetic field. By applying an electric field of 400 kV/m along the \mathbf{z} -direction during the measurements, parts of the polycrystalline ferromagnetic thin film fabricated on top of ferroelastic a -domains are strained, since these a -domains are transformed to c -domains. The following strain tensors of the BaTiO₃ substrate derived from molecular dynamics simulations performed under $E = 4$ MV/m and $E = 0$ MV/m are used for the description of the ferroelastic domain transformations:

$$\begin{aligned} \epsilon_{c^{\text{dep}} \rightarrow c} &= \begin{pmatrix} -0.0002 & 0 & 0 \\ 0 & -0.0002 & 0 \\ 0 & 0 & 0.0005 \end{pmatrix} \\ \epsilon_{a_1^{\text{dep}} \rightarrow c} &= \begin{pmatrix} -0.0091 & 0 & 0 \\ 0 & -0.0002 & 0 \\ 0 & 0 & 0.0094 \end{pmatrix}. \end{aligned} \quad (8.5)$$

Strain components smaller than 10^{-4} are not displayed. The strain tensor $\epsilon_{a_2^{\text{dep}} \rightarrow c}$ can be obtained by interchanging the 11 and 22 component of $\epsilon_{a_1^{\text{dep}} \rightarrow c}$. The strained regions of the ferromagnetic thin film cause an angular dependence of the magnetization, which is different for regions of the ferromagnetic thin film deposited on top

of a_1 - or a_2 -domains. The angular dependence of the magnetization of a 50 nm thick FeCo thin film deposited onto a BaTiO₃ substrate recorded in different external magnetic field strengths is shown in Fig. 8.17(a). The measurements were carried out at 300 K with an electric field of 400 kV/m applied along the \mathbf{z} -direction. Before the measurements, the FeCo thin film was magnetized along the \mathbf{x} -direction ($\phi = 0^\circ$) using a magnetic field of 1 T. The angular sweeps were then recorded three times in both positive and negative directions of rotation in an external magnetic field with constant magnitude. The third back and forth scans are displayed in Fig. 8.17(a). The in-plane angles in which the magnetization exhibits a minimum value mark the direction of a magnetically hard direction. At these positions the measurements carried out rotating the sample in positive and negative direction do not coincide. The difference as a function of rotation direction can be attributed to an energy barrier ΔE describing the energy required to nucleate and unpin domains (see Appendix B). Therefore, a finite energy barrier ΔE is needed to simulate the angular dependent magnetization displayed in Fig. 8.17(a). The value of $\Delta E/M_s = 7.5$ mT is chosen such that the angles at which the incoherent switching takes place are reproduced by the simulation shown in Fig. 8.17(b). Using magnetoelastic theory on the basis of the ab initio calculated strain components of the BaTiO₃ substrate the best fit between experiment and simulation was found assuming a concentration of a -domains during the deposition of $x_{a_1}^{\text{dep}} = 18\%$ and $x_{a_2}^{\text{dep}} = 40\%$. We note that the discontinuity observed at around $\phi = 200^\circ$ gives evidence for the presence of both a -domains. Furthermore, the k value, which describes the strength of the magnetoelastic coupling was found to be $k = (0.42 \pm 0.05)$. Using these values, the FeCo/BaTiO₃ hybrid structure is entirely described in terms of magnetoelastic effects and the temperature dependence of the magnetization can be simulated by utilizing the phase diagram obtained from molecular dynamics (see Fig. 8.14). For the simulation the ferroelastic domain evolution schematically shown in Fig. 8.15 (III) is assumed.

The experimental results and the simulation of the temperature dependent magnetization for different external magnetic field strengths applied along the \mathbf{x} - and \mathbf{y} -direction of a FeCo/BaTiO₃ hybrid structure are depicted in Fig. 8.18. The data were recorded while decreasing the temperature from 300 K to 180 K after aligning the magnetization into a well-defined state using an external magnetic field of 1 T.

The simulations with an external magnetic field \mathbf{H} aligned along the \mathbf{y} -direction (see Figs. 8.18(c) and (d)) of the FeCo/BaTiO₃ hybrid structure reproduce the experimental results fairly well. Discrepancies can be observed for $\mathbf{H} \parallel \mathbf{x}$ displayed in Figs. 8.18(a) and (b). Since all magnetoelastic simulations presented throughout this chapter assume magnetic single domain states, the difference between simulation and experiment at low magnetic field strengths might be attributed to the presence of a magnetic multi-domain state in the ferromagnetic thin film. By comparing the magnetic field orientation along the \mathbf{x} - and \mathbf{y} -direction, a strong in-plane magnetic anisotropy is visible throughout the investigated temperature range. While the large concentration of a_2 -domains is responsible for the magnetic anisotropy observable in the tetragonal phase of BaTiO₃ ($T_{\text{exp.}} \geq 280$ K; $T_{\text{MD}} \geq 245$ K), the difference in the magnetic behavior for $\mathbf{H} \parallel \mathbf{x}$ and $\mathbf{H} \parallel \mathbf{y}$ in the orthorhombic (188 K $\leq T_{\text{exp.}} < 280$ K;

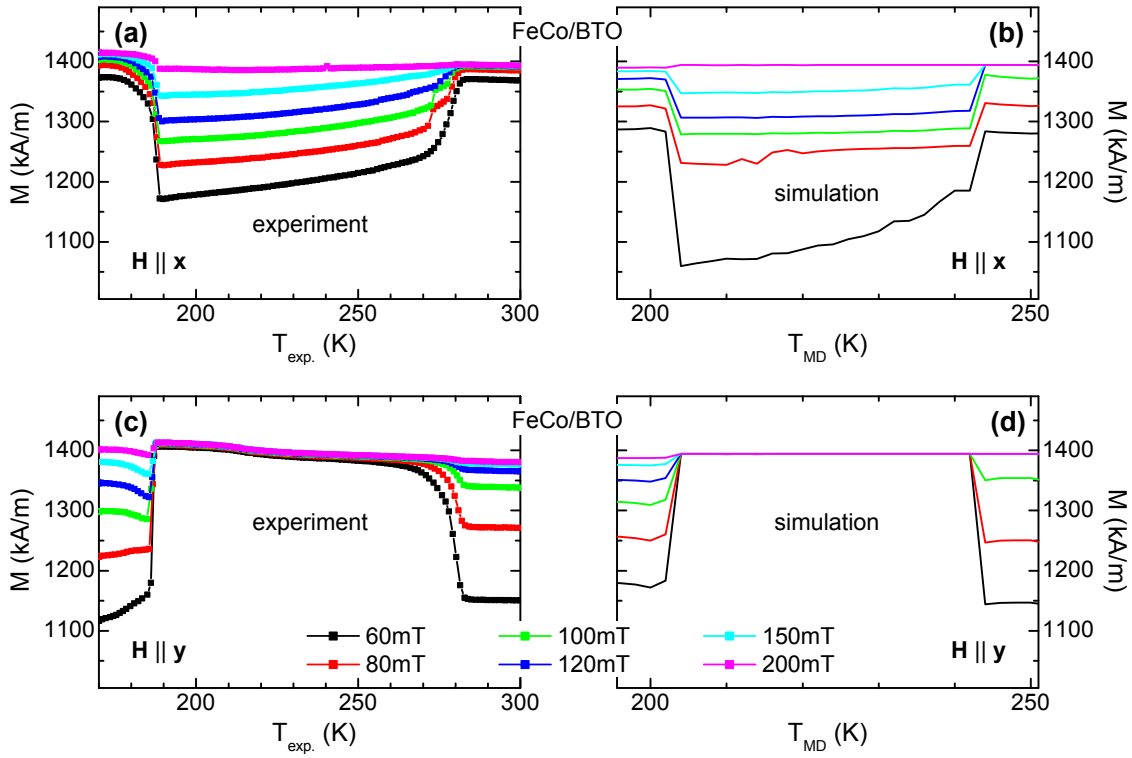


Figure 8.18: Experimental results ((a), (c)) and simulations ((b), (d)) for the magnetization as a function of temperature and external magnetic field strength of a FeCo(50 nm)/BaTiO₃ hybrid structure. The magnetic field was applied along the ((a) and (b)) x - and ((c) and (d)) y -direction. The temperature of the experiment is denoted as $T_{\text{exp.}}$, and the temperature axis of the simulation as T_{MD} . The ferroelastic domain evolution $c \rightarrow o_{23} \rightarrow r_3$ was assumed for the calculation. Furthermore, the volume fraction of a -domains during the deposition was set to $x_{a_1}^{\text{dep}} = 18\%$ and $x_{a_2}^{\text{dep}} = 40\%$, and an attenuation of the magnetoelastic coupling of $k = (0.42 \pm 0.05)$ was used.

$202 \text{ K} \leq T_{\text{MD}} < 245 \text{ K}$) and rhombohedral phase ($T_{\text{exp.}} < 188 \text{ K}$; $T_{\text{MD}} < 202 \text{ K}$) can mainly be attributed to o_{23} -domains and r_3 -domains, respectively. Despite of large magnetoelastic coupling constants λ_{100} and λ_{111} in FeCo the changes of the magnetization projection at the phase transitions of BaTiO₃ do not exceed 25%. This is due to the low k value of only $k = 0.42$ in this particular FeCo/BaTiO₃ sample. This low k value illustrates an imperfect elastic coupling of the FeCo and the BaTiO₃ substrate.

However, k values up to $k = 0.80$ can be achieved in Ni/BaTiO₃ samples measured shortly after the deposition. As an example, the results of temperature dependent magnetization measurements and simulations recorded for different magnetic field strengths of a Ni/BaTiO₃ hybrid structure are displayed in Fig. 8.19. The external magnetic field was applied along the y -direction. An excellent agreement between experiment and simulation was obtained for $x_{a_1}^{\text{dep}} = 13\%$, $x_{a_2}^{\text{dep}} = 24\%$, and $k = (0.80 \pm 0.05)$. Figure 8.19 reveals that changes of the magnetization across the ferroelastic phase transitions of more than 80% can be realized in Ni/BaTiO₃ hybrid

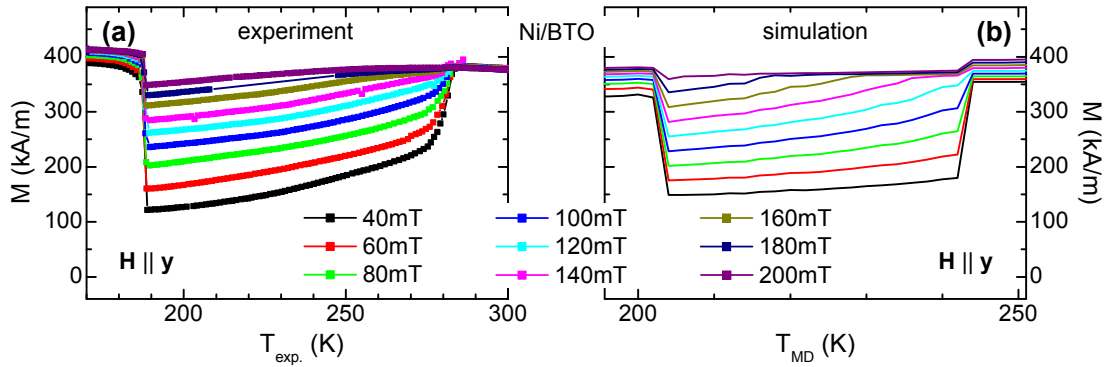


Figure 8.19: Temperature dependent magnetization (a) measured and (b) simulated for different magnetic field strengths of a 50 nm thick Ni thin film deposited on BaTiO₃. The external magnetic field was applied along the y -direction. The simulations were performed using the ferroelastic domain evolution $c \rightarrow o_{23} \rightarrow r_3$, as well as $x_{a_1}^{\text{dep}} = 13\%$, $x_{a_2}^{\text{dep}} = 24\%$, and $k = (0.80 \pm 0.05)$.

structures. The reason for the difference in the k values for different samples has not yet been conclusively resolved. One explanation might be the presence of fatigue effects, which lead to a reduction of the strain transfer from the BaTiO₃ substrate into the ferromagnetic thin film.

In total, the temperature dependent magnetic behavior of FM/BaTiO₃ hybrid structures based on FeCo and Ni can be well simulated on the basis of magnetoelastic theory. In analogy to the previous sections, a proportional constant k has to be included to account for a diminished coupling between the ferromagnetic thin film and the BaTiO₃ substrate. Furthermore, with the knowledge of the domain configuration during the fabrication of these structures, predictions of the magnetic behavior of FM/BaTiO₃ hybrid structures based on ab initio calculations are possible. This new approach of combining ab initio strain calculations and magnetoelastic theory pave the way to engineer new multiferroic composite hybrid structures.

8.4 Electric field control of magnetism in FM/BaTiO₃ hybrid structures

In the field of multiferroic composite structures, the electric field control of the magnetization is by far the most important functionality. In recent years, the discovery of giant sharp and persistent converse magnetoelectric effects in FM/BaTiO₃ multiferroic composite structures triggered an increase in research activity in this field [20]. However, detailed studies on magnetization changes due to electric fields applied to the BaTiO₃ substrate are scarce. In this section, the electric field control of the magnetization in FM/BaTiO₃ hybrid structures is discussed for two important cases. First, the control of the magnetization at room temperature, i.e., in the tetragonal phase of the BaTiO₃ substrate, is highly desirable for applications. Furthermore, enhanced magnetoelectric effects are expected applying the electric

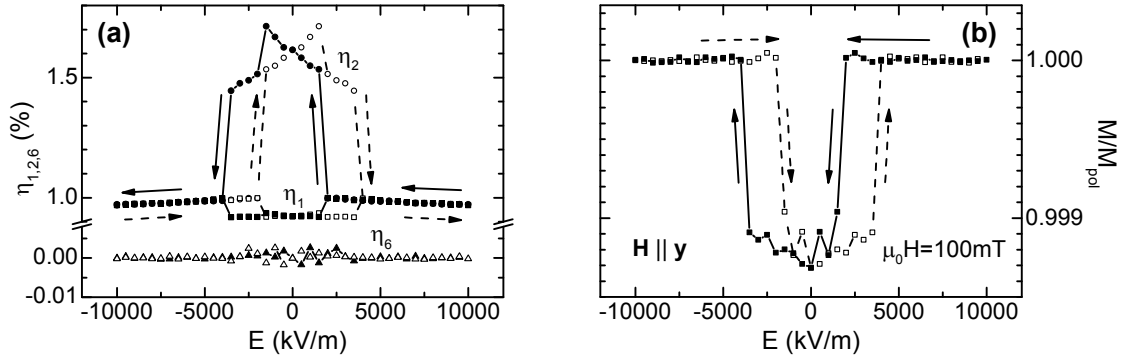


Figure 8.20: (a) Average homogeneous in-plane strain components η_i ($i = 1, 2, 6$) of BaTiO_3 as a function of the applied electric field E calculated employing molecular dynamics simulations in the tetragonal phase at $T_{\text{MD}} = 261$ K using the same parameters as for the simulations shown in Fig. 7.3. The strains are calculated relative to the lattice constant 0.3948 nm, which is derived from local density approximation calculations. (b) Electric field dependence of the magnetization projection onto the external magnetic field direction simulated for a $\text{Fe}_3\text{O}_4/\text{BaTiO}_3$ hybrid structure on the basis of the strain components η_i ($i = 1, 2, 6$) shown in (a). The magnetization is normalized to the value M_{pol} for $E = 10000$ kV/m. The magnetic field was assumed to be aligned along the y -direction (cf. Fig. 8.13) with a magnetic field strength of $\mu_0 H = 100$ mT. Full symbols denote the down sweep from $+10000$ kV/m to -10000 kV/m and the up sweep (-10000 kV/m \rightarrow $+10000$ kV/m) is marked by open symbols.

field along non-polar directions, e.g., along the z -direction (cf. Fig. 8.13) in the orthorhombic phase of BaTiO_3 .

8.4.1 BaTiO_3 in the tetragonal phase

The manipulation of the magnetization by electric fields at room temperature is one of the most important tasks in today's spintronic devices. Therefore, the converse magnetoelectric response of FM/ BaTiO_3 hybrid structures measured at 300 K is discussed in detail in the following.

Two region model of FM/ BaTiO_3 hybrid structures

The expected electric field dependence of the magnetization in the tetragonal phase of BaTiO_3 can be calculated by means of molecular dynamics simulations. Using the same parameters as in Section 8.2, the molecular dynamics simulations yield average homogeneous in-plane strain components η_i ($i = 1, 2, 6$) of BaTiO_3 as shown in Fig. 8.20(a). Thus, the electric field dependence can be separated into two parts. At high electric fields ($E > |4000$ kV/m), a ferroelastic single domain state is present and the strain dependence is only caused by the converse linear piezoelectric effect. However, around zero electric field, ferroelastic domains are expected, which results in large deviations of the average strain components. In particular, the in-plane strain components η_1 and η_2 have different values, imposing tensile strain along the y -direction into the overlying ferromagnetic thin film in FM/ BaTiO_3 hybrid

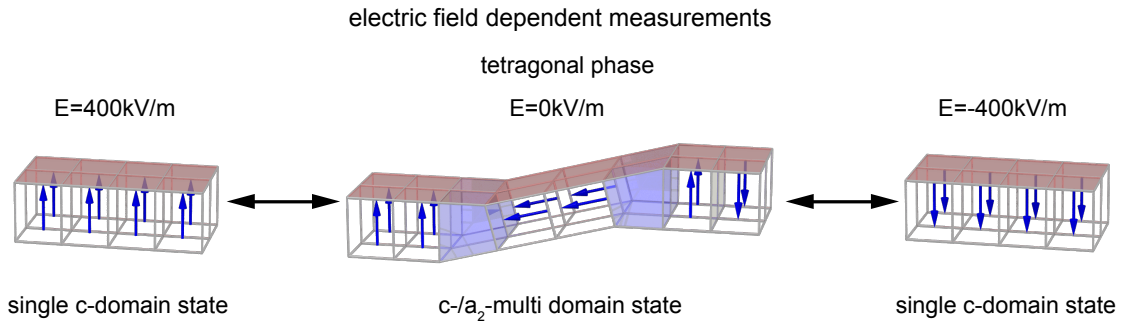


Figure 8.21: Schematic illustration of the electric field control of the magnetization in the tetragonal phase of BaTiO₃. The overlying ferromagnetic thin film is marked in red. A ferroelastic/ferroelectric multi-domain state is expected at $E = 0$ kV/m with ferroelastic 90°- and ferroelectric 180°-domain walls (marked in light blue) (cf. Fig. 7.4). The ferroelectric polarization \mathbf{P} is denoted by blue arrows.

structures. As expected, this tensile strain alters the magnetization of the ferromagnetic thin film. Using magnetoelastic theory, the change of the magnetization projection along the external magnetic field of a Fe₃O₄/BaTiO₃ hybrid structure can be simulated on the basis of the in-plane strain components of BaTiO₃ shown in Fig. 8.20(a) (cf. Section 6.2.4). While no variation of the normalized magnetization is visible for high electric fields, a small change of the magnetization is observed for electric fields smaller than $E < |4000 \text{ kV/m}|$, i.e., in the ferroelastic multi-domain state of the BaTiO₃ substrate (see Fig. 8.20(b)). Thus, in the absence of in-plane shear strains ($\eta_6 = 0$), ferroelastic domain switching, which imposes large strains into the clamped ferromagnetic thin film, is essential to realize converse magnetoelectric effects in FM/BaTiO₃ hybrid structures.

Therefore, the converse magnetoelectric effect should be strongly dependent on the ferroelastic multi-domain state in the BaTiO₃ substrate. Figure 8.21 schematically shows the ferroelastic domain evolution of a FM/BaTiO₃ hybrid structure using miscut BaTiO₃ substrates. As evident from x-ray diffraction measurements shown in Fig. 8.16, poled BaTiO₃ substrates exhibit a single c -domain state imposing uniform strain in the overlying ferromagnetic thin film, which was fabricated at temperatures well above the ferroelectric Curie temperature of BaTiO₃, at high electric fields ($E > 400 \text{ kV/m}$) applied across the hybrid structure along the \mathbf{z} -direction. Upon decreasing the electric field the BaTiO₃ substrate crosses from a ferroelastic single domain state into a mixed a_2 - and c -domain state. By reaching the coercive electric field of the BaTiO₃, the number of a_2 -domains attains its maximum value. Therefore, two types of regions are created at low electric fields. One type consists of parts of the ferromagnetic thin film on top of ferroelastic c -domains, while the other corresponds to areas clamped to ferroelastic a_2 -domains. Further decreasing the electric field yields a single c -domain configuration again and the same strain state as for high positive electric fields is achieved (see Fig. 8.20(a)).

The ferroelastic multi-domain state at low electric fields and the impact on the overlying ferromagnetic thin film due to different imposed strains can be investigated

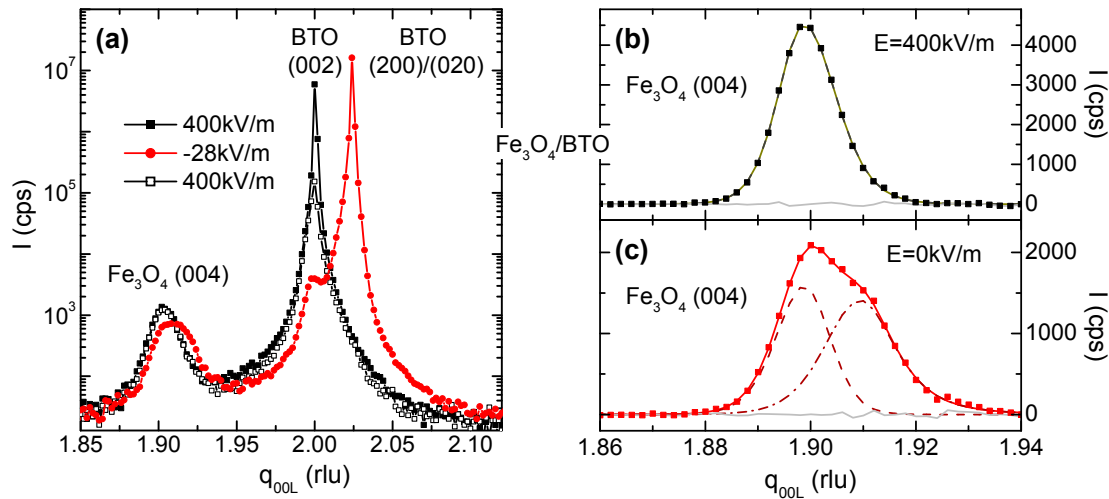


Figure 8.22: (a) q_{L00} scans around the BaTiO_3 (002) reflection recorded at different electric fields applied across a $\text{Fe}_3\text{O}_4/\text{BaTiO}_3$ structure. The measurements (full and open symbols) were carried out at the BM28 beamline at the ESRF. The lines are guides to the eye. (b), (c) The influence of different strain states on the Fe_3O_4 (004) reflection was investigated in more detail on a second $\text{Fe}_3\text{O}_4/\text{BaTiO}_3$ sample. The profile of the Fe_3O_4 (004) reflection were fitted using Pearson VII peak functions (solid black and red lines). (c) At $E = 0$ kV/m, two different peak functions are needed to reproduce the experimental data (dashed red lines). The gray lines display the difference between the experimental data (full symbols) and the peak profile fits (solid lines) in (b) and (c).

by performing x-ray diffraction measurements on a crystalline FM/ BaTiO_3 hybrid structure. For example, Fig. 8.22(a) shows q_{L00} scans around the BaTiO_3 (002) reflection recorded at different electric fields applied across the $\text{Fe}_3\text{O}_4/\text{BaTiO}_3$ structure. The measurements were carried out at the BM28 beamline at the ESRF using synchrotron radiation. At $E = 400$ kV/m, the BaTiO_3 substrate yields only one reflection at $q_{L00} = 2.0$ rlu (cf. full black symbols in Fig. 8.22(a)). Again, this confirms that a single ferroelastic c -domain configuration can be obtained at this electric field strength. By reducing the electric field to values close to the coercive field of BaTiO_3 , a second reflection around $q_{L00} \approx 2.03$ rlu emerges, which is caused by a_2 -domains in the BaTiO_3 substrate (cf. full red symbols in Fig. 8.22(a)). Upon increasing the electric field to the starting value of $E = 400$ kV/m, the first measurement is reproduced, i.e., a pure c -domain state is restored (cf. open black symbols in Fig. 8.22(a)). The effect of the imposed strain on the Fe_3O_4 thin film was investigated in more detail around the Fe_3O_4 (004) reflection on a second $\text{Fe}_3\text{O}_4/\text{BaTiO}_3$ hybrid structure (Figs. 8.22(b) and (c)). The profile of the Fe_3O_4 (004) reflection obtained by applying an electric field of $E = 400$ kV/m can be well fitted using a single Pearson VII peak function [666] (see Fig. 8.22(b)). In contrast, at $E = 0$ kV/m the intensity of the reflection is reduced while a second peak occurs close to the first one (see Fig. 8.22(c)). Two different peak functions are needed to reproduce this situation. While the position of the first profile is almost the same as for the measurement recorded at $E = 400$ kV/m and can therefore be attributed to regions of the Fe_3O_4 thin film on

top of c -domains, the second profile is located at higher q_{L00} -values. The intensity of the emerging second peak is caused by scattering of x-ray light on parts of the Fe₃O₄ thin film clamped to a_2 -domains. Thus, this result confirms the two region model schematically shown in Fig. 8.21 around $E = 0$ kV/m. The induced out-of-plane strain of the Fe₃O₄ thin film of $\eta_3 = -(0.0053 \pm 0.0003)$ can be calculated using the difference in position of the two profiles $\Delta q_{L00} = (0.0102 \pm 0.0005)$ rlu. By employing the Poisson ratio 0.33 [549], the in-plane strains $\eta_1 = 0$ and $\eta_2 = (0.0107 \pm 0.0006)$ are obtained. This is in excellent agreement with the theoretical value of $\eta_2 = 0.0105$ caused by the transformation of c -domains into a_2 -domains. Therefore, in principle, a perfect strain transmission from the BaTiO₃ substrate into the ferromagnetic thin film, i.e. $k^c = 1$, is observed experimentally.

Due to the tensile strain imposed by the ferroelastic a_2 -domains in the ferromagnetic thin film, the magnetization of those parts of the thin film, which are clamped to these a_2 -domains, changes. In contrast, in the following, it is assumed that the magnetic properties of the ferromagnetic thin film on top of c -domain regions stay unaffected. Furthermore, any effects caused by ferroelastic 90°-domain walls are neglected. Therefore, the mixed ferroelastic domain state at low electric fields induces a heterogeneous magnetic state in the ferromagnetic thin film. However, it is further assumed that each type of region can still be described by a magnetic single domain state exhibiting a well defined macroscopic magnetization. Hence, the change of the total magnetization as a function of the applied electric field $M(E)$ should be an indirect measure of the emerging a_2 -domains.

Magnetic response of FM/BaTiO₃ hybrid structures as a function of the applied electric field at 300 K

As discussed above, the magnetic response of FM/BaTiO₃ hybrid structures as a function of applied electric field $M(E)$ is strongly dependent on the number of a_2 -domains. As an example, Figure 8.23(a) shows the projection of the magnetization on the field direction as a function of the electric field $M(E)$ of a 100 nm thick Ni thin film deposited on a BaTiO₃ substrate, taken at a constant magnetic field $\mu_0 H$ applied along the \mathbf{y} -direction of the BaTiO₃ substrate. Each $M(E)$ loop is recorded after saturating the magnetization at $\mu_0 H = 1000$ mT. Reversible changes of the magnetization projection M up to 20 % are observed. Furthermore, the $M(E)$ loops exhibit a butterfly-like shape. This demonstrates that the variation of the magnetization is indeed caused by strain effects and resembles the simulated $M(E)$ loops shown in Fig. 8.20(a). Thus, other effects, such as electric field effects, can be neglected and the converse magnetoelectric effect displayed in Fig. 8.23(a) is purely strain-mediated. At $\mu_0 H = 0$ mT, the $M(E)$ curve recorded while decreasing the electric field from 400 kV/m to -400 kV/m (down loop) does not reach its initial value for saturating E field strengths with the corresponding $M(E)$ curve measured with increasing the electric field (up loop). This is clear evidence for irreversible magnetic domain effects induced by electric fields E . By increasing the external magnetic field $\mu_0 H$, the irreversible magnetic domain effects are suppressed and the maximum magnetization change ΔM decreases roughly exponentially with increasing the ex-

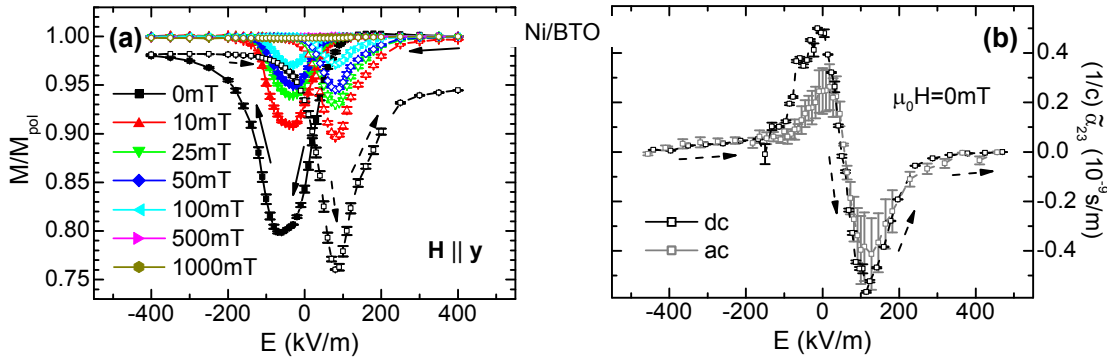


Figure 8.23: (a) Magnetization M as a function of the applied electric field E of a 100 nm Ni thin film deposited on a BaTiO₃ substrate, measured at different magnetic field strengths. The electric field is applied along the z -direction and the magnetic field along the y -direction of the BaTiO₃ substrate. The projection of the magnetization on the external magnetic field direction M is normalized to the value M_{pol} obtained at $E = 400$ kV/m. The down loop ($+400$ kV/m \rightarrow -400 kV/m) is marked by full symbols and the up loop (-400 kV/m \rightarrow $+400$ kV/m) by open symbols. The lines are guides to the eye. (b) Comparison of the linear pseudo-magnetoelectric coupling coefficient $\frac{1}{c}\tilde{\alpha}_{23}^c$ obtained from dc (black symbols) and ac (gray symbols) SQUID magnetometry measurements at $\mu_0 H = 0$ mT. For clarity, only one direction of the electric field sweep is displayed.

ternal magnetic field strength. The changes of the magnetization as a function of the applied electric field is largest at $\mu_0 H = 0$ mT, reaching nearly 20%, which is in good agreement with previous measurements in La_{0.67}Sr_{0.33}MnO₃/BaTiO₃ hybrid structures [20]. Of course, the maximum magnitude of the electric field induced changes of M in FM/BaTiO₃ hybrid structures is strongly dependent on the number of a -domains and thus different samples can only quantitatively be compared.

On the basis of the magnetization changes ΔM , a pseudo linear magnetoelectric coupling coefficient $\tilde{\alpha}_{23,\text{dc}}^c$ can be estimated from the equation $\frac{1}{c}\tilde{\alpha}_{23,\text{dc}}^c = \mu_0 \Delta M_y / \Delta E_z$ (cf. Eq. (6.12)). However, using the ac option of a SQUID magnetometer (cf. Section 2.3.1), the linear magnetoelectric coupling coefficient $\frac{1}{c}\tilde{\alpha}_{23,\text{ac}}^c = \mu_0 \partial M_y / \partial E_z$ can directly be measured. In this case, an ac electric field with an amplitude of $E_{\text{ac}} = 40$ kV/m and a frequency of 10 Hz is superimposed on the dc electric field E . $\frac{1}{c}\tilde{\alpha}_{23,\text{dc}}^c$ and $\frac{1}{c}\tilde{\alpha}_{23,\text{ac}}^c$ thus obtained are shown in Fig. 8.23(b) as a function of the dc electric field E . Over the whole electric field range, both pseudo linear magnetoelectric coupling coefficients are in quantitative agreement. The slight difference can be attributed to the large time constant involved in the accumulation of a -domains in the BaTiO₃ substrate. However, a maximum coupling constant of around $\frac{1}{c}\tilde{\alpha}_{23}^c \approx 0.4 \times 10^{-9}$ s/m is observed, which is around one order of magnitude lower than in (LaSr)MnO₃/BaTiO₃ hybrid structures [20, 667]. This can mainly be attributed to the strain dependence of the magnetic Curie temperature in (LaSr)MnO₃, which has larger effects on room temperature magnetization measurements than for Ni/BaTiO₃ hybrid structures, since the Curie temperature of (LaSr)MnO₃ is around 350 K. However, the measured pseudo converse magnetoelectric coupling coefficient is in good agreement with multilayer capacitors based

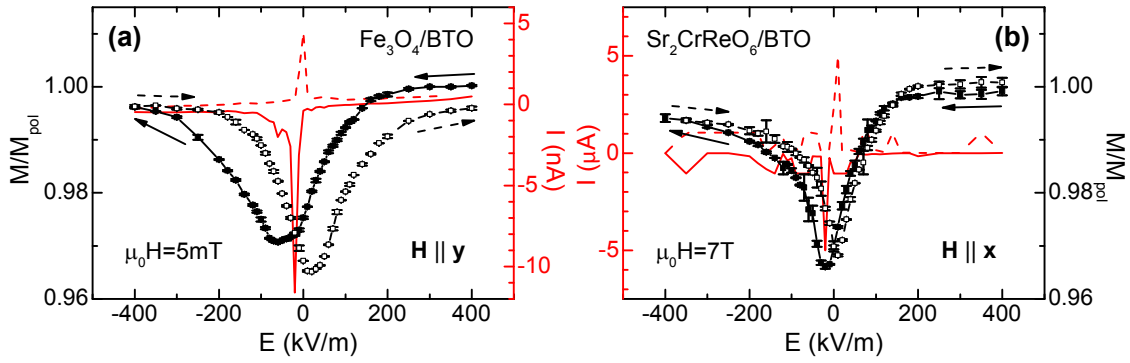


Figure 8.24: Variation of the magnetization M as a function of the applied electric field E for (a) $\text{Fe}_3\text{O}_4/\text{BaTiO}_3$ and (b) $\text{Sr}_2\text{CrReO}_6/\text{BaTiO}_3$ hybrid structures (black symbols). The projection of the magnetization on the external magnetic field direction M is again normalized using the value M_{pol} measured at $E = 400 \text{ kV/m}$. The simultaneously measured dielectric current I across the BaTiO_3 substrate (red line) reveals sharp peaks, which can be identified by displacement currents of BaTiO_3 at the coercive electric fields.

on BaTiO_3 using Ni as electrode material [668].

As discussed in Section 6.2.2, the magnetoelectric effect α_{ij}^c of composite hybrid structures can be obtained by scaling the pseudo magnetoelectric effect $\tilde{\alpha}_{ij}^c$ by $d^m/(d^p + d^m)$, which accounts for the finite thickness of the piezoelectric layer d^p (BaTiO_3) and the magnetostrictive thin film d^m (Ni). In case of the Ni/BaTiO_3 hybrid structure, $d^m/(d^p + d^m)$ yields 2×10^{-4} and the maximum converse linear magnetoelectric effect is found to be $\frac{1}{c}\alpha_{23} \approx 0.8 \times 10^{-13} \text{ s/m}$, which is around one order of magnitude lower than the magnetoelectric effect of the prototype magnetoelectric intrinsic material Cr_2O_3 [104]. Therefore, the magnitude of the converse linear magnetoelectric effect in composite hybrid structures is comparable or even less than in intrinsic magnetoelectric materials due to the unfavorable thickness ratio. However, the observed magnetoelectric effect is robust at room temperature, which has not been established for intrinsic magnetoelectric materials up to now.

A finite variation of the magnetization as a function of the applied electric field is also obtained in epitaxial FM/ BaTiO_3 hybrid structures. Figures 8.24(a) and (b) show $M(E)$ curves measured in $\text{Fe}_3\text{O}_4/\text{BaTiO}_3$ and $\text{Sr}_2\text{CrReO}_6/\text{BaTiO}_3$ hybrids. In both systems a behavior similar to Ni/BaTiO_3 is obtained. Again, the largest change of the magnetization is observed around the electric coercive fields of BaTiO_3 , which are marked by the displacement currents. (cf. red curves in Figs. 8.24(a) and (b)). In $\text{Sr}_2\text{CrReO}_6/\text{BaTiO}_3$ hybrids, a pronounced strain-mediated converse magnetoelectric effect can be obtained even at an external magnetic field strength of $\mu_0 H = 7 \text{ T}$. Unfortunately, the strong dependence of magnetization changes in FM/ BaTiO_3 hybrids on the ferroelastic domain configuration of the BaTiO_3 substrate prevent a definite conclusion on the optimal choice for the magnetic material in multiferroic composite structures.

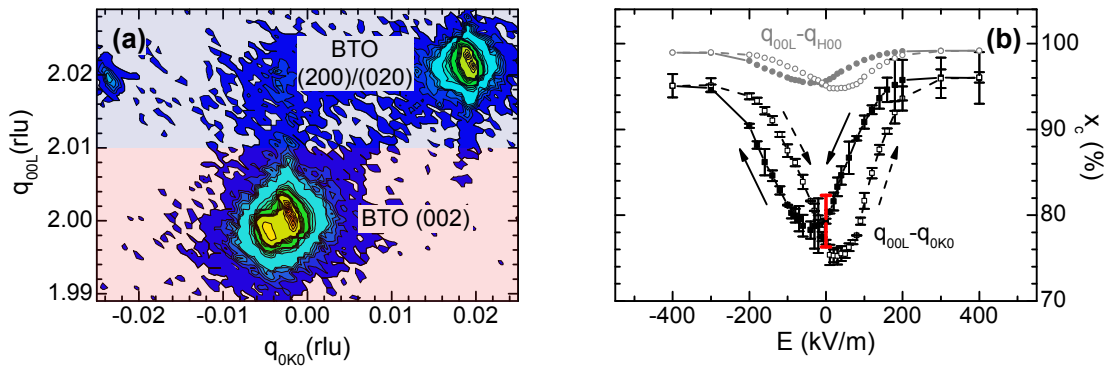


Figure 8.25: X-ray diffraction of a $\text{Fe}_3\text{O}_4/\text{BaTiO}_3$ hybrid structure around BaTiO_3 (002) with different electric fields E applied across the BaTiO_3 substrate. The alignment was carried out at the beginning of the measurement series at $E = 400$ kV/m. (a) As an example, the reciprocal space mapping of the q_{00L} - q_{0K0} plane at $E = 0$ kV/m is shown. Ferroelastic c -domains (BaTiO_3 (002)) as well as tilted a -domains (BaTiO_3 (200)/(020)) are clearly observable. To obtain the volume fraction of the c -domains $x_c = I_{q_{00L} \leq 2.01 \text{ rlu}} / I_{\text{total}}$ with $I_{\text{total}} = I_{q_{00L} \leq 2.01 \text{ rlu}} + I_{q_{00L} > 2.01 \text{ rlu}}$ as a function of the applied electric field E , the intensity for $q_{00L} \leq 2.01$ rlu (red shaded area) and for $q_{00L} > 2.01$ rlu (blue shaded area) is integrated. (b) $x_c(E)$ derived by mapping the q_{00L} - q_{0K0} plane (black symbols) and the q_{00L} - q_{H00} plane (gray symbols), respectively. The red error bar depicts the maximum uncertainty, which includes the finite penetration depth of the x-rays.

Simulation of converse magnetoelectric effects at 300 K in a $\text{Fe}_3\text{O}_4/\text{BaTiO}_3$ hybrid structure

To simulate the magnetic response of a $\text{Fe}_3\text{O}_4/\text{BaTiO}_3$ hybrid structure as a function of the applied electric field using the two region model, first of all the electric field dependence of the ferroelastic domain configuration in the BaTiO_3 substrate has to be obtained. Different methods are established to reveal the ferroelastic domain configuration [260]. Since c - and a_2 -domains exhibit different unit cell dimensions as well as a change in the polarization direction, the Bragg angle and the intensity of the respective Bragg reflection is affected. Therefore, the indirect observation of domain changes under the influence of electric fields can be undertaken by means of x-ray diffraction [669, 670]. In principle, when an electric field is applied, the BaTiO_3 substrate is strained due to two main effects, pure linear piezoelectric response, which slightly affects the lattice dimensions, and domain switching. In first order, the linear piezoelectric response can be neglected (cf. Section 8.2). Therefore, we only concentrate on domain switching. Starting from the critical field strength needed for creating a single domain state by reducing the electric field, 180° and 90° domain switching can occur (cf. Fig. 8.21), which can be detected using x-ray diffraction techniques. Since reorientation of the polarization by 90° causes a change of the Bragg angle, 90° domain switching can easily be observed by x-ray diffraction [669, 671, 672]. In contrast, 180° domain switching, which does not affect the ferroelastic domain configuration, but contribute to x-ray diffraction measurements under applied electric field, necessitates x-ray scattering due to anomalous dispersion. In

the kinematical approximation the diffracted intensity of a Bragg reflection is given by Eq. 2.1 (cf. Section 2.1.3). In case of BaTiO₃, the most significant contribution of the anomalous dispersion to the scattered intensity comes from f''_{Ba} . The intensity can therefore be approximated by [672]

$$\begin{aligned} I(hkl) \propto & |F_{f''=0}|^2 + f''_{\text{Ba}}{}^2 + 2f''_{\text{Ba}}{}^2 f_{\text{Ti}}^0 (-1)^{h+k+l} \sin(2\pi \cdot l \cdot \Delta z(\text{Ti})) \\ & + 2f''_{\text{Ba}}{}^2 f_{\text{O}}^0 (-1)^{h+k} \sin(2\pi \cdot l \cdot \Delta z(\text{O1})) \\ & + 2f''_{\text{Ba}}{}^2 f_{\text{O}}^0 [(-1)^{h+l} + (-1)^{k+l}] \sin(2\pi \cdot l \cdot \Delta z(\text{O2})), \end{aligned} \quad (8.6)$$

where $|F_{f''=0}|^2$ denotes the scattering amplitude in the absence of anomalous dispersion and $\Delta z(\text{Ti}) = 0.00135$ nm, $\Delta z(\text{O1}) = -0.00245$ nm, $\Delta z(\text{O2}) = -0.0015$ nm the displacements of the Ti and O atom at the different sites in the space group $P4mm$. f_{O}^0 is the atomic form factor and therefore the Fourier transform of the electron density around the O atom. For photon energies far from any absorption edges of the atoms, the total scattering amplitude f_j of the atom j is in good approximation equal to f_{O}^0 . However, close to an absorption edge, resonance effects become significant and the scattering amplitude for Ba is written as the normal atomic form factor plus a complex anomalous dispersion term $f'_{\text{Ba}} + if''_{\text{Ba}}$. Using Cu $K\alpha$ radiation of a standard x-ray tube with wavelength 0.15406 nm and energy 8.05 keV, the energy of the L_1 -edge of Ba (5.989 keV) is slightly lower. Since Eq. (8.6) depends on Δz , a change of the polarization by 180° causes a change in intensity by 2–5% depending on the BaTiO₃ hkl reflection [672]. Reeuwijk and coworkers indeed found intensity changes due to anomalous scattering in 100 nm thick BaTiO₃ films using Cu $K\alpha$ radiation [673]. Therefore, anomalous scattering in BaTiO₃ thin films is expected using a standard x-ray tube.

For the experimental determination of the volume fraction of the ferroelastic domains x_c , x-ray diffraction measurements around BaTiO₃ (002) were carried out. Figure 8.25(a) shows a reciprocal space map around the BaTiO₃ (002) reflection recorded with $E = 0$ kV/m. The intensity due to x-ray diffraction from ferroelastic c -domains and tilted a_2 -domains are clearly visible. The integrated intensity for $q_{00L} \leq 2.01$ rlu (c -domains) and for $q_{00L} > 2.01$ rlu (a_2 -domains) can be used to determine the volume fraction of these domains near the surface of the BaTiO₃ substrate. From the ratio of the integrated intensities $R = I_{q_{00L} \leq 2.01 \text{ rlu}} / I_{q_{00L} > 2.01 \text{ rlu}}$, the volume fraction of c -domains can be estimated as follows: $x_c = R / (1 + R) = I_{q_{00L} \leq 2.01 \text{ rlu}} / I_{\text{total}}$ with $I_{\text{total}} = I_{q_{00L} \leq 2.01 \text{ rlu}} + I_{q_{00L} > 2.01 \text{ rlu}}$ [674]. The resulting volume fraction of c -domains x_c as a function of the applied electric field strength E is displayed in Fig. 8.25(b). As discussed in Section 8.2, due to the utilization of miscut BaTiO₃ substrates, only mapping the q_{00L} - q_{0K0} plane (full symbols) yields the correct information of the c -domain volume fraction (see Fig. 8.11). For comparison, the derived volume fraction of c -domains obtained by mapping the q_{00L} - q_{H00} plane is also included in Fig. 8.25(b) (open symbols). The large difference of the volume fractions x_c again demonstrates the existence of tilted a_2 -domains in miscut BaTiO₃ substrates. However, butterfly-like $x_c(E)$ loops are observed, which is typical for 90° ferroelastic domain switching. Furthermore, the change of the volume fraction

of c -domains resembles $\epsilon(E)$ traces of bulk ferroelectric materials. By comparing x_c recorded at $E = 400 \text{ kV/m}$ and $E = -400 \text{ kV/m}$, a difference of 1% is observable. This might be caused by an additional scattering intensity based on anomalous dispersion described by Eq. (8.6). However, the large uncertainties do not allow an unambiguous interpretation of this result and a modulation technique would be more suitable to investigate this issue [675].

For the calculation of strain-mediated converse magnetoelectric effects in FM/BaTiO₃ hybrid structures, the ferroelastic domain configuration at the surface of the BaTiO₃ substrate is essential, since these domains are directly coupled to the overlying ferromagnetic thin film. As x-rays penetrate into the sample, the obtained fraction of ferroelastic c -domains is an average value. The penetration depth depends on the absorption coefficient μ of the investigated material and the incident angle of the x-ray beam. In case of q_{00L} -scans using BaTiO₃, the penetration depth can be calculated to $\tau(\theta) = \sin \theta / 2\mu = \lambda l / (4a \cdot \mu) = 0.611 \mu\text{m} \cdot l$ [68], where l denotes the Miller index. By comparing the volume fraction of ferroelastic c -domains obtained by x-ray diffraction measurements performed around BaTiO₃ (001) ($l = 1$) and BaTiO₃ (002) ($l = 2$) at $E = 0 \text{ kV/m}$ using different FM/BaTiO₃ hybrid structures, an uncertainty of less than $\pm 3\%$ is obtained due to the finite penetration depth, which is exemplarily shown in Fig. 8.25(b) by the red error bar. This significant error could be attributed to an abnormally high fraction of a -domains, that is observed at the surface of BaTiO₃ [669, 676]. Furthermore, a difference of the domain configuration at the edge of the BaTiO₃ substrate is also expected. X-ray diffraction measurements, which were recorded using pinhole collimation, reveal deviations of the volume fraction of ferroelastic c -domains of about $\pm 6\%$. However, since the converse magnetoelectric response of the whole sample is investigated using SQUID magnetometry, the average fraction of ferroelastic c -domains displayed in Fig. 8.25(b) is used for the following calculations.

With the knowledge of the ferroelastic domain state of the BaTiO₃ substrate as a function of the applied electric field $x_c(E)$, the strain tensor of the overlying Fe₃O₄ thin film can be calculated using the method described in Section 6.2.3 based on the in-plane strain components η_i with $i = 1, 2, 6$ of BaTiO₃. The in-plane components of the strain tensor are calculated by employing molecular dynamics simulations at a temperature of $T_{\text{MD}} = 261 \text{ K}$, which corresponds to $T_{\text{exp.}} \approx 300 \text{ K}$ in the experiment. Additionally, the epitaxial strain of the Fe₃O₄ thin film has to be taken into account. As discussed in Section 7.2.1, Fe₃O₄ thin films on BaTiO₃ exhibit large tensile out-of-plane strain of +1.2% and isotropic in-plane strain of -1.2% at room temperature. Both values were determined, while $E = 400 \text{ kV/m}$ was applied across the hybrid structure, i.e., in a well defined ferroelastic state of the BaTiO₃ substrate. Using these strain values, the strain tensors of the Fe₃O₄ thin film on top of ferroelastic c -domains ϵ_c and a_2 -domains ϵ_a can be calculated as follows:

$$\epsilon_c = \begin{pmatrix} -0.012 & 0 & 0 \\ 0 & -0.012 & 0 \\ 0 & 0 & 0.012 \end{pmatrix}; \epsilon_a = \begin{pmatrix} -0.012 & 0 & 0 \\ 0 & -0.003 & 0 \\ 0 & 0 & 0.008 \end{pmatrix}. \quad (8.7)$$

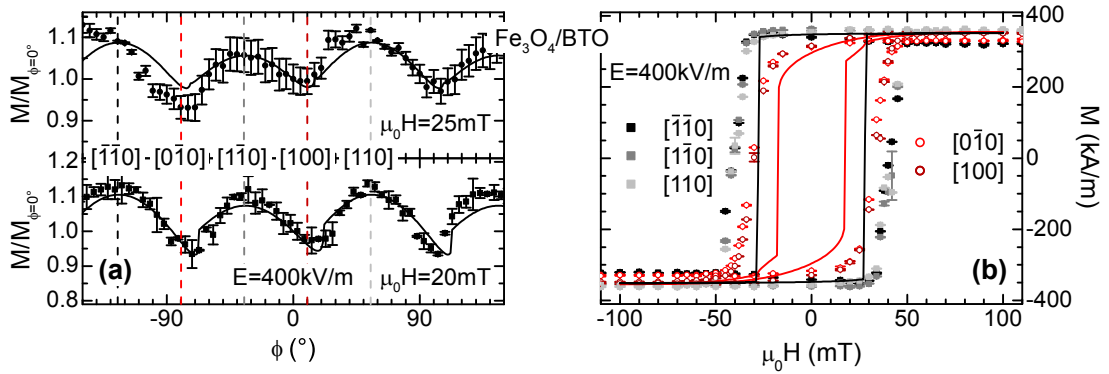


Figure 8.26: Angular dependent magnetization measurements (symbols) carried out on a Fe_3O_4 (38 nm)/ BaTiO_3 hybrid structure at $T = 300 \text{ K}$ and an electric field of $E = 400 \text{ kV/m}$ applied along the z -direction. (a) The magnetic anisotropy of the Fe_3O_4 thin film can be determined by magnetometry measurements for different in-plane orientations ϕ of the applied magnetic field. $\phi = 0^\circ$ marks the x -direction of the BaTiO_3 substrate. Since the BaTiO_3 substrate exhibits an in-plane misalignment of 10° , the BaTiO_3 $[100]$ direction does not coincide with $\phi = 0^\circ$. By employing Eq. (6.4), the simulation (solid lines) of the angular dependence yields a magnetic cubic anisotropy of Fe_3O_4 with an anisotropy field of $K_c/M = (-19 \pm 1) \text{ mT}$. (b) $M(H)$ hysteresis measured with the magnetic field aligned on different crystallographic in-plane orientations. The parameter derived from (a) are used to simulate the $M(H)$ loops under the assumption of incoherent spin switching with $\Delta E/M_s = 32 \text{ mT}$ (solid lines) (cf. Appendix B).

In Eq. (8.7), strain components smaller than 10^{-5} are ignored. Assuming an ideal coupling between Fe_3O_4 and the BaTiO_3 substrate, Eq. (8.7) reveals that the formation of a_2 -domains reduces the compressive epitaxial strain in the y -direction. For the simulation of magnetization changes as a function of applied electric fields, effects caused by the converse linear dielectric effect are neglected. Using Eq. (8.7), the projection of the magnetization M along an applied magnetic field can be calculated within the described two region model by

$$M(E) = x_c(E) \cdot M_c + (1 - x_c(E)) \cdot M_a, \quad (8.8)$$

where M_c and M_a denote the projections of the magnetization along the external field of Fe_3O_4 thin film areas on top of ferroelastic c -domains and a_2 -domains, respectively. M_c and M_a are derived by minimizing the modified thermodynamic potential $\tilde{g}^{(m)}$ described in Section 6.2.1. Since $\text{Fe}_3\text{O}_4/\text{BaTiO}_3$ is a crystalline hybrid structure, the determination of the crystalline magnetic anisotropy of Fe_3O_4 is a prerequisite for the calculation of M_c and M_a calculations. For this purpose, SQUID magnetometry measurements on a $\text{Fe}_3\text{O}_4/\text{BaTiO}_3$ hybrid structure were carried out for different in-plane orientations ϕ of the applied magnetic field. To ensure a well defined ferroelastic single c -domain state, an electric field of $E = 400 \text{ kV/m}$ was applied across the hybrid structure during the measurements. The angular dependent magnetization displayed in Fig. 8.26(a) recorded at constant magnetic field strengths of 20 mT and 25 mT reveal a four-fold symmetry, which is a clear sign of a magnetic cubic anisotropy of the Fe_3O_4 thin film. The trace of the angular

dependence at constant strain can be simulated by means of Eq. (6.4). The best fit between experiment and simulation was obtained using a cubic anisotropy field of $K_c/M = (-19 \pm 1)$ mT. This value is in good agreement with ferromagnetic resonance measurements performed on a $\text{Fe}_3\text{O}_4/\text{BaTiO}_3$ hybrid structure without any electric field applied. These measurements were carried out by Mathias Weiler during his diploma thesis [677].⁴ A misalignment of the sample of 4° with respect to the rotating axis was assumed to account for the different magnetization values measured along the $\langle 100 \rangle$ directions. The cubic anisotropy of the Fe_3O_4 thin film is also observable by magnetic hysteresis measurements $M(H)$ carried out for different orientations of the external magnetic field (see Fig. 8.26(b)). Since x-ray diffraction measurements on this sample reveal an in-plane misalignment of the BaTiO_3 unit cell of 10° with respect to the substrate edges, the crystallographic orientation of the $\text{Fe}_3\text{O}_4/\text{BaTiO}_3$ hybrid structure slightly differs from the respective ϕ angles, which are determined relative to the substrate edges (cf. Fig. 8.26(a)). The magnetic hysteresis curves $M(H)$ measured with the applied magnetic field aligned either along $\langle 110 \rangle$ or $\langle 100 \rangle$ directions of the Fe_3O_4 thin film are nearly indistinguishable, which further proves that the Fe_3O_4 thin film exhibits a cubic symmetry. In addition, the $M(H)$ curves reveal magnetically easy directions along $\langle 110 \rangle$ and hard directions along $\langle 100 \rangle$. By using the anisotropy behavior determined by the simulations of the angular dependence of the magnetization at constant magnetic field strength displayed in Fig. 8.26(a), the magnetization as a function of the applied magnetic field was calculated for a magnetic field orientation of $[100]$ and $[110]$. The simulation was carried out under the assumption of an incoherent spin switching using an energy barrier of $\Delta E/M_s = 32$ mT. This value was obtained by the simulation of the magnetic hysteresis of a Fe_3O_4 thin film deposited on a lattice matched MgO substrate (see Appendix B). While the shape of the $M(H)$ curves are well described, the coercive fields are underestimated (cf. Fig. 8.26(b)). As discussed in Appendix B, this can be attributed to additional pinning centers in $\text{Fe}_3\text{O}_4/\text{BaTiO}_3$ hybrid structures compared to Fe_3O_4 thin films on MgO substrates. However, the relative magnetization dependence can be well described.

With the knowledge of the magnetic anisotropy at $E = 400$ kV/m, the remaining unknown parameter k , which characterizes the magnetoelastic coupling strength of the $\text{Fe}_3\text{O}_4/\text{BaTiO}_3$ hybrid structure and the difference of the magnetostrictive strain for Fe_3O_4 thin films and bulk materials (cf. Section 6.2.3), can be determined by $M(H)$ loops measured under different electric fields applied to the BaTiO_3 substrate. In Figs. 8.27(a) and (b), $M(H)$ loops with the applied magnetic field aligned along the \mathbf{x} -direction ($\phi = 0^\circ$) as well as along the \mathbf{y} -direction ($\phi = 90^\circ$) of the BaTiO_3 substrate are shown. An electric field of $E = 400$ kV/m and $E = -60$ kV/m was applied across the hybrid structure during the measurements. While the magnetization as a function of the applied magnetic field for $\mathbf{H} \parallel \mathbf{x}$ and $\mathbf{H} \parallel \mathbf{y}$ at $E = 400$ kV/m resembles $M(H)$ loops recorded with $\mathbf{H} \parallel [100]$ (cf. Fig. 8.26(b)), the resulting $M(H)$ loops for an electric field of $E = -60$ kV/m are superpositions of Fe_3O_4 thin film

⁴Ferromagnetic resonance measurements on FM/ BaTiO_3 hybrid structures under finite applied electric fields are not applicable mainly due to the high dielectric constant of BaTiO_3 (see Ref. [677]).

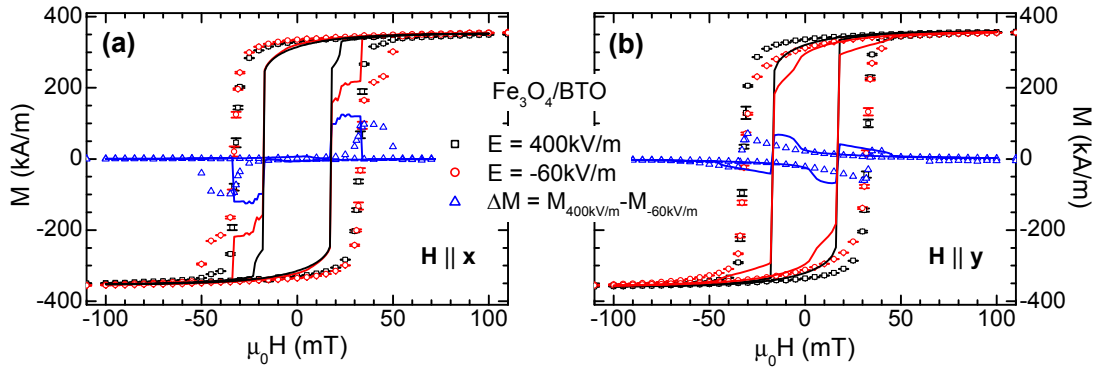


Figure 8.27: Magnetization as a function of the applied magnetic field for (a) $\mathbf{H} \parallel \mathbf{x}$ and (b) $\mathbf{H} \parallel \mathbf{y}$ recorded at $E = 400$ kV/m (black open symbols) and $E = -60$ kV/m (red open symbols) in $\text{Fe}_3\text{O}_4(38 \text{ nm})/\text{BaTiO}_3$. The maximum converse magnetoelectric effect can be estimated from the difference of both measurements $\Delta M = M_{400\text{ kV/m}} - M_{-60\text{ kV/m}}$ (blue open symbols). The magnetic hysteresis loops were simulated by using $K_c/M = (-19 \pm 1)$ mT, a magnetoelastic coupling strength of $k = (0.42 \pm 0.02)$, a volume fraction of ferroelastic c -domains at $E = -60$ kV/m of $x_c = (79 \pm 3)\%$ as well as an energy barrier of $\Delta E/M_s = 32$ mT (solid lines).

regions, which are located on top of ferroelastic c -domains and a_2 -domains. This is manifested in a two step magnetization reversal for $\mathbf{H} \parallel \mathbf{x}$. By using the magnetoelastic coupling strength $k = (0.42 \pm 0.02)$ as well as a volume fraction of ferroelastic c -domains at $E = -60$ kV/m of $x_c = (79 \pm 3)\%$ (see Fig. 8.25(b)), the two step reversal process for $\mathbf{H} \parallel \mathbf{x}$ and the relative magnetization dependence as a function of the applied magnetic field for $\mathbf{H} \parallel \mathbf{y}$ can be well simulated (solid lines in Figs. 8.27(a) and (b)). The difference in the coercive fields can again be attributed to a high density of pinning centers in this hybrid structure.

Now, we are ready to simulate the converse magnetoelectric effect in $\text{Fe}_3\text{O}_4/\text{BaTiO}_3$ hybrid structures on the basis of the simple two region model described by Eq. (8.8), using the magnetic and magnetoelastic parameters determined above. The similar electric field dependence of the magnetization and the volume fraction of ferroelastic c -domains in the BaTiO_3 substrate shown in Fig. 8.28(a) further confirms the use of the two region model as the starting point for the simulation of the converse magnetoelectric effect at fixed magnetic field strengths. Although, the magnitude of the converse magnetoelectric effect, which can be estimated by the difference of the magnetization $\Delta M = M_{400\text{ kV/m}} - M_{-60\text{ kV/m}}$ recorded at $E = 400$ kV/m and $E = -60$ kV/m, is expected to be largest around the magnetic coercive field of Fe_3O_4 (cf. Figs. 8.27(a) and (b)), magnetic field strengths well above the saturation field are used to simulate the electric field dependence of the magnetization to ensure a magnetic single domain state in each region of the ferromagnetic layer. Figure 8.28(b) shows an excellent agreement between experiment and simulation for a magnetic field orientation of $\mathbf{H} \parallel \mathbf{y}$ and two different magnetic field strengths. This proves that the electric field dependence of the magnetization of FM/BaTiO₃ hybrid structures can be well described within the two region model for magnetic fields well above the saturation field.

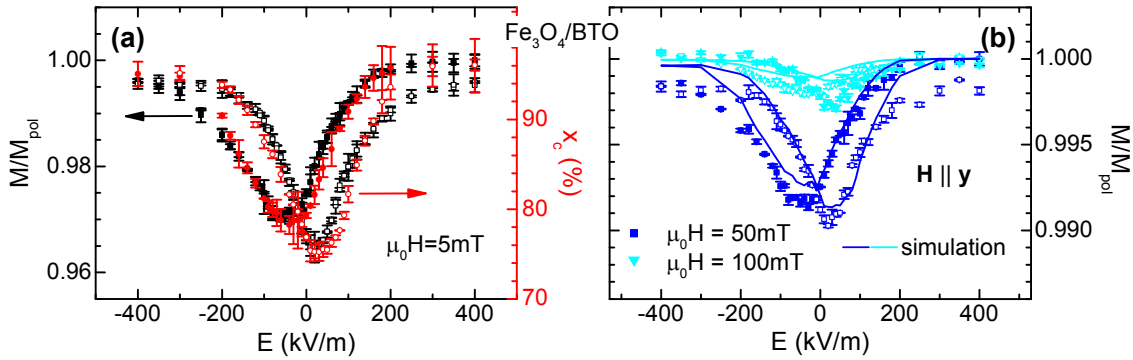


Figure 8.28: (a) Measured normalized magnetization M/M_{pol} (black symbols) and volume fraction of ferroelastic c -domains x_c (red symbols) as a function of the applied electric field E . Both reveal an almost identical dependence. (b) Measured (symbols) and simulated (solid lines) converse magnetoelectric effect for a magnetic field orientation of $\mathbf{H} \parallel \mathbf{y}$ and two different magnetic field strengths well above the saturation magnetic field in $\text{Fe}_3\text{O}_4(38 \text{ nm})/\text{BaTiO}_3$.

Local measurement of the converse magnetoelectric effect using angle dependent magnetoresistance measurements

All above measurements of the electric field dependence of the magnetization in this section were performed using a SQUID magnetometer. Within this technique, the total magnetic moment integrated over the whole sample volume is measured. By using angle-dependent magnetoresistance (ADMR) measurements, the magnetic anisotropy can be observed on a local scale (cf. Section 2.3.3). Exploiting the particular domain configuration of miscut BaTiO_3 substrates (see Fig. 8.13), the Hall bar used for magnetotransport measurements can be defined in such a way, that the measured longitudinal resistivity ρ_{xx} (transverse resistivity ρ_{xy}) is a series (parallel) connection of different regions exhibiting a certain strain state. This is shown in Fig. 8.29(a) for a 50 nm thick Ni thin film deposited on a BaTiO_3 substrate. The a_2 - c -domain structure is clearly observable in this micrograph. Furthermore, the probed $220 \mu\text{m} \times 80 \mu\text{m}$ area of the polycrystalline Ni thin films is marked by a red shaded rectangle. The ADMR measurements were carried out with the current direction \mathbf{j} along the pseudo-cubic $[010]_{\text{pc}}$ direction of the BaTiO_3 substrate and ρ_{xx} as well as ρ_{xy} were recorded at fixed magnetic field strength under different in-plane orientations of the magnetic field. To simulate the experimental data in the context of the discussed two region model, the volume fraction of the c -domains x_c , which are present in the BaTiO_3 substrate at a certain electric field strength was determined by x-ray diffraction around the $\text{BaTiO}_3(002)$ reflection in the same way as described above. The result is shown in Fig. 8.29(b). To exclude effects stemming from the edges of the BaTiO_3 substrate, a pinhole with 1 mm in diameter was used to confine the x-ray beam size. However, since the x-ray diffraction measurements were performed after the deposition of Ni on BaTiO_3 and before the fabrication process of the Hall bar pattern, the x-ray diffraction and the transport measurements might be carried out on different areas. Nevertheless, with the knowledge of the

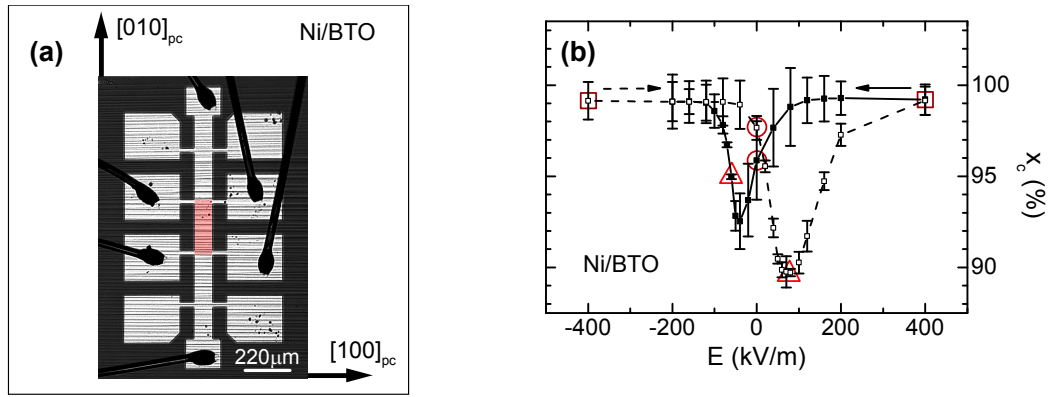


Figure 8.29: Angle-dependent magnetoresistance (ADMR) measurement performed on a Ni(50 nm)/BaTiO₃ hybrid structure. (a) The optical microscope image shows the relative alignment of a Ni Hall bar, which was patterned by optical lithography and ion milling, with respect to the pseudo-cubic axes of the BaTiO₃ substrate. The a_2 - c -domain walls are clearly visible by dark lines. The Hall bar is aligned perpendicular to these lines. The probed $220 \mu\text{m} \times 80 \mu\text{m}$ area of the polycrystalline Ni thin films is marked by a red shaded rectangle. The longitudinal and transverse voltage measured along and across the current direction arise from $E_{xx} = \mathbf{j} \cdot \mathbf{E}$ and $E_{xy} = \mathbf{t} \cdot \mathbf{E}$ with $\mathbf{j} \parallel [010]_{\text{pc}}$ and $\mathbf{t} \parallel [\bar{1}00]_{\text{pc}}$. (b) To simulate the ADMR measurements, the volume fraction of c -domains x_c was measured using x-ray diffraction around the BaTiO₃ (002) reflection (symbols). The lines are guides to the eye. To exclude effects stemming from the edges of the BaTiO₃ substrate, a pinhole with 1 mm in diameter was used to confine the x-ray beam size. ADMR measurements were performed at different electric fields marked by the red open symbols.

volume fraction of the c -domains x_c in the sample as well as the strength of the magnetoelastic coupling $k = (0.23 \pm 0.02)$ determined by ferromagnetic resonance measurements shown in Fig. 8.12, we are set to simulate the experimental results.

Since, in case of polycrystalline ferromagnetic thin films, the ferromagnetic material is deposited in an unstrained state on a certain ferroelastic domain configuration of the BaTiO₃ substrate at room temperature, the dependence of the magnetization as a function of the applied electric field in Ni/BaTiO₃ hybrid structures has to be calculated with respect to the unknown ferroelastic domain state present during the fabrication process. Therefore, we first determine the initial volume fraction of ferroelastic a - and c -domains ($x_{a_1}^{\text{dep}}$, $x_{a_2}^{\text{dep}}$, x_c^{dep}) during the deposition, by simulating the experimental results with an electric field of 400 kV/m applied to the hybrid structure. Even though, Figure 8.29(b) reveals a small but finite a_2 -domain concentration at 400 kV/m ($x_c < 1$), we neglect these a_2 -domains and assume a ferroelastic single c -domain state at this particular electric field. The observed longitudinal resistivity ρ_{xx} is a series connection of resistivities stemming from Ni regions, which are grown on top of a - and c -domains: $\rho_{xx} = x_c^{\text{dep}} \cdot \rho_{xx}^c + x_{a_1}^{\text{dep}} \cdot \rho_{xx}^{a_1} + x_{a_2}^{\text{dep}} \cdot \rho_{xx}^{a_2}$. The resistivities ρ_{xx}^c , $\rho_{xx}^{a_1}$, and $\rho_{xx}^{a_2}$ can now be calculated on the basis of magnetoelastic theory using the strain tensors depicted in Eq. (8.5). Equivalently, the transverse resistivity can be simulated by $(\rho_{xy})^{-1} = x_c^{\text{dep}} \cdot (\rho_{xy}^c)^{-1} + x_{a_1}^{\text{dep}} \cdot (\rho_{xy}^{a_1})^{-1} + x_{a_2}^{\text{dep}} \cdot (\rho_{xy}^{a_2})^{-1}$.

Figures 8.30(a) and (b) shows the longitudinal ρ_{xx} and transverse ρ_{xy} resistivity measured at 300 K for different magnetic field strengths. The resistivity parameters

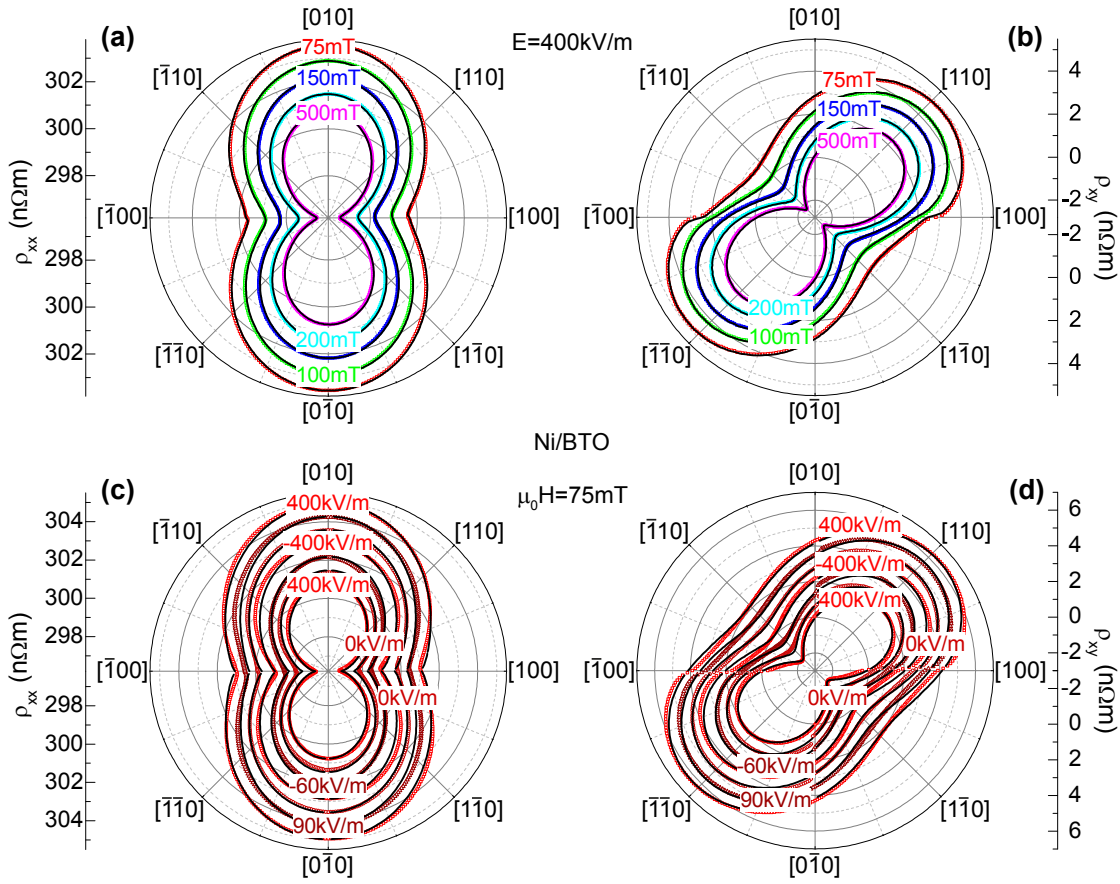


Figure 8.30: Angle-dependent longitudinal resistivity ρ_{xx} (a) and transverse resistivity ρ_{xy} (b) measured with an electric field of $E = 400$ kV/m applied across the Ni/BaTiO₃ hybrid structure at constant external magnetic field strengths. ρ_{xx} (c) and ρ_{xy} (d) recorded with an applied magnetic field of $\mu_0 H = 75$ mT at different electric fields (400 kV/m, 0 kV/m, -60 kV/m, -400 kV/m, 0 kV/m, 90 kV/m, 400 kV/m). The direction of the external magnetic field is denoted with respect to the pseudo-cubic directions of the BaTiO₃ substrate. Before each measurement, the magnetization was aligned into a well-defined initial state in an external magnetic field of $\mu_0 H = 1$ T along $[010]_{pc}$ at constant electric field applied across the hybrid structure. Then, the magnetic field strength was reduced to the measuring field and the angular scan was started. The experimental data are displayed by open symbols and the simulation of the angle-dependent magnetoresistance by black solid lines. The data are shifted by a constant offset for better visibility.

$\rho_0 = 296.96$ nΩm, $\rho_1 = 4.06$ nΩm, and $\rho_2 = 4.55$ nΩm are deduced from ADMR measurements recorded at a magnetic field of $\mu_0 H = 500$ mT. These parameters are kept constant for different magnetic fields. Furthermore, to reduce the number of free fit parameters, ρ_0 , ρ_1 and ρ_2 are assumed to be the same for Ni regions exposed to different strain. This is obviously not true, since piezoresistance effects are neglected (cf. Section 8.1.2). To account for these effects, the experimental data recorded at fixed electric fields applied across the hybrid structure were scaled by a factor between 0.995 and 1. In theory, the resistivity parameters ρ_1 and ρ_2 should be identical for an “ideal” polycrystalline material. However, ρ_1 and ρ_2 differ by 12%, which can

be attributed to a preferred orientation of Ni grains during the growth process. A perfect agreement between experiment and simulation can be obtained by assuming a volume fraction of a -domains of $x_{a_1}^{\text{dep}} = 0$ and $x_{a_2}^{\text{dep}} = (0.25 \pm 0.02)$ during the deposition, which yields a volume fraction of c -domains of $x_c^{\text{dep}} = 1 - x_{a_2}^{\text{dep}} = (0.75 \pm 0.02)$ (see Figs. 8.30(a) and (b)). These domain concentrations are the starting point to describe ADMR measurements at different electric fields applied across the Ni/BaTiO₃ hybrid. As indicated by red symbols in Fig. 8.29(b), ADMR measurements were performed at 400 kV/m, 0 kV/m, -60 kV/m, -400 kV/m, 0 kV/m, 90 kV/m, and 400 kV/m. Using the measured volume fraction of c -domains x_c , the longitudinal resistivity ρ_{xx} and transverse resistivity ρ_{xy} was calculated. Note that there are no free parameters in the simulation. In Figs. 8.30(c) and (d), the experimental data as well as the simulation for ρ_{xx} and ρ_{xy} performed at a constant external magnetic field strength of $\mu_0 H = 75$ mT are shown. While a good agreement between experiment and simulation is mainly observed for the longitudinal resistivity ρ_{xx} , the simulation of the transverse resistivity ρ_{xy} differs slightly along the pseudo-cubic [100]_{pc} direction of the BaTiO₃ substrate. This can be mainly attributed to the insufficient determination of the volume fraction of the ferroelastic domains beneath the probed area of the Ni thin film.

However, Figure 8.29 reveals that the magnetic properties of Ni/BaTiO₃ hybrid structures can be described locally by angle-dependent magnetoresistance (ADMR) measurements. Therefore, not only macroscopic magnetometry measurements are well described on the basis of the simple two region model (cf. Fig. 8.28(b)), but also small structures. Note that a ferroelastic domain control is a prerequisite for simulations of the longitudinal ρ_{xx} and transverse resistivity ρ_{xy} (cf. Fig. 8.29(a)).

The limit of the two region model: Irreversible and reversible magnetization switching by an electric field

Figures 8.28 and 8.30 demonstrate that the simple two region model is sufficient to explain converse magnetoelectric effects in FM/BaTiO₃ hybrid structures at magnetic fields larger than the saturation fields of the respective ferromagnetic material used in the FM/BaTiO₃ hybrid structure. However, detailed magnetization measurements with $\mathbf{H} \parallel \mathbf{y}$ reveal changes of the coercive field $\mu_0 H_c$ for different electric fields applied across Ni/BaTiO₃ hybrid structures, which cannot be explained in the context of the two region model alone.

Figure 8.31 shows the magnetization as a function of the applied external magnetic field aligned along $\mathbf{H} \parallel \mathbf{y}$ for two different electric fields. As evident in Fig. 8.31, the $M(H)$ loop measured at $E = -60$ kV/m does not only reveal a reduction of the magnetization below $\mu_0 H = 200$ mT, but also a change in the coercive field from $\mu_0 H_c = 5.5$ mT to 5.0 mT. Therefore, the coercive field can be manipulated by around 10% via electric fields in this sample. This value is by a factor of two smaller than the one reported recently in Fe/BaTiO₃ hybrid structures [678]. However, the two region model must be extended to simulate these effects. Up to now, the converse magnetoelectric effects are simulated by taking only the volume fraction of ferroelastic c - and a_2 -domains into account. In this context, the imposed strain

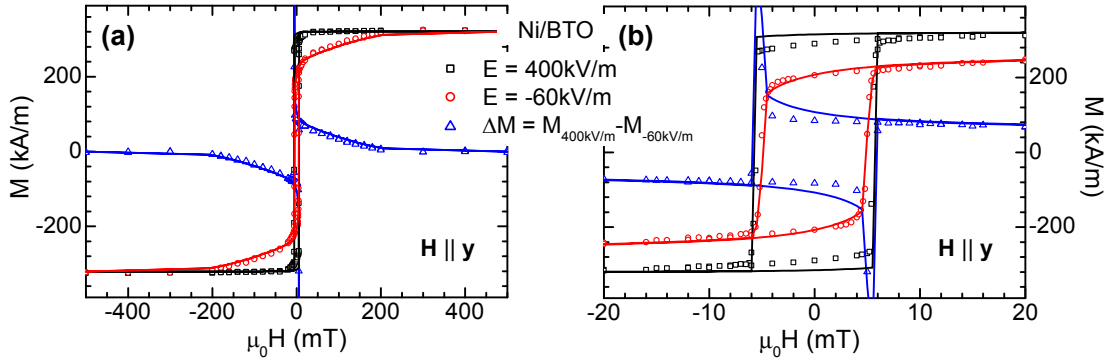


Figure 8.31: (a) and (b) Magnetic hysteresis loops $M(H)$ measured with $E = 400$ kV/m (black) and $E = -60$ kV/m (red) applied across a Ni(50 nm)/BaTiO₃ hybrid structure. The magnetic field was aligned along the y direction. To estimate the maximum magnetoelectric effect, the difference $\Delta M = M_{400\text{ kV/m}} - M_{-60\text{ kV/m}}$ is shown in blue. The best agreement between simulation (solid lines) and experiment (open symbols) was obtained for a magnetoelastic coupling strength of $k = (0.80 \pm 0.02)$ as well as an assumed domain configuration during the deposition of $x_c = (45 \pm 3)\%$ and $x_{a_2}^{\text{dep}} = (55 \pm 3)\%$. Furthermore, an energy barrier of $\Delta E/M_s = 11$ mT was used to account for the formation of domains and pinning effects. Furthermore, an uniaxial anisotropy is included into the simulation (see Fig. 8.12). Upon reducing the electric field to $E = -60$ kV/m, $(28 \pm 2)\%$ a_2 -domains are formed.

tensor caused by each ferroelastic domain is taken as a constant and the electric field dependence, i.e., converse piezoelectric effects, was neglected. However, these effects can shift the magnetic switching field to higher and lower values.

X-ray diffraction is a suitable method to investigate the converse piezoelectric effect [679, 680]. In the case of the BaTiO₃ substrate, x-ray diffraction measurements were performed around the asymmetric BaTiO₃ (024) reflection with different electric fields applied across the sample. Since the electric field changes the interplanar spacing d_{HKL} and therefore the scattering vector \mathbf{q}_{HKL} in the reciprocal space, a three-dimensional mapping of the BaTiO₃ (024) reflection has to be carried out. For this purpose, reciprocal space maps with different in-plane orientations of the sample were recorded (see Fig. 8.11) and the scattering vector $\mathbf{q}_{024}(E)$ as a function of the electric field is determined. In Figs. 8.32(a)-(c), the influence of a finite electric field applied across the BaTiO₃ on the scattering vector $\Delta \mathbf{q} = \mathbf{q}_{024}(E) - \mathbf{q}_{024}(E = 0)$ is shown. While the large uncertainties in Δq_x prevent an interpretation of the electric field dependence, the electric field alters the components Δq_y and Δq_z . To exclude temperature instabilities or drift effects, x-ray diffraction measurements are performed for decreasing the electric field strength from 400 kV/m to -400 kV/m (full symbols) and increasing it again to 400 kV/m (open symbols). By comparing both measurement series, a small hysteresis is visible due to the ferroelectric nature of BaTiO₃. In the limit of the linear theory of elasticity, the elastic strain tensor based on the converse piezoelectric effect can be calculated from Figs. 8.32(a)-(c).

Under the influence of a finite strain ϵ_{ij} a unit-cell vector \mathbf{a}_k in the real space changes according to $a_i^\epsilon = (1 + \epsilon_{ij})a_j^0$ ($i, j = 1, 2, 3$), where a_i^ϵ denotes the strained vector component and a_j^0 the vector component at $E = 0$. With the definition of

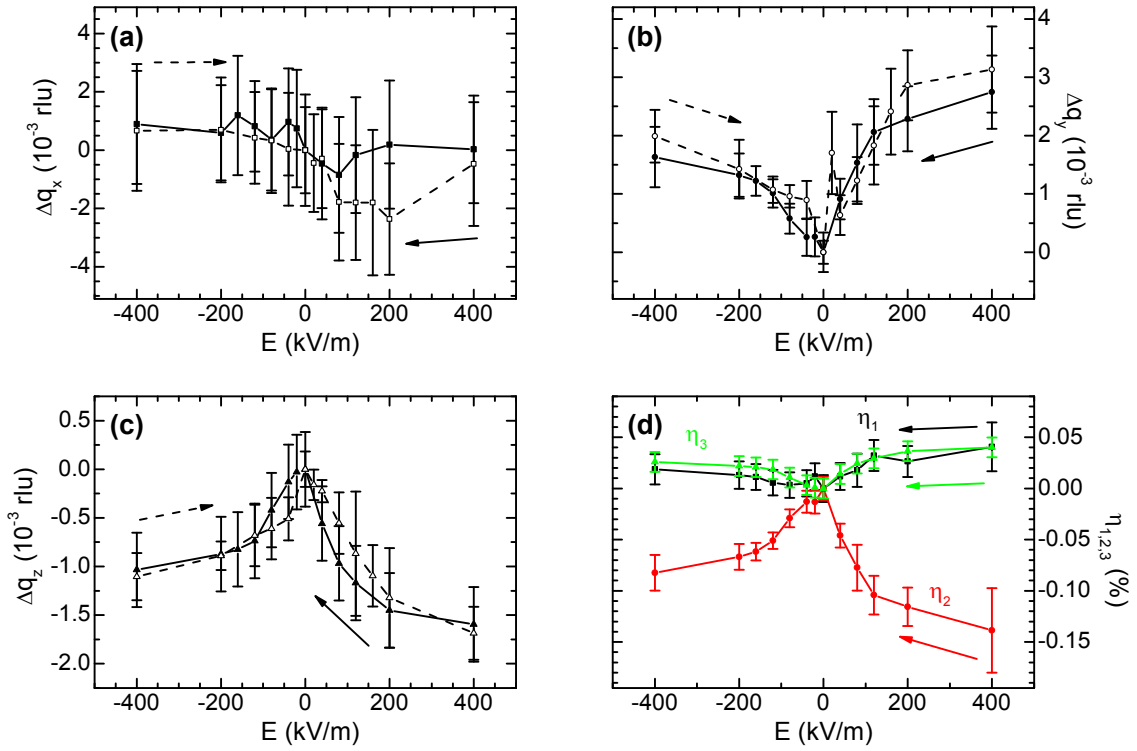


Figure 8.32: Variation of the asymmetric BaTiO₃ (024) reflection under different electric fields applied across the BaTiO₃ substrate. The change of the (a) x -, (b) y -, and (c) z - component of the scattering vector $\mathbf{q}_{024}(E)$ with respect to $\mathbf{q}_{024}(E=0)$ is determined by performing reciprocal space maps around BaTiO₃ (024) with different in-plane orientations of the sample. For each electric field strength, 20 reciprocal space maps were recorded varying the in-plane orientation by 0.25°. The x-ray diffraction measurements were performed for decreasing the electric field strength from 400 kV/m to -400 kV/m (line and full symbols) and increasing it again to 400 kV/m (dashed line and open symbols). (d) The elastic strain components η_i are derived from Δq_i in the limit of the linear theory of elasticity. Due to the large error in Δq_x , η_1 is calculated using the BaTiO₃ Poisson ratio of $\nu = 0.29$. For clarity, only the electric field sweep $+400$ kV/m $\rightarrow -400$ kV/m is shown.

the base vectors \mathbf{b}_l of the reciprocal space $\mathbf{a}_k \cdot \mathbf{b}_l = 2\pi\delta_{kl}$ ($k, l = 1 - 3$), where δ_{kl} denotes the Kronecker delta, the components of a base vector can be expressed as

$$b_i^\epsilon = \frac{1}{1 + \epsilon_{ij}} b_j^0 \simeq (1 - \epsilon_{ij}) b_j^0. \quad (8.9)$$

In the approximation of the linear theory of elasticity, higher than first powers of ϵ_{ij} are neglected [680]. Since all reciprocal lattice vectors can be expressed as a linear combination of \mathbf{b}_l , any reciprocal lattice vector transforms according to Eq. 8.9. Therefore, the strain components in the matrix notation η_i can be derived from Δq_i displayed in Figs. 8.32(a)-(c) by $\eta_i = -\Delta q_i / q_i^0$ ($i = 1, 2, 3$), neglecting any shear strains. Due to the large error in Δq_x , η_1 is calculated using the BaTiO₃ Poisson ratio of $\nu = 0.29$ [643]. The resulting strain components η_i are shown in Fig. 8.32(d). All three components are in the order of 0.1% and thus one order of magnitude smaller

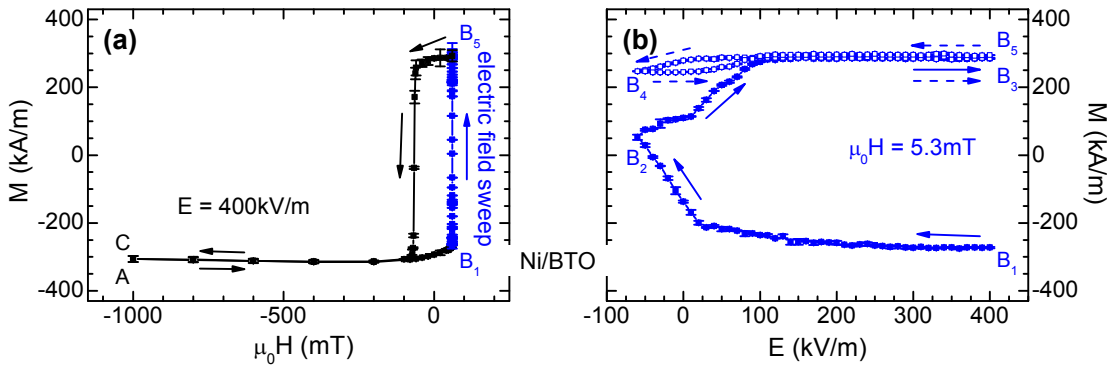


Figure 8.33: (a) Irreversible switching of the magnetization via electric field measured in a Ni(50 nm)/BaTiO₃ hybrid structure. (b) Evolution of the magnetization during the electric field sweep from +400 kV/m (B₁) to -60 kV/m (B₂) and back to +400 kV/m (B₃) at a constant magnetic field strength of $\mu_0 H = +5.2$ mT. The second electric field sweep (+400 kV/m (B₃) \rightarrow -60 kV/m (B₄) \rightarrow +400 kV/m (B₅)) is indicated by open symbols.

than the strain imposed by the generation of ferroelastic a_2 -domains. On the other hand, these values are by far larger than the induced in-plane strain calculated from the piezoelectric modulus d_{ij} of BaTiO₃ (cf. Section 7.1). Furthermore, the symmetry of the tetragonal phase $4mm$ does not allow a difference in the in-plane strain components η_1 and η_2 for an electric field applied in any direction. Therefore, the result in Fig. 8.32(d) is surprising and can only be explained by extrinsic effects due to the particular ferroelastic domain configuration displayed in Fig. 8.13. In this context, polarization rotation might be one reason for the large piezoelectric response evident in Fig. 8.32(d) [484].

However, by including the electric field dependence of $\eta_i(E)$ into the two region model, the $M(H)$ loops can be nicely simulated (solid lines in Fig. 8.31). Therefore, the difference in the coercive field $\mu_0 H_c$ for $E = 400$ kV/m and $E = -60$ kV/m are caused by magnetoelastic effects based on the converse piezoelectric effect.

The electric field control of the coercive field $\mu_0 H_c(E)$ in Ni/BaTiO₃ can be utilized to irreversibly switch the magnetization \mathbf{M} . This is shown in Fig. 8.33. After preparing \mathbf{M} in a well-defined state at $\mu_0 H = -100$ mT and $E = 400$ kV/m, the external magnetic field strength is increased from $\mu_0 H = -100$ mT (A) to $\mu_0 H = +5.2$ mT (B₁) at a constant electric field of $E = 400$ kV/m. At point (B₁), the magnetization \mathbf{M} has not yet switched, and is therefore essentially oriented antiparallel to the external magnetic field in a metastable state. This situation is shown in Fig. 8.34(a). The calculated $\tilde{g}^{(m)}/M_s$ trace using an external magnetic field of $\mu_0 H = -100$ mT reveals that the magnetization orientation is aligned along the global minimum of $\tilde{g}^{(m)}/M_s$ at around $m_2 \approx -1$ (A), i.e., almost parallel to the external magnetic field. By increasing the magnetic field strength to $\mu_0 H = +5.2$ mT (B₁), the magnetization remains close to $m_2 \approx -1$. Up to this magnetic field, no switching of the magnetization occurs, since the energy difference $\Delta\tilde{g}^{(m)}/M_s$ of the local minima at around $m_2 \approx -1$ and the global minima at around $m_2 \approx +1$ is smaller than the energy barrier of $\Delta E/M_s = 11$ mT needed to generate magnetic domains and overcome

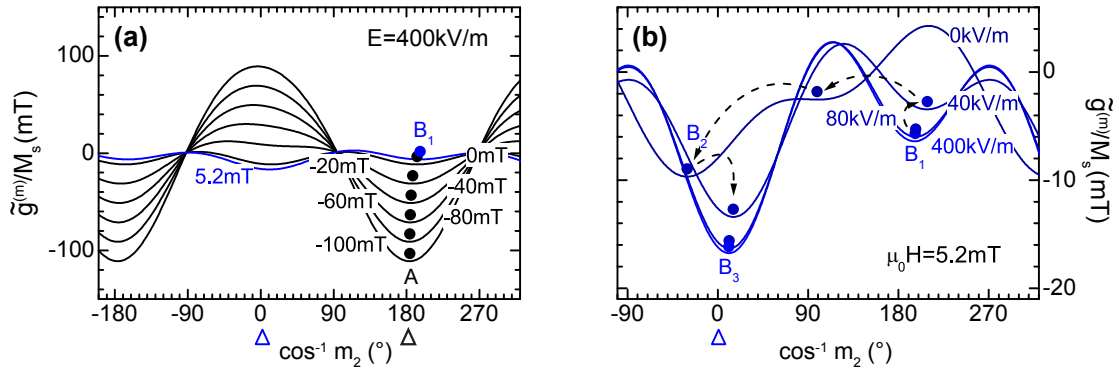


Figure 8.34: Illustration of the irreversible switching process of the magnetization via electric fields in Ni/BaTiO₃. (a) Calculated free enthalpy density contours $\tilde{g}^{(m)}/M_s$ normalized to the saturation magnetization M_s as a function of the external magnetic field. A constant electric field of $E = 400$ kV/m is assumed to be applied to the Ni/BaTiO₃ hybrid structure. The minima of $\tilde{g}^{(m)}/M_s$ and therefore the magnetization orientations are marked by black and blue full circles. Furthermore, the directions of the external magnetic field for negative magnetic field strengths (black curves) and $\mu_0 H = +5.2$ mT (blue line) are indicated by black and blue open triangles. (b) $\tilde{g}^{(m)}/M_s$ calculated at $\mu_0 H = +5.2$ mT for different electric fields (blue lines). The irreversible coherent switching of the magnetization is indicated by dashed black arrows.

pinning effects in the Ni/BaTiO₃ sample (cf. Appendix B).⁵ Due to local fluctuations of the magnetization caused by finite temperature or sample inhomogeneities, which are not considered in our simulations, some magnetic moments switch already at lower magnetic field strengths and reduce the magnetization. This might also be the reason for the difference of the simulated and measured $M(H)$ loop for $E = 400$ kV/m at low magnetic field strengths shown in Fig. 8.31(b). However, the main part of the magnetization is aligned antiparallel to the external magnetic field at point (B₁). Reducing the electric field strength from +400 kV/m (B₁) to -60 kV/m (B₂) at the constant magnetic field of $\mu_0 H = +5.2$ mT then results in an almost demagnetized Ni thin film with a multi-domain state and thus a low magnetization of $M = 52.7$ kA/m (see Fig. 8.33(b)). Upon increasing the electric field again from -60 kV/m (B₂) to +400 kV/m (B₃), the magnetization \mathbf{M} aligns along the external magnetic field as evident from the large positive magnetization 290 kA/m. A subsequent scan of the electric field from +400 kV/m to -60 kV/m and back (B₃ → B₄ → B₅) only reduces the magnetization by about 20% but does not switch the magnetization again. Thus, Fig. 8.33 demonstrates that the magnetization \mathbf{M} can be switched irreversibly by sweeping the electric field only. To restore the initial state, the external magnetic field must be decreased from $\mu_0 H = +5.2$ mT to $\mu_0 H = -100$ mT (B₃ → C) at constant electric field $E = 400$ kV/m.

To explain the irreversible switching process, we trace the minimum of $\tilde{g}^{(m)}/M_s$ as a function of the applied electric field at a constant magnetic field of $\mu_0 H = +5.2$ mT (see Fig. 8.34(a)). Starting at 400 kV/m (B₁), the magnetization is oriented close to $m_2 = -1$. While almost no changes are observed by decreasing the electric field to

⁵The energy barrier is determined by simulating the magnetic hysteresis shown in Fig. 8.31.

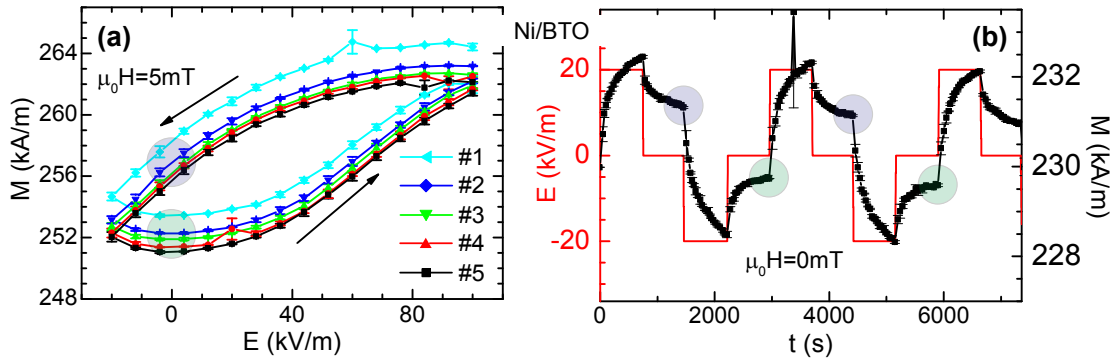


Figure 8.35: (a) $M(E)$ minor loops of Ni(50 nm)/BaTiO₃ measured at a constant external magnetic field of $\mu_0 H = 5$ mT by sweeping the electric field in a small range from $E = +100$ kV/m to -20 kV/m and back to $+100$ kV/m after aligning the magnetization into a well-defined state using an external magnetic field of $\mu_0 H = 1$ T. The electric field sequence was repeated five times (#1-#5). (b) Two different remanent magnetic states, which are indicated by full circles, can be achieved by applying the electric field sequence $+0.2$ kV/m \rightarrow 0 kV/m \rightarrow -0.2 kV/m \rightarrow 0 kV/m (red line) across the structure.

80 kV/m, which is in agreement with the experimental data shown in Fig. 8.33(b), a coherent switching of the magnetization ($m_2 \approx -1 \rightarrow m_2 \approx 0 \rightarrow m_2 \approx +1$) is observed between 40 kV/m and 0 kV/m. Increasing the external electric field to 40 kV/m, the orientation of the magnetization aligns almost parallel to the external magnetic field. Any further variation of the external electric field causes only minor changes of the magnetization, since the magnetization direction remains in the global minimum close to $m_2 \approx +1$ (B_3). Therefore, Figure 8.34(a) discloses, that the non-volatile irreversible magnetization switching is caused by a continuous coherent magnetization reorientation explainable on the basis of the elastic strain components η_i derived using x-ray diffraction. However, to improve the agreement between experiment and simulation, the elastic strain components η_i resulting from the converse piezoelectric effect should be determined in more detail. Furthermore, a broad Gaussian distribution of the energy barrier, which takes a broad distribution of domain pinning effects into account, should be included into the simulation [681].

Figure 8.33(b) reveals a hysteretic $M(E)$ behavior of the second electric field sweep ($B_3 \rightarrow B_4 \rightarrow B_5$) with two different values of the magnetization at $E = 0$ kV/m, depending on the sweep history. This is illustrated in more detail in Fig. 8.35(a). After aligning the magnetization into a well-defined state using an external magnetic field of $\mu_0 H = 1$ T, the electric field dependence of the Ni/BaTiO₃ hybrid structure is measured in a small range from $E = +100$ kV/m to -20 kV/m and back to $+100$ kV/m. The electric field sequence was repeated several times in a row. While a small drift of the magnetization is observed up to the third minor loop (#1-#3), the fourth and fifth measurements (#4, #5) are almost identical. This demonstrates that the two different magnetization states at $E = 0$ kV/m are stable in time after performing four electric field sweeps. The hysteretic $M(E)$ behav-

ior can be attributed to the ferroelastic nature of the BaTiO₃ substrate leading to non-linearities of the converse piezoelectric response. In particular, under weak-field conditions, irreversible elastic domain wall effects play a dominant role. While reversible contributions result in a linear behavior, irreversible effects can be expressed by a quadratic dependence [682, 683]. This is in analogy to ferromagnetic hysteresis described by the Rayleigh law [684].

Considering the Ni/BaTiO₃ hybrid structure macroscopically as a new, homogeneous system [423], the remanent magnetization of this system can even be switched from one electro-remanent state to another and back to the initial state, by applying the electric field sequence $+0.2 \text{ kV/m} \rightarrow 0 \text{ kV/m} \rightarrow -0.2 \text{ kV/m} \rightarrow 0 \text{ kV/m}$ across the structure (see Fig. 8.35(b)). Therefore, two different remanent states can be realized electrically in Ni/BaTiO₃ hybrid structures. We note that the electric field strengths to achieve a remanent switching based on ferroelastic domain effects are low compared to electric fields needed to switch the polarization, as required, e.g., in ferroelectric random access memories.

In total, the manipulation of the ferromagnetic magnetization via electric fields was discussed in detail in different FM/BaTiO₃ hybrid structures with FM = Ni, Fe₃O₄, Sr₂CrReO₆ at room temperature. In particular, pure electrical reversible and irreversible switching of the magnetization was achieved. The magnetization changes were found to be purely strain mediated and could be explained by a two region model. At low electric fields ($E < 400 \text{ kV/m}$) two types of regions can be distinguished. One type consists of parts of the ferromagnetic thin film on top of ferroelastic c -domains and the other can be identified by areas clamped to ferroelastic a_2 -domains. While, at first glance, ferromagnetic thin films on top of c -domains as well as of 90° -domain walls are assumed to be not affected by the electric field, the formation of ferroelastic a_2 -domains induces strain in the overlying ferromagnetic thin film and alters the magnetization due to magnetoelastic effects. This two region model is adequate to describe electric field induced magnetization changes in FM/BaTiO₃ hybrid structures carried out at magnetic field strengths larger than the saturation field of the ferromagnetic thin film. However, at lower magnetic fields, magnetization variations due to the converse piezoelectric effect of c - and a_2 -domains have to be taken into account.

8.4.2 BaTiO₃ in the orthorhombic phase

In terms of application, the control of the magnetization in FM/BaTiO₃ hybrid structures at room temperature is certainly the most important aspect. However, high electromechanical response can be observed by polarization rotation from a rhombohedral or orthorhombic state to a tetragonal one induced by external electric fields [484]. Therefore, large magnetoelectric effects in FM/BaTiO₃ hybrid structures are expected in the orthorhombic phase of BaTiO₃ at 270 K with the electric field applied along the \mathbf{z} -direction.

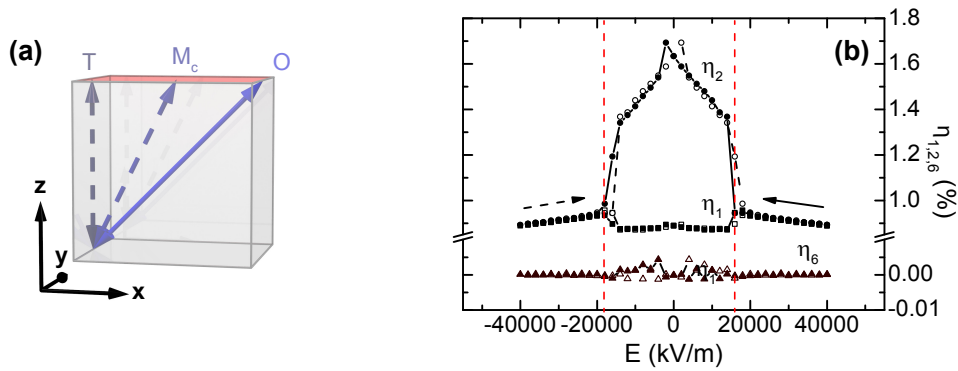


Figure 8.36: (a) Schematic illustration of the symmetry changes during the switching process of the ferroelectric polarization in the nominal orthorhombic phase with the electric field applied along the z -direction. T , M_c , O denote the tetragonal, monoclinic, and orthorhombic symmetries and the blue arrows the ferroelectric polarization P in each symmetry. (b) In-plane strain components η_i ($i = 1, 2, 6$) as a function of the applied electric field E calculated via molecular dynamics simulations in the nominally orthorhombic phase at $T_{MD} = 232$ K. The critical fields $E_{T \rightarrow M_c}$ and $E_{M_c \rightarrow T}$ are marked by vertical red dashed lines.

Expected magnetization changes of $\text{Fe}_3\text{O}_4/\text{BaTiO}_3$ hybrids with BaTiO_3 in the orthorhombic phase

While the tetragonal symmetry is preserved during the switching of the polarization of a perfect BaTiO_3 crystal at room temperature, the polarization reversal in the orthorhombic phase of BaTiO_3 with an electric field applied along the z -direction is a multi-step process (see Fig. 8.36(a)). At sufficiently high values of the electric field E , the polarization \mathbf{P} is aligned parallel to the external electric field along $[001]_{pc}$ exhibiting a tetragonal symmetry (T). Decreasing the external electric field, a phase transition from the tetragonal to the monoclinic M_c symmetry occurs at a critical field $E_{T \rightarrow M_c}$. In the monoclinic M_c phase the polarization \mathbf{P} is aligned along $[u0v]_{pc}$ with ($u \neq v$) $[664]$. Further reducing the electric field strength leads to a rotation of the polarization \mathbf{P} towards the $[101]_{pc}$ direction in the $(010)_{pc}$ plane. At $E = 0$ kV/m both strain components are equal and BaTiO_3 exhibits an orthorhombic symmetry (O). The second switching occurs at the coercive field, at which the polarization \mathbf{P} reverses. After the polarization reversal, the polarization rotates away from the $[\bar{1}0\bar{1}]_{pc}$ direction with decreasing the electric field. At the critical field $E_{M_c \rightarrow T}$, the phase transition from the M_c phase to the tetragonal phase takes place. Therefore, the electric polarization reversal in the nominal orthorhombic phase is characterized by two switching processes. First, the polarization switches from the tetragonal T to the monoclinic M_c symmetry and second, a polarization reversal takes place within the monoclinic M_c symmetry. Furthermore, a rotation of the polarization is observable in the monoclinic M_c phase.

The multi-step process of the polarization reversal is expected to have significant impact on the strain state of the BaTiO_3 substrate and therefore should alter the magnetization in FM/ BaTiO_3 hybrid structures. Using molecular dynamics simu-

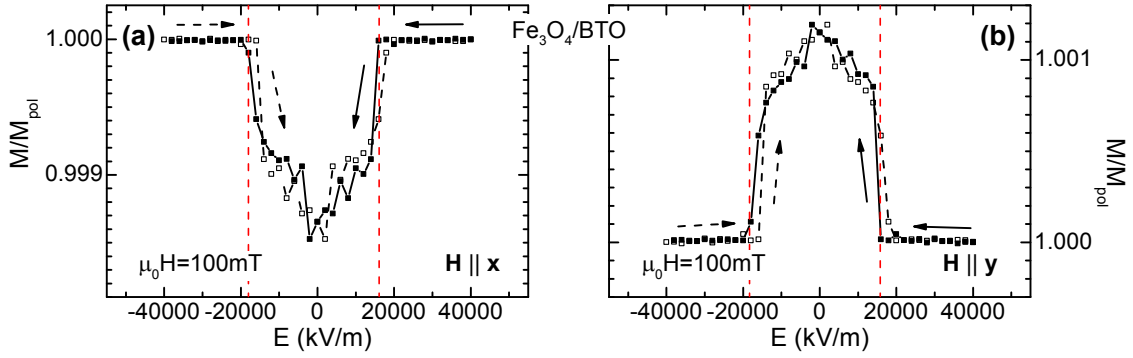


Figure 8.37: Projection of the magnetization on the external magnetic field direction as a function of the applied electric field $M(E)$ of a $\text{Fe}_3\text{O}_4/\text{BaTiO}_3$ hybrid structure calculated on the basis of the in-plane strain components η_i ($i = 1, 2, 6$) derived by molecular dynamics simulations (cf. Fig. 7.2(b)). The external magnetic field was aligned along (a) $\mathbf{H} \parallel \mathbf{x}$ and (b) $\mathbf{H} \parallel \mathbf{y}$ and a magnetic field strength of $\mu_0 H = 100 \text{ mT}$ were used for the simulation. The magnetization is normalized to the value M_{pol} obtained at $E = 40000 \text{ kV/m}$. Again, the critical fields $E_{T \rightarrow M_c}$ and $E_{M_c \rightarrow T}$ are marked by vertical red dashed lines.

lation, the strain components η_i and the polarization as a function of the electric field were calculated at $T_{\text{MD}} = 232 \text{ K}$, which corresponds to $T_{\text{exp.}} \approx 270 \text{ K}$ (see Fig. 8.14). In contrast to Fig. 7.3, higher electric field strengths are considered in the simulation shown in Fig. 8.36(b). At electric fields larger than $E > 16000 \text{ kV/m}$, where the polarization is parallel to the external electric field, the strain response is caused by the converse linear piezoelectric effect. However, since no difference between the in-plane strain components is observed, no variation of the magnetization in FM/BaTiO₃ hybrid structures is expected in this electric field range (cf. Section 6.2.4). The situation changes when the electric field strength is reduced. At the first critical field $E_{T \rightarrow M_c} = 16000 \text{ kV/m}$, when the crystal transforms to the monoclinic M_c symmetry, large discontinuities of the strain components are visible (see Fig. 8.36(b)). Furthermore, the in-plane isotropy is broken, leading to a large difference of η_1 and η_2 of more than 0.5%. This should cause large changes of the magnetization of the clamped ferromagnetic thin film. Within the monoclinic M_c phase, the rotation of the polarization results in an increase of the strain component η_2 . The second discontinuity of the electric field dependence of the strain components occurs at the coercive field $E \approx -2000 \text{ kV/m}$ at which the polarization reverses. Below this electric field strength, the BaTiO₃ crystal enters the polarization rotation region and at the critical field $E_{M_c \rightarrow T}$, the phase transition from the M_c phase to the tetragonal phase takes place. Therefore, the strain behavior is almost symmetric with respect to $E \approx -2000 \text{ kV/m}$ and ferroelastic domain switching may play a minor role.

On the basis of the calculated in-plane strain components η_i ($i = 1, 2, 6$), the normalized magnetization as a function of the applied electric field can now be simulated in a $\text{Fe}_3\text{O}_4/\text{BaTiO}_3$ hybrid structure. To carry out the simulation, the magnetic and magnetoelastic parameters determined in Section 8.4.1 are used. To

emulate the experiment, the general sequence of the simulation is as follows. First, the magnetization component along the external magnetic field, which was aligned either along \mathbf{x} or \mathbf{y} , during cooling down from 300 K to 270 K was calculated on the basis of the calculated strain components shown in Fig. 8.14 using a magnetic field strength of 1 T. At 270 K, which corresponds to $T_{\text{MD}} = 232$ K in the simulation, the magnetic field strength is reduced to the measuring field of 100 mT and the electric field dependence of the magnetization is simulated using all 6 strain components η_i , which are calculated at $T_{\text{MD}} = 232$ K with different electric fields applied. Figures 8.37 (a) and (b) reveal a maximum change of the magnetization of about 0.1%, which is comparable with magnetoelastic effects measured at room temperature (see Fig. 8.28(b)). As expected, no variation of the magnetization is visible for electric fields larger than $E > 16000$ kV/m, i.e., in the tetragonal symmetry. However, reducing the electric field strength, when the crystal enters the monoclinic M_c phase, large magnetoelectric effects are observable at the critical electric field $E_{T \rightarrow M_c}$. Furthermore, smaller changes of the magnetization is simulated around the coercive fields at around $E \approx -2000$ kV/m. In total, the $M(E)$ loops resembles the electric field dependence of the strain component $\eta_2(E)$ shown in Fig. 8.36(b). Therefore, the converse magnetoelectric effect in the nominal orthorhombic phase is not expected to be caused by ferroelastic domain switching as it is the case in the tetragonal symmetry but should also be achieved considering a ferroelastic single-domain state in the BaTiO₃ substrate.

Magnetic response of FM/BaTiO₃ hybrid structures as a function of the applied electric field at 270 K

In contrast to the predictions from theory, totally different electric field dependencies of the magnetization is observed experimentally. In Fig. 8.38, the projection of the magnetization onto the external magnetic field direction of FM/BaTiO₃ hybrid structures as a function of the applied electric field using different ferromagnetic materials are shown. A strongly asymmetric behavior is detected in all FM/BaTiO₃ hybrid structures. While almost no changes of the magnetization projection is detected by decreasing the electric field from 400 kV/m down to the corresponding coercive field, gradual magnetization changes are observed below this electric field strength. Whether the magnetization projection increases or decreases depends on the sign of the magnetostrictive constant λ_{100} . Very recently, a similar dependence of the magnetic coercive field as a function of the applied electric field measured at 250 K on Fe/BaTiO₃ hybrid structures was reported by Brivio and coworkers [685]. Therefore, the asymmetric behavior of the $M(E)$ loops is no experimental artifact. By comparing Fig. 8.38 and Fig. 8.37, it seems that only the magnetization dependence for $E > 0$ kV/m was measured, as a result of a large shift of the ferroelectric hysteresis. Since the displacement currents also shown in Fig. 8.38 are nearly symmetric with respect to $E = 0$ kV/m, a distortion or shift of the hysteresis loop, as speculated by Brivio *et al.* [685], is not the reason for the asymmetric behavior. Furthermore, the magnetization behavior displayed in Fig. 8.38 does not change by increasing the maximum electric field strength up to $E \leq 1000$ kV/m (not shown

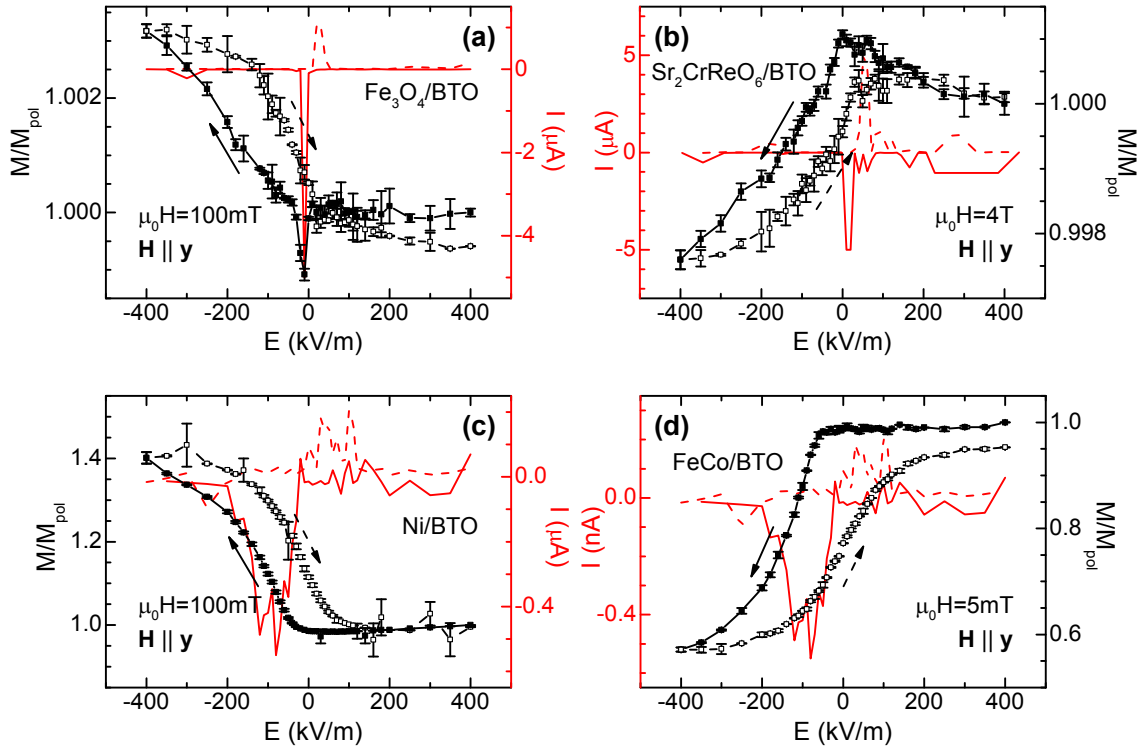


Figure 8.38: $M(E)$ loops measured at 270 K of BaTiO₃ (BTO) based hybrid structures with (a) Fe₃O₄, (b) Sr₂CrReO₆, (c) Ni, and (d) FeCo used as ferromagnetic material. M_{pol} denotes the magnetization value obtained at $E = 400$ kV/m. The measurements were carried out with the applied magnetic field aligned along $\mathbf{H} \parallel \mathbf{y}$ but under different magnetic field strengths. The peaks in the current (red lines), which is flowing across the hybrid structure during the measurement, can be attributed to displacement currents and thus indicates the coercive electric fields of BaTiO₃.

here). At higher field strengths, electrical breakdown was observed. Therefore, it seems that the electric field strength needed to align the polarization of the BaTiO₃ substrate parallel to the external electric field, i.e., in a tetragonal symmetry, could not be reached experimentally. However, even if the tetragonal phase is not obtained, a different behavior is expected (see Fig. 8.37).

As the electric field can alter the magnetization $\mathbf{M}(M, m_i)$ by changing its magnitude M and the direction of the magnetization vector m_i , in-plane angular dependent magnetometry measurements were performed at constant magnetic field strength of 5 mT and with different electric fields applied to the FeCo/BaTiO₃ hybrid structure to resolve changes in the magnetic anisotropy. FeCo was chosen as the ferromagnetic material, since the high saturation magnetization causes a large demagnetization field forcing the magnetization to stay in the film plane. Similar to the $M(E)$ loop displayed in Fig. 8.38(d), no difference of the angular dependent magnetization is observed between $E = 400$ kV/m and $E = 0$ kV/m (see Fig. 8.39(a)). Further decreasing the electric field to $E = -100$ kV/m, $E = -200$ kV/m, and $E = -400$ kV/m, not only a reduction of the maximum magnetization M_{max} by 22% but also a shift of the $M(\phi)$ curve by 40° is observed. The same type of mea-

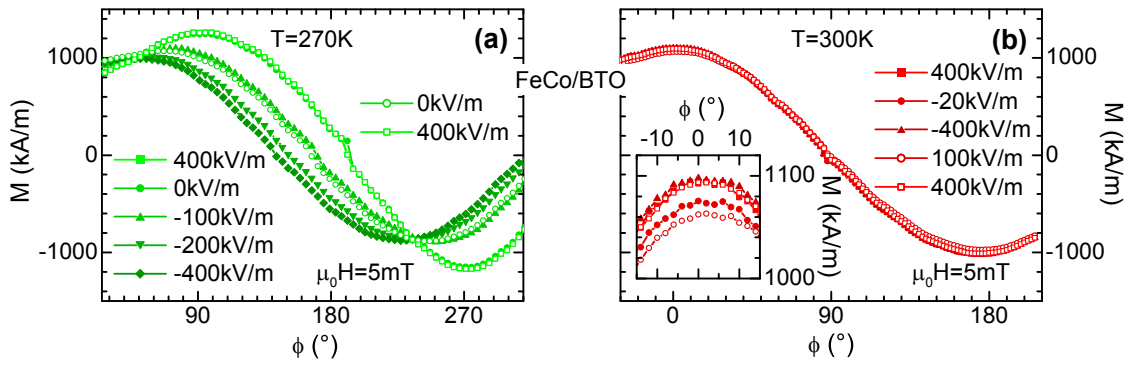


Figure 8.39: Angular dependent magnetization measured using a magnetic field strength of $\mu_0 H = 5 \text{ mT}$ at (a) 270 K and (b) 300 K on a FeCo/BaTiO₃ hybrid structure under different electric fields applied. The down loop of the electric field (+400 kV/m \rightarrow -400 kV/m) is marked by full symbols, while the up loop (-400 kV/m \rightarrow +400 kV/m) is denoted by open symbols. $\phi = 0^\circ$ coincides with the x -direction of the BaTiO₃ substrate (cf. Fig. 8.13). Before each measurement, the magnetization was first aligned to a well-defined initial state along $\phi = 90^\circ$ ($\phi = 0^\circ$) for 270 K (300 K) in an external magnetic field of $\mu_0 H = 1 \text{ T}$. Afterwards the angular measurement were repeated three times. An enlargement of the angular dependent magnetization measured at 300 K around $\phi = 0^\circ$ is shown in the inset of (b).

surement carried out at 300 K is shown in Fig. 8.39(b) for comparison. At 300 K, a reduction of the magnetization M_{max} and only a marginal shift of the $M(\phi)$ curve is detectable for electric field strengths $|E| < 400 \text{ kV/m}$. From the comparison between the angular dependent magnetization measurements performed at 300 K and 270 K, the reduction of M_{max} visible in Fig. 8.39(a) can mainly be attributed to domain formation. Therefore, the change of the magnetization for electric field strengths $E < 0 \text{ kV/m}$ visible in Fig. 8.39(a) might be due to ferroelastic domain formation in BaTiO₃ at negative electric fields. In contrast, since almost no changes of the magnetization are observed in the field range between $E = 400 \text{ kV/m}$ and $E = 0 \text{ kV/m}$, the ferroelastic state seems to be unchanged in this electric field range.

Simulation of converse magnetoelectric effects at 270 K in a Fe₃O₄/BaTiO₃ hybrid structure

As discussed in the previous section, the knowledge of the ferroelastic behavior in the BaTiO₃ as a function of the applied electric field is a prerequisite for the simulation of the asymmetric converse magnetoelectric effects measured at 270 K in FM/BaTiO₃ hybrid structures. The ferroelastic state of the BaTiO₃ substrate was investigated by performing x-ray diffraction measurements around the (103) reflection of BaTiO₃ at 270 K with an electric field of $E = 400 \text{ kV/m}$ and $E = 0 \text{ kV/m}$. The BaTiO₃ (103) reflection measured under an electric field of $E = 400 \text{ kV/m}$ applied is found to be split into three peaks (cf. Fig. 8.40(a)), which is a clear indication of the monoclinic M_c phase [686]. As shown in Fig. 8.40(b), almost the same pattern is observed after decreasing the electric field to zero. Therefore, the monoclinic M_c phase is stable in the electric field range $E = 400 \text{ kV/m}$ to $E = 0 \text{ kV/m}$. Further-

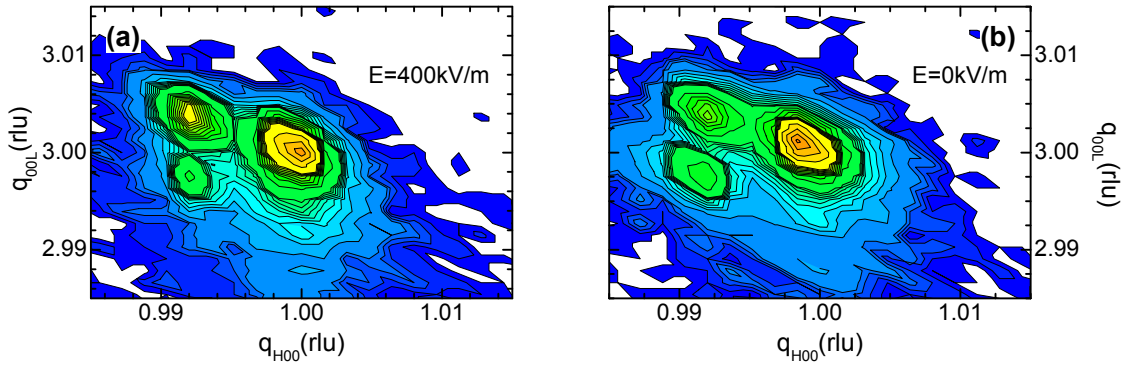


Figure 8.40: X-ray diffraction measurements around BaTiO₃ (103) carried out at 270 K with an electric field of (a) 400 kV/m and (b) 0 kV/m.

more, the expected orthorhombic symmetry seems to be absent at $E = 0$ kV/m. These findings are in agreement with the experimental data recently published by Cao and coworkers [687]. Therefore, the almost constant magnetization behavior for $E = 400$ kV/m \rightarrow $E = 0$ kV/m can indeed be attributed to a constant ferroelastic state of the BaTiO₃ substrate. Note that one crucial step in the stabilization of the monoclinic M_c phase at $E = 0$ kV/m seems to be crossing the tetragonal-orthorhombic phase transition under field-cooled condition [686].

Decreasing the electric field to $E = -400$ kV/m, the angular dependent magnetization measurements displayed in Fig. 8.39(a) suggest the formation of ferroelastic domains in the BaTiO₃ substrate. Again using x-ray diffraction at $T = 270$ K the appearance of ferroelastic domains should be detectable. Figure 8.41(a) shows a reciprocal space map around the BaTiO₃ (002) reflection recorded at $E = 400$ kV/m. To trace the position of the BaTiO₃ (002) reflection as a function of the applied electric field, q_{00L} -scans at $q_{0K0} = 0$ rlu were performed under different electric fields applied to the BaTiO₃ substrate (Fig. 8.41(b)). In the electric field range between $E = 400$ kV/m and $E = 0$ kV/m, a single peak at BaTiO₃ (002) is observed. The second peak located around $q_{00L} \approx 2.015$ rlu is caused by the diffraction from a minor concentration of orthorhombic o_{12} -domains. At negative electric field strengths, the BaTiO₃ (002) reflection is shifted to higher q_{00L} values and a second peak emerges at $q_{00L} \approx 1.995$ rlu. The peaks might be attributed to orthorhombic o_{23} -domains with $q_{00L} = 2.015$ rlu and o_{13} -domains with $q_{00L} \approx 1.995$ rlu. By increasing the electric field to $E = 0$ kV/m the second peak vanishes again. Thus, x-ray diffraction measurements around BaTiO₃ (002) reveal an asymmetric behavior in the context of crystalline domain formation and changes of the lattice spacing. Similar to Fig. 8.32, the strain components η_i ($i = 1, 2, 3$) can be calculated using Eq. (8.9). However, in contrast to Fig. 8.32, Figure 8.41(b) provides only a one dimensional information on the scattering vector. Since a slight strain dependence of the strain component η_1 was observed at $T = 300$ K (cf. Fig. 8.32), η_1 is assumed to be zero at $T = 270$ K. Within this assumption, the strain components η_3 can be derived from Fig. 8.41(b) and η_2 can be calculated using a Poisson ratio of 0.29 [378]. Both strain components are depicted in Fig. 8.41(c) and Fig. 8.41(d) for orthorhombic o_{23} - and o_{13} -domains,

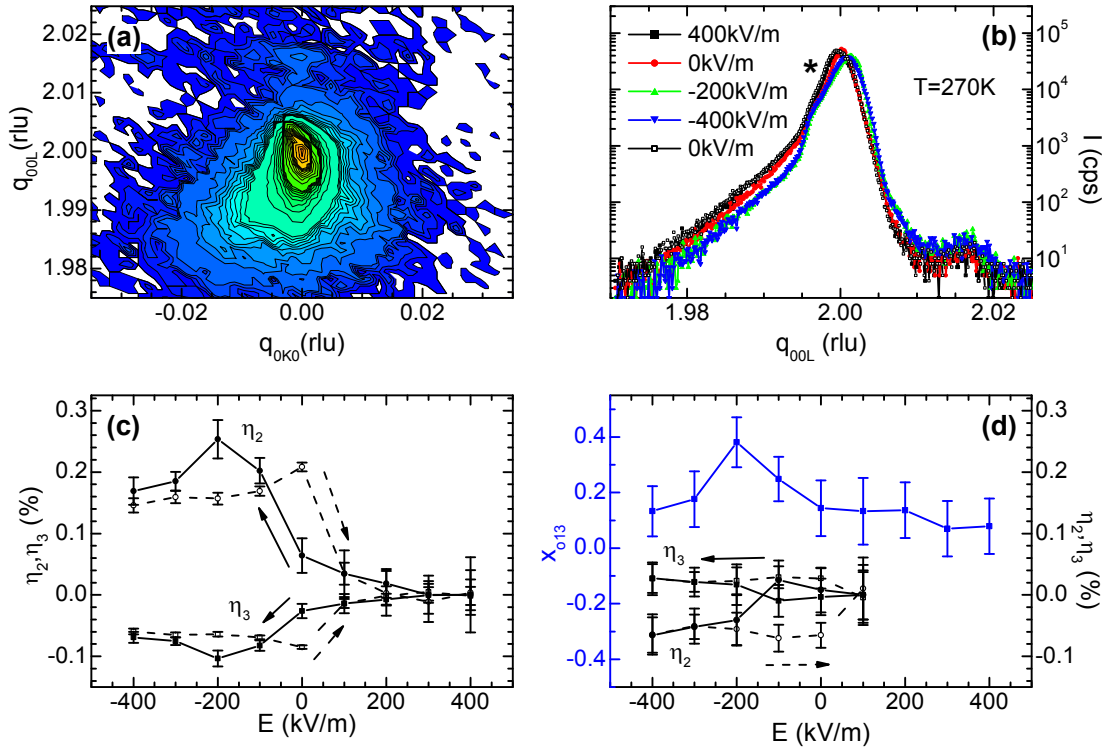


Figure 8.41: (a) X-ray diffraction measurements around BaTiO₃ (002) recorded at 270 K with an electric field of 400 kV/m applied across the BaTiO₃ substrate. (b) q_{00L} -scans at $q_{0K0} = 0$ r.l.u. measured in different electric fields E . The second peak emerging at negative electric fields is marked by the asterisk. (c), (d) Strain components η_2 , η_3 as a function of the applied electric field E of the (c) main peak and the (d) second peak calculated under the assumption of $\eta_1 = 0$. The down loop (+400 kV/m \rightarrow -400 kV/m) is marked by full symbols, while the up loop (-400 kV/m \rightarrow +400 kV/m) is denoted by open symbols. The volume fraction x_{o13} of the second peak, which is derived from one dimensional q_{00L} -scans, is shown in blue.

respectively. Furthermore, the volume fraction of o_{13} -domains x_{o13} is derived from the intensity ratio of both reflections visible in Fig. 8.41(b) (see Fig. 8.41(d)).

Using these values, the electric field dependence of the magnetization can be calculated for a Fe₃O₄/BaTiO₃ hybrid structure in the same way as described for Fig. 8.37. A magnetic field of $\mu_0 H = 100$ mT was used for the simulation, since irreversible $M(E)$ -effects are observed at lower magnetic field strengths (Fig. 8.42(a)). At this magnetic fields, large changes of the magnetization projection of unknown origin were observed around $E = 0$ kV/m. However, the result of the simulation as well as the experimental data for $\mu_0 H = 100$ mT are shown in Fig. 8.42(b). While the asymmetric electric field dependence is more or less in good agreement with the experimental results, the change of the magnetization component is much too low. This discrepancy between simulation and experiment can mainly be attributed to the insufficient determination of the strain tensor of BaTiO₃ at $T = 270$ K as well as the volume fraction of the ferroelastic domains, which is limited due to experimental restrictions. However, Fig. 8.39 and Fig. 8.42(b) reveal that the observed

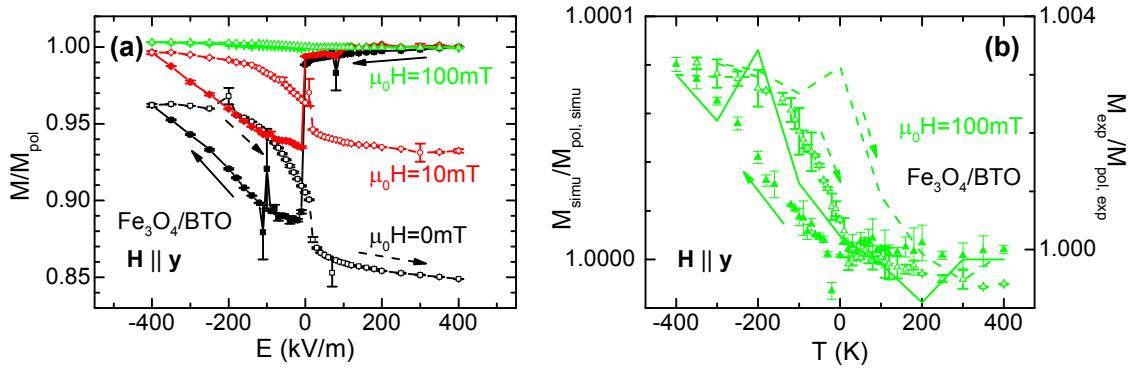


Figure 8.42: (a) $M(E)$ loops at low magnetic field strength measured on a $\text{Fe}_3\text{O}_4/\text{BaTiO}_3$ hybrid structure. The lines are guides to the eye. (b) Experiment (symbols) and simulation (lines) of the electric field dependence of the magnetization carried out at $\mu_0 H = 100$ mT. The simulation was performed on the basis of the strain components η_2, η_3 derived in Fig. 8.41.

electric field dependence of the magnetization might be based on the formation of ferroelastic domains in the BaTiO_3 substrate.

In total, in contrast to the tetragonal symmetry at room temperature, a magnetoelectric behavior very different from the theoretically expected one was observed experimentally at $T = 270$ K. In theory, applying an electric field on a non-polar direction, e.g. along the \mathbf{z} -direction in the orthorhombic phase, yields large in-plane strain effects due to polarization rotation. Therefore, strong converse magnetoelectric effects are expected even in single domain ferroelastic substrates. However, x-ray diffraction measurements disclosed a stable monoclinic M_c -symmetry from $E = +400$ kV/m down to $E = 0$ kV/m, which results in a constant electric field dependence of the magnetization. At negative electric fields, the BaTiO_3 substrate might decompose into ferroelastic domains starting at the coercive electric field. These ferroelastic domains certainly have great influence on the magnetoelectric properties. Using x-ray diffraction measurements, the strain state caused by the ferroelastic domains and their electric field dependence were investigated in the BaTiO_3 substrate. However, magnetoelastic simulations based on the derived strain components reveal that these measurements just provide a first hint on the reason for the asymmetric magnetoelectric behavior observed at 270 K.

8.5 Summary

In this chapter, strain-mediated magnetoelectric effects in ferromagnetic thin films (FM) deposited on ferroelastic BaTiO_3 substrates were discussed. FM/ BaTiO_3 hybrid structures based on epitaxial $\text{Fe}_3\text{O}_4/\text{BaTiO}_3$ and $\text{Sr}_2\text{CrReO}_6/\text{BaTiO}_3$ systems as well as on polycrystalline FM/ BaTiO_3 structures using Ni and FeCo thin films were studied. Since BaTiO_3 crystals exhibit different ferroelastic phases (cf. Section 7.1), BaTiO_3 was employed to manipulate the strain state of the overlying ferromagnetic thin film. With this method, the magnetic response of different ferro-

magnetic materials can be studied under different strain conditions. In this sense, FM/BaTiO₃ hybrid structures have been used over the past ten years [447].

In our FM/BaTiO₃ hybrid structures large changes of the physical properties as a function of temperature were observed. In particular, a strong modification of the magnetic anisotropy in Sr₂CrReO₆/BaTiO₃ hybrids was detected upon crossing the ferroelastic phase transition of the BaTiO₃ substrate. While an isotropic magnetic state was found in the rhombohedral phase of the BaTiO₃ substrate, a large in-plane magnetic anisotropy is observed at 270 K, i.e., in the orthorhombic symmetry of BaTiO₃. This can be attributed to large magnetoelastic effects present in Sr₂CrReO₆ thin films. Therefore, indeed, the magnetic properties of Sr₂CrReO₆ seems to be highly sensitive to strain effects imposed by the ferroelastic BaTiO₃ substrate.

Using different experimental techniques, such as ferromagnetic resonance and angle dependent magnetoresistance measurements, modifications of the magnetic anisotropy were observed in Fe₃O₄/BaTiO₃ and Ni/BaTiO₃ hybrids as well. However, as it has become clear in the first part of this chapter, a control of the ferroelastic domain configuration in the BaTiO₃ substrate is mandatory to correlate the experimental results with theoretical simulations in a quantitative way. Therefore, ferroelastic domain engineering is an important task in magnetostrictive/piezoelectric hybrid structures using ferroelastic materials as the piezoelectric layer. In this chapter, it was shown that a specific ferroelastic domain configuration can be obtained by using miscut BaTiO₃ substrates. These substrates exhibit not only one type of ferroelastic *a*-domains at room temperature, but also allows to select particular domains in the orthorhombic and rhombohedral phase of BaTiO₃. By exploiting the properties of miscut ferroelastic BaTiO₃ substrates with an electric field applied along the out-of-plane direction, the calculation of the magnetic response of FeCo/BaTiO₃ and Ni/BaTiO₃ as a function of temperature was achieved on the basis of *ab initio* molecular dynamics simulations in combination with magnetoelastic theory. Moreover, magnetization changes of more than 80% were experimentally observed at the ferroelastic phase transitions of BaTiO₃ in Ni/BaTiO₃ hybrids.

Using BaTiO₃ substrates as piezoelectric layer in multiferroic hybrid structures does not only allow to examine the physical properties of the overlying ferromagnetic thin film under constant applied electric field and different temperature, but also admits the investigation of strain-mediated magnetoelectric effects. Two different important cases were considered in this chapter. First, converse magnetoelectric effects were investigated at room temperature, i.e., in the tetragonal phase of BaTiO₃, and second, the magnetic response of FM/BaTiO₃ hybrid structures as a function of the applied electric field was examined at 270 K, since in the orthorhombic phase of BaTiO₃ large converse piezoelectric effects are expected.

Since the manipulation of the magnetization as a function of the applied electric field at room temperature is highly desirable for applications in today's spintronic devices, large and robust converse magnetoelectric effects are an important issue. At this temperature, a finite variation of the magnetization as a function of the applied electric field was observed in all investigated FM/BaTiO₃ hybrid structures. Since the converse magnetoelectric effect is strongly dependent on the ferroelastic domain configuration, a definite conclusion on the optimal choice of the magnetic material

could not be drawn. However, using a two region model, which accounts for the different magnetic states of areas of the ferromagnetic thin film on top of ferroelastic c - and a_2 -domains leading to a magnetic heterogeneous state, the electric field dependent magnetization variation was well simulated for magnetic fields larger than the saturation field of the respective ferromagnetic layer. This two region model was even used to describe the magnetic behavior on a local scale. However, as it has become clear from the magnetic properties of Ni/BaTiO₃ hybrid structures, this model is insufficient to explain the variation of the magnetic coercive field of up to 10% as a function of the applied electric field. To simulate these changes, the converse piezoelectric effect of ferroelastic c - and a_2 -domains has to be taken into account. Including converse piezoelectric effects, which were quantified from x-ray diffraction, into the two region model, an excellent agreement between experiment and simulation was obtained. Furthermore, by exploiting the electric field dependence of the magnetic coercive field, an electric field induced irreversible switching of the magnetization was achieved. Moreover, even a reversible switching between two non-volatile remanent magnetic states based on irreversible ferroelastic domain effects in the BaTiO₃ substrate was obtained in Ni/BaTiO₃ hybrid structures. This demonstrates that FM/BaTiO₃ hybrid structures are interesting candidates for strain-mediated non-volatile magnetic memory devices.

However, these changes are based on a multi-ferroelastic domain configuration in the BaTiO₃, which imposes a magnetically heterogeneous state in the overlying ferromagnetic thin film. For applications, electrically controllable non-volatile remanent magnetic reorientations are desirable, i.e., switching the magnetization of a single domain state from one distinct orientation to another. This requires two homogeneous in-plane strain states exhibiting a preferential elongation in a certain direction, which might be realized using ferroelastic crystals with a specific orientation. To illustrate the magnetic response of hybrid structures based on such ferroelastic crystals, in the following, we address a practicable concept, which allows to control the remanent magnetization by an electric field leading to non-volatile switching of the remanent magnetization in a single domain state.

By using (011) oriented $[\text{Pb}(\text{Mg}_{1/3}\text{Nb}_{2/3})\text{O}_3]_{1-x}[\text{PbTiO}_3]_x$ (PMN-PT) crystals as ferroelectric layer in multiferroic hybrids, the realization of a nonvolatile reorientation of the magnetization might be feasible, since PMN-PT crystals provide large electric field induced in-plane strain changes along the y -direction due to non-180° polarization reorientation [487, 688]. Considering a composite hybrid, which is built up by a ferromagnetic thin film exhibiting a crystalline cubic anisotropy deposited onto a (011)-PMN-PT substrate, the magnetization direction can be, in principle, reoriented by 90° forced by the linear converse piezoelectric effect of the PMN-PT crystal. Since the preferred elongation direction is parallel to one of the two magnetic hard directions of the ferromagnetic thin film, in this example, the two easy directions are energetically degenerate, which results in two different magnetic domains after the switching process. Therefore, a finite rotation of the magnetic easy direction of the ferromagnetic thin film with respect to the preferential direction of the piezoelectric elongation of the (011) -PMN-PT substrate is essential to achieve a magnetic single-domain reorientation of the magnetization. This might be achieved

by using a post-annealed buffer layer, which consists of an adequate material system [689]. The resulting FM/PMN-PT hybrid structure with Fe_3O_4 as magnetostrictive material as well as the epitaxial relation of both layers are schematically shown in Fig. 8.43(a). To illustrate the nonvolatile switching of the remanent magnetization, energy density contours of the modified magnetic Gibbs potential $\tilde{g}^{(m)}/M_s$ (cf. Section 6.2) as a function of the magnetization orientation m_2 are calculated assuming a difference of the [100] directions of the Fe_3O_4 thin film and the PMN-PT substrate of 10° attained by the buffer layer as well as a small cubic anisotropy $K_c/M_s = -2 \text{ mT}$.⁶ To derive $\tilde{g}^{(m)}/M_s$ traces for different imposed strain states, the measured converse piezoelectric response of a (011)-PMN-PT substrate $\epsilon_{ij}^{(e)}(E)$ as discussed in Ref. [688] is used. The calculated $\tilde{g}^{(m)}/M_s$ dependence on the magnetization direction m_2 for three different electric fields is shown in Fig. 8.43(c). Starting at $\mathbf{M} \parallel [1\bar{1}0]$ and $E = 0 \text{ kV/m}$ (cf. ① in the upper panel of Fig. 8.43(c)), the direction of the magnetization m_1 , which is determined by the local minimum of the $\tilde{g}^{(m)}/M_s$ curve, slightly changes by increasing the electric field to $E = 40 \text{ kV/m}$. Further increase of the electric field strength leads to a coherent magnetization rotation to $\mathbf{M} \parallel [110]$ at $E = 100 \text{ kV/m}$ (cf. ② in the upper panel of Fig. 8.43(c)). By removing the electric field, the switching process of the magnetization by 90° is complete (cf. ③ in the upper panel of Fig. 8.43(c)). Further reorientation of the magnetization by 90° can be realized by exploiting the linear electric field dependence of the converse piezoelectric effect of (011)-PMN-PT as the electric field is decreased to $E = -100 \text{ kV/m}$ (cf. ③ \rightarrow ④ \rightarrow ⑤ in the lower panel of Fig. 8.43(c)). Therefore, a sequential non-volatile reorientation of the magnetization by 90° can, in principle, be obtained within the described model. The corresponding orientation of the magnetization with respect to the [100] direction together with the expected projection of the magnetization along this axis is shown in Fig. 8.43(d) upon applying the electric field sequence 0 kV/m ① \rightarrow 100 kV/m ② \rightarrow -100 kV/m ④ \rightarrow $+100 \text{ kV/m}$ ⑥ \rightarrow 0 kV/m ⑦. Thus, electrical addressable non-volatile spintronic devices exhibiting low power consumption might be feasible on the basis of multiferroic composite hybrid structures. Therefore, ferromagnetic/ferroelectric hybrid structures are indeed interesting material composites in the field of spintronic memories.

In contrast to the converse magnetoelectric effects of FM/ BaTiO_3 measured in the tetragonal phase of BaTiO_3 , the magnetic response of FM/ BaTiO_3 hybrid structures observed in the orthorhombic phase of BaTiO_3 , was found to be completely different than expected from theory. SQUID magnetometry measurements revealed an asymmetric behavior of the magnetization projection along the external magnetic field as a function of the applied electric field with respect to $E = 0$. X-ray diffraction measurements carried out in the orthorhombic phase of BaTiO_3 suggest a ferroelastic multi-domain state in the BaTiO_3 substrate at negative electric fields and magnetoelastic simulations reveal that the asymmetric electric field dependence might be

⁶Strained (011) oriented Fe_3O_4 thin films might exhibit an additional uniaxial anisotropy (see Ref. [690]).

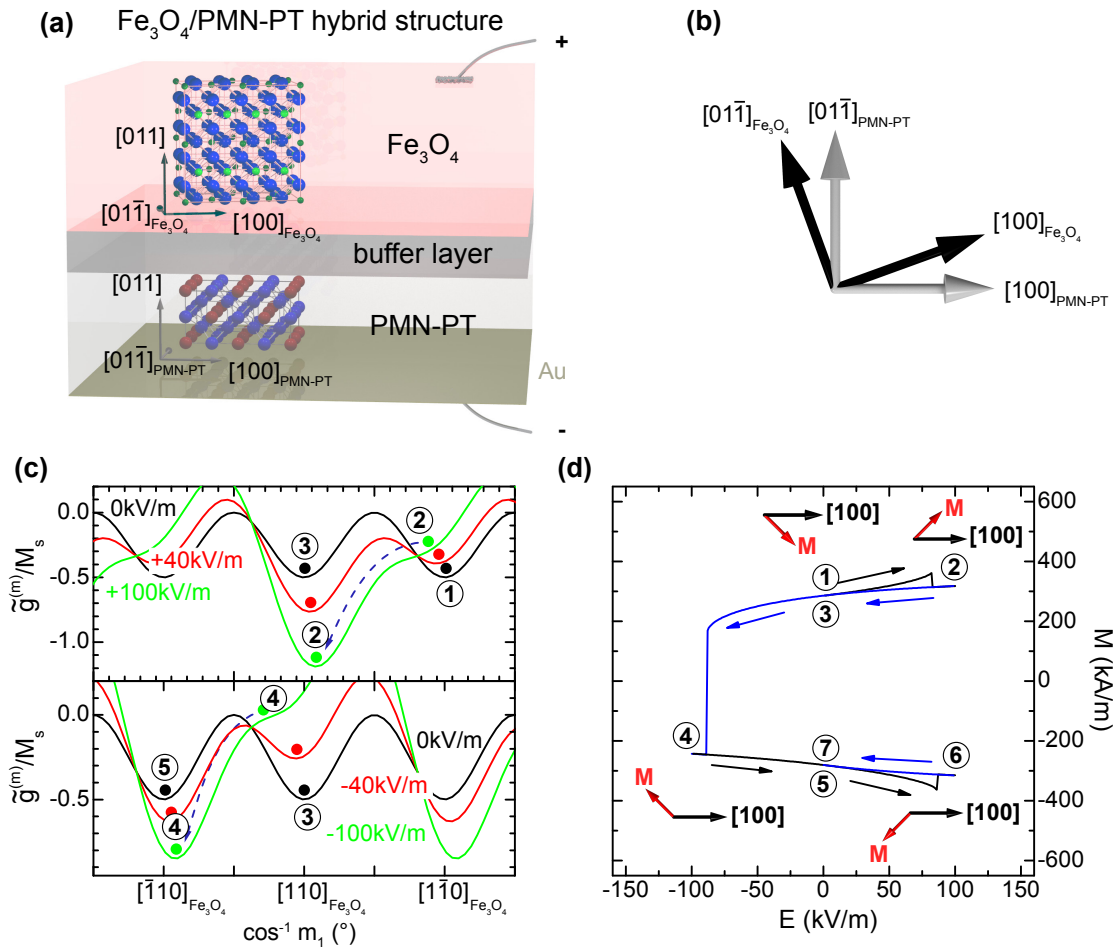


Figure 8.43: (a) Schematic representation of a multiferroic Fe₃O₄/PMN-PT hybrid structure using a (011) oriented [Pb(Mg_{1/3}Nb_{2/3})O₃]_{1-x}[PbTiO₃]_x (PMN-PT) substrate. (b) The buffer layer maintains different epitaxial relation of the Fe₃O₄ thin film with respect to the PMN-PT substrate ($[100]_{\text{Fe}_3\text{O}_4} \parallel [100]_{\text{PMN-PT}}$, $[01\bar{1}]_{\text{Fe}_3\text{O}_4} \parallel [01\bar{1}]_{\text{PMN-PT}}$). (c) To illustrate a nonvolatile sequential reorientation of the remanent magnetization by 90°, Gibbs free energy density contours $\tilde{g}^{(m)}/M_s$ (cf. Section 6.2) as a function of the magnetization orientation m_2 are calculated assuming a difference of the [100] directions of the Fe₃O₄ thin film and the PMN-PT substrate of 10° as well as a small cubic anisotropy with a cubic anisotropy field of $K_c/M_s = -2$ mT. Furthermore, the converse piezoelectric response of the (011) oriented PMN-PT substrate obtained by Wu and coworkers [688] was used to derive $\tilde{g}^{(m)}/M_s$ traces for different strain states, i.e., different electric fields applied along the [011] direction of the PMN-PT substrate. The upper (lower) panel shows the evolution of the magnetization orientation with positive (negative) electric fields applied across the Fe₃O₄/PMN-PT hybrid. The magnetization aligns along the local minima of the $\tilde{g}^{(m)}/M_s$ traces which are marked by vertical arrows. The reorientation of the magnetization indicated by dashed arrows was modeled as a coherent rotation process. The evolution of the magnetization projection $M = M_s m_1$ upon applying the electric field sequence 0 kV/m \rightarrow 100 kV/m \rightarrow -100 kV/m \rightarrow +100 kV/m \rightarrow 0 kV/m is shown in (d).

caused by different strain states imposed in the overlying ferromagnetic thin film. However, as long as a detailed picture of the converse piezoelectric response of mis-

cut BaTiO₃ substrates is not resolved, the presented calculations should be regarded as preliminary.

In total, in contrast to the critical position of Vaz *et al.* [424], who stated that details of the strain modulation of multiferroic hybrid structures can be more complex than a simple elastic coupling, converse magnetoelectric effects in FM/BaTiO₃ hybrids measured at room temperature can be well simulated by means of magnetoelastic theory on the basis of the ferroelastic domain configuration in the BaTiO₃ substrate. Furthermore, a concept for further experiments is introduced aiming at the realization of electrical controllable non-volatile reorientations of the remanent magnetization of a ferromagnetic/ferroelectric hybrid system.

Chapter 9

Thin film heterostructures based on FM/BaTiO₃ multiferroic composites

As discussed in the previous chapter, FM/BaTiO₃ hybrid structures are promising candidates for next-generation multifunctional devices, since reversible and irreversible magnetization control via electric fields can be realized at room temperature. However, to implement these structures in micro-devices, magnetoelectric thin film heterostructures based on FM/BaTiO₃ layers have to be demonstrated. In case of strain-mediated magnetoelectric thin film heterostructures three different kinds of composite thin films can be distinguished according to the microstructure of the thin films: 0-3, 1-3, and 2-2 type structures (cf. Section 6.1) [425, 443]. A substantial magnetoelectric coupling was demonstrated in 0-3 and 1-3 type structures, which are based on magnetic nanoparticles or magnetic pillars embedded in ferroelectric thin films, due to efficient strain coupling as well as a reduced clamping effect by the substrate [425, 446, 691, 692]. However, the design and control of such structures remains an experimental challenge [693]. Furthermore, high leakage currents caused by the low resistance of the magnetic pillars hamper the direct determination of the magnetoelectric coefficients. These issues are avoided in 2-2 type horizontal heterostructures (cf. Fig. 6.2(b2)), which are easier to fabricate than vertical structures. On the other hand, due to large in-plane elastic constraint caused by the rigid substrate, horizontal heterostructures are expected to exhibit weaker strain-mediated magnetoelectric effects [694]. Anyhow, the observation of the direct magnetoelectric effect in 2-2 type horizontal NiFe₂O₄/BaTiO₃ heterostructures [695] confirms the possible use of these systems in multifunctional microelectronic devices. Interestingly, although the 2-2 type horizontal heterostructures are the most widely investigated magnetoelectric composites made by using numerous ferroelectrics (e.g. BaTiO₃, Pb(Zr_xTi_{1-x})O₃, BiFeO₃) and magnetic materials (Fe₃O₄, NiFe₂O₄, CoFe₂O₄, La_{0.7}Sr_{0.3}MnO₃) [695–702], the number of studies on the converse linear magnetoelectric coefficient are small [21, 693]. In the following, we therefore focus on the electric field control of magnetization, i.e., the converse magnetoelectric effect in 2-2 type horizontal FM/BaTiO₃ heterostructures (cf. Fig. 6.2(b2)). We start by discussing the physical properties of BaTiO₃ thin films theoretically and experimentally.

9.1 BaTiO₃ thin films

Since the magnitude of the converse linear magnetoelectric effect in BaTiO₃-based multiferroic 2-2 type horizontal heterostructures mainly depends on the quality and physical properties of the BaTiO₃ layer, the understanding of the theoretical and experimental behavior of BaTiO₃ thin films is essential for the realization of FM/BaTiO₃ heterostructures. Therefore, the ferroelectric and ferroelastic properties of BaTiO₃ thin films are first discussed in the context of molecular dynamics simulations. In particular, the difference between BaTiO₃ thin films clamped to a rigid substrate and free-standing bulk-like BaTiO₃ layers is outlined. Afterwards, the physical properties of BaTiO₃ thin films deposited on Nb:SrTiO₃ are discussed in detail.

9.1.1 BaTiO₃ thin films investigated by molecular dynamics simulations

The physical behavior of ferroelectric and/or ferroelastic thin films can largely differ from their bulk behavior. In particular, it is well known that ferroelectric thin films are highly sensitive to strain effects (cf. Part I of this thesis). In recent years, this subject has received increasing attention, since a large enhancement of the transition temperature as well as the ferroelectric polarization as a function of strain was observed in ferroelectric thin films [245, 251, 458, 703]. This opens the door to tailor the desired physical properties in such thin films.

Strain can be imposed in thin films by pseudomorphic growth onto suitable substrates. Other sources of finite strain state are, e.g., the presence of crystalline defects or different thermal expansion coefficients of the substrate and the thin film. The latter results in a temperature dependent strain state of the thin film. However, even at vanishing strain, ferroelectric and/or ferroelastic thin films behave differently as compared to free-standing thin films due to the two dimensional clamping effect caused by the rigid substrates.¹ To study this effect in more detail, molecular dynamics simulations were performed under short circuit conditions. Again, the open source code FERAM was utilized for the simulation [513]. Figure 9.1(a) illustrates the model used to simulate a ferroelectric thin film with thickness d_{FE} sandwiched between two electrodes [704, 705]. Within this model, the electrodes were treated as perfect electrostatic mirrors. The electrostatic image of an electric dipole in the ferroelectric film is, of course, a dipole with the same magnitude inside the electrode but with different directions. While the z -direction is the same, the x - and y -directions are opposite to the real dipole (cf. Fig. 9.1(a)). This leads to a “head-to-tail” arrangement of the electric dipoles across the electrodes. Due to the electrostatic image, the length of the periodic structure d_{MD} becomes twice as large as the supercell (cf. Fig. 9.1(a)). Therefore, a doubly periodic boundary condition was used for the simulation. This is in contrast to single periodic boundary condition ($d_{\text{MD}} = d_{\text{FE}}$) used for the simulation of bulk BaTiO₃ (cf. Section 7.1).

¹Throughout this chapter, the substrate is considered as thick and rigid. Therefore, we neglect any influence of the overlying BaTiO₃ thin film on the substrate.

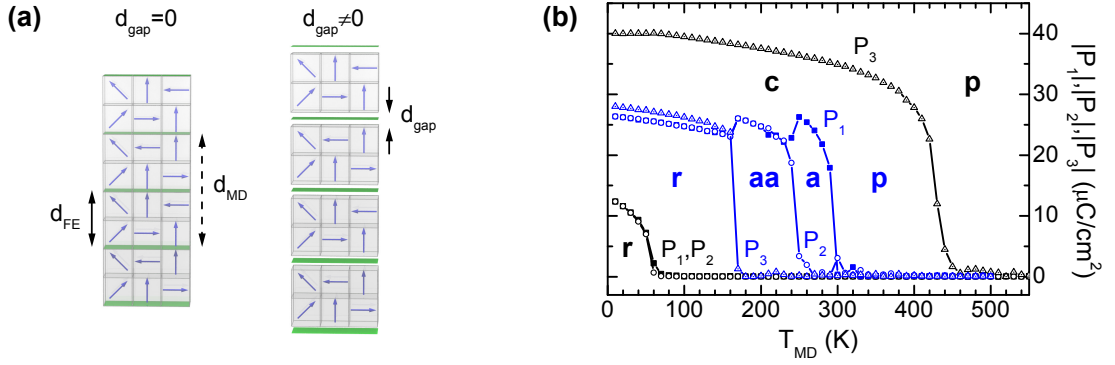


Figure 9.1: Molecular dynamics simulations of BaTiO₃ thin films under short-circuit conditions. (a) Schematic illustration of the model used to simulate a ferroelectric thin film with thickness of $d_{\text{FE}} = 2$ unit cells sandwiched between perfect ($d_{\text{gap}} = 0$) and imperfect electrodes ($d_{\text{gap}} \neq 0$). The electrodes (green planes) are treated as perfect electrostatic mirrors, which increases the periodic boundary condition to $d_{\text{MD}} = 2(d_{\text{FE}} + d_{\text{gap}})$ compared to $d_{\text{MD}} = d_{\text{FE}}$ in case of the simulation of bulk BaTiO₃. (b) Temperature dependence of the ferroelectric polarization $\mathbf{P} = (P_1, P_2, P_3)$ for BaTiO₃ thin films without any elastic constraints (blue) and for epitaxial BaTiO₃ thin films with $\epsilon_{ij} = 0$ for $ij = 11, 22, 12$ derived from molecular dynamics simulations assuming perfect electrodes ($d_{\text{gap}} = 0$) (black). At each temperature the system was thermalized with 40000 time steps and an averaging of 40000 calculations was performed afterwards. The different phases are labeled according to Pertsev *et al.* [458]: paraelectric p-phase ($P_1 = P_2 = P_3 = 0$), tetragonal *a*-phase ($P_1 \neq 0, P_2 = P_3 = 0$), tetragonal *c*-phase ($P_1 = P_2 = 0, P_3 \neq 0$) orthorhombic *aa*-phase ($P_1 = P_2 \neq 0, P_3 = 0$), and monoclinic *r*-phase ($P_1 = P_2 \neq 0, P_3 \neq 0$).

To account for imperfect electrodes, a gap between the ferroelectric thin film and the electrodes was introduced. The gap d_{gap} is an indication how effective the electrodes compensate the depolarization field, which can be determined in a simple electrostatic model by²

$$E_{\text{d}} = -\frac{1}{\epsilon_0} \frac{d_{\text{gap}}}{d_{\text{FE}} + d_{\text{gap}}} \mathbf{P} \cdot \hat{\mathbf{n}}. \quad (9.1)$$

$\hat{\mathbf{n}}$ denotes an unitary vector normal to the surface pointing outwards. Therefore, the periodic boundary condition yields $d_{\text{MD}} = 2(d_{\text{FE}} + d_{\text{gap}})$ and simulations under the assumption of perfect electrodes ($d_{\text{gap}} = 0$) as well as “bad” electrodes ($d_{\text{gap}} = 1$)³ can be carried out. Note that the existence of a “dead” or “passive” dielectric layer between the ferroelectric thin film and the electrodes, which causes imprint effects, can also be treated within the simple model shown in Fig. 9.1(a), since Ghosez and coworkers showed that this situation is formally equivalent to the incomplete screening model [706].

First, we discuss the ferroelectric properties of BaTiO₃ thin films in between perfect electrodes. The following simulations are performed using a supercell of the

²An overview of more detailed models for the calculation of electric depolarization fields on imperfect electrodes can be found in Ref. [706].

³ $d_{\text{gap}}, d_{\text{MD}}$ and d_{FE} are in units of number of the unit cells.

size of $16 \times 16 \times 16$, since no thickness dependence of the ferroelectric properties are expected for $d_{\text{FE}} = 16$ [705]. Furthermore, at each temperature the system was thermalized with 40000 time steps and an averaging of 40000 calculations was performed afterwards. Figure 9.1(b) shows the results of temperature dependent molecular dynamics simulations of the electric polarization $\mathbf{P} = (P_1, P_2, P_3)$ of a BaTiO_3 thin film under vanishing epitaxial in-plane strain with two different elastic boundary conditions. In one case, the BaTiO_3 thin film is allowed to expand and contract freely (cf. blue symbols in Fig. 9.1(b)), while a perfect clamping of the thin film is assumed in the second case (cf. black symbols in Fig. 9.1(b)), i.e., the in-plane strain components are fixed in the whole temperature range to $\epsilon_{ij} = 0$ ($ij = 11, 22, 12$). In the former case, a bulk-like phase diagram was obtained (cf. Fig. 7.1) with transition temperatures which are again underestimated with respect to the experimental obtained values (cf. Section 7.1). By comparing these results with simulations of bulk BaTiO_3 (cf. Fig. 7.1), a small reduction of the ferroelectric transition temperatures is observable.

By symmetry, six possible phases are allowed in BaTiO_3 thin films. Using the notation introduced by Pertsev et al. [458], the phases can be labeled as the paraelectric high temperature p -phase ($P_1 = P_2 = P_3 = 0$), the tetragonal a - ($P_1 \neq 0, P_2 = P_3 = 0$) and c -phase ($P_1 = P_2 = 0, P_3 \neq 0$), the orthorhombic aa -phase ($P_1 = P_2 \neq 0, P_3 = 0$), the monoclinic r -phase ($P_1 = P_2 \neq 0, P_3 \neq 0$), and the ac -phase ($P_1 \neq 0, P_2 = 0, P_3 \neq 0$), where the polarization lies on one of the faces. In case of vanishing epitaxial constraints, four phases are observable. In the presence of in-plane elastic constraints, the simulations yield totally different results. First, the ferroelectric transition temperature is strongly enhanced and second, only three different phases are visible in the whole temperature range. Figure 9.1(b) reveals that in case of epitaxial thin films deposited on a rigid substrate the two dimensional clamping effect results in a different sequence of phase transitions $p \rightarrow c \rightarrow r$, whereas no orthorhombic aa -phases or orthorhombic-like ac -phases are visible. Furthermore, the phase transitions seem to be of second order.

Repeating the simulation shown in Fig. 9.1(b) for different in-plane strain states, the dependence of the ferroelectric polarization as a function of the misfit strains and temperature, so called ‘‘Pertsev diagrams’’, can be obtained. Assuming a pseudomorphic growth of the ferroelectric thin film on a suitable substrate without any dislocation and a perfect clamping between thin film and substrate, the in-plane strain state of the ferroelectric thin film is equal to the misfit strain. In Fig. 9.2(a) the phase diagram obtained by assuming perfect electrodes ($d_{\text{gap}} = 0$) is shown. The diagram is in agreement with the temperature-epitaxial strain phase diagram reported by Paul *et al.* for ultrathin BaTiO_3 thin films [705]. Figure 9.2(a) reveals that only three different ferroelectric phases are visible. No ac -phases are observed at any strain state in the whole temperature range. This is in contrast to ‘‘Pertsev diagrams’’ obtained by utilizing a Landau-Ginzburg-Devonshire phenomenological theory [458, 707]. However, these phase diagrams have to be taken with care, since a small change in the set of parameters can lead to different results [707]. One striking feature of the phase diagram depicted in Fig. 9.2(a) is the asymmetric strain dependence of the paraelectric-ferroelectric transition temperatures with respect to

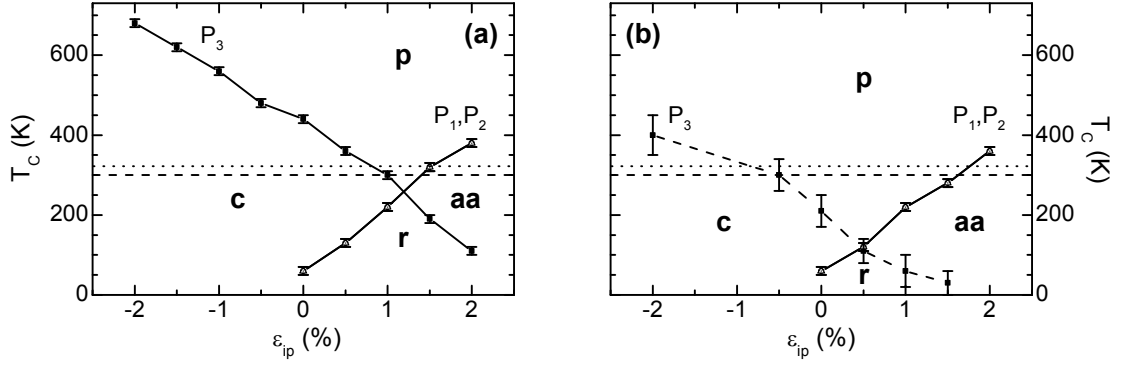


Figure 9.2: Temperature-strain phase diagrams (“Pertsev diagrams”) derived from molecular dynamics simulations assuming (a) perfect ($d_{\text{gap}} = 0$) and (b) imperfect electrodes ($d_{\text{gap}} = 1$). The phase transition temperatures of the polarization $\mathbf{P} = (P_1, P_2, P_3)$ are marked by open and full symbols. The horizontal dashed and dotted lines mark the transition temperatures of a BaTiO₃ thin film simulated without any elastic constraints (cf. Fig. 9.1(b)) and of bulk BaTiO₃ simulations (cf. Fig. 7.2), respectively. The simulations were performed under the same conditions as used for the simulation of $\mathbf{P}(T)$ (Fig. 9.1(b)). In the case of imperfect electrodes, the out-of-plane component P_3 is two orders of magnitude smaller than in simulations with $d_{\text{gap}} = 0$ and the transition temperatures derived from P_3 should be taken with care.

$\epsilon_{\text{ip}} = 0$. This is the main difference to the “Pertsev diagram” calculated by Diéguez and coworkers using a similar first-principles based model Hamiltonian approach as described in Section 7.1 [707]. The asymmetric behavior can be attributed to surface/interface induced enhancement of the normal component of the polarization [706] and therefore to the electrode model shown in Fig. 9.1(a) [705]. Thus, a compressive strain of around $\epsilon_{\text{ip}} = -1.2\%$ has to be applied to compensate the increase in T_c . A similar asymmetric phase diagram with respect to epitaxial strain was observed in $(\text{PbTiO}_3)_1/(\text{PbZrO}_3)_1$ superlattices [708]. Since the transition temperature of BaTiO₃ thin films without any elastic restrictions determined by molecular dynamics simulations is around 300 K (cf. Fig. 9.1(b)), Figure 9.2(a) reveals that epitaxial strain increases the transition temperature of BaTiO₃ thin films except around $\epsilon_{\text{ip}} = -1.2\%$. This emphasizes the strong coupling between strain and polarization in perovskite oxides [260].

When BaTiO₃ thin films are sandwiched between imperfect electrodes ($d_{\text{gap}} = 1$), the phase diagram is different compared to simulations assuming perfect electrodes (Fig. 9.2(b)). Using imperfect electrodes, the depolarization field (Eq. 9.1) does not vanish and suppresses the z -component of the polarization P_3 [705]. No clear phase transitions of P_3 were observed in the simulations. Furthermore, since P_3 is two orders of magnitude smaller than in simulations with $d_{\text{gap}} = 0$, the depicted transition temperatures for P_3 in Fig. 9.2(b) should be taken with care. However, looking closer to the domain configuration during the simulations, stripe-like domains with polarization along the z -direction which form arbitrary patterns in the (001) planes are observed [705]. Therefore, the out-of-plane polarization decomposes into stripe-like domains due to the strong depolarization field. Thus, while the out-of-plane com-

ponent of the polarization is highly affected by imperfect electrodes, the in-plane components reveal only a minor dependence on d_{gap} . By comparing Figs. 9.2(a) and (b), a small reduction of the transition temperatures of P_1 and P_2 are visible in case of imperfect electrodes.

In total, the interplay and competition between the epitaxial strain imposed by the substrate, which tends to enhance the ferroelectricity, the depolarization field that tends to suppress the latter, and the interface and surface effects result in a wealth of different phases [706].

9.1.2 BaTiO₃ thin films fabricated by pulsed-laser deposition

On the experimental side, substantial effort was devoted to fabricate high-quality BaTiO₃ thin films using various techniques, such as pulsed laser deposition [251, 709], molecular beam epitaxy [251, 710], chemical vapor deposition [711, 712], magnetron sputtering [713, 714] and spin coating [715], since BaTiO₃ is attractive for many applications such as multilayer piezoelectric actuators, transducers, electro-optical devices, thin film capacitors, electro-optical devices, and composite magnetoelectric multiferroics [425, 716]. In case of strain-mediated magnetoelectric 2-2 type heterostructures, BaTiO₃ thin films with large piezoelectric response and low surface roughness providing a good interfacial coupling between the ferromagnetic thin film and the BaTiO₃ layer are essential. Therefore, while an imperfect elastic coupling of the BaTiO₃ thin film to the substrate is desirable, the elastic bonding of the overlying ferromagnetic thin film on the BaTiO₃ layer should be perfect. The former can be realized by depositing BaTiO₃ thin films on substrates exhibiting a large lattice mismatch forcing the BaTiO₃ layer to relax in the first monolayers. Nonetheless, the BaTiO₃ thin films should exhibit good crystalline and surface qualities to realize a perfect interface between the ferromagnetic layer and the BaTiO₃ thin film.

The crystallinity and the surface morphology can be improved by using low oxygen partial pressure during the deposition of BaTiO₃ [717]. However, low oxygen pressure results in high densities of oxygen vacancies, which degrade the ferroelectric/ferroelastic properties of BaTiO₃. In addition, the ferroelectric properties are highly sensitive to the crystal structure and stresses between thin film and substrate [245, 251, 718]. Due to the formation of dislocations, these stresses can be reduced significantly. In BaTiO₃ thin films fabricated on SrTiO₃ (001) substrates, fully relaxed thin films can be obtained for thicknesses larger than 200 nm [719]. Additionally, the structural properties can be modified by oxygen vacancies. Thin films deposited under low oxygen pressures ($p_{\text{O}_2} < 5 \times 10^{-2}$ mbar) exhibit a tetragonal symmetry with $c/a > 1$, while $c/a < 1$ is observed in thin films fabricated under higher oxygen pressures ($p_{\text{O}_2} > 5 \times 10^{-2}$ mbar) [718, 720]. Therefore, c -axis and a -axis oriented BaTiO₃ thin films can be fabricated by simply varying the oxygen pressure during the fabrication process. In the context of device applications, c -axis BaTiO₃ films are desirable for ferroelectric memory applications, while a -axis oriented BaTiO₃ thin films are interesting for electric-optical applications [721]. For strain-mediated magnetoelectric 2-2 type heterostructures with an electric field applied along the out-of-plane direction, a -axis oriented BaTiO₃ thin films might be

the better choice, since an enhanced converse piezoelectric response is expected in these thin films compared to *c*-axis oriented BaTiO₃ thin films [717].

These results demonstrate the importance of controlling the oxygen pressure during the growth process. In the course of this thesis, BaTiO₃ thin films were fabricated using an oxygen pressure in the range of 7.5×10^{-3} mbar to 1.5×10^{-1} mbar. In this range, the ratio between Ti and Ba should be nearly constant, while the Ba/O ratio should vary, creating oxygen vacancies below $p_{\text{O}_2} < 1 \times 10^{-1}$ mbar [722]. In the following, we focus on BaTiO₃ thin films fabricated using two different sets of deposition parameters. While the laser fluence on the target and the repetition rate were fixed at 1.0 J/cm^2 and 2 Hz, respectively, the oxygen pressure during the deposition was set to $p_{\text{O}_2} = 7.5 \times 10^{-3}$ mbar and $p_{\text{O}_2} = 1.0 \times 10^{-1}$ mbar, i.e., in the oxygen deficient and the nominally stoichiometric regime. To get highly crystalline BaTiO₃ thin films with low surface roughness the temperature of the substrate during the deposition was optimized to $T_s = 793 \text{ K}$ in case of $p_{\text{O}_2} = 7.5 \times 10^{-3}$ mbar and $T_s = 898 \text{ K}$ for $p_{\text{O}_2} = 1.0 \times 10^{-1}$ mbar.

As discussed in Part I, SrRuO₃ seems to be the ideal candidate for an electrode material on the basis of perovskite structures. However, due to the ferromagnetic ground state of SrRuO₃ below around 150 K (cf. Section 4.3), any magnetization measurement, which is based on an integral method, is affected by the signal stemming from SrRuO₃ for $T \lesssim 150 \text{ K}$. Alternatively, Nb doped SrTiO₃ substrates can be used as electrode material, since Nb:SrTiO₃ can be considered as a *n*-doped degenerated semiconductor with an electron density of $n = 2 \times 10^{18} \text{ cm}^{-3}$ [261] and therefore satisfies the requirements of an electrode material in short circuit ferroelectric heterostructures. Furthermore, Nb:SrTiO₃ substrates are diamagnetic and are therefore suitable for magnetoelectric composite heterostructures. Moreover, the lattice mismatch between BaTiO₃ and Nb:SrTiO₃ at the growth temperatures is around 3%. Thus, critical thickness of pseudomorphic growth is small, and the epitaxial strain of BaTiO₃ thin films should completely relax in the first monolayers. As mentioned above, the large lattice mismatch is favorable for elastic decoupling of the BaTiO₃ thin film and the Nb:SrTiO₃ substrate, which might result in large piezoelectric responses.

Structural properties of BaTiO₃ thin films

The structural properties of BaTiO₃ thin films fabricated either using an oxygen pressure of $p_{\text{O}_2} = 7.5 \times 10^{-3}$ mbar or $p_{\text{O}_2} = 1.0 \times 10^{-1}$ mbar were investigated using x-ray diffraction (XRD) and high resolution transmission electron microscopy (TEM). Furthermore, the surface morphology was examined by atomic force microscopy (AFM).

The results of XRD measurements carried out at room temperature on 440 nm and 310 nm thick BaTiO₃ films deposited under oxygen deficient and nominal stoichiometric conditions are depicted in Fig. 9.3. XRD scans around BaTiO₃ (002) reveal an enhanced out-of-plane lattice parameter of $c = (0.4004 \pm 0.0005) \text{ nm}$ compared to $c = (0.3998 \pm 0.0005) \text{ nm}$ of a BaTiO₃ thin film grown under nominally stoichiometric conditions (Figs. 9.3(a) and (b)). This might be explained by either different strain

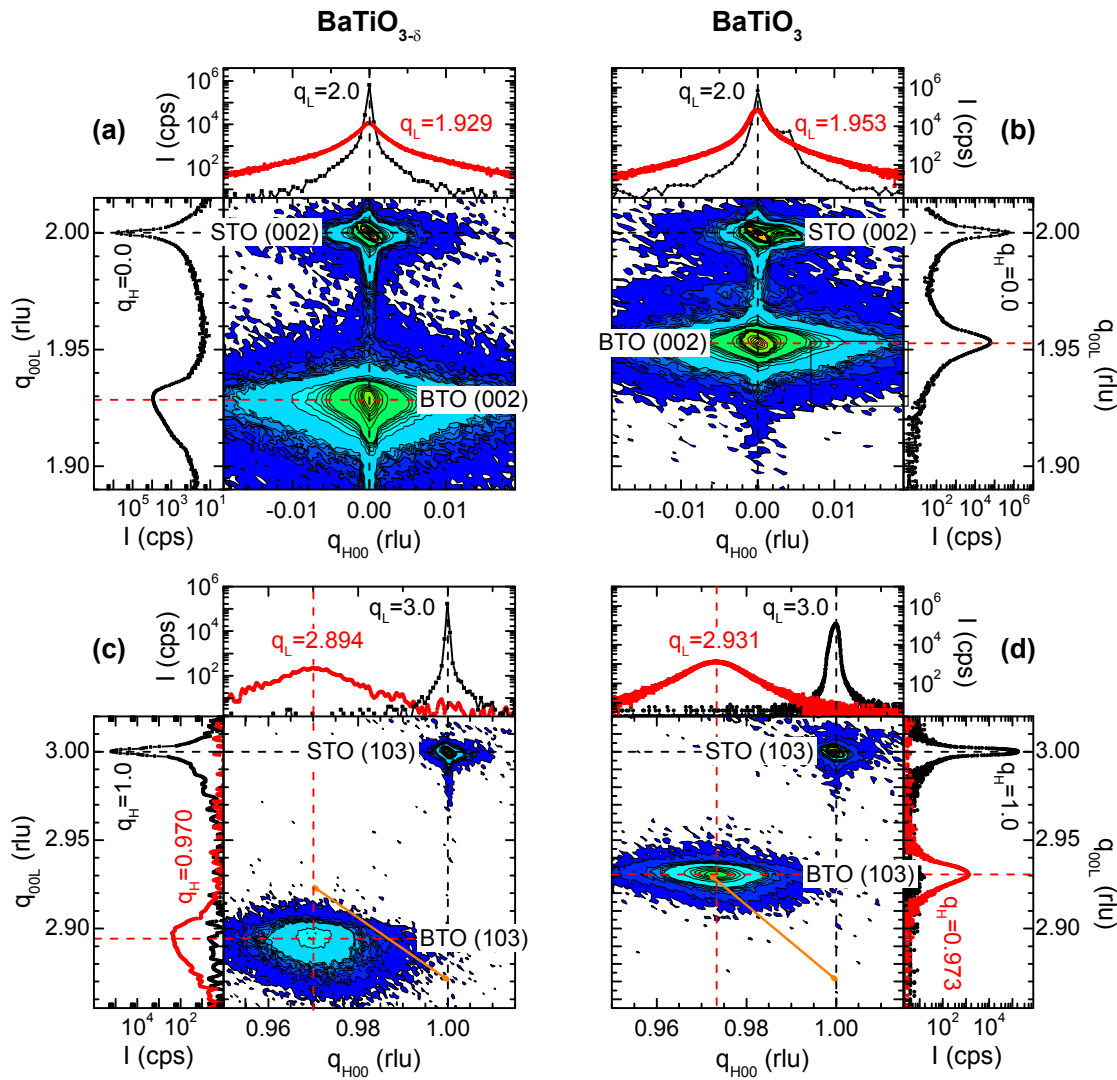


Figure 9.3: X-ray diffraction measurements around (a), (b) BaTiO_3 (002) and (c), (d) BaTiO_3 (103) of two BaTiO_3 thin films deposited on Nb:SrTiO_3 substrates using an oxygen pressure of (a), (c) $p_{\text{O}_2} = 7.5 \times 10^{-3}$ mbar ($\text{BaTiO}_{3-\delta}$) and (b), (d) $p_{\text{O}_2} = 1.0 \times 10^{-1}$ mbar (BaTiO_3). The former thin film exhibits a thickness of 440 nm and the latter of 310 nm. The orange thick lines in (c) and (d) represent the relaxation of misfit strain from coherent thin films at $q_{\text{H}00} = 1$ rlu to fully relaxed BaTiO_3 thin films at $q_{\text{H}00} \approx 0.971$ rlu.

states of both thin films or by oxygen vacancies. The former can be investigated by performing XRD measurements around the asymmetric BaTiO_3 (103) reflection, which is displayed in Figs. 9.3(c) and (d). Both thin films exhibit the same in-plane but different out-of-plane lattice constants, which can mainly be explained by the presence of oxygen vacancies in case of BaTiO_3 thin films fabricated under oxygen deficient conditions. Oxygen vacancies normally lead to an expansion of the unit cell. However, as the thin films are elastically clamped to the substrate in the in-plane a - b -plane, the expansion is only visible in an enhancement of the out-of-

plane lattice constant. The presence of oxygen vacancies is further evident from the calculation of the lattice volumes. From Figs. 9.3(c) and (d) lattice volumes of $V^{1/3} = 0.4019$ nm and $V^{1/3} = 0.4006$ nm. The latter is equal to the bulk value, are derived. Therefore, indeed, BaTiO₃ thin films fabricated at $p_{\text{O}_2} = 7.5 \times 10^{-3}$ mbar exhibit a finite density of oxygen vacancies, which leads to an enlargement of the lattice volume. In contrast, almost stoichiometric BaTiO₃ thin films with an unit cell volume equal to the bulk value can be obtained using an oxygen pressure of $p_{\text{O}_2} = 1.0 \times 10^{-1}$ mbar.⁴ Furthermore, in agreement with Zhao and coworkers [718], BaTiO_{3- δ} thin films grown under oxygen-deficient conditions are *c*-axis oriented, while thin films under stoichiometric conditions are *a*-axis oriented.

Due to the large lattice mismatch between BaTiO₃ and the Nb:SrTiO₃ substrate, fully relaxed BaTiO₃ thin films are expected for thickness larger than 200 nm. By using the bulk lattice constants of BaTiO₃ measured by Shebanov [496] and a Poisson ratio of $\nu^{\text{BTO}} = 0.29$ [643], the relaxation line of BaTiO₃ thin films deposited on Nb:SrTiO₃ substrates can be calculated (orange lines in Figs. 9.3(c) and (d)). For this calculation, it is assumed that misfit dislocations, which reduce the in-plane lattice strain, are created only at the growth temperature due to a suppression of dislocation glides at lower temperatures [723]. Figures 9.3(c) and (d) reveal that the BaTiO₃ (103) reflection of the stoichiometric BaTiO₃ thin film appears close to the position of thin films which exhibit no misfit strain, while the position of the BaTiO₃ (103) reflection obtained from XRD measurements on oxygen deficient BaTiO_{3- δ} thin films is shifted to lower q_{L00} -values. This further proves finite non-stoichiometric effects in these thin films. However, Figures 9.3(c) and (d) disclose that BaTiO₃ thin films exhibit an intrinsic strain of 0.50% and 0.35% for oxygen pressures of $p_{\text{O}_2} = 7.5 \times 10^{-3}$ mbar and $p_{\text{O}_2} = 1.0 \times 10^{-1}$ mbar used during the deposition. The finite strain state can mainly be attributed to different thermal expansion coefficients of BaTiO₃ and SrTiO₃ [718, 720], resulting in strained BaTiO₃ thin films during cooling down from the deposition temperatures.

A striking feature of x-ray diffraction measurements on oxygen deficient BaTiO_{3- δ} samples is the asymmetric shape of the diffraction lines of the BaTiO₃ reflections in the out-of-plane direction (see Figs. 9.3(a) and (c)). This can be attributed to a gradual relaxation of misfit strain, which creates strain field gradients in these samples. In contrast, Figures 9.3(b) and (d) reveal symmetrical diffraction lines around BaTiO₃ (002) and BaTiO₃ (103) of BaTiO₃ thin films fabricated under stoichiometric conditions. In a more quantitative way, the inhomogeneous strain can be estimated by using the Williamson-Hall relation (cf. Section 4.4.1). This formalism yields an inhomogeneous strain of 0.23% and 0.06% for the oxygen deficient BaTiO_{3- δ} thin film and the stoichiometric sample displayed in Fig. 9.3, respectively. Therefore, the strain relaxation takes place over a significant number of BaTiO₃ unit cells in BaTiO_{3- δ} thin films creating intrinsic strains in the out-of-plane direction, while in BaTiO₃ thin films deposited under stoichiometric conditions the misfit strain is released in the first monolayers. This suggests the presence of a high den-

⁴The terms oxygen deficient and stoichiometric BaTiO₃ thin films are used to distinguish between both types of BaTiO₃ thin films although the BaTiO₃ thin film fabricated under an oxygen pressure of $p_{\text{O}_2} = 1.0 \times 10^{-1}$ mbar is certainly not fully stoichiometric.

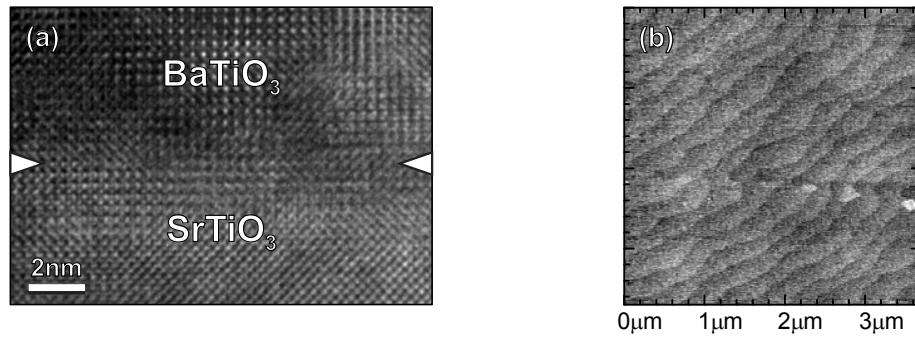


Figure 9.4: (a) High-resolution TEM micrograph of a 130 nm thick $\text{BaTiO}_{3-\delta}$ thin film grown on a Nb:SrTiO_3 substrate at $p_{\text{O}_2} = 7.5 \times 10^{-3}$ mbar. The interface is marked by white triangles. (b) Atomic force microscope image of the same thin film. The measurements were performed by (a) Sven-Martin Hühne (Universität Bonn) and (b) Denny Köhler (Technische Universität Dresden).

sity of misfit dislocations at the interface between the Nb:SrTiO_3 substrate and the BaTiO_3 thin film. Furthermore, as stated above, the clamping of the BaTiO_3 thin film might be incomplete in these thin films, which might result in finite converse linear magnetoelectric effects.

However, in both cases, BaTiO_3 thin films with high crystalline quality can be obtained, which is confirmed by low full widths at half maximum of 0.04° - 0.07° of rocking curves around BaTiO_3 (002). These values demonstrate that the crystalline quality is comparable to fully-strained BaTiO_3 thin films grown on better lattice-matched substrates like GdScO_3 and DyScO_3 [251].

The good crystalline quality is further demonstrated by high resolution TEM microscopy shown in Fig. 9.4(a). A well-ordered crystalline structure of the BaTiO_3 thin film is visible. Furthermore, a step-terrace structure is observed by probing the surface morphology using atomic force microscopy. While a surface roughness of $0.59 \text{ nm}_{\text{RMS}}$ was observed in a 130 nm thick oxygen deficient $\text{BaTiO}_{3-\delta}$ thin film, a moderate increase of the surface roughness to $1.3 \text{ nm}_{\text{RMS}}$ was detected using a 310 nm thick BaTiO_3 thin film fabricated under stoichiometric conditions. These results suggest an improved morphology by using low oxygen partial pressure during the fabrication process. Therefore, while the misfit strain is relaxed in the first monolayers in BaTiO_3 thin films fabricated under stoichiometric conditions, the surface roughness is reduced in oxygen deficient $\text{BaTiO}_{3-\delta}$ thin films, which might result in an improved elastic coupling between the $\text{BaTiO}_{3-\delta}$ layer and the overlying magnetostrictive thin film in strain-mediated magnetoelectric heterostructures.

Besides the excellent structural quality of BaTiO_3 thin films, good ferroelastic and ferroelectric properties are essential for ferroelectric layers in magnetoelectric 2-2 type heterostructures. Since the ferroelectric and ferroelastic order parameters are coupled in BaTiO_3 (cf. Section 7.1), the ferroelectric and ferroelastic behavior of BaTiO_3 thin films can be tested by observing the elastic and electric properties, respectively. To investigate the onset of ferroelectricity, x-ray diffraction measurements as a function of temperature were carried out around Nb:SrTiO_3 (002)

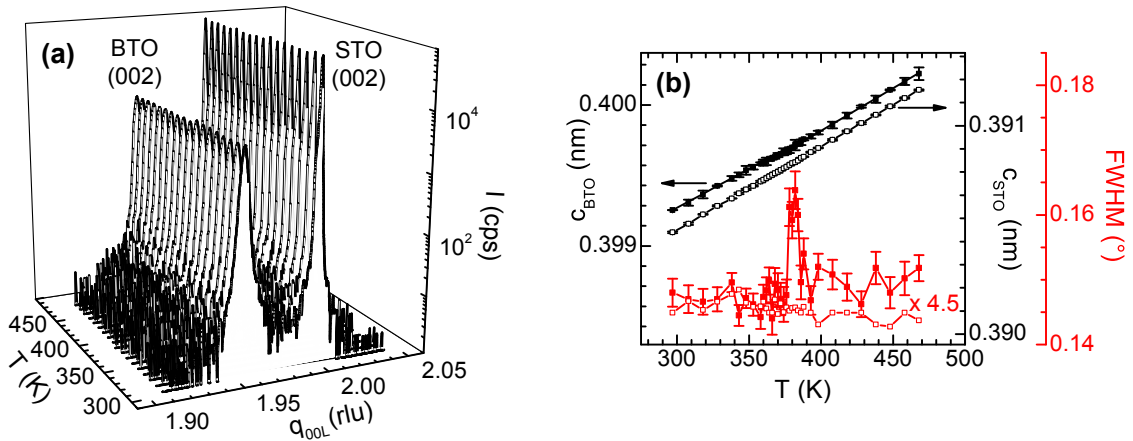


Figure 9.5: (a) X-ray diffraction measurements around Nb:SrTiO₃ (002) as a function of temperature of a 310 nm thick BaTiO₃ thin film fabricated under stoichiometric conditions. (b) The Nelson-Riley method was used to derive the out-of-plane lattice parameter c_{BTO} of BaTiO₃ (full symbols) and c_{STO} of Nb:SrTiO₃ (open symbols). The full width at half maximum (FWHM) of the BaTiO₃ (004) reflection measured along the q_{L00} -direction (red full symbols) broadens at the phase transition compared to the FWHM of the Nb:SrTiO₃ substrate (red open symbols), which is multiplied by 4.5 for better visibility.

(Fig. 9.5(a)). At first glance, no transition is visible in the investigated temperature range. In particular, no peak splitting is observed around 393 K, which is the case in bulk BaTiO₃ (cf. Fig. 8.1). In contrast to bulk BaTiO₃, the symmetry of the high temperature paraelectric phase is lowered from cubic to tetragonal due to the elastic clamping of the BaTiO₃ thin film on the substrate. Therefore, no change of the crystalline symmetry takes place crossing the paraelectric-ferroelectric phase transition in BaTiO₃ thin films.

By using the Nelson-Riley method (cf. Section 2.1.3), the out-of-plane lattice parameter of BaTiO₃ (c_{BTO}) and Nb:SrTiO₃ (c_{STO}) were derived. The resulting evolution of both lattice parameters as a function of temperature is displayed in Fig. 9.5(b). By comparing the temperature dependence of $c_{\text{BTO}}(T)$ and $c_{\text{STO}}(T)$, a small decrease of the thermal expansion α_{BTO} from $\alpha_{\text{BTO}} = 1.5 \times 10^{-5} \text{ K}^{-1}$ to $\alpha_{\text{BTO}} = 1.4 \times 10^{-5} \text{ K}^{-1}$ is observable above and below $T \approx 380 \text{ K}$. The change in slope of the out-of-plane lattice parameter $c_{\text{BTO}}(T)$ at high temperatures can be associated with the ferroelectric transition temperature in BaTiO₃ thin films [251, 724, 725]. In contrast to the discontinuous change of the lattice parameter in bulk crystals (cf. Fig. 8.1), the clamping of the BaTiO₃ thin film on the Nb:SrTiO₃ substrate causes a smooth change of the out-of-plane lattice parameter $c_{\text{BTO}}(T)$, since the in-plane lattice parameter can not expand or contract freely. As the ferroelastic and ferroelectric degrees of freedom are coupled in BaTiO₃, the smooth change of $c_{\text{BTO}}(T)$ indicates a second-order type phase transition in BaTiO₃ thin films. This is also predicted by theory [458] and molecular dynamics simulations (cf. Section 9.1.1).

The phase transition is more obvious in the full width at half maximum (FWHM) of the diffraction peak measured along the q_{00L} -direction [720, 726]. In Fig. 9.5(b),

the FWHM of the BaTiO₃ (004) and the Nb:SrTiO₃ (004) reflections are displayed as a function of temperature. Clearly, a peak broadening of BaTiO₃ (004) is visible at $T = (381 \pm 5)$ K, which can be attributed to the ferroelastic/ferroelectric transition temperature T_c . The broadening of the BaTiO₃ (004) Bragg peak might be explained by strain relaxation due to ferroelastic domain formation. In general, a multi-domain formation is favored if the stored elastic energy of one monodomain can be diminished by embedding a second domain orientation [268]. Therefore, the domain structure is governed by the interplay of elastic relaxation due to a mixed domain pattern and the possible additional formation of misfit dislocations, if electric effects due to imperfect screening of the depolarization field are neglected. However, the peak broadening takes place only at the transition temperature (see Fig. 9.5(b)). Above and below T_c , the FWHM has comparable values. This is contrary to the assumption of a multi-domain state present at temperatures well below T_c . Therefore, a mixed domain pattern is only expected around the transition temperature.

In thin films fabricated under a low oxygen pressure of $p_{O_2} = 7.5 \times 10^{-3}$ mbar almost the same transition temperature $T_c = (380 \pm 8)$ K was observed as a smooth change of the temperature dependence of the out-of-plane lattice parameter $c_{\text{BTO}}(T)$. The similar transition temperature can be explained by the small difference in the epitaxial strain of both types of BaTiO₃ thin films [727]. However, no peak broadening was observed. Following the arguments above, no strain relaxation due to the formation of a ferroelastic multi-domain state might take place in these thin films. This can be explained by a stronger bonding of these thin films to the Nb:SrTiO₃ substrate compared to stoichiometric BaTiO₃ thin films.

The phase transition temperature of BaTiO₃ thin films ($T_c \approx 380$ K) determined by x-ray diffraction is lower compared to the bulk value of $T_{c\text{bulk}} = 393$ K (cf. Section 7.1). The difference can not be explained by oxygen non-stoichiometric effects, since almost the same transition temperature is observed for BaTiO₃ thin films fabricated using different oxygen pressures during the deposition. As discussed in Section 9.1.1, the transition temperature is highly sensitive to the strain state of the BaTiO₃ thin film. Molecular dynamics simulations reveal that the transition temperature of BaTiO₃ exhibiting an in-plane strain of 0.5% is enhanced compared to BaTiO₃ thin films without clamping. However, it is nearly the same as for the simulation of bulk BaTiO₃ (cf. Fig. 9.2(a)). Therefore, the finite strain state in the investigated BaTiO₃ thin films might also be not the explanation for the experimentally observed reduction of T_c in BaTiO₃ thin films. As pointed out in Section 7.1, a variation of the Curie temperature can be attributed to different Ti concentration in BaTiO₃ [493]. Therefore, a Ba:Ti ratio, which differs from one, might explain the reduction of the Curie temperature T_c .

Dielectric properties of BaTiO₃ thin films

As discussed above, changes in the oxygen content of BaTiO₃ thin films should strongly influence the dielectric and ferroelectric properties [722, 728, 729]. Furthermore, molecular dynamics simulations reveal that the ferroelectric state of BaTiO₃ thin films is sensitive to strain and imperfect screening of the surface charges due

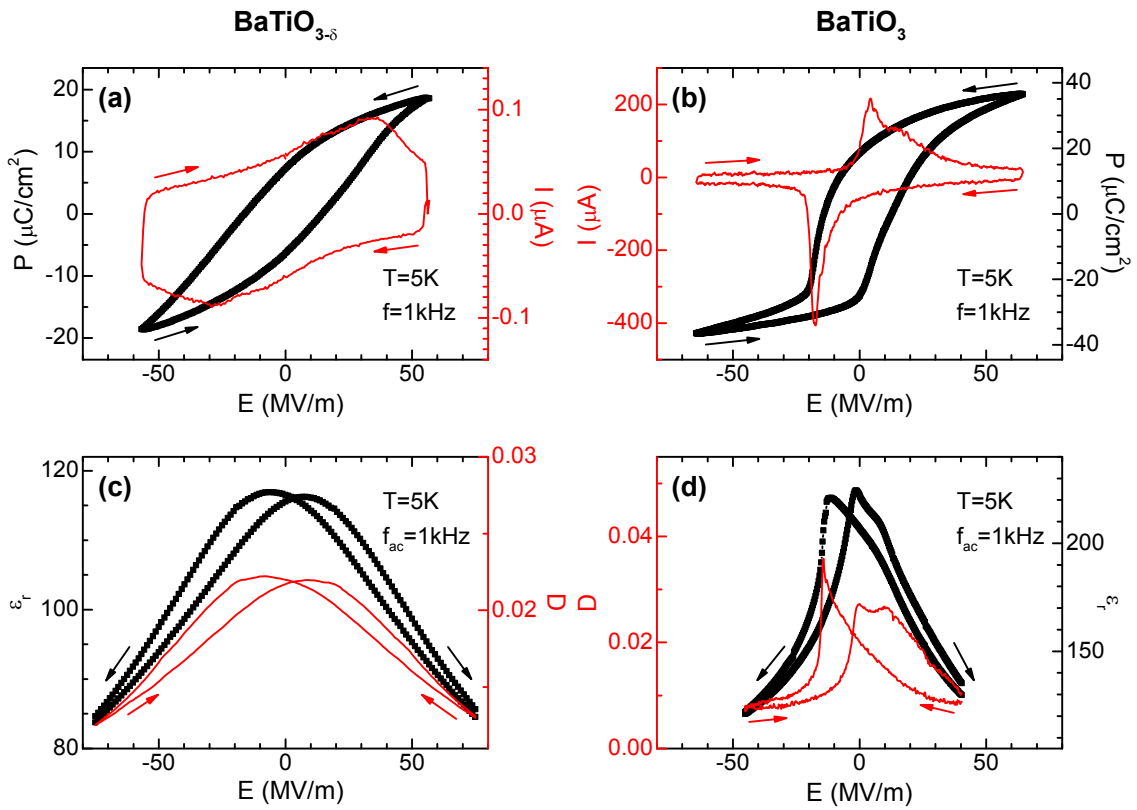


Figure 9.6: Electric field E dependence of (a),(b) the ferroelectric polarization P and the current I as well as (c), (d) the real part of the dielectric constant ϵ_r and the dielectric loss D . The polarization P was measured with the dynamic hysteresis measurement mode using a frequency of 1 kHz. An imposed small AC signal with a voltage level of 25 mV and a frequency of 1 kHz were used to derive the dielectric properties in (c), (d). Both types of measurement were carried out at 5 K on (a), (c) an oxygen deficient $\text{BaTiO}_{3-\delta}$ thin film with a thickness of 310 nm and (b), (d) on a (440 nm) BaTiO_3 sample fabricated under almost stoichiometric conditions.

to “bad” electrodes (cf. Section 9.1.1). Moreover, a transition from the ferroelectric c -phase to the r -phase upon lowering the temperature of BaTiO_3 thin films under tensile strain of around 0.5% is observable in these simulations (cf. Fig. 9.2). Therefore, the out-of-plane component of the polarization measured at low temperature in the r phase of BaTiO_3 is expected to be slightly reduced compared to the tetragonal c -phase. However, no transition from the tetragonal c -phase into the rhombohedral r phase was observed experimentally. As discussed in the following, this can mainly be attributed to extrinsic effects, such as high leakage currents or incomplete screening of the depolarization field, which affect the polarization measurements.

In Fig. 9.6, the electric polarization and the real part of the dielectric permittivity are compared as a function of the electric field. The data are obtained on a 440 nm thick oxygen deficient $\text{BaTiO}_{3-\delta}$ film and a (310 nm) BaTiO_3 sample fabricated under almost stoichiometric conditions. The non-saturated polarization hysteresis $P(E)$ loop of the oxygen deficient sample recorded using the dynamic hysteresis

measurement mode (cf. Section 2.2.1) is clearly dominated by leakage current effects even at 5 K (Fig. 9.6(a)) [5, 89]. The high leakage current is mainly caused by oxygen vacancies, which significantly alter the electric properties of BaTiO₃ thin films, since oxygen vacancies act as donors of charge carriers after ionization [730]. As pointed out in Section 4.5.2, a finite density of oxygen vacancies can reduce the Schottky barrier between the electrode material and the ferroelectric thin film. This implies that the leakage currents are strongly influenced by the electrode material [731]. Here we used Au as the top electrode and Nb:SrTiO₃ as the bottom electrode. Nb:SrTiO₃ can be considered as a *n*-doped degenerated semiconductor exhibiting a band gap of 3.2 eV [261, 732]. Although the electron density of Nb:SrTiO₃ ($n \approx 2 \times 10^{18} \text{ cm}^{-3}$) is much smaller than in normal metals, in principle, it should be sufficient to screen a polarization in the order of $20 \mu\text{C}/\text{cm}^2$ [260]. However, a reduction of the carrier concentration by two orders of magnitude was found at the surface of Nb:SrTiO₃, which leads to band bending and charge trapping at the film-substrate interface in the accumulation state [733]. This can cause a shift of the hysteresis loop on the voltage axis, i.e., imprint effects [91]. Furthermore, an insulating surface layer might form, if Nb:SrTiO₃ is exposed to oxygen at temperatures larger than 773 K [734]. Therefore, Nb:SrTiO₃ is obviously not the best electrode material in context of dielectric measurements, but it is still suitable for magnetoelectric measurements, since it is diamagnetic.

Due to the elongation of the out-of-plane lattice constant caused by oxygen vacancies, which enhances the tetragonality c/a , a larger saturation polarization P_s is expected than for the BaTiO₃ samples deposited under stoichiometric conditions, when other effects related to oxygen vacancies are neglected [722]. In spite of the difficulty to determine the saturation polarization P_s in oxygen deficient samples due to the absence of any saturation, the $P(E)$ loops displayed in Figures 9.6(a) and (b) reveal that P_s does not seem to be enhanced in our BaTiO_{3- δ} samples. This is in contrast to Li and coworkers [722], who reported an increase of the saturation polarization P_s in oxygen deficient samples caused by an enhancement of the tetragonality (c/a) driven by oxygen deficiency. Therefore, this result suggests that oxygen vacancies rather diminish the ferroelectric properties. However, stoichiometric BaTiO₃ thin films exhibit large saturation polarizations P_s up to $40 \mu\text{C}/\text{cm}^2$. This value is comparable to the saturation polarizations P_s published by other groups [714, 719, 735], but it is much smaller than the value $P_s \approx 70 \mu\text{C}/\text{cm}^2$ measured in strained BaTiO₃ thin films deposited on DyScO₃ substrates [251].

Not only the shape of the $P(E)$ loop was found to be strongly affected by the different oxygen content in the BaTiO₃ samples, but also the coercive fields E_c are significantly smaller in BaTiO₃ samples fabricated under stoichiometric conditions (cf. Figs. 9.6(a) and (b)).⁵ The large coercive fields of around 30 MV/m in oxygen deficient BaTiO_{3- δ} samples can be attributed to large inhomogeneous strains detected by x-ray diffraction in these samples (cf. Section 9.1.2). In almost stoichiometric BaTiO₃ thin films a coercive field of around 10 MV/m was measured. This value is in agreement with the coercive fields reported in Ref. [719] (and references

⁵Since imprint effects are detectable in all $P(E)$ loops, the coercive field E_c is determined by $E_c = (E_{c+} - E_{c-})/2$ using the positive E_{c+} and negative electric fields E_{c-} at $I = |I_{\text{max}}|$.

therein), but much larger than the characteristic coercive field $E_c \approx 0.1$ MV/m of bulk BaTiO₃ [492]. This large enhancement of the coercive field cannot only be explained by strain effects [736]. Interfacial passive layers between the ferroelectric thin film and the electrode [737], domain nuclei formation [738], imperfect screening of the polarization charges by the electrodes resulting in large depolarization fields [719], and point defects such as dislocations [739] also could play a significant role. The existence of an imperfect screening of the polarization charges mainly due to the Nb:SrTiO₃ bottom electrode is also reflected in the asymmetric shape of the $P(E)$ hysteresis loop shown in Fig. 9.6(b). This asymmetric behavior reveals the effect of charge compensation due to a semiconducting electrode [740]. This suggests, that at least the surface region of the Nb:SrTiO₃ substrate behaves like a normal n -doped semiconductor in BaTiO₃ thin films fabricated under high oxygen pressure $p_{\text{O}_2} \geq 1.0 \times 10^{-1}$ mbar. Considering a semiconductor as electrode, large band bending and electron depletion is required to compensate negative ionic charges from the ferroelectric polarization. This causes a large depolarization field in the ferroelectric, since the charge compensation is incomplete. On the other hand, screening of positive ionic charges can be readily achieved by electron accumulation with small band bending. The different band bending effects causing accumulation and depletion of the majority carriers result in different depolarization fields and stability of the ferroelectric polarization [741].

A further striking feature of our BaTiO₃ samples fabricated under high oxygen pressure $p_{\text{O}_2} \geq 1.0 \times 10^{-1}$ mbar is the observation of two peaks in the current response, while increasing the electric field from -65 MV/m to $+65$ MV/m (Fig. 9.6(b)). In principle, the polarization reversal can be accomplished either by the growth of existing domains antiparallel to the applied field, by domain-wall motion, or by the nucleation and growth of new antiparallel domains [260]. Both processes are strongly dependent on the presence of defects. For example, the domain wall motion was found to be a disorder-controlled creep process in Pb(Zr_{0.2}Ti_{0.8})O₃ thin films, which results from the competition between elastic behavior and pinning in a disorder potential [742]. In addition, inhomogeneous domain nucleation and growth was observed in disordered ferroelectric thin film capacitors [743]. Furthermore, trapped space charges located at the interface between the ferroelectric thin film and the electrodes can cause double peak structures in dielectric measurements [744]. This is confirmed in the electric field dependence of the real part of the complex dielectric constant ε_r displayed in Fig. 9.6(d).

Not only an additional peak in the up sweep from -45 MV/m to $+45$ MV/m is observable in the $\varepsilon_r(E)$ response of BaTiO₃ thin films deposited under high oxygen pressure ($p_{\text{O}_2} \geq 1.0 \times 10^{-1}$ mbar), but also an increase of the dielectric constant ε_r compared to the oxygen deficient BaTiO_{3- δ} sample displayed in Fig. 9.6(c). Allredge and coworkers instead observed a smaller in-plane dielectric constant for a -axis oriented Ba_{0.5}Sr_{0.5}TiO₃ thin films than for c -axis oriented samples and attributed this behavior to strain effects [745]. Therefore, the enhanced dielectric constant ε_r might be attributed to extrinsic effects, such as an additional interface capacitance due to space charges located at the interface between BaTiO₃ thin films and Nb:SrTiO₃ structures in case of BaTiO₃ thin films fabricated under

$p_{\text{O}_2} = 1.0 \times 10^{-1}$ mbar [744]. Furthermore, an expected high density of threading dislocations, which create local strain effects in oxygen deficient $\text{BaTiO}_{3-\delta}$ thin films (cf. Fig. 9.3(a)), can cause dielectric degradation in these thin films [252].

In summary, state of the art BaTiO_3 thin films with excellent crystalline quality were fabricated on Nb:SrTiO₃ substrates under different oxygen pressures. While BaTiO_3 thin films deposited using an oxygen pressure of $p_{\text{O}_2} = 1.0 \times 10^{-1}$ mbar are almost stoichiometric, thin films fabricated at $p_{\text{O}_2} = 7.5 \times 10^{-3}$ mbar exhibit a large density of oxygen vacancies. X-ray diffraction measurements carried out on both types of BaTiO_3 thin films reveal a nearly complete relaxation of the misfit strain. The relaxation process seems to take place in the first monolayers in case of almost stoichiometric BaTiO_3 thin films, while large inhomogeneous strains are observed in oxygen deficient $\text{BaTiO}_{3-\delta}$ thin films. However, $\text{BaTiO}_{3-\delta}$ thin films exhibit smaller surface roughness compared to stoichiometric BaTiO_3 thin films. Therefore, in the context of 2-2 type multiferroic composite heterostructures, the elastic coupling between the BaTiO_3 layer and the magnetostrictive thin film, which is deposited on top of BaTiO_3 , is expected to be stronger in case of oxygen deficient $\text{BaTiO}_{3-\delta}$ thin films due to the lower surface roughness, while larger piezoelectric responses might take place for oxygen stoichiometric BaTiO_3 thin films. The ferroelectric and dielectric properties were found to be strongly affected by the different oxygen content in BaTiO_3 thin films. In $\text{BaTiO}_{3-\delta}$ thin films, oxygen vacancies generate large leakage currents even at 5 K. In contrast, for BaTiO_3 thin films fabricated on Nb:SrTiO₃ substrates at higher oxygen pressures ($p_{\text{O}_2} \geq 1.0 \times 10^{-1}$ mbar), the dielectric and ferroelectric properties suggest a dead layer at the interface between the BaTiO_3 thin film and the Nb:SrTiO₃ substrate, which results in finite imprint effects and an incomplete compensation of the surface charges. A detailed discussion on the dielectric properties of our BaTiO_3 thin films can be found in the diploma thesis of Daniel Pantel [70].

9.2 FM/ BaTiO_3 multiferroic composite heterostructures

On the basis of BaTiO_3 thin films deposited on Nb:SrTiO₃ substrates, the fabrication of FM/ BaTiO_3 multiferroic composite heterostructures is viable (cf. Fig. 6.2(b2)). Two different types of multiferroic composites are considered in this section: epitaxial and non-epitaxial 2-2 type heterostructures. To realize epitaxial multiferroic 2-2 type heterostructures, Fe_3O_4 thin films were deposited in-situ on top of BaTiO_3 layers using pulsed laser deposition. Furthermore, non-epitaxial 2-2 type FM/ BaTiO_3 /Nb:SrTiO₃ heterostructures were fabricated using polycrystalline FeCo thin films evaporated directly on BaTiO_3 films.

In the following, the physical properties of these 2-2 type multiferroic composite heterostructures based on BaTiO_3 or $\text{BaTiO}_{3-\delta}$ thin films are discussed. We start by modeling the converse linear magnetoelectric effect employing the inverse magnetoelastic effect.

9.2.1 Modeling of FM/BaTiO₃ heterostructures

The simulation of FM/BaTiO₃ heterostructures is demanding, since the elastic response of the BaTiO₃ thin film deposited on a rigid substrate is unknown due to large clamping effects. As shown in Fig. 9.1(b), the strong elastic coupling between the BaTiO₃ thin film and the substrate has huge impact on the ferroelectric properties. While in the limit of BaTiO₃ thin films, which can move freely in all directions, a bulk like phase diagram was observed, molecular dynamics simulations reveal a quite different phase diagram for elastically constrained epitaxial BaTiO₃ thin films. However, as discussed in Chapter 6, an electric field dependence of the in-plane strain components η_k is essential to observe converse magnetoelectric effects in strain-mediated composite systems. Therefore, while a perfect clamping of the BaTiO₃ layer and the overlying ferromagnetic thin film is desirable, the elastic coupling between the BaTiO₃ thin film and the rigid substrate has to be weakened. In case of BaTiO₃ thin films, which are allowed to expand and contract without any elastic constraints, the largest possible converse magnetoelectric effects are expected.

By using molecular dynamics simulations, the strain variation as a function of the applied electric field can be derived in case of BaTiO₃ thin films, which are elastically decoupled from the substrate. With this information, the manipulation of the magnetization as a function of the electric field $M(E)$ can be computed by employing magnetoelastic effects (cf. Section 6.2). This situation is similar to FM/BaTiO₃ composite hybrid structures discussed in the previous chapter. Two different temperatures were chosen to calculate the strain dependence of BaTiO₃ thin films. First, the strain tensor of BaTiO₃ thin films in the tetragonal a -phase at $T_{\text{MD}} = 250$ K (cf. Fig. 9.1(b)), which is close to room temperature in reality, were determined.

The results of these calculations are depicted in Fig. 9.7(a). Since the electric field is applied along the z -direction of the BaTiO₃ thin film, ferroelastic c -domains are energetically more favorable than a -domains at high electric fields. At $|E| \gtrsim 10$ MV/m, the electric field dependence of the in-plane strain components is determined by the converse linear piezoelectric effect leading to identical in-plane strain components ($\eta_1 = \eta_2$). Around zero electric field, ferroelastic domain switching from tetragonal c -domains to a -domains occurs. This leads to large differences of the in-plane strain components η_1 and η_2 . As expected, the shear component η_6 is negligible in the tetragonal phase. In analogy to the previous chapter, the manipulation of the magnetization can now be derived by minimizing the modified Gibbs free energy $\tilde{g}^{(\text{m})}$ of the ferromagnetic thin film (cf. Eq. 6.4) and assuming a perfect clamping between the ferromagnetic thin film and the BaTiO₃ layer ($k = 1$). As an example, the elastic and magnetic properties of a polycrystalline Ni thin film is used throughout this section.

The variation of the projection of the magnetization along the external magnetic field is displayed in Fig. 9.7(b). A constant magnetization is visible in the electric field range of ferroelastic c -domains ($|E| \gtrsim 10$ MV/m), where $\eta_i(E)$ is caused by the linear converse piezoelectric effect (cf. Section 6.29). However, the large strain difference of η_1 and η_2 due to ferroelastic a -domains results in tremendous changes

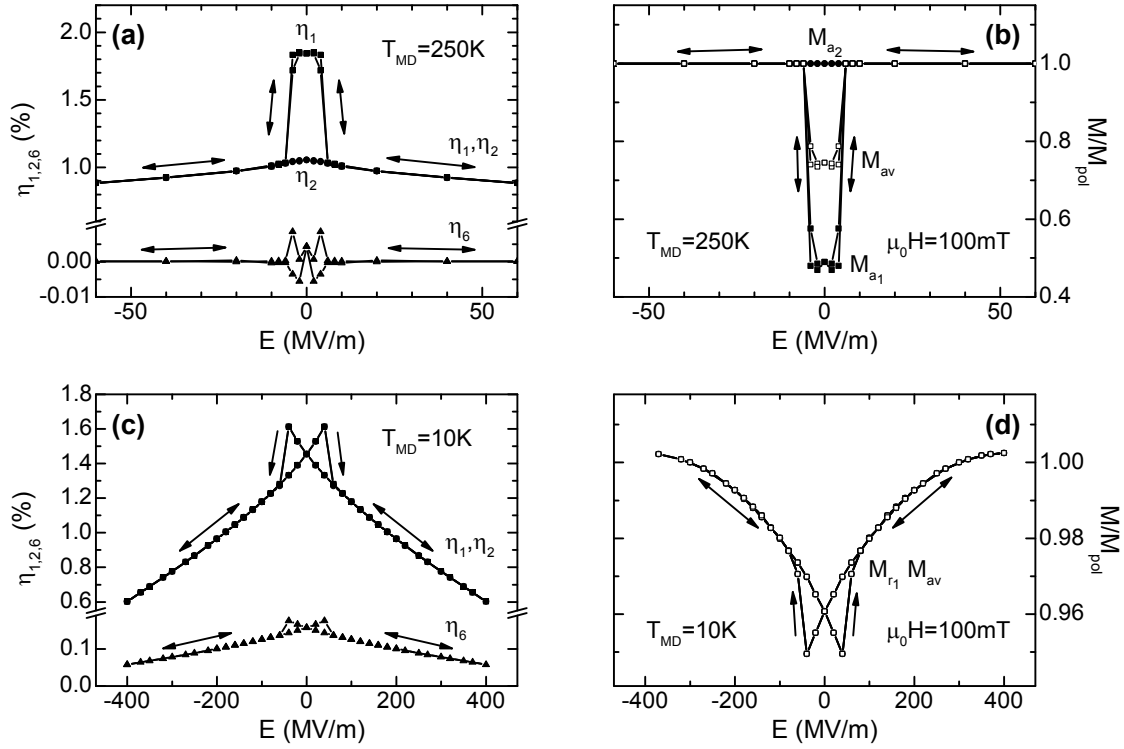


Figure 9.7: Molecular dynamics simulations of BaTiO₃ thin films under short-circuit conditions carried out at (a) $T_{MD} = 250$ K and (c) $T_{MD} = 10$ K. The BaTiO₃ thin film was allowed to expand and contract freely and the electric field was applied along the z -direction. Using the calculated in-plane strain components $\eta_k = \eta_k^{(e)}$ with $k = 1, 2, 6$ of the BaTiO₃ thin film, which are calculated with respect to the lattice constant of 0.3948 nm, the variation of the magnetization of the overlying ferromagnetic thin film was derived by minimizing the modified Gibbs free energy $\tilde{g}^{(m)}$ (cf. Eq. 6.4) for an external magnetic field $\mu_0 H = 100$ mT ((b), (d)) using the elastic and magnetic properties of a polycrystalline Ni thin film. Furthermore, a perfect clamping between the Ni thin film and the BaTiO₃ layer was assumed ($\eta_k = \eta_k^{(e)} = \eta_k^{(m)}$). To account for the different ferroelastic domains in the tetragonal phase at $T_{MD} = 250$ K, $M(E)$ loops for $c \leftrightarrow a_1 \leftrightarrow c$ (M_{a_1}) and $c \leftrightarrow a_2 \leftrightarrow c$ (M_{a_2}) were calculated. M_{av} (open symbols) are the average values of both loops. At $T_{MD} = 10$ K, the $M(E)$ loops on the basis of different rhombohedral domains (M_{r_1}) are the same, thus M_{av} (open symbols) is equal to M_{r_1} (full symbols).

of the magnetization projection of the Ni thin film of up to 50% even at a magnetic field strength of 100 mT. Since the probability of creating a_1 - and a_2 -domains around zero electric fields is the same, $M(E)$ loops for $c \leftrightarrow a_1 \leftrightarrow c$ (M_{a_1}) and $c \leftrightarrow a_2 \leftrightarrow c$ (M_{a_2}) were calculated and the average magnetization (M_{av}) was determined (cf. open symbols in Fig. 9.7(b)), which still exhibits a large variation as a function of the electric field. However, Figures 9.7(a) and (b) disclose that finite strain-mediated converse magnetoelectric effects in FM/BaTiO₃ heterostructures can only be realized by ferroelastic domain switching at room temperature.

In contrast to $T_{MD} = 250$ K, a finite manipulation of the magnetization projection in the range of the linear converse piezoelectric effect can be observed at $T_{MD} =$

10 K, i.e., in the rhombohedral r -phase (cf. Fig. 9.1). While molecular dynamics simulations reveal indistinguishable strain components η_1 and η_2 , finite in-plane shear strains η_6 are visible (Fig. 9.7(c)). The variation of η_6 as a function of the applied electric field causes finite converse magnetoelectric effects, which is displayed in Fig. 9.7(d). Since the same $M(E)$ loop is derived for all possible rhombohedral domains, the average variation of the magnetization (M_{av}) is equal to assuming a ferroelastic single domain state (M_{r_1}) (cf. open symbols in Fig. 9.7(d)). Figs. 9.7(b) and (d) disclose that the change of the magnetization projection of up to 5% at $T_{\text{MD}} = 10$ K is much smaller compared to $T_{\text{MD}} = 250$ K.

As the strain components $\eta_i = \eta_i^{(e)}$ with $i = 1, 2, 6$ were determined in the limit of vanishing clamping between the BaTiO₃ thin film and the rigid substrate as well as perfect elastic coupling at the interface between the ferromagnetic Ni layer and the BaTiO₃ thin film, the $M(E)$ loops displayed in Figs. 9.7(b) and (d) are the upper limit of converse magnetoelectric effects in Ni/BaTiO₃ composite heterostructures at each temperature. However, a perfectly clamped BaTiO₃ thin film on the rigid substrate clearly describes the lower limit. In this case, the resulting strain is a sum of the piezoelectric strain $\eta_i^{(e)} = d_{ki}E_k$, and the mechanical strain $\eta_i^{(e)} = s_{ik}\sigma_k$, where d_{ki} , s_{ik} , E_k , and σ_k denote the piezoelectric modulus, the elastic compliance, the electric field, and the mechanical stress of the BaTiO₃ layer [112]. Assuming an ideal elastic bonding of the BaTiO₃ thin film on a cubic substrate with an in-plane misfit strain of $\eta_1^{(e)} = \eta_2^{(e)}$ and $\eta_6^{(e)} = 0$, the remaining out-of-plane strain component can be calculated to $\eta_3^{(e)} = d_{33}E_3 + 2s_{12}/(s_{11} + s_{12})(\eta_1^{(e)} - d_{31}E_3)$ [746]. Therefore, only the out-of-plane strain component of the BaTiO₃ thin film depends on the electric field, while the in-plane components are fixed. Since this has no effect on the elastic strain tensor of the ferromagnetic thin film $\epsilon_{ij}^{(m)}$ on top of BaTiO₃, no manipulation of the magnetization as a function of the electric field based on magnetoelastic effects is observable. Therefore, the release of the elastic clamping between the BaTiO₃ thin film and the substrate is essential.

The most important possibility to reduce the clamping is the formation of dislocation at the interface. In BaTiO₃ thin films deposited on SrTiO₃ substrates, a dense and regular network of dislocations is formed at the interface for thickness larger than 200 nm [747]. The orthogonal dislocation network is composed by two dislocation lines with Burgers vectors $\mathbf{b} \parallel [100]$ and $\mathbf{b} \parallel [010]$. However, as mentioned in the previous chapter, if dislocations are not mobile, their presence alone does not reduce the elastic coupling between the thin film and the substrate. Therefore, glides, which are driven by the Peach-Koehler force [748], of a large number of dislocations are necessary to reduce the elastic interaction between the BaTiO₃ thin film and the rigid SrTiO₃ substrate.

However, BaTiO₃ thin films totally decoupled from the SrTiO₃ substrate, which means the existence of large plastic deformations at the interface, are not expected. Therefore, as switching of ferroelastic domains requires large changes of the in-plane strain (cf. Fig. 9.7(a)), ferroelastic domain reorientation is hampered in case of finite substrate clamping [721]. Thus, the large converse magnetoelectric effects calculated at $T_{\text{MD}} = 250$ K is hardly observable in experiments. If the polarization reversal takes place without creating ferroelastic a -domains, no variation of

the magnetization is visible at $T_{\text{MD}} = 250 \text{ K}$, since the in-plane strains are equal in case of ferroelastic c -domains. However, at magnetic field strengths lower than the saturation field needed to create a magnetic single domain state, a finite converse magnetoelectric effect is observed, assuming a magnetic field dependence of the magnetostrictive strain $\lambda_{ij}(H)$ and an imperfect clamping of the BaTiO_3 layer on the substrate. While the former leads to a magnetic field dependence of the components of the magnetoelastic coupling tensor B_{ijkl} in the bulk limit (cf. Section 6.2), the latter results in a finite variation of the in-plane strain components of the BaTiO_3 layer and therefore to an electric field dependent strain tensor $\epsilon_{ij}^{(m)}(E)$ of the overlying magnetostrictive thin film. Thus, the magnetoelastic contribution $u_{\text{magel}}^{(m)}$ of the internal energy density of the magnetostrictive thin film depends on the external magnetic *and* electric field. As discussed in Section 6.2, in the limit of a well defined, homogeneous magnetization, the converse linear magnetoelectric effect can be expressed as (cf. Eq. (6.11))

$$\begin{aligned} \alpha_{ij} &= -\mu_0 c \frac{\partial^2 \bar{g}^{(c)}}{\partial H_i \partial E_j} = -\mu_0 c \frac{d^{(m)}}{d^{(e)} + d^{(m)}} \frac{\partial^2 u_{\text{magel}}^{(m)}}{\partial H_i \partial E_j} \\ &= -\mu_0 c \frac{d^{(m)}}{d^{(e)} + d^{(m)}} \frac{\partial^2}{\partial H_i \partial E_j} \left(B_{ijkl} \epsilon_{ij}^{(m)} m_k m_l \right). \end{aligned} \quad (9.2)$$

Since the tensor components of B_{ijkl} are directly proportional to the magnetostrictive strain λ in the bulk limit (cf. Section 6.2.1), Eq. (9.2) reveals that the linear magnetoelectric effect is expected to depend on the magnetic field derivative of the magnetostrictive strain $-\left(\frac{\partial \lambda_{ij}}{\partial H_i}\right)$ as well as on the electric field derivative of the strain tensor $\frac{\partial \epsilon_{ij}^{(m)}}{\partial E_j}$. However, since the magnetostrictive response is highly correlated to the magnetic domain structure in ferromagnetic materials (e.g. Ref. [749]), the strong dependence of λ_{ij} on the magnetic field H is mainly due to the presence of magnetic domains. In this case, the magnetization of the magnetostrictive thin film may no longer be described as $\mathbf{M} = M_s \cdot \mathbf{m}$ with the unit vector \mathbf{m} of the magnetization direction (cf. Section 6.2). However, Equation. (9.2) can be regarded as an approximation of the converse linear magnetoelectric effect in the limit of a “pseudo” single domain state.

Neglecting ferroelastic domain switching in BaTiO_3 thin films, which exhibits a finite elastic coupling to the rigid substrate, the electric field dependence of the strain tensor $\epsilon_{ij}^{(e)}(E)$ of BaTiO_3 is caused only by the converse linear piezoelectric effect. Assuming a perfect elastic coupling of the magnetostrictive thin film deposited on top of the BaTiO_3 layer, the electric field derivative of the strain tensor $\frac{\partial \epsilon_{ij}^{(m)}}{\partial E_j}$ is therefore expected to be neither a function of the electric nor of the magnetic field. In contrast, due to the strong correlation of the magnetostrictive strain λ_{ij} and the magnetic domain state, λ_{ij} is not expected to be a linear function of the magnetic field in the whole magnetic field range. As an example, Figure 9.8(a) shows the magnetostrictive strain $\bar{\lambda}$ measured on polycrystalline Ni bulk samples as a function of the external magnetic field. The data were taken from Ref. [750]. Starting with a demagnetized

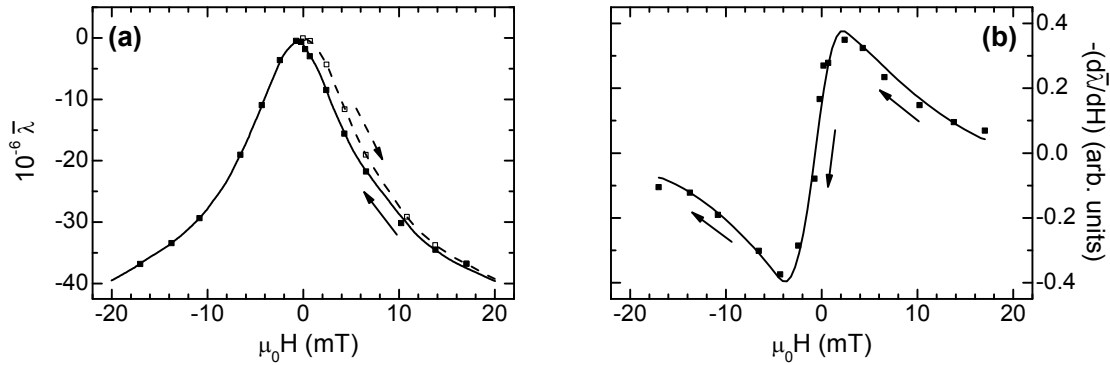


Figure 9.8: (a) Magnetic field dependence of the magnetostrictive strain $\bar{\lambda}$ (solid line and full symbols) of polycrystalline Ni. The initial magnetostrictive curve $\bar{\lambda}(H)$ is marked by a dashed line and open symbols. Since the converse linear magnetoelectric effect is expected to be a function of the derivative of the magnetostrictive strain, $-\left(\frac{\partial \bar{\lambda}}{\partial H}\right)$ as a function of the external magnetic field is shown in (b). The solid and dashed lines are guides to the eye. The data were taken from Ref. [750].

sample at $\mu_0 H = 0$ mT, which consists of a number of magnetic domains leading to a vanishing magnetostriction, domain wall displacement takes place by introducing a moderate positive external magnetic field (dashed line in Fig. 9.8(a)). Further increase of the magnetic field strength leads to domain rotation and saturation of the magnetization in the higher magnetic field region [464]. Therefore, the magnetic field dependence of $\bar{\lambda}(H)$ is a quadratic function around zero external magnetic field, increases about linearly at intermediate magnetic field strengths, and finally reaches its saturation value λ_s , which is equal to the magnetostriction constant $\bar{\lambda}^{\text{bulk}}$ defined in Eq. (6.7). The linear dependence near the inflection point of the $\bar{\lambda}(H)$ curve is often interpreted as a “pseudo” piezomagnetic effect in analogy to the converse piezoelectric effect in dielectric materials [464, 751]. The derivative of the $\bar{\lambda}(H)$ curve can now be calculated. Since $-\left(\frac{\partial \bar{\lambda}}{\partial H}\right)$ is a strong function of the external magnetic field (Fig. 9.8(b)), the converse linear magnetoelectric effect is expected to be highly magnetic field dependent.

In total, assuming elastically decoupled BaTiO₃ thin films, bulk like converse magnetoelectric effects, which are mainly caused by ferroelastic domain switching and shear strains in the BaTiO₃ layer, are expected in multiferroic 2-2 type heterostructures. However, in case of a finite clamping of the BaTiO₃ thin films on the rigid substrate, ferroelastic domain switching is unlikely and no variation of the magnetization as a function of the applied electric field should be observed at room temperature for magnetic fields larger than the saturation field needed to ensure a magnetic single domain state. Moreover, in case of a magnetic multi-domain state in the magnetostrictive layer, finite converse linear magnetoelectric effects are expected due to an incomplete coupling of the BaTiO₃ layer on the substrate which results in an electric field dependent strain tensor $\epsilon_{ij}^{(m)}(E)$ of the magnetostrictive layer and due to a magnetic field dependence of the magnetostrictive strain $\lambda_{ij}(H)$. Both conditions are necessary to observe a converse linear magnetoelectric effect

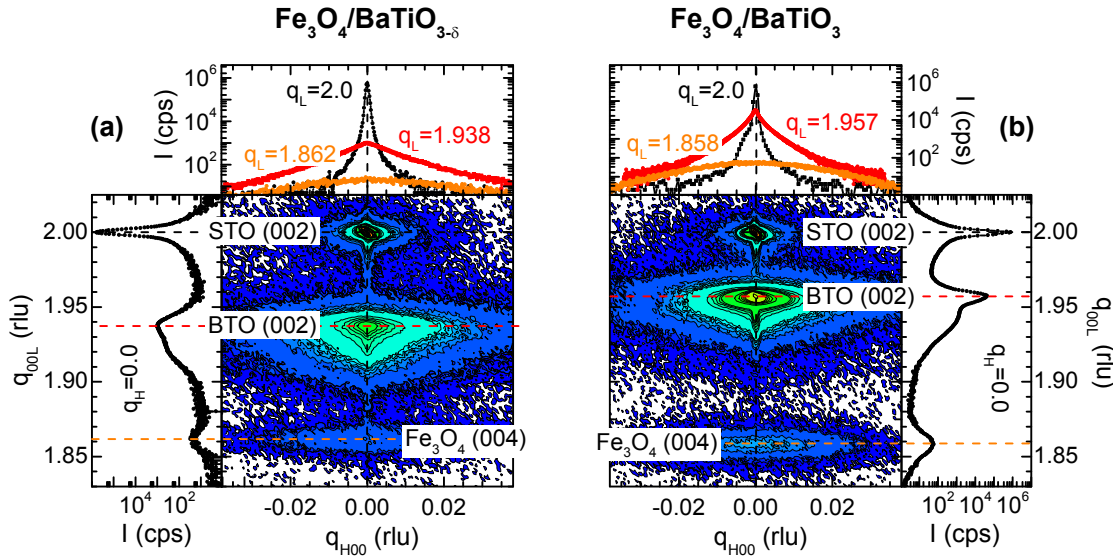


Figure 9.9: X-ray diffraction measurements around Nb:SrTiO₃ (002) carried out on two Fe₃O₄/BaTiO₃/Nb:SrTiO₃ heterostructures. The structures are based on BaTiO₃ thin films fabricated using an oxygen pressure of (a) $p_{\text{O}_2} = 7.5 \times 10^{-3}$ mbar (Fe₃O₄/BaTiO_{3- δ}) and (b) $p_{\text{O}_2} = 1.0 \times 10^{-1}$ mbar (Fe₃O₄/BaTiO₃).

in 2-2 type heterostructures exhibiting a strong but incomplete elastic coupling between the piezoelectric layer and the substrate. In this case, the converse linear magnetoelectric effect is expected to be highly magnetic field dependent.

9.2.2 Epitaxial 2-2 type Fe₃O₄/BaTiO₃ heterostructures

Epitaxial multiferroic 2-2 type heterostructures were realized using Fe₃O₄ thin films, which were deposited on top of BaTiO₃ thin films using the same deposition parameters as described in Section 7.2.1. We again used BaTiO₃ thin films fabricated under nearly stoichiometric conditions ($p_{\text{O}_2} = 1.0 \times 10^{-1}$ mbar) as well as under low oxygen pressure ($p_{\text{O}_2} = 7.5 \times 10^{-3}$ mbar).

The crystalline quality of Fe₃O₄/BaTiO₃ 2-2 type heterostructures is shown in Figs. 9.9(a) and (b). For both cases, a crystalline growth of Fe₃O₄ was obtained. The full width at half maximum (FWHM) of the rocking curves of the Fe₃O₄ (004) peak were found to be around 0.8° , which is comparable to FWHM values of Fe₃O₄ thin films deposited on BaTiO₃ substrates (cf. Section 7.2.1). However, a small difference of the out-of-plane lattice constant is detectable. For Fe₃O₄ thin films deposited on top of oxygen deficient BaTiO_{3- δ} thin films, a lattice constant of $c_{\text{Fe}_3\text{O}_4} = (0.8390 \pm 0.0005)$ nm was obtained (see Fig. 9.9(a)), while Fe₃O₄ thin films fabricated on almost stoichiometric BaTiO₃ thin films exhibit a small elongation of the unit cell with a lattice constant of $c_{\text{Fe}_3\text{O}_4} = (0.8400 \pm 0.0005)$ nm (see Fig. 9.9(b)). By comparing these values with the lattice constant of Fe₃O₄ in bulk form ($a_{\text{Fe}_3\text{O}_4} = 0.83941$ nm), x-ray diffraction measurements disclose that the lattice constants of both Fe₃O₄ thin films are nearly fully relaxed. The slight tensile strain of

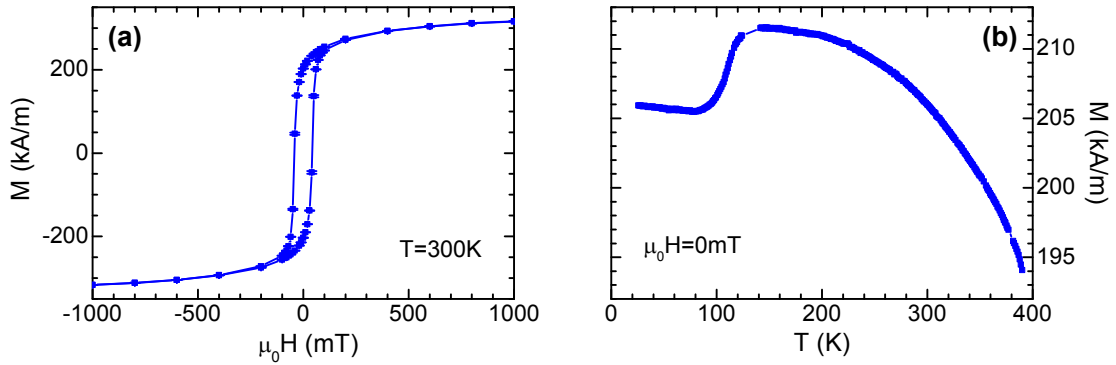


Figure 9.10: Magnetic properties of a Fe₃O₄/BaTiO₃/Nb:SrTiO₃ heterostructure with BaTiO₃ fabricated under stoichiometric conditions using an oxygen pressure of $p_{\text{O}_2} = 1.0 \times 10^{-1}$ mbar. (a) The magnetic hysteresis loop measured at 300 K reveals a high saturation magnetization of around 315 kA/m. (b) The temperature dependence of the remanent magnetization discloses a distinct Verwey transition at (113 ± 2) K. The data were recorded in zero magnetic field with decreasing temperature after magnetizing at 390 K and 1 T.

0.07% in the out-of-plane direction of Fe₃O₄ thin films fabricated on almost stoichiometric BaTiO₃ thin films might be attributed to a slight oxygen non-stoichiometry and to strain effects during the growth process.

Nevertheless, the magnetic properties of Fe₃O₄ thin films deposited on either BaTiO₃ or BaTiO_{3- δ} layers are nearly identical. As an example, Figure 9.10 shows the magnetic field and temperature dependence of the magnetization of a 52 nm thick Fe₃O₄ film fabricated on a BaTiO₃ (440 nm) layer deposited under stoichiometric conditions. The magnetic hysteresis displayed in Fig. 9.10(a) reveals a high saturation magnetization of around 315 kA/m. Furthermore, the rounded shape of the $M(H)$ -loop resembles more Fe₃O₄ thin films on MgO substrates than on BaTiO₃ substrates (cf. Fig. 7.11). This suggests the presence of a significant amount of anti-phase boundaries in the Fe₃O₄ thin film (cf. Section 7.2.1).

Since the Verwey transition is considered as a hallmark for the correct stoichiometry in Fe₃O₄ thin films, the distinct Verwey transition visible in the temperature dependence of the remanent magnetization suggests that our thin films exhibit the correct iron oxide phase (Fig. 9.10(b)). However, the Verwey transition takes place at $T_V = (113 \pm 2)$ K, which is comparable to T_V in Fe₃O₄ thin films fabricated on BaTiO₃ substrates, but lower than the transition temperature of 121 K reported for stoichiometric Fe₃O₄ thin films (cf. Section 7.2.1). Since the lattice of Fe₃O₄ thin films fabricated on BaTiO₃ layers is almost fully relaxed, the Verwey transition is not affected by strain effects. Therefore, the reduction of the transition temperature is most likely caused by a slight oxygen non-stoichiometry. By using the dependence of the Verwey transition on the oxygen content of Fe_{3(1- δ)}O₄ described in Section 7.2.1, the Verwey transition of (113 ± 2) K can be explained by a slight non-stoichiometry of $\delta \simeq 0.0021$. However, in contrast to epitaxial free-standing FM/BaTiO₃ hybrids (cf. Fig. 8.2), no abrupt changes of the magnetization of Fe₃O₄/BaTiO₃ heterostructures were observed as a function of temperature.

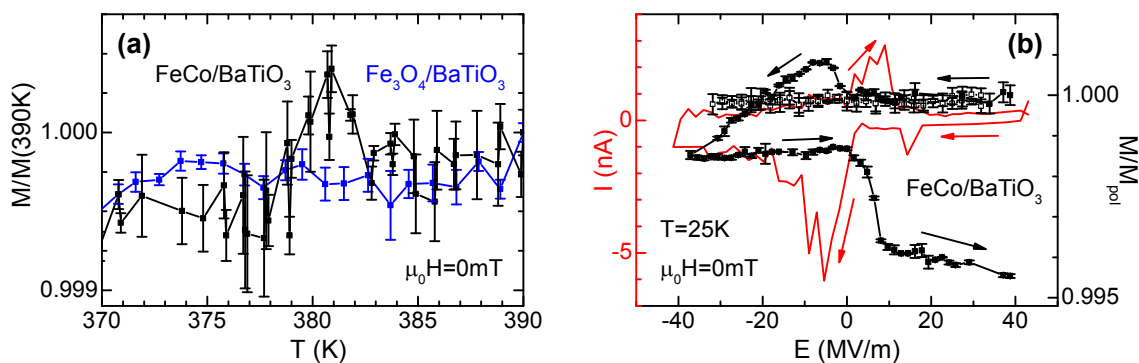


Figure 9.11: (a) Temperature dependence of the remanent magnetization around the ferroelastic transition temperature of the BaTiO_3 thin film carried out on a $\text{Fe}_3\text{O}_4/\text{BaTiO}_3$ (blue symbols) and $\text{FeCo}/\text{BaTiO}_3$ (black symbols) 2-2 type heterostructure. (b) Converse magnetoelectric effect measured at 25 K on a $\text{FeCo}/\text{BaTiO}_3$ heterostructure for zero magnetic field applied. Two different types of $\text{FeCo}/\text{BaTiO}_{3-\delta}$ heterostructures thin films were investigated, based on nominally stoichiometric BaTiO_3 thin films (full symbols) and on $\text{BaTiO}_{3-\delta}$ with $\delta \neq 0$ (open symbols). The data were recorded at $\mu_0H = 0$ mT after applying a magnetic field of 1 T. The current response of the $\text{FeCo}/\text{BaTiO}_3$ heterostructure is displayed in red. The magnetization is normalized to its value at 390 K in panel (a) and to $M_{\text{pol}} = M(40 \text{ MV/m})$ in panel (b).

In summary, epitaxial multiferroic 2-2 type heterostructures based on Fe_3O_4 and BaTiO_3 thin films were fabricated. The crystalline quality of the Fe_3O_4 thin films is similar to Fe_3O_4 thin films deposited directly on BaTiO_3 substrates. Moreover, the Fe_3O_4 thin films exhibit a high saturation magnetization and a distinct Verwey transition at $T_V = (113 \pm 2)$ K. The reduction of T_V as compared to high quality single crystals can be explained by a slight oxygen non-stoichiometry. However, no changes of the magnetization neither at the ferroelastic phase transition of BaTiO_3 thin films at around 380 K nor as a function of the applied electric field (not shown) was found in these epitaxial multiferroic 2-2 type composite heterostructures.

9.2.3 Non-epitaxial 2-2 type $\text{FeCo}/\text{BaTiO}_3$ heterostructures

In contrast to epitaxial 2-2 type composite heterostructures, which are fabricated exclusively by pulsed laser deposition, non-epitaxial heterostructures were realized using polycrystalline FeCo evaporated via electron beam evaporation in-situ on BaTiO_3 thin films grown by pulsed laser deposition. A gold gap with a thickness of 10 nm was evaporated on top of FeCo to prevent oxidation. After the deposition, the $\text{FeCo}/\text{BaTiO}_3$ heterostructure was patterned into a cylindrical structure with a diameter of $500 \mu\text{m}$ as shown in Fig. 6.2(b2). This structure allows to apply a well defined electric field along the z -direction so that the investigation of converse magnetoelectric effects is possible.

In contrast to epitaxial $\text{Fe}_3\text{O}_4/\text{BaTiO}_3$ multiferroic composite heterostructures, a clear variation of the remanent magnetization is observed around the ferroelastic phase transition of the BaTiO_3 thin film. The temperature dependence of the nor-

malized remanent magnetization around $T_c \approx 380$ K carried out on a FeCo/BaTiO₃ heterostructure based on a BaTiO₃ thin film fabricated using almost stoichiometric conditions is shown in Fig. 9.11(a). For comparison, the magnetization as a function of temperature of an epitaxial Fe₃O₄/BaTiO₃ heterostructure (blue symbols) is also depicted in Fig. 9.11(a). While no variation of the magnetization can be observed for epitaxial Fe₃O₄/BaTiO₃ heterostructures, a distinct change of the magnetization is visible for FeCo/BaTiO₃ composites (cf. black symbols in Fig. 9.11(a)) in the same way as the FWHM of the BaTiO₃ (004) reflection changes in temperature dependent x-ray diffraction measurements (cf. Fig. 9.5(b)). Therefore, the variation of the magnetization might be attributed to a ferroelastic multi-domain state present at the phase transition of the BaTiO₃ thin film. This observation suggests an imperfect clamping of the BaTiO₃ layer on the Nb:SrTiO₃ substrate, which makes the investigation of finite converse linear magnetoelectric effects possible. Indeed, Figure 9.11(b) reveals changes of the magnetization as a function of the applied electric field measured on FeCo/BaTiO₃ heterostructures at 25 K for $\mu_0 H = 0$ mT (cf. full black symbols in Fig. 9.11(b)). Since the large variations of the magnetization are correlated to the ferroelectric switching currents caused by the BaTiO₃ layer (cf. red curves in Fig. 9.11), these changes are no experimental artifacts and are correlated to the ferroelectric and/or ferroelastic properties of BaTiO₃. Interestingly, finite converse magnetoelectric effects are only observable using BaTiO₃ thin films fabricated under stoichiometric conditions and no electric field induced changes of the magnetization were observed on Fe₃O₄/BaTiO_{3- δ} 2-2 type heterostructures (cf. black open symbols in Fig. 9.11(b)). Therefore, BaTiO₃ thin films fabricated under almost stoichiometric conditions are suitable for magnetoelectric 2-2 type heterostructures.

From magnetoelastic theory, the observed variation of the magnetization by an electric field at low temperature ($T = 25$ K) in the rhombohedral symmetry, which is expected by molecular dynamics simulations (cf. Section 9.1.1), should be caused by a finite converse piezoelectric response of the in-plane shear strain component of the BaTiO₃ layer $\epsilon_{12}^{(e)}$ (cf. Section 9.2.1). Since the BaTiO₃ thin films are still clamped to the Nb:SrTiO₃ substrate, Fig. 9.11(b) suggests that only a small variation of the shear strain component occurs in the BaTiO₃ layer. Furthermore, the simulation presented in Section 9.2.1 is based on a magnetic single domain state. However, Figure 9.11(b) reveals that the $M(E)$ -loop is not closed, leading to two different magnetic states at $E = 40000$ kV/m depending on the sweep direction. Similar irreversible converse magnetoelectric effects were observed for free-standing FM/BaTiO₃ hybrid structures using an external magnetic field of $\mu_0 H = 0$ T (cf. Fig. 8.23(a)). But, in contrast to FM/BaTiO₃ hybrid structures, no significant variations of the magnetization projection were detected for external magnetic fields larger than the saturation field of the ferromagnetic thin film in FeCo/BaTiO₃ heterostructures.

This is confirmed by magnetic hysteresis measurements under different electric fields E applied across a FeCo(50 nm)/BaTiO₃(310 nm) 2-2 heterostructure carried out at 25 K. Figure 9.12(a) reveals that the magnetic hysteresis loops are the same for different electric fields in the limit of the experimental uncertainty. Therefore, the electric field dependence of the magnetization displayed in Fig. 9.11(b) might be caused by reversible and irreversible magnetic domain effects, which are only

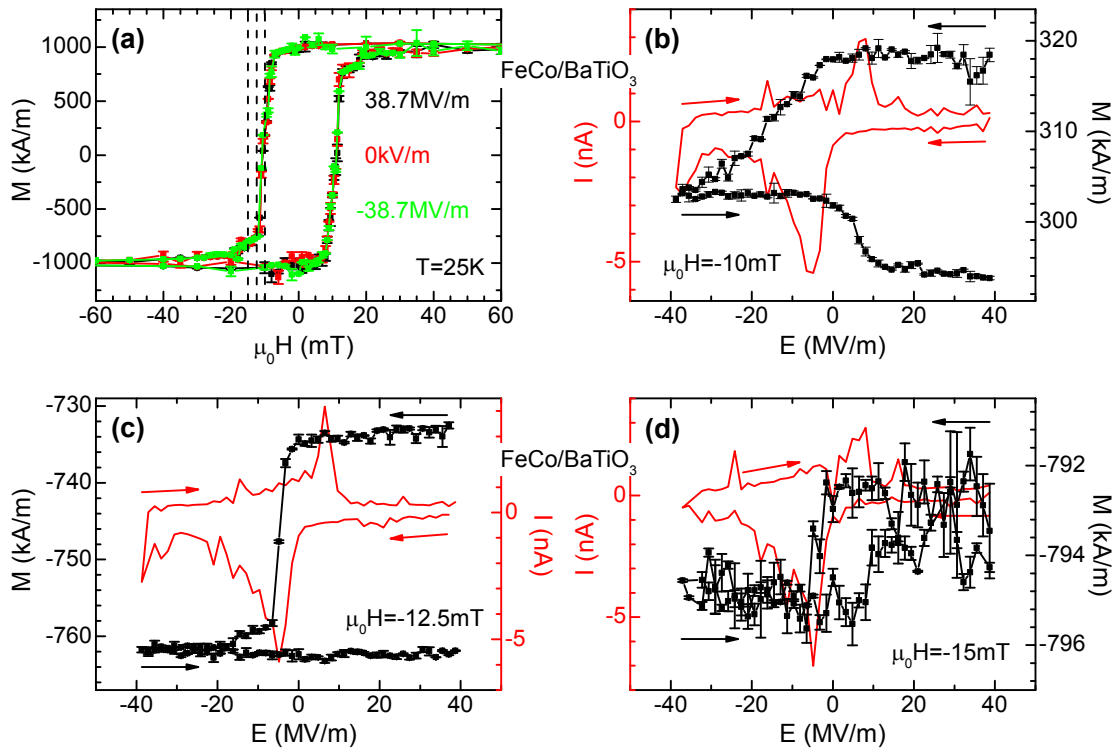


Figure 9.12: (a) $M(H)$ loops measured on a FeCo(50 nm)/BaTiO₃(310 nm) 2-2 heterostructure with different electric fields E applied. The measurements were carried out at 25 K. (b)-(d) $M(E)$ loop (full symbols) and current response (red line) recorded on the same sample at 25 K using different magnetic field strengths, which are marked by dashed lines in (a). Each $M(E)$ loops was recorded after magnetizing the sample to saturation in an external magnetic field of 1 T.

observable close to the magnetic coercive field. Indeed, large converse magnetoelectric effects up to 8% were detected using magnetic field strengths around -10 mT (Figs. 9.11(b) and (c)). However, at $\mu_0 H = -15$ mT, a weak variation of the magnetization as a function of the electric field is still visible (Fig. 9.11(d)). This $M(E)$ loop is reminiscent of ferroelectric $P(E)$ loops and might therefore be caused by nonvanishing influences of surface charges.

If the $M(E)$ loops displayed in Figs. 9.12(b)-(d) were repeatedly cycled, the 2-2 heterostructure reaches almost a demagnetized state. Figure 9.13(a) shows the variation of the magnetization M and the applied electric field E as a function of time t carried out on a FeCo(50 nm)/BaTiO₃(310 nm) 2-2 heterostructure at 25 K with a magnetic field strength of -10 mT. At the beginning, the sample was magnetized to saturation using an external magnetic field of 1 T. Each electric field cycle continuously reduces the magnetization until the sample reaches an almost demagnetized state. Therefore, at this magnetic field, the electric field induces irreversible magnetic domain effects in such a way that no net magnetization is measured after a few electric field cycles. This further confirms that the finite manipulation of the magnetization by an electric field visible in Figs. 9.12(b)-(d) is mainly caused by changes of the magnetic domain state in the ferromagnetic thin film. This is in contrast

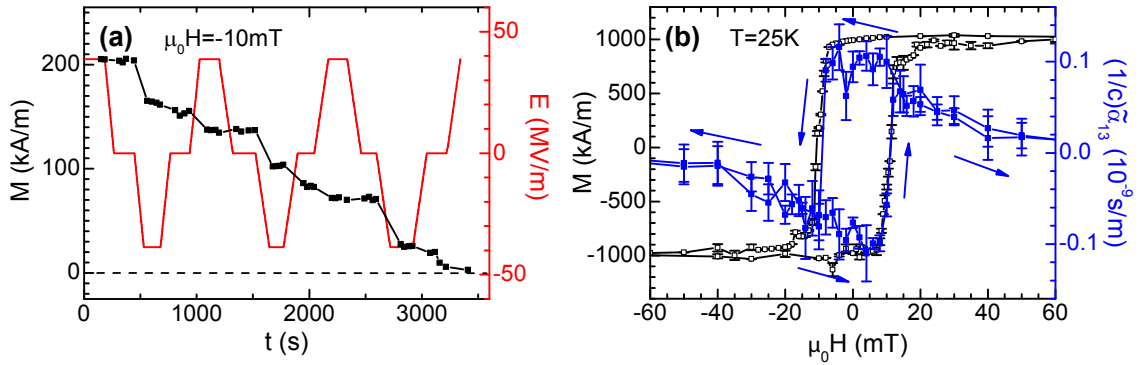


Figure 9.13: (a) Variation of the magnetization M (full symbols) and the applied electric field E (red line) as a function of time t measured on a FeCo(50 nm)/BaTiO₃(310 nm) 2-2 heterostructure at 25 K with a magnetic field strength of -10 mT. The demagnetized state ($M = 0$ kA/m) is marked by a horizontal dashed line. (b) Converse magnetoelectric constant $\frac{1}{c}\tilde{\alpha}_{13}$ (blue full symbols) as a function of the in-plane magnetic field strength. The measurements were carried out at 25 K on the same heterostructure utilizing the ac option of a SQUID magnetometer. An ac electric field with an amplitude of $E_{ac} = 38.7$ MV/m and a frequency of $f = 10$ Hz was used. A magnetic field strength of 0.1 T was applied before taking each magnetic field point. For comparison, the magnetic hysteresis $M(H)$ recorded with $E = 0$ kV/m is shown by black open symbols.

to free-standing FM/BaTiO₃ hybrid structures, where magnetic domain effects can mostly be neglected (cf. Fig. 8.35). Recently, reversible and irreversible magnetic domain effects induced by electric fields could be observed in multiferroic composite heterostructures by several groups using magnetic force microscopy and Lorentz microscopy [752–754]. Therefore, the control of the local magnetic structure by electric fields seems possible in these devices. This is not surprising. Even a small variation of the strain state caused by converse piezoelectric effects in the ferroelectric layer should result in changes of the ferromagnetic domain structure, since the domain pattern is determined by the minimum of the total free energy. This energy can be written as a sum of the exchange energy, the energy of the magnetic anisotropy, a stray field contribution, the energy of external stresses and magnetostriction as well as the Zeeman energy term [755]. Therefore, elastic deformations of the ferromagnetic thin film should lead to variations of the ferromagnetic domain pattern, as the total energy is modified. These variations not only affect the magnetization but also influences the magnetostrictive response. In this case, Section 9.2.1 discloses that a finite converse linear magnetoelectric effect should be observable, which is based on the magnetic field dependence of the magnetostrictive strain $\lambda_{ij}(H)$ and is therefore expected to be highly dependent on the strength of the external magnetic field.

To measure the converse magnetoelectric effect α_{13} of the FeCo(50 nm)/BaTiO₃ (310 nm) 2-2 heterostructure, the ac option of the SQUID magnetometer (cf. Section 2.3.1) was utilized. However, contrary to the measurements of the linear magnetoelectric coupling coefficient on FM/BaTiO₃ hybrid samples (cf. Fig. 8.23(b)), an ac electric field with an amplitude as large as $E_{ac} = 38.7$ MV/m and a frequency

of $f = 10$ Hz was used. Therefore, the converse pseudo magnetoelectric response $\frac{1}{c}\tilde{\alpha}_{13}$ of the 2-2 heterostructure at different magnetic field strengths displayed in Fig. 9.13(b) originates from probing the whole $M(E)$ loop. Before each measurement, an magnetic field of 0.1 T was first applied and then the magnetic field was lowered to the measurement field. Starting at $\mu_0 H = +60$ mT, the pseudo linear magnetoelectric response increases upon decreasing the magnetic field strength and reaches its maximum value of $\frac{1}{c}\tilde{\alpha}_{13} \approx 0.1 \times 10^{-9}$ s/m at the magnetic coercive field. A 180° phase difference is observed, when the magnetization of the FeCo thin film reverses. Further reduction of the magnetic field strength result in an almost zero value of the converse magnetoelectric constant. The dependence of the converse linear magnetoelectric constant $\frac{1}{c}\tilde{\alpha}_{13}(H)$ on the magnetic field dependence of the magnetization $M(H)$ is further obvious by comparing $\frac{1}{c}\tilde{\alpha}_{13}(H)$ and $M(H)$ hysteresis measurements. Figure 9.13(b) reveals that a finite converse magnetoelectric response was only detected around zero magnetic field, i.e., in the magnetic field range where magnetic domains are expected. This situation is similar to magneto-electric effects observed in laminate structures consisting of thick layers of CoFe_2O_4 as well as NiFe_2O_4 and lead zirconate titanate fabricated by lamination and sintering [105, 456, 756]. However, the strong correlation of the converse linear magnetoelectric constant on the magnetic domain structure confirms the theoretical consideration in Section 9.2.1. Therefore, Figure 9.13(b) suggests that indeed $\alpha_{13}(H)$ is strongly dependent on the magnetic field derivative of the magnetostrictive strain $-\left(\frac{\partial\lambda_{ij}}{\partial H_i}\right)$. Thus, a large value of $\frac{\partial\lambda_{ij}}{\partial H_i}$ is desirable to realize 2-2 type magnetoelectric heterostructures in the case of finite elastic substrate clamping. In the limit of linear response, high values of $\frac{\partial\lambda_{ij}}{\partial H_i}$ might be found in piezomagnetic material systems rather than in magnetostrictive ones [757].

In summary, BaTiO_3 thin film based epitaxial and non-epitaxial multiferroic composite heterostructures were successfully fabricated. While no variation of the magnetization projection along the external magnetic field was observed in epitaxial $\text{Fe}_3\text{O}_4/\text{BaTiO}_3$ multiferroic heterostructures neither at the ferroelastic phase transition of BaTiO_3 nor as a function of any applied electric field, a finite inverse magnetoelastic and converse magnetoelectric effects were detected in non-epitaxial 2-2 type $\text{FeCo}/\text{BaTiO}_3$ heterostructures. However, these effects were only observed in heterostructures based on BaTiO_3 thin films deposited under stoichiometric conditions. Detailed investigations of the manipulation of the magnetization by an electric field in $\text{FeCo}/\text{BaTiO}_3$ heterostructures reveal irreversible magnetic domain effects induced by the converse piezoelectric effect in the BaTiO_3 layer. Furthermore, a finite converse linear magnetoelectric effect was observed, which was found to be strongly magnetic field dependent and therefore mainly based on the magnetic field derivative of the magnetostrictive strain.

9.3 Summary

In summary, 2-2 type multiferroic heterostructures based on BaTiO_3 were investigated in detail in this chapter. To this end, the properties of BaTiO_3 thin films were

examined experimentally and theoretically using molecular dynamics simulations. These simulations revealed a strong dependence of the ferroelectric properties of BaTiO₃ thin films on elastic constraints imposed by the rigid non-ferroelectric substrate. While BaTiO₃ thin films, which are allowed to expand and contract freely, exhibit a bulk like phase diagram, the strong elastic coupling of BaTiO₃ thin films on a rigid substrate on the one hand leads to an increase of the ferroelectric transition temperature and on the other hand to a reduction of the number of the possible ferroelectric phases. Furthermore, the influence of “bad” electrodes, which do not fully screen the ferroelectric depolarization field, were simulated. As a result, the in-plane components of the ferroelectric polarization are expected to exhibit a minor dependence on the quality of the electrodes. In contrast, the out-of-plane component of the polarization is highly affected by imperfect electrodes decomposing into a multi-domain state.

Experimentally, state of the art BaTiO₃ thin films were fabricated by pulsed laser deposition under different oxygen pressures. X-ray diffraction, transmission electron microscopy and atomic force microscopy revealed that these BaTiO₃ thin films deposited on Nb:SrTiO₃ substrates exhibit an excellent crystalline quality as well as a low surface roughness. However, x-ray diffraction measurements suggested the presence of a large amount of oxygen vacancies in BaTiO_{3- δ} thin films fabricated under low oxygen pressure of $p_{\text{O}_2} = 7.5 \times 10^{-3}$ mbar and a gradual relaxation of the misfit strain. In contrast, the values of the lattice parameters and the unit cell volumes of BaTiO₃ thin films using an oxygen pressure of $p_{\text{O}_2} = 1.0 \times 10^{-1}$ mbar during the deposition indicate an almost stoichiometric composition of BaTiO₃. Furthermore, x-ray diffraction line profile analysis revealed a negligible intrinsic strain, which suggest an abrupt strain relaxation within the first monolayers in these BaTiO₃ thin films accompanied with a large density of dislocations. However, an increase of the surface roughness compared to BaTiO_{3- δ} thin films fabricated under low oxygen pressure was detected. The ferroelectric properties of both types of BaTiO₃ thin films disclosed a strong dependence on the oxygen pressure. While oxygen deficient BaTiO_{3- δ} thin films exhibit large leakage currents due to oxygen vacancies, a dielectric dead layer, which is mainly formed by oxidation of the Nb:SrTiO₃ surface, at the interface between the BaTiO₃ thin film and the Nb:SrTiO₃ substrate was found for almost stoichiometric BaTiO₃ thin films.

In the context of BaTiO₃ based 2-2 type multiferroic heterostructures, large converse magnetoelectric effects are expected for BaTiO₃ thin films, which are elastically decoupled from the rigid Nb:SrTiO₃ substrate. On the other hand, a perfect clamping of the overlying ferromagnetic thin film on the BaTiO₃ layer is desirable. The above mentioned results suggest that the former issue is expected to be larger in BaTiO₃ thin films fabricated under almost stoichiometric conditions, since a high density of dislocations within the first monolayers is supposed in these thin films. On the other hand, the improved surface morphology of BaTiO_{3- δ} thin films might enhance the elastic coupling between the ferromagnetic thin film and the BaTiO_{3- δ} layer.

In the second part of this chapter, epitaxial Fe₃O₄/BaTiO₃ thin film heterostructures fabricated using pulsed laser deposition as well as non-epitaxial FeCo/BaTiO₃

thin film structures were discussed. While neither converse magnetoelectric effects nor any magnetoelastic effects were observed in epitaxial $\text{Fe}_3\text{O}_4/\text{BaTiO}_3$ heterostructures, finite changes of the magnetization at the ferroelastic phase transition of BaTiO_3 thin films and converse magnetoelectric effects were found in $\text{FeCo}/\text{BaTiO}_3$ type heterostructures. However, these magnetization variations were only visible in $\text{FeCo}/\text{BaTiO}_3$ heterostructures based on almost stoichiometric BaTiO_3 thin films. This suggests that the elastic coupling between BaTiO_3 thin films fabricated under nominally stoichiometric conditions is indeed incomplete leading to a finite magnetoelectric effect. A detailed analysis of the converse linear magnetoelectric coupling reveals that these effects are largest at the magnetic coercive field and are strongly correlated to strain induced changes of the magnetic domain state. In particular, the magnetic field dependence of the converse linear magnetoelectric coupling was found to be similar to the magnetic field derivative of the magnetostriction strain.

This chapter revealed that a key requirement for larger converse magnetoelectric coupling in further experiments is the elastic decoupling between the piezoelectric layer and the rigid substrate leading to enhanced converse piezoelectric effects.

Chapter 10

Extrinsic multiferroic composite structures: Conclusions and Outlook

The strain-mediated manipulation of the magnetization by an electric field is the focus of the second part of this thesis. To this end, we investigated extrinsic multiferroic composite structures in which two or more submaterials are elastically coupled to each other. Such composites are expected to exhibit large and robust magnetoelectric effects even at room temperature. These effects arise from strain induced crystal deformations of the magnetic layer, which alter the magnetization caused by the inverse effect of magnetostriction. Therefore, the magnetoelectric effect can be described as a product property, converting an applied electric field to strain changes in one constituent, which force variations of the magnetization in the elastically coupled second component. Two different approaches to realize multiferroic composite structures were discussed. Both are based on a 2-2-type horizontal strain-mediated scheme, in which magnetostrictive/piezoelectric structures are fabricated by depositing ferromagnetic thin films onto ferroelectric layers. In the first approach, free-standing hybrid structures were realized by using a bulk ferroelectric substrate (cf. Chapter 8). However, for applications in micro-devices, magnetoelectric thin film heterostructures based on multiferroic composites have to be realized. Therefore, the second approach utilizes the elastic properties of ferroelectric thin films, which were first deposited on a suitable substrate (cf. Chapter 9). In the following, we review our key results, and give an outlook for strain-mediated converse magnetoelectric effects in composite structures.

Summary

The main advantage of extrinsic multiferroic composite structures is the possibility to select and optimize each constituent in order to enhance the desired magnetoelectric coupling (cf. Chapter 7). In particular, the intrinsic upper limit of the magnetoelectric effect in single-phase multiferroic materials, which is given by the geometric mean of the corresponding electric and magnetic susceptibilities (cf. Chapter 3), is overcome in extrinsic multiferroic composites. In this thesis, BaTiO_3 was chosen as ferroelectric material. In BaTiO_3 , (i) linear converse piezoelectric effects and (ii) electric field controlled ferroelastic domain switching cause changes of the

strain state, which allows for a manipulation of the magnetization in the overlying ferromagnetic thin film. Furthermore, (iii) BaTiO₃ exhibits different ferroelastic phases, which can be selected by simply varying the temperature (cf. Section 7.1). For the ferromagnetic constituent, various single crystalline as well as polycrystalline ferromagnetic materials were considered. In addition to well known ferromagnetic materials, such as Fe₃O₄, Ni, and FeCo, the physical properties of Sr₂CrReO₆ films, which are potential candidates for spintronic devices, were studied for the first time (cf. Section 7.2).

One key result of this thesis is based on topic (iii), the phase transitions of BaTiO₃. We used BaTiO₃ substrates to study magnetoelastic effects of different ferromagnetic materials by simply varying the temperature of multiferroic composite hybrid structures (cf. Section 8.1). However, since the magnetic response of FM/BaTiO₃ hybrids is highly dependent on the ferroelastic domain configuration of the BaTiO₃ substrates, a control of these domains in each phase of the BaTiO₃ substrate is essential to describe the experimental results in a quantitative way. Therefore, miscut BaTiO₃ substrates were used to create a well-defined strain state in the multiferroic hybrid structures (cf. Section 8.2). On the basis of these substrates, the magnetoelastic response of ferromagnetic thin films deposited on top were modeled using molecular dynamics simulations in combination with magnetoelastic theory. An excellent agreement between experiment and theory was obtained, confirming the possibility to predict the magnetoelastic response of FM/BaTiO₃ hybrid systems in a quantitative manner. This new approach paves the way to predict the magnetoelastic behavior of new multiferroic hybrids, since the calculations are only based on material constants and the strength of the elastic coupling between both layers (cf. Section 8.3).

These simulations are also applicable to calculate the magnetoelectric responses at a given temperature in multiferroic hybrid structures. As the manipulation of the magnetization by electric fields is a main challenge in today's spintronic applications, converse magnetoelectric effects were investigated at room temperature, i.e., in the tetragonal phase of BaTiO₃, as well as in the orthorhombic phase at 270 K (cf. Section 8.4). In both cases, large changes of the magnetization of up to 40% were observed experimentally. However, while the electrical control of the magnetization in multiferroic hybrids could be well simulated in the tetragonal phase of BaTiO₃ in the context of a two region model, which accounts for the magnetic heterogeneous state created by the simultaneous existence of ferroelastic *a*₂- and *c*-domains in the BaTiO₃ substrate, the asymmetric response as a function of the applied electric field observed in the orthorhombic phase could only be explained qualitatively. Therefore, further experiments are needed to elucidate the converse magnetoelectric response of FM/BaTiO₃ hybrid structures in the orthorhombic phase of BaTiO₃. In contrast, a detailed experimental and theoretical understanding of the magnetic behavior of FM/BaTiO₃ hybrids was developed in the tetragonal phase of BaTiO₃ at 300 K. These experiments, together with the simulation approach, are a second key outcome of this thesis. In particular, it was demonstrated that FM/BaTiO₃ hybrid structures are promising candidates for next-generation multifunctional spintronic devices, since reversible switching between two non-volatile remanent mag-

netic states was demonstrated in experiment.

For commercial multifunctional micro-devices, the realization of thin film heterostructures with finite converse magnetoelectric effects is mandatory. In this spirit, epitaxial and non-epitaxial FM/BaTiO₃ multiferroic 2-2 type heterostructures were fabricated on rigid Nb:SrTiO₃ substrates (cf. Chapter 9). While neither magnetoelastic nor magnetoelectric effects were observed for multiferroic heterostructures based on epitaxial Fe₃O₄ deposited on BaTiO₃ thin films, non-epitaxial FeCo/BaTiO₃ thin film 2-2 type heterostructures revealed finite variations of the magnetization based on reversible and irreversible magnetic domain effects induced by the converse piezoelectric effect of the BaTiO₃ layers. The converse magnetoelectric response does not only show a strong dependence on the properties of the ferromagnetic material, but also on the growth conditions of the BaTiO₃ layer. Multiferroic FeCo/BaTiO₃ heterostructures with BaTiO₃ thin films deposited at a high oxygen pressure of $p_{O_2} = 1.0 \times 10^{-1}$ mbar exhibited a finite magnetoelectric effect, while no magnetoelectric effect was found in FeCo/BaTiO₃ heterostructures built-up from oxygen deficient BaTiO_{3- δ} layers fabricated at $p_{O_2} = 7.5 \times 10^{-3}$ mbar. This might be attributed to two mechanisms. First, the physical properties of BaTiO_{3- δ} degrade in the presence of oxygen vacancies and second, only a gradual relaxation of the mismatch strain was observed in oxygen deficient BaTiO_{3- δ} thin films, while BaTiO₃ thin films fabricated under almost stoichiometric conditions exhibited negligible intrinsic strains, i.e., are fully relaxed. This suggests that the epitaxial strain is relaxed within the first monolayers of BaTiO₃. Therefore, the elastic coupling between the BaTiO₃ thin films deposited at $p_{O_2} = 1.0 \times 10^{-1}$ mbar and the rigid Nb:SrTiO₃ substrate might be reduced due to the presence of a high density of dislocations at the interface. However, a finite elastic coupling is still present, since multiferroic FeCo/BaTiO₃ heterostructures do not behave as a free-standing FM/BaTiO₃ structure. In particular, a strong dependence of the converse linear magnetoelectric effect on the applied magnetic field is evident in experiment. This can be explained by assuming that the converse linear magnetoelectric coupling is a function of the magnetic field derivative of the magnetostriction constant (cf. Section 9.2). Therefore, at magnetic fields larger than the saturation field of the ferromagnet, no magnetoelectric response was measured, while the magnetoelectric coupling was found to be largest around the magnetic coercive field. These measurements disclosed that a converse magnetoelectric coupling is achievable even in multiferroic heterostructures exhibiting elastic constraints due to the rigid substrate.

Conclusions and Outlook

As summarized above, in case of free-standing composite hybrids based on BaTiO₃ substrates large and robust manipulations of the magnetization were achieved as a function of temperature at constant electric field as well as a function of the electric field at constant temperature. However, these effects are mainly caused by modifying the ferroelastic multi-domain state in the BaTiO₃ substrate imposing a heterogeneous magnetic configuration in the overlying ferromagnetic thin film. For further applications, it is necessary to control or avoid this heterogeneous magnetic state.

The former can be, for example, achieved by patterning ferroelectric/ferroelastic domains in the ferroelastic layer [758]. Due to magnetoelastic coupling of the overlying ferromagnetic thin film, an electrically controlled magnetic domain pattern might be realized within this method. By considering domain wall scattering in such systems, sharp resistivity changes are expected in the ferromagnetic layer due to the presence and absence of electrically controlled magnetic domain walls, which could be exploited in memory devices [759]. On the other hand, switching of ferroelastic domains from one single-domain state to another single-domain state in the ferroelastic layer circumvents electrically driven magnetic inhomogeneities in the overlying ferromagnetic thin film, since a homogeneous strain state is imposed into the ferromagnetic thin film. For example, ferroelastic a -domains can switch to c -domains via electric fields in BaTiO₃. But not every a -domain can recover its position in the absence of the electric field once it was switched into a c -orientation [760]. Furthermore, a preferential elongation direction in the plane of the ferromagnetic thin film is needed to switch the magnetization in the film plane. Therefore, the realization of ferroelastic single-domain switching from, for example, a_1 - to c -domains and back is demanding in bulk BaTiO₃. However, in Section 8.5, a practicable concept for further experiments on non-volatile and persistent electrical control of magnetization reorientations was given on the basis of ferroelectric (011) oriented $[\text{Pb}(\text{Mg}_{1/3}\text{Nb}_{2/3})\text{O}_3]_{1-x}[\text{PbTiO}_3]_x$ crystals. This example furthermore demonstrates that ferromagnetic/ferroelectric hybrid structures are indeed a viable approach for non-volatile memory devices.

The electrical control of the remanent magnetization orientation in spintronic devices is only one example of potential applications of multiferroic composites. Hybrids that exhibit large magnetoelectric effects at room temperature with low power consumption are further capable for a range of technological applications, such as current sensors, microwave devices, resonators, transducers, filters or phase shifters (see Refs. [21, 425, 443, 450] and references therein). In particular, multiferroic multilayer ceramic capacitors are very promising in the field of magnetic field sensors, due to their low cost [668, 761]. In addition, multiferroic composite hybrids can be used for harvesting magnetic and mechanical energy [762, 763]. This is of great importance, since the generation and storage of energy will be one of the most pressing technological challenges in the future. Furthermore, in recent years, left-handed materials have become an exciting subject in the field of fundamental research due to their unique electromagnetic properties including negative phase velocity and negative refraction [764]. Such materials can be realized by multiferroic composite hybrids, which allows to electrically and magnetically tune the left-handed transition in such devices [106, 765].

Although multiferroic composites are, in principle, ready for practical applications, the following important issues remain to be solved [425]:

First, as the magnetoelectric interaction of strain-mediated multiferroic composite structures is induced across the interface, a good elastic contact with effective strain transfer between the magnetostrictive and piezoelectric layer is a prerequisite for high magnetoelectric effects. Therefore, the deposition process of the magnetostrictive thin film on the piezoelectric layer is a key issue. By choosing suitable ferroelectric

and magnetic materials, a reduction of crystalline defects such as dislocations can be obtained in the case of pseudomorphic growth. In this limit, the coupling constant k^c as defined in Chapter 6 should be close to 1.

Second, a clear fatigue behavior was observed in FM/BaTiO₃ hybrid structures, which reduces the converse magnetoelectric response of the hybrid structure as a function of the number of electrical cycles (cf. Section 8.3). This can be attributed to two effects. First, mechanical fatigue can occur in the BaTiO₃ crystal, which diminishes the converse piezoelectric strain, and second, the elastic coupling of the ferromagnetic thin film on the BaTiO₃ substrate might be reduced due to the formation of crystalline defects. In contrast to ferroelectric fatigue effects, there is a lack in the understanding of mechanical fatigue, which is of particular technological importance [425].

Third, to ensure scalability of possible memory devices based on strain-mediated multiferroic hybrids, large and robust magnetoelectric effects are essential even if the lateral size of the memory cell is reduced below 1 μm . Therefore, it will be important to investigate to which extent possible size effects affect the magnetoelectric response [21].

Fourth, the frequency dependence and the dynamics of the magnetoelectric coupling is another important issue in multiferroic composites [21]. Since the magnetoelectric coupling is mediated by strain in these systems, an enhancement of the magnetoelectric response is expected, when the frequency of the driving field is tuned close to the resonance phenomena of the system, such as the electromechanical and ferromagnetic resonances [450]. Moreover, theoretical calculations predict a giant magnetoelectric effect, if the frequencies of the electromechanical and ferromagnetic resonances overlap, i.e., at the magnetoacoustic resonance [766]. However, this is yet to be verified. In the past, various studies on the frequency dependence of the magnetoelectric coupling were based on laminate structures, i.e., bonded bilayers with micrometer thicknesses [450], but only few reports are available on the high-frequency dependence of the magnetoelectric response in composite hybrids or heterostructures up to now [767–770]. However, epitaxial composite hybrids and heterostructures are critically important in particular for future high-frequency device applications.

Today's memory devices exhibit a memory cell array formed on a suitable substrate. Therefore, the realization of the strain-mediated concept of ferromagnetic/ferroelectric hybrid structures in thin film form is mandatory. Chapter 9 revealed that the converse magnetoelectric effect in ferromagnetic/ferroelectric thin film heterostructures strongly depends on the degree of elastic decoupling of the piezoelectric layer and the substrate. Therefore, we address different possibilities to enhance the elastic release from the stiff substrate in the following.

The most obvious method of increasing the converse piezoelectric effect of the piezoelectric layer is to release it from the stiff substrate using etching techniques or focused ion beam milling [752, 771]. However, the fabrication of free-standing structures is not appropriate for low cost, high density memory devices. Furthermore, since the passive region is still clamped to the substrate, bending of the heterostructure occurs at the active region, which induces inhomogeneous strain into

the overlying magnetostrictive thin film. Another possibility to reduce the elastic constraint on the piezoelectric layer is to deposit a buffer layer on the substrate first. This buffer layer can release the misfit strain due to the formation of crystal defects and act as a bottom electrode in multiferroic heterostructures [21]. Furthermore, using $\text{PbZr}_x\text{Ti}_{1-x}\text{O}_3$ as piezoelectric material, an enhanced piezoelectric response can be obtained by fabricating a $\text{PbZr}_x\text{Ti}_{1-x}\text{O}_3$ bilayer comprised of a tetragonal layer with $x = 0.3$ deposited on top of a rhombohedral layer with $x = 0.7$. The resulting ferroelastic domain arrangement in the tetragonal layer is more tethered to the Zr-rich rhombohedral layer than to the stiff substrate, which results in a three times larger piezoelectric response compared to constrained single-layered $\text{PbZr}_x\text{Ti}_{1-x}\text{O}_3$ thin films [772]. Further decrease of the clamping between the piezoelectric layer and the substrate can be achieved by fabricating magnetoelectric elements with lateral dimensions of less than $10\ \mu\text{m}$ [773].

The above described methods are different possibilities to enhance the converse piezoelectric effect of the piezoelectric layer, which should lead to finite magneto-electric effects in 2-2 type multiferroic heterostructures. However, a complete elastic decoupling of the piezoelectric layer from the rigid substrate is difficult to achieve in experiment. Therefore, the imposed in-plane strain might not be sufficient to realize large magnetization reorientations in the overlying ferromagnetic thin film. Nevertheless, using pseudomorphic growth of the ferromagnetic layer, the misfit strain between the ferromagnetic and the piezoelectric material can be tailored such that the elastic energy is equal to the demagnetization energy of the ferromagnetic thin film. At this critical misfit strain, the magnetization orientation can largely be influenced by an additionally imposed strain stemming from the converse piezoelectric effect of the piezoelectric layer. If the total in-plane strain is enhanced the magnetization rotates perpendicular to the film surface, while a reduction of the in-plane strain state relative to the misfit strain forces the magnetization to stay in the plane of the ferromagnetic film.¹ Therefore, switching of the magnetization from an in-plane direction to the out-of-plane direction might be achieved in 2-2 type multiferroic heterostructures even in the presence of substantial substrate clamping [774, 775]. However, if the magnetic thin film exhibits a preferential direction of the magnetization in the film plane, a magnetic multi-domain state occurs while the magnetization is reoriented from the out-of-plane to the in-plane direction. Thus, reorientation of the remanent magnetization of a single domain state takes only place for magnetically isotropic materials. Therefore, even in the case of 2-2 type multiferroic heterostructures, switching of the magnetization on the basis of magnetoelastic effects seems to be possible by engineering the material properties of the magnetostrictive and piezoelectric layers.

In conclusion, the study of layered composite multiferroics presented in the second part of this thesis shows strong and persistent converse magnetoelectric effects. Moreover, a better understanding of the physical mechanisms is derived not only experimentally but also theoretically. This could prove very useful for future applications in the field of spintronic devices.

¹We here assume ferromagnetic thin films exhibiting a magnetization, which lies in the film plane for vanishing external fields and strain.

Appendix A

Multiferroic double perovskite $\text{Bi}_2\text{CrFeO}_6$ thin films

In searching for new multiferroic compounds exhibiting a strong ferroelectric and ferromagnetic polarization, Bi containing double perovskites $\text{Bi}_2\text{BB}'\text{O}_6$ have received renewed interest. In particular, recent attention has focused on $\text{Bi}_2\text{CrFeO}_6$, as an enhanced magnetism and multiferroic behavior at room temperature was reported [412, 413]. However, theory calculations [417] as well as studies on thin films [415] and bulk samples [416] are in contradiction to these findings. To investigate this controversy, the magnetic properties of $\text{Bi}_2\text{CrFeO}_6$ thin films were examined during this thesis.

In the double perovskite structure $A_2\text{BB}'\text{O}_6$, the transition metal ions B and B' occupy the octahedral site alternately along the [111] direction resulting in a rock-salt lattice (cf. Figs. A.1(a) and (b)). This can be exploited to artificially fabricate double perovskites by alternately growing ABO_3 and $\text{AB}'\text{O}_3$ unit cell layers. As an example, a ferromagnetic spin order was realized in LaCrO_3 - LaFeO_3 superlattices by employing this technique [776]. In the course of this thesis, $\text{Bi}_2\text{CrFeO}_6$ thin films were fabricated on SrRuO_3 -buffered as well as directly on (111) oriented $\text{Nb}:\text{SrTiO}_3$ substrates. Since the above described method failed to realize $\text{Bi}_2\text{CrFeO}_6$ thin films, the results, which are discussed in the following, are based on thin films grown by pulsed laser deposition using a single stoichiometric $\text{Bi}_{2.4}\text{CrFeO}_6$ target.

One crucial parameter of double perovskites is the B/B' order, since antisite defects significantly can alter the physical properties (cf. Section 7.2.2). In principle, the $\text{ABO}_3/\text{AB}'\text{O}_3$ sublattice order is strongly dependent on the difference of the ionic charges and the ionic radii of the B and B' cations. Since, Cr^{3+} and Fe^{3+} have very similar ionic radii [233], a spontaneous ordering is not expected for thin films fabricated from a single $\text{Bi}_{2.4}\text{CrFeO}_6$ target. However, Fig. A.1(c) reveals a superstructure peaks at $(0.5\ 0.5\ 0.5)_{\text{pc}}$, which is caused by the alternating ordering of the $\text{BiCrO}_3/\text{BiFeO}_3$ sublattices along the pseudo-cubic $[111]_{\text{pc}}$ direction. The spontaneous ordering was found to be highly dependent on the deposition parameters, in analogy to the recent publication on the fabrication of $\text{La}_2\text{CrFeO}_6$ [620]. However, since the deposition window of the fabrication of single-phase Bi containing perovskite-like thin films is narrow (cf. Fig. 4.2), a detailed investigation of this issue could not be carried out. Parasitic phases were formed easily when the deposition parameters differed slightly from those which were found optimal for the growth of BiFeO_3 and BiCrO_3 thin films.

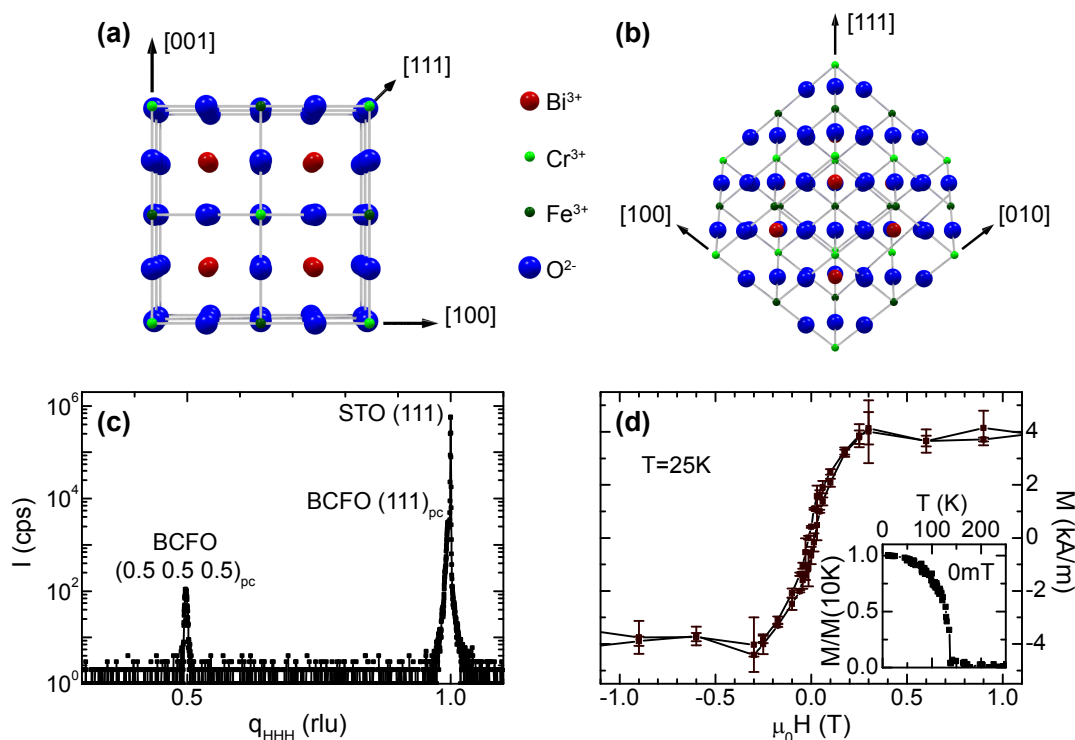


Figure A.1: Schematic illustration of the double perovskite $\text{Bi}_2\text{CrFeO}_6$ crystal structure in a cubic $Fm\bar{3}m$ symmetry along the (a) [001] and (b) [111] direction. (c) X-ray diffraction of a 20 nm thick $\text{Bi}_2\text{CrFeO}_6$ (BCFO) film fabricated on a (111) oriented Nb:SrTiO₃ substrate with $q_H = q_K = q_L$. The finite intensity observed at the pseudo-cubic reflection BCFO $(0.5\ 0.5\ 0.5)_{pc}$ indicates a finite ordering of the BiCrO₃/BiFeO₃ sublattices. (d) The magnetic hysteresis loop measured at $T = 25\text{ K}$ reveals a saturation magnetization of about 4 kA/m. The normalized remanent magnetization versus temperature is shown in the inset.

The magnetic properties of a 20 nm thick $\text{Bi}_2\text{CrFeO}_6$ film is depicted in Fig. A.1(d). A ferromagnetic behavior with a saturation magnetization of around 4 kA/m, which is slightly larger than in single BiFeO₃ and BiCrO₃ thin films (cf. Figs. 4.20 and 4.40), was found in this thin film. Therefore, the results reported by Nechache and coworkers [412], who found an enhanced magnetism with a saturation magnetization of around 15 kA/m in epitaxial BiFeO₃/BiCrO₃ heterostructures, could not be confirmed in our measurements. Furthermore, the temperature dependence of the remanent magnetization depicted in the inset of Fig. A.1(d) revealed a magnetic transition temperature of around 150 K. Thus, these measurements suggest that a room temperature multiferroic behavior in $\text{Bi}_2\text{CrFeO}_6$ is unlikely, which is in agreement with by theory calculations [417].

Appendix B

Modeling of magnetization hysteresis in ferromagnetic materials

There have been many efforts in the past to develop analytical models to analyze the magnetization reversal process in ferromagnetic materials. The most successful models are summarized in Refs. [777, 778]. We here use a macrospin model, which is known as the Stoner-Wohlfarth model [779]. This is the simplest method that is adequate enough to describe the physics of ferromagnetic materials exhibiting a single domain state. In this limit, the constant exchange energy forces all spins to align parallel to each other, i.e., the magnetization does not vary in space and is homogeneous throughout the sample. Therefore, the minimum of the Gibbs free energy density $\tilde{g}^{(m)}$, which determines the magnetization direction m_i , does not depend on the exchange energy and is only a function of the magnetic anisotropy $u_{\text{ani}}^{(m)}$, the elastic energy $u_{\text{el}}^{(m)}$, the magnetoelastic contribution $u_{\text{magel}}^{(m)}$, the demagnetization energy $u_{\text{demag}}^{(m)}$, and the external magnetic field H_i (see Section 6.2). As an example, the magnetic field dependence of the magnetization of a polycrystalline Ni thin film under a strain state of

$$\epsilon^{\text{Ni}} = \begin{pmatrix} -0.0005 & 0 & 0 \\ 0 & 0.0012 & 0 \\ 0 & 0 & -0.0004 \end{pmatrix}$$

can be described within this model.¹ The projection of the magnetization along the direction of the external magnetic field, which is aligned along the \mathbf{y} -direction, obtained by SQUID magnetometry is depicted in Fig. B.1(a). Since the equilibrium orientation of the magnetization \mathbf{m} is given by the minimum of the Gibbs free energy density $\tilde{g}^{(m)}$, the magnetization component along the \mathbf{y} -direction $M_2 = M_s \cdot m_2$ can be calculated within the film plane (cf. red solid line in Fig. B.1(a)). The Gibbs free energy density $\tilde{g}^{(m)}$ contours normalized to the saturation magnetization M_s of 400 kA/m, which is determined by SQUID magnetometry and shown in Fig. B.1(b) reveals that the direction of the magnetization indicated by red full circles follows the global minimum of the free energy density upon decreasing the magnetic field strength from +50 mT to -50 mT. Therefore, the magnetization reversal can be

¹A standard Cartesian coordinate system is used throughout this example.

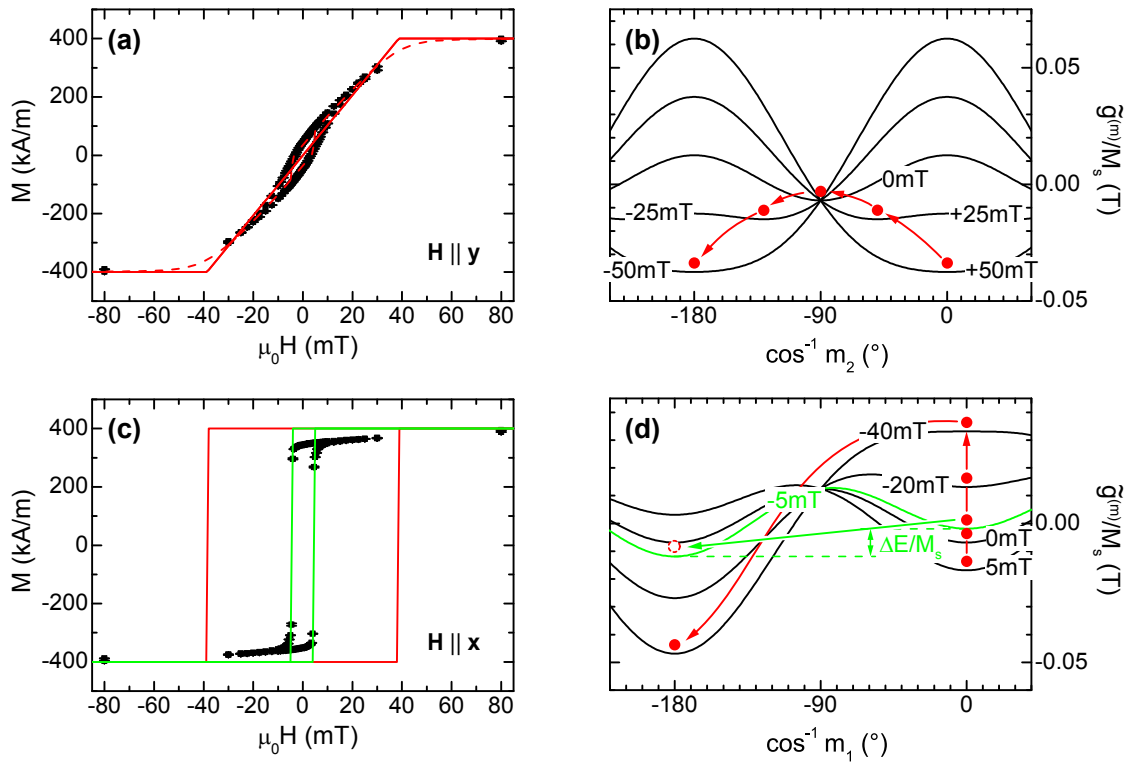


Figure B.1: (a), (c) Experimental results (black full symbols) obtained by SQUID magnetometry and simulation (solid lines) derived on the basis of a macrospin model for the magnetization reversal of a Ni thin film under a certain strain state. The magnetic field was applied either along the (a) y -direction or (c) x -direction. The corresponding Gibbs free energy density $\tilde{g}^{(m)}$ contours for different magnetic field strengths as a function of the magnetization direction m_2 and m_1 are depicted in (b) and (d), respectively. The local minima of $\tilde{g}^{(m)}$, which determine the magnetization direction, are marked by red full circles in case of a coherent spin rotation process. The incoherent spin switching process, which results in the magnetic hysteresis displayed by the green line in (c), is denoted by the green arrow in (d).

described as a *coherent spin rotation* process. Note that the agreement between simulation and experiment can be improved even more by assuming a misalignment of 5° of the external magnetic field with respect to the y -direction of the sample (cf. red dashed line in Fig. B.1(a)).

However, in contrast to $H \parallel y$, the magnetic field dependence of the magnetization obtained with the external magnetic field applied along the x -direction (Fig. B.1(c)) can only be explained by considering *incoherent spin switching* around the coercive magnetic fields in addition to *coherent spin rotation*. Omitting *incoherent spin switching*, the orientation of the magnetization m_1 follows the local minimum of the Gibbs free energy density at 0° as the magnetic field strength is decreased from 5 mT to -40 mT (cf. Fig. B.1(d)). As apparent from Fig. B.1(d), a coherent spin switching takes place at -40 mT due to the appearance of an inflection point in the Gibbs free energy density at $m_2 = 1$. This process results in a magnetic hysteresis $M(H)$ (cf. red line in Fig. B.1(c)) exhibiting a coercive field, which is largely overestimated

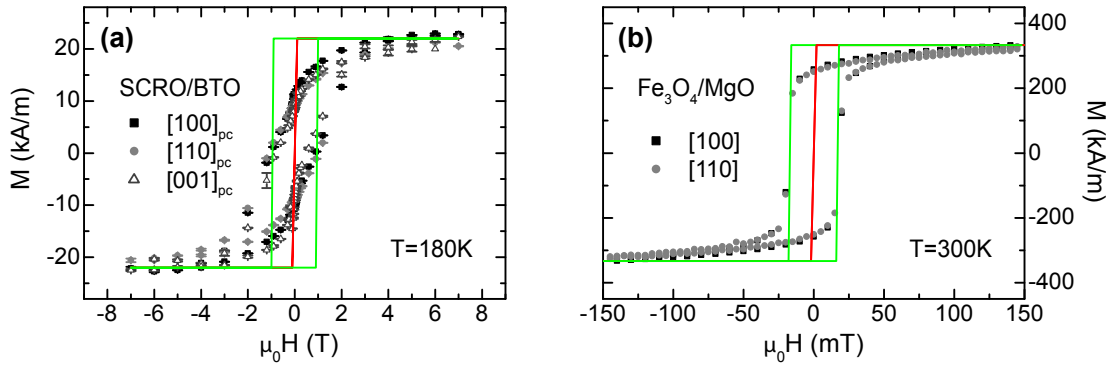


Figure B.2: Magnetic field dependence of a (a) $\text{Sr}_2\text{CrReO}_6/\text{BaTiO}_3$ hybrid system as well as a (b) Fe_3O_4 thin film deposited on a MgO substrate. The similar magnetic response on magnetic fields applied along different directions (open and closed symbols) demonstrates a magnetic isotropic behavior of $\text{Sr}_2\text{CrReO}_6/\text{BaTiO}_3$ structures in the rhombohedral phase of BaTiO_3 at 180 K as well as negligible in-plane anisotropy for Fe_3O_4 thin films on MgO substrates. Employing the method of incoherent magnetization switching, the experimentally observed finite coercive field can be simulated (green solid line), while no coercive field is obtained in the limit of coherent spin switching (red solid line). The experimental data in (b) are taken from the PhD thesis of Andrea Nielsen[?].

compared to the experimental value. This evidently shows that additional effects should be considered, such as domain nucleation and expansion. The formation energy of domain walls can be described by a surface energy, which is a function of the anisotropy energy density, the exchange integral, the spin quantum number, and the lattice parameter [460, 780]. For iron or nickel, this energy is of the order of $0.1 - 0.2 \mu\text{J}/\text{cm}^2$ [780, 781]. Now, considering the movement of a 180° domain of surface area A through a distance Δx , the energy loss can be calculated by $\Delta E^{(p)} = nE_p A \Delta x$, where E_p is the pinning energy per unit volume and n denotes the number of pinning sites [782]. This movement results in a change of the magnetic moment by $\Delta m = 2M_s A \Delta x$. Therefore, the change of the Gibbs free energy density results in $\Delta g^{(p)} = \frac{nE_p}{2M_s} \Delta M = q \Delta M$, where q is a microstructural parameter proportional to the pinning site density and to the pinning energy [777]. Within this context, the magnetization reversal of the Ni thin film depicted in Fig. B.1(c) takes place at an external magnetic field of -5 mT , due to *incoherent magnetization switching*. At this magnetic field strength, the energy difference $\Delta E/M_s = 10 \text{ mT}$ of the local minimum located at 0° and the global free energy density minimum is larger than the energy needed to create and unpin magnetic domain walls. Therefore, domains are formed and expand rapidly throughout the sample, until a final state is reached, which can again be described in the context of a macrospin model [780]. In our calculation the energy barrier $\Delta E/M_s$ is taken as a free parameter to reproduce the experimentally obtained magnetic switching fields. This energy barrier is determined for each thin film by either measuring the magnetic hysteresis characteristic $M(H)$ (cf. Fig. 8.4) or by determining the angular dependence of the magnetization for positive and negative rotational direction of the magnetic field (cf. Fig. 8.17) and is

taken as a constant value. However, this is only a first approximation, since $\Delta E/M_s$ is expected to be a function of the applied magnetic field as well as the imposed strain state [783].

Figure B.2 shows two examples of determining the energy barrier $\Delta E/M_s$. For the $\text{Sr}_2\text{CrReO}_6/\text{BaTiO}_3$ hybrid structure, a magnetically isotropic behavior has been found in the rhombohedral phase of BaTiO_3 at 180 K (see Fig. B.2(a)). In the limit of coherent spin switching, no hysteresis is expected in this case (cf. red line in Fig. B.2(a)). To account for the finite coercive fields, the described method of incoherent magnetization switching using an energy barrier of $\Delta E/M_s = 0.9 \text{ T}$ has been applied (cf. green line in Fig. B.2(a)). This value is used to simulate the magnetic hysteresis shown in Fig. 8.4. The second example deals with Fe_3O_4 based thin films. Since Fe_3O_4 thin films on BaTiO_3 substrates exhibit a pronounced magnetic anisotropy in the whole measured temperature range of $180 \text{ K} < T < 390 \text{ K}$, the nearly isotropic magnetic in-plane behavior of Fe_3O_4 thin films fabricated on MgO substrates is used to determine the energy barrier $\Delta E/M_s$ (see Fig. B.2(b)). In this case, a value of $\Delta E/M_s = 32 \text{ mT}$ is obtained. Using this value, Section 8.4.1 demonstrates that the magnetic reversal in $\text{Fe}_3\text{O}_4/\text{BaTiO}_3$ hybrid structures can only be described qualitatively, which can mainly be attributed to additional pinning centers in Fe_3O_4 thin films deposited on BaTiO_3 substrates.

List of publications

- A. Brandlmaier, S. Geprägs, M. S. Brandt, R. Gross, and S. T. B. Goennenwein, *Towards voltage-controlled nonvolatile magnetization switching*, in preparation for publication.
 - A. Brandlmaier, M. Brasse, S. Geprägs, M. Weiler, R. Gross, and S. T. B. Goennenwein, *Magneto-optical imaging of voltage-controlled magnetization reorientation*, submitted for publication (2011).
17. A. Brandlmaier, S. Geprägs, G. Woltersdorf, R. Gross, and S. T. B. Goennenwein, *Nonvolatile, reversible electric-field controlled switching of remanent magnetization in multifunctional ferromagnetic/ferroelectric hybrids*, Journal of Applied Physics **110**, 043913 (2011).
 16. M. Opel, S. Geprägs, E. P. Menzel, A. Nielsen, D. Reisinger, K.-W. Nielsen, A. Brandlmaier, F. D. Czeschka, M. Althammer, M. Weiler, S. T. B. Goennenwein, J. Simon, M. Svete, W. Yu, S.-M. Hühne, W. Mader, and R. Gross, *Novel multifunctional materials based on oxide thin films and artificial heteroepitaxial multilayers*, Physica Status Solidi A **208**, 232 (2011).
 15. S. Geprägs, A. Brandlmaier, M. Opel, R. Gross, and S. T. B. Goennenwein, *Electric field controlled manipulation of the magnetization in Ni/BaTiO₃ hybrid structures*, Applied Physics Letters **96**, 142509 (2010).
 14. F. Czeschka, S. Geprägs, M. Opel, S. T. B. Goennenwein, and R. Gross, *Giant magnetic anisotropy changes in Sr₂CrReO₆ thin films on BaTiO₃*, Applied Physics Letters **95**, 062508 (2009).
 13. S. Geprägs, F. Czeschka, M. Opel, S. T. B. Goennenwein, W. Yu, W. Mader, and R. Gross, *Epitaxial growth and magnetic properties of Sr₂CrReO₆ thin films*, Journal of Magnetism and Magnetic Materials **321**, 2001 (2009).
 12. D. Venkateshvaran, M. Althammer, A. Nielsen, S. Geprägs, M. S. Ramachandra Rao, S. T. B. Goennenwein, M. Opel, and R. Gross, *Epitaxial Zn_xFe_{3-x}O₄ thin films: A spintronic material with tunable electrical and magnetic properties*, Physical Review B **79**, 134405 (2009).
 11. M. Weiler, A. Brandlmaier, S. Geprägs, M. Althammer, M. Opel, C. Bihler, H. Huebl, M. S. Brandt, R. Gross, and S. T. B. Goennenwein, *Voltage controlled inversion of magnetic anisotropy in a ferromagnetic thin film at room temperature*, New Journal of Physics **11**, 013021 (2009).

10. C. Bihler, M. Althammer, A. Brandlmaier, S. Geprägs, M. Weiler, M. Opel, W. Schoch, W. Limmer, R. Gross, M. S. Brandt, and S. T. B. Goennenwein, *Ga_{1-x}Mn_xAs/piezoelectric actuator hybrids: A model system for magnetoelastic magnetization manipulation*, Physical Review B **78**, 045203 (2008).
9. A. Brandlmaier, S. Geprägs, M. Weiler, A. Boger, M. Opel, H. Huebl, C. Bihler, M. S. Brandt, B. Botters, D. Grundler, R. Gross, and S. T. B. Goennenwein, *In situ manipulation of magnetic anisotropy in magnetite thin films*, Physical Review B **77**, 104445 (2008).
8. S. T. B. Goennenwein, M. Althammer, C. Bihler, A. Brandlmaier, S. Geprägs, M. Opel, W. Schoch, W. Limmer, R. Gross, and M. S. Brandt, *Piezo-voltage control of magnetization orientation in a ferromagnetic semiconductor*, Physica Status Solidi (RRL) **2**, 96 (2008).
7. S. Geprägs, M. Opel, S. T. B. Goennenwein, and R. Gross, *Multiferroic materials based on artificial thin film heterostructures*, Philosophical Magazine Letters **87**, 141 (2007).
6. S. Geprägs, P. Majewski, R. Gross, C. Ritter, and L. Alff, *Electron doping in the double perovskite La_xA_{2-x}CrWO₆ with A=Sr and Ca*, Journal of Applied Physics **99**, 08J102 (2006).
5. P. Majewski, S. Geprägs, O. Sanganas, M. Opel, R. Gross, F. Wilhelm, A. Rogalev, and L. Alff, *X-ray magnetic circular dichroism study of Re 5d magnetism in Sr₂CrReO₆*, Applied Physics Letters **87**, 202503 (2005).
4. P. Majewski, S. Geprägs, A. Boger, M. Opel, A. Erb, R. Gross, G. Vaitheeswaran, V. Kanchana, A. Delin, F. Wilhelm, A. Rogalev, and L. Alff, *Magnetic moments of W 5d in Ca₂CrWO₆ and Sr₂CrWO₆ double perovskites*, Physical Review B **72**, 132402 (2005).
3. P. Majewski, S. Geprägs, A. Boger, M. Opel, L. Alff, and R. Gross, *Epitaxial growth of electron doped double perovskites La_xA_{2-x}CrWO₆ with A = Sr and Ca*, Journal of Magnetism and Magnetic Materials **290**, 1154 (2005).
2. N. Rama, M. S. Ramachandra Rao, V. Sankaranarayanan, P. Majewski, S. Geprägs, M. Opel, and R. Gross, *A-site-disorder-dependent percolative transport and Griffiths phase in doped manganites*, Physical Review B **70**, 224424 (2004).
1. J. B. Philipp, P. Majewski, D. Reisinger, S. Geprägs, M. Opel, A. Erb, L. Alff, and R. Gross, *Magneto-resistance and magnetic properties of the double perovskites*, Acta Physica Polonica A **105**, 7 (2004).

Acknowledgements

Finally, I would like to thank all the people who supported me and gave their important contributions to this work:

- Prof. Dr. Rudolf Gross for giving me the opportunity to work in the magnetism group of the WMI and for his support at all stages of my scientific work. The stimulating discussions and his deep physical knowledge were always very helpful.
- Dr. Matthias Opel and Dr. habil. Sebastian T. B. Gönnerwein for their supervision and kind help. They always provided me with valuable ideas and helpful comments. I am also grateful for their careful reading of my thesis and many great moments during various different conferences.
- Andreas Brandlmaier, for sharing all the up's and down's during this thesis. I am grateful for the true friendship we have.
- All the diploma students for their great work and contributions to this study (in order of appearance): Oliver Sanganas, Franz Czeschka, Mathias Weiler, Matthias Althammer, Daniel Pantel, Matthias Brasse, and Michael Wagner.
- The current and former Ph.D. colleagues in the magnetism group, in particular: Matthias Althammer, Andreas Brandlmaier, Franz Czeschka, Johannes Lotze and Mathias Weiler.
- All the current office mates Prof. Dr. B. S. Chandrasekhar, Hans-Martin Eiter, and Florian Kretzschmar for the great atmosphere. In particular, the discussions with Prof. Dr. B. S. Chandrasekhar helped me to keep my investigations focused on the key aspects of magnetoelectric multiferroics.
- Thomas Brenninger for his professional support on all technical issues, making impossible things possible. I enjoyed working with you a lot.
- The WMI workshop staff, in particular Robert Müller and Helmut Thies, for doing an outstanding job in fabricating numerous newly designed components.
- Dr. habil. Andreas Erb for helping me in fabricating polycrystalline samples.
- The whole WMI staff for their great support regarding all aspects of scientific work as well as the friendly working atmosphere.
- Prof. Dr. Martin S. Brandt and his group for all the useful discussions in the Walt(h)er seminar.

- Dr. Dan Mannix for the great time during the measurement periods at the ESRF and the Diamond light source.
- Prof. Dr. L. Eng, Prof. Dr. C. Loppacher-Voirol, Dr. Denny Köhler for the PFM and MFM investigations of our samples.
- Prof. Dr. W. Mader, Sven-Martin Hühne, Matthias Svete, and Dr. Wentao Yu for the TEM studies.
- My friends for their unlimited support.
- I am deeply grateful to my parents, who have always supported and encouraged me in all imaginable situations.
- Finally, and most of all, I would like to thank my wife for her continuous encouragement, patience, and love. I dedicate this thesis to you and our beloved daughter Sarah Katharina.

Bibliography

- [1] H. Schmid, *Ferroelectrics* **252**, 41 (2001).
- [2] J. F. Scott, *Nat. Mater.* **6**, 256 (2007).
- [3] M. Gajek, M. Bibes, S. Fusil, K. Bouzehouane, J. Fontcuberta, A. Barthelemy, and A. Fert, *Nat. Mater.* **6**, 296 (2007).
- [4] F. Yang, M. H. Tang, Z. Ye, Y. C. Zhou, X. J. Zheng, J. X. Tang, J. J. Zhang, and J. He, *J. Appl. Phys.* **102**, 044504 (2007).
- [5] M. Dawber, K. M. Rabe, and J. F. Scott, *Rev. Mod. Phys.* **77**, 1083 (2005).
- [6] J. F. Scott, *Science* **315**, 954 (2007).
- [7] A. Ney, C. Pampuch, R. Koch, and K. H. Ploog, *Nature* **425**, 485 (2003).
- [8] W. Eerenstein, N. D. Mathur, and J. F. Scott, *Nature* **442**, 759 (2006).
- [9] M. Bibes and A. Barthelemy, *Nat. Mater.* **7**, 425 (2008).
- [10] W. Cao, H. H. Cudney, and R. Waser, *Proc. Natl. Acad. Sci.* **96**, 8330 (1999).
- [11] W. F. Brown, R. M. Hornreich, and S. Shtrikman, *Phys. Rev.* **168**, 574 (1968).
- [12] R. Ramesh, *Nature* **461**, 1218 (2009).
- [13] G. Catalan and J. F. Scott, *Adv. Mater.* **21**, 2463 (2009).
- [14] N. A. Spaldin, S.-W. Cheong, and R. Ramesh, *Phys. Today* **63**, 38 (2010).
- [15] H. Béa, M. Gajek, M. Bibes, and A. Barthélémy, *J. Phys.: Condens. Matter* **20**, 434221 (2008).
- [16] H. Béa and P. Paruch, *Nat. Mater.* **8**, 168 (2009).
- [17] J. Hu, Z. Li, Y. H. Lin, and C. W. Nan, *Phys. Stat. Sol. (RRL)* **4**, 106 (2010).
- [18] R. Thomas, J. F. Scott, D. N. Bose, and R. S. Katiyar, *J. Phys.: Condens. Matter* **22**, 423201 (2010).
- [19] N. A. Hill, *J. Phys. Chem. B* **104**, 6694 (2000).
- [20] W. Eerenstein, M. Wiora, J. L. Prieto, J. F. Scott, and N. D. Mathur, *Nat. Mater.* **6**, 348 (2007).

- [21] J. Ma, J. Hu, Z. Li, and C.-W. Nan, *Adv. Mater.* **23**, 1061 (2011).
- [22] H. Schmid, *J. Phys.: Condens. Matter* **20**, 434201 (2008).
- [23] N. A. Spaldin and M. Fiebig, *Science* **309**, 391 (2005).
- [24] A. Brandlmaier, *Magnetization control in multifunctional devices*, Ph.D. thesis, Technische Universität München (2011).
- [25] S. Cheong and M. Mostovoy, *Nat. Mater.* **6**, 13 (2007).
- [26] T. Kimura, T. Goto, H. Shintani, K. Ishizaka, T. Arima, and Y. Tokura, *Nature* **426**, 55 (2003).
- [27] D. Lebeugle, D. Colson, A. Forget, and M. Viret, *Appl. Phys. Lett.* **91**, 022907 (2007).
- [28] Fujitsu, Press Release 2 (2006).
- [29] D. Lebeugle, D. Colson, A. Forget, M. Viret, A. M. Bataille, and A. Gukasov, *Phys. Rev. Lett.* **100**, 227602 (2008).
- [30] S. Lee, W. Ratcliff, II, S.-W. Cheong, and V. Kiryukhin, *Appl. Phys. Lett.* **92**, 192906 (2008).
- [31] S. Lee, T. Choi, W. Ratcliff, R. Erwin, S.-W. Cheong, and V. Kiryukhin, *Phys. Rev. B* **78**, 100101 (2008).
- [32] J. Wang, J. B. Neaton, H. Zheng, V. Nagarajan, S. B. Ogale, B. Liu, D. Viehland, V. Vaithyanathan, D. G. Schlom, U. V. Waghmare, N. A. Spaldin, K. M. Rabe, M. Wuttig, and R. Ramesh, *Science* **299**, 1719 (2003).
- [33] N. A. Hill, P. Battig, and C. Daul, *J. Phys. Chem. B* **106**, 3383 (2002).
- [34] D. H. Kim, H. N. Lee, M. Varela, and H. M. Christen, *Appl. Phys. Lett.* **89**, 162904 (2006).
- [35] J. C. Wojdeł and J. Íñiguez, *Phys. Rev. Lett.* **103**, 267205 (2009).
- [36] C. Darie, C. Goujon, M. Bacia, H. Klein, P. Toulemonde, P. Bordet, and E. Suard, *Solid State Sci.* **12**, 660 (2010), international Symposium on Structure-Property Relationships in Solid-State Materials.
- [37] C. Goujon, C. Darie, M. Bacia, H. Klein, L. Ortega, and P. Bordet, *J. Phys.: Conf. Ser.* **121**, 022009 (2008).
- [38] H. Béa, M. Bibes, A. Barthélémy, K. Bouzehouane, E. Jacquet, A. Khodan, J.-P. Contour, S. Fusil, F. Wyczisk, A. Forget, D. Lebeugle, D. Colson, and M. Viret, *Appl. Phys. Lett.* **87**, 072508 (2005).

- [39] B. Hjörvarsson and R. Pentcheva, in *Magnetic Heterostructures*, Springer Tracts in Modern Physics, Vol. 227, edited by H. Zabel and S. Bader (Springer Berlin / Heidelberg, 2008) pp. 1–44.
- [40] J. Schuler, *Ferromagnetische Einzelladungs-Transistoren*, Ph.D. thesis, Technische Universität München (2005).
- [41] BalTec, <http://www.baltec.com>.
- [42] P. R. Willmott and J. R. Huber, *Rev. Mod. Phys.* **72**, 315 (2000).
- [43] R. K. Singh and J. Narayan, *Phys. Rev. B* **41**, 8843 (1990).
- [44] H. M. Christen and G. Eres, *J. Phys.: Condens. Matter* **20**, 264005 (2008).
- [45] L. Martin, Y. Chu, and R. Ramesh, *Mater. Sci. Eng., R* **68**, 89 (2010).
- [46] K.-W. Nielsen, *Ursache der magnetischen Kopplung in Kobalt-dotiertem ZnO*, Ph.D. thesis, Technische Universität München (2007).
- [47] M. Althammer, S. Geprägs, T. Brenninger, S. Goennenwein, M. Opel, and R. Gross, *New laser beam optics for the laser MBE system*, Tech. Rep. (Walther-Meissner-Institut, 2009).
- [48] B. Blass, *Epitaxie und Magnetismus dünner Schichten des Ferrimagneten Magnetit*, Diploma thesis, Technische Universität München (2002).
- [49] O. P. Sanganas, *Untersuchung der magnetischen Wechselwirkung von Strontium-basierten Doppelperowskiten*, Diploma thesis, Technische Universität München (2005).
- [50] Y. P. Wang, L. Zhou, M. F. Zhang, X. Y. Chen, J.-M. Liu, and Z. G. Liu, *Appl. Phys. Lett.* **84**, 1731 (2004).
- [51] S. Geprägs, *Elektronendotierung und strukturelle Effekte in ferromagnetischen Doppelperowskiten*, Diploma thesis, Technische Universität München (2004).
- [52] D. Reisinger, *Magnetit in ultradünnen, epitaktischen Schichtsystemen für die Spinelektronik*, Ph.D. thesis, Technische Universität München (2004).
- [53] G. Koster, B. L. Kropman, G. J. H. M. Rijnders, D. H. A. Blank, and H. Rogalla, *Appl. Phys. Lett.* **73**, 2920 (1998).
- [54] T. Ohnishi, K. Shibuya, M. Lippmaa, D. Kobayashi, H. Kumigashira, M. Oshima, and H. Koinuma, *Appl. Phys. Lett.* **85**, 272 (2004).
- [55] J. A. Hooton and W. J. Merz, *Phys. Rev.* **98**, 409 (1955).
- [56] G. Pearson and W. Feldmann, *J. Phys. Chem. Solids* **9**, 28 (1959).

- [57] C.-G. Duan, S. S. Jaswal, and E. Y. Tsymbal, *Phys. Rev. Lett.* **97**, 047201 (2006).
- [58] J. A. Venables, G. D. T. Spiller, and M. Hanbucken, *Rep. Prog. Phys.* **47**, 399 (1984).
- [59] H. Brune, *Surf. Sci. Rep.* **31**, 125 (1998).
- [60] G. J. H. M. Rijnders, G. Koster, D. H. A. Blank, and H. Rogalla, *Appl. Phys. Lett.* **70**, 1888 (1997).
- [61] J. Klein, *Epitaktische Heterostrukturen aus dotierten Manganaten*, Ph.D. thesis, Universität Köln (2001).
- [62] W. Braun, *Applied RHEED* (Springer Tracts in Modern Physics, 1999).
- [63] G. Koster, *Artificially layered oxides by pulsed laser deposition*, Ph.D. thesis, University Twente (1999).
- [64] A. Ichimiya and P. I. Cohen, *Reflection high-energy electron diffraction* (Cambridge University Press, 2004).
- [65] <http://www.esrf.eu/UsersAndScience/Experiments/CRG/BM28/>.
- [66] <http://www.diamond.ac.uk/Home/Beamlines/I16.html>.
- [67] www.spring8.or.jp.
- [68] M. Birkholz, *Thin Film Analysis by X-Ray Scattering: Techniques for Structural Characterization*, 1st ed. (Wiley-VCH Verlag GmbH & Co. KGaA, 2005).
- [69] R. Bartolini, "Electron beam dynamics in storage rings," www.adams-institute.ac.uk/ (2010).
- [70] D. Pantel, *Elektrische und magnetische Eigenschaften multifunktionaler Dünnschichtstrukturen*, Diploma thesis, Technische Universität München (2008).
- [71] T. Möller and J. Falta, *Forschung mit Synchrotronstrahlung* (Vieweg+Teubner, 2010).
- [72] M. A. Krivoglaz, *X-Ray and Neutron Diffraction in Nonideal Crystals*, illustrated edition ed. (Springer, Berlin, 1995).
- [73] M. A. Krivoglaz, *Diffuse Scattering of X-Rays and Neutrons by Fluctuations* (Springer-Verlag, 1996).
- [74] U. Pietsch, V. Holý, and T. Baumbach, *High-Resolution X-ray Scattering* (Springer, 2004).

- [75] G. Catalan, B. Noheda, J. McAneney, L. J. Sinnamon, and J. M. Gregg, *Phys. Rev. B* **72**, 020102 (2005).
- [76] T. Ungár and A. Borbély, *Appl. Phys. Lett.* **69**, 3173 (1996).
- [77] B. Cullity and S. Stock, *Elements of X-Ray Diffraction*, 3rd ed. (Prentice Hall, 2001).
- [78] J. B. Nelson and D. P. Riley, *Proc. Phys. Soc.* **57**, 160 (1945).
- [79] S. W. Lovesey and S. P. Collins, *X-ray Scattering and Absorption by Magnetic Materials* (Oxford University Press, USA, 1996).
- [80] N. Tanaka, *Sci. Technol. Adv. Mater.* **9**, 014111 (2008).
- [81] W. Yu, *Atomic resolution studies of In₂O₃ ZnO compounds on aberration corrected electron microscopes*, Ph.D. thesis, Rheinischen Friedrich-Wilhelms-Universität Bonn (2009).
- [82] *TF Analyzer 2000*.
- [83] *HP 4284a LCR Meter*.
- [84] S. Geprägs, D. Pantel, S. Goennenwein, M. Opel, R. Gross, D. Köhler, U. Zerweck, L. M. Eng, and C. Loppacher, *Ferroelectric Properties of BaTiO₃ Thin Films*, Tech. Rep. (Walther-Meissner-Institut, 2007).
- [85] R. Waser, U. Böttger, and S. Tiedke, *Polar Oxides: Properties, Characterization, and Imaging*, 1st ed. (Wiley-VCH Verlag GmbH & Co. KGaA, 2004).
- [86] T. Schmitz, K. Prume, B. Reichenberg, A. Roelofs, R. Waser, and S. Tiedke, *J. Europ. Cer. Soc.* **24**, 1145 (2004).
- [87] R. Meyer, R. Waser, K. Prume, T. Schmitz, and S. Tiedke, *Appl. Phys. Lett.* **86**, 142907 (2005).
- [88] C. B. Sawyer and C. H. Tower, *Phys. Rev.* **35**, 269 (1930).
- [89] J. F. Scott, *J. Phys.: Condens. Matter* **20**, 021001 (2008).
- [90] D. Bolten, U. Böttger, and R. Waser, *J. Appl. Phys.* **93**, 1735 (2003).
- [91] R. Waser, ed., *Nanoelectronics and Information Technology* (Wiley-VCH, 2005).
- [92] S. V. Kalinin, A. N. Morozovska, L. Q. Chen, and B. J. Rodriguez, *Rep. Prog. Phys.* **73**, 056502 (2010).
- [93] D. Köhler, *Rasterkraftmikroskopische Untersuchungen der elektrischen und magnetischen Eigenschaften multiferroischer Systeme*, Ph.D. thesis, Technische Universität Dresden (2010).

- [94] P. Borisov, A. Hochstrat, V. V. Shvartsman, and W. Kleemann, *Rev. Sci. Instrum.* **78**, 106105 (2007).
- [95] I. Quantum Design, *MPMS XL Manuals*, Quantum Design (1999).
- [96] M. K. Althammer, *Magneto-galvanische Effekte und Verspannungen in dünnen ferromagnetischen Filmen*, Diploma thesis, Technische Universität München (2007).
- [97] M. A. Wagner, *Winkelaufgelöster Magnetotransport an ferromagnetischen dünnen Filmen*, Diploma thesis, Technische Universität München (2009).
- [98] R. R. Birss, *Symmetry and magnetism*, edited by E. Wohlfarth (North-Holland Publishing Company - Amsterdam, 1964).
- [99] W. Limmer, M. Glunk, J. Daeubler, T. Hummel, W. Schoch, R. Sauer, C. Bihler, H. Huebl, M. S. Brandt, and S. T. B. Goennenwein, *Phys. Rev. B* **74**, 205205 (2006).
- [100] T. McGuire and R. Potter, *IEEE Trans. Magn.* **11**, 1018 (1975).
- [101] P. J. Curie, *Oeuvres de Pierre Curie* (Gordon and Breach Science Publishers, 1894).
- [102] L. Landau and E. Lifshitz, *Electrodynamics Of Continuous Media* (Pergamon Press, 1984).
- [103] I. E. Dzyaloshinskii, *JETP* **10**, 628 (1959).
- [104] D. N. Astrov, *JETP* **11**, 708 (1960).
- [105] M. Fiebig, *J. Phys. D: Appl. Phys.* **38**, R123 (2005).
- [106] M. Fiebig, V. V. Eremenko, and I. E. Chupis, *Magnetoelectric Interaction Phenomena in Crystals: Proceedings of the NATO ARW on Magnetoelectric Interaction Phenomena in Crystals, Sudak, Ukraine ... II: Mathematics, Physics and Chemistry*, 1st ed. (Springer Netherlands, 2004).
- [107] T. H. O'Dell, *The Electrodynamics of Magneto-electric Media* (North-Holland Publishing Company, 1970).
- [108] E. J. Post, *Formal Structure Of Electromagnetics* (Nort, 1962).
- [109] J. P. Rivera, *Eur. Phys. J. B* **71**, 299 (2009), 10.1140/epjb/e2009-00336-7.
- [110] E. Ascher, *Phys. Status Solidi B* **65**, 677 (1974).
- [111] T. H. O'Dell, *Philos. Mag.* **13**, 921 (1966).
- [112] J. Nye, *Physical Properties of Crystals* (Oxford University Press, 1985).

- [113] D. G. Sannikov, *Ferroelectrics* **219**, 177 (1998).
- [114] Y. Popov, A. Kadomtseva, D. Belov, G. Vorobaev, and A. Zvezdin, *JETP Letters* **69**, 330 (1999), 10.1134/1.568032.
- [115] N. A. Spaldin, M. Fiebig, and M. Mostovoy, *J. Phys.: Condens. Matter* **20**, 434203 (2008).
- [116] A. Scaramucci, *On ferroelectricity of magnets*, Ph.D. thesis, University of Groningen (2010).
- [117] S. L. Hou and N. Bloembergen, *Phys. Rev.* **138**, A1218 (1965).
- [118] M. J. Cardwell, *Philos. Mag.* **20**, 1087 (1969).
- [119] E. Ascher, *Philos. Mag.* **17**, 149 (1968).
- [120] H. Grimmer, *Acta Cryst.* **A48**, 266 (1992).
- [121] E. Ascher, *Phys. Lett. A* **46**, 125 (1973).
- [122] R. E. Newnham, *Am. Mineralogist* **59**, 906 (1974).
- [123] B. B. V. Aken, J. Rivera, H. Schmid, and M. Fiebig, *Nature* **449**, 702 (2007).
- [124] J. Kreisel and M. Kenzelmann, *Europhys. News* **40**, 4 (2009).
- [125] R. Seshadri and N. A. Hill, *Chem. Mater.* **13**, 2892 (2001).
- [126] B. B. V. Aken, T. T. Palstra, A. Filippetti, and N. A. Spaldin, *Nat. Mater.* **3**, 164 (2004).
- [127] M. Fiebig, T. Lottermoser, D. Frohlich, A. V. Goltsev, and R. V. Pisarev, *Nature* **419**, 818 (2002).
- [128] J. van den Brink and D. I. Khomskii, *J. Phys.: Condens. Matter* **20**, 434217 (2008).
- [129] N. Ikeda, H. Ohsumi, K. Ohwada, K. Ishii, T. Inami, K. Kakurai, Y. Murakami, K. Yoshii, S. Mori, Y. Horibe, and H. Kito, *Nature* **436**, 1136 (2005).
- [130] X. S. Xu, M. Angst, T. V. Brinzari, R. P. Hermann, J. L. Musfeldt, A. D. Christianson, D. Mandrus, B. C. Sales, S. McGill, J.-W. Kim, and Z. Islam, *Phys. Rev. Lett.* **101**, 227602 (2008).
- [131] M. Alexe, M. Ziese, D. Hesse, P. Esquinazi, K. Yamauchi, T. Fukushima, S. Picozzi, and U. Gösele, *Adv. Mater.* **21**, 4452 (2009).
- [132] K. Yamauchi, T. Fukushima, and S. Picozzi, *Phys. Rev. B* **79**, 212404 (2009).
- [133] K. Yamauchi and S. Picozzi, *Phys. Rev. Lett.* **105**, 107202 (2010).

- [134] Y. J. Choi, H. T. Yi, S. Lee, Q. Huang, V. Kiryukhin, and S.-W. Cheong, *Phys. Rev. Lett.* **100**, 047601 (2008).
- [135] M. Mostovoy, *Phys. Rev. Lett.* **96**, 067601 (2006).
- [136] J. J. Betouras, G. Giovannetti, and J. van den Brink, *Phys. Rev. Lett.* **98**, 257602 (2007).
- [137] T. Zhao, A. Scholl, F. Zavaliche, K. Lee, M. Barry, A. Doran, M. P. Cruz, Y. H. Chu, C. Ederer, N. A. Spaldin, R. R. Das, D. M. Kim, S. H. Baek, C. B. Eom, and R. Ramesh, *Nat. Mater.* **5**, 823 (2006).
- [138] P. Borisov, A. Hochstrat, X. Chen, W. Kleemann, and C. Binek, *Phys. Rev. Lett.* **94**, 117203 (2005).
- [139] F. Sugawara, S. Iiida, Y. Syono, and S. Ito Akimoto, *J. Phys. Soc. Jpn.* **25**, 1553 (1968).
- [140] P. Royen and K. Swars, *Angewandte Chemie* **69**, 779 (1957).
- [141] F. Kubel and H. Schmid, *Acta Cryst.* **B46**, 698 (1990).
- [142] P. Fischer, M. Polomska, I. Sosnowska, and M. Szymanski, *J. Phys. C: Solid State Phys.* **13**, 1931 (1980).
- [143] I. Sosnowska, T. P. Neumaier, and E. Steichele, *J. Phys. C: Solid State Phys.* **15**, 4835 (1982).
- [144] J. R. Teague, R. Gerson, and W. J. James, *Solid State Commun.* **8**, 1073 (1970).
- [145] J. Moreau, C. Michel, R. Gerson, and W. James, *J. Phys. Chem. Solids* **32**, 1315 (1971).
- [146] G. A. Smolenskii and I. E. Chupis, *Soviet Physics Uspekhi* **25**, 475 (1982).
- [147] S. Niitaka, M. Azuma, M. Takano, E. Nishibori, M. Takata, and M. Sakata, *Solid State Ionics* **172**, 557 (2004), proceedings of the Fifteenth International Symposium on the Reactivity of Solids.
- [148] A. A. Belik, S. Iikubo, K. Kodama, N. Igawa, S. Shamoto, and E. Takayama-Muromachi, *Chem. Mater.* **20**, 3765 (2008).
- [149] M. Murakami, S. Fujino, S.-H. Lim, L. G. Salamanca-Riba, M. Wuttig, I. Takeuchi, B. Varughese, H. Sugaya, T. Hasegawa, and S. E. Lofland, *Appl. Phys. Lett.* **88**, 112505 (2006).
- [150] M. Murakami, S. Fujino, S.-H. Lim, C. J. Long, L. G. Salamanca-Riba, M. Wuttig, I. Takeuchi, V. Nagarajan, and A. Varatharajan, *Appl. Phys. Lett.* **88**, 152902 (2006).

- [151] A. David, P. Boullay, R. V. K. Mangalam, N. Barrier, and W. Prellier, *Appl. Phys. Lett.* **96**, 221904 (2010).
- [152] V. R. Palkar, J. John, and R. Pinto, *Appl. Phys. Lett.* **80**, 1628 (2002).
- [153] S. Y. Yang, F. Zavaliche, L. Mohaddes-Ardabili, V. Vaithyanathan, D. G. Schlom, Y. J. Lee, Y. H. Chu, M. P. Cruz, Q. Zhan, T. Zhao, and R. Ramesh, *Appl. Phys. Lett.* **87**, 102903 (2005).
- [154] S. Iakovlev, C.-H. Solterbeck, M. Kuhnke, and M. Es-Souni, *J. Appl. Phys.* **97**, 094901 (2005).
- [155] R. R. Das, D. M. Kim, S. H. Baek, C. B. Eom, F. Zavaliche, S. Y. Yang, R. Ramesh, Y. B. Chen, X. Q. Pan, X. Ke, M. S. Rzchowski, and S. K. Streiffer, *Appl. Phys. Lett.* **88**, 242904 (2006).
- [156] J. F. Ihlefeld, A. Kumar, V. Gopalan, D. G. Schlom, Y. B. Chen, X. Q. Pan, T. Heeg, J. Schubert, X. Ke, P. Schiffer, J. Orenstein, L. W. Martin, Y. H. Chu, and R. Ramesh, *Appl. Phys. Lett.* **91**, 071922 (2007).
- [157] J. Wang, H. Zheng, Z. Ma, S. Prasertchoung, M. Wuttig, R. Droopad, J. Yu, K. Eisenbeiser, and R. Ramesh, *Appl. Phys. Lett.* **85**, 2574 (2004).
- [158] Y.-H. Chu, Q. Zhan, L. Martin, M. Cruz, P.-L. Yang, G. Pabst, F. Zavaliche, S.-Y. Yang, J.-X. Zhang, L.-Q. Chen, D. Schlom, I.-N. Lin, T.-B. Wu, and R. Ramesh, *Adv. Mater.* **18**, 2307 (2006).
- [159] D. S. Rana, K. Takahashi, K. R. Mavani, I. Kawayama, H. Murakami, M. Tonouchi, T. Yanagida, H. Tanaka, and T. Kawai, *Phys. Rev. B* **75**, 060405 (2007).
- [160] H. Béa, M. Bibes, S. Fusil, K. Bouzehouane, E. Jacquet, K. Rode, P. Bencok, and A. Barthélémy, *Phys. Rev. B* **74**, 020101 (2006).
- [161] S. J. Clark and J. Robertson, *Appl. Phys. Lett.* **94**, 022902 (2009).
- [162] J. Lu, A. Günther, F. Schrettle, F. Mayr, S. Krohns, P. Lunkenheimer, A. Pimenov, V. D. Travkin, A. A. Mukhin, and A. Loidl, *Eur. Phys. J. B* **75**, 10 (2010).
- [163] C. P. Flynn, *Phys. Rev. Lett.* **57**, 599 (1986).
- [164] A. F. M. dos Santos, A. K. Cheetham, W. Tian, X. Pan, Y. Jia, N. J. Murphy, J. Lettieri, and D. G. Schlom, *Appl. Phys. Lett.* **84**, 91 (2004).
- [165] M.-W. Chu, I. Szafraniak, R. Scholz, C. Harnagea, D. Hesse, M. Alexe, and U. Gosele, *Nat. Mater.* **3**, 87 (2004).
- [166] I. Vrejoiu, G. Lea Rhun, L. Pintilie, D. Hesse, M. Alexe, and U. Gösele, *Adv. Mater.* **18**, 1657 (2006).

- [167] M. Plekh and M. Tyunina, *Appl. Phys. Lett.* **97**, 062902 (2010).
- [168] G. Koster, G. J. H. M. Rijnders, D. H. A. Blank, and H. Rogalla, *Appl. Phys. Lett.* **74**, 3729 (1999).
- [169] A. G. Schrott, J. A. Misewich, V. Nagarajan, and R. Ramesh, *Appl. Phys. Lett.* **82**, 4770 (2003).
- [170] Y. Kato, Y. Kaneko, H. Tanaka, and Y. Shimada, *Jpn. J. Appl. Phys.* **47**, 2719 (2008).
- [171] C. B. Eom, R. J. Cava, R. M. Fleming, J. M. Phillips, R. B. vanDover, J. H. Marshall, J. W. P. Hsu, J. J. Krajewski, and W. F. P. Jr., *Science* **258**, 1766 (1992).
- [172] M. Schultz, S. Levy, J. W. Reiner, and L. Klein, *Phys. Rev. B* **79**, 125444 (2009).
- [173] H. N. Lee, H. M. Christen, M. F. Chisholm, C. M. Rouleau, and D. H. Lowndes, *Appl. Phys. Lett.* **84**, 4107 (2004).
- [174] M. Mlynarczyk, K. Szot, A. Petraru, U. Poppe, U. Breuer, R. Waser, and K. Tomala, *J. Appl. Phys.* **101**, 023701 (2007).
- [175] H. N. Lee, H. M. Christen, M. F. Chisholm, C. M. Rouleau, and D. H. Lowndes, *Nature* **433**, 395 (2005).
- [176] M. Ziese, I. Vrejoiu, E. Pippel, P. Esquinazi, D. Hesse, C. Etz, J. Henk, A. Ernst, I. V. Maznichenko, W. Hergert, and I. Mertig, *Phys. Rev. Lett.* **104**, 167203 (2010).
- [177] J. Shin, A. Y. Borisevich, V. Meunier, J. Zhou, E. W. Plummer, S. V. Kalinin, and A. P. Baddorf, *ACS Nano* **4**, 4190 (2010).
- [178] A. Hartmann, M. Neilson, R. Lamb, K. Watanabe, and J. Scott, *Appl. Phys. A* **70**, 239 (2000).
- [179] S. Aggarwal, I. G. Jenkins, B. Nagaraj, C. J. Kerr, C. Canedy, R. Ramesh, G. Velasquez, L. Boyer, and J. J. T. Evans, *Appl. Phys. Lett.* **75**, 1787 (1999).
- [180] T. Morimoto, O. Hidaka, K. Yamakawa, O. Arisumi, H. Kanaya, T. Iwamoto, Y. Kumura, I. Kunishima, and S. ichi Tanaka, *Jpn. J. Appl. Phys.* **39**, 2110 (2000).
- [181] Y. S. Kim, J. Y. Jo, D. J. Kim, Y. J. Chang, J. H. Lee, T. W. Noh, T. K. Song, J.-G. Yoon, J.-S. Chung, S. I. Baik, Y.-W. Kim, and C. U. Jung, *Appl. Phys. Lett.* **88**, 072909 (2006).
- [182] A. Callaghan, C. W. Moeller, and R. Ward, *Inorg. Chem.* **5**, 1572 (1966).

- [183] G. Cao, S. McCall, M. Shepard, J. E. Crow, and R. P. Guertin, *Phys. Rev. B* **56**, 321 (1997).
- [184] S. Geller, *J. Chem. Phys.* **24**, 1236 (1956).
- [185] J. C. Jiang and X. Q. Pan, *Philos. Mag. Lett.* **80**, 271 (2000).
- [186] F. He, B. O. Wells, Z.-G. Ban, S. P. Alpay, S. Grenier, S. M. Shapiro, W. Si, A. Clark, and X. X. Xi, *Phys. Rev. B* **70**, 235405 (2004).
- [187] A. M. Glazer, *Acta Cryst.* **B28**, 3384 (1972).
- [188] J. J. Randall and R. Ward, *J. Am. Chem. Soc.* **81**, 2629 (1959).
- [189] P. B. Allen, H. Berger, O. Chauvet, L. Forro, T. Jarlborg, A. Junod, B. Revaz, and G. Santi, *Phys. Rev. B* **53**, 4393 (1996).
- [190] I. I. Mazin and D. J. Singh, *Phys. Rev. B* **56**, 2556 (1997).
- [191] R. Bouchard and J. Gillson, *Mater. Res. Bull.* **7**, 873 (1972).
- [192] L. Klein, J. S. Dodge, C. H. Ahn, J. W. Reiner, L. Mieville, T. H. Geballe, M. R. Beasley, and A. Kapitulnik, *J. Phys.: Condens. Matter* **8**, 10111 (1996).
- [193] G. Rijnders, D. H. A. Blank, J. Choi, and C.-B. Eom, *Appl. Phys. Lett.* **84**, 505 (2004).
- [194] J. Choi, C. B. Eom, G. Rijnders, H. Rogalla, and D. H. A. Blank, *Appl. Phys. Lett.* **79**, 1447 (2001).
- [195] W. Hong, H. N. Lee, M. Yoon, H. M. Christen, D. H. Lowndes, Z. Suo, and Z. Zhang, *Phys. Rev. Lett.* **95**, 095501 (2005).
- [196] B. AXS, "Leptos," <http://www.bruker-axs.com>.
- [197] A. Vailionis, W. Siemons, and G. Koster, *Appl. Phys. Lett.* **93**, 051909 (2008).
- [198] M. Ziese, I. Vrejoiu, and D. Hesse, *Phys. Rev. B* **81**, 184418 (2010).
- [199] A. T. Zayak, X. Huang, J. B. Neaton, and K. M. Rabe, *Phys. Rev. B* **74**, 094104 (2006).
- [200] J. C. Jiang, W. Tian, X. Q. Pan, Q. Gan, and C. B. Eom, *Appl. Phys. Lett.* **72**, 2963 (1998).
- [201] D. B. Kacedon, R. A. Rao, and C. B. Eom, *Appl. Phys. Lett.* **71**, 1724 (1997).
- [202] Q. Gan, R. A. Rao, and C. B. Eom, *Appl. Phys. Lett.* **70**, 1962 (1997).
- [203] R. A. Rao, Q. Gan, and C. B. Eom, *Appl. Phys. Lett.* **71**, 1171 (1997).

- [204] G. Herranz, F. Sánchez, J. Fontcuberta, M. V. García-Cuenca, C. Ferrater, M. Varela, T. Angelova, A. Cros, and A. Cantarero, *Phys. Rev. B* **71**, 174411 (2005).
- [205] S. S. Kim, T. S. Kang, and J. H. Je, *J. Appl. Phys.* **90**, 4407 (2001).
- [206] Z. Fang, N. Nagaosa, K. S. Takahashi, A. Asamitsu, R. Mathieu, T. Ogasawara, H. Yamada, M. Kawasaki, Y. Tokura, and K. Terakura, *Science* **302**, 92 (2003).
- [207] A. Kanbayasi, *J. Phys. Soc. Jpn.* **41**, 1876 (1976).
- [208] Q. Gan, R. A. Rao, C. B. Eom, J. L. Garrett, and M. Lee, *Appl. Phys. Lett.* **72**, 978 (1998).
- [209] M. Shikano, T.-K. Huang, Y. Inaguma, M. Itoh, and T. Nakamura, *Solid State Commun.* **90**, 115 (1994).
- [210] F. L. Marrec, A. Demuer, D. Jaccard, J.-M. Triscone, M. K. Lee, and C. B. Eom, *Appl. Phys. Lett.* **80**, 2338 (2002).
- [211] Y. Kats, L. Klein, J. W. Reiner, T. H. Geballe, M. R. Beasley, and A. Kapitulnik, *Phys. Rev. B* **63**, 054435 (2001).
- [212] L. Klein, J. Dodge, C. Ahn, G. Snyder, T. Geballe, M. Beasley, and A. Kapitulnik, *Phys. Rev. Lett.* **77**, 2774 (1996).
- [213] D. Kim, B. L. Zink, F. Hellman, S. McCall, G. Cao, and J. E. Crow, *Phys. Rev. B* **67**, 100406 (2003).
- [214] L. M. Wang, H. E. Horng, and H. C. Yang, *Phys. Rev. B* **70**, 014433 (2004).
- [215] R. Palai, H. Huhtinen, J. F. Scott, and R. S. Katiyar, *Phys. Rev. B* **79**, 104413 (2009).
- [216] A. Grutter, F. Wong, E. Arenholz, M. Liberati, A. Vailionis, and Y. Suzuki, *Appl. Phys. Lett.* **96**, 082509 (2010).
- [217] G. Herranz, F. Sánchez, N. Dix, D. Hrabovsky, I. C. Infante, J. Fontcuberta, M. V. García-Cuenca, C. Ferrater, and M. Varela, *Appl. Phys. Lett.* **89**, 152501 (2006).
- [218] B. Dabrowski, M. Avdeev, O. Chmaissem, S. Kolesnik, P. W. Klamut, M. Maxwell, and J. D. Jorgensen, *Phys. Rev. B* **71**, 104411 (2005).
- [219] W. Siemons, G. Koster, A. Vailionis, H. Yamamoto, D. H. A. Blank, and M. R. Beasley, *Phys. Rev. B* **76**, 075126 (2007).
- [220] R. V. Chopdekar, Y. Takamura, and Y. Suzuki, *J. Appl. Phys.* **99**, 08F503 (2006).

- [221] A. F. Marshall, L. Klein, J. S. Dodge, C. H. Ahn, J. W. Reiner, L. Mieville, L. Antagonazza, A. Kapitulnik, T. H. Geballe, and M. R. Beasley, *J. Appl. Phys.* **85**, 4131 (1999).
- [222] L. Klein, Y. Kats, A. F. Marshall, J. W. Reiner, T. H. Geballe, M. R. Beasley, and A. Kapitulnik, *Phys. Rev. Lett.* **84**, 6090 (2000).
- [223] S. C. Gausepohl, M. Lee, K. Char, R. A. Rao, and C. B. Eom, *Phys. Rev. B* **52**, 3459 (1995).
- [224] M. Izumi, K. Nakazawa, Y. Bando, Y. Yoneda, and H. Terauchi, *J. Phys. Soc. Jpn.* **66**, 3893 (1997).
- [225] J. H. Cho, Q. X. Jia, X. D. Wu, S. R. Foltyn, and M. P. Maley, *Phys. Rev. B* **54**, 37 (1996).
- [226] H. C. Yang, S. H. Liu, L. M. Wang, and H. E. Horng, *J. Appl. Phys.* **85**, 5792 (1999).
- [227] R. Mathieu, C. U. Jung, H. Yamada, A. Asamitsu, M. Kawasaki, and Y. Tokura, *Phys. Rev. B* **72**, 064436 (2005).
- [228] Y. Kats, I. Genish, L. Klein, J. W. Reiner, and M. R. Beasley, *Phys. Rev. B* **70**, 180407 (2004).
- [229] W. Kaiser, *Spinabhängiger Transport in Magnetit*, Diploma thesis, Technische Universität München (2006).
- [230] S. C. Gausepohl, M. Lee, R. A. Rao, and C. B. Eom, *Phys. Rev. B* **54**, 8996 (1996).
- [231] R. Mathieu, A. Asamitsu, H. Yamada, K. S. Takahashi, M. Kawasaki, Z. Fang, N. Nagaosa, and Y. Tokura, *Phys. Rev. Lett.* **93**, 016602 (2004).
- [232] D. Arnold, K. Knight, F. Morrison, and P. Lightfoot, *Phys. Rev. Lett.* **102** (2009), 10.1103/PhysRevLett.102.027602.
- [233] R. D. Shannon, *Acta Cryst.* **A32**, 751 (1976).
- [234] H. Béa, M. Bibes, M. Sirena, G. Herranz, K. Bouzehouane, E. Jacquet, S. Fusil, P. Paruch, M. Dawber, J.-P. Contour, and A. Barthélémy, *Appl. Phys. Lett.* **88**, 062502 (2006).
- [235] X. Qi, M. Wei, Y. Lin, Q. Jia, D. Zhi, J. Dho, M. G. Blamire, and J. L. MacManus-Driscoll, *Appl. Phys. Lett.* **86**, 071913 (2005).
- [236] G. Xu, H. Hiraka, G. Shirane, J. Li, J. Wang, and D. Viehland, *Appl. Phys. Lett.* **86**, 182905 (2005).
- [237] L. Yan, H. Cao, J. Li, and D. Viehland, *Appl. Phys. Lett.* **94**, 132901 (2009).

- [238] K. Saito, A. Ulyanenkov, V. Grossmann, H. Röss, L. Bruegemann, H. Ohta, T. Kurosawa, S. Ueki, and H. Funakubo, *Jpn. J. Appl. Phys.* **45**, 7311 (2006).
- [239] H. Béa, M. Bibes, S. Petit, J. Kreisel, and A. Barthélémy, *Philos. Mag. Lett.* **87**, 165 (2007).
- [240] C. J. M. Daumont, S. Farokhipoor, A. Ferri, J. C. Wojdeł, J. Íñiguez, B. J. Kooi, and B. Noheda, *Phys. Rev. B* **81**, 144115 (2010).
- [241] R. J. Zeches, M. D. Rossell, J. X. Zhang, A. J. Hatt, Q. He, C.-H. Yang, A. Kumar, C. H. Wang, A. Melville, C. Adamo, G. Sheng, Y.-H. Chu, J. F. Ihlefeld, R. Erni, C. Ederer, V. Gopalan, L. Q. Chen, D. G. Schlom, N. A. Spaldin, L. W. Martin, and R. Ramesh, *Science* **326**, 977 (2009).
- [242] I. C. Infante, S. Lisenkov, B. Dupé, M. Bibes, S. Fusil, E. Jacquet, G. Geneste, S. Petit, A. Courtial, J. Juraszek, L. Bellaiche, A. Barthélémy, and B. Dkhil, *Phys. Rev. Lett.* **105**, 057601 (2010).
- [243] J. Li, J. Wang, M. Wuttig, R. Ramesh, N. Wang, B. Ruetter, A. P. Pyatakov, A. K. Zvezdin, and D. Viehland, *Appl. Phys. Lett.* **84**, 5261 (2004).
- [244] D. Kan and I. Takeuchi, *J. Appl. Phys.* **108**, 014104 (2010).
- [245] D. G. Schlom, L.-Q. Chen, C.-B. Eom, K. M. Rabe, S. K. Streiffer, and J.-M. Triscone, *Ann. Rev. Mater. Res.* **37**, 589 (2007).
- [246] H. Béa, B. Dupé, S. Fusil, R. Mattana, E. Jacquet, B. Warot-Fonrose, F. Wilhelm, A. Rogalev, S. Petit, V. Cros, A. Anane, F. Petroff, K. Bouzehouane, G. Geneste, B. Dkhil, S. Lisenkov, I. Ponomareva, L. Bellaiche, M. Bibes, and A. Barthélémy, *Phys. Rev. Lett.* **102**, 217603 (2009).
- [247] B. Dupé, I. C. Infante, G. Geneste, P.-E. Janolin, M. Bibes, A. Barthélémy, S. Lisenkov, L. Bellaiche, S. Ravy, and B. Dkhil, *Phys. Rev. B* **81**, 144128 (2010).
- [248] D. Ricinschi, K.-Y. Yun, and M. Okuyama, *J. Phys.: Condens. Matter* **18**, L97 (2006).
- [249] A. J. Hatt, N. A. Spaldin, and C. Ederer, *Phys. Rev. B* **81**, 054109 (2010).
- [250] W. Eerenstein, F. D. Morrison, J. Dho, M. G. Blamire, J. F. Scott, and N. D. Mathur, *Science* **307**, 1203a (2005).
- [251] K. J. Choi, M. Biegalski, Y. L. Li, A. Sharan, J. Schubert, R. Uecker, P. Reiche, Y. B. Chen, X. Q. Pan, V. Gopalan, L.-Q. Chen, D. G. Schlom, and C. B. Eom, *Science* **306**, 1005 (2004).
- [252] C. L. Canedy, H. Li, S. P. Alpay, L. Salamanca-Riba, A. L. Roytburd, and R. Ramesh, *Appl. Phys. Lett.* **77**, 1695 (2000).

- [253] I. B. Misirlioglu, A. L. Vasiliev, M. Aindow, S. P. Alpay, and R. Ramesh, *Appl. Phys. Lett.* **84**, 1742 (2004).
- [254] V. Nagarajan, C. L. Jia, H. Kohlstedt, R. Waser, I. B. Misirlioglu, S. P. Alpay, and R. Ramesh, *Appl. Phys. Lett.* **86**, 192910 (2005).
- [255] J. X. Zhang, B. Xiang, Q. He, J. Seidel, R. J. Zeches, P. Yu, S. Y. Yang, C. H. Wang, Y.-H. Chu, L. W. Martin, A. M. Minor, and R. Ramesh, *Nat. Nanotechnol.* **6**, 98 (2011).
- [256] CrysTec, *SrTiO₃ for Research and Development*, Tech. Rep. (Crystec GmbH, Köpenicker Strasse 325, 12555 Berlin, Germany).
- [257] H. T. Stokes, E. H. Kisi, D. M. Hatch, and C. J. Howard, *Acta Cryst.* **B58**, 934 (2002).
- [258] D. Pandey, A. K. Singh, and S. Baik, *Acta Cryst.* **A64**, 192 (2008).
- [259] U. M. Gebhardt, *Strukturelle Relaxation von epitaktischen, dünnen La/Sr-Manganitfilmen in Abhängigkeit von der Schichtdicke*, Ph.D. thesis, Universität Stuttgart (2007).
- [260] M. Lines and A. Glass, *Principles and Applications of Ferroelectric and Related Materials* (Oxford University Press, 1977).
- [261] O. N. Tufte and P. W. Chapman, *Phys. Rev.* **155**, 796 (1967).
- [262] Y. H. Chu, T. Zhao, M. P. Cruz, Q. Zhan, P. L. Yang, L. W. Martin, M. Huijben, C. H. Yang, F. Zavaliche, H. Zheng, and R. Ramesh, *Appl. Phys. Lett.* **90**, 252906 (2007).
- [263] D. H. Kim, H. N. Lee, M. D. Biegalski, and H. M. Christen, *Appl. Phys. Lett.* **92**, 012911 (2008).
- [264] H. Liu, K. Yao, P. Yang, Y. Du, Q. He, Y. Gu, X. Li, S. Wang, X. Zhou, and J. Wang, *Phys. Rev. B* **82**, 064108 (2010).
- [265] T. C. T. Ting and T. Chen, *Int. J. Mech. Appl. Math.* **58**, 73 (2005).
- [266] L. You, N. T. Chua, K. Yao, L. Chen, and J. Wang, *Phys. Rev. B* **80**, 024105 (2009).
- [267] J. Matthews and A. Blakeslee, *J. Cryst. Growth* **27**, 118 (1974).
- [268] J. S. Speck and W. Pompe, *J. Appl. Phys.* **76**, 466 (1994).
- [269] S. Venkatesan, A. Vlooswijk, B. J. Kooi, A. Morelli, G. Palasantzas, J. T. M. De Hosson, and B. Noheda, *Phys. Rev. B* **78**, 104112 (2008).
- [270] J. Chen, W. Wang, J.-B. Li, and G. Rao, *J. Alloys Compd.* **459**, 66 (2008).

- [271] J. D. Bucci, B. K. Robertson, and W. J. James, *J. Appl. Crystallogr.* **5**, 187 (1972).
- [272] L. B. Freund, *J. Mech. Phys. Solids* **38**, 657 (1990).
- [273] N. Farag, M. Bobeth, W. Pompe, A. E. Romanov, and J. S. Speck, *J. Appl. Phys.* **97**, 113516 (2005).
- [274] S. K. Streiffer, C. B. Parker, A. E. Romanov, M. J. Lefevre, L. Zhao, J. S. Speck, W. Pompe, C. M. Foster, and G. R. Bai, *J. Appl. Phys.* **83**, 2742 (1998).
- [275] Y.-H. Chu, M. Cruz, C.-H. Yang, L. Martin, P.-L. Yang, J.-X. Zhang, K. Lee, P. Yu, L.-Q. Chen, and R. Ramesh, *Adv. Mater.* **19**, 2662 (2007).
- [276] H. W. Jang, D. Ortiz, S. Baek, C. M. Folkman, R. R. Das, P. Shafer, Y. Chen, C. T. Nelson, X. Pan, R. Ramesh, and C. Eom, *Adv. Mater.* **21**, 817 (2009).
- [277] A. E. Romanov, M. J. Lefevre, J. S. Speck, W. Pompe, S. K. Streiffer, and C. M. Foster, *J. Appl. Phys.* **83**, 2754 (1998).
- [278] J. Seidel, L. W. Martin, Q. He, Q. Zhan, Y. Chu, A. Rother, M. E. Hawkrigde, P. Maksymovych, P. Yu, M. Gajek, N. Balke, S. V. Kalinin, S. Gemming, F. Wang, G. Catalan, J. F. Scott, N. A. Spaldin, J. Orenstein, and R. Ramesh, *Nat. Mater.* **8**, 229 (2009).
- [279] S. Gariglio, N. Stucki, J.-M. Triscone, and G. Triscone, *Appl. Phys. Lett.* **90**, 202905 (2007).
- [280] V. M. Kaganer, R. Köhler, M. Schmidbauer, R. Opitz, and B. Jenichen, *Phys. Rev. B* **55**, 1793 (1997).
- [281] H. J. Kim, S. H. Oh, and H. M. Jang, *Appl. Phys. Lett.* **75**, 3195 (1999).
- [282] L. Nicola, E. V. der Giessen, and M. E. Gurtin, *J. Mech. Phys. Solids* **53**, 1280 (2005).
- [283] G. Williamson and W. Hall, *Acta Metallurgica* **1**, 22 (1953).
- [284] I. Vartanyants, C. Ern, W. Donner, H. Dosch, and W. Caliebe, *Appl. Phys. Lett.* **77**, 3929 (2000).
- [285] E. J. Mittemeijer and U. Welzel, *Z. Kristallogr.* **223**, 552 (2008).
- [286] S. P. Alpay, I. B. Misirlioglu, V. Nagarajan, and R. Ramesh, *Appl. Phys. Lett.* **85**, 2044 (2004).
- [287] J. Wu and J. Wang, *J. Appl. Phys.* **106**, 054115 (2009).

- [288] S. H. Baek, H. W. Jang, C. M. Folkman, Y. L. Li, B. Winchester, J. X. Zhang, Q. He, Y. H. Chu, C. T. Nelson, M. S. Rzchowski, X. Q. Pan, R. Ramesh, L. Q. Chen, and C. B. Eom, *Nat. Mater.* **9**, 309 (2010).
- [289] F. Zavaliche, S. Y. Yang, T. Zhao, Y. H. Chu, M. P. Cruz, C. B. Eom, and R. Ramesh, *Phase Transitions* **79**, 991 (2006).
- [290] N. Balke, S. Choudhury, S. Jesse, M. Huijben, Y. H. Chu, A. P. Baddorf, L. Q. Chen, R. Ramesh, and S. V. Kalinin, *Nat Nano* **4**, 868 (2009).
- [291] H. Béa, M. Bibes, X.-H. Zhu, S. Fusil, K. Bouzehouane, S. Petit, J. Kreisel, and A. Barthélémy, *Appl. Phys. Lett.* **93**, 072901 (2008).
- [292] F. Zavaliche, R. R. Das, D. M. Kim, C. B. Eom, S. Y. Yang, P. Shafer, and R. Ramesh, *Appl. Phys. Lett.* **87**, 182912 (2005).
- [293] H. Zheng, F. Straub, Q. Zhan, P.-L. Yang, W.-K. Hsieh, F. Zavaliche, Y.-H. Chu, U. Dahmen, and R. Ramesh, *Adv. Mater.* **18**, 2747 (2006).
- [294] G. Catalan, H. Béa, S. Fusil, M. Bibes, P. Paruch, A. Barthélémy, and J. F. Scott, *Phys. Rev. Lett.* **100**, 027602 (2008).
- [295] S. V. Kiselev, R. P. Ozerov, and G. Zhadanov, *Doklady Physics* **7**, 742 (1963), 10.1134/S1028335810010015.
- [296] C. Ederer and N. A. Spaldin, *Phys. Rev. B* **71**, 060401 (2005).
- [297] I. Dzyaloshinsky, *J. Phys. Chem. Solids* **4**, 241 (1958).
- [298] T. Moriya, *Phys. Rev.* **120**, 91 (1960).
- [299] C. Ederer and C. J. Fennie, *J. Phys.: Condens. Matter* **20**, 434219 (2008).
- [300] B. Dupé, S. Prosandeev, G. Geneste, B. Dkhil, and L. Bellaiche, *Phys. Rev. Lett.* **106**, 237601 (2011).
- [301] C. J. Fennie, *Phys. Rev. Lett.* **100**, 167203 (2008).
- [302] D. Albrecht, S. Lisenkov, W. Ren, D. Rahmedov, I. A. Kornev, and L. Bellaiche, *Phys. Rev. B* **81**, 140401 (2010).
- [303] R. de Sousa and J. E. Moore, *Phys. Rev. Lett.* **102**, 249701 (2009).
- [304] C. J. Fennie, *Phys. Rev. Lett.* **102**, 249702 (2009).
- [305] D. Lebeugle, A. Mougin, M. Viret, D. Colson, J. Allibe, H. Béa, E. Jacquet, C. Deranlot, M. Bibes, and A. Barthélémy, *Phys. Rev. B* **81**, 134411 (2010).
- [306] M. B. Holcomb, L. W. Martin, A. Scholl, Q. He, P. Yu, C.-H. Yang, S. Y. Yang, P.-A. Glans, M. Valvidares, M. Huijben, J. B. Kortright, J. Guo, Y.-H. Chu, and R. Ramesh, *Phys. Rev. B* **81**, 134406 (2010).

- [307] J. Herrero-Albillos, G. Catalan, J. A. Rodriguez-Velamazán, M. Viret, D. Colson, and J. F. Scott, *J. Phys.: Condens. Matter* **22**, 256001 (2010).
- [308] M. Ramazanoglu, W. Ratcliff, Y. J. Choi, S. Lee, S.-W. Cheong, and V. Kiryukhin, *Phys. Rev. B* **83**, 174434 (2011).
- [309] A. Zvezdin, A. Kadomtseva, S. Krotov, A. Pyatakov, Y. Popov, and G. VorobeV, *J. Magn. Magn. Mater.* **300**, 224 (2006), the third Moscow International Symposium on Magnetism 2005.
- [310] F. Bai, J. Wang, M. Wuttig, J. Li, N. Wang, A. P. Pyatakov, A. K. Zvezdin, L. E. Cross, and D. Viehland, *Appl. Phys. Lett.* **86**, 032511 (2005).
- [311] H. Béa, M. Bibes, F. Ott, B. Dupé, X.-H. Zhu, S. Petit, S. Fusil, C. Deranlot, K. Bouzehouane, and A. Barthélémy, *Phys. Rev. Lett.* **100**, 017204 (2008).
- [312] A. J. Millis, T. Darling, and A. Migliori, *J. Appl. Phys.* **83**, 1588 (1998).
- [313] F. Tsui, M. C. Smoak, T. K. Nath, and C. B. Eom, *Appl. Phys. Lett.* **76**, 2421 (2000).
- [314] J. Scola, W. Noun, E. Popova, A. Fouchet, Y. Dumont, N. Keller, P. Lejay, I. Sheikin, A. Demuer, and A. Pautrat, *Phys. Rev. B* **81**, 174409 (2010).
- [315] S. Lim, M. Murakami, W. Sarney, S. Ren, A. Varatharajan, V. Nagarajan, S. Fujino, M. Wuttig, I. Takeuchi, and L. Salamanca-Riba, *Adv. Funct. Mater.* **17**, 2594 (2007).
- [316] Y. Popov, A. Zvezdin, G. VorobeV, A. Kadomtseva, V. A. Murashev, and D. N. Rakov, *JETP Letters* **57**, 69 (1993).
- [317] I. S. Jacobs, H. F. Burne, and L. M. Levinson, *J. Appl. Phys.* **42**, 1631 (1971).
- [318] A. Kadomtseva, A. Zvezdin, Y. Popov, A. Pyatakov, and G. Vorobaev, *JETP Letters* **79**, 571 (2004).
- [319] G. Le Bras, D. Colson, A. Forget, N. Genand-Riondet, R. Tourbot, and P. Bonville, *Phys. Rev. B* **80**, 134417 (2009).
- [320] C.-H. Yang, T. Koo, and Y. Jeong, *Solid State Commun.* **134**, 299 (2005).
- [321] B. Ruetter, S. Zvyagin, A. P. Pyatakov, A. Bush, J. F. Li, V. I. Belotelov, A. K. Zvezdin, and D. Viehland, *Phys. Rev. B* **69**, 064114 (2004).
- [322] S. Chikazumi, *Physics of Ferromagnetism*, edited by C. G. JR (Oxford University Press, 1997).
- [323] A. K. Zvezdin and A. P. Pyatakov, *Phys. Status Solidi B* **246**, 1956 (2009).
- [324] Z. V. Gabbasova, M. D. Kuz'min, A. K. Zvezdin, I. S. Dubenko, V. A. Murashov, D. N. Rakov, and I. B. Krynetsky, *Phys. Lett. A* **158**, 491 (1991).

- [325] M. Daraktchiev, G. Catalan, and J. F. Scott, *Phys. Rev. B* **81**, 224118 (2010).
- [326] M. K. Singh, W. Prellier, M. P. Singh, R. S. Katiyar, and J. F. Scott, *Phys. Rev. B* **77**, 144403 (2008).
- [327] B. Ramachandran and M. S. R. Rao, *Appl. Phys. Lett.* **95**, 142505 (2009).
- [328] L. W. Martin, Y.-H. Chu, M. B. Holcomb, M. Huijben, P. Yu, S.-J. Han, D. Lee, S. X. Wang, and R. Ramesh, *Nano Lett.* **8**, 2050 (2008), pMID: 18547121.
- [329] X. He, Y. Wang, N. Wu, A. N. Caruso, E. Vescovo, K. D. Belashchenko, P. A. Dowben, and C. Binek, *Nat Mater* **9**, 579 (2010).
- [330] N. Wu, X. He, A. L. Wysocki, U. Lanke, T. Komesu, K. D. Belashchenko, C. Binek, and P. A. Dowben, *Phys. Rev. Lett.* **106**, 087202 (2011).
- [331] Z. V. Gareeva and A. K. Zvezdin, *Phys. Stat. Sol. (RRL)* **3**, 79 (2009).
- [332] Z. V. Gareeva and A. K. Zvezdin, *Europhys. Lett.* **91**, 47006 (2010).
- [333] A. Lubk, S. Gemming, and N. A. Spaldin, *Phys. Rev. B* **80**, 104110 (2009).
- [334] V. G. Prokhorov, G. G. Kaminsky, J. M. Kim, T. W. Eom, J. S. Park, Y. P. Lee, V. L. Svetchnikov, G. G. Levchenko, Y. M. Nikolaenko, and V. A. Khokhlov, *Low Temp. Phys.* **37**, 129 (2011).
- [335] L. W. Martin, *Dalton Transactions* **39**, 10813 (2010).
- [336] F. Sugawara, S. Iida, Y. Syono, and S. Ito Akimoto, *J. Phys. Soc. Jpn.* **20**, 1529 (1965).
- [337] T. Kimura, S. Kawamoto, I. Yamada, M. Azuma, M. Takano, and Y. Tokura, *Phys. Rev. B* **67**, 180401 (2003).
- [338] I. Solovyev and Z. Pchelkina, *JETP Letters* **89**, 597 (2009), 10.1134/S0021364009120029.
- [339] C. J. M. Daumont, D. Mannix, S. Venkatesan, G. Catalan, D. Rubi, B. J. Kooi, J. T. M. D. Hosson, and B. Noheda, *Journal of Physics: Condensed Matter* **21**, 182001 (2009).
- [340] P. Mandal, A. Iyo, Y. Tanaka, A. Sundaresan, and C. N. R. Rao, *J. Mater. Chem.* **20**, 1646 (2010).
- [341] A. A. Belik, H. Yusa, N. Hirao, Y. Ohishi, and E. Takayama-Muromachi, *Inorg. Chem.* **48**, 1000 (2009).
- [342] J. Ding, Y. Yao, and L. Kleinman, *J. Appl. Phys.* **109**, 103905 (2011).

- [343] A. A. Belik, T. Kolodiazhnyi, K. Kosuda, and E. Takayama-Muromachi, *J. Mater. Chem.* **19**, 1593 (2009).
- [344] G. Carbone, *Structural and magnetic studies of strained thin films of $La_{2/3}Ca_{1/3}MnO_3$* , Ph.D. thesis, Max-Planck-Institut für Metallforschung Stuttgart (2004).
- [345] H. Yang, Z. H. Chi, L. D. Yao, W. Zhang, F. Y. Li, C. Q. Jin, and R. C. Yu, *J. Appl. Phys.* **100**, 044105 (2006).
- [346] S. Trolier-McKinstry, M. D. Biegalski, J. Wang, A. A. Belik, E. Takayama-Muromachi, and I. Levin, *J. Appl. Phys.* **104**, 044102 (2008).
- [347] C. R. Serrao, A. K. Kundu, S. B. Krupanidhi, U. V. Waghmare, and C. N. R. Rao, *Phys. Rev. B* **72**, 220101 (2005).
- [348] V. Westphal, W. Kleemann, and M. D. Glinchuk, *Phys. Rev. Lett.* **68**, 847 (1992).
- [349] C. Elissalde and J. Ravez, *J. Mater. Chem.* **11**, 1957 (2001).
- [350] P. Lunkenheimer, V. Bobnar, A. V. Pronin, A. I. Ritus, A. A. Volkov, and A. Loidl, *Phys. Rev. B* **66**, 052105 (2002).
- [351] S. Kamba, D. Nuzhnyy, M. Savinov, J. Šebek, J. Petzelt, J. Prokleška, R. Haumont, and J. Kreisel, *Phys. Rev. B* **75**, 024403 (2007).
- [352] S. J. Clark and J. Robertson, *Appl. Phys. Lett.* **90**, 132903 (2007).
- [353] C. Ang, J. F. Scott, Z. Yu, H. Ledbetter, and J. L. Baptista, *Phys. Rev. B* **59**, 6661 (1999).
- [354] C. Ang, L. E. Cross, Z. Yu, R. Guo, A. S. Bhalla, and J. H. Hao, *Appl. Phys. Lett.* **78**, 2754 (2001).
- [355] H. Yang, Y. Q. Wang, H. Wang, and Q. X. Jia, *Appl. Phys. Lett.* **96**, 012909 (2010).
- [356] H. Yang, M. Jain, N. A. Suvorova, H. Zhou, H. M. Luo, D. M. Feldmann, P. C. Dowden, R. F. DePaula, S. R. Foltyn, and Q. X. Jia, *Appl. Phys. Lett.* **91**, 072911 (2007).
- [357] X. Fang and T. Kobayashi, *Appl. Phys. A* **69**, S587 (1999).
- [358] W. Sachtler, G. Dorgelo, and A. Holscher, *Surface Science* **5**, 221 (1966).
- [359] A. M. Cowley and S. M. Sze, *J. Appl. Phys.* **36**, 3212 (1965).
- [360] Y. Xu, X. Hao, J. Meng, D. Zhou, and F. Gao, *J. Phys.: Condens. Matter* **21**, 236006 (2009).

- [361] G. W. Pabst, L. W. Martin, Y.-H. Chu, and R. Ramesh, *Appl. Phys. Lett.* **90**, 072902 (2007).
- [362] S. M. Sze, *Physics of Semiconductor Devices* (Wiley-Interscience, 1981).
- [363] X. Qi, J. Dho, R. Tomov, M. G. Blamire, and J. L. MacManus-Driscoll, *Appl. Phys. Lett.* **86**, 062903 (2005).
- [364] K. S. Cole and R. H. Cole, *J. Chem. Phys.* **9**, 341 (1941).
- [365] C. P. de Araujo, J. F. Scott, and G. W. Taylor, eds., *Ferroelectric Thin Films: Synthesis and Basic Properties* (Gordon and Breach Publisher, 1996).
- [366] X. Chen, A. I. Kingon, L. Mantese, O. Auciello, and K. Y. Hsieh, *Integr. Ferroelectr.* **3**, 355 (1993).
- [367] M. Schumacher and R. Waser, *Integr. Ferroelectr.* **22**, 109 (1998).
- [368] O. Lohse, *Verlustmechanismus in ferroelektrischen keramischen Dünnschichtkondensatoren für hochintegrierte nicht-flüchtige Halbleiterspeicher*, Ph.D. thesis, RWTH Aachen (2001).
- [369] D. R. Wolters and J. J. van der Schoot, *J. Appl. Phys.* **58**, 831 (1985).
- [370] A. Jonscher, *IEEE Trans. Electr. Ins.* **27**, 407 (1992).
- [371] O. Lohse, M. Grossmann, U. Boettger, D. Bolten, and R. Waser, *J. Appl. Phys.* **89**, 2332 (2001).
- [372] Y.-H. Kim and J.-J. Kim, *Phys. Rev. B* **55**, R11933 (1997).
- [373] W. L. Warren, B. A. Tuttle, D. Dimos, G. E. Pike, H. N. Al-Shareef, R. Ramesh, J. T. Evans, and J. Jr, *Jpn. J. Appl. Phys.* **35**, 1521 (1996).
- [374] K. Abe, S. Komatsu, N. Yanase, K. Sano, and T. Kawakubo, *Jpn. J. Appl. Phys.* **36**, 5846 (1997).
- [375] D. Nagasawa and H. Nozawa, *Jpn. J. Appl. Phys.* **38**, 5406 (1999).
- [376] Z. Zhuang, H. MP, S. DM, and N. RE, *Mater. Res. Bull.* **22**, 1329 (1987).
- [377] N. Ray and U. V. Waghmare, *Phys. Rev. B* **77**, 134112 (2008).
- [378] A. A. Belik, N. Tsujii, H. Suzuki, and E. Takayama-Muromachi, *Inorg. Chem.* **46**, 8746 (2007).
- [379] A. A. Belik and E. Takayama-Muromachi, *J. Phys.: Conf. Ser.* **165**, 012035 (2009).
- [380] R. O'Handley, *Modern Magnetic Materials: Principals and Applications* (Wiley-Interscience, 2000).

- [381] F. Radu and H. Zabel, *Magnetic Heterostructures*, edited by H. Zabel and S. D. Bader, Vol. 227 (Springer Berlin Heidelberg, Berlin, Heidelberg, 2008).
- [382] M. Fecioru-Morariu, *Exchange bias of metallic ferro-/antiferromagnetic bilayers*, Ph.D. thesis, RWTH Aachen (2008).
- [383] S. Giri, M. Patra, and S. Majumdar, *J. Phys.: Condens. Matter* **23**, 073201 (2011).
- [384] A. P. Malozemoff, *Phys. Rev. B* **35**, 3679 (1987).
- [385] W. H. Meiklejohn, *J. Appl. Phys.* **33**, 1328 (1962).
- [386] W. H. Meiklejohn and C. P. Bean, *Phys. Rev.* **105**, 904 (1957).
- [387] P. J. van der Zaag, Y. Ijiri, J. A. Borchers, L. F. Feiner, R. M. Wolf, J. M. Gaines, R. W. Erwin, and M. A. Verheijen, *Phys. Rev. Lett.* **84**, 6102 (2000).
- [388] T. Ambrose and C. L. Chien, *J. Appl. Phys.* **83**, 6822 (1998).
- [389] C. Papusoi, J. Hauch, M. Fecioru-Morariu, and G. Guntherodt, *J. Appl. Phys.* **99**, 123902 (2006).
- [390] F. Nolting, A. Scholl, J. Stohr, J. W. Seo, J. Fompeyrine, H. Siegwart, J. Locquet, S. Anders, J. Luning, E. E. Fullerton, M. F. Toney, M. R. Scheinfein, and H. A. Padmore, *Nature* **405**, 767 (2000).
- [391] H. Ohldag, A. Scholl, F. Nolting, S. Anders, F. U. Hillebrecht, and J. Stöhr, *Phys. Rev. Lett.* **86**, 2878 (2001).
- [392] A. Hochstrat, C. Binek, X. Chen, and W. Kleemann, *J. Magn. Magn. Mater.* **272-276**, 325 (2004), proceedings of the International Conference on Magnetism (ICM 2003).
- [393] V. Laukhin, V. Skumryev, X. Martí, D. Hrabovsky, F. Sánchez, M. V. García-Cuenca, C. Ferrater, M. Varela, U. Lüders, J. F. Bobo, and J. Fontcuberta, *Phys. Rev. Lett.* **97**, 227201 (2006).
- [394] S. M. Wu, S. A. Cybart, P. Yu, M. D. Rossell, J. X. Zhang, R. Ramesh, and R. C. Dynes, *Nat. Mater.* **9**, 756 (2010).
- [395] V. Skumryev, V. Laukhin, I. Fina, X. Martí, F. Sánchez, M. Gospodinov, and J. Fontcuberta, *Phys. Rev. Lett.* **106**, 057206 (2011).
- [396] G. Lawes and G. Srinivasan, *J. Phys. D: Appl. Phys.* **44**, 243001 (2011).
- [397] P. Rovillain, M. Cazayous, Y. Gallais, A. Sacuto, R. P. S. M. Lobo, D. Lebeugle, and D. Colson, *Phys. Rev. B* **79**, 180411 (2009).
- [398] M. Ramazanoglu, W. Ratcliff, H. T. Yi, A. A. Sirenko, S.-W. Cheong, and V. Kiryukhin, *Phys. Rev. Lett.* **107**, 067203 (2011).

- [399] E. K. H. Salje, *Philos. Trans. R. Soc. London, Ser. A* **368**, 1163 (2010).
- [400] G. Hammerl and N. Spaldin, *Science* **332**, 922 (2011).
- [401] M. Liu, J. Lou, S. Li, and N. X. Sun, *Adv. Funct. Mater.* **21**, 2593 (2011).
- [402] K. Takahashi, N. Kida, and M. Tonouchi, *Phys. Rev. Lett.* **96**, 117402 (2006).
- [403] J. F. Scott, *MRS Bulletin* **35**, 227 (2010).
- [404] S. R. Basu, L. W. Martin, Y. H. Chu, M. Gajek, R. Ramesh, R. C. Rai, X. Xu, and J. L. Musfeldt, *Appl. Phys. Lett.* **92**, 091905 (2008).
- [405] S. Y. Yang, L. W. Martin, S. J. Byrnes, T. E. Conry, S. R. Basu, D. Paran, L. Reichertz, J. Ihlefeld, C. Adamo, A. Melville, Y.-H. Chu, C.-H. Yang, J. L. Musfeldt, D. G. Schlom, I. J. W. Ager, and R. Ramesh, *Appl. Phys. Lett.* **95**, 062909 (2009).
- [406] T. Choi, S. Lee, Y. J. Choi, V. Kiryukhin, and S. Cheong, *Science* **324**, 63 (2009).
- [407] I. V. Solovyev and Z. V. Pchelkina, *New J. Phys.* **10**, 073021 (2008).
- [408] J. A. McLeod, Z. V. Pchelkina, L. D. Finkelstein, E. Z. Kurmaev, R. G. Wilks, A. Moewes, I. V. Solovyev, A. A. Belik, and E. Takayama-Muromachi, *Phys. Rev. B* **81**, 144103 (2010).
- [409] Y. Uratani, T. Shishidou, F. Ishii, and T. Oguchi, *Jpn. J. Appl. Phys.* **44**, 7130 (2005).
- [410] S. Kanungo and T. Saha-Dasgupta, *Phys. Rev. B* **83**, 104104 (2011).
- [411] P. Ravindran, R. Vidya, O. Eriksson, and H. Fjellvag, *Adv. Mater.* **20**, 1353 (2008).
- [412] R. Nechache, P. Gupta, C. Harnagea, and A. Pignolet, *Appl. Phys. Lett.* **91**, 222908 (2007).
- [413] R. Nechache, C. V. Cojocaru, C. Harnagea, C. Nauenheim, M. Nicklaus, A. Ruediger, F. Rosei, and A. Pignolet, *Adv. Mater.* **23**, 1724 (2011).
- [414] R. Nechache, C. Harnagea, S. Licoccia, E. Traversa, A. Ruediger, A. Pignolet, and F. Rosei, *Appl. Phys. Lett.* **98**, 202902 (2011).
- [415] D. H. Kim, H. N. Lee, M. D. Biegalski, and H. M. Christen, *Appl. Phys. Lett.* **91**, 042906 (2007).
- [416] M. R. Suchomel, C. I. Thomas, M. Allix, M. J. Rosseinsky, A. M. Fogg, and M. F. Thomas, *Appl. Phys. Lett.* **90**, 112909 (2007).
- [417] P. Baettig, C. Ederer, and N. A. Spaldin, *Phys. Rev. B* **72**, 214105 (2005).

- [418] S. Picozzi and C. Ederer, *J. Phys.: Condens. Matter* **21**, 303201 (2009).
- [419] Q. Zhang, C. H. Kim, Y. H. Jang, H. J. Hwang, and J. H. Cho, *Appl. Phys. Lett.* **96**, 152901 (2010).
- [420] H. Naganuma, S. Yasui, K. Nishida, T. Iijima, H. Funakubo, and S. Okamura, *J. Appl. Phys.* **109**, 07D917 (2011).
- [421] C. J. Fennie and K. M. Rabe, *Phys. Rev. Lett.* **97**, 267602 (2006).
- [422] J. H. Lee, L. Fang, E. Vlahos, X. Ke, Y. W. Jung, L. F. Kourkoutis, J. Kim, P. J. Ryan, T. Heeg, M. Roeckerath, V. Goian, M. Bernhagen, R. Uecker, P. C. Hammel, K. M. Rabe, S. Kamba, J. Schubert, J. W. Freeland, D. A. Muller, C. J. Fennie, P. Schiffer, V. Gopalan, E. Johnston-Halperin, and D. G. Schlom, *Nature* **466**, 954 (2010).
- [423] J. van Suchtelen, *Philips Res. Rep.* **27**, 28 (1972).
- [424] C. A. F. Vaz, J. Hoffman, C. H. Ahn, and R. Ramesh, *Adv. Mater.* **22**, 2900 (2010).
- [425] C.-W. Nan, M. I. Bichurin, S. Dong, D. Viehland, and G. Srinivasan, *J. Appl. Phys.* **103**, 031101 (2008).
- [426] M. Weisheit, S. Fähler, A. Marty, Y. Souche, C. Poinsignon, and D. Givord, *Science* **315**, 349 (2007).
- [427] H. J. A. Molegraaf, J. Hoffman, C. A. F. Vaz, S. Gariglio, D. van der Marel, C. H. Ahn, and J.-M. Triscone, *Adv. Mater.* **21**, 3470 (2009).
- [428] C. A. F. Vaz, J. Hoffman, Y. Segal, J. W. Reiner, R. D. Grober, Z. Zhang, C. H. Ahn, and F. J. Walker, *Phys. Rev. Lett.* **104**, 127202 (2010).
- [429] V. Garcia, M. Bibes, L. Bocher, S. Valencia, F. Kronast, A. Crassous, X. Moya, S. Enouz-Vedrenne, A. Gloter, D. Imhoff, C. Deranlot, N. D. Mathur, S. Fusil, K. Bouzehouane, and A. Barthélémy, *Science* **327**, 1106 (2010).
- [430] A. J. Hatt and N. A. Spaldin, *Appl. Phys. Lett.* **90**, 242916 (2007).
- [431] M. Fechner, I. V. Maznichenko, S. Ostanin, A. Ernst, J. Henk, P. Bruno, and I. Mertig, *Phys. Rev. B* **78**, 212406 (2008).
- [432] M. K. Niranjana, J. P. Velev, C.-G. Duan, S. S. Jaswal, and E. Y. Tsymlal, *Phys. Rev. B* **78**, 104405 (2008).
- [433] J. M. Rondinelli, M. Stengel, and N. A. Spaldin, *Nat. Nanotechnol.* **3**, 46 (2008).
- [434] I. V. Ovchinnikov and K. L. Wang, *Phys. Rev. B* **78**, 012405 (2008).
- [435] J. D. Burton and E. Y. Tsymlal, *Phys. Rev. B* **80**, 174406 (2009).

- [436] H. Ohno, D. Chiba, F. Matsukura, T. Omiya, E. Abe, T. Dietl, Y. Ohno, and K. Ohtani, *Nature* **408**, 944 (2000).
- [437] H. Tanaka, J. Zhang, and T. Kawai, *Phys. Rev. Lett.* **88**, 027204 (2001).
- [438] C. Thiele, K. Dörr, L. Schultz, E. Beyreuther, and W.-M. Lin, *Appl. Phys. Lett.* **87**, 162512 (2005).
- [439] D. Chiba, M. Sawicki, Y. Nishitani, Y. Nakatani, F. Matsukura, and H. Ohno, *Nature* **455**, 515 (2008).
- [440] I. Stolichnov, S. W. E. Riestler, H. J. Trodahl, N. Setter, A. W. Rushforth, K. W. Edmonds, R. P. Champion, C. T. Foxon, B. L. Gallagher, and T. Jungwirth, *Nat. Mater.* **7**, 464 (2008).
- [441] Y. Yamada, K. Ueno, T. Fukumura, H. T. Yuan, H. Shimotani, Y. Iwasa, L. Gu, S. Tsukimoto, Y. Ikuhara, and M. Kawasaki, *Science* **332**, 1065 (2011).
- [442] C.-W. Nan, *Phys. Rev. B* **50**, 6082 (1994).
- [443] Y. Wang, J. Hu, Y. Lin, and Ce-Wen-Nan, *NPG Asia Mater.* **2**, 61 (2010).
- [444] A. M. J. G. Run, D. R. Terrell, and J. H. Scholing, *J. Mater. Sci.* **9**, 1710 (1974), 10.1007/BF00540771.
- [445] J. Ryu, A. V. Carazo, K. Uchino, and H.-E. Kim, *Jpn. J. Appl. Phys.* **40**, 4948 (2001).
- [446] H. Zheng, J. Wang, S. E. Loffland, Z. Ma, L. Mohaddes-Ardabili, T. Zhao, L. Salamanca-Riba, S. R. Shinde, S. B. Ogale, F. Bai, D. Viehland, Y. Jia, D. G. Schlom, M. Wuttig, A. Roytburd, and R. Ramesh, *Science* **303**, 661 (2004).
- [447] M. K. Lee, T. K. Nath, C. B. Eom, M. C. Smoak, and F. Tsui, *Appl. Phys. Lett.* **77**, 3547 (2000).
- [448] J. G. Wan, X. W. Wang, Y. J. Wu, M. Zeng, Y. Wang, H. Jiang, W. Q. Zhou, G. H. Wang, and J.-M. Liu, *Appl. Phys. Lett.* **86**, 122501 (2005).
- [449] R. Newnham, D. Skinner, and L. Cross, *Mater. Res. Bull.* **13**, 525 (1978).
- [450] G. Srinivasan, *Ann. Rev. Mater. Res.* **40**, 153 (2010).
- [451] A. Brandlmaier, S. Geprägs, M. Weiler, A. Boger, M. Opel, H. Huebl, C. Bihler, M. S. Brandt, B. Botters, D. Grundler, R. Gross, and S. T. B. Goennenwein, *Phys. Rev. B* **77**, 104445 (2008).
- [452] S. T. B. Goennenwein, M. Althammer, C. Bihler, A. Brandlmaier, S. Geprägs, M. Opel, W. Schoch, W. Limmer, R. Gross, and M. S. Brandt, *Phys. Stat. Sol. (RRL)* **2**, 96 (2008).

- [453] C. Bihler, M. Althammer, A. Brandlmaier, S. Geprägs, M. Weiler, M. Opel, W. Schoch, W. Limmer, R. Gross, M. S. Brandt, and S. T. B. Goennenwein, *Phys. Rev. B* **78**, 045203 (2008).
- [454] M. Weiler, A. Brandlmaier, S. Geprägs, M. Althammer, M. Opel, C. Bihler, H. Huebl, M. S. Brandt, R. Gross, and S. T. B. Goennenwein, *New J. Phys.* **11**, 013021 (2009).
- [455] M. I. Bichurin, V. M. Petrov, S. V. Averkin, and E. Liverts, *J. Appl. Phys.* **107**, 053904 (2010).
- [456] G. Srinivasan, E. T. Rasmussen, J. Gallegos, R. Srinivasan, Y. I. Bokhan, and V. M. Laletin, *Phys. Rev. B* **64**, 214408 (2001).
- [457] I. A. Osaretin and R. G. Rojas, *Phys. Rev. B* **82**, 174415 (2010).
- [458] N. A. Pertsev, A. G. Zembilgotov, and A. K. Tagantsev, *Phys. Rev. Lett.* **80**, 1988 (1998).
- [459] D. Sander, *Rep. Prog. Phys.* **62**, 809 (1999).
- [460] C. Kittel, *Rev. Mod. Phys.* **21**, 541 (1949).
- [461] H. Mueller, *Phys. Rev.* **58**, 805 (1940).
- [462] W. P. Mason, *Phys. Rev.* **82**, 715 (1951).
- [463] L. Landau and E. Lifshitz, *Theory of elasticity* (Elsevier Ltd., 1986).
- [464] E. du Trémolet de Lacheisserie, *Magnetostriction: Theory and Applications of Magnetoelasticity* (CRC Press, 1993).
- [465] E. W. Lee, *Rep. Prog. Phys.* **18**, 184 (1955).
- [466] S. Blügel, Institute of Solid State Research (IFF) .
- [467] H. B. Callen and N. Goldberg, *J. Appl. Phys.* **36**, 976 (1965).
- [468] N. S. Akulov, *Zeitschrift für Physik A Hadrons and Nuclei* **66**, 533 (1930), 10.1007/BF01402036.
- [469] S. W. Sun and R. C. O’Handley, *Phys. Rev. Lett.* **66**, 2798 (1991).
- [470] M. Weber, R. Koch, and K. H. Rieder, *Phys. Rev. Lett.* **73**, 1166 (1994).
- [471] Z. Tian, D. Sander, and J. Kirschner, *Phys. Rev. B* **79**, 024432 (2009).
- [472] M. Komelj and M. Fähnle, *Phys. Rev. B* **65**, 212410 (2002).
- [473] S. Blundell, *Magnetism in Condensed Matter* (Oxford University Press, 2001).

- [474] S. B. T. Gönnerwein, *Two-Dimensional Electron Gases and Ferromagnetic Semiconductors: Materials for Spintronic*, Ph.D. thesis, Technische Universität München (2003).
- [475] M. J. Haun, E. Furman, S. J. Jang, H. A. McKinstry, and L. E. Cross, *J. Appl. Phys.* **62**, 3331 (1987).
- [476] W. Cao, *Ferroelectrics* **375**, 28 (2008).
- [477] J. J. Yang, Y. G. Zhao, H. F. Tian, L. B. Luo, H. Y. Zhang, Y. J. He, and H. S. Luo, *Appl. Phys. Lett.* **94**, 212504 (2009).
- [478] J.-H. Kim, K.-S. Ryu, J.-W. Jeong, and S.-C. Shin, *Appl. Phys. Lett.* **97**, 252508 (2010).
- [479] N. Hur, S. Park, P. A. Sharma, J. S. Ahn, S. Guha, and S. Cheong, *Nature* **429**, 392 (2004).
- [480] E. Ascher, H. Rieder, H. Schmid, and H. Stössel, *J. Appl. Phys.* **37**, 1404 (1966).
- [481] K. Dörr, O. Bilani-Zeneli, A. Herklotz, A. Rata, K. Boldyreva, J. Kim, M. Dekker, K. Nenkov, L. Schultz, and M. Reibold, *Eur. Phys. J. B* **71**, 6 (2009).
- [482] Y. Moritomo, A. Asamitsu, and Y. Tokura, *Phys. Rev. B* **51**, 16491 (1995).
- [483] R. Lengsdorf, M. Ait-Tahar, S. S. Saxena, M. Ellerby, D. I. Khomskii, H. Micklitz, T. Lorenz, and M. M. Abd-Elmeguid, *Phys. Rev. B* **69**, 140403 (2004).
- [484] H. Fu and R. E. Cohen, *Nature* **403**, 281 (2000).
- [485] P. Marcus and F. Jona, *J. Phys. Chem. Solids* **55**, 1513 (1994), special Symposium in Honor of Professor Arthur S. Nowick.
- [486] P. M. Marcus, *Phys. Rev. B* **53**, 7460 (1996).
- [487] S.-E. Park and T. R. ShROUT, *J. Appl. Phys.* **82**, 1804 (1997).
- [488] W. L. Bond, W. P. Mason, and H. J. McSkimin, *Phys. Rev.* **82**, 442 (1951).
- [489] H. Kato, T. Okuda, Y. Okimoto, Y. Tomioka, Y. Takenoya, A. Ohkubo, M. Kawasaki, and Y. Tokura, *Appl. Phys. Lett.* **81**, 328 (2002).
- [490] D. Serrate, J. M. D. Teresa, and M. R. Ibarra, *J. Phys.: Condens. Matter* **19**, 023201 (2007).
- [491] G. Vaitheeswaran, V. Kanchana, and A. Delin, *Appl. Phys. Lett.* **86**, 032513 (2005).

- [492] F. Jona and G. Shirane, *Ferroelectric crystals*, edited by R. Smoluchowski and N. Kurti (Pergamon Press, 1962).
- [493] K. ichi Sakayori, Y. Matsui, H. Abe, E. Nakamura, M. Kenmoku, T. Hara, D. Ishikawa, A. Kokubu, K. ichi Hirota, and T. Ikeda, *Jpn. J. Appl. Phys.* **34**, 5443 (1995).
- [494] H. D. Megaw, *Nature* **155**, 484 (1945).
- [495] H. F. Kay and P. Vousden, *Philos. Mag.* **40**, 1019 (1949).
- [496] L. A. Shebanov, *Phys. Status Solidi A* **65**, 321 (1981).
- [497] W. J. Merz, *Phys. Rev.* **76**, 1221 (1949).
- [498] W. J. Merz, *Phys. Rev.* **88**, 421 (1952).
- [499] G. Sheng, J. X. Zhang, Y. L. Li, S. Choudhury, Q. X. Jia, Z. K. Liu, and L. Q. Chen, *Appl. Phys. Lett.* **93**, 232904 (2008).
- [500] W. Cochran, *Adv. Phy.* **9**, 387 (1960).
- [501] E. A. Stern, *Phys. Rev. Lett.* **93**, 037601 (2004).
- [502] J. Harada, J. D. Axe, and G. Shirane, *Phys. Rev. B* **4**, 155 (1971).
- [503] B. Ravel, E. A. Stern, R. I. Vedrinskii, and V. Kraizman, *Ferroelectrics* **206**, 407 (1998).
- [504] B. D. Chapman, E. A. Stern, S.-W. Han, J. O. Cross, G. T. Seidler, V. Gavrilatshchenko, R. V. Vedrinskii, and V. L. Kraizman, *Phys. Rev. B* **71**, 020102 (2005).
- [505] R. Comes, M. Lambert, and A. Guinier, *Solid State Commun.* **6**, 715 (1968).
- [506] B. c. v. Zalar, A. Lebar, J. Seliger, R. Blinc, V. V. Laguta, and M. Itoh, *Phys. Rev. B* **71**, 064107 (2005).
- [507] M. I. Marqués, *Phys. Rev. B* **71**, 174116 (2005).
- [508] M. I. Marqués and J. A. Gonzalo, *Ferroelectrics* **337**, 51 (2006).
- [509] W. Zhong, D. Vanderbilt, and K. M. Rabe, *Phys. Rev. Lett.* **73**, 1861 (1994).
- [510] W. Zhong, D. Vanderbilt, and K. M. Rabe, *Phys. Rev. B* **52**, 6301 (1995).
- [511] R. D. King-Smith and D. Vanderbilt, *Phys. Rev. B* **49**, 5828 (1994).
- [512] U. V. Waghmare, B. P. Burton, and E. J. Cockayne, *Ferroelectrics* **291**, 187 (2003).
- [513] T. Nishimatsu, “Feram code,” <http://loto.sourceforge.net/feram/>.

- [514] T. Nishimatsu, U. V. Waghmare, Y. Kawazoe, and D. Vanderbilt, *Phys. Rev. B* **78**, 104104 (2008).
- [515] S. Tinte, J. Iniguez, K. M. Rabe, and D. Vanderbilt, *Phys. Rev. B* **67**, 064106 (2003).
- [516] P. N. Keating, *Phys. Rev.* **145**, 637 (1966).
- [517] R. Car and M. Parrinello, *Phys. Rev. Lett.* **55**, 2471 (1985).
- [518] S. D. Bond, B. J. Leimkuhler, and B. B. Laird, *J. Comp.Phys.* **151**, 114 (1999).
- [519] G. H. Kwei, A. C. Lawson, S. J. L. Billinge, and S. W. Cheong, *J. Phys. Chem.* **97**, 2368 (1993).
- [520] T. Nishimatsu, M. Iwamoto, Y. Kawazoe, and U. V. Waghmare, *Phys. Rev. B* **82**, 134106 (2010).
- [521] Z. Wu and R. E. Cohen, *Phys. Rev. B* **73**, 235116 (2006).
- [522] E. B. Tadmor, U. V. Waghmare, G. S. Smith, and E. Kaxiras, *Acta Mater.* **50**, 2989 (2002).
- [523] J. Paul, T. Nishimatsu, Y. Kawazoe, and U. V. Waghmare, *Appl. Phys. Lett.* **93**, 242905 (2008).
- [524] A. Schaefer, H. Schmitt, and A. Dörr, *Ferroelectrics* **69**, 253 (1986).
- [525] R. Tazaki, D. Fu, M. Itoh, M. Daimon, and S. ya Koshihara, *J. Phys.: Condens. Matter* **21**, 215903 (2009).
- [526] D. Damjanovic, F. Brem, and N. Setter, *Appl. Phys. Lett.* **80**, 652 (2002).
- [527] S.-E. Park, S. Wada, L. E. Cross, and T. R. ShROUT, *J. Appl. Phys.* **86**, 2746 (1999).
- [528] R. W. Cahn, *Adv. Phy.* **3**, 363 (1954).
- [529] J. Hlinka and P. Márton, *Phys. Rev. B* **74**, 104104 (2006).
- [530] P. Marton, I. Rychetsky, and J. Hlinka, *Phys. Rev. B* **81**, 144125 (2010).
- [531] J. Fousek and V. Janovec, *J. Appl. Phys.* **40**, 135 (1969).
- [532] C. Kittel, *Solid State Commun.* **10**, 119 (1972).
- [533] Q. Zhang and W. A. Goddard, *Appl. Phys. Lett.* **89**, 182903 (2006).
- [534] P. W. Forsbergh, *Phys. Rev.* **76**, 1187 (1949).
- [535] R. G. Rhodes, *Acta Cryst.* **4**, 105 (1951).

- [536] E. J. W. Verwey and E. L. Heilmann, *J. Chem. Phys.* **15**, 174 (1947).
- [537] C. G. Shull, E. O. Wollan, and W. C. Koehler, *Phys. Rev.* **84**, 912 (1951).
- [538] J. A. Duffy, J. W. Taylor, S. B. Dugdale, C. Shenton-Taylor, M. W. Butchers, S. R. Giblin, M. J. Cooper, Y. Sakurai, and M. Itou, *Phys. Rev. B* **81**, 134424 (2010).
- [539] M. Fonin, R. Pentcheva, Y. S. Dedkov, M. Sperlich, D. V. Vyalikh, M. Scheffler, U. Rüdiger, and G. Güntherodt, *Phys. Rev. B* **72**, 104436 (2005).
- [540] R. Pentcheva, F. Wendler, H. L. Meyerheim, W. Moritz, N. Jedrecy, and M. Scheffler, *Phys. Rev. Lett.* **94**, 126101 (2005).
- [541] Z. Zhang and S. Satpathy, *Phys. Rev. B* **44**, 13319 (1991).
- [542] H.-T. Jeng and G. Y. Guo, *Phys. Rev. B* **65**, 094429 (2002).
- [543] Y. S. Dedkov, U. Rüdiger, and G. Güntherodt, *Phys. Rev. B* **65**, 064417 (2002).
- [544] M. Fonin, Y. S. Dedkov, R. Pentcheva, U. Rüdiger, and G. Güntherodt, *J. Phys.: Condens. Matter* **20**, 142201 (2008).
- [545] P. Seneor, A. Fert, J.-L. Maurice, F. Montaigne, F. Petroff, and A. Vaurès, *Appl. Phys. Lett.* **74**, 4017 (1999).
- [546] M. Bibes and A. Barthelemy, *IEEE Trans. Electron Devices* **54**, 1003 (2007).
- [547] K. I. Arai, K. Ohmori, N. Tsuya, and S. Iida, *Phys. Status Solidi A* **34**, 325 (1976).
- [548] S. Kale, S. M. Bhagat, S. E. Loffland, T. Scabarozzi, S. B. Ogale, A. Orozco, S. R. Shinde, T. Venkatesan, B. Hannoyer, B. Mercey, and W. Prellier, *Phys. Rev. B* **64**, 205413 (2001).
- [549] H. Schwenk, S. Bareiter, C. Hinkel, B. L'Éthi, Z. Kakol, A. Koslowski, and J. M. Honig, *Eur. Phys. J. B* **13**, 491 (2000), 10.1007/s100510050060.
- [550] F. Walz, *J. Phys.: Condens. Matter* **14**, R285 (2002).
- [551] J. García and G. Subías, *J. Phys.: Condens. Matter* **16**, R145 (2004).
- [552] E. Verwey, *Nature* **144**, 327 (1939).
- [553] W. C. Hamilton, *Phys. Rev.* **110**, 1050 (1958).
- [554] M. E. Fleet, *Acta Cryst.* **B37**, 917 (1981).
- [555] C. Medrano, M. Schlenker, J. Baruchel, J. Espeso, and Y. Miyamoto, *Phys. Rev. B* **59**, 1185 (1999).

- [556] J. P. Wright, J. P. Attfield, and P. G. Radaelli, *Phys. Rev. B* **66**, 214422 (2002).
- [557] Y. Joly, J. E. Lorenzo, E. Nazarenko, J.-L. Hodeau, D. Mannix, and C. Marin, *Phys. Rev. B* **78**, 134110 (2008).
- [558] H.-T. Jeng, G. Y. Guo, and D. J. Huang, *Phys. Rev. B* **74**, 195115 (2006).
- [559] E. J. Verwey, P. W. Haayman, and F. C. Romeijn, *J. Chem. Phys.* **15**, 181 (1947).
- [560] C. H. Li, *Phys. Rev.* **40**, 1002 (1932).
- [561] L. R. Bickford, *Rev. Mod. Phys.* **25**, 75 (1953).
- [562] G. S. Parks and K. K. Kelley, *J. Phys. Chem.* **30**, 47 (1926).
- [563] R. W. Millar, *J. Am. Chem. Soc.* **51**, 215 (1929).
- [564] E. Verwey and P. Haayman, *Physica* **8**, 979 (1941).
- [565] T. Toyoda, S. Sasaki, and M. Tanaka, *Am. Mineralogist* **84**, 294 (1999).
- [566] R. J. Goff, J. P. Wright, J. P. Attfield, and P. G. Radaelli, *J. Phys.: Condens. Matter* **17**, 7633 (2005).
- [567] E. Nazarenko, J. E. Lorenzo, Y. Joly, J. L. Hodeau, D. Mannix, and C. Marin, *Phys. Rev. Lett.* **97**, 056403 (2006).
- [568] M. Bimbi, G. Allodi, R. De Renzi, C. Mazzoli, and H. Berger, *Phys. Rev. B* **77**, 045115 (2008).
- [569] J. Schlappa, C. Schüßler-Langeheine, C. F. Chang, H. Ott, A. Tanaka, Z. Hu, M. W. Haverkort, E. Schierle, E. Weschke, G. Kaindl, and L. H. Tjeng, *Phys. Rev. Lett.* **100**, 026406 (2008).
- [570] J. García, G. Subías, M. G. Proietti, H. Renevier, Y. Joly, J. L. Hodeau, J. Blasco, M. C. Sánchez, and J. F. Bézar, *Phys. Rev. Lett.* **85**, 578 (2000).
- [571] J. García, G. Subías, M. G. Proietti, J. Blasco, H. Renevier, J. L. Hodeau, and Y. Joly, *Phys. Rev. B* **63**, 054110 (2001).
- [572] G. Subias, J. Garcia, J. Blasco, M. Grazia Proietti, H. Renevier, and M. Concepción Sánchez, *Phys. Rev. Lett.* **93**, 156408 (2004).
- [573] F. Zhou and G. Ceder, *Phys. Rev. B* **81**, 205113 (2010).
- [574] M. Matsubara, Y. Shimada, T. Arima, Y. Taguchi, and Y. Tokura, *Phys. Rev. B* **72**, 220404 (2005).
- [575] G. T. Rado and J. M. Ferrari, *Phys. Rev. B* **15**, 290 (1977).

- [576] S. B. Wilkins, S. Di Matteo, T. A. W. Beale, Y. Joly, C. Mazzoli, P. D. Hatton, P. Bencok, F. Yakhou, and V. A. M. Brabers, *Phys. Rev. B* **79**, 201102 (2009).
- [577] S. D. Matteo, *J. Phys.: Conf. Ser.* **190**, 012008 (2009).
- [578] M. Ziese, “private communication,” (2010).
- [579] H. F. Tian, T. L. Qu, L. B. Luo, J. J. Yang, S. M. Guo, H. Y. Zhang, Y. G. Zhao, and J. Q. Li, *Appl. Phys. Lett.* **92**, 063507 (2008).
- [580] C. A. F. Vaz, J. Hoffman, A.-B. Posadas, and C. H. Ahn, *Appl. Phys. Lett.* **94**, 022504 (2009).
- [581] Y. S. Koo, K. M. Song, N. Hur, J. H. Jung, T.-H. Jang, H. J. Lee, T. Y. Koo, Y. H. Jeong, J. H. Cho, and Y. H. Jo, *Appl. Phys. Lett.* **94**, 032903 (2009).
- [582] G. E. Sterbinsky, B. W. Wessels, J.-W. Kim, E. Karapetrova, P. J. Ryan, and D. J. Keavney, *Appl. Phys. Lett.* **96**, 092510 (2010).
- [583] M. S. Park, J.-H. Song, and A. J. Freeman, *Phys. Rev. B* **79**, 024420 (2009).
- [584] D. Venkateshvaran, *Fabrication and Characterization of $Zn_xFe_{3-x}O_4$ Epitaxial Films*, Master’s thesis, Technische Universität München (2008).
- [585] O. Madelung, U. Rössler, and M. Schulz, eds., *Non-Tetrahedrally Bonded Binary Compounds II*, Vol. 41D (Springer-Verlag, Berlin/Heidelberg, 2000).
- [586] S. K. Arora, R. G. S. Sofin, I. V. Shvets, and M. Luysberg, *J. Appl. Phys.* **100**, 073908 (2006).
- [587] M. Luysberg, R. G. S. Sofin, S. K. Arora, and I. V. Shvets, *Phys. Rev. B* **80**, 024111 (2009).
- [588] D. T. Margulies, F. T. Parker, M. L. Rudee, F. E. Spada, J. N. Chapman, P. R. Aitchison, and A. E. Berkowitz, *Phys. Rev. Lett.* **79**, 5162 (1997).
- [589] W. Eerenstein, T. T. M. Palstra, S. S. Saxena, and T. Hibma, *Phys. Rev. Lett.* **88**, 247204 (2002).
- [590] A. M. Bataille, L. Ponson, S. Gota, L. Barbier, D. Bonamy, M. Gautier-Soyer, C. Gatel, and E. Snoeck, *Phys. Rev. B* **74**, 155438 (2006).
- [591] S. Celotto, W. Eerenstein, and T. Hibma, *Eur. Phys. J. B* **36**, 271 (2003), 10.1140/epjb/e2003-00344-7.
- [592] A. Fernández-Pacheco, J. Orna, J. M. D. Teresa, P. A. Algarabel, L. Morellon, J. A. Pardo, M. R. Ibarra, E. Kampert, and U. Zeitler, *Appl. Phys. Lett.* **95**, 262108 (2009).
- [593] J. P. Shepherd, J. W. Koenitzer, R. Aragón, J. Spal/ek, and J. M. Honig, *Phys. Rev. B* **43**, 8461 (1991).

- [594] G. K. Rozenberg, G. R. Hearne, M. P. Pasternak, P. A. Metcalf, and J. M. Honig, *Phys. Rev. B* **53**, 6482 (1996).
- [595] S. Todo, N. Takeshita, T. Kanehara, T. Mori, and N. Môri, *J. Appl. Phys.* **89**, 7347 (2001).
- [596] G. A. Samara, *Phys. Rev. Lett.* **21**, 795 (1968).
- [597] J. Spalek, A. Kozłowski, Z. Tarnawski, Z. Kałol, Y. Fukami, F. Ono, R. Zach, L. J. Spalek, and J. M. Honig, *Phys. Rev. B* **78**, 100401 (2008).
- [598] Y. Ding, D. Haskel, S. G. Ovchinnikov, Y.-C. Tseng, Y. S. Orlov, J. C. Lang, and H.-k. Mao, *Phys. Rev. Lett.* **100**, 045508 (2008).
- [599] F. m. c. Baudelet, S. Pascarelli, O. Mathon, J.-P. Itié, A. Polian, and J.-C. Chervin, *Phys. Rev. B* **82**, 140412 (2010).
- [600] K. Kobayashi, T. Kimura, H. Sawada, K. Terakura, and Y. Tokura, *Nature* **395**, 677 (1998).
- [601] H. Asano, N. Koduka, K. Imaeda, M. Sugiyama, and M. Matsui, *IEEE Trans. Magn.* **41**, 2811 (2005).
- [602] D. S. Donoso, *Spin Dependent Transport in Double Perovskites and Magnetic Nanostructures*, Ph.D. thesis, University of Zaragoza (2005).
- [603] Y. Krockenberger, K. Mogare, M. Reehuis, M. Tovar, M. Jansen, G. Vaitheeswaran, V. Kanchana, F. Bultmark, A. Delin, F. Wilhelm, A. Rogalev, A. Winkler, and L. Alff, *Phys. Rev. B* **75**, 020404 (2007).
- [604] D. D. Sarma, P. Mahadevan, T. Saha-Dasgupta, S. Ray, and A. Kumar, *Phys. Rev. Lett.* **85**, 2549 (2000).
- [605] J. Kanamori and K. Terakura, *J. Phys. Soc. Jpn.* **70**, 1433 (2001).
- [606] Z. Fang, K. Terakura, and J. Kanamori, *Phys. Rev. B* **63**, 180407 (2001).
- [607] T. Yamamoto, J. Liimatainen, J. Linden, M. Karppinen, and H. Yamauchi, *J. Mater. Chem.* **10**, 2342 (2000).
- [608] P. Majewski, *Magnetischer Austauschmechanismus und Magnetotransport in ferromagnetischen Doppelperowskiten $A_2BB'O_6$* , Ph.D. thesis, Technische Universität München (2006).
- [609] P. Majewski, S. Geprägs, O. Sanganas, M. Opel, R. Gross, F. Wilhelm, A. Rogalev, and L. Alff, *Appl. Phys. Lett.* **87**, 202503 (2005).
- [610] P. Majewski, S. Geprägs, A. Boger, M. Opel, A. Erb, R. Gross, G. Vaitheeswaran, V. Kanchana, A. Delin, F. Wilhelm, A. Rogalev, and L. Alff, *Phys. Rev. B* **72**, 132402 (2005).

- [611] M. Sikora, C. Kapusta, M. Borowiec, C. J. Oates, V. Prochazka, D. Rybicki, D. Zajac, J. M. D. Teresa, C. Marquina, and M. R. Ibarra, *Appl. Phys. Lett.* **89**, 062509 (2006).
- [612] A. Winkler, N. Narayanan, D. Mikhailova, K. G. Bramnik, H. Ehrenberg, H. Fuess, G. Vaitheeswaran, V. Kanchana, F. Wilhelm, A. Rogalev, A. Kolchinskaya, and L. Alff, *New J. Phys.* **11**, 073047 (2009).
- [613] J. Gopalakrishnan, A. Chattopadhyay, S. B. Ogale, T. Venkatesan, R. L. Greene, A. J. Millis, K. Ramesha, B. Hannoyer, and G. Marest, *Phys. Rev. B* **62**, 9538 (2000).
- [614] J. B. Philipp, P. Majewski, L. Alff, A. Erb, R. Gross, T. Graf, M. S. Brandt, J. Simon, T. Walther, W. Mader, D. Topwal, and D. D. Sarma, *Phys. Rev. B* **68**, 144431 (2003).
- [615] J. M. De Teresa, D. Serrate, J. Blasco, M. R. Ibarra, and L. Morellon, *Phys. Rev. B* **69**, 144401 (2004).
- [616] D. Serrate, J. M. D. Teresa, P. A. Algarabel, C. Marquina, J. Blasco, M. R. Ibarra, and J. Galibert, *J. Phys.: Condens. Matter* **19**, 436226 (2007).
- [617] M. Komelj, *Phys. Rev. B* **82**, 012410 (2010).
- [618] H. Asano, N. Kozuka, A. Tsuzuki, and M. Matsui, *Appl. Phys. Lett.* **85**, 263 (2004).
- [619] J. Orna, L. Morellon, P. Algarabel, J. Pardo, C. Magen, M. Varela, S. Pennycook, J. D. Teresa, and M. Ibarra, *J. Magn. Magn. Mater.* **322**, 1217 (2010), proceedings of the Joint European Magnetic Symposia.
- [620] S. Chakraverty, A. Ohtomo, and M. Kawasaki, *Appl. Phys. Lett.* **97**, 243107 (2010).
- [621] L. Balcells, J. Navarro, M. Bibes, A. Roig, B. Martínez, and J. Fontcuberta, *Appl. Phys. Lett.* **78**, 781 (2001).
- [622] A. Venimadhav, F. Sher, J. Attfield, and M. Blamire, *Solid State Commun.* **138**, 314 (2006).
- [623] F. D. Czeschka, *Strukturelle, elektrische und magnetische Eigenschaften dünner Sr_2CrReO_6 Schichten für die Spinelektronik*, Diploma thesis, Technische Universität München (2007).
- [624] J. A. Alonso, M. T. Casais, M. J. Martinez-Lope, J. L. Martinez, P. Velasco, A. Munoz, and M. T. Fernandez-Diaz, *Chem. Mater.* **12**, 161 (2000).
- [625] I. V. Solovyev, *Phys. Rev. B* **65**, 144446 (2002).

- [626] R. P. Panguluri, S. Xu, Y. Moritomo, I. V. Solovyev, and B. Nadgorny, *Appl. Phys. Lett.* **94**, 012501 (2009).
- [627] J. Navarro, L. Balcells, F. Sandiumenge, M. Bibes, A. Roig, B. Mart \tilde{A} nez, and J. Fontcuberta, *J. Phys.: Condens. Matter* **13**, 8481 (2001).
- [628] J. M. Michalik, J. M. D. Teresa, C. Ritter, J. Blasco, D. Serrate, M. R. Ibarra, C. Kapusta, J. Freudenberger, and N. Kozlova, *Europhys. Lett.* **78**, 6 (2007).
- [629] C. Meneghini, S. Ray, F. Liscio, F. Bardelli, S. Mobilio, and D. D. Sarma, *Phys. Rev. Lett.* **103**, 046403 (2009).
- [630] J. B. Goodenough and R. I. Dass, *Int. J. Inorg. Mater.* **2**, 3 (2000).
- [631] T. Asaka, X. Z. Yu, Y. Tomioka, Y. Kaneko, T. Nagai, K. Kimoto, K. Ishizuka, Y. Tokura, and Y. Matsui, *Phys. Rev. B* **75**, 184440 (2007).
- [632] C. Kittel, *Introduction to Solid State Physics* (Oldenbourg Verlag, 1991).
- [633] H. Danan, A. Herr, and A. J. P. Meyer, *J. Appl. Phys.* **39**, 669 (1968).
- [634] N. Ashcroft and D. Mermin, *Solid State Physics* (Oldenbourg Verlag, 2001).
- [635] R. R. Birss and E. W. Lee, *Proc. Phys. Soc.* **76**, 502 (1960).
- [636] G. A. Alers, J. R. Neighbours, and H. Sato, *J. Phys. Chem. Solids* **13**, 40 (1960).
- [637] A. E. Clark, J. B. Restorff, M. WunFogle, D. Wu, and T. A. Lograsso, *J. Appl. Phys.* **103**, 07B310 (2008).
- [638] T. Sourmail, *Prog. Mater. Sci.* **50**, 816 (2005).
- [639] R. C. Hall, *J. Appl. Phys.* **31**, S157 (1960).
- [640] D. Bonnenberg, K. A. Hempel, and H. P. J. Wijn, *3d, 4d and 5d Elements, Alloys and Compounds*, edited by H. Wijn, Vol. 19a (Springer-Verlag, Berlin/Heidelberg, 1986).
- [641] J. W. Shih, *Phys. Rev.* **46**, 139 (1934).
- [642] A. Y. Liu and D. J. Singh, *Phys. Rev. B* **46**, 11145 (1992).
- [643] D. Berlincourt and H. Jaffe, *Phys. Rev.* **111**, 143 (1958).
- [644] D. Dale, A. Fleet, J. D. Brock, and Y. Suzuki, *Appl. Phys. Lett.* **82**, 3725 (2003).
- [645] P. W. Bridgman, *Phys. Rev.* **42**, 858 (1932).
- [646] C. S. Smith, *Phys. Rev.* **94**, 42 (1954).

- [647] R. L. Parker and A. Krinsky, *J. Appl. Phys.* **34**, 2700 (1963).
- [648] G. C. Kuczynski, *Phys. Rev.* **94**, 61 (1954).
- [649] Y. P. Shkolnikov, K. Vakili, E. P. D. Poortere, and M. Shayegan, *Appl. Phys. Lett.* **85**, 3766 (2004).
- [650] S. U. Jen, C. C. Yu, C. H. Liu, and G. Y. Lee, *Thin Solid Films* **434**, 316 (2003).
- [651] E. Kloholm, *J. Vac. Sci. Technol.* **10**, 235 (1973).
- [652] S. U. Jen, T. C. Wu, and C. H. Liu, *J. Magn. Magn. Mater.* **256**, 54 (2003).
- [653] J. M. De Teresa, M. R. Ibarra, J. Blasco, J. García, C. Marquina, P. A. Algarabel, Z. Arnold, K. Kamenev, C. Ritter, and R. von Helmolt, *Phys. Rev. B* **54**, 1187 (1996).
- [654] T. Taniyama, K. Akasaka, D. Fu, and M. Itoh, *J. Appl. Phys.* **105**, 07D901 (2009).
- [655] M. Adachi, Y. Akishige, T. Asahi, K. Deguchi, K. Gesi, K. Hasebe, T. Hikita, T. Ikeda, Y. Iwata, M. Komukae, T. Mitsui, E. Nakamura, N. Nakatani, M. Okuyama, T. Osaka, A. Sakai, E. Sawaguchi, Y. Shiozaki, T. Takenaka, K. Toyoda, T. Tsukamoto, and T. Yagi, in *Oxides*, Vol. 36A1, edited by Y. Shiozaki, E. Nakamura, and T. Mitsui (Springer-Verlag, Berlin/Heidelberg, 2002) pp. 1–12.
- [656] A. Brandlmaier, *Magnetische Anisotropie in dünnen Schichten aus Magnetit*, Diploma thesis, Technische Universität München (2006).
- [657] C. Chappert, K. L. Dang, P. Beauvillain, H. Hurdequint, and D. Renard, *Phys. Rev. B* **34**, 3192 (1986).
- [658] L. McGuigan, R. C. Barklie, R. G. S. Sofin, S. K. Arora, and I. V. Shvets, *Phys. Rev. B* **77**, 174424 (2008).
- [659] L. M. Eng, *Nanotechnology* **10**, 405 (1999).
- [660] A. Gruverman and A. Kholkin, *Rep. Prog. Phys.* **69**, 2443 (2006).
- [661] H. Janocha and W. Cao, in *Adaptronics and Smart Structures* (Springer Berlin Heidelberg, 2007) pp. 29–53, 10.1007/978-3-540-71967-0_3.
- [662] S. Wada, *Next-Generation Actuators Leading Breakthroughs*, edited by T. Higuchi, K. Suzumori, and S. Tadokoro (Springer London, London, 2010).
- [663] J. van den Boomgaard and A. M. J. G. van Run, *Solid State Commun.* **19**, 405 (1976).
- [664] D. Vanderbilt and M. H. Cohen, *Phys. Rev. B* **63**, 094108 (2001).

- [665] J. Paul, T. Nishimatsu, Y. Kawazoe, and U. V. Waghmare, *Phys. Rev. B* **80**, 024107 (2009).
- [666] M. M. H. Jnr, V. G. Veeraraghavan, H. Rubin, and P. G. Winchell, *J. Appl. Crystallogr.* **10**, 66 (1977).
- [667] K. Ban, M. Gomi, T. Shundo, and N. Nishimura, *IEEE Trans. Magn.* **41**, 2793 (2005).
- [668] C. Israel, S. Kar-Narayan, and N. D. Mathur, *Appl. Phys. Lett.* **93**, 173501 (2008).
- [669] E. C. Subbarao, M. C. McQuarrie, and W. R. Buessem, *J. Appl. Phys.* **28**, 1194 (1957).
- [670] D. D. Fong and C. Thompson, *Ann. Rev. Mater. Res.* **36**, 431 (2006).
- [671] K. S. Lee, Y. K. Kim, S. Baik, J. Kim, and I. S. Jung, *Appl. Phys. Lett.* **79**, 2444 (2001).
- [672] S. J. van Reeuwijk, K. Karakaya, H. Graafsma, and S. Harkema, *J. Appl. Crystallogr.* **37**, 193 (2004).
- [673] S. van Reeuwijk, *Deformations in Crystals Induced by External Electric Fields*, Ph.D. thesis, University of Twente (2002).
- [674] M. J. Hoffmann, H. Kungl, J.-T. Reszat, and S. Wagner, "Characterization of pzt-ceramics by high-resolution x-ray analysis," in *Polar Oxides* (Wiley-VCH Verlag GmbH & Co. KGaA, 2005) pp. 137–150.
- [675] I. Fujimoto, *Phys. Rev. Lett.* **40**, 941 (1978).
- [676] A. G. Chynoweth, *Phys. Rev.* **102**, 705 (1956).
- [677] M. Weiler, *Magnetization control in multiferroic heterostructures*, Master's thesis, Technische Universität München (2007).
- [678] S. Sahoo, S. Polisetty, C.-G. Duan, S. S. Jaswal, E. Y. Tsymbal, and C. Binek, *Phys. Rev. B* **76**, 092108 (2007).
- [679] A. S. Bhalla, D. N. Bose, E. W. White, and L. E. Cross, *Phys. Status Solidi A* **7**, 335 (1971).
- [680] G. R. Barsch, *Acta Cryst.* **A32**, 575 (1976).
- [681] P. R. Stone, C. Bihler, M. Kraus, M. A. Scarpulla, J. W. Beeman, K. M. Yu, M. S. Brandt, and O. D. Dubon, *Phys. Rev. B* **78**, 214421 (2008).
- [682] D. Damjanovic and M. Demartin, *J. Phys. D: Appl. Phys.* **29**, 2057 (1996).
- [683] V. Mueller, H. Beige, and Q. M. Zhang, *Ferroelectrics* **222**, 295 (1999).

- [684] L. Rayleigh, *Philos. Mag.* **23**, 225 (1887).
- [685] S. Brivio, D. Petti, R. Bertacco, and J. C. Cezar, *Appl. Phys. Lett.* **98**, 092505 (2011).
- [686] Z. Chen, Z. Luo, Y. Qi, P. Yang, S. Wu, C. Huang, T. Wu, J. Wang, C. Gao, T. Sritharan, and L. Chen, *Appl. Phys. Lett.* **97**, 242903 (2010).
- [687] H. Cao, C. P. Devreugd, W. Ge, J. Li, D. Viehland, H. Luo, and X. Zhao, *Appl. Phys. Lett.* **94**, 032901 (2009).
- [688] T. Wu, A. Bur, P. Zhao, K. P. Mohanchandra, K. Wong, K. L. Wang, C. S. Lynch, and G. P. Carman, *Appl. Phys. Lett.* **98**, 012504 (2011).
- [689] A. Ishii, Y. Takano, S. Arisawa, T. Hatano, and K. Togano, *Physica C* **372-376**, 600 (2002).
- [690] D. T. Margulies, F. T. Parker, F. E. Spada, R. S. Goldman, J. Li, R. Sinclair, and A. E. Berkowitz, *Phys. Rev. B* **53**, 9175 (1996).
- [691] F. Zavaliche, T. Zhao, H. Zheng, F. Straub, M. P. Cruz, P.-L. Yang, D. Hao, and R. Ramesh, *Nano Lett.* **7**, 1586 (2007).
- [692] B. Liu, T. Sun, J. He, and V. P. Dravid, *ACS Nano* **4**, 6836 (2010).
- [693] R. Ramesh and N. A. Spaldin, *Nat. Mater.* **6**, 21 (2007).
- [694] C.-W. Nan, G. Liu, Y. Lin, and H. Chen, *Phys. Rev. Lett.* **94**, 197203 (2005).
- [695] C. Deng, Y. Zhang, J. Ma, Y. Lin, and C.-W. Nan, *J. Appl. Phys.* **102**, 074114 (2007).
- [696] P. Murugavel, P. Padhan, and W. Prellier, *Appl. Phys. Lett.* **85**, 4992 (2004).
- [697] M. P. Singh, W. Prellier, L. Mechin, C. Simon, and B. Raveau, *J. Appl. Phys.* **99**, 024105 (2006).
- [698] S. Ryu, J. H. Park, and H. M. Jang, *Appl. Phys. Lett.* **91**, 142910 (2007).
- [699] Y. G. Ma, W. N. Cheng, M. Ning, and C. K. Ong, *Appl. Phys. Lett.* **90**, 152911 (2007).
- [700] Y. Zhang, C. Deng, J. Ma, Y. Lin, and C.-W. Nan, *Appl. Phys. Lett.* **92**, 062911 (2008).
- [701] S.-T. Zhang, Y. Zhang, Z.-L. Luo, M.-H. Lu, Z.-B. Gu, and Y.-F. Chen, *Appl. Surf. Sci.* **255**, 5092 (2009).
- [702] Z. Li, Y. Wang, Y. Lin, and C. Nan, *Phys. Rev. B* **79**, 180406 (2009).
- [703] J. George A. Rossetti, L. E. Cross, and K. Kushida, *Appl. Phys. Lett.* **59**, 2524 (1991).

- [704] M. Dawber, P. Chandra, P. B. Littlewood, and J. F. Scott, *J. Phys.: Condens. Matter* **15**, L393 (2003).
- [705] J. Paul, T. Nishimatsu, Y. Kawazoe, and U. V. Waghmare, *Phys. Rev. Lett.* **99**, 077601 (2007).
- [706] P. Ghosez and J. Junquera, *cond-mat/0605299* (2006).
- [707] O. Diéguez, S. Tinte, A. Antons, C. Bungaro, J. B. Neaton, K. M. Rabe, and D. Vanderbilt, *Phys. Rev. B* **69**, 212101 (2004).
- [708] C. Bungaro and K. M. Rabe, *Phys. Rev. B* **69**, 184101 (2004).
- [709] M. G. Norton, K. P. B. Cracknell, and C. B. Carter, *J. Am. Ceram. Soc.* **75**, 1999 (1992).
- [710] R. A. McKee, F. J. Walker, J. R. Conner, E. D. Specht, and D. E. Zelmon, *Appl. Phys. Lett.* **59**, 782 (1991).
- [711] B. S. Kwak, K. Zhang, E. P. Boyd, A. Erbil, and B. J. Wilkens, *J. Appl. Phys.* **69**, 767 (1991).
- [712] T. Schneller and R. Waser, *Ferroelectrics* **267**, 293 (2002).
- [713] K. Fujimoto, Y. Kobayashi, and K. Kubota, *Thin Solid Films* **169**, 249 (1989).
- [714] N. Yanase, K. Abe, N. Fukushima, and T. Kawakubo, *Jpn. J. Appl. Phys.* **38**, 5305 (1999).
- [715] M. C. Gust, N. D. Evans, L. A. Momoda, and M. L. Mecartney, *J. Am. Ceram. Soc.* **80**, 2828 (1997).
- [716] G. H. Haertling, *J. Am. Ceram. Soc.* **82**, 797 (1999).
- [717] J. Hiltunen, D. Seneviratne, H. Tuller, J. Lappalainen, and V. Lantto, *J. Electroceram.* **22**, 395 (2009), 10.1007/s10832-008-9443-0.
- [718] T. Zhao, F. Chen, H. Lu, G. Yang, and Z. Chen, *J. Appl. Phys.* **87**, 7442 (2000).
- [719] A. Petraru, N. A. Pertsev, H. Kohlstedt, U. Poppe, R. Waser, A. Solbach, and U. Klemradt, *J. Appl. Phys.* **101**, 114106 (2007).
- [720] M. E. Marssi, F. L. Marrec, I. A. Lukyanchuk, and M. G. Karkut, *J. Appl. Phys.* **94**, 3307 (2003).
- [721] K. Lee and S. Baik, *Ann. Rev. Mater. Res.* **36**, 81 (2006).
- [722] C. L. Li, Z. H. Chen, Y. L. Zhou, and D. F. Cui, *J. Phys.: Condens. Matter* **13**, 5261 (2001).

- [723] R. Dittmann, R. Plonka, E. Vasco, N. A. Pertsev, J. Q. He, C. L. Jia, S. Hoffmann-Eifert, and R. Waser, *Appl. Phys. Lett.* **83**, 5011 (2003).
- [724] S. K. Streiffer, J. A. Eastman, D. D. Fong, C. Thompson, A. Munkholm, M. V. Ramana Murty, O. Auciello, G. R. Bai, and G. B. Stephenson, *Phys. Rev. Lett.* **89**, 067601 (2002).
- [725] F. He and B. O. Wells, *Appl. Phys. Lett.* **88**, 152908 (2006).
- [726] B. Dkhil, E. Defayé, and J. Guillian, *Appl. Phys. Lett.* **90**, 022908 (2007).
- [727] S. Lee, Z.-K. Liu, M.-H. Kim, and C. A. Randall, *J. Appl. Phys.* **101**, 054119 (2007).
- [728] G. Y. Yang, E. C. Dickey, C. A. Randall, D. E. Barber, P. Pinceloup, M. A. Henderson, R. A. Hill, J. J. Beeson, and D. J. Skamser, *J. Appl. Phys.* **96**, 7492 (2004).
- [729] G. Y. Yang, G. D. Lian, E. C. Dickey, C. A. Randall, D. E. Barber, P. Pinceloup, M. A. Henderson, R. A. Hill, J. J. Beeson, and D. J. Skamser, *J. Appl. Phys.* **96**, 7500 (2004).
- [730] T. Zhao, Z.-H. Chen, F. Chen, H.-B. Lu, G.-Z. Yang, and H.-S. Cheng, *Appl. Phys. Lett.* **77**, 4338 (2000).
- [731] B. Nagaraj, S. Aggarwal, T. K. Song, T. Sawhney, and R. Ramesh, *Phys. Rev. B* **59**, 16022 (1999).
- [732] K. W. Blazey, *Phys. Rev. Lett.* **27**, 146 (1971).
- [733] H.-M. Christen, J. Mannhart, E. J. Williams, and C. Gerber, *Phys. Rev. B* **49**, 12095 (1994).
- [734] I. Burn and S. Neirman, *J. Mater. Sci.* **17**, 3510 (1982), 10.1007/BF00752196.
- [735] D. J. Kim, J. Y. Jo, Y. S. Kim, Y. J. Chang, J. S. Lee, J.-G. Yoon, T. K. Song, and T. W. Noh, *Phys. Rev. Lett.* **95**, 237602 (2005).
- [736] N. A. Pertsev, J. R. Contreras, V. G. Kukhar, B. Hermanns, H. Kohlstedt, and R. Waser, *Appl. Phys. Lett.* **83**, 3356 (2003).
- [737] P. K. Larsen, G. J. M. Dormans, D. J. Taylor, and P. J. van Veldhoven, *J. Appl. Phys.* **76**, 2405 (1994).
- [738] J. Y. Jo, Y. S. Kim, T. W. Noh, J.-G. Yoon, and T. K. Song, *Appl. Phys. Lett.* **89**, 232909 (2006).
- [739] Y. L. Li, S. Y. Hu, S. Choudhury, M. I. Baskes, A. Saxena, T. Lookman, Q. X. Jia, D. G. Schlom, and L. Q. Chen, *J. Appl. Phys.* **104**, 104110 (2008).
- [740] I. P. Batra, P. Wurfel, and B. D. Silverman, *Phys. Rev. B* **8**, 3257 (1973).

- [741] X. Du and I.-W. Chen, *J. Appl. Phys.* **83**, 7789 (1998).
- [742] P. Paruch, T. Giamarchi, T. Tybell, and J.-M. Triscone, *J. Appl. Phys.* **100**, 051608 (2006).
- [743] D. J. Kim, J. Y. Jo, Y. S. Kim, and T. K. Song, *J. Phys. D: Appl. Phys.* **43**, 395403 (2010).
- [744] F. M. Pontes, E. R. Leite, E. Longo, J. A. Varela, E. B. Araujo, and J. A. Eiras, *Appl. Phys. Lett.* **76**, 2433 (2000).
- [745] L. M. B. Alldredge, J. C. Woicik, W. Chang, S. W. Kirchoefer, and J. M. Pond, *Appl. Phys. Lett.* **91**, 052909 (2007).
- [746] K. Lefki and G. J. M. Dormans, *J. Appl. Phys.* **76**, 1764 (1994).
- [747] H. P. Sun, W. Tian, X. Q. Pan, J. H. Haeni, and D. G. Schlom, *Appl. Phys. Lett.* **84**, 3298 (2004).
- [748] K. W. Schwarz, *J. Appl. Phys.* **85**, 108 (1999).
- [749] S. H. Xie, X. Y. Liu, Y. C. Zhou, and J. Y. Li, *J. Appl. Phys.* **109**, 063911 (2011).
- [750] C. W. Heaps, *Phys. Rev.* **42**, 108 (1932).
- [751] A. S. Borovik-Romanov, *Ferroelectrics* **162**, 153 (1994).
- [752] T. Brintlinger, S.-H. Lim, K. H. Baloch, P. Alexander, Y. Qi, J. Barry, J. Melngailis, L. Salamanca-Riba, I. Takeuchi, and J. Cumings, *Nano Lett.* **10**, 1219 (2010), PMID: 20199031.
- [753] T.-K. Chung, G. P. Carman, and K. P. Mohanchandra, *Appl. Phys. Lett.* **92**, 112509 (2008).
- [754] T.-K. Chung, S. Keller, and G. P. Carman, *Appl. Phys. Lett.* **94**, 132501 (2009).
- [755] A. Hubert and R. Schäfer, *Magnetic Domains* (Springer Berlin Heidelberg, Berlin, Heidelberg, 1998).
- [756] G. Srinivasan, E. T. Rasmussen, and R. Hayes, *Phys. Rev. B* **67**, 014418 (2003).
- [757] P. Lukashev, R. F. Sabirianov, and K. Belashchenko, *Phys. Rev. B* **78**, 184414 (2008).
- [758] D. Li and D. A. Bonnell, *Ann. Rev. Mater. Res.* **38**, 351 (2008).
- [759] J.-M. Hu, Z. Li, J. Wang, J. Ma, Y. H. Lin, and C. W. Nan, *J. Appl. Phys.* **108**, 043909 (2010).

- [760] W. Pan, Q. Zhang, A. S. Bhalla, and L. E. Cross, *J. Am. Ceram. Soc.* **71**, C (1988).
- [761] C. Israel, N. D. Mathur, and J. F. Scott, *Nat. Mater.* **7**, 93 (2008).
- [762] S. Dong, J. Zhai, J. F. Li, D. Viehland, and S. Priya, *Appl. Phys. Lett.* **93**, 103511 (2008).
- [763] X. Dai, Y. Wen, P. Li, J. Yang, and G. Zhang, *Sensors and Actuators A* **156**, 350 (2009).
- [764] Q. Zhao, J. Zhou, F. Zhang, and D. Lippens, *Mater. Today* **12**, 60 (2009).
- [765] H. Zhao, L. Kang, J. Zhou, Q. Zhao, L. Li, L. Peng, and Y. Bai, *Appl. Phys. Lett.* **93**, 201106 (2008).
- [766] M. I. Bichurin, V. M. Petrov, O. V. Ryabkov, S. V. Averkin, and G. Srinivasan, *Phys. Rev. B* **72**, 060408 (2005).
- [767] A. S. Tatarenko, V. Gheevarghese, and G. Srinivasan, *Electron. Lett.* **42**, 540 (2006).
- [768] Y. K. Fetisov and G. Srinivasan, *Appl. Phys. Lett.* **88**, 143503 (2006).
- [769] S. Davis, A. Baruth, and S. Adenwalla, *Appl. Phys. Lett.* **97**, 232507 (2010).
- [770] M. Weiler, L. Dreher, C. Heeg, H. Huebl, R. Gross, M. S. Brandt, and S. T. B. Goennenwein, *Phys. Rev. Lett.* **106**, 117601 (2011).
- [771] T.-K. Chung, K. Wong, S. Keller, K. L. Wang, and G. P. Carman, *J. Appl. Phys.* **106**, 103914 (2009).
- [772] V. Anbusathaiah, D. Kan, F. C. Kartawidjaja, R. Mahjoub, M. A. Arredondo, S. Wicks, I. Takeuchi, J. Wang, and V. Nagarajan, *Adv. Mater.* **21**, 3497 (2009).
- [773] V. Nagarajan, A. Roytburd, A. Stanishevsky, S. Prasertchoung, T. Zhao, L. Chen, J. Melngailis, O. Auciello, and R. Ramesh, *Nat. Mater.* **2**, 43 (2003).
- [774] N. A. Pertsev, *Phys. Rev. B* **78**, 212102 (2008).
- [775] J.-M. Hu and C. W. Nan, *Phys. Rev. B* **80**, 224416 (2009).
- [776] K. Ueda, H. Tabata, and T. Kawai, *Science* **280**, 1064 (1998).
- [777] F. Liorzou, B. Phelps, and D. Atherton, *IEEE Trans. Magn.* **36**, 418 (2000).
- [778] D. C. Jiles, X. Fang, and W. Zhang, in *Handbook of Advanced Magnetic Materials*, edited by Y. Liu, D. J. Sellmyer, and D. Shindo (Springer US, 2006) pp. 745–779.

-
- [779] E. Stoner and E. Wohlfarth, *IEEE Trans. Magn.* **27**, 3475 (1991).
- [780] X. Liu, W. L. Lim, L. V. Titova, M. Dobrowolska, J. K. Furdyna, M. Kutrowski, and T. Wojtowicz, *J. Appl. Phys.* **98**, 063904 (2005).
- [781] D. Snowden, *Magnetoresistance of Thermally Deposited Nickel Films*, Ph.D. thesis, Harvey Mudd College (2004).
- [782] D. Jiles and D. Atherton, *J. Magn. Magn. Mater.* **61**, 48 (1986).
- [783] D. C. Jiles and D. L. Atherton, *J. Appl. Phys.* **55**, 2115 (1984).